DESY 01-123F vol. 4
DESY-LC-REV-2001-062
December 2001

Physics and Experimentation at a Linear Electron–Positron Collider

Volume 4: The THERA Book. Electron–Proton Scattering at $\sqrt{s} \sim 1$ TeV

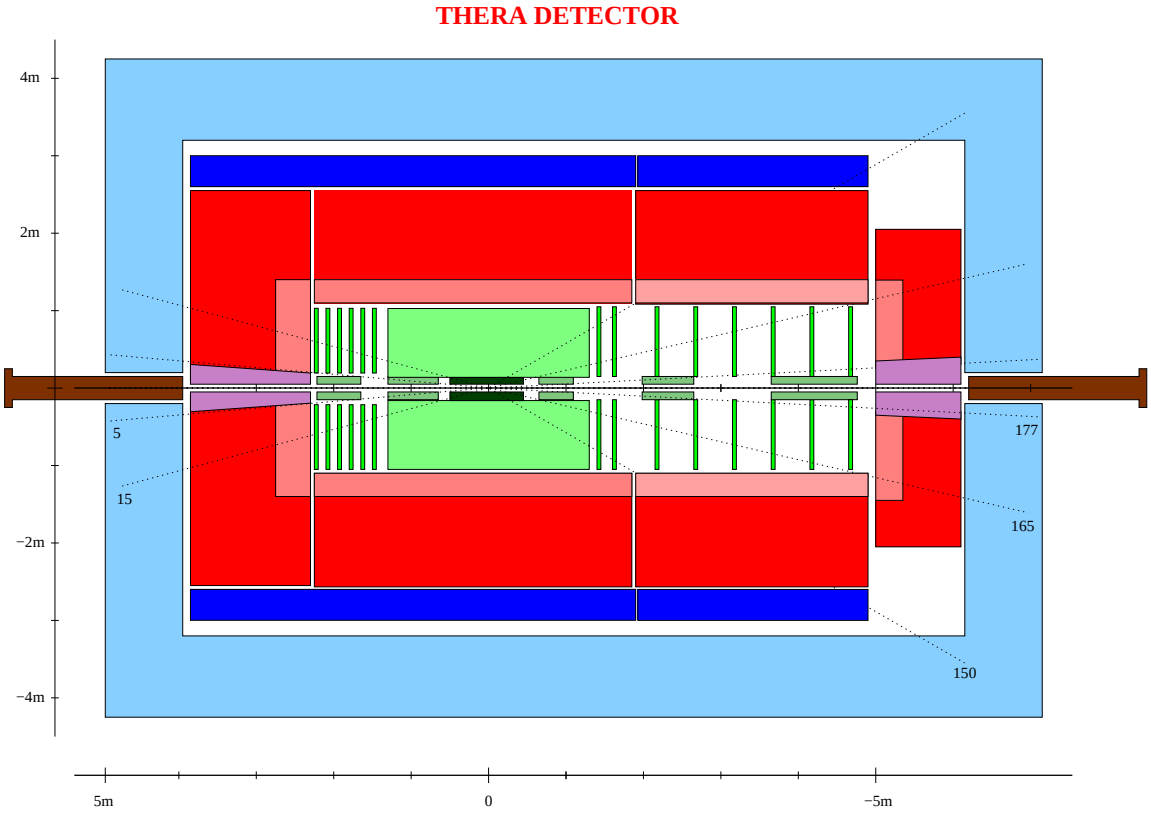

Editors: U. Katz, M. Klein, A. Levy and S. Schlenstedt

ISSN 0418-9833

DESY 01-123F vol. 4
DESY-LC-REV-2001-062
December 2001

Physics and Experimentation at a Linear Electron–Positron Collider

Volume 4: The THERA Book. Electron–Proton Scattering at $\sqrt{s} \sim 1$ TeV

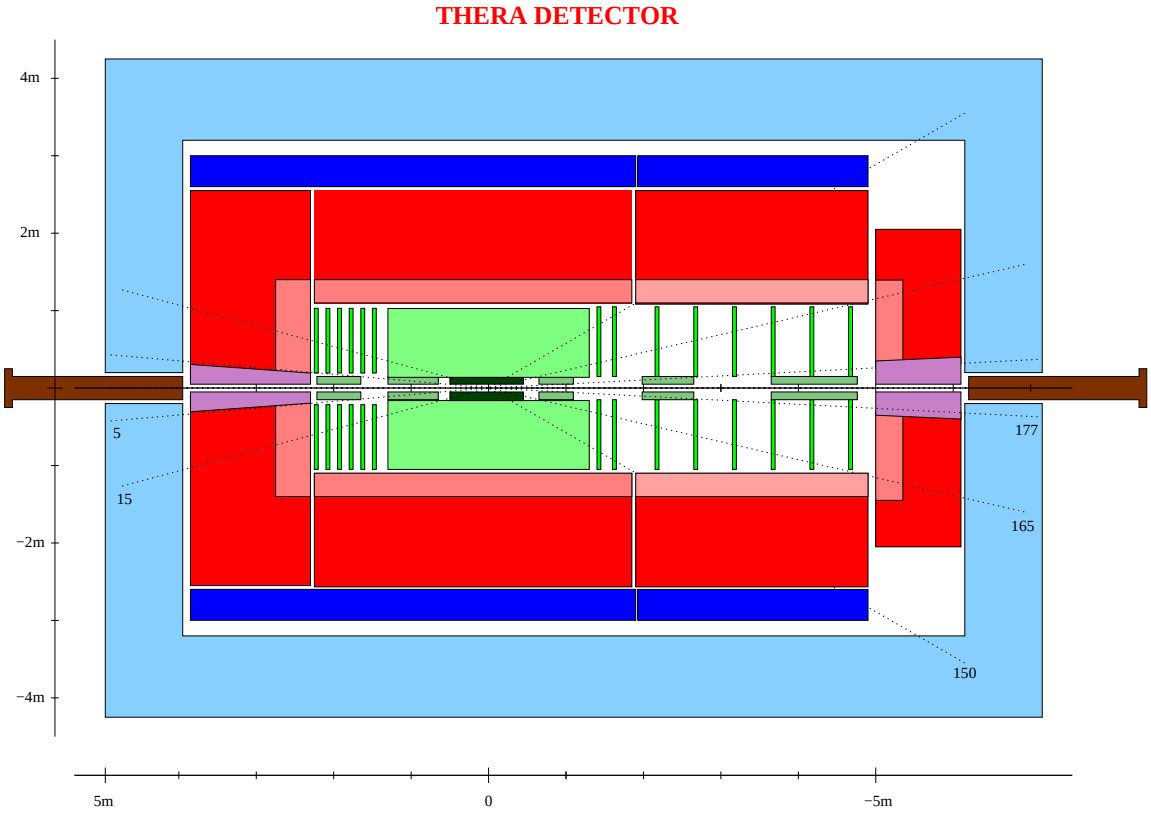

Editors: U. Katz, M. Klein, A. Levy and S. Schlenstedt

ISSN 0418-9833

Publisher:
DESY
Deutsches Elektronen-Synchroton
Notkestraße 85, D-22607 Hamburg
Germany
`http://www.desy.de`
E-mail: desyinfo@desy.de

Member of the Hermann von Helmholtz Association
of National Research Centers (HGF)

Reproduction including extracts is permitted
subject to crediting the source.

The picture on the front page shows a version of
the low-x THERA detector with an extended coil.

This volume collects original contributions for THERA, a future electron-nucleon collider operating in the TeV energy range, which can be realised combining the $e^{\pm}$ linear accelerator TESLA with the proton ring accelerator HERA at DESY. The material presented here has been worked out during the preparation of the TESLA Technical Design Report in the years 2000 and 2001. The THERA option was discussed in a series of meetings involving about 100 physicists. These meetings are documented on `http:/www-zeuthen.desy.de/thera`.

Working Groups and Convenors:

Low x and Diffraction	E Levin (U Tel Aviv) A Levy (U Tel Aviv) P Newman (U Birmingham)
Tests of QCD and MC Simulation	H Jung (U Lund) L Lönnblad (U Lund) H Spiesberger (U Mainz)
Heavy Flavours	K Daum (U Wuppertal) L Gladilin (U Hamburg, Moscow)
Photon Structure	J Butterworth (UC London) M Krawczyk (U Warsawa) S Söldner-Rembold (CERN/U Freiburg)
High Q^2 and BSM	M Kuze (KEK) K Long (IC London) E Perez (Saclay)
Detector and Machine	J Crittenden (U Bonn) U Katz (U Bonn/ U Erlangen) M Klein (DESY Zeuthen) D Pitzl (DESY Hamburg) S Schlenstedt (DESY Zeuthen) U Schneekloth (DESY Hamburg) F Willeke (DESY Hamburg)
eA Scattering	M Strikman (Penn State)
Real Photon-Proton Interactions	S Sultansoy (Ankara)
Polarisation	A Deshpande (Yale U) E Rondio (U Warsawa)

Contents

1 Introduction to the THERA Book **1**

2 THERA: Electron–Proton Scattering at $\sqrt{s} \sim 1$ TeV **3**
2.1 Introduction 5
2.2 Physics with THERA 7
2.2.1 Low-x physics 7
2.2.2 Proton structure and quantum chromodynamics 15
2.2.3 Searches for new particles or phenomena 25
2.2.4 Resolving the partonic structure of the photon 28
2.3 Experimentation at THERA 32
2.3.1 Collision of TESLA electrons with HERA protons 32
2.3.2 A detector for THERA 38
2.4 Further Options 42
2.4.1 Electron–nucleus scattering 42
2.4.2 Real photon–proton scattering 46
2.4.3 Polarised protons 48
2.5 Summary 51

3 Low-x Physics **63**
3.1 Small-x Evolution of Wilson Lines 63
I. Balitsky
3.1.1 Small-x *vs* Q^2 evolution. 63
3.1.2 High-energy asymptotics as a scattering from the shock-wave field 65
3.1.3 Regularized Wilson-line operators 71
3.1.4 One-loop evolution of Wilson-line operators 74
3.1.5 BFKL pomeron from the evolution of Wilson-line operators . . 78
3.1.6 Non-linear evolution of Wilson lines as functional integral 81
3.1.7 Nuclear structure functions 86
3.1.8 Conclusion 89
3.2 Perturbative Evolution at Small x 93
G. Altarelli, R.D. Ball and S. Forte
3.2.1 Introduction 93
3.2.2 Duality of small x evolution 94
3.2.3 The Double–Leading expansion 96
3.2.4 Resummation 99

3.2.5 Predictions for THERA 101
3.3 High Density QCD at THERA 107
E. Gotsman, E. Levin, M. Lublinsky, U. Maor,
E. Naftali and K. Tuchin
3.3.1 Introduction: Our hopes and main goals at THERA 107
3.3.2 Our model 112
3.3.3 Predictions for THERA 115
3.3.4 Resume 123
3.4 Small x Physics and Forward Jet Production at THERA 129
H. Jung and L. Lönnblad
3.4.1 Introduction 129
3.4.2 Initial State QCD Cascade 131
3.4.3 Conclusion 133
3.5 Gluon Saturation and the Color Glass Condensate 136
E. Iancu and L. McLerran
3.5.1 Introduction 136
3.5.2 The Color Glass Condensate 137
3.5.3 Quantum evolution and BFKL 140
3.5.4 The quantum evolution of the CGC 142
3.5.5 Recovering some known results 146
3.5.6 Solving the RGE: Saturation and Universality 147
3.6 Saturation at low $\mathbf{x}$ 160
E. Levin
3.6.1 Introduction 160
3.6.2 Qualitative Picture of Interaction in DIS at low $\mathbf{x}$ 161
3.6.3 Non-linear Evolution 168
3.6.4 Initial conditions: 172
3.6.5 Saturation scale $\mathbf{Q_s}(\mathbf{x})$ 173
3.6.6 A new scaling in the saturation region. 175
3.6.7 Parton densities at THERA and LHC energies 178
3.6.8 Summary 180
3.7 Saturation and Unitarity of Hadronic Structure Functions 186
Yu.V. Kovchegov
3.7.1 "Phase Diagram" of High Energy QCD 186
3.7.2 Qualitative Picture of Saturation 187
3.7.3 Evolution equation from the dipole model 190
3.7.4 Double Logarithmic Limit 196
3.7.5 Approximate Solution of the Nonlinear Evolution Equation . . . 198
3.7.6 Asymptotic Behavior of the F_2 Structure Function 203
3.7.7 Diffractive Dissociation Including Multiple Pomeron Exchanges 205
3.8 Diffractive Production of Neutral Vector Mesons 212
J.A. Crittenden
3.8.1 Introduction 212
3.8.2 Lessons from HERA 215

3.8.3 Requirements on the performance of machine and detector . . . 218
3.8.4 Conclusions 220

4 Proton Structure and Quantum Chromodynamics 224
4.1 Heavy Quark Production Measurements at THERA 224
L. Gladilin and I. Redondo
4.1.1 Introduction 225
4.1.2 Heavy quark photoproduction and proton gluon structure 226
4.1.3 Heavy quark production in neutral current DIS 229
4.1.4 Charm production in charged current DIS 235
4.1.5 Summary 237
4.2 High-p_T Jet Production 240
B. Pötter
4.2.1 Introduction 240
4.2.2 Next-to-leading order calculations 240
4.2.3 Jet Production at THERA 241
4.2.4 Summary 244
4.3 Jet Photoproduction at THERA 247
M. Klasen
4.3.1 Motivation 247
4.3.2 Dijet Cross Section 248
4.3.3 Results 249
4.3.4 Conclusion 253
4.4 Precision Tests of Perturbative QCD at THERA 256
W.L. van Neerven
4.4.1 Introduction. 256
4.4.2 Light cone dominance and sum rules. 257
4.4.3 Heavy flavour production. 262
4.4.4 Comparison between electro-production and photo- and hadro-production. 267
4.5 Heavy Quark Production in the Semihard QCD Approach at THERA . 272
S.P. Baranov and N.P. Zotov
4.5.1 Introduction 272
4.5.2 The semihard QCD approach 273
4.5.3 Numerical results 276
4.6 Charged-current Deep Inelastic Scattering at THERA 283
K. Nagano
4.6.1 Introduction 283
4.6.2 Double differential cross-section measurement 284
4.6.3 The d-quark density at high-x 285
4.6.4 Determination of the propagator mass 286
4.6.5 Summary 287

5 Searches for New Particles or Phenomena 288
5.1 Contact Interactions, Large Extra Dimensions and Leptoquarks 288
A.F. Żarnecki
5.1.1 Contact Interactions 288
5.1.2 Large Extra Dimensions 289
5.1.3 Leptoquarks 290
5.1.4 Analysis method 294
5.1.5 THERA running 296
5.1.6 Results 296
5.1.7 Summary 301
5.2 Pair Production of Supersymmetric Particles 311
M. Corradi
5.2.1 Introduction 311
5.2.2 Selectron and Squark Production 312
5.2.3 Selectron and Neutralino Production 314
5.2.4 Conclusions 314
5.3 Search for Excited Fermions at THERA 316
M. Kuze
5.3.1 Introduction 316
5.3.2 Results 316
5.3.3 Conclusions 317

6 Resolving the Partonic Structure of the Photon 319
6.1 Reach of Future Colliders in Probing the Structure of the Photon . . . 319
M. Krawczyk, S. Söldner-Rembold and M. Wing
6.1.1 Introduction 319
6.1.2 The THERA kinematic region in comparison with other colliders 321
6.1.3 Summary 322
6.2 Inclusive Dijet Photoproduction and the Resolved Photon at THERA . 324
M. Wing
6.2.1 Introduction 324
6.2.2 Photoproduction from HERA to THERA 326
6.2.3 Cross section definition 327
6.2.4 Results 328
6.2.5 Discussion 330
6.2.6 Summary 333
6.3 Heavy Quark Photoproduction at THERA 336
P. Jankowski, M. Krawczyk and M. Wing
6.3.1 Introduction 336
6.3.2 Leading order QCD predictions of charm quark production . . . 337
6.3.3 MC predictions of dijet production with charm and beauty quarks 340
6.3.4 Summary 343
6.4 The Prompt Photon Photoproduction at THERA 347
M. Krawczyk and A. Zembrzuski

6.4.1 Introduction 347
6.4.2 The NLO cross section 347
6.4.3 The results 350
6.4.4 Summary 351
6.5 On the Importance of the Contribution of the Longitudinal Virtual Photon... 353
U. Jezuita-Dąbrowska and M. Krawczyk
6.5.1 Introduction 353
6.5.2 Factorisation of the one-photon exchange cross sections for the inclusive and semi-inclusive unpolarised lepton-nucleon scattering 355
6.5.3 Azimuthal angle distribution for the semi-inclusive process . . . 358
6.5.4 Numerical results 359
6.5.5 Conclusions 363

7 Electron-Nucleus Scattering 369
7.1 Electron-Nucleus Collisions at THERA 369
L. Frankfurt, V. Guzey, M. McDermott and M. Strikman
7.1.1 Executive Summary 369
7.1.2 Introduction 370
7.1.3 The black body limit and its signals in DIS final states 375
7.1.4 Unitarity constraints for electron-nucleus DIS 384
7.1.5 Nuclear shadowing and diffraction 387
7.1.6 Experimental considerations 398
7.1.7 Conclusions 399

8 Real Photon-Proton Scattering 403
8.1 Gamma Options of the THERA Collider 403
O. Çakir, A. K. Çiftçi, S. Sultansoy, Ö. Yavaş and M. Yilmaz
8.1.1 Introduction 403
8.1.2 Luminosity considerations 403
8.1.3 Physics goals 405

1 Introduction to the THERA Book

This document is a result of a study within the TESLA Technical Design Report at DESY, Hamburg. It was carried out during the years 2000/01 with the aim of investigating the feasibility and the physics interest of an *ep* collider, THERA, which scatters polarized leptons ($e^{\pm}$) from TESLA off protons, or nuclei, accelerated in the HERA proton ring. With lepton energies of $E_e = 250-800\,\mathrm{GeV}$ and proton energies of $E_p = 300-1000\,\mathrm{GeV}$, THERA can reach center-of-mass energies of 1 TeV and beyond. Estimated annual luminosities between 40 and $250\,\mathrm{pb}^{-1}$, for energy ratios E_e/E_p between 1/4 and 1, respectively, would allow THERA to complement the TeV-scale exploration with the next generation of $\mathrm{e}^+\mathrm{e}^-$ and *pp* colliders. THERA is a natural successor of the HERA collider, extending the kinematic limits of the photon virtuality, Q^2, up to more than $10^6\,\mathrm{GeV}^2$, and that of the Bjorken x variable down to 10^{-7}.

Lepton probes represent the cleanest way to explore the structure of matter. THERA will allow to access dimensions as small as 10^{-19} m, a factor of thousand below the scale where partons were first observed in deep inelastic scattering and five times smaller than resolved at HERA.

In the past, lepton–nucleon scattering has been an excellent ground for investigating strong-interaction physics and for developing Quantum Chromodynamics (QCD). The HERA collider greatly improved our understanding of QCD, especially in the low-x region. However, the current experimental and theoretical assessment of QCD is far from complete. QCD predicts the existence of a variety of as yet unknown new forms of hadron matter, such as quark-gluon plasma, or color superconductivity, which are all related to large-distance QCD interactions. In order to fully establish QCD as one of the cornerstones in our picture of fundamental interactions, further research is necessary which should help to elucidate intricate features of QCD and also to find qualitatively new QCD phenomena. Investigating small-x *ep* reactions at THERA, where the coherence length is about 10^4 fm and the parton densities are high will be a major step in this direction.

Physics at THERA leads far beyond the low-x domain. In this book, many aspects of the exciting physics at THERA are described. These include the role of heavy flavors in strong interactions and the very high Q^2 region and searches for physics beyond the Standard Model, such as quark compositeness and leptoquarks. Extremely important options are high energy physics with real photons, deep inelastic lepton scattering on nuclei, and *ep* collisions with polarized beams.

While one can try to extrapolate the current wisdom to the THERA range, only experimental data in this new kinematic domain will substantiate the view on this physics and will undoubtedly lead to new insights. This book presents the foundations of a new *ep* machine in the TeV range.

We gratefully acknowledge the enthusiastic, ingenious work and contributions of many theorists and experimentalists to this THERA book, and we thank the DESY directorate for encouragement and support.

U. Katz, M. Klein, A. Levy and S. Schlenstedt, editors

2 THERA: Electron–Proton Scattering at $\sqrt{s} \sim 1$ TeV

A Contribution to the TESLA Technical Design Report
13. Feb. 2001

H. Abramowicz[41], S.P. Baranov[21], J. Bartels[17], W. Bialowons[13], R. Brinkmann[13], O. Çakır[4], A. Caldwell[12], V. Chekelian[32,31], A.K. Çiftçi[4], J.G. Conteras[14], M. Corradi[7], J.A. Crittenden[8], J. Dainton[23], K. Daum[45], A. Deshpande[46,39], D. Eckstein[13], E. Elsen[13], B. Foster[9], L. Frankfurt[41], E. Gabathuler[23], J. Gassner[38], U. Gensch[13], I. Ginzburg[33], L. Gladilin[44], M. Glück[14], N. Gogitidze[21], K. Golec-Biernat[17], E. Gotsman[41], T. Greenshaw[23], V. Guzey[2], P. Jankowski, U. Jezuita-Dabrowska[42], H. Jung[13], U.F. Katz[8], R. Klanner[13,17], M. Klasen[17], M. Klein[13], B. Kniehl[17], H. Koru[5], P. Kostka[13], H. Kowalski[13], M. Krawczyk[42], T. Kurča[20], M. Kuze[19], P. Landshoff[10], T. Laštovička[37], B. Levchenko[30], E. Levin[41], A. Levy[41], K. Long[24], L. Lönnblad[25], U. Maor[41], M. McDermott[23], K. Nagano[19], T. Naumann[13], W. van Neerven[22], P. Newman[6], N. Nikolaev[18], C. Pascaud[34], E. Perez[40], D. Pitzl[13], B. Pötter[32], G. Rädel[1], V. Ravindran[3], I. Redondo[26], E. Reya[14], A. De Roeck[11], E. Rondio[43], J. Ruan[15], W. Schäfer[18], S. Schlenstedt[13], P. Schleper[13], U. Schneekloth[13], S. Söldner-Rembold[16,11], H. Spiesberger[27], U. Stösslein[13], M. Strikman[36], S. Sultansoy[5], K. Tuchin[41], W.K. Tung[29], R. Wallny[47], D. Waters[35], P. Wesolowski[13], F. Willeke[13], M. Wing[28], Ö. Yavaş[4], M. Yılmaz[5], A.F. Żarnecki[42], A. Zembrzuski[42], A. Zhokin[31], V. Zoller[31], N.P. Zotov[30]

[1] RWTH Aachen, Germany
[2] University of Adelaide, Australia
[3] Mehta Research Institute of Mathematics and Mathematical Physics, Allahabad, India
[4] Ankara University, Turkey
[5] Gazi University, Ankara, Turkey
[6] University of Birmingham, UK
[7] INFN Bologna, Italy
[8] Universität Bonn, Germany
[9] University of Bristol
[10] Cambridge University, UK
[11] CERN, Geneva, Switzerland
[12] Columbia University, Nevis Labs, Irvington, USA
[13] DESY, Hamburg and Zeuthen, Germany
[14] Universität Dortmund, Germany
[15] East China Normal University, Shanghai, P.R. China
[16] Universität Freiburg, Germany
[17] Universität Hamburg, Germany
[18] Forschungszentrum Jülich, Germany
[19] KEK, Tsukuba, Japan
[20] Institute of Experimental Physics, Košice, Slovak Republic
[21] Lebedev Physical Institute, Moscow, Russia
[22] University of Leiden, The Netherlands
[23] University of Liverpool, UK
[24] Imperial College London, UK
[25] Lund University, Sweden
[26] Universidad Autónoma de Madrid, Spain
[27] Universität Mainz, Germany
[28] McGill University, Montreal, Canada
[29] Michigan State University, East Lansing, USA
[30] Moscow State University, Russia
[31] ITEP, Moscow, Russia
[32] MPI für Physik, München, Germany
[33] Institute of Mathematics, Novosibirsk, Russia
[34] LAL, Orsay, France
[35] University of Oxford, UK
[36] Pennsylvania State University, New Kensington, USA
[37] Charles University, Prague, Czech Republic
[38] PSI, Villingen, Switzerland
[39] RIKEN-BNL Research Center, Upton, USA
[40] DAPNIA-CEA/Saclay, Gif sur Yvette, France
[41] Tel Aviv University, Israel
[42] Warsaw University, Poland
[43] Institute for Nuclear Studies, Warsaw, Poland
[44] Weizmann Institute, Rehovot, Israel
[45] Universität Wuppertal, Germany
[46] Yale University, New Haven, USA
[47] Universität Zürich, Switzerland

2.1 Introduction

The elementary nature of the electron makes it a good probe to study the structure of the proton in deep inelastic *ep* interactions [1]. Previous fixed-target deep inelastic scattering (DIS) experiments have discovered the partonic structure of the nucleon and established Quantum Chromodynamics (QCD) as the correct field theory of quark–gluon interactions at small distances.

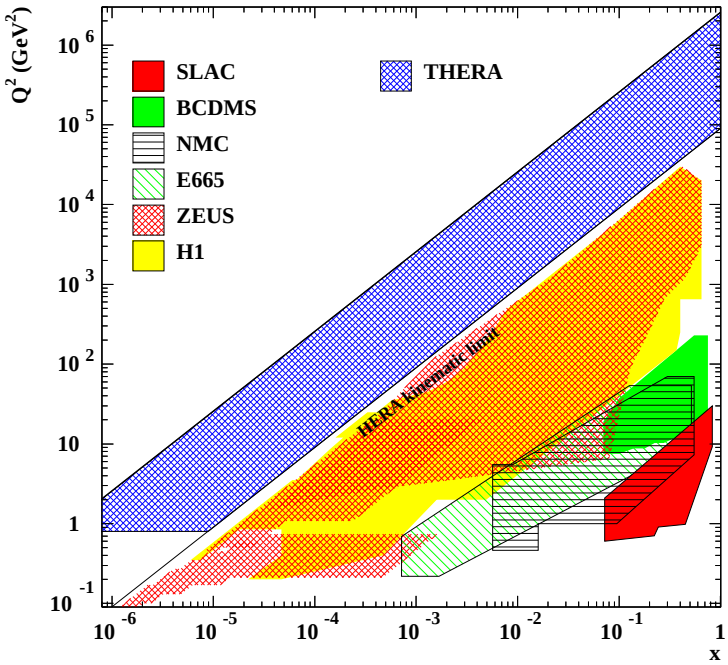

Figure 1: *The kinematic plane in deep inelastic lepton–proton scattering, showing the regions covered by fixed-target scattering experiments and by the HERA experiments, and the extension of the kinematic range by the THERA collider with an ep centre-of-mass energy squared of* $s = 2.56 \times 10^6\, GeV^2$. *The variables* x *and* Q^2 *denote the Bjorken scaling variable and the negative square of the four-momentum transfer between lepton and proton, respectively.*

HERA [2], the first electron–proton collider, has been a major step forward in accelerator technology and has resulted in a number of fundamental physics observations: the discovery of the rise of the proton structure function $F_2(x, Q^2)$ towards low Bjorken x, which is related to a large gluon density in the proton; the discovery of hard diffractive scattering in DIS and the confirmation of the pointlike nature of the partons down to distances of about 10^{-18} m. The HERA measurements at low Q^2 have initiated intense studies of the transition between QCD radiation at small distances and non-perturbative parton dynamics at large transverse distances, which has become a central issue in modern strong interaction theory.

THERA[1] uses polarised electrons or positrons from the linear accelerator TESLA at energies of 250–800 GeV and brings them into collision with high-energy protons (500 GeV to 1 TeV) from HERA in the West Hall on the DESY site. THERA will thus extend the investigation of deep inelastic scattering into an as yet unexplored kinematic region (Fig. 1), yielding complementary information to hadron–hadron and e^+e^- colliders in the TeV energy range.

At low x, THERA offers the possibility of uncovering a new strong-interaction do-

[1]The acronym THERA symbolises a combination of TESLA and HERA. It also is the name of a Greek island, which in the Doric period was called Kalliste, most beautiful.

main of parton saturation, which would be a substantial step towards an understanding of confinement. Processes such as jet production in the proton beam direction or heavy flavour production at low x, studies of the partonic structure of the photon and a precision measurement of the strong interaction coupling constant α_s make THERA an excellent facility for investigating strong and electroweak interaction dynamics. Finally, the high centre-of-mass energy will open a new window for the observation of new particles or interactions, such as leptoquarks, supersymmetric particles or contact interactions, the helicity structure of which could be particularly well investigated at THERA.

With centre-of-mass energies beyond 1 TeV, structures in the proton with sizes down to 10^{-19} m will be resolved. In the history of the exploration of the basic structure of matter, illustrated in Fig. 2, THERA thus represents a new major step.

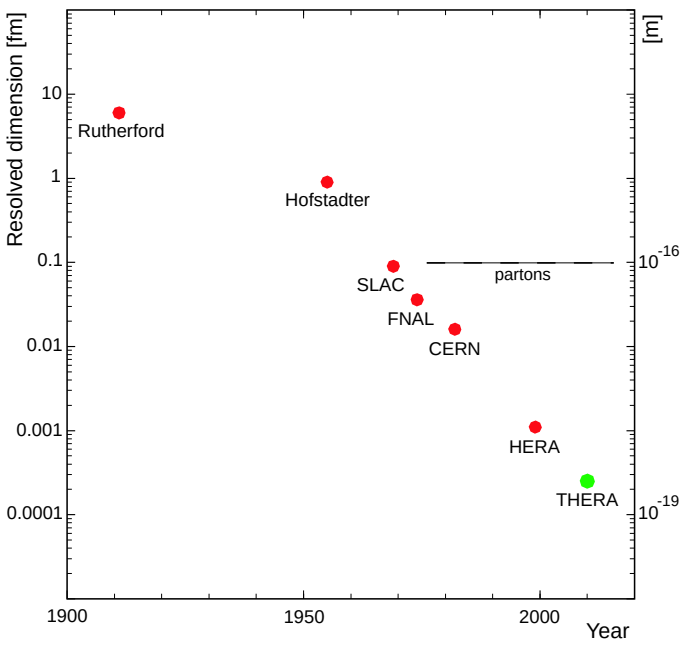

Figure 2: *The development over time of the resolution power of experiments exploring the inner structure of matter, from the Rutherford experiment to THERA.*

The electron–proton scattering programme at THERA can be greatly extended by accelerating nuclei or polarised protons in the HERA ring, or with real photon–proton scattering using laser light backscattered off the electron beam. Thus THERA can be a unique long-term, cost-effective facility for inelastic lepton–hadron scattering in an unexplored range.

The structure of this appendix[2] is the following: In Sect. 2.2 the physics subjects studied are discussed, and the major physics possibilities are highlighted. In Sect. 2.3 the THERA machine layout and luminosity estimates, as well as the concept of a THERA detector, are presented. Sect. 2.4 presents briefly the physics options of running the THERA facility in $\vec{e}A$, $\vec{\gamma}p$ and $\vec{e}\vec{p}$ mode. A brief summary is given in Sect. 2.5.

[2]This appendix summarises studies of a group of about one hundred physicists. Most of the results are available on the web (`http://www.ifh.de/thera`) and will be documented in more detail in a separate volume [3].

2.2 Physics with THERA

2.2.1 Low-x physics

From the measurement of the differential cross section $d^2\sigma/dx\,dQ^2$ in inclusive deep-inelastic lepton–proton scattering, $\ell p \to \ell X$, the proton structure function $F_2(x, Q^2)$ is determined. In the naive Quark Parton Model (QPM), F_2 is interpreted as the sum of the momentum densities of quarks and anti-quarks in the proton, weighted with their charge squares. The variable x is interpreted as the fraction of the proton's longitudinal momentum carried by the struck quark. According to the relation $x = Q^2/sy$ (where y is the fractional energy carried by the exchanged current), every step towards higher centre-of-mass energy, $\sqrt{s}$, leads deeper into the unexplored region of low x.

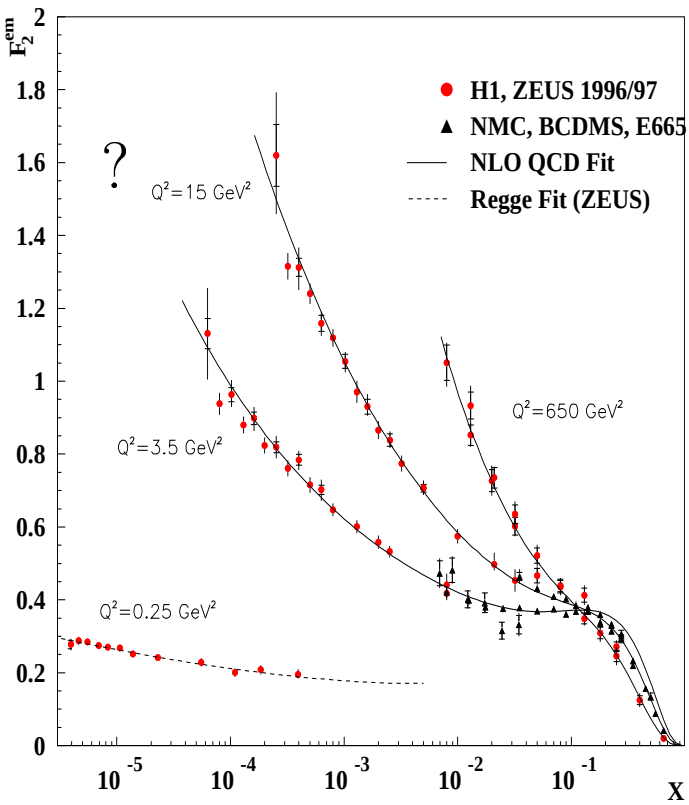

Figure 1: *The proton structure function $F_2(x, Q^2)$ as measured in fixed-target μp scattering at large x, and in ep scattering at HERA. The solid curves show a fit using the next-to-leading order QCD evolution equations. The dashed curve for the lowest-Q^2 data is a fit using Regge theory. The structure function in the low-x region represents the sea-quark component of the proton. With THERA, the kinematic range will be extended by a further order of magnitude towards lower x. The expected behaviour of F_2 in this new region is hotly debated.*

The high-energy collider HERA and its experiments have extended the kinematic (x, Q^2) region for DIS by about two orders of magnitude. As can be seen in Fig. 1, the structure function F_2 as measured at HERA [4, 5] and thus the sea-quark density rises by a large factor towards low x, and the increase becomes stronger with increasing Q^2. The data in the DIS region were found to be well described by the QCD evolution equations [6], which are based on the renormalisation group equations and the operator product expansion. Figure 1 also illustrates that the behaviour of the data [7] at low $Q^2 < 1\,\mathrm{GeV}^2$ is completely different, showing a slower, logarithmic rise, which is typical for the energy dependence of soft hadronic processes.

Much of the understanding of strong interaction dynamics is derived from the study

of Q^2 dependences in DIS. The HERA experiments have found that $F_2(x, Q^2)$ at fixed small values of x strongly rises with Q^2. In the standard QCD evolution equations, the derivative $(\partial F_2/\partial \ln Q^2)_x$ at fixed low x is, at leading order, proportional to the product of the strong interaction coupling constant, α_s, and the gluon momentum density, xg. Thus the rise of F_2 with Q^2 as measured at HERA implies a large gluon density in the proton, which increases towards low x (see Fig. 2). However, it remains an open question whether the underlying evolution equations strictly hold at the lowest x values, in spite of neglecting large logarithms of the type $\ln(1/x)$ and possible unitarity effects. Data at lower x and larger Q^2 are required to resolve this issue. Theoretical QCD developments regarding DIS at low x are discussed in Sect. 2.2.2.1.

In the HERA collider experiments a number of observables have been studied which provide insight into strong interaction dynamics independently of F_2 and are also sensitive to the behaviour of the gluon distribution at low x. Examples are the longitudinal structure function $F_L \propto \alpha_s xg$ [4], the production of vector mesons like J/ψ [8, 9] ($\propto (\alpha_s xg)^2$) and the charm structure function F_2^c [10, 11]. The successful description of these and further measurements with a single set of parton distribution functions of the proton has been a major success of perturbative QCD.

Due to the high density of quarks and gluons, qualitatively new signatures are expected in the low-x region of THERA. An extrapolation of the rise of F_2 to lower x, as indicated by Fig. 1, would at some point violate the unitarity limit of virtual photon–proton scattering. An upper limit on xg is obtained from the unitarity requirement

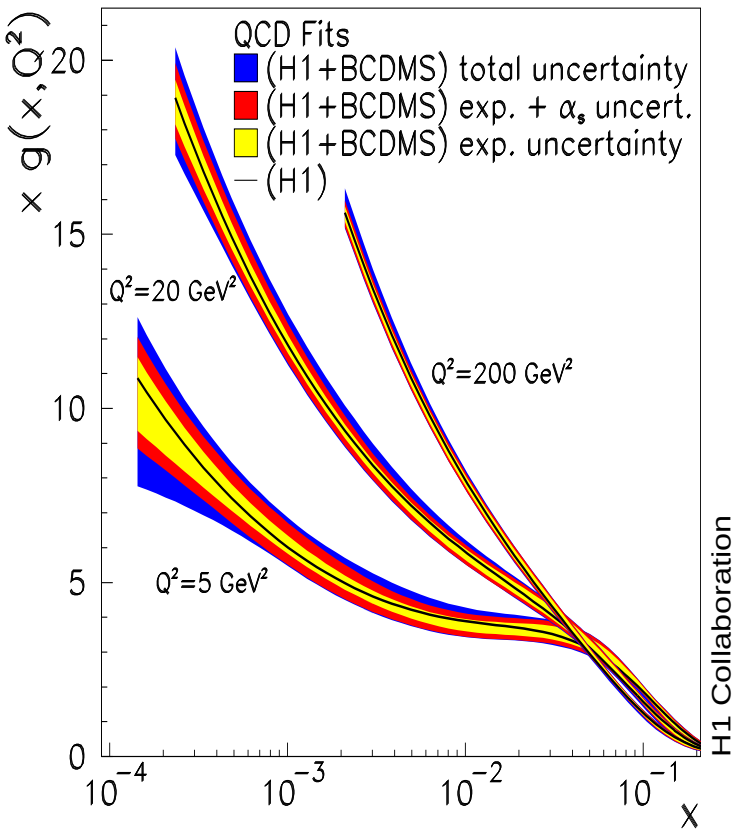

Figure 2: *Gluon momentum distribution measured at HERA, extracted within the framework of the conventional evolution equations of perturbative QCD. The gluon distribution is sensitive to the understanding of heavy flavour production at low x and Q^2. The behaviour of the gluon density in the kinematic range of THERA is a hotly debated issue which has to be resolved experimentally.*

that the inelastic cross section of the interaction of a small dipole[3] [13–15] with the proton may not exceed the transverse proton size πR^2. This leads to an approximate constraint [16, 17]

$$xg(x, Q^2) \leq \frac{1}{\pi N_c \alpha_s(Q^2)} Q^2 R^2 \simeq \frac{Q^2}{\alpha_s} , \tag{2.2.1}$$

where N_c is the number of colours and Q^2 is given in GeV^2. Given the strong rise of xg towards low x (Fig. 2), it seems likely that the unitarity limit is reached in the THERA kinematic range and that therefore this rise eventually becomes tamed. As discussed in Sect. 2.4.1, it is possible that these effects are amplified in electron–nucleus scattering. In any case, understanding deep inelastic structure functions in the THERA range is of crucial relevance for the description of high-energy cross sections at hadron colliders and astro-particle physics experiments [18, 19].

Saturation may be connected with a novel, high parton density state of QCD, between the low-density region of partons and the region of confinement. The transition from the perturbative range of small distances to the physics at large distances is currently being intensively studied, using data from the HERA collider experiments on the total virtual-photon proton cross section as well as on elastic vector meson production and diffraction. Despite the success of phenomenological models, however, a consistent theoretical description remains elusive [20][4], and a significant extension of the kinematic range in deep inelastic scattering is required.

2.2.1.1 The high-density QCD phase and confinement

The deep inelastic scattering process can be viewed as a fluctuation of the incoming proton into a cloud of constituents which is subsequently scanned by the virtual photon. The life-time of the cloud, $\tau \approx 1/Mx$, is considerably longer than the photon interaction time (M being the proton mass). Therefore the photon takes 'snapshots' of the 'frozen' proton cloud with a resolution $\Delta r \approx 1/\sqrt{Q^2}$. The x and Q^2 dependence of the proton structure may be viewed as sketched in Fig. 3.

HERA data and theoretical studies suggest that hadrons have a qualitatively different structure in three domains:

[3] Theoretical descriptions of DIS at low x frequently use a frame in which the proton is at rest. In the high-energy limit, low-x processes factorise into a virtual photon fluctuation to a hadronic system at large distances from the proton target, which is followed by a brief interaction with the target and subsequent hadronic final state formation over a longer period. The simplest fluctuation, which dominates for systems with small transverse size, is a quark–antiquark state which forms a colour-triplet dipole. This view is attractive for describing inclusive DIS at low x as well as suitable for vector meson production and diffractive processes. It has been successfully used and developed much further in recent years, as is reviewed in [12].

[4] This is reminiscent of a situation about 100 years ago before Planck successfully solved the black-body radiation problem bridging the gap between Wien's law and the Rayleigh–Jeans formula. In analogy to the ultraviolet catastrophe, i.e. the divergence of the Rayleigh–Jeans law at small wavelengths, the proton structure function F_2 cannot grow indefinitely as x approaches zero.

1. The *domain of perturbative QCD* with small-size constituents which are distributed in a hadron with rather low density (the region below the solid line in Fig. 3). Reacting partons are resolved with a resolution determined as $\Delta r \approx 1/Q$.

2. The *QCD domain of high parton density* [21, 22] but small coupling, where the density is too large to use the established perturbative QCD methods (the region above the solid line). Theoretical studies suggest that the size of the partons in this region is effectively determined by an x dependent resolution scale, $Q_S(x)$: $\Delta r \approx 1/Q_S(x)$ [23].

3. The *non-perturbative QCD domain*, in which the QCD coupling α_s is large, Regge theory applies and the confinement of quarks and gluons occurs. New theoretical methods must be developed to explore this region (left of the dash-dotted line).

According to [17, 24] the HERA data suggest the existence of the high-density QCD domain in which a new scaling law for the virtual photon–proton cross section may apply [25]. However, the HERA data can also be described without such an assumption [17, 26]. At THERA, such investigations can be performed at larger Q^2 for a given x, i.e. more safely inside the region of small α_s. Thus the extension of the kinematic range is crucial to the distinction and analysis of these states of matter.

It is well known that in the short-distance limit (i.e. in the perturbative QCD domain), quarks and gluons are the proper degrees of freedom of the QCD Lagrangian. To describe the transition from short to long distances, however, one needs to consider degrees of freedom beyond quarks and gluons. Approaches based on colour dipole formation as the first stage in this transition are promising.

Understanding the confinement of quarks and gluons is still a challenge to theorists. Deep inelastic scattering provides two approaches to study this phenomenon. Firstly, the experimental data at high energies suggest some properties of confinement, such

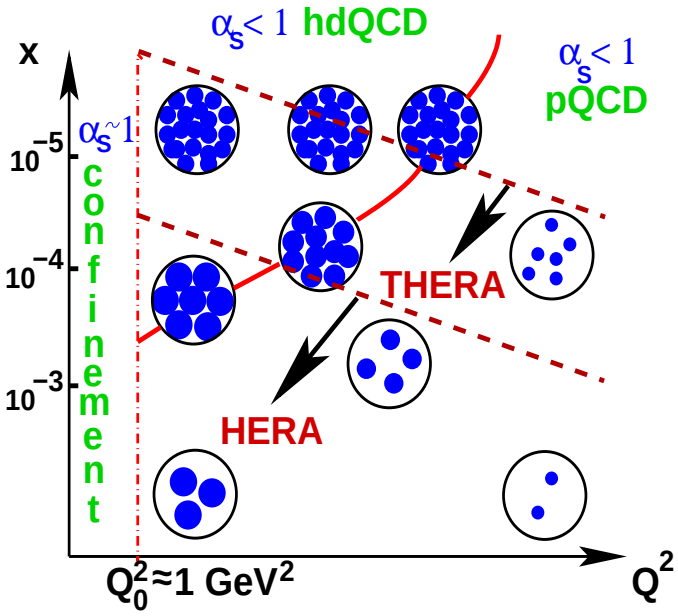

Figure 3: *Snapshots of the proton constituents (full dots) taken with different resolution ($\Delta r \approx 1/Q$) at different values of x. The solid line shows the estimated position of the transition from the perturbative region to the high-density phase of QCD (hdQCD). The resolution scale diminishes with Q^2 in the pQCD region but with x in the hdQCD region. The vertical dash-dotted line delimits the confinement region. The dashed lines and the corresponding arrows indicate the HERA and THERA measurement ranges. The observation of signatures allowing the identification of the various regions is a challenge for THERA.*

as factorisation, the space-time picture or the quark model. These hint at the effective degrees of freedom and at which type of effective Lagrangian may be used for developing a microscopic theory at high energies. Secondly, DIS data allow the matching of perturbative and non-perturbative QCD domains to be studied by investigating low-Q^2 virtual-photon proton scattering. Clearly, a solution to the confinement problem of hadrons has fundamental implications.

2.2.1.2 Vector-meson production

Investigations of vector meson production at HERA have provided insights into the dynamics of both soft and hard diffractive processes [27] (for a review see [28]). The high flux of quasi-real photons from the electron beam permitted detailed measurements of both elastic and proton-dissociative photoproduction of ρ^0, ω, ϕ, J/ψ, and Υ mesons. Power-law scaling with the photon–proton centre-of-mass energy, W, was observed, as is illustrated by Fig. 4. The steep energy dependence measured for J/ψ mesons inspired a number of theoretical approaches based on perturbative QCD [29–31].

In the theory of light vector mesons, the photon virtuality [16, 33–36] and the momentum transferred to the proton [37–40] were introduced as hard scales. These calculations demonstrated remarkable sensitivity to the gluon density, since the cross sections were shown to be proportional to $(xg)^2$. With large THERA data samples, covering a variety of vector meson species, remaining theoretical uncertainties can be

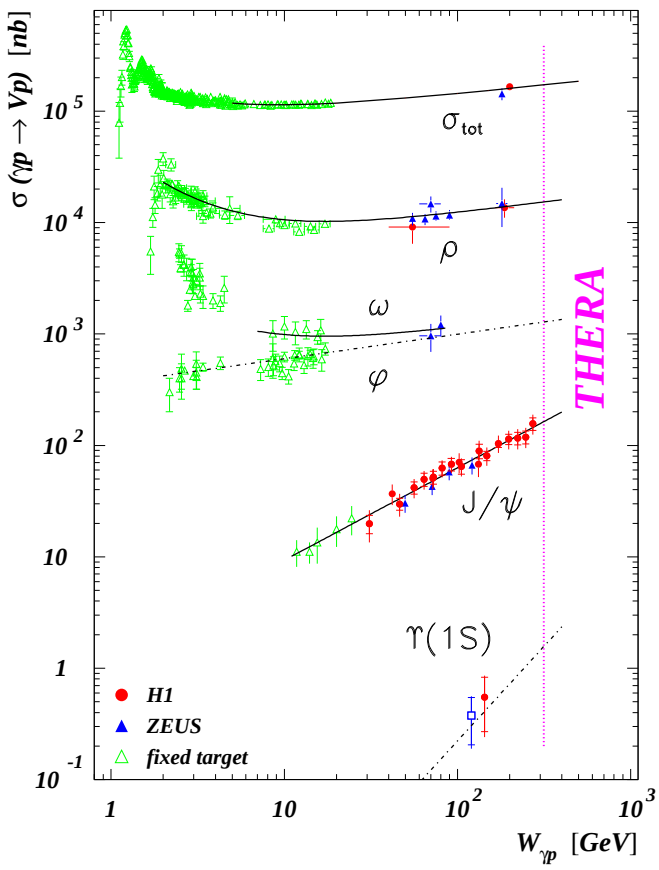

Figure 4: *Energy dependence of the total γp cross section and the elastic vector meson photoproduction cross sections for ρ^0, ω, ϕ, J/ψ, and Υ mesons. Here W is the photon–proton centre-of-mass energy. The plot is reproduced from [32]. Since the production cross section of heavy vector mesons is proportional to $(xg)^2$, measurements in the THERA range of W up to 1 TeV may be sensitive to saturation.*

tackled, such that elastic vector meson production could become a competitive means of extracting the gluon density. Of particular interest is the question whether the rise of the J/ψ cross section towards large W (Fig. 4) is tamed, for example by unitarity effects, or indeed persists [26]. Because of the enlarged cross section and W range, the investigation of Υ meson production [41, 42] will become an important topic at THERA.

Whereas perturbative QCD is applicable where hard scales are present, long-range strong-interaction dynamics apply to the forward production of light vector mesons at low Q^2. The transition between these two regimes is studied by scanning Q^2 or the square of the four-momentum transfer at the proton vertex, t, allowing comparisons to hadronic interactions. Of particular interest is the possibility of determining the transverse interaction size which may grow with energy [17, 26, 43], as given by the slope of the Pomeron trajectory, α'. Due to the weakness of the energy dependence in such long-distance processes, the extension of the energy reach is essential to provide sensitivity to α'.

The programme of vector meson measurements will benefit not only from the extended kinematic reach but as well from the improved coverage of the THERA detector at small angles and from tagging systems in both the proton and electron beam directions, designed with the benefit of the experience obtained at HERA.

2.2.1.3 Hard diffractive scattering

A striking result at HERA has been the abundance of diffractive processes of the type $ep \to eXp$ [44, 45] in DIS, where the proton remains intact with only a small loss in momentum. Deep inelastic scattering at low x thus became, rather unexpectedly, an important process for the understanding of one of the oldest puzzles of high energy physics, the nature of diffraction [46]. The mechanism responsible for diffraction remains unsettled, and its investigation will profit enormously from the extended phase space available at THERA. Since total, elastic and diffractive cross sections are closely related via the optical theorem, it is clear that a correct description of diffractive processes must be an integral part of any consistent theory of low-x physics [47–49].

The diffractive contribution to F_2 has been measured in the form of a structure function $F_2^{D(3)}(x_{I\!P}, \beta, Q^2)$. Here, as illustrated in Fig. 5a, $x_{I\!P}$ is the fractional proton longitudinal momentum loss and $\beta = x/x_{I\!P}$ is the fraction of the exchanged longitudinal momentum carried by the quark coupling to the virtual photon. Figures 5b,c show the kinematic regions in which diffractive processes can be measured at HERA and at THERA. An extension of approximately an order of magnitude towards lower β or $x_{I\!P}$ is obtained at fixed Q^2.

The hard scale supplied by the photon virtuality has encouraged perturbative QCD approaches to diffractive DIS. A QCD factorisation theorem has recently been proven for the process [50], implying that diffractive parton densities at fixed $x_{I\!P}$ can be defined, which should describe both the scaling violations of $F_2^{D(3)}$ and exclusive final state cross sections such as those for high-p_t jet production. HERA data have shown that the diffractive parton densities are dominated by gluons at large β [51]. The region

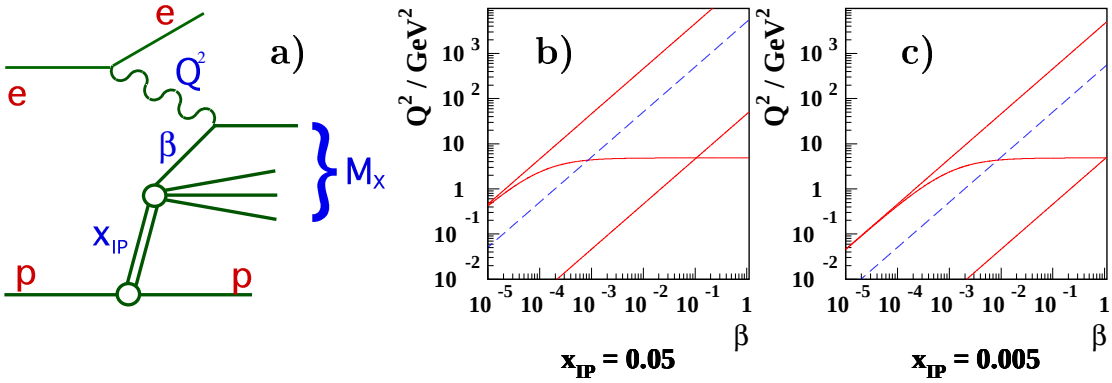

Figure 5: *(a) Feynman diagram of diffractive ep scattering, with the kinematic quantities indicated in blue. (b,c) The accessible kinematic plane in β and Q^2 for diffractive DIS at two different values of $x_{I\!P}$. The solid red lines show the limits imposed by the cuts $0.001 < y < 1$ and $\theta_e < 179.5°$ for THERA, with electrons of 250 GeV and protons of 920 GeV. The dashed blue lines show the kinematic limit at HERA.*

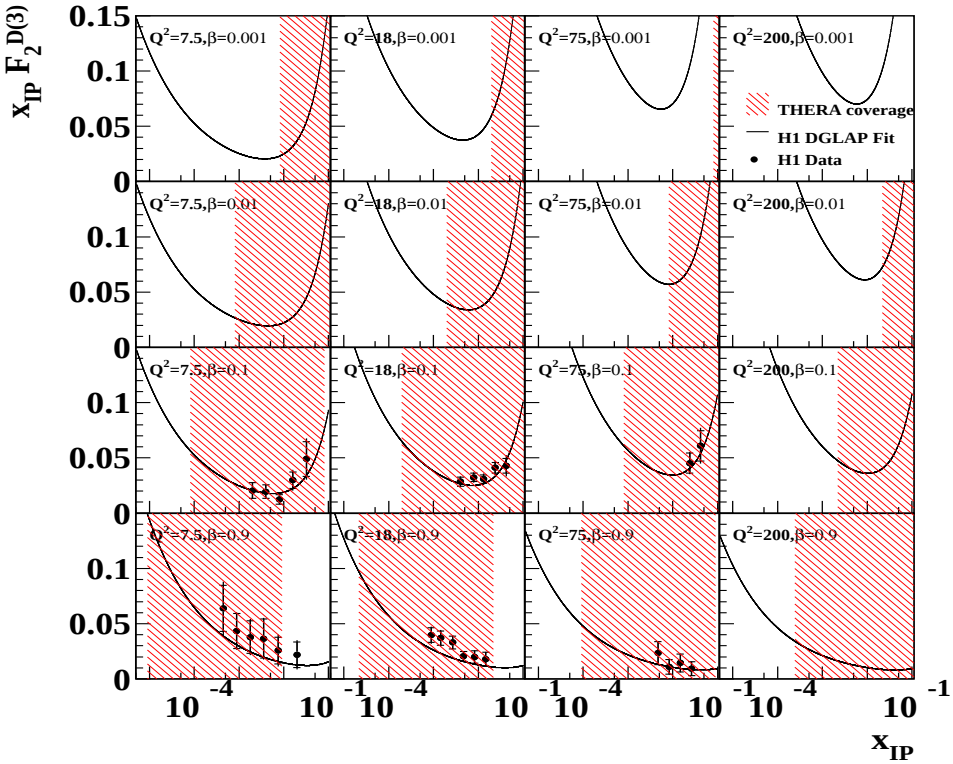

Figure 6: *Illustration of the kinematic coverage for measurements of $F_2^{D(3)}(x_{I\!P}, \beta, Q^2)$ at HERA and at THERA. The accessible $x_{I\!P}$ range is shown for selected values of β and Q^2. Appropriate HERA data points from [44] are also shown. The curves are extrapolations of QCD fits to data with $\beta < 0.65$ from [44]. The shaded areas show the region of extended coverage at THERA (920 GeV protons, 250 GeV electrons).*

$\beta \lesssim 0.05$ remains poorly explored at HERA.

In the proton rest-frame approach, diffractive DIS is considered as the elastic scattering of the proton with $q\bar{q}$ and $q\bar{q}g$ partonic fluctuations of the virtual photon. The scattering has been modelled either in terms of multiple interactions in the non-perturbative colour field of the proton [52, 53] or in terms of the exchange of a pair of perturbative gluons [24, 54, 55]. THERA data in an extended phase space will be very powerful in distinguishing between these different approaches.

From combined analyses of diffractive and inclusive $\gamma^* p$ cross sections, it has been suggested that the regime of parton saturation, expected as the unitarity limit is approached, is already reached at HERA [24]. Diffractive data are crucial for this sort of analysis, since for fixed x, saturation is expected to set in at larger Q^2 values in the diffractive than in the inclusive cross section. Although the presence or absence of saturation effects in diffraction at HERA is hotly debated, it is likely that the effect will be clearly visible in the extended low-x range at THERA.

Figure 6 indicates the regions in which measurements of $F_2^{D(3)}$ will be possible at THERA, together with selected data points from HERA. Extrapolations of a QCD fit to HERA data [44] based on DGLAP evolution of the diffractive parton distributions are also shown. THERA measurements at lower β will allow the precise determination of diffractive parton densities in the region of low momentum fraction. The extended

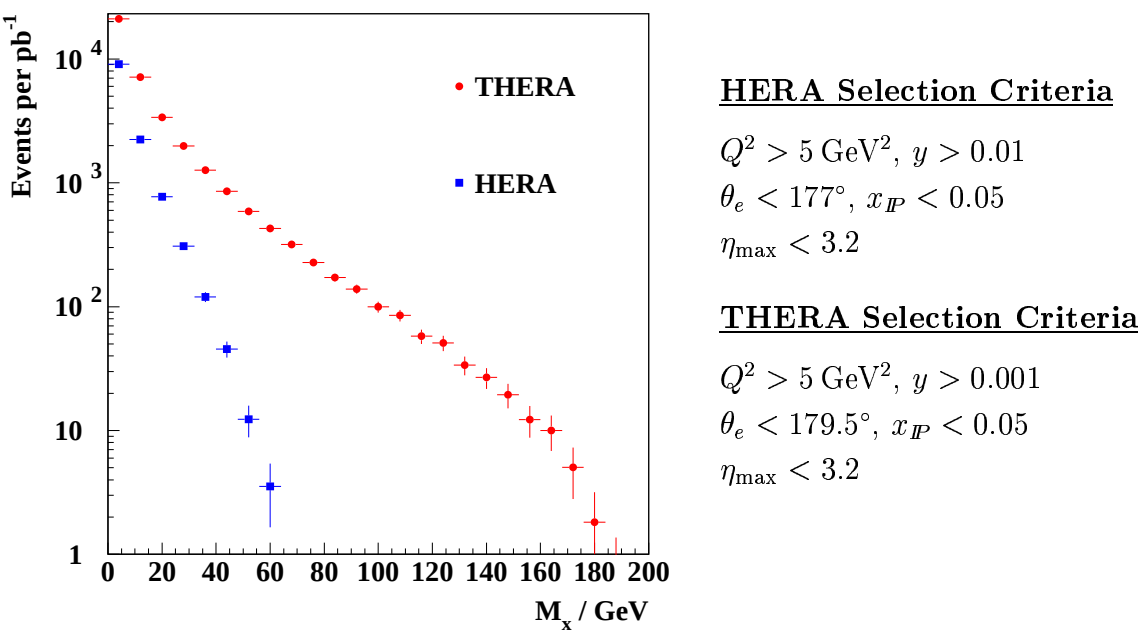

Figure 7: *Event yields per unit luminosity for the process $ep \to eXp$ after applying the quoted selection criteria at THERA (920 GeV protons, 250 GeV electrons) and HERA. The yields are shown as a function of the mass M_X and are based on an ad hoc extrapolation of a QCD fit to HERA data [44].*

range in $x_{I\!P}$ will allow an improved determination of the energy dependence of diffractive DIS from the combined HERA and THERA data. This will lead to detailed tests of the hypothesis of 'Regge' factorisation of the $x_{I\!P}$ dependence from the Q^2 and β dependences, as would be expected for a universal pomeron exchange [56].

Further tests of QCD models of diffraction and an improved understanding of the gluonic degrees of freedom are achievable by studies of hadronic final state cross sections involving additional hard scales due to the presence of charm or high-p_t jets. At HERA, the limited reach in M_X (see Fig. 5a) seriously restricts the phase space for charm and dijet production and implies that these final states can only be studied at rather large $x_{I\!P}$. As can be seen from Fig. 7, the values of M_X reached at THERA for $x_{I\!P} < 0.05$ are larger by a factor of around 3 than in the HERA case.

In diffractive events the proton can remain intact or dissociate into a low-mass hadronic system. In this sense diffractive events are directly sensitive to the conditions required to preserve the hadronic bound state. A detailed comparative study of diffractive events with and without proton dissociation could reveal information about confinement. Such an analysis can be performed if the outgoing proton beam-line is instrumented with detectors to tag the final-state protons (leading-proton spectrometer).

2.2.2 Proton structure and quantum chromodynamics

Deep-inelastic scattering has been crucial in the development of Quantum Chromodynamics since the observation of the logarithmic pattern of scaling violations in $F_2(x, Q^2)$. Over the past decades, precision measurements of structure functions and studies of final state characteristics have deepened the understanding of QCD. With the access to very low values of Bjorken x in the deep inelastic region, the exploration of extremely high Q^2 values at high luminosity, and an extension of the transverse momentum phase space, THERA promises new insights into the structure of QCD.

2.2.2.1 Perturbative QCD and structure functions

The measurements of structure functions in DIS have been accompanied by remarkable progress in QCD calculations. Both the splitting functions, to second order in α_s, and the coefficient functions, to order α_s^3, are calculated [57], and the NNLO calculation of the splitting functions is in progress. The current measurements of $F_2(x, Q^2)$ in the kinematic range of HERA are very well described by the twist-2 evolution equations, even in a range in which significant higher-twist effects and specific higher-order small-x effects were previously expected. The phenomenological success of joint determinations of the coupling constant α_s and the gluon distribution xg, together with the quark distributions, is impressive [4, 58] and has led to precise measurements of these quantities. Parton densities to NLO have been extracted over a wide kinematic range from HERA F_2 and other cross section data [59–61]. With data in the kinematic domain of THERA, both at lower x and larger Q^2, the precision of these quantities will further improve significantly (see below).

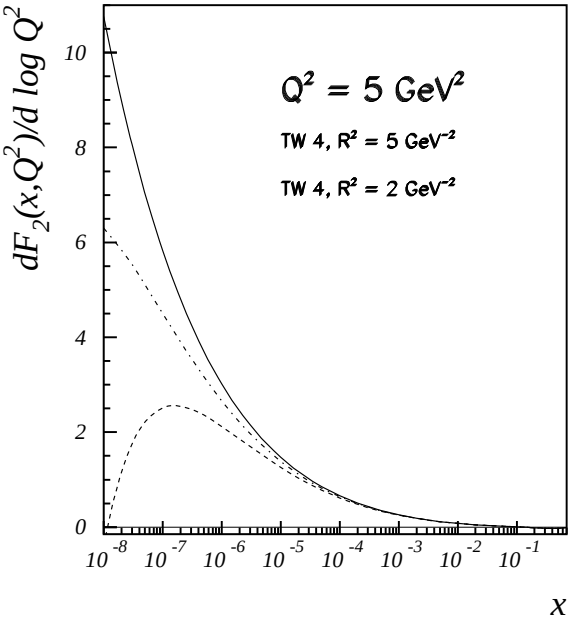

Figure 8: *The slope $\partial F_2(x,Q^2)/\partial \log Q^2$ at $Q^2 = 5\,GeV^2$ [62]. Full line: leading-order twist-2 contributions (parameterisation [61]); dash-dotted line: slope including the twist-4 contribution with a screening radius of $R^2 = 5\,GeV^{-2}$; dashed line: $R^2 = 2\,GeV^{-2}$.*

As was discussed above, an important question is how the low-x growth in F_2 as observed at HERA is tamed to satisfy the unitarity bound. Higher-order corrections to the twist-2 terms diminish the growth but do not lead to a saturation as $x \to 0$. One can expect that unitarity is restored by higher-twist contributions. First studies of these effects have been performed [62, 63] in approaches based on the light-cone expansion. Numerical results on the slope $\partial F_2/\partial \log Q^2$ for specific choices of twist-4 screening radii R are depicted in Fig. 8, showing that one may indeed probe these effects in the kinematic domain of THERA, $x \gtrsim 10^{-6}$ (see also [64]). Rather large higher twist effects [65, 66] may be seen in measurements of the longitudinal structure function F_L.

The apparent success of the complete fixed-order calculations in describing F_2 in the small-x domain is puzzling theoretically. Starting from the BFKL approximation and resumming the most singular pieces, large corrections were predicted both for the anomalous dimensions [67, 68] and for the coefficient functions [69]. Recently, large next-to-leading order resummed gluon anomalous dimensions were found [70], however with opposite sign. This led to the conclusion that they have to be stabilised by resumming even higher orders [71–73]. Formally, sub-leading terms were found to be quantitatively as important as the resummed 'leading' terms due to the strong rise of the gluon and sea quark densities in the small-x domain. This requires the knowledge of the coefficient functions also for the range of medium values of x [71, 73], where resummations are not possible. More theoretical work is needed to further develop perturbative QCD. This will be stimulated by a continuing experimental programme and data in an extended range.

Ultimately, in the regime of extremely low values of x and small Q^2, one expects that the light-cone expansion does not apply anymore. For this kinematic domain new theoretical concepts have still to be developed.

2.2.2.2 Forward jet production

In order to understand strong-interaction dynamics, inclusive cross section measurements and their interpretations have to be complemented by the investigation of the hadronic final state. At HERA, the description of details of the final states, for example in forward jet production at low x, requires to consider resolved photon structure effects in addition to the pure DGLAP evolution. However, an extension of the phase space as provided by THERA is necessary to distinguish between a DGLAP-based calculation with an additional resolved virtual photon contribution, which mimics non-k_t-ordered (i.e. non-pure-DGLAP) contributions at present energies, and small-x evolution as modelled by the BFKL [67, 68] or CCFM [74] equations. The CCFM evolution equation, based on the principle of colour coherence, is equivalent to BFKL for $x \to 0$ and reproduces the DGLAP equation for large x.

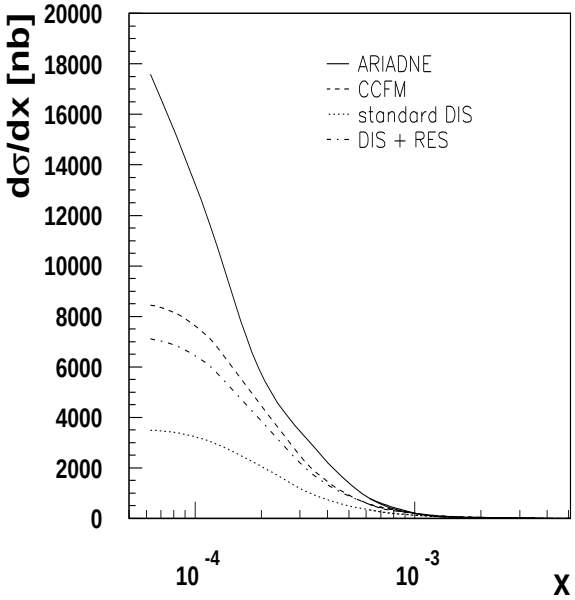

Figure 9: *Forward-jet cross section as a function of x in different models for $0.5 < p_t^2/Q^2 < 2$ and a minimum polar jet angle of $1°$. The measurements at HERA are limited to $x \gtrsim 2 \times 10^{-3}$.*

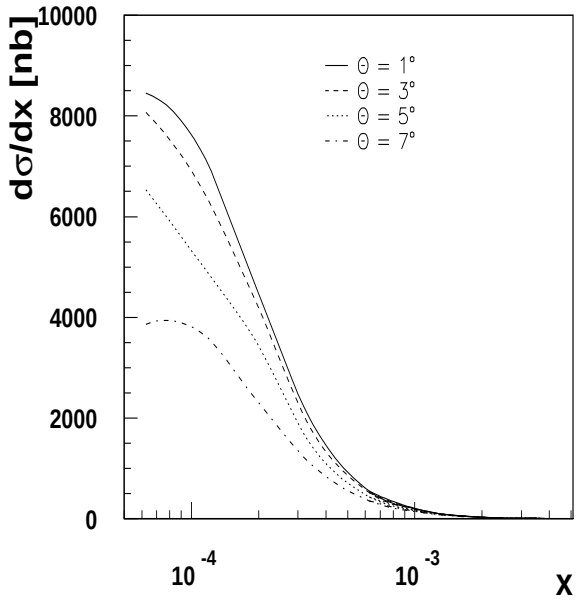

Figure 10: *Forward-jet cross section as a function of x obtained from CCFM for $0.5 < p_t^2/Q^2 < 2$, for different values of the minimum jet angle.*

At THERA the differences between these approaches become striking. In Fig. 9 the cross section for forward jet production [75] is shown as a function of x. Whereas the measurement at HERA is limited to $x \gtrsim 2 \times 10^{-3}$, the available x range at THERA is extended by one order of magnitude towards lower x. At THERA the CCFM approach predicts a much larger cross section than the model with resolved virtual photon contributions added, giving the unique opportunity to identify a new QCD regime, which can only be described by new small-x evolution equations. This not only allows us

to distinguish between the different approaches, but also to study details of the QCD cascade, which at small x includes unintegrated parton densities [48]. THERA will be the only place where these parton densities can be measured, and where the small-x parton dynamics can be clearly studied.

In Fig. 10 the forward jet cross section is shown for different minimal jet angles. On the experimental side this requires complete acceptance both in the electron and proton direction down to the lowest possible angles. From the size of the cross section $d\sigma/dx$ one would like to reach at least $\theta \sim 3°$ for the forward jet measurement, desirably even $\theta \sim 1°$. The luminosity required for such measurements is of the order of $10\,\mathrm{pb}^{-1}$.

2.2.2.3 Measurement of the strong coupling constant α_s

The accurate determination of α_s has been a central issue in many high-energy experiments which revealed a logarithmic dependence of α_s with Q^2, thereby confirming the property of asymptotic freedom of QCD (for a review see [76]). A precise measurement of this coupling constant is very important for the calculation of strong interaction processes and for unified field theories [77]. Inclusive deep inelastic scattering is particularly suitable to determine $\alpha_s(Q^2)$ because the predictions of QCD at large space-like momentum transfer can be derived in a rigorous way, based on the operator product expansion, and are free of additional assumptions like quark–hadron duality, assumptions concerning the behaviour of quark and gluon condensates, or assumptions regarding the absence or parametrisation of power corrections. The precision of QCD predictions in inclusive DIS is only limited by the present ability to evaluate perturbative corrections to sufficiently high orders. DIS measurements are therefore a unique opportunity to test QCD in a stringent way which is superior to e^+e^- annihilation and pp collisions.

Present DIS measurements of α_s [4, 58, 78] have about the accuracy of and are consistent with the world-averaged determinations of α_s. Improving these analyses is a challenge to the experimental precision and the theoretical calculations. The extension of the (x, Q^2) range and the envisaged cross section uncertainties at THERA of 1–3% lead to an estimated error [79] on $\alpha_s(M_Z^2)$ of about 0.3–0.5%, which is smaller than the current theoretical uncertainty [80] dominated by the choice of the renormalisation scale.

Reduction of the theoretical uncertainty requires the calculation of the complete 3-loop anomalous dimensions needed for NNLO QCD analyses. First results for a series of fixed moments have been obtained already [81] on the way to the complete solution. Based on these results, numerical investigations have been performed on the 3-loop splitting functions [80, 82].

Since THERA extends the Q^2 range and provides p_T values up to almost 100 GeV for jet production [83], the predictions of perturbative QCD become more reliable. Thus measurements of dijet cross sections promise to yield complementary and more accurate information on α_s and the gluon distribution than has presently been achieved at HERA [84, 85].

2.2.2.4 Heavy-flavour physics

In the last years, heavy-flavour production in *ep* scattering has become a subject of intense research in perturbative QCD (see [86, 87] and references therein).

Heavy quarks are produced copiously in *ep* collisions. The total charm and beauty cross sections at HERA are of the order of 1 μb and 10 nb, respectively. Charm production at HERA has been studied by the H1 and ZEUS collaborations in both the photoproduction and DIS regimes [10, 88, 89]. General agreement with pQCD expectations was observed in the DIS case, while a description of the charm photoproduction cross sections is more problematic for present pQCD calculations. The first measured beauty photoproduction cross sections at HERA [90] lie above the fixed-order next-to-leading order (NLO) QCD predictions [91]. No measurements of beauty production in the DIS regime at HERA have been performed so far.

An increase of the centre-of-mass energy of *ep* collisions from about 300 GeV at HERA to $\sim$ 1 TeV at THERA will result in an increase of the total charm and beauty production cross sections by factors $\sim$ 3 and $\sim$ 5, respectively [92, 93].

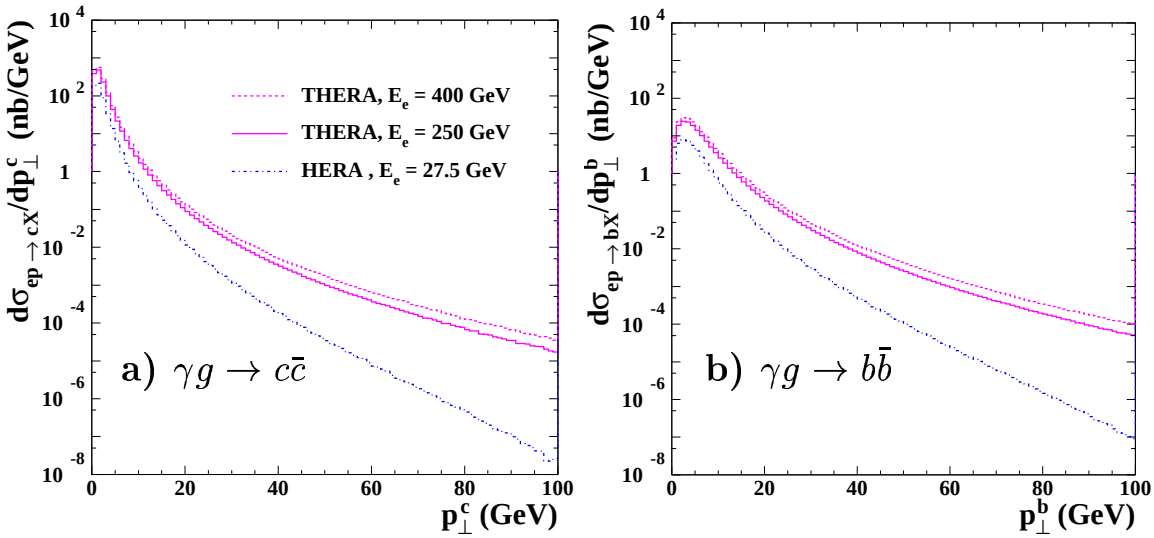

Figure 11: *The contribution of photon–gluon fusion to the differential cross sections $d\sigma/dp_\perp$ for (a) charm and (b) beauty production calculated in NLO QCD for $Q^2 < 1$ GeV^2. The solid and dashed violet curves show the predictions for THERA operation with an electron energy of 250 GeV and 400 GeV, respectively, and $E_p = 920$ GeV. The predictions for the HERA case are indicated by the dash-dotted blue curves.*

Figure 11 compares the contributions of photon–gluon fusion to the differential cross sections $d\sigma/dp_\perp^{c,b}$ ($p_\perp^{c,b}$ denoting the quark transverse momentum) at HERA and THERA, calculated within NLO QCD [91] for $Q^2 < 1$ GeV^2. The difference between the heavy quark production cross sections at THERA and HERA increases with increasing $p_\perp^{c,b}$, thereby creating the opportunity to measure charm and beauty quarks at THERA in a wider transverse momentum range. Such measurements will provide a solid basis for testing the fixed-order, resummed, and k_t-factorisation [94] pQCD calculations.

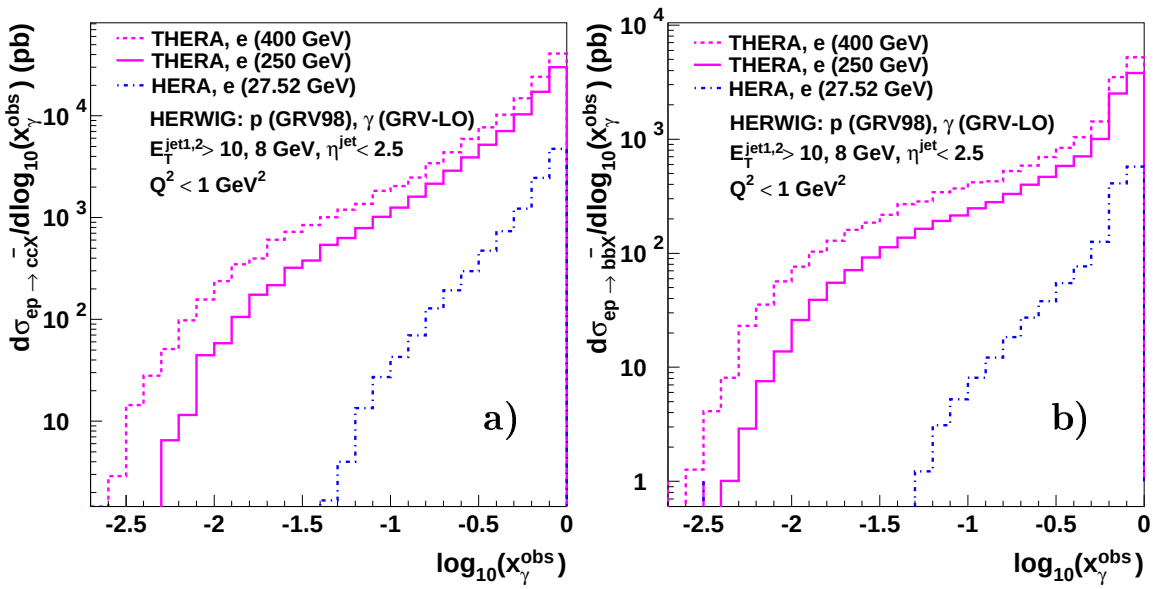

Figure 12: *The differential cross sections $d\sigma/d\log_{10} x_\gamma^{\rm obs}$ for (a) charm and (b) beauty dijet photoproduction as calculated in LO with the Monte Carlo generator HERWIG. The cross sections are shown for THERA, for a proton beam energy of* 920 *GeV and electrons with* 250 *GeV (solid magenta) and* 400 *GeV (dashed magenta), and for HERA (dashed blue).*

The reconstruction of two jets in heavy-quark photoproduction events provides an opportunity to study the gluon and heavy-quark structure of the photon [10, 88, 89]. The fraction of the photon energy contributing to the dijet photoproduction,

$$x_\gamma^{\rm obs} = \frac{\sum_{\rm jet1,2}(E_T^{\rm jet}\ e^{-\eta^{\rm jet}})}{2E_\gamma}\ , \tag{2.2.2}$$

has been found a useful observable for the investigation of the photon structure function. Here, $E_T^{\rm jet}$ and $\eta^{\rm jet}$ are the jet transverse energy and pseudorapidity, respectively, and the summation is over the two jets with highest $E_T^{\rm jet}$ within the accepted $\eta^{\rm jet}$ range. Figure 12 compares $d\sigma/d\log_{10} x_\gamma^{\rm obs}$ for charm and beauty photoproduction ($Q^2 < 1\,{\rm GeV}^2$) at HERA and THERA. The cross sections have been calculated in LO with the Monte Carlo generator HERWIG [95]. The difference between the heavy-quark dijet photoproduction cross sections at THERA and HERA increases towards smaller $x_\gamma^{\rm obs}$ values. The gluon and heavy quark structure of the photon can be studied only for $x_\gamma^{\rm obs} \gtrsim 0.1$ at HERA. The transition to the THERA energy regime will provide an opportunity to probe the structure down to at least $x_\gamma^{\rm obs} = 10^{-2}$ [92]. The gluon and heavy quark structure of the photon at THERA will be measured at rather large scale values stemming from the high E_T values of two reconstructed jets. Thus the measurements will provide complementary information to the results of future e^+e^- and $\gamma\gamma$ colliders [92].

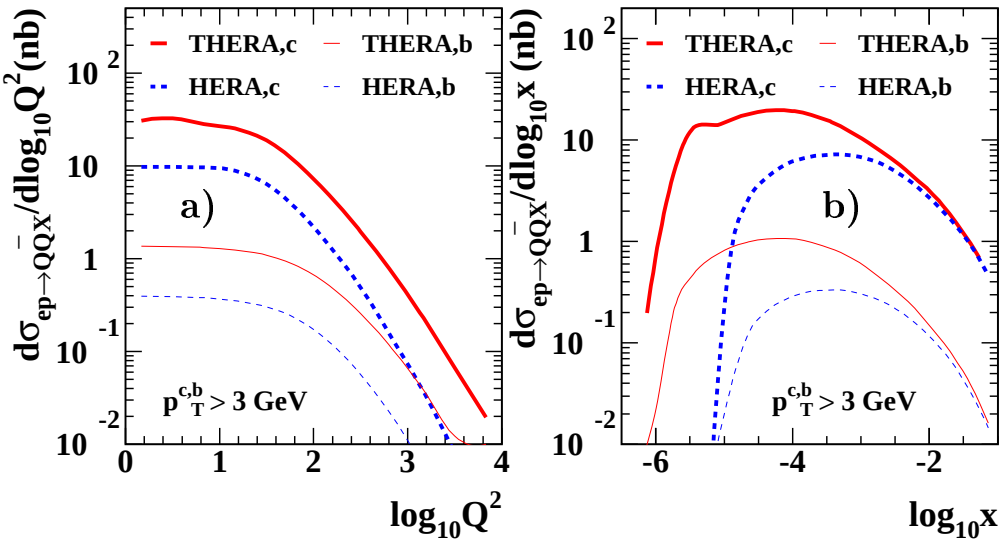

Figure 13: *The differential cross sections for charm (thick curves) and beauty (thin curves) production in neutral current DIS calculated in NLO QCD, (a) $d\sigma/d\log_{10}Q^2$ and (b) $d\sigma/d\log_{10}x$. The cross sections at THERA (solid curves) and HERA (dashed curves) are compared.*

The kinematic limits of DIS at THERA are one order of magnitude higher in Q^2 and one order smaller in x with respect to those at HERA. Figure 13 shows the differential cross sections $d\sigma/d\log_{10}Q^2$ and $d\sigma/d\log_{10}x$ for charm and beauty production in neutral current (NC) DIS calculated with the NLO code of [96]. The THERA cross sections are shifted towards smaller x values with respect to those at HERA. They are significantly above the HERA cross sections at all Q^2. Thus THERA will open new kinematic regions where the charm and beauty contributions to the proton structure function, F_2^c and F_2^b, can be extracted [93]. The measurement of charm production at large Q^2 will provide an opportunity to test the resummed pQCD calculations which treat the charm quark as a massless parton [97]. Charm production in the process of photon–gluon fusion at low Q^2 values will serve for the determination of the gluon structure of the proton in the as yet unexplored kinematic range $10^{-5} < x_g < 10^{-4}$ [93].

The theoretical description of charm production in charged current (CC) DIS is challenging [98]. The special interest in this process is caused by its sensitivity to the proton strange-quark density which is rather poorly known [99]. However, no measurement of CC charm production has been performed so far at HERA due to the small signal cross section ($\sim$ 10 pb). According to a HERWIG calculation, the cross sections for both LO CC charm production processes, $W^+s \to c$ and $W^+g \to c\bar{s}$, will be more than 6 times larger at THERA than at HERA. The differential cross sections $d\sigma/d\log_{10}Q^2$ for CC charm production are shown in Fig. 14. The THERA cross sections are shifted towards larger Q^2 with respect to those at HERA. They are one order of magnitude larger than the HERA cross sections at large Q^2 values, thereby creating the opportunity to study charm production in CC DIS at THERA [93].

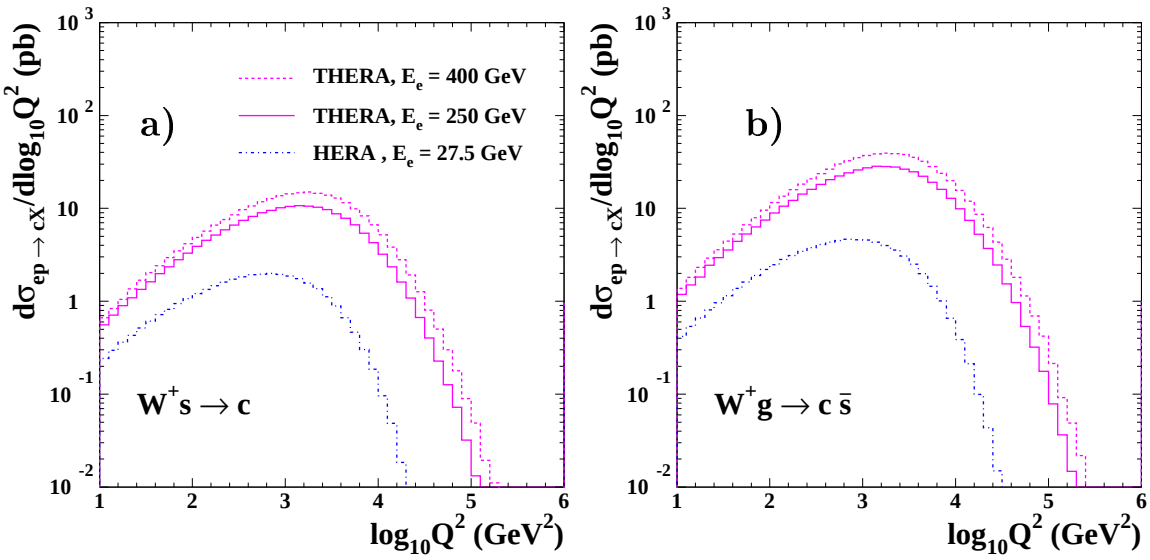

Figure 14: *The differential cross sections $d\sigma/d\log_{10} Q^2$ for charm production in charged current DIS, (a) from the strange sea and (b) from boson–gluon fusion, calculated with the LO Monte Carlo generator HERWIG. The cross sections are shown for THERA for a proton beam energy of* 920 *GeV and electrons with* 250 *GeV (solid magenta) and* 400 *GeV (dashed magenta), and for HERA (dashed blue).*

In conclusion, studies of charm and beauty production at THERA will provide unique new information about the proton and photon structures in as yet unexplored kinematic ranges.

2.2.2.5 Electroweak structure functions

In the THERA range of very high $Q^2 > M_Z^2$, the NC cross section receives comparable contributions from the exchange of photons, of Z bosons and from their interference. This is illustrated in Fig.15 showing the reduced NC cross section, $\sigma_r = \sigma_{NC}/Y_+$, defined by the relation

$$\sigma_{NC} = \frac{d^2\sigma_{NC}^{\pm}}{dx\, dQ^2} \frac{Q^4 x}{2\pi\alpha^2} = Y_+ \mathbf{F_2}^{\pm} + Y_- \mathbf{xF_3}^{\pm} \tag{2.2.3}$$

with $Y_\pm = (1 \pm (1-y)^2)$ and the fine structure constant α. Due to the Z exchange contribution, a new structure function combination $\mathbf{xF_3}$ occurs in NC [100, 101] (for a comprehensive review see [102]), which in the QPM measures a combination of the u and d valence quark distributions $q_v = q - \bar{q}$. Therefore deep inelastic NC scattering at very high Q^2 is sensitive to the quark flavours, in contrast to low Q^2, where the structure function F_2 measures only the weighted sum $\sum_q Q_q^2(q + \bar{q})$ of quark and anti-quark distributions.

Similarly, in CC scattering, the double differential cross section is given by

$$\frac{d^2\sigma^{\pm}_{CC}}{dxdy} = \frac{G_F^2}{2\pi} \cdot \left(\frac{M_W^2}{Q^2 + M_W^2}\right)^2 \cdot s \cdot \frac{1 \pm \lambda}{2} \cdot [Y_+ W_2^{\pm} \mp Y_- x W_3^{\pm}] \,, \tag{2.2.4}$$

where M_W is the CC propagator mass and G_F the Fermi constant. For a given beam charge, the cross section contains two structure functions which, in the QPM, are given by the following sums over the u- and d-type parton distributions:

$$\begin{aligned} W_2^{+(-)} &= 2x \sum (q_{d(u)} + \bar{q}_{u(d)}) \\ xW_3^{+(-)} &= 2x \sum (q_{u(d)} - \bar{q}_{d(u)}) \,. \end{aligned} \tag{2.2.5}$$

The cross section is proportional to s (which at THERA is equivalent to a beam energy of about 10^3 TeV in a neutrino fixed-target experiment). Combining NC and CC

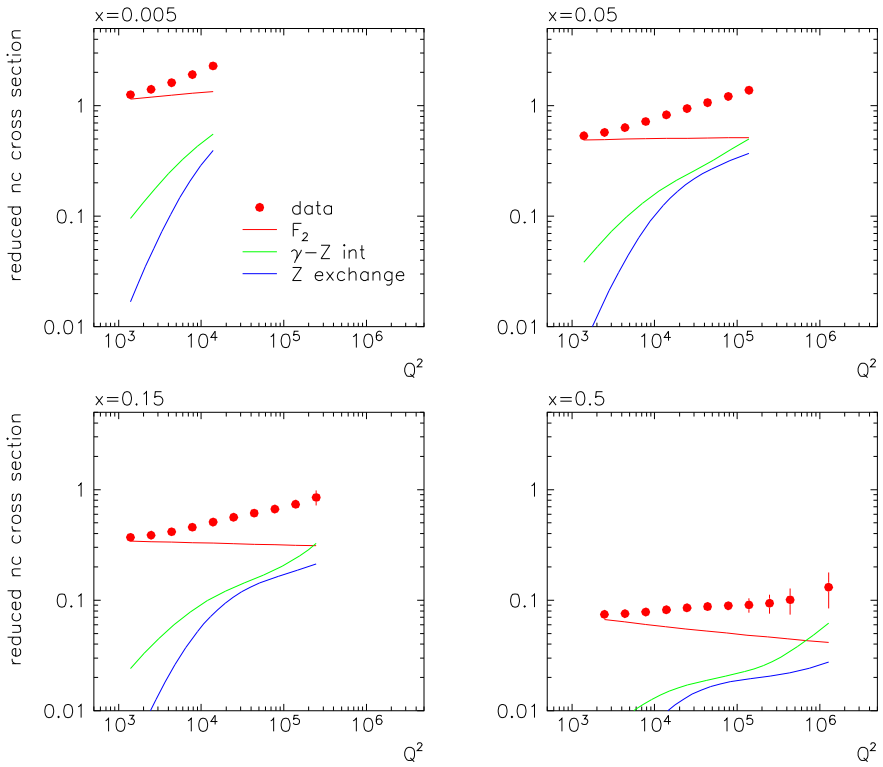

Figure 15: *Simulation of a measurement of the reduced NC DIS cross section at THERA in unpolarised electron scattering, for an integrated luminosity of* $200\,pb^{-1}$. *The error bars are a convolution of statistical and estimated systematic uncertainties. The curves represent the fraction of the one-photon exchange (red, top), of the* γZ *interference (green, middle) and of the pure* Z *exchange (blue, bottom). Towards very high* Q^2, *depending on the lepton beam charge and polarisation, the* Z *exchange contributions become increasingly important.*

$e^{\pm}p$ cross sections for different lepton polarisations, a complete unfolding [103] of the up and down quark and anti-quark distributions can be envisaged at THERA, with much higher accuracy than at HERA due to the extended Q^2 range which enhances the electroweak contributions to the cross section. The approximate symmetry of the electron and proton beam energies furthermore allows access to the up and down valence quark distributions up to very large x. This is of advantage over the standard method to access d_v at large x which relies on a comparison of proton and neutron structure functions and thus is subject to uncertain nuclear binding corrections, see [104]. The combination with the results of future high-statistics neutrino experiments [105] will permit important, flavour dependent tests of QCD.

The coverage of the full x range from about 0.005 to 1 in the region of high Q^2 at THERA is also essential for testing rigorous theoretical predictions in CC scattering [106], such as the Adler sum rule, $\int_0^1 (W_2^+ - W_2^-)dx/x = 2$, the Bjorken sum rule, $\int_0^1 (W_1^+ - W_1^-)dx = 1$, and the Gross–Llewellyn-Smith sum rule, $\int_0^1 (W_3^+ + W_3^-)dx = 6$. While the Adler sum rule holds independently of QCD, the two latter relations test QCD and are subject to higher-twist corrections which are negligible in the very high Q^2 range of THERA.

Various measurements of electroweak quantities can be performed at THERA, e.g. of the light-quark couplings, of the gauge boson masses in the space-like region and of parity violation at very high Q^2 via polarisation asymmetries in NC scattering, similarly to the pioneering experiment [107]. Utilising the high degree of lepton-beam polarisation at TESLA, one can search with much increased sensitivity for the existence of right handed currents in the new energy range which would prevent the CC cross section $\sigma^{\pm}$ from vanishing at $\lambda \to \mp 1$ (cf. eq. 2.2.4). Such a measurement at THERA for a luminosity of $100\,\mathrm{pb}^{-1}$ is illustrated in Fig. 16 for $\sqrt{s} = 1$ TeV.

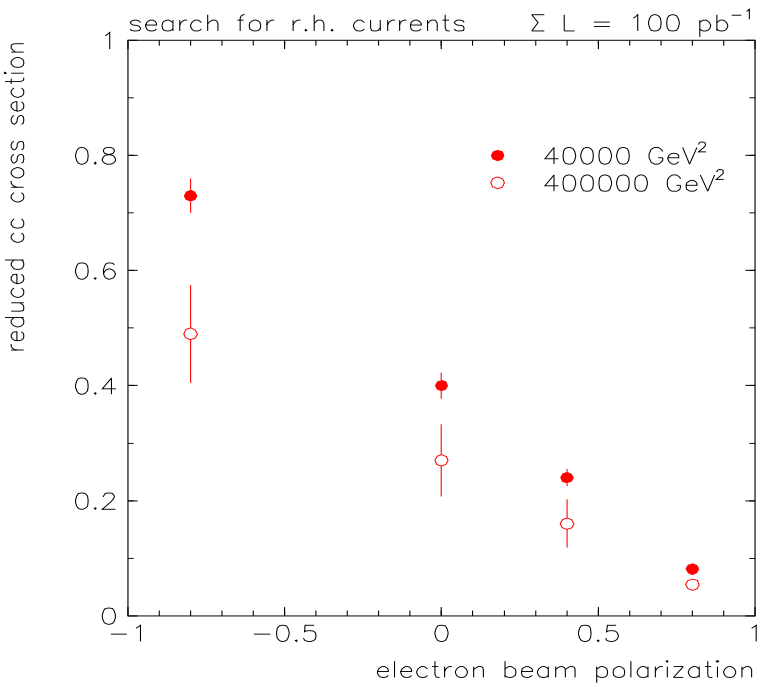

Figure 16: *Search for right-handed currents in CC scattering at THERA using a measurement of the electron–proton CC cross section as a function of the electron beam polarisation, λ. This simulation assumes a total integrated luminosity of $100\,pb^{-1}$ distributed over four measurements at different λ.*

The extension towards the electroweak region of very high $Q^2 \sim 10^5\,\mathrm{GeV}^2$ and the coverage of the full x range make THERA an excellent facility for the exploration of the partonic nucleon structure and the test of the electroweak theory. If new interactions and particles will be found in the TeV range of energy, THERA will not only explore these but as well be crucial in accurately determining the parton distributions which have to be known for the interpretation of the new phenomena.

2.2.3 Searches for new particles or phenomena

2.2.3.1 Leptoquarks and squarks

The *ep* collider THERA, providing both baryonic and leptonic quantum numbers in the initial state, naturally offers the possibility to search for new bosons possessing couplings to an electron–quark pair. Such particles could be squarks in supersymmetry with R-parity violation ($\not{R}_p$), or leptoquark (LQ) bosons [108] which appear in various unifying theories beyond the Standard Model (SM).

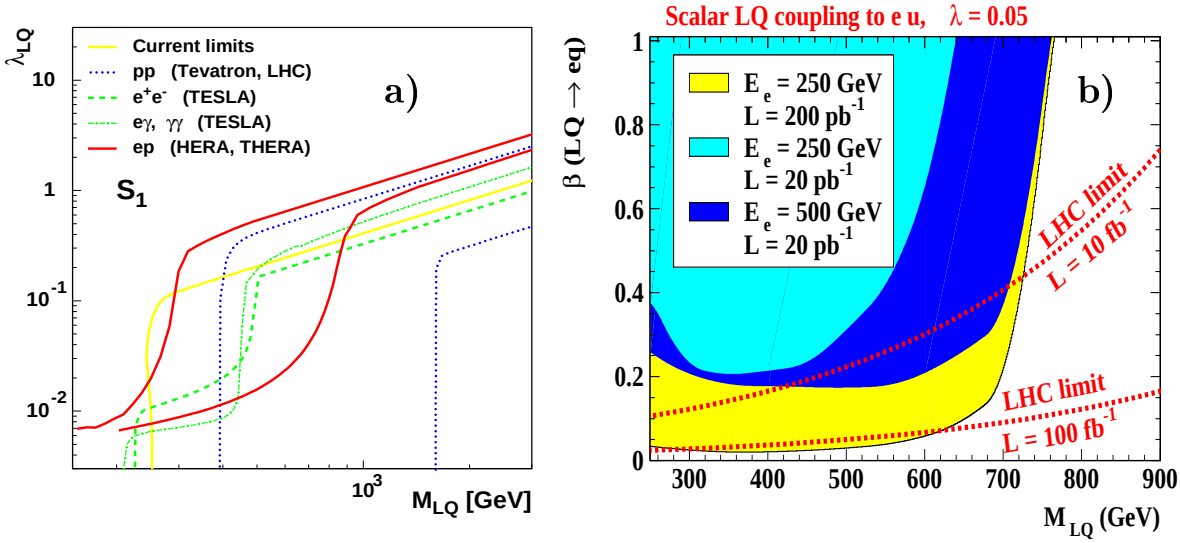

Figure 17: *(a) Mass-dependent upper bounds on the LQ coupling λ as expected at THERA (lower solid red curve, $E_e = 250\,GeV$, $E_p = 920\,GeV$, $100\,pb^{-1}$ of e^-p data), HERA (upper solid red curve, $2 \times 400\,pb^{-1}$ of $e^{\pm}p$ data), TESLA ($E_e = 250\,GeV$, $100\,fb^{-1}$ of ee, $e\gamma$ or $\gamma\gamma$ data), Tevatron (upper dotted curve, $10\,fb^{-1}$) and LHC (lower dotted curve, $\sqrt{s} = 14\,TeV$, $100\,fb^{-1}$). Upper limits as obtained from a global fit of various existing data sets [108] are also shown by the solid yellow curve. (b) Typical expected mass-dependent sensitivities on the branching ratio $\beta(LQ \to eq)$ of a LQ decaying to eq, at THERA for two different values of the lepton beam energy and at LHC; the coloured regions (the domains above the dashed red curves) would be probed by THERA (LHC).*

Leptoquarks (or $\not{R}_p$ squarks) with masses up to the kinematic limit, $\sqrt{s}$, could be singly produced as s-channel resonances by the fusion of the incoming electron with

a quark coming from the proton, with largest cross section when a valence quark in the proton participates in the fusion. For LQs decaying into an electron and a quark, the final state is similar to that of high-Q^2 NC DIS. For masses above the kinematic limit, LQ exchange can be parameterised by a contact interaction and could affect the measured high-Q^2 NC DIS cross section.

The sensitivity to LQs is discussed here either in the strict context of the BRW phenomenological ansatz [109], where the decay branching ratios are fixed by the model, or in the context of generic models allowing for arbitrary branching ratios.

For one of the scalar LQs described by the BRW model, with fermion number $F = 2$ (i.e. coupling to an e^- and a valence quark), the expected THERA sensitivity on the Yukawa coupling λ at the LQ-e-q vertex is illustrated in Fig. 17a as a function of the LQ mass, and compared to that of HERA-II, TESLA and hadron colliders [110]. THERA will improve the bounds expected from the full data sample of HERA by typically one order of magnitude, and its sensitivity will be significantly better than that of TESLA in the mass range 0.5–1 TeV, for a lepton beam energy of 250 GeV. However, the sensitivity of the LHC to pair-produced LQs should extend up to LQ masses of $\sim$ 2 TeV, independently of λ. The LHC will thus probe the mass domain where resonant LQ production could be possible at THERA. This statement remains valid in 'generic' models, where the branching ratio $\beta(\mathrm{LQ} \to eq)$ of the LQ to decay into eq is not fixed but treated as a free parameter, as shown in Fig. 17b.

	$S_{0,L}$	$S_{1,L}$	$\tilde{S}_{0,R}$	$S_{0,R}$	$S_{1/2,L}$	$\tilde{S}_{1/2,L}$	$S_{1/2,R}$
$S_{0,L}$		β_ν	P_e	P_e			
$S_{1,L}$	β_ν		P_e	P_e		e^+/e^-	
$\tilde{S}_{0,R}$	P_e	P_e		P_p			
$S_{0,R}$	P_e	P_e	P_p				
$S_{1/2,L}$						P_p	P_e
$\tilde{S}_{1/2,L}$		e^+/e^-			P_p		P_e
$S_{1/2,R}$					P_e	P_e	

Table 2.2.1: *Discrimination between LQs with different quantum numbers by using the lepton beam charge (e^+/e^-) or e/p polarisation (P_e, P_p). The nomenclature of [111] has been used to label the different scalar LQ species described by the BRW model, in which the branching ratio β_ν of the LQs is known.*

If a LQ directly accessible at THERA is discovered elsewhere, THERA will be the ideal machine to disentangle the quantum numbers of this resonance and to study its properties, as illustrated in table 2.2.1: the angular distribution of the final-state lepton easily discriminates between a scalar or vector resonance; the fermion number is obtained by comparing the signal cross section in e^+p and e^-p collisions; the polarisation P_e of the lepton beam determines the chirality structure of the LQ coupling. In addition, the fact that a signal in the CC channel could also be observed provides another

discriminating variable in LQ models where the branching ratio $\beta_\nu = \beta(\mathrm{LQ} \to \nu q)$ is known. Further discrimination between LQs coupling to eu or ed would need e.g. proton beam polarisation, P_p [112].

Finally, THERA allows direct measurements of LQ couplings in the range 10^{-1}–10^{-2} for given LQ branching ratios. In contrast, pp and $p\bar{p}$ colliders are only sensitive to larger couplings via lepton-pair production induced by t-channel LQ exchange.

2.2.3.2 Contact interactions

The sensitivity of THERA to generic $eeqq$ four-fermion contact interactions (CI) has been studied in detail. Besides the exchange of very massive LQs, such CI terms can be used to parameterise any new physics process (e.g. exchange of new bosons, compositeness) appearing at an energy scale above the centre-of-mass energy. At THERA, $eeqq$ four-fermion terms would interfere (constructively or destructively) with NC DIS and thus affect the measured NC DIS Q^2 distribution. Various CI models can be considered, depending on the chiral structure of the new interaction and on the flavours of the involved quarks. CI models which violate parity are already severely constrained by the precise measurements of atomic parity violation. For models conserving parity, scales up to $\sim 18\,\mathrm{TeV}$ could be probed at THERA, extending considerably beyond the existing bounds. The LHC collider should be able to probe even larger scales. However, should an $eeqq$ CI be within its reach, THERA would give deeper insights on the chiral structure of this new interaction by exploiting the lepton beam polarisation. For general CI models involving all possible flavour and chiral structures, searches at THERA and LHC will be to a large extent complementary.

2.2.3.3 Large extra dimensions

The t-channel exchange of Kaluza–Klein gravitons in models with large extra dimensions [113] would also affect the Q^2 distribution of the observed NC DIS events. Compactification scales up to $\sim 2.8\,\mathrm{TeV}$ could be probed at THERA. However, the existence of extra dimensions corresponding to much larger scales should be detected by the analysis of dijet events at the LHC. It has been conjectured that fermions with different gauge quantum numbers are localised on different 'branes' in the full space-time [114]. For accessible compactification scales, relevant and complementary information on this fermion localisation could be provided by TESLA and THERA, in contrast to the LHC, where the two-gluon initial state would dominate the cross section.

2.2.3.4 Excited leptons

The single production of excited leptons (electrons, e^*, and neutrinos, ν^*) at THERA can proceed via the t-channel exchange of a gauge boson. Assuming an equal coupling, f, of the e^*e pair to $U(1)$ and $SU(2)$ bosons, the expected sensitivity to f/Λ has been studied as a function of the e^* mass M_{e^*} (here Λ denotes the compositeness scale [115]). For $f/\Lambda = 1/M_{e^*}$, excited electrons could be detected up to masses of $\sim 1\,\mathrm{TeV}$ at THERA with a luminosity of $200\,\mathrm{pb}^{-1}$ and beam energies of $800\,\mathrm{GeV}$.

A similar sensitivity is expected for excited neutrinos. This extends far beyond the current bounds of HERA and LEP. Pair production of e^* and ν^* at the LHC should probe this mass domain independently of the unknown couplings.

2.2.4 Resolving the partonic structure of the photon

In high-energy processes, the photon exhibits a "hadronic structure". At low Bjorken x, the photon structure function $F_2^\gamma(x, \hat{Q}^2)$ is expected to behave like the proton F_2, i.e. to increase towards lower x at sufficiently large $\hat{Q}^2$, where $\hat{Q}^2$ is the scale used to probe the quasi-real photon. Unique expectations for the photon are the logarithmic rise of the hadronic structure function with the scale, $\hat{Q}^2$, and a large quark density at large x. Observations of these phenomena are basic tests of QCD and essential to understanding the structure of the photon.

The ep collider THERA offers the opportunity to study the partonic structure of the photon in terms of the variable x_γ, which measures the fraction of the photon momentum participating in the hard interaction. At lowest order, x_γ is equal to unity for 'direct process' (Fig. 18a), whereas 'resolved processes' (Fig. 18b) are characterised by a smaller x_γ. THERA extends the kinematic range in x_γ by approximately one order of magnitude towards smaller values with respect to existing colliders (HERA and LEP) and significantly increases the accessible hard scale $\hat{Q}^2 = p_T^2$, i.e. the square of the parton transverse momenta (corresponding to Q^2 in deep inelastic $e\gamma$ scattering).

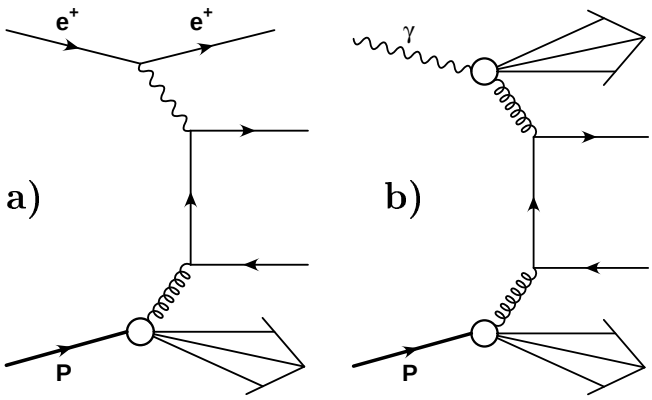

Figure 18: *Examples of LO (a) direct photon and (b) resolved photon processes in ep collisions.*

Photoproduction ($Q^2 < 1\,\mathrm{GeV}^2$) of particles (hadrons or prompt photons) or jets at high transverse momenta provides information on the gluonic content of the quasi-real photon (Fig. 18b), complementary to that from deep inelastic $e\gamma$ scattering. The photoproduction of dijets, heavy quarks and prompt photons has been studied [92, 116, 117], with the emphasis on the potential of THERA to yield information on the structure of the real photon. The possibility of measuring the structure of the virtual photon at THERA has also been considered [118]. In addition, it has been demonstrated that a first determination of the spin structure of the photon at THERA appears feasible for luminosities significantly exceeding $\mathcal{O}(10\,\mathrm{pb}^{-1})$ [119].

Good knowledge of the hadronic interactions of the photon is important for future

high energy physics investigations, e.g. for determining the Standard Model background in searches for new particles. The present situation is not satisfactory, as data for some processes, such as photoproduction of dijets at HERA, are not in agreement with existing NLO QCD calculations [120, 121]. The level of agreement for processes involving resolved virtual photons is even more problematic.

2.2.4.1 Kinematics and comparison with other colliders

A first estimate of the benefits of THERA can be obtained by comparing the kinematic reach of THERA ($\sqrt{s} \approx 1\,\mathrm{TeV}$) with that of LEP ($\sqrt{s} \approx 200\,\mathrm{GeV}$), HERA ($\sqrt{s} \approx 300\,\mathrm{GeV}$) and a future linear e^+e^- collider, TESLA, ($\sqrt{s} \approx 500\,\mathrm{GeV}$). Of interest for this section are the minimal accessible x_γ,

$$x_\gamma^{\min}\Big|_{e^+e^-} = \frac{p_T e^{\pm\eta_{\mathrm{CM}}}}{2E_e - p_T e^{\mp\eta_{\mathrm{CM}}}}\,, \qquad x_\gamma^{\min}\Big|_{ep} = \frac{E_p p_T e^{-\eta_{\mathrm{LAB}}}}{2E_e E_p - E_e p_T e^{\eta_{\mathrm{LAB}}}}\,, \tag{2.2.6}$$

the range of the hard scale, $\hat{Q}^2$, and the pseudorapidity, η, of the jets in resolved-photon events which determines the geometrical acceptance of the detector.

In Fig. 19a, the minimum photon momentum fraction, $x_\gamma^{\min}$, for a fixed transverse momentum of $p_T = 10\,\mathrm{GeV}$, is shown as a function of the laboratory-frame pseudorapidity for e^+e^- and ep colliders. It can be seen that for a given η, THERA accesses $x_\gamma^{\min}$ values that are an order of magnitude smaller than at HERA. The minimum x_γ at TESLA would also be beyond the reach of LEP and HERA. However, smaller values of x_γ can be accessed at THERA than at TESLA in the very forward direction ($\eta_{\mathrm{LAB}}^{ep} > 2$), reaching a minimum for the given transverse momentum at $\eta_{\mathrm{LAB}}^{ep} \approx 4.6$. This demonstrates the need for an instrumentation of the very forward direction at THERA which allows an accurate measurement of jets up to the rapidities discussed here.

The accessible regions in $\hat{Q}^2$ and x or x_γ are shown in Fig. 19b, taking into account restrictions imposed by limited detector acceptance. Typical kinematic selection criteria are imposed, as indicated in Fig. 19b for LEP and HERA. The same cuts have also been applied for the TESLA and THERA studies, although it is hoped that the future experiments would have improved acceptance in the very forward and backward regions. Although the e^+e^- machines will yield the lowest values of x, the ep machines can probe smaller values of x_γ for a given $\hat{Q}^2$. In particular, THERA will provide valuable additional information on the structure of the photon down to $x_\gamma \sim 0.01$ at high p_T, thus complementing TESLA and the current experiments.

2.2.4.2 Jet production

Inclusive dijet and charm production at THERA have been studied and compared with what is currently achievable at HERA [92, 116, 122]. Heavy quark production at THERA is discussed in Sect. 2.2.2.4. Here the focus is on the potential of the THERA collider in testing the partonic content of the photon using jets and heavy quarks as tools. In dijet production, the observable x_γ^{obs}, defined as the fraction of the photon

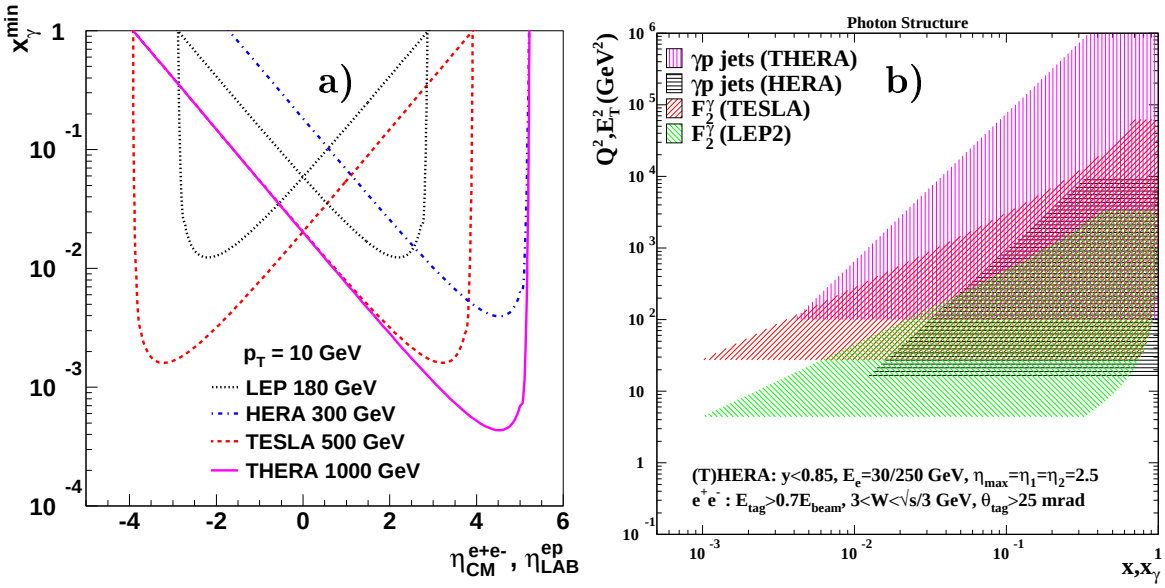

Figure 19: *(a) The minimum photon momentum fraction, $x_\gamma^{\min}$, as a function of the rapidity in the centre-of-mass frame for e^+e^- colliders and in the laboratory frame for ep colliders. (b) Range in $\hat{Q}^2$ (Q^2 or p_T^2) versus x or x_γ with kinematic cuts reflecting a realistic detector acceptance (indicated at the bottom of the figure). The kinematic reach of THERA is compared with that of TESLA, HERA and LEP2.*

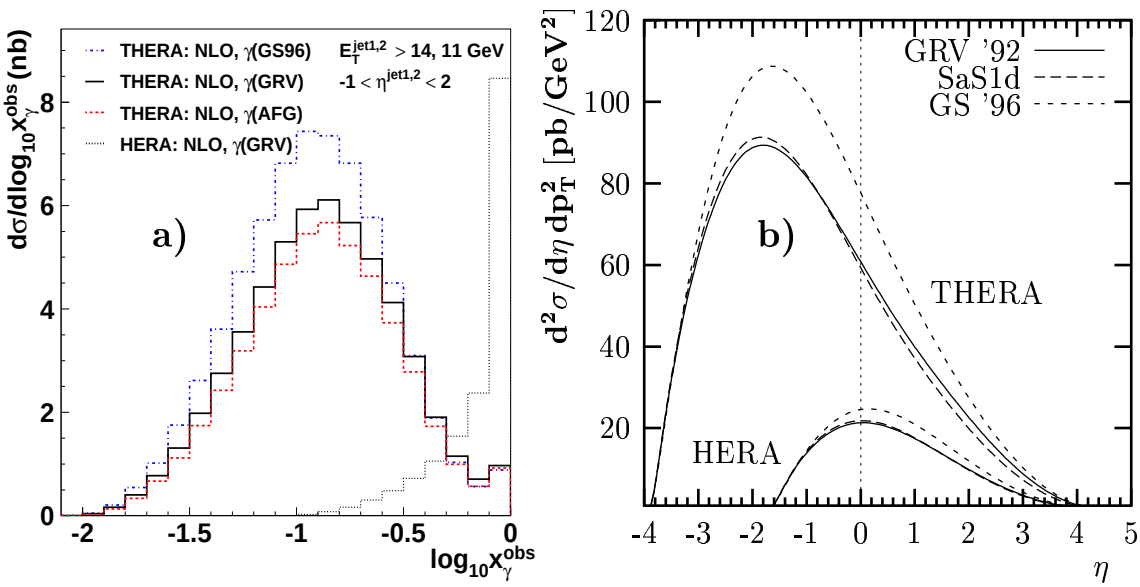

Figure 20: *(a) The differential cross section, $d\sigma/d\log_{10} x_\gamma^{\rm obs}$, for inclusive dijet photoproduction at HERA and THERA as predicted by a NLO calculation. (b) The differential cross section for photoproduction of charm in ep reactions, $ep \to e\, c\bar{c}\, X$, at $p_T = 10$ GeV calculated in LO in the massless (VFNS) scheme.*

energy producing the two jets of highest transverse energy (see eq. 2.2.2), is used as an estimator for x_γ [123]. The cross section $d\sigma/d\log_{10} x_\gamma^{\rm obs}$ in NLO [124, 125] is shown in Fig. 20a. It can be seen that the prediction for HERA is strongly peaked at $x_\gamma^{\rm obs}$ close to unity, whereas the predictions for THERA peak at $x_\gamma^{\rm obs} \sim 0.1$. Differences of up to 50% between the results for different structure function sets [126–130] are observed. The charm cross section $d^2\sigma/d\eta dp_T^2$ from a LO calculation for $p_T = 10\,$GeV is peaked at $\eta \approx 0$ for HERA and at $\eta \approx -2$ for THERA (see Fig. 20b). The cross section maximum at THERA is enhanced by a factor of about 5 as compared to HERA. Again, some sensitivity to the choice of the photon parton parametrisation is evident. For THERA, the cross section ratio of resolved to direct photoproduction of charm exceeds unity at $\eta > -3.5$ and rapidly increases with growing η (see Fig. 21).

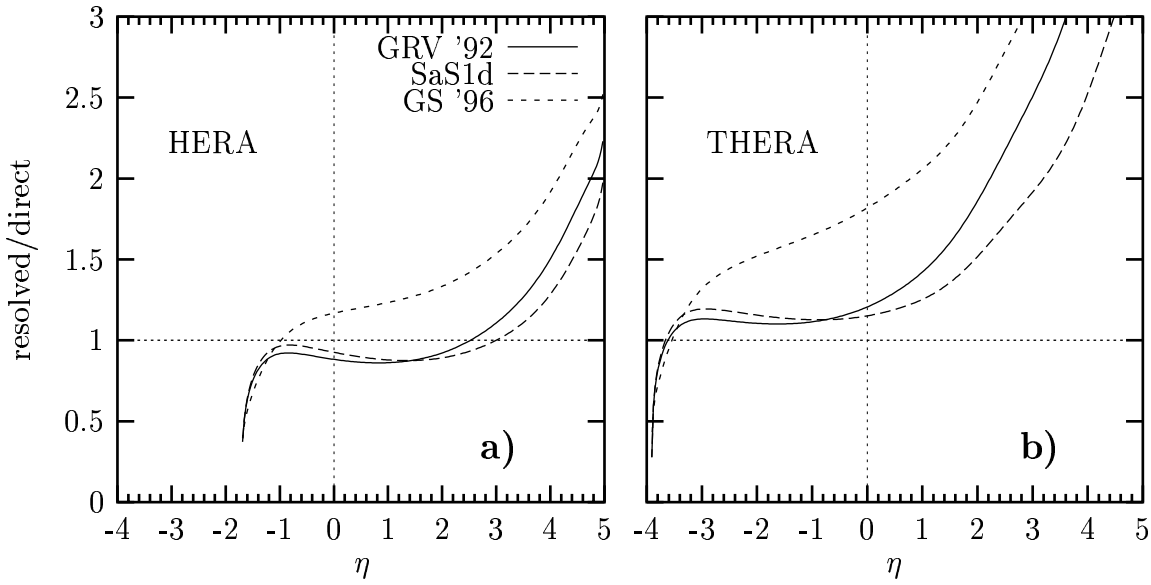

Figure 21: *The ratio of the resolved to the direct contributions to the charm photoproduction cross sections $d^2\sigma/d\eta dp_T^2$ in ep reactions at $p_T = 10$ GeV, (a) for HERA and (b) for THERA. The cross sections have been calculated to LO in the massless (VFNS) scheme, using the CTEQ5L parton distribution set for the proton and three different LO parton distribution sets for the photon.*

2.2.4.3 Prompt photon production

Prompt photon photoproduction, $ep \to \gamma X$ (the deep inelastic Compton scattering process), allows the photon structure to be studied in yet another way [117]. For example, calculations demonstrate that in the forward region ($\eta_\gamma > 0$) the Compton process is dominated by the reaction ($gq \to \gamma q$) with a cross section nearly ten times larger than at HERA and extending to larger transverse momenta of the photon. Thus prompt photon production will allow the gluonic content of the photon to be probed.

2.3 Experimentation at THERA

2.3.1 Collision of TESLA electrons with HERA protons

The achievable luminosity for THERA, the TESLA–HERA electron proton collider, is constrained by the electron beam power, the intra-beam scattering which limits the emittance of the proton beam, and the β-function of the protons which is achievable within the practical limits of focusing at the interaction point (IP). In the limit of ultra-short bunches and assuming head-on collisions, round beams, and equal transverse beam sizes for electrons and protons at the crossing point, the luminosity L is given by

$$L = \frac{N_e N_p f_b \gamma_p}{4\pi \varepsilon_p \beta^*} \,, \tag{2.3.1}$$

where ε_p is the normalised proton beam emittance or mean square beam size divided by the betatron parameter β^*, N_e and N_p are the numbers of electrons and protons per bunch, f_b is the collision frequency, and γ_p is the proton Lorentz factor. Once the energy of the electron beam is chosen, the total electron beam current ($I_e = N_e \cdot e \cdot f_b$) is limited by the allowed electron beam power or $I_e = e \cdot P_e/E_e$. The luminosity L is independent of the bunch charge N_e and the collision frequency f_b as long as their product, expressed by the beam power P_e, is constant. The luminosity can thus be written in the following form:

$$L = 4.8 \times 10^{30}\,\mathrm{cm}^{-2}\,\mathrm{s}^{-1} \cdot \frac{N_p}{10^{11}} \frac{10^{-6}\,\mathrm{m}}{\varepsilon_p} \frac{\gamma_p}{1066} \frac{10\,\mathrm{cm}}{\beta^*} \frac{P_e}{22.6\,\mathrm{MW}} \frac{250\,\mathrm{GeV}}{E_e} \,. \tag{2.3.2}$$

2.3.1.1 Proton phase space density

The ratio N_p/ε_p is called beam brightness. In conjunction with a certain bunch length and energy spread of the protons it is a measure of the phase space density. The beam brightness is limited by space charge forces in the low-energy part of the accelerator chain. But also at high energy, the beam brightness is subject to slow decay due to Coulomb scattering of protons within the bunch, the so-called intra-beam scattering (IBS) [131], which, in the presence of dispersion, leads to emittance growth. The limitation of beam brightness depends on the longitudinal charge density and thus on the bunch length σ_p. This is, however, also a critical parameter at collision since it limits the effective size of the proton beam at the IP. For long bunches (large σ_p compared to β^*), collisions occur at significantly increased cross sections due to the quadratic increase of β as a function of the distance s from the IP (hourglass effect). In addition, the finite bunch length reduces the effective proton beam cross section in case of a crossing angle. For given radio-frequency (RF) focusing forces, the bunch length is given by the longitudinal emittance, which is also subject to limitation by space charge effects at low energy and to slow growth due to IBS at high energy. Due to practical limitations of the RF focusing system and dynamical stability considerations, there is only a limited range for optimising the bunch length within these constraints. At low energy, one wants to maximise the bunch length to achieve maximum brightness. At

high energies, at collisions, one wants minimum bunch length to achieve the minimum effective beam cross section.

Taking these general limitations into account, an IBS growth time of 2.9 hours results for a 1 TeV proton beam in HERA with an initial transverse normalised emittance of $\varepsilon_p = 1 \times 10^{-6}$ m, an initial bunch length of $\sigma_p = 10$ cm, and an initial relative energy spread of $\sigma_{p\epsilon} = 1.1 \times 10^{-4}$. The longitudinal growth time is just 2 hours. This determines the luminosity lifetime and must be considered as an upper limit for the proton density. In order to achieve smaller proton beam emittance, emittance cooling is required. For example, to reduce the emittance by a factor of five, cooling times of 12 min must be achieved to balance the IBS emittance growth. Up to this point, no such powerful cooling systems are available. This leads to the conclusion, that a proton beam normalised emittance in the order of $\varepsilon_p = 1 \times 10^{-6}$ m with $N_p = 10^{11}$ has to be considered as a minimum for HERA. It represents quite a challenge to achieve the corresponding beam brightness in the injector chain. At present, the best beam brightness values achieved in the DESY III synchrotron are in the range of $N_p/\varepsilon_p = 1.3 \times 10^{11}/3 \times 10^{-6}$ m [132] which falls short by a factor of 2.3 to the target value of $10^{11}/10^{-6}$ m. Electron cooling in the lower energy stages [133] may be necessary to achieve the target value. Active feedback to damp injection oscillations might be needed in the higher energy stages. The conclusion is that the target values of $N_p = 10^{11}$, $\varepsilon_p = 10^{-6}$ m, $\sigma_p = 16$ cm and $\sigma_{p\epsilon} = 1.1 \times 10^{-4}$ constitute an ambitious but maybe not unrealistic goal for the phase space density of an LC–ring electron–proton collider at HERA.

2.3.1.2 Interaction region layout

Small values of the β-function β^* at the IP are essential for high luminosity. The β-function is limited by the chromaticity of the protons which is generated in the low-β quadrupole magnets, by aperture limitations in connection with a maximum achievable field gradient in the quadrupole magnets and by the proton bunch length. As chromaticity and maximum beam size grow linearly with the final focus quadrupole distance from the IP, for fixed β^*, it is desirable to focus electrons and protons simultaneously, thereby minimising the distance of the quadrupole magnets to the IP. At 1 TeV proton energy, the bunch length should be 10 cm or longer for adequate IBS life times. In addition, in order to avoid the excitation of synchro-betatron resonances of the protons by the electrons the crossing angle must be limited to a few mrad. This is supported by recent tracking calculations [134]. Additional beam separation technique is thus required, possibly using soft magnetic separation.

Figure 1 shows a component layout and the resulting envelope functions that meet the requirements. The layout has been designed for a ratio of proton to electron energies of 1 TeV/300 GeV and is taken from previous work on electron–proton colliders based on a LC–ring combination [135]. The electron beam is focused by a superconducting quadrupole triplet which is placed at 5 m from the IP and two doublets which give a β^* of 97 cm at the IP and also low β at 25 m and 50 m from the IP. At these latter positions strong quadrupoles for the protons are placed which, because of the low

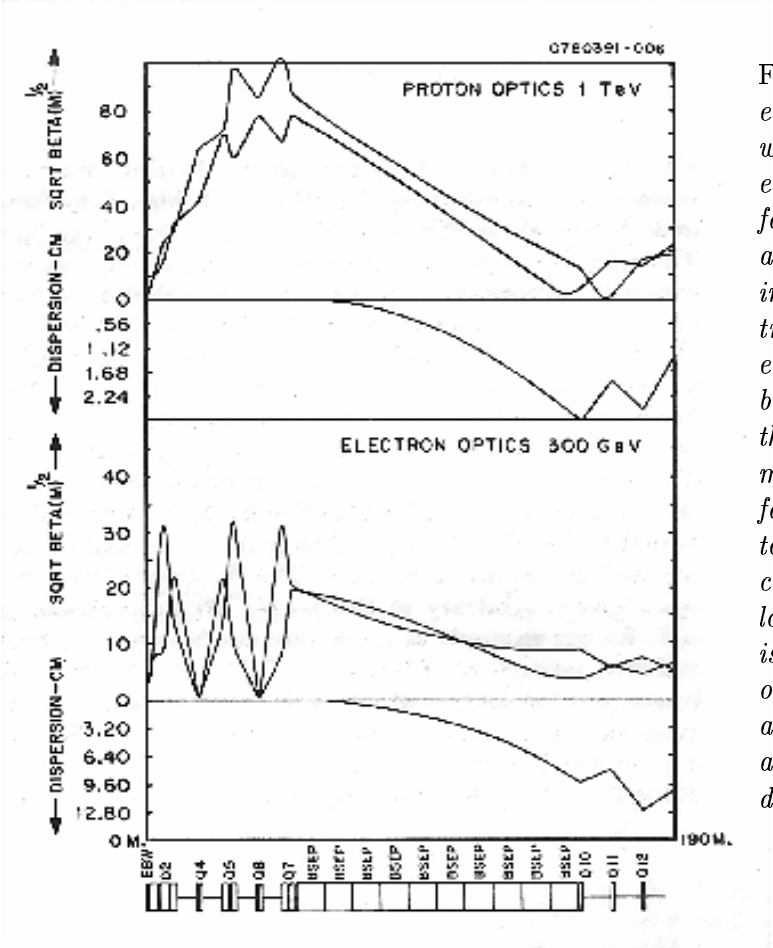

Figure 1: *Possible layout for an electron–proton interaction region, which works for proton/electron energy ratios between one and four. The case for* 1 *TeV protons and* 300 *GeV electrons as presented in [135] is shown. One quadrupole triplet and two doublets focus the electron beam strongly. At the beam envelope waists in between these lenses, strong quadrupole magnets are placed which help to focus primarily the protons. After the two beams are properly focused, at* 70 *m from the IP, a long soft quadrupole magnet, which is aligned along the electron beam orbit, smoothly bends the protons away. This arrangement avoids any extra upstream synchrotron radiation by the beam separation.*

electron β there, have minimum influence on the electrons while effecting a β^* of 10 cm for the protons. The quadrupole gradients are 150 T/m, the lengths of the quadrupoles vary between 2 and 4 m to achieve a good optical match. An aperture of 30 mm appears to be technically feasible but very challenging since it requires peak fields of 9 T. The beta function of the protons reach values of 1000 m at the maximum in the low-beta quadrupoles. This corresponds to ten standard deviations of the proton beam size and appears to be acceptable based on HERA operational experience. A 100 m long separator magnet, which is placed at 60 m distance from the IP, acts to separate the two beams. It is a soft, defocusing quadrupole ($G = 10$ T/m) which is aligned along the electron orbit while the protons pass off-centre and receive a deflection. A tiny crossing angle of 0.05 mrad avoids the first parasitic crossing at 65 m and provides the required small initial pre-separation of the two beams. This arrangement avoids any extra upstream synchrotron radiation by the beam separation magnets. It is remarkable, that this scheme is very flexible as far as the energy ratio of the beams is concerned. It allows to separate beams with a ratio of beam energies between one and four.

The electron beam is focused by the beam–beam interaction at the IP as well as the outgoing lenses. Inclusion of the beam–beam interaction in the linear optics shows that the e-beam is still well behaved on its way out. Full separation is achieved at 50 m from the IP.

The trajectory of the TESLA beam line is planned to be tangential to the HERA Straight Section West. The beam separation scheme is designed such that no bends in the electron beam lines are necessary for the incoming electron beam. However, the outgoing protons receive a kick of 14 mrad and a radial displacement of 468 mm. This could be compensated by disabling the first superconducting dipole magnet for the outgoing protons, accompanied by a small correction kick of 1 mrad and a radial shift of the IP by approximately 524 mm away from the centre of the ring. The final geometry of the TESLA tunnel and beam line should take this into account. The outgoing electrons are allowed to receive a bending angle which would shorten the separation section on the other side considerably. The additional space made available in this way is needed to restore the proton orbit for incoming protons, making use of the now available dipole magnet from the other side. A complete layout of the geometry has not yet been designed.

2.3.1.3 Luminosity estimate

In Table 2.3.1, the parameters of an (e-LC)-(p-ring) collider based on TESLA and HERA parameters are summarised. In calculating the luminosity, the limitations in β and proton beam brightness as discussed in the previous sections as well as the hourglass effect and the effect of a crossing angle have been taken into account. Assuming a bunch length of 10 cm to be possible, the hourglass reduction factor is 0.9. Even a tiny crossing angle of $\theta = 0.05$ mrad changes the cross section and thus the luminosity by 6%. Combining all these numbers yields a luminosity of $L = 4.1 \times 10^{30}\,\mathrm{cm}^{-2}\,\mathrm{s}^{-1}$ when operating TESLA at $E_e = 250$ GeV and HERA at $E_p = 1$ TeV. In a year of running this luminosity corresponds to about $40\,\mathrm{pb}^{-1}$ assuming an efficiency of 60% and 200 days of operation.

If THERA is operated with equal electron and proton energies, the focusing could be made much more efficient. Such an energy setting is not favourable for low x physics because the electron would be scattered even closer to the electron beam direction than in the asymmetric energy case. This constraint, however, is not important for high-Q^2 studies, for which, on the other hand, maximising the luminosity is of utmost importance.

With equal beam energies, a single low-beta doublet could be used to focus the beam to beta functions as small as 1 cm. The superconducting quadrupole magnets need to have a length of $l = 3$ m, and would be placed starting at 2 m from the IP. An aperture of 20 mm would correspond to 10 times the r.m.s. beam size in these magnets. A peak field of 5 T would be required to produce the gradients needed in this setup. The magnet cryostat would have an estimated outer diameter of 40 cm. The detector would have to provide space for these magnets by giving up small-angle detector acceptance. The strong hourglass effect in this situation, with 16 cm bunch length and 1 cm beta function, must be overcome following a proposal by Dohlus and Brinkmann [136] which features a moving β-waist around the IP due to time-dependent focusing by introduction of RF quadrupoles. This way, the minimum β-function occurs at the location and time where the e-beam collides with a slice of the proton beam

electron beam parameters	
electron energy	$E_e = 250\,\mathrm{GeV}$
number of electrons per bunch	$N_e = 2 \times 10^{10}$
bunch length	$\sigma_{se} = 0.3\,\mathrm{mm}$
invariant emittance	$\varepsilon = 100 \times 10^{-6}\,\mathrm{m}$
beta function at IP	$\beta_{x,y} = 0.5\,\mathrm{m}$
electron tune shift	$\Delta\nu_y = 0.228$
disruption	$D = 0.02$
bunch spacing	$t_{be} = t_{bp} = 211.37\,\mathrm{ns}$
RF frequency	$f = 1301\,\mathrm{MHz}$
accelerating gradient	$g = 23.4\,\mathrm{MV/m}$
beam pulse length	$T_p = 1.19\,\mathrm{ms}$
number of bunches	$56 \times (94 + 6$ empty bunches$)$
duty cycle	$d = 0.5\%$
repetition rate	$f_r = 5\,\mathrm{Hz}$
beam power	$P_b = 22.6\,\mathrm{MW}$
proton beam parameters	
proton energy	$E_p = 1\,\mathrm{TeV}$
number of protons per bunch	$N_p = 10^{11}$
number of bunches	$N_{pb} = 94$
beam current	$I_p = 71\,\mathrm{mA}$
bunch length	$\sigma_p = 10\,\mathrm{cm}$
beta functions at IP	$\beta^*_{xp} = 10\,\mathrm{cm}$
normalised emittance	$\varepsilon_p = 1 \times 10^{-6}\,\mathrm{m}$
IBS growth time transv./long.	$\tau_s = 2.88\,\mathrm{h}, \tau_x = 2.0\,\mathrm{h}$
collider parameters	
hourglass reduction factor	$R = 0.9$
crossing angle	$\theta = 0.05\,\mathrm{mrad}$
luminosity	$L = 4.1 \times 10^{30}\,\mathrm{cm}^{-2}\,\mathrm{s}^{-1}$

Table 2.3.1: *Main parameters of an electron–proton collider based on HERA and TESLA.*

and the beam size remains uniform during the whole collision time. In the horizontal plane, the beam size would be dominated by the crossing angle and the β-function can be relaxed to 3 cm. The luminosity which can be achieved in this scenario is estimated to be $L = 2.5 \times 10^{31}\,\mathrm{cm}^{-2}\,\mathrm{s}^{-1}$ for $E_e = E_p = 500\,\mathrm{GeV}$. This scenario uses both arms of TESLA, which is possible due to the standing-wave type cavities in the superconducting LC. With the TESLA machine upgraded in power, energies as high as 400 GeV per arm are envisaged, which for THERA opens the possibility to run at $E_e = E_p = 800\,\mathrm{GeV}$. This provides a maximum energy in *ep* scattering of $\sqrt{s} = 1.6\,\mathrm{TeV}$ at an estimated luminosity of $1.6 \times 10^{31}\,\mathrm{cm}^{-2}\,\mathrm{s}^{-1}$. Thus with equal beam energies and a dynamic focusing system, integrated luminosities of about $200\,\mathrm{pb}^{-1}$ per year are in reach for THERA.

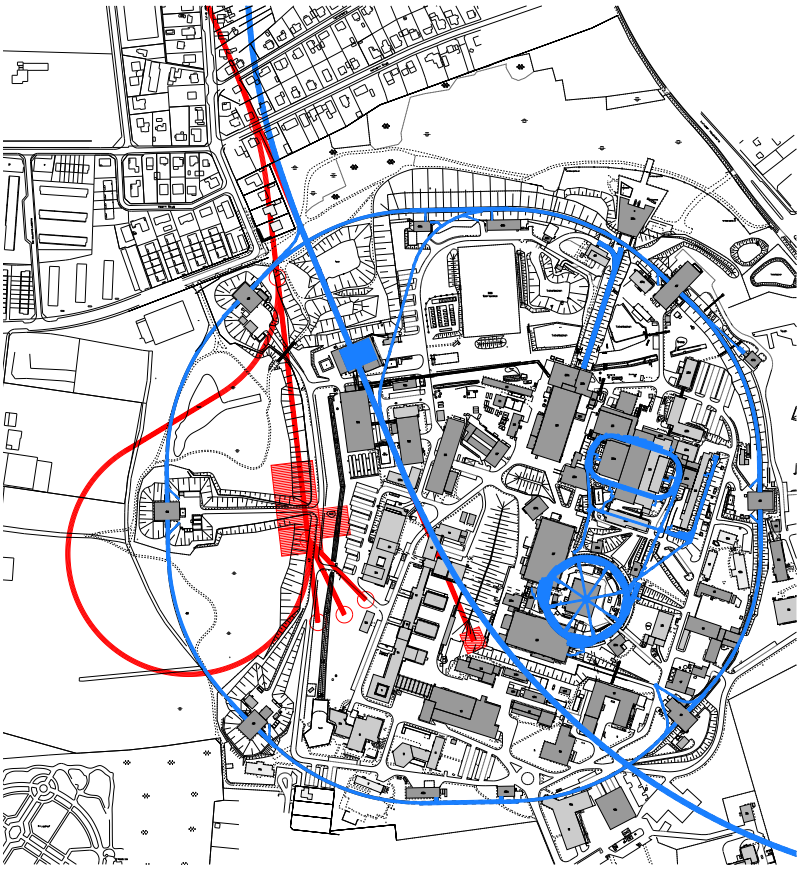

Figure 2: *Site of THERA: TESLA (red) is foreseen to be built tangentially to the HERA ring (blue) such that electrons from North hit protons in the West Hall on the DESY site. The PETRA ring is seen which serves as a pre-accelerator for HERA protons. The PETRA lepton injection line will be instrumented with superconducting magnets to arrange protons travelling clockwise in HERA. After collision the TESLA electrons will be dumped on site.*

2.3.1.4 Auxiliary systems

The THERA accelerator site at DESY is shown in Fig. 2. Electrons or positrons are injected at the far North end into the linac and accelerated up to full energy. A dedicated THERA electron gun and a short injector unit will be necessary. In order to operate the *ep* collider, the protons have to travel clockwise around HERA. For injecting the proton beam, the current lepton injection line has to be used, whose strong bends require superconducting magnets for a 40 GeV proton beam. The slope of the line is a problem for the cryogenic supply of these magnets, which however can presumably be solved. The electron beam lines into and out of HERA require civil engineering work including two long slits of the HERA tunnel. A beam dump similar to the TESLA beam dump has to be foreseen, which would fit on the DESY site. Two types of superconducting quadrupoles for the new interaction region have to be provided with five magnets each and cryogenic supply. Beam pipes, support, power supplies, beam diagnostics and controls are required. In addition, faster kicker magnets are needed to provide the desired bunch spacing. In order to achieve the envisaged beam brightness, electron cooling in PETRA will most likely be required.

2.3.2 A detector for THERA

The electron–proton scattering kinematics governs the design of the THERA detector. Roughly speaking, there are three detector regions which have to match different requirements: the forward[5] part, where the final-state energies are limited by the proton beam energy, E_p; the central part, where particles with transverse momenta up to $\sqrt{s}/2$ can be produced; the backward part, where the final-state energies are limited by the electron beam energy, E_e. The forward part thus has to match similar criteria as at HERA, whereas the backward part has to cope with much higher energies. The central part bridges these two extremes.

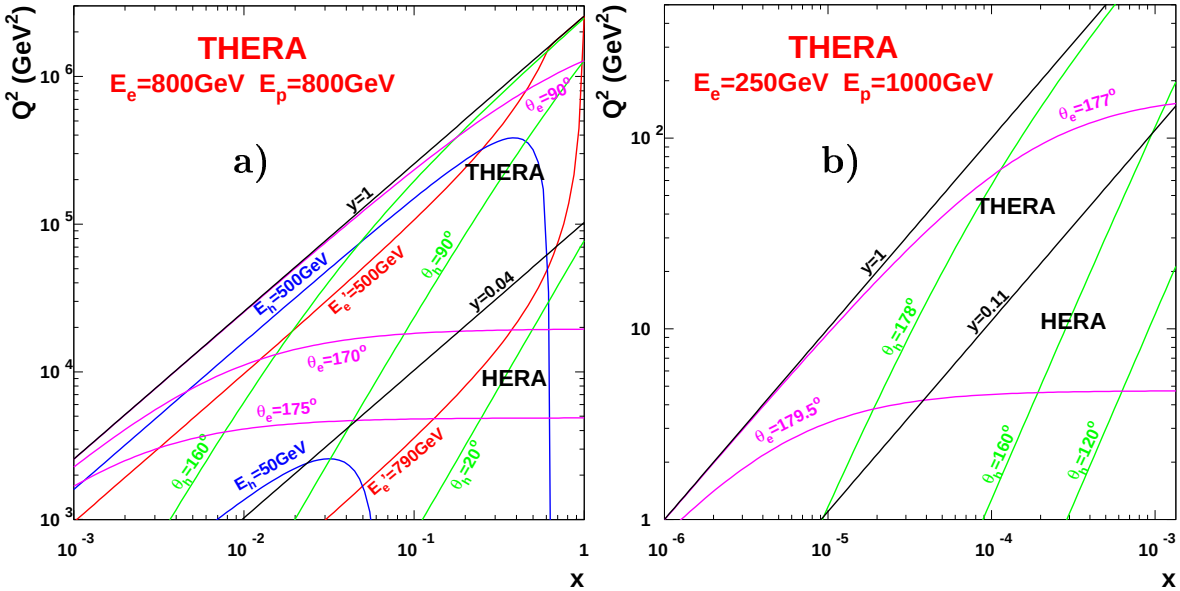

Figure 3: *Kinematic range covered by THERA, (a) at high x and Q^2 for $E_e = E_p = 800\,GeV$ ($\sqrt{s} = 1.6\,TeV$), and (b) at low x and Q^2 for beam energies of $E_e = 250\,GeV$ and $E_p = 1\,TeV$ ($\sqrt{s} = 1\,TeV$). The lines for $y = 0.04$ in (a) and $y = 0.11$ in (b) indicate the kinematic limit of HERA. Lines of constant E'_e (red), E_h (blue), θ_e (magenta) and θ_h (green) are indicated. In (b), E_h and E'_e are given approximately by yE_e and $(1-y)E_e$, respectively. Note that for low x both the electron and the jet are scattered into the backward region, illustrating the strong boost of the electron–quark system in this kinematic region.*

The coverage of the (x, Q^2) plane for DIS at large $Q^2 > 10^3\,\mathrm{GeV}^2$ is shown in Fig. 3a for the maximum THERA centre-of-mass energy envisaged (see Sect. 2.3.1.3). The final-state electrons have energies, E'_e, of hundreds of GeV and are scattered at backward and central angles, θ_e. The current jets emerge at a broad spectrum of angles, θ_h, hitting the forward, central and backward detector parts with energies, E_h, which

[5] A coordinate system is defined according to the HERA conventions, with the origin in the interaction point (IP) and the z axis pointing in the proton beam direction, referred to as forward.

are approaching E_p at highest x and E_e at highest y.

The kinematic properties of low-x reactions are illustrated in Fig. 3a. The most striking features of such events are the very small deflection of the electrons and their large energies of $E'_e \approx (1-y)\,E_e$, exceeding the corresponding values in the HERA backward region by one order of magnitude. As can be seen from this figure, Q^2 values of a few GeV^2 can be accessed only with electron scattering angles close to 180° (θ_e as large as 179.5° is e.g. required to reach $Q^2 = 4E_eE'_e\cos^2(\theta_e/2) \simeq 2\,\mathrm{GeV}^2$ at $y = 0.5$ for $E_e = 250\,\mathrm{GeV}$). Simultaneously, the current jets are also scattered into the backward direction, with energies $E_h \approx y\,E_e$.

The backward region of the THERA detector is therefore of central importance for low-x investigations and has to be newly designed, since the corresponding HERA detector components cannot provide the required energy containment and angular coverage. The extension in z of the very backward detector part (i.e. at largest θ) depends critically on the beam-pipe radius which can be as small as 2 cm because of the absence of synchrotron radiation from bends of the incoming electron beam near the interaction region. The beam-pipe will have exit windows with 2π azimuthal coverage to minimise shower development and multiple scattering.

Based on the experience of experimentation at HERA and a simulations of THERA DIS events and kinematics, a design study of the THERA detector has been performed [137].

The *operation* of the THERA experiment is envisaged in two phases aiming at low-x physics and high-Q^2 physics, respectively. Accordingly, the THERA detector is foreseen to be modular in its structure. Detectors near the beam-pipe and the extended backward part should be removable for high-luminosity operation, which will require the installation of focusing magnets as close as possible to the interaction point. Characteristic parameters of both phases are summarised in Table 2.3.2.

Magnetic field: A homogenous solenoidal magnetic field, extending over almost 10 m in z could be provided by the H1 and ZEUS coils which can be operated at 1–1.5 T. The mechanical stability of such an arrangement and the design of the support structure have not yet been investigated.

The *calorimeter* has to be almost 4π-hermetic in order to be able to reconstruct the longitudinal energy-momentum balance, $E-p_z$, which is essential for DIS event identification and reconstruction. The required energy resolutions are roughly $15\%/\sqrt{E(\mathrm{GeV})}$ for electromagnetic and $40\%/\sqrt{E(\mathrm{GeV})}$ for hadronic energy measurements, with additional constant terms of about 1%. These resolution requirements can be met by presently available calorimeter technology as e.g. employed by the HERA collaborations. In particular, one might consider to equip the forward and central calorimeter regions with the H1 LAr calorimeter, and to use the instrumented iron structure of the H1 detector. The reconstruction of forward-jet final states requires position reconstruction and energy flow measurements down to polar scattering angles of about 1°. Thus, a new calorimeter with enhanced granularity will have to be constructed for the very forward region, i.e. $\theta < 5°$ ('forward plug').

In the backward direction, the calorimeter must be able to provide energy and position measurement for the scattered electrons with energies close to the electron

	low-x configuration	high-Q^2 configuration	
electron beam energy, E_e	250 GeV	500 GeV	800 GeV
proton beam energy, E_p	1 TeV	500 GeV	800 GeV
c.m.s. energy, $\sqrt{s}$	1.0 TeV	1.0 TeV	1.6 TeV
luminosity [$10^{30}\,\mathrm{cm}^{-2}\,\mathrm{s}^{-1}$]	4	25	16
distance focusing magnet – IP	5 m	2 m	2 m
backward electron acceptance	$\theta_e < 179.7°$	$\theta_e < 175°$	$\theta_e < 175°$
forward calorimetric acceptance	$\theta_h > 1°$	$\theta_h > 5°$	$\theta_h > 5°$

Table 2.3.2: *Operation parameters of THERA. The first phase with standard beam energies and luminosity will focus on low-x physics. A subsequent, higher-luminosity phase is envisaged which will concentrate on high-Q^2 physics. In this high-Q^2 phase, both arms of TESLA are used for acceleration of electrons to achieve maximum energy. Note that the maximum Q^2 is given by $s = 4E_eE_p$. Choosing $E_e = E_p$ is favourable for maximising the luminosity (see Sect. 2.3.1). An electron energy of* 800 *GeV energy can be obtained after the TESLA power upgrade, while* 500 *GeV are available already in the first stage of TESLA.*

beam energy, at angles up to 179.7°. Furthermore, hadronic energy measurement and reliable electron/hadron separation are required in the same energy and angular range to fully cover low-x reactions, in which both the electron and the hadronic state are scattered into a narrow cone in the e beam direction (see Fig. 3a). These requirements necessitate a high-resolution, fine-grain calorimeter with sufficient depth to contain electron and hadronic energy deposits of several 100 GeV. Particularly stringent constraints are present for the calorimeter part close to the beam-pipe, which is envisaged to be constructed as a separate module ('backward plug').

Tracking: Tracks will be reconstructed in silicon strip detector telescopes near the beam-pipe and an arrangement of outer tracking detectors. These may consist of a cylindrical central chamber and, for example, of planes of straw-tube or drift-chamber detectors in the forward and the extended backward regions, with hit resolutions of about 150 μm.

Electron identification near $\theta_e = 179.5°$ will be achieved using a combination of the calorimetric information and the data from a track detector which has sufficient resolution to determine the charge of particles with momenta up to E_e and will be positioned in front of the backward plug calorimeter. Low-x charm and beauty physics requires the reconstruction of tracks with momenta of a few GeV at scattering angles up to 179°. It has been verified with simulation studies [138] that the required angular acceptance and momentum resolution can be provided using 6-inch silicon strip detectors with hit resolutions of about 20 μm. These detectors will be arranged in 5-plane modules, which are mounted around the beam pipe and cover the full range of polar and azimuthal angles. The backward tracker response was simulated in some detail, and resolutions of about 15 MeV for the $D^0 \to K\pi$ mass reconstruction and of about

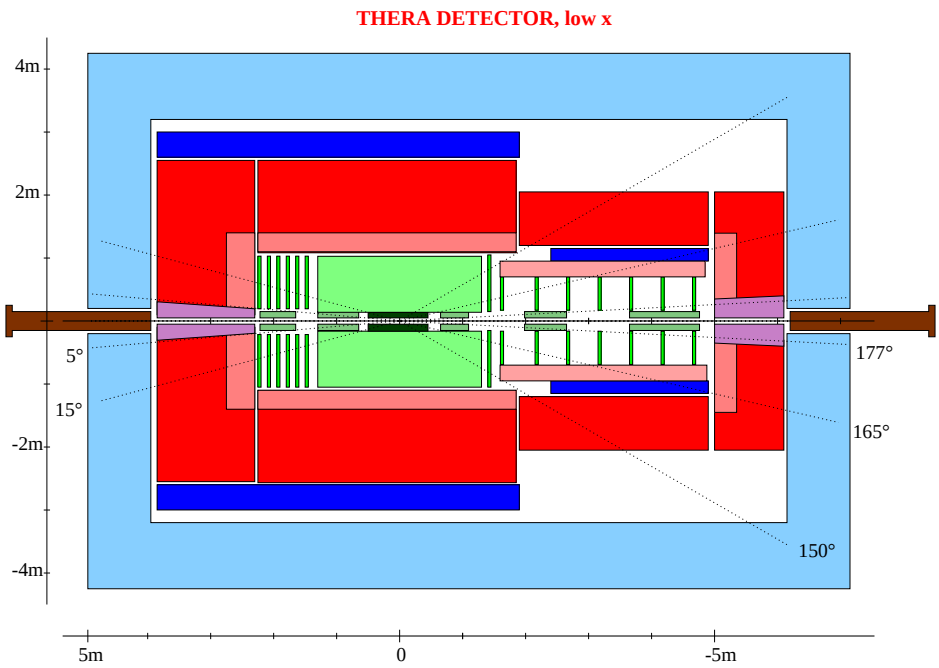

Figure 4: *Basic design of the THERA detector in the low-x configuration. The electrons enter from left, the protons from right. Around the beam-pipe, modules of 6-inch silicon strip detectors are positioned (dark-green). Tracking is complemented by planar and circular track chambers (light-green). Electromagnetic (pink) and hadronic (red) calorimetry ensures hermetic, accurate reconstruction of the final-state energy depositions. A homogenous, solenoidal field over 9 m length is provided by the large-diameter H1 coil and the smaller ZEUS coil (blue). The return yoke iron structure (light-blue) is instrumented for shower tail catching and muon detection. The focusing magnets (brown) are placed near the plug calorimeters (magenta).*

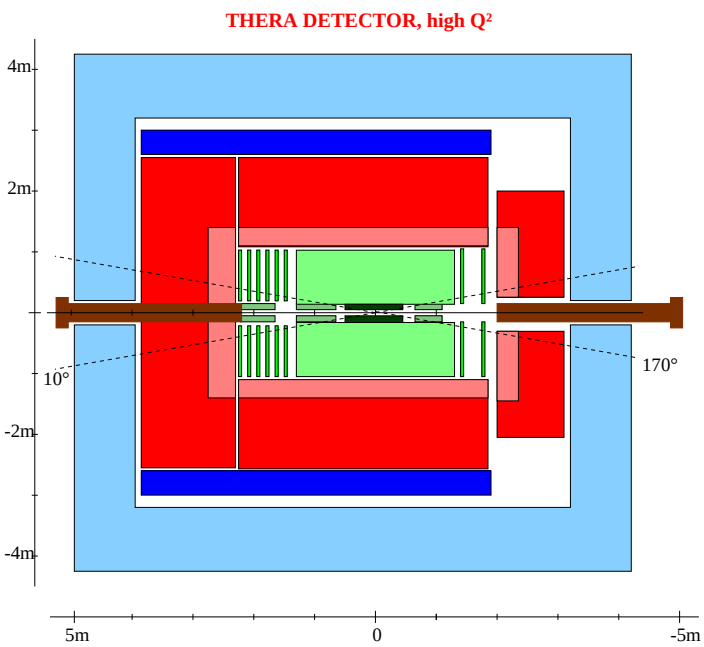

Figure 5: *Basic design of the THERA detector in the high-Q^2 configuration. This detector is similar in its basic layout to Figure 4, with the backward detector part and the ZEUS coil removed and the iron structure shortened correspondingly. Removal of the large/small angle trackers and the forward/backward plug calorimeters permits the focusing magnets to be placed much nearer to the interaction point than in the low-x phase.*

0.5 MeV for the $D^* - D^0$ mass difference were obtained. The tiny transverse size of the interaction spot (roughly 20 μm diameter) is of great advantage for momentum measurement and in particular for tagging heavy-flavour decays by reconstructing impact parameters and secondary vertices.

Muon chambers outside the calorimeter are required in the full acceptance range of the detector, preferentially also backwards at small angles for heavy-flavour physics.

Tagging of electrons and photons in the electron beam direction is necessary for luminosity measurements, control of radiative corrections and for identifying photoproduction events, in particular in the context of exclusive measurements. The detection of protons and neutrons in the proton beam direction is needed, or at least supportive, for investigations of diffractive reaction channels. It appears feasible to include these different tagging detectors in the interaction region; however, no effort has been made to design them at this stage.

It is concluded that low-x physics at THERA, while representing the challenge of measuring the scattered electron so close to the beam-pipe, can be studied with a detector design following the above considerations, as shown in Fig. 4. The design is sufficiently modular to allow for a detector reconfiguration suitable for the THERA high-Q^2 phase (see Fig. 5).

The construction of the THERA detector can be based on the large experience with the collider detectors at HERA and is not expected to exceed their cost.

2.4 Further Options

2.4.1 Electron–nucleus scattering

Deep inelastic scattering of nuclei is a classical way of studying the space-time picture of strong interactions, (see [139] for a recent review). So far DIS data on nuclei are only available for $x \gtrsim 0.003$, see e.g. Fig. 1 (reproduced from [139]).

The prime motive for using nuclear beams at THERA is to advance much deeper into the region of high parton densities than it would be possible in the electron–proton mode. Based on the dependence of various observables on the nucleon number, A, measurements at THERA would provide decisive tests and a number of valuable cross checks of various ideas about the QCD state in the high-density limit (for a summary see [141–143]). Effects to be investigated would include the saturation of gluon and quark densities [144, 145] (discussed in Sect. 2.2.1) or a large reduction of the nuclear gluon density [146], g_A, as compared to the incoherent sum $g_A = Ag_N$ of the individual nucleon densities, g_N (*leading-twist shadowing*). Indeed, the small-x gluon densities per unit area at central impact parameters in nuclei (i.e. at small transverse distances from the centre of the nucleus) are enhanced as compared to the nucleon case by a factor $(g_A/\pi R_A^2)/(g_N/\pi r_N^2) \approx A^{1/3} g_A/Ag_N$, which is as large as 6 for $A = 200$ if $g_A \approx Ag_N$ is assumed. The unitarity constraint (see eq. 2.2.1 for a nucleon target), requiring that the total inelastic cross section of the interaction of a small dipole with the nucleus cannot exceed πR_A^2 (*the black body limit*), implies the presence of large screening effects and nonlinear dynamics in eA scattering at THERA. In particular,

it implies that in the interaction of small colour-octet dipoles with nuclei at central impact parameters the gluon density per nucleon (i.e. the ratio of the gluon density averaged over a small range of central impact parameters and the number of nucleons, $A_{\rm eff}$, in the corresponding nuclear volume) cannot exceed [16, 147]

$$\left.\frac{xg_A(x,Q^2)}{A_{\rm eff}}\right|_{\rm central} \leq 3A^{-1/3}Q^2\,({\rm GeV}^2) \overset{A=200}{\approx} 0.5\,Q^2\,({\rm GeV}^2)\ . \qquad (2.4.1)$$

Note that this ratio would be equal to xg_N if the nucleon fields would add incoherently. The upper bound in eq. 2.4.1 can be compared e.g. with $xg_N(x{=}10^{-3}, Q^2{=}4\,{\rm GeV}^2) \geq 5$ in the current parton distribution fits. One concludes that strong modifications of the gluon field in heavy nuclei (as compared to the incoherent sum of the nucleon fields) appear to be unavoidable in a wide (x, Q^2) range to be covered by THERA.

A significant part of these modifications required to satisfy the unitarity constraints is the leading-twist reduction of the gluon and quark parton densities (shadowing) related to the leading-twist diffraction observed at HERA [146]. The rest should be due to nonlinear effects. The kinematic range where nonlinear effects are expected to be large is illustrated in Fig. 2 for scattering of small-size colour-triplet and colour-octet dipoles off nuclei, taking into account the leading-twist shadowing. For central impact parameters the limits are much stronger – the limit for the inclusive scattering off a nucleus with a given A corresponds to the limit at central impact parameters for a nucleus with $A' \approx A/3.5$, so that the inclusive curves for $A = 40$ are the same as the curves for central scattering off carbon (the subtraction of the contribution from scattering at peripheral impact parameters can be performed by studying cross sections for a series of nuclei, e.g. for $A, A/4, \ldots$ [141]). The interaction strength in this domain may reach values close to the black body limit and can be studied at THERA in a wide x range as a function of the parton density (i.e. the number of nucleons at the impact parameter

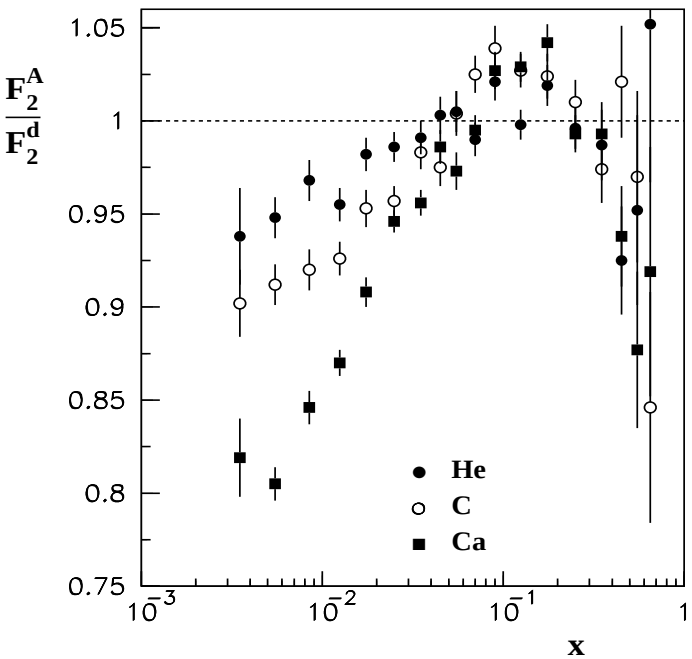

Figure 1: *NMC data [140] for the structure function ratio $F_2^{\rm A}/F_2^{\rm d}$ per nucleon for ^4He, ^{12}C and ^{40}Ca for $Q^2 \geq 0.7\,GeV^2$. THERA would extend these measurements by three orders of magnitude to $x \simeq 10^{-5}$.*

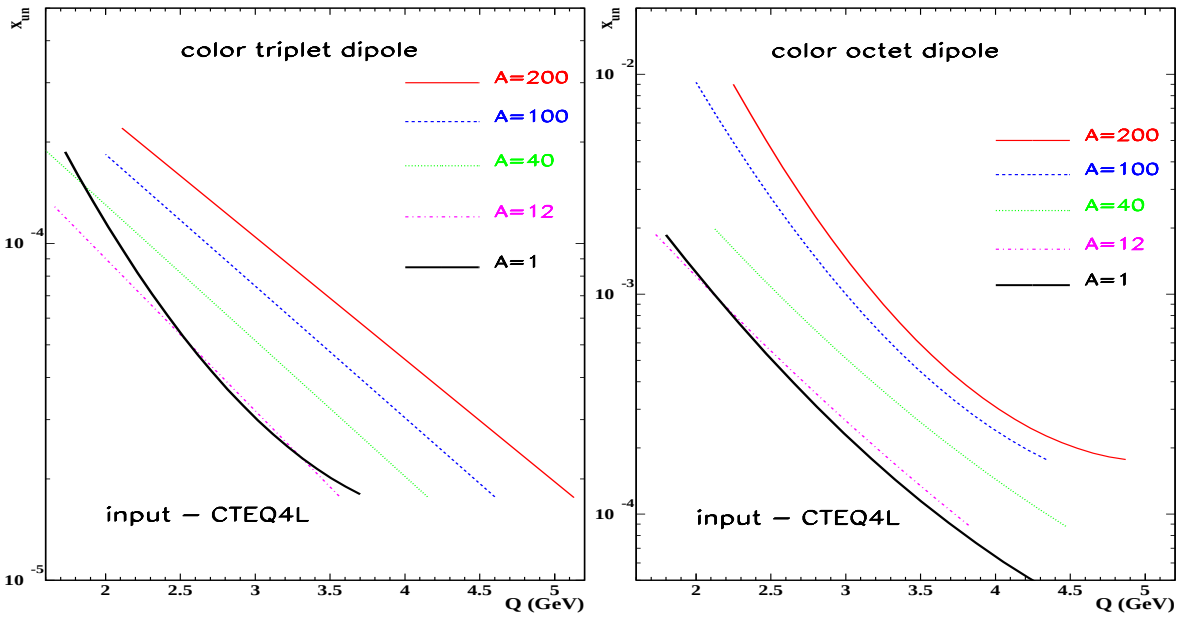

Figure 2: *Unitarity boundaries in the* $(x, \sqrt{Q^2})$*-plane for (a) the inelastic* $q\bar{q}$ *(colour triplet)–nucleus and (b) the* $q\bar{q}g$ *(colour octet)–nucleus cross sections for nuclei with* $A =$ 12, 40, 100 *and* 200. *The unitarity boundaries for the inelastic* $q\bar{q}$*– and* $q\bar{q}g$*–nucleon cross sections are indicated as black solid lines.*

of the probe), which is impossible for the case of *ep* scattering. In a number of models [148, 149] the shadowing in the leading twist is assumed to be small, resulting in a much larger range of (x, Q^2) where nonlinear effects should dominate (see plots in [142]).

One can see from the figure that the measurement of central scattering for $A = 40$ (which requires data from a set of isoscalar nuclei with $A \leq 40$ for the subtraction of the peripheral part) would access limits corresponding to inclusive scattering off nuclei with $A \sim 200$ and hence extend the Q^2 unitarity boundary by a at least a factor of two at x values of $\sim 10^{-4}$. This gain would allow the observation of nonlinear effects in a Q^2 range which is indisputably perturbative, at least for *ep* scattering.

It will be possible to reveal unambiguously the new high-density regime of DIS at small-x eA collisions via studies of a number of inclusive observables and the A-dependence of the properties of the final states. Several gold-plated observables are listed in the following. For illustration, expectations based on the black body limit scenario [16, 147, 150, 151] are considered (which is rather closely related to the saturation scenario [144, 145, 148, 149, 152, 153]), though nonlinear effects could tame the increase of the interaction strength before this limit is reached.

Inclusive observables

In the black body limit, the relation $F_2^A \propto 2\pi R_A^2 Q^2 \ln(1/x)$ holds for $Q^2 \leq Q^2_{\rm bbl}(x)$, where $Q^2_{\rm bbl}(x)$ denotes the maximal value of Q^2 for which the total inelastic cross section of the interaction of a small colour dipole of transverse size $\propto 1/Q$ with a heavy nucleus is equal to the black body limit, πR_A^2. The scale $Q^2_{\rm bbl}(x)$ increases with

A. The measurement of the scaling violation of $F_2^A(x, Q^2)$ provides direct access to the dynamics of the interaction of the small dipoles with nuclei and hence yields detailed information about the relevance of the black body limit for $\gamma^* A$ scattering. Direct tests of the onset of the black body regime in the gluon channel may be possible via measurements of $\sigma_L(eA)$ and the study of dijet production in $\gamma^* A$ scattering.

Another signal for approaching the black body limit would be an A dependence of the transverse momentum (p_t) spectrum of the partons: the average p_t rises with $Q^2_{\rm bbl}(x)$, $\langle p_t \rangle \sim Q_{\rm bbl}$ [148, 149], resulting in an A dependence of the leading hadron spectrum in the current fragmentation region at values of Feynman x close to one: the multiplicity will decrease with A [151] and the average p_t^2 at $x_F \sim 1$ should be proportional to $Q^2_{\rm bbl}$. Such a gross violation of the QCD factorisation theorem for leading hadron production in DIS will provide one of the model independent signals for the onset of the black body regime.

Diffractive observables

For experimental investigations, three classes of diffractive electron–nucleus interactions have to be considered: *diffractive dissociation* with meson production in the nucleus fragmentation region, *nuclear break-up* producing nuclear fragments (mostly neutrons and protons) in the forward direction, and *coherent scattering*, where the nucleus stays intact. The separation of these three classes from non-diffractive reactions is very similar to the selection of diffractive events in the *ep* case. The contribution of diffractive dissociation to the overall diffractive cross section is significantly smaller than in the *ep* case. The experimental signatures for this reaction class are similar to *ep* scattering since the energy flow in the forward direction is expected to have almost the same topology. Calorimetric coverage down to $\theta \lesssim 1°$ in the forward region (see Sect. 2.3.2) will allow the detection of most dissociative reactions. Nuclear break-up is expected to constitute about 10% of the coherent diffraction for a wide range of model parameters. Forward detectors similar to the forward neutron calorimeters (FNC) of the HERA collider experiments will be needed to distinguish these two processes [142].

Inclusive DIS diffraction provides a direct test of how close the interaction is to the black body limit, where the probability of coherent diffraction is close to 50% of the total cross section [150, 154–156]. The same is true for partial cross sections such as for charm production or dijet production in γA scattering. Moreover, since the interaction is stronger in the gluon channel, the diffractive cross section should be close to 50% of the corresponding total cross section in a wider (x, Q^2) range [146]. The differential cross section of diffractive production of states with mass $M_X^2 \leq Q^2_{\rm bbl}$ is also predicted in a model-independent way, see [151]. Another signature of the black body limit is that for $M_X^2 \leq Q^2_{\rm bbl}$ the production of high-p_t jets is strongly enhanced: $\langle (p_t^{\rm jet})^2 \rangle = 3M_X^2/20$.

Exclusive DIS diffraction, the production of vector mesons in the process $\gamma^* + A \to V + A$, provides a clean experimental signature if the V decay products are in the detector acceptance. This will be the case for light vector mesons if either Q^2 or $|t|$ (the square of the momentum transfer at the nucleon vertex) are sufficiently high, and for J/ψ and Υ mesons over the full kinematic range. The separation of coherent and incoherent events will require the same experimental techniques as for inclusive studies

and can in addition make use of the very steep diffractive peak expected for coherent processes. Exclusive DIS diffraction yields a direct answer to the fundamental question: Are heavy nuclei transparent for high-energy small objects like J/ψ or Υ mesons? In the region of $x \sim 0.02$, evidence for colour transparency was obtained [157] by the observation that the coherent J/ψ production amplitude is proportional to $AF_A(t)$, where $F_A(t)$ is the nuclear form factor. This colour transparency regime corresponds to the propagation of a small dipole through a thick target with very small absorption. At small $x \lesssim 0.01$, a qualitatively new phenomenon – colour opacity – is expected: a strong absorption of the small dipoles propagating through the nuclei. In the black body limit the increase of the cross section with A will be reduced to $A^{2/3}$ as compared to $A^{4/3}$ in the colour transparency limit. QCD also predicts the absolute cross section for the vector meson production in the black body limit. The THERA kinematic range would allow for studying the interplay of colour transparency and colour opacity in a wide (x, Q^2) range and distinguishing between various models of shadowing for the interaction of small dipoles. In particular, the eikonal model [144] leads to a much smaller colour opacity effect than the leading-twist models of gluon shadowing based on the dominance of gluons in the diffractive structure functions [146].

Measurements with deuteron beams (which probably can be polarised without installation of Siberian snakes using a novel technique suggested by A. Skrinsky [158]) would allow the investigation of low-x physics in reaction channels which cannot be induced by Pomeron exchange ('non-vacuum channels') by combining inclusive measurements and techniques of neutron tagging [141]. Measurements of non-vacuum exchange would be given by the structure function differences $F_2^p - F_2^n$ or $g_1^p - g_1^n$. Electron–deuteron scattering would also allow an interesting test of the Gottfried sum rule, $\int_0^1 (F_2^p - F_2^n)\, dx/x = 1/3 + 2/3 \int_0^1 (\bar{u} - \bar{d})\, dx$, in a new kinematic range.

To summarise, the use of nuclear beams would increase in a major way the THERA potential for the study of nonlinear QCD phenomena. Several measurements, especially in the diffractive channels, will determine in an unambiguous way whether the black body regime is reached and explore in detail a new QCD state of matter produced at small x. Most of these measurements will require rather modest luminosities of 1–10 pb^{-1} per nucleus [141]. It would be possible to explore the nonlinear regime in a Q^2 range extended by at least a factor of 2 with respect to ep scattering by performing measurements on a series of nuclei with $A \leq 40$, e.g. $A = 2, 4, 16, 40$.

2.4.2 Real photon–proton scattering

At a linear collider, laser light can be Compton-backscattered off the high-energy electron beam, offering the unique opportunity [159–161] to run THERA as a real-photon nucleon collider. As has been studied in detail in [159, 162], the luminosity for a γp machine depends on the distance z between the conversion region and the interaction point and also on the laser and electron beam helicities. An increase of z reduces the luminosity but also reduces the energy spread of the photon beam. A careful optimisation of the operation parameters such as the photon and electron beam helicities and the collision angle between the photon and proton beams is required. The basic

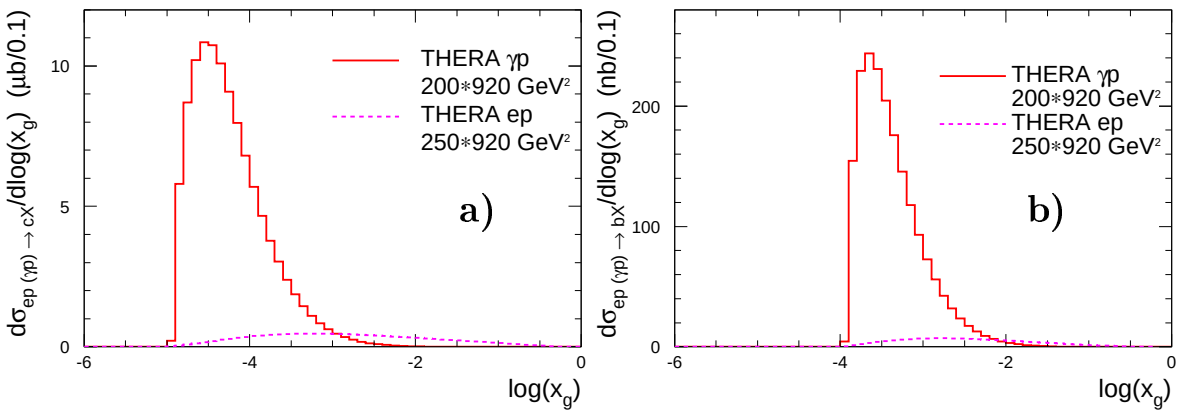

Figure 3: *Dependence of the differential cross section of (a) charm and (b) beauty production on x_g in γp and ep scattering at THERA.*

scheme for converting the TESLA electron beam into a high-energy photon beam is described in appendix I, *The Photon Collider at TESLA*, of this Technical Design Report. Given the much larger beam size of the protons, the interaction of the laser with the electron beam can happen several meters away from the photon–proton interaction point and thus outside of the detector. Photon–proton luminosities of order 30% of the electron–proton luminosities can be achieved.

Compton backscattering yields a beam of photons with about 80% of the electron beam energy on average, with a full width of approximately 15%. The resulting photon–proton interactions allow studies of many of the physics issues discussed above, e.g. heavy flavour production or photon structure, with much enhanced sensitivity. This is illustrated in Fig. 3 which compares the differential cross sections of charm and beauty production in γp scattering and in ep scattering as functions of the gluon fractional momentum in the proton, x_g. The cross section gain at low x_g is striking. A similar observation holds for the differential cross section with respect to the photon energy fraction, $x_\gamma^{\rm obs}$ (see eq. 2.2.2), carried by the produced dijet system in charm and beauty events as is shown in Fig. 4.

The main physics goals of a THERA-based γp collider [160, 163] are:

- a measurement of the total γp cross section at the TeV scale;
- high-statistics studies of heavy-quark production (roughly $10^8, 10^6, 10^2$ events per year for $c\bar{c}$, $b\bar{b}$, $t\bar{t}$ production);
- investigation of the partonic structure of real photons;
- single production of W bosons and top quarks;
- search for excited quarks (u^* and d^*) with masses up to 1 TeV;
- search for fourth-family quarks, Q, produced via anomalous γcQ, γuQ (Q=t_4, u_4), γsd_4 or γdd_4 couplings.

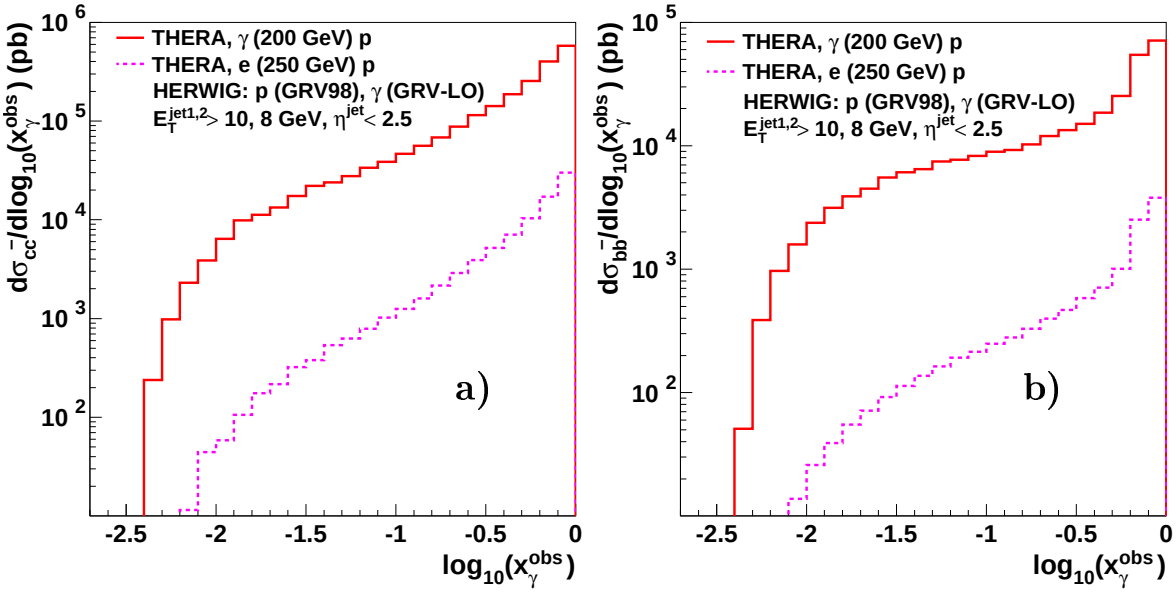

Figure 4: *Differential cross sections with respect to $x_\gamma^{\rm obs}$ for (a) charm and (b) beauty production for the γp and ep options of THERA.*

The photon polarisation will provide important additional information in all these measurements. In addition, a γp collider with a longitudinally polarised proton beam will be a powerful tool for investigating the spin structure of the proton.

Of particular interest is the photon–nucleus (γA) collider option of THERA (see Sect. 2.4.1 and [160, 163]) which, besides all the investigations mentioned above for the γp mode, allows for example detailed studies of quark–gluon plasma formation at very high temperature but relatively low nuclear density, or of multi-quark clusters in nuclei.

2.4.3 Polarised protons

The detailed study of the nucleon spin structure was initiated by the EMC muon experiment [164], which found that the quark contribution to the nucleon spin is surprisingly small and that hence the nucleon spin cannot be understood within the naive quark parton model. Since then a wealth of data from fixed-target experiments on spin structure has been accumulated and spin theory became much more sophisticated. The puzzling question of the nucleon spin composition is still unresolved (for the present status see [165]). The importance of extending the kinematic range of spin physics by an *ep* collider has been investigated and emphasised in a series of workshops on polarised *ep* physics at HERA [166–168].

In polarised DIS, the spin-dependent terms only make a small contribution to the total cross section. They can be extracted from measurements of cross section differences for interactions with opposite relative orientations of lepton and nucleon helicities, in which the spin-independent contributions cancel. A classic quantity is the

spin structure function g_1, which measures the weighted sum of polarised quark distribution functions Δq and is approximately related to the cross section asymmetry, $A_{||} = (\sigma_{\uparrow\downarrow} - \sigma_{\uparrow\uparrow})/(\sigma_{\uparrow\downarrow} + \sigma_{\uparrow\uparrow})$, by:

$$g_1 \simeq \frac{F_2}{2x} \cdot \frac{A_{||}}{\lambda_e \lambda_p} \cdot \frac{y^2 + 2(1-y)}{y(2-y)} \,. \tag{2.4.2}$$

Eq. 2.4.2 illustrates the need for high polarisations, λ_e and λ_p, and a preference for measurements at large values of y. The electron polarisation at TESLA will be high, $\lambda_e \simeq 0.8$. Polarisations $\lambda_p \simeq 0.6$ may be achieved in the HERA proton ring. From eq. 2.4.2 it can be deduced that integrated luminosities exceeding $100\,\mathrm{pb}^{-1}$ per polarisation state are necessary for studying the proton spin structure in a quantitative manner. Therefore, dedicated high-luminosity e–nucleus ring facilities are under discussion [169, 170] with typical energies of $\sqrt{s} \simeq 50\,\mathrm{GeV}$. High-statistics fixed target experiments are being carried out at CERN, DESY and SLAC and proposed to be pursued at TESLA [171].

The outstanding advantage of the THERA facility is the large extension of the kinematic range. Due to the very large centre-of-mass energy, $\sqrt{s} \simeq 1\,\mathrm{TeV}$, the Q^2 evolution can be tested, the x range expanded to much lower x and exploratory measurements be performed. In spin physics these comprise for example inclusive polarised deep inelastic scattering and spin asymmetries in jet and dijet production. For the first time, spin effects will be measurable in polarised DIS through electroweak asymmetries in CC and NC scattering.

The study of spin-dependent effects would be extended to low x and allow for a test of the Q^2 evolution of g_1 towards highest $Q^2 \simeq 10^4\,\mathrm{GeV}^2$. Important information on the spin structure can be obtained from data on the asymmetry in the production of two jets (dijets) or of two hadrons. The polarised gluon distribution ΔG can be accessed with dijet events, as was demonstrated in [172] for HERA operation with polarised protons. For THERA, the asymmetries, calculated with MEPJET and GSA, are about 6% at $x = 0.05$ and smaller than 0.5% for $x < 0.001$. A further source of information about gluon polarisation at low x is charm production which occurs with high cross section at THERA (see Sect. 2.2.2.4).

Inclusive measurements in DIS are sensitive to the sum of all quark flavours. To extract flavour-dependent spin information, one presently uses semi-inclusive scattering, an area being actively pursued in fixed-target experiments [165]. In the very high Q^2 range of THERA, however, CC interactions are a new and promising way to access flavour-specific spin information, independently of fragmentation effects which hinder semi-inclusive analyses. Thus CC scattering has been considered here as an example to illustrate the THERA potential for investigating the polarised proton structure at high Q^2.

In the CC e^+p and e^-p scattering cross sections, asymmetries can be defined as

$$A^{W^\mp} = \frac{d\sigma^{W^\mp}_{\uparrow\downarrow} - d\sigma^{W^\mp}_{\uparrow\uparrow}}{d\sigma^{W^\mp}_{\uparrow\downarrow} + d\sigma^{W^\mp}_{\uparrow\uparrow}} = \frac{\pm 2b g_1^{W^\mp} + a g_5^{W^\mp}}{a F_1^{W^\mp} \pm b F_3^{W^\mp}} \approx \frac{g_5^{W^\mp}}{F_1^{W^\mp}} \tag{2.4.3}$$

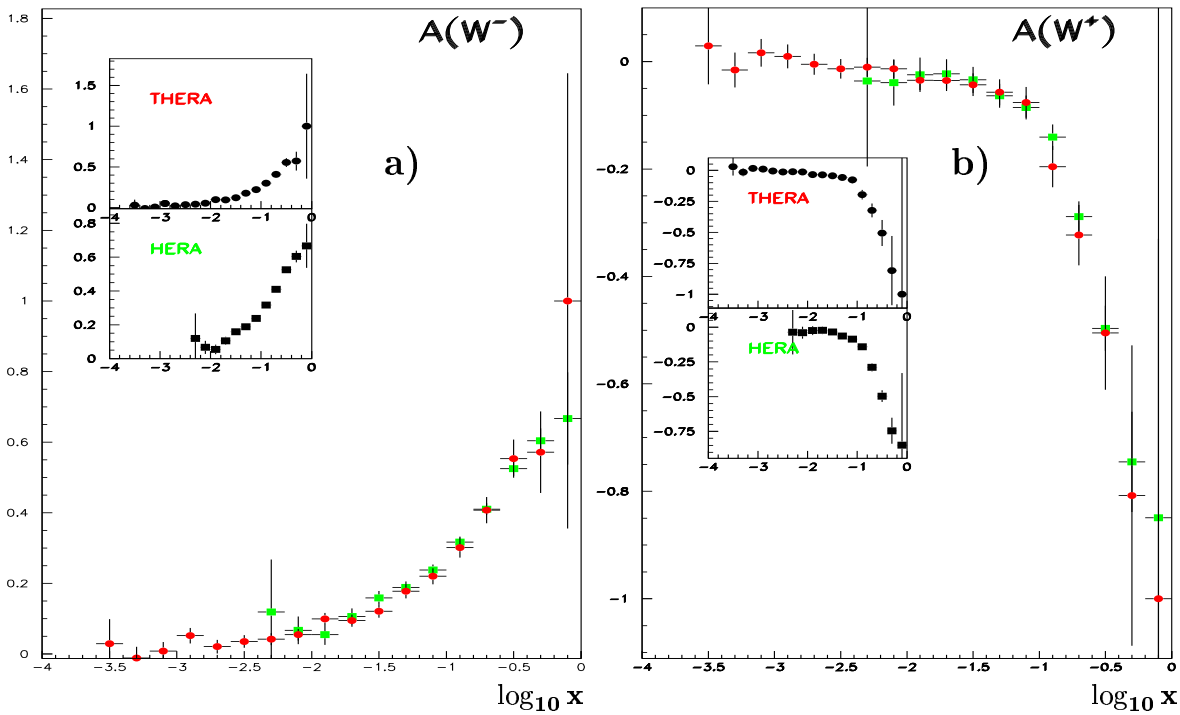

Figure 5: *Simulated measurements of (a) the asymmetry A^{W^-} and (b) of A^{W^+} in CC scattering as functions of x, as expected at the HERA and THERA facilities with polarised proton beams. Note that this representation hides the large differences in the Q^2 range of the HERA and THEA measurements, respectively.*

with $a = 2(y^2 - 2y + 2)$ and $b = y(2 - y)$, $g_5^{W^-} = \Delta u + \Delta c - \Delta\bar{d} - \Delta\bar{s}$ and $g_5^{W^+} = \Delta d + \Delta s - \Delta\bar{u} - \Delta\bar{c}$. A simulation study has been performed for the measurement of this asymmetry, requiring the total missing transverse momentum to exceed 12 GeV. From $A^{W^\mp}$ measurements, the new structure functions g_5 [173] can be extracted following the method used in [174]. The results for $A^{W^\pm}$ are shown in Fig. 5, for a luminosity of 100 pb^{-1} for each polarisation combination, assuming full polarisation. The error bars indicate the statistical precision of the measurement. The results are compared with simulated asymmetry measurements for polarised HERA operation, which will access lower Q^2 at a given x. THERA will allow such asymmetry measurements to be performed in the CC channel for x values down to below 10^{-3}, thus extending the range accessible to HERA by one order of magnitude in x and by even more compared to the projected electron–nucleus colliders. It is expected that $g_5^{W^+}$ can be measured at THERA in the region $x \gtrsim 10^{-2}$, while for electron scattering the asymmetries are large enough to allow for a measurement of $g_5^{W^-}$ down to $x \simeq 10^{-3}$. Both g_5 structure functions are related by a Bjorken sum rule which is valid for very large Q^2 [106].

If any deviation from the Standard Model is found, such as R-parity violating SUSY [175], leptoquarks [112] or instantons [176], it will be particularly interesting to study the helicity-specific properties of the corresponding objects in $\vec{e}\vec{p}$ scattering at THERA.

2.5 Summary

A new electron–proton collider, THERA, based on the linear accelerator TESLA and the proton ring HERA, can be built at DESY. With electron energies between 250 and 800 GeV and proton energies between 500 GeV and 1 TeV, THERA opens a new, unexplored energy range in deep inelastic lepton–nucleon scattering. Design considerations of the THERA facility lead to preliminary estimates of the achievable luminosity between 4 and $25 \times 10^{30}\,\mathrm{cm}^{-2}\,\mathrm{s}^{-1}$ (corresponding to annual luminosities between about $40\,\mathrm{pb}^{-1}$ and $250\,\mathrm{pb}^{-1}$), depending on the beam energies. Relying on the experience and some components of the H1 and ZEUS experiments at HERA, a detector design is presented which promises to allow successful experimentation at THERA at the required level of accuracy and in the full kinematic range. Operation of THERA can be envisaged to proceed in two phases, one dedicated to the physics at very low Bjorken x and the other to extremely high momentum transfers Q^2.

A study is presented of those physics subjects which, based on present results of HERA and theoretical extrapolations, are considered to most likely govern the future physics of deep inelastic scattering and photoproduction in the TeV energy range. Important aims of THERA are the understanding of strong interactions in the presence of high parton densities, a coherent description of the transition from small to large distances and the exploration of new particles and phenomena. The detection of the complete final state and high accuracy in the measurements allow a rich experimental and theoretical programme of research to be performed in the unexplored region. This will test QCD as the theory of strong interactions in much more depth than could be reached so far.

The results of the THERA studies [3] can be summarised as follows:

- The extension of the kinematic range down to $x \simeq 10^{-6}$ allows access to the high-parton-density domain and its detailed exploration in the deep-inelastic regime. Studies of the saturation phase of matter are expected to yield insight into the question of confinement. These studies require the measurements of inclusive DIS, of light and heavy vector meson production and of diffraction. These results will allow the transition from the perturbative to the non-perturbative QCD regime to be understood much better than presently.

- The measurement of proton structure functions at THERA will be essential for determining quark and gluon distributions in the proton in an unexplored kinematic region. This will be crucial for a consistent theoretical description of low-x phenomena, which so far is elusive, and also for understanding the interactions at hadron colliders and of highest-energy cosmic particles.

- The nature of diffraction will be studied in a much extended phase space region of the fractional proton longitudinal momentum loss, x_{IP}, and the ratio $\beta = x/x_{IP}$. The rise of the diffractive structure function $F_2^{D(3)}$ will be explored accurately, which, together with the inclusive F_2, constitutes one of the key measurements to investigate the properties of the saturation region.

- The study of forward-going jets at THERA is expected to reveal the mechanism for the evolution of QCD radiation at low x. The increased range for the Q^2 evolution of parton densities will allow a precision measurement of α_s to the level of 0.5%. This is accompanied by major theoretical efforts to calculate QCD to next-to-next-to-leading order.

- The total cross sections for charm and beauty production are expected to increase by factors of three and five, respectively, as compared to HERA. This will allow the structure functions F_2^c and F_2^b to be measured precisely, heavy-quark QCD predictions to be tested and the gluon distribution in the proton to be determined from the photon–gluon fusion process at much lower x.

- THERA will operate beyond the electroweak unification scale and is thus a truly 'electroweak interaction machine'. The measurement of neutral and charged current cross sections will allow the flavour content of the proton to be unfolded at very high Q^2 and large x, including the region near $x = 1$.

- THERA will probe physics beyond the Standard Model. In particular, leptoquarks or squarks in supersymmetry with R-parity violation can be produced and their couplings determined in a rather complete manner. THERA is very sensitive to four-fermion contact interactions and probes compactification scales up to about 2.8 TeV via t-channel exchange of Kaluza–Klein gravitons in models with large extra dimensions. THERA will extend the searches for excited fermions to masses of up to 1 TeV.

- The photon structure will be resolved at harder scales and lower x_γ. The higher cross section for heavy-flavour production will permit the charm and bottom content of the quasi-real and virtual photon to be explored. Photon structure studies at THERA will be complementary to the investigations in $\gamma\gamma$ and $e\gamma$ reactions at TESLA.

- The acceleration of nuclei in HERA allows the investigation of electron–nucleus scattering in a very high energy range. This may lead deep into the region of high parton densities at low x and to phenomena such as saturation or large leading-twist shadowing. In eA collisions, coherent diffraction is expected to represent about half of the total interaction cross section.

- A further option of THERA consists in colliding a high-energy quasi-monochromatic beam of real photons, produced by backscattering laser light off the TESLA electron beam, with the proton beam from HERA. This would extend the field of real-photoproduction studies into the TeV range and would allow for high-statistics studies of heavy-quark production at low x.

- Polarised proton–electron scattering at THERA allows the study of the spin structure of the proton and its theoretical interpretation in QCD to be extended into an hitherto unexplored kinematic range of low x and large Q^2.

THERA represents a unique, cost-effective facility for investigating the structure of matter down to distances of about 10^{-19} m. As such it continues the long tradition of lepton–nucleon scattering experiments. Similarly to HERA, which has been the *ep* companion of the *pp* and e^+e^- colliders Tevatron and LEP, the THERA facility will yield information complementary to the LHC and to TESLA, utilising the rich physics potential of deep inelastic scattering in the TeV range of energy.

References

[1] R.P. Feynman, *Photon–Hadron Interactions.* Benjamin, New York, 1972.

[2] G.A. Voss and B.H. Wiik, Ann. Rev. Nucl. Part. Sci. **44**, 413 (1994).

[3] *The THERA Book*, Report DESY-LC-REV-2001-062, 2001. `http://www.desy.de/~lcnotes`.

[4] H1 Coll., C. Adloff et al., *Deep inelastic inclusive ep scattering at low x and a determination of* α_s. Preprint DESY-00-181 (hep-ex/0012053), 2000. Subm. to Eur. Phys. J.

[5] ZEUS Coll., *Measurement of the proton structure function* F_2 *in* e^+p *collisions at HERA.* Subm. to *ICHEP2000*, Osaka, Japan, paper 412, 2000.

[6] V.N. Gribov and L.N. Lipatov, Sov. J. Nucl. Phys. **15**, 438 (1972);
G. Altarelli and G. Parisi, Nucl. Phys. **B 126**, 298 (1977);
Yu.L. Dokshitzer, Sov. Phys. JETP **46**, 641 (1977).

[7] ZEUS Coll., J. Breitweg et al., Phys. Lett. **B 487**, 53 (2000).

[8] ZEUS Coll., J. Breitweg et al., Eur. Phys. J. **C 6**, 603 (1999).

[9] H1 Coll., C. Adloff et al., Phys. Lett. **B 483**, 23 (2000).

[10] ZEUS Coll, J. Breitweg et al., Eur. Phys. J. **C 12**, 35 (2000).

[11] H1 Coll., *Measurement of* $D^{*\pm}$ *production and* F_2^c *in DIS.* Subm. to *ICHEP2000*, Osaka, Japan, paper 313, 2000.

[12] M.F. McDermott, *The dipole picture of small x physics: A summary of the Amirim meeting.* Preprint DESY-00-126 (hep-ph/0008260), 2000.

[13] A.H. Mueller, Nucl. Phys. **B 415**, 373 (1994).

[14] N.N. Nikolaev and B.G. Zakharov, Z. Phys. **C 49**, 607 (1991).

[15] N.N. Nikolaev and B.G. Zakharov, Z. Phys. **C 64**, 631 (1994).

[16] L. Frankfurt, W. Koepf and M. Strikman, Phys. Rev. **D 54**, 3194 (1996).

[17] E. Gotsman et al., *Has HERA reached a new QCD regime? (Summary of our view).* Preprint DESY-00-149 (hep-ph/0010198), 2000.

[18] M. Glück, S. Kretzer and E. Reya, Astropart. Phys. **11**, 327 (1999).

[19] J. Kwiecinski, A.D. Martin and A.M. Stasto, *Penetration of the earth by ultrahigh-energy neutrinos and the parton distributions inside the nucleon.* Preprint hep-ph/9905307, 1999. Talk at *34th Rencontres de Moriond: QCD and Hadronic Interactions*, Les Arcs, France.

[20] J. Bartels and H. Kowalski, *Diffraction at HERA and the confinement problem.* Preprint DESY-00-154 (hep-ph/0010345), 2000.

[21] L.V. Gribov, E.M. Levin and M.G. Ryskin, Phys. Rept. **100**, 1 (1983).

[22] A.H. Mueller and J. Qiu, Nucl. Phys. **B 268**, 427 (1986).

[23] E. Levin, *Low-x physics.* Preprint hep-ph/0010272, 2000. Talk at *Diffraction 2000, Centraro, Italy.*

[24] K. Golec-Biernat and M. Wüsthoff, Phys. Rev. **D 60**, 114023 (1999).

[25] A.M. Stasto, K. Golec-Biernat and J. Kwiecinski, Phys. Rev. Lett. **86**, 596 (2001).

[26] L. Frankfurt, M. McDermott and M. Strikman, *A fresh look at diffractive J/ψ photoproduction at HERA, with predictions for THERA.* Preprint hep-ph/0009086, 2000.

[27] B. Naroska, *New results on vector meson production at HERA.* Preprint hep-ex/0006010, 2000. Contrib. to *35th Rencontres de Moriond: QCD and High Energy Hadronic Interactions*, Les Arcs, France.

[28] J.A. Crittenden, *Exclusive Production of Neutral Vector Mesons at the Electron–Proton Collider HERA*, Springer Tracts in Modern Physics, Vol. 140. Springer, Berlin, Heidelberg, 1997.

[29] M.G. Ryskin, Z. Phys. **C 57**, 89 (1993).

[30] L.Frankfurt, W. Koepf and M. Strikman, Phys. Rev. **D 57**, 512 (1998).

[31] M.G. Ryskin et al., Z. Phys. **C 76**, 231 (1997).

[32] P. Merkel, *Diffractive Photoproduction of Heavy Vector Mesons at HERA.* Ph.D. Thesis, University of Hamburg, Report DESY-THESIS-1999-030, 1999.

[33] S.J. Brodsky et al., Phys. Rev. **D 50**, 3134 (1994).

[34] J.C. Collins, L. Frankfurt and M. Strikman, Phys. Rev. **D 56**, 2982 (1997).

[35] A.D. Martin, M.G. Ryskin and T. Teubner, Phys. Rev. **D 55**, 4329 (1997).

[36] J. Nemchik et al., Phys. Lett. **B 374**, 199 (1996).

[37] D.Yu. Ivanov, Phys. Rev. **D 53**, 3564 (1996).

[38] I.F. Ginzburg and D.Yu. Ivanov, Phys. Rev. **D 54**, 5523 (1996).

[39] S.J. Brodsky et al., Phys. Lett. **B 449**, 306 (1999).

[40] J.R. Forshaw and M.G. Ryskin, Z. Phys. **C 68**, 137 (1995).

[41] A.D. Martin, M.G. Ryskin and T. Teubner, Phys. Lett. **B 454**, 339 (1999).

[42] L.L. Frankfurt, M.F. McDermott and M. Strikman, JHEP **9902**, 002 (1999).

[43] A. Levy, Phys. Lett. **B 424**, 191 (1998).

[44] H1 Coll., C. Adloff et al., Z. Phys. **C 76**, 613 (1997).

[45] ZEUS Coll., J. Breitweg et al., Eur. Phys. J. **C 6**, 43 (1999).

[46] E.L. Feinberg and I.Y. Pomerantchuk, Nuovo Cim. Suppl. **III(4)**, 652 (1956);
F.E. Low, Phys. Rev. **D 12**, 163 (1975);
S. Nussinov, Phys. Rev. Lett. **34**, 1286 (1975).

[47] J. Bartels, J. Phys. **G 26**, 481 (2000).

[48] J. Kwiecinski, *Introduction to low x physics and diffraction.* Preprint hep-ph/0102018, 2001.

[49] P.V. Landshoff, *Pomeron physics: An update.* Preprint DAMTP-2000-122 (hep-ph/0010315), 2000. Talk at *Diffraction 2000*, Centraro, Italy.

[50] J.C. Collins, Phys. Rev. **D 57**, 3051 (1998). Erratum in Phys. Rev. **D 61** 019902 (2000).

[51] ZEUS Coll., J. Breitweg et al., Eur. Phys. J. **C 5**, 41 (1998);
H1 Coll., C. Adloff et al., *Diffractive jet production in deep-inelastic e^+p collisions at HERA.* Preprint DESY-00-174 (hep-ex/0012051), 2000. Subm. to Eur. Phys. J.

[52] W. Buchmüller, M.F. McDermott and A. Hebecker, Nucl. Phys. **B 487**, 283 (1997). Erratum in Nucl Phys. **B 500**, 621 (1997).

[53] W. Buchmüller, T. Gehrmann and A. Hebecker, Nucl. Phys. **B 537**, 477 (1999).

[54] J. Bartels, H. Lotter and M. Wüsthoff, Phys. Lett. **B 379**, 239 (1996). Erratum in Phys. Lett. **B 382**, 449 (1996);
J. Bartels, H. Jung and M. Wüsthoff, Eur. Phys. J. **C 11**, 111 (1999).

[55] E. Gotsman, E. Levin and U. Maor, Nucl. Phys. **B 493**, 354 (1997).

[56] G. Ingelman and P.E. Schlein, Phys. Lett. **B 152**, 256 (1985).

[57] E. Zijlstra and W. van Neerven, Nucl. Phys. **B 417**, 61 (1994). Erratum in Nucl. Phys **B 426**, 245 (1994);
J. Blümlein and S. Kurth, Phys. Rev. **D 60**, 014018 (1999);
E. Remiddi and J.A.M. Vermaseren, Int. J. Mod. Phys. **A 15**, 725 (2000);
J. Blümlein, Comput. Phys. Comm. **133**, 76 (2000);
S. Moch and J.A.M. Vermaseren, Nucl. Phys. **B 573**, 853 (2000).

[58] J. Santiago and F.J. Ynduráin, Nucl. Phys. **B 563**, 45 (1999).

[59] CTEQ Coll., H.L. Lai et al., Eur. Phys. J. **C 12**, 375 (2000).

[60] A.D. Martin et al., Eur. Phys. **C 4**, 463 (1998).

[61] M. Glück, E. Reya and A. Vogt, Eur. Phys. J. **C 5**, 461 (1998).

[62] J. Blümlein et al., *Twist-4 gluon recombination corrections for deep inelastic structure functions.* Preprint DESY-01-007 (hep-ph/0102025), 2000.

[63] J. Bartels and C. Bontus, Phys. Rev. **D 61**, 034009 (2000);
J. Bartels, C. Bontus and H. Spiesberger, *Factorization of twist four gluon operator contributions.* Preprint DESY-99-118 (hep-ph/9908411), 1999.

[64] M.A. Kimber, J. Kwiecinski and A.D. Martin, *Gluon shadowing in the low x region probed by the LHC.* Preprint PPP-01-01 (hep-ph/0101099), 2001.

[65] J. Bartels, K. Golec-Biernat and K. Peters, Eur. Phys. J. **C 17**, 121 (2000).

[66] E. Gotsman et al., *Higher twists and maxima for DIS on proton in high density QCD region.* Preprint TAUP-2644-2000 (hep-ph/0008280), 2000.

[67] E.A. Kuraev, L.N. Lipatov and V.S. Fadin, Sov. Phys. JETP **44**, 443 (1976).

[68] E.A. Kuraev, L.N. Lipatov and V.S. Fadin, Sov. Phys. JETP **45**, 199 (1977);
I.I. Balitsky and L.N. Lipatov, Sov. J. Nucl. Phys. **28**, 822 (1978).

[69] S. Catani and F. Hautmann, Nucl. Phys. **B 427**, 475 (1994).

[70] V.S. Fadin and L.N. Lipatov, Phys. Lett. **B 429**, 127 (1998).

[71] J. Blümlein, J. Phys. **G 19**, 1695 (1993);
J. Blümlein and W.L. van Neerven, Phys. Lett. **B 450**, 412 (1999);
J. Blümlein, *QCD evolution of structure functions at small x.* Preprint hep-ph/9909449, 1999. Lectures at *Ringberg Workshop: New Trends in HERA Physics*, Ringberg Castle, Tegernsee, Germany.

[72] G. Altarelli, R.D. Ball and S. Forte, Nucl. Phys. **B 575**, 313 (2000).

[73] R.K. Ellis, F. Hautmann and B.R. Webber, Phys. Lett. **B 348**, 582 (1995).

[74] M. Ciafaloni, Nucl. Phys. **B 296**, 49 (1988);
S. Catani, F. Fiorani and G. Marchesini, Phys. Lett. **B 234**, 339 (1990);
S. Catani, F. Fiorani and G. Marchesini, Nucl. Phys. **B 336**, 18 (1990);
G. Marchesini, Nucl. Phys. **B 445**, 49 (1995).

[75] H. Jung and L. Lönnblad, *Forward jet production at THERA*, in *The THERA Book* [3].

[76] S. Bethke, J. Phys. **G 26**, R27 (2000).

[77] C. Quigg, *Perspectives in high-energy physics.* Preprint hep-ph/0002080, 2000. Review Lecture at ICFA School on Instrumentation in Elementary Particle Physics, Istanbul, Turkey.

[78] S.I. Alekhin and A.L. Kataev, Nucl. Phys. **A 666**, 179 (2000).

[79] M. Klein, C. Pascaud and R. Wallny, *QCD analysis of structure function measurements*, in *The THERA Book* [3].

[80] W.L. van Neerven and A. Vogt, Nucl. Phys. **B 568**, 263 (2000).

[81] S. Larin, T. van Ritbergen and J.A.M. Vermaseren, Nucl. Phys. **B 427**, 41 (1994);
S. Larin et al., Nucl. Phys. **B 492**, 338 (1997);
A. Retey and J.A.M. Vermaseren, *Some higher moments of deep inelastic structure functions at next-to-next-to-leading order of perturbative QCD.* Preprint NIKHEF-2000-018 (hep-ph/0007294), 2000.

[82] W. van Neerven and A. Vogt, Nucl. Phys. **B 588**, 345 (2000);
W.L. van Neerven and A. Vogt, Phys. Lett. **B 490**, 111 (2000).

[83] B. Pötter, *High-p_t jet production*, in *The THERA Book* [3].

[84] H1 Coll., C. Adloff et al., *Measurement and QCD analysis of jet cross-sections in deep inelastic positron–proton collisions at $\sqrt{s}$ of* 300 *GeV.* Preprint DESY-00-145 (hep-ex/0010054), 2000. Subm. to Eur. Phys. J.

[85] ZEUS Coll., *Measurement of differential cross sections for dijet production in neutral current DIS at high Q^2 and determination of α_s.* Subm. to *ICHEP2000*, Osaka, Japan, paper 420, 2000.

[86] W.-K. Tung, *The heavy quark parton oxymoron – a mini-review of heavy quark production theory in pQCD*, in *Proc. 5th Int. Workshop on Deep Inelastic Scattering and QCD (DIS97), Chicago, IL, USA*, eds. J. Repond and D. Krakauer, p. 1014. American Institute of Physics, Woodbury, NY, 1997. Also in preprint hep-ph/9706480.

[87] A. Chuvakin, J. Smith and B.W. Harris, *Variable flavor number schemes versus fixed order perturbation theory for charm quark electroproduction.* Preprint YITP-SB-00-68 (hep-ex/0010350), 2000.

[88] H1 Coll., C. Adloff et al., Nucl. Phys. **B 545**, 21 (1999).

[89] ZEUS Coll., J. Breitweg et al., Eur. Phys. J. **C 6**, 67 (1999).

[90] H1 Coll., C. Adloff et al., Phys. Lett. **B 467**, 156 (1999);
ZEUS Coll., J. Breitweg et al., *Measurement of open beauty production in photoproduction at HERA.* Preprint DESY-00-166 (hep-ex/0011081), 2000. Subm. to Eur. Phys. J.

[91] S. Frixione et al., Nucl. Phys. **B 412**, 225 (1994);
M.L. Mangano, P. Nason and G. Ridolfi, Nucl. Phys. **B 373**, 295 (1992).

[92] P. Jankowski, M. Krawczyk and M. Wing, *Heavy quark production at THERA*, in *The THERA Book* [3].

[93] L Gladilin and I. Redondo, *Heavy quark production measurements at THERA*, in *The THERA Book* [3].

[94] S.P. Baranov and N.P. Zotov, *Heavy quark production in the semihard approach at THERA*, in *The THERA Book* [3].

[95] G. Marchesini et al., Comp. Phys. Comm. **67**, 465 (1992).

[96] B.W. Harris and J. Smith, Phys. Rev. **D 57**, 2806 (1998).

[97] J. Amundson et al., JHEP **0010**, 031 (2000). Also in hep-ph/0005221;
A. Chuvakin, J. Smith and B.W. Harris, *Variable flavor number schemes versus fixed order perturbation theory for charm quark electroproduction.* Preprint YITP-SB-00-68 (hep-ph/0010350), 2000.

[98] M. Buza and W.L. van Neerven, Nucl. Phys. **B 500**, 301 (1997);
R.S. Thorne and R.G. Roberts, *A variable number flavor scheme for charged current heavy flavor structure functions.* Preprint RAL-TR-2000-048 (hep-ph/0010344), 2000.

[99] V. Barone, C. Pascaud and F. Zomer, *A new global analysis of DIS data and the strange sea distribution*, in *Proc. Workshop on Light-Cone QCD and Nonperturbative Hadron Physics, Adelaide, Australia, 1999*, p. 167. 2000. Also in preprint hep-ph/0004268.

[100] E. Derman, Phys. Rev. **D 7**, 2755 (1973).

[101] M. Klein and T. Riemann, Z. Phys. **C 24**, 151 (1984).

[102] U.F. Katz, *Deep-Inelastic Positron–Proton Scattering in the High-Momentum-Transfer Regime of HERA*, Springer Tracts in Modern Physics, Vol. 168. Springer, Berlin Heidelberg, 2000.

[103] J. Blümlein et al., Z. Phys. **C 45**, 501 (1990).

[104] S. Kuhlmann et al., Phys. Lett. **B 476**, 291 (2000).

[105] J.G. Morfin, Nucl. Phys. Proc. Suppl. **79**, 664 (1999);
C. Albright et al., *Physics at a neutrino factory.* Report FERMILAB-FN-492 (hep-ex/0008064), 2000.

[106] W. van Neerven, *Precison tests of perturbative QCD at THERA.* Talk at THERA meeting, Hamburg, 2000.
`http://www.ifh.de/thera/agenda_18oct.html`.

[107] C.Y. Prescott et al., Phys. Lett. **B 77**, 347 (1978).

[108] A.F. Żarnecki, Eur. Phys. J. **C 17**, 695 (2000).

[109] W. Buchmüller, R. Rückl and D. Wyler, Phys. Lett. **B 191**, 442 (1987). Erratum in Phys. Lett. **B 448** 320 (1999).

[110] A.F. Żarnecki, *Leptoquark searches at future colliders.* Preprint hep-ph/0006335, 2000. Subm. to *ICHEP2000*, Osaka, Japan, abstract 193.

[111] A. Djouadi et al., Z. Phys. **C 46**, 679 (1990).

[112] P. Taxil, E. Tuğcu and J.M. Virey, Eur. Phys. J. **C 14**, 165 (2000).

[113] N. Arkani-Hamed, S. Dimopoulos and G. Dvali, Phys. Lett. **B 429**, 263 (1998);
N. Arkani-Hamed, S. Dimopoulos and G. Dvali, Phys. Rev. **D 59**, 086004 (1999).

[114] N. Arkani-Hamed and M. Schmaltz, Phys. Rev. **D 61**, 033005 (2000).

[115] K. Hagiwara, D. Zeppenfeld and S. Komamiya, Z. Phys. **C 29**, 115 (1985).

[116] M. Wing, *Inclusive dijet photoproduction and the resolved photon at THERA*, in *The THERA Book* [3].

[117] M. Krawczyk and A. Zembrzuski, *Prompt photon production at THERA*, in *The THERA Book* [3].

[118] U. Jezuita-Dabrowska and M. Krawczyk, *On the importance of the interference terms and longitudinal virtual photon contribution at THERA*, in *The THERA Book* [3].

[119] M. Stratmann, *Determining the spin structure of the photon at future colliders.* Preprint hep-ph/0006285, 2000. Contrib. to *DIS2000*, Liverpool.

[120] ZEUS Coll., J. Breitweg et al., Euro. Phys. J. **C 11**, 35 (1999);
ZEUS Coll., *The structure of the photon and the dynamics of resolved-photon processes in dijet photoproduction.* Subm. to *ICHEP2000*, Osaka, Japan, paper 418, 2000;
ZEUS Coll., *Measurement of dijet photoproduction at high transverse energies at HERA.* Subm. to *EPS-HEP99*, Tampere, Finland, paper 540, 1999.

[121] M. Krawczyk, A. Zembrzuski and M. Staszel, *Survey of present data on photon structure functions and resolved photon processes.* Preprint IFT-99-15 (hep-ph/0011083), 2000. Subm. to Phys. Rept.

[122] M. Klasen, *Jet photoproduction at THERA*, in *The THERA Book* [3].

[123] ZEUS Coll., M. Derrick et al., Phys. Lett. **B 348**, 665 (1995).

[124] S. Frixione, Z. Kunszt and A. Signer, Nucl. Phys. **B 467**, 399 (1996);
S. Frixione, Nucl. Phys. **B 507**, 295 (1997).

[125] S. Frixione and G. Ridolfi, Nucl. Phys. **B 507**, 315 (1997).

[126] L.E. Gordon and J.K. Storrow, Nucl. Phys. **B 489**, 405 (1997).

[127] M. Glück, E. Reya and A. Vogt, Phys. Rev. **D 45**, 3986 (1992).

[128] M. Glück, E. Reya and A. Vogt, Phys. Rev. **D 46**, 1973 (1992).

[129] P. Aurenche, J.P. Guillet and M. Fontannaz, Z. Phys. **C 64**, 621 (1994).

[130] G.A. Schuler and T. Sjöstrand, Z. Phys. **C 68**, 607 (1995).

[131] A. Piwinski, *Intrabeam scattering*, in *Proc. 9th Int. Conf. on High Energy Accelerators, Stanford (1974)*, p. 405. 1975.

[132] J. Maidment. Private communication, 2001.

[133] K. Balewski et al., Nucl. Instrum. Meth. **A 441**, 274 (2000).

[134] T. Sen, *Crossing angle option for HERA.* Report DESY-HERA-96-02, 1996.

[135] M. Tigner, B. Wiik and F. Willeke, *An electron–proton collider in the TeV range*, in *Proc. IEEE Particle Accelerator Conference, San Francisco*, p. 2910. 1991.

[136] R. Brinkmann and M. Dohlus, *A method to overcome the bunch length limitations on β_p^* for electron–proton colliders.* Report DESY-M-95-11, 1995.

[137] J. Crittenden et al., *A detector for THERA*, in *The THERA Book* [3].

[138] L. Gladilin et al., *The backward silicon tracker for THERA*, in *The THERA Book* [3].

[139] G. Piller and W. Weise, Phys. Rept. **330**, 1 (2000).

[140] New Muon Coll., P. Amaudruz et al., Nucl. Phys. **B 441**, 3 (1995).

[141] M. Arneodo et al., *Nuclear beams in HERA*, in *Proc. Workshop on Future Physics at HERA*, eds. G. Ingelman, A. De Roeck and R. Klanner, p. 887. Hamburg, Germany, DESY, 1996.

[142] L. Frankfurt and M. Strikman, *Small-x phenomena in eA collisions*, in *The THERA Book* [3].

[143] *Proc. Nuclear Theory Summer Meeting on eRHIC*, eds. L. McLerran and R. Venugopalan, 2000. Report BNL-52606.

[144] A.H. Mueller, Nucl. Phys. **B 335**, 115 (1990).

[145] E. Iancu, A. Leonidov and L. McLerran, *Nonlinear gluon evolution in the color glass condensate. I.* Preprint SACLAY-T00-166 (hep-ph/0011241), 2000.

[146] L. Frankfurt and M. Strikman, Eur. Phys. J. **A 5**, 293 (1999).

[147] L. Frankfurt, V. Guzey and M. Strikman, J. Phys. **G 27**, R23 (2001).

[148] L. McLerran and R. Venugopalan, Phys. Rev. **D 50**, 2225 (1994).

[149] L. McLerran and R. Venugopalan, Phys. Rev. **D 59**, 094002 (1999).

[150] V.N. Gribov, Sov. Phys. JETP **30**, 709 (1970).

[151] M. McDermott et al., Eur. Phys. J. **C 16**, 641 (2000).

[152] A.H. Mueller, Nucl. Phys. **B 558**, 285 (1999).

[153] Y.V. Kovchegov, A.H. Mueller and S. Wallon, Nucl. Phys. **B 507**, 367 (1997).

[154] N.N. Nikolaev, B.G. Zakharov and V.R. Zoller, Z. Phys. **A 351**, 435 (1995).

[155] L.L. Frankfurt and M.I. Strikman, Phys. Lett. **B 382**, 6 (1996).

[156] E. Gotsman et al., Phys. Lett. **B 492**, 47 (2000).

[157] B.H. Denby et al., Phys. Rev. Lett. **52**, 795 (1984).

[158] A. Skrinsky, *Prospects for polarized electron nuclei colliders*, in *Proc. Workshop on Physics With Electron Polarized Ion Collider (EPIC99)*, eds. L.C. Bland, J.T. Londergan and A.P. Szczepaniak. 1999.

[159] A.K. Çiftçi et al., Nucl. Instrum. Meth. **A 365**, 317 (1995).

[160] R. Brinkmann et al., *Linac-ring type colliders: Fourth way to TeV scale.* Preprint DESY-97-239 (physics/9712023), 1997.

[161] S. Sultansoy, *The post-HERA era: Brief review of future lepton hadron and photon hadron colliders.* Preprint DESY-99-159 (hep-ph/9911417), 1999.

[162] S.F. Sultanov, *Prospects of the future ep and γp colliders: Luminosity and physics.* Report IC/89/409, ICTP, Trieste, 1989.

[163] S. Sultansoy, Turkish J. Phys. **22**, 575 (1998).

[164] EMC Coll., J. Ashman et al., Phys. Lett. **B 206**, 364 (1988);
EMC Coll., J. Ashman et al., Nucl. Phys. **B 328**, 1 (1989).

[165] N.C.R. Makins, *Spin physics.* Talk at *DIS2000*, Liverpool, `hep.ph.liv.ac.uk/~disproc/plenary1/makins.ps.gz`, 2000;
U. Stösslein, *Summary of the spin programme (PWG1).* Talk at *DIS2000*, Liverpool, `hep.ph.liv.ac.uk/~disproc/plenary2/PWG1/stoesslein`, 2000.

[166] *Proc. Workshop on Future Physics at HERA*, eds. G. Ingelman, A. De Roeck and R. Klanner, 1996.

[167] *Proc. Workshop Deep Inelastic Scattering off Polarized Targets: Theory Meets Experiment*, ed. J. Blümlein et al., Report DESY-97-200, 1997.

[168] A. Deshpande, *The physics case for polarized protons at HERA*, in *Proc. Workshop on Polarized Protons at High Energies – Accelerator Challenges and Physics Opportunities*, eds. A. De Roeck, D. Barber and G. Rädel. 1999.

[169] *An electron ring collider at RHIC.* Proc. *2nd eRHIC Workshop*, Yale, 2000. Report BNL-52592.

[170] *An electron ring at RHIC and EIC.* Proc. *2nd Workshop on an Electron Ion Collider (EIC)*, Boston, 2000.

[171] TESLA-N Study Group, M. Anselmino et al., *Electron scattering with polarized targets at TESLA.* Preprint DESY-00-160 (hep-ph/0011299), 2000. Also in this volume.

[172] A. De Roeck et al., Eur. Phys. J. **C 6**, 121 (1999).

[173] J. Blümlein, RIKEN Rev. **28**, 126 (2000). Also in hep-ph/9912550.

[174] J.G. Contreras, A. De Roeck and M. Maul, *A study on Δu and Δd in charged current events using polarized beams at HERA*, in *Proc. Workshop on Physics with Polarized Protons at HERA, Hamburg*, p. 103. 1998. Also in preprint hep-ph/9711418.

[175] J. Ellis, S. Lola and K. Sridhar, Phys. Lett. **B 408**, 252 (1997).

[176] N. Kochelev, *Instantons, spin crisis and high Q^2 anomaly at HERA*, in *Proc. Workshop on Physics with Polarized Protons at HERA, Hamburg*, p. 225. 1997. `http://www.desy.de/~gehrt/heraspin/proclist.html`.

3 Low-x Physics

3.1 Small-x Evolution of Wilson Lines

I. Balitsky
Department of Physics, Old Dominion University
Norfolk, VA 23529
and
Theory Group, Jefferson Lab, Newport News, VA 23606
e-mail: balitsky@jlab.org

3.1.1 Small-x *vs* Q^2 evolution.

The great success of pQCD in describing the Q^2 behavior of structure functions of deep inelastic scattering (DIS) can be traced back to the fact that the Q^2 dependence is governed by DGLAP evolution equations which have two remarkable properties: (i) they are linear equations, and (ii) the evolution at high Q^2 is not affected by the non-perturbative physics. The latter property is due to the fact that the DGLAP evolution is based on the factorization of the amplitude in the "hard" part coming from the transverse momenta $k_\perp^2 > \mu^2$ and the "soft" part coming from low $k_\perp^2 < \mu^2$ where μ is the factorization scale. The contributions from hard momenta give the coefficient functions in front of the light-cone operators formed by the soft contributions. The factorization scale μ^2 serves as a normalization point for these operators. Taking $\mu^2 = Q^2$, we get the usual result that the Q^2 dynamics is governed by the renorm-group equations for the light-cone operators. A very important property of this factorization is that the coefficient functions are purely perturbative. Indeed, the effective coupling constant is determined by characteristic transverse momenta so that the contributions coming from large $k_\perp^2 > \mu^2$ are perturbative as long as μ^2 is sufficiently large. The non-perturbative physics enters the game only when we lower the normalization point μ^2 down to the typical hadronic scale ($\sim$ 1GeV). The higher-order terms of perturbative expansion (for both the coefficient functions and the anomalous dimensions of the light-cone operators) lie in the same framework of linear evolution and lead to the corrections $\sim \alpha_s, \alpha_s^2$ etc. Therefore if we compare the measurements of structure functions at, for

example, 5 GeV and 10 GeV, we rely only on pQCD and the linear character of the DGLAP equations makes this comparison especially simple.

The situation for the small-x DIS is more complicated. If one presses on with the DGLAP evolution, the higher-loop contributions become enhanced by additional factors $\ln x_B$ and the perturbative expansion of the coefficient functions and the anomalous dimensions breaks down calling for the small-x resummation. In pQCD, the small-x asymptotics is described in the leading logarithmic approximation (LLA) by the BFKL pomeron [1]. It is possible to reformulate the BFKL equation as an evolution equation where the relevant operators are Wilson lines - infinite gauge links [2]. Indeed, at high energies the particles move so fast that their trajectories can be approximated by straight lines collinear to their velocities. (Strictly speaking, if we produce in a high-energy collision two clusters of particles with different rapidities, they perceive each other as moving at a great speed along the straight lines). The proper degrees of freedom for the fast particles moving along the straight lines are the (infinite) gauge factors ordered along the straight line [3, 4]. The two-Wilson-line operator corresponding to the fast-moving quark-antiquark pair is called a color dipole [5–8]. We will demonstrate later that the evolution of this dipole with respect to the slope of Wilson lines reproduces the BFKL equation.

Unfortunately, the theoretical status of the BFKL evolution is not as clear as the DGLAP one (for the review, see [9]). The biggest problem is the lack of unitarity: the power behavior of the BFKL cross section violates the Froissart bound and therefore, in order get the true asymptotics at small x, we must go beyond the LLA. At this step, we face a new problem. In the DGLAP case, the sub-leading logarithms follow the same general pattern of linear DGLAP equation and the problem is purely technical: calculating the loop corrections to the kernels. In the case of small-x evolution there are also α_s corrections to the BFKL kernel [10, 11], but, on the top of that, there are the unitarity corrections which lie outside the framework of the BFKL equation. At small α_s and x, these corrections seem to dominate over the NLO BFKL ones [12, 13].

Another problem with the BFKL evolution is infrared instability. We can safely apply pQCD to the small-x DIS if the characteristic transverse momenta of the gluons $k_\perp$ in the gluon ladder are large. For the the first few diagrams, one can check by explicit calculation that the characteristic $k_\perp^2$ are $\sim Q^2$. However, as x decreases, it turns out that the characteristic transverse momenta in the middle of the gluon ladder drift to $\Lambda_{\rm QCD}$ making the application of pQCD questionable. This is related to the fact that the operator expansion for the high-energy scattering is based on the factorization in the rapidity [14] rather than the factorization in transverse momenta. Unlike the usual light-cone expansion, the high-energy expansion in Wilson operators does not have the additional meaning of perturbative *vs* non-perturbative separation – both the coefficient functions and the matrix elements have perturbative and non-perturbative parts. This happens because, as I mentioned above, the coupling constant in a scattering process is determined by the scale of the transverse momenta. When we use the factorization in hard ($k_\perp > \mu$) and soft ($k_\perp < \mu$) momenta, we calculate the coefficient functions perturbatively (because $\alpha_s(k_\perp > \mu)$ is small) whereas the matrix elements are non-perturbative. Conversely, when we factorize the amplitude in

rapidity, both fast and slow parts have contributions coming from the regions of large and small $k_\perp$. In this sense, the small-x evolution in QCD is not protected from the IR side in the same way as the DGLAP evolution is: in order to compare the two structure functions measured at different (small) values of x the pQCD may be insufficient and, in order to explain the small-x behavior of structure functions, it may be necessary to take into account the interplay between the hard and soft pomeron.

Recently, an idea has emerged that these two difficulties may cancel each other out. Consider the DIS from the heavy nuclei where the large density sets the saturation scale Q_s [15, 16] which effectively cuts the integration over $k_\perp$ even at relatively low energy. As we shall see below, the small-x evolution in this case is nonlinear which leads to the growth of the saturation scale with energy, see the discussion in Refs. [17–20]. It is natural to assume that even for the DIS from the nucleon where there is no saturation at low energies, the saturation scale at sufficiently small x may be generated by the nonlinear evolution itself. Indeed, the linear BFKL evolution, which describes the parton splitting, leads to the gluon density increasing as $x^{-12\ln 2\alpha_s/pi}$ at small x. This growth , however, cannot last forever - for example, it would violate the unitary bound. Thus, at some point the parton recombination, described by the nonlinear evolution, must balance the effects of parton splitting so the partons will reach the state of the saturation [15, 17, 21, 22]. In this high-density regime the coupling constant is small but the characteristic fields are large, making a perfect case for the application of the semiclassical QCD methods [23–30]. The high-density regime of QCD can serve as a bridge between the domain of pQCD and the "real" non-perturbative QCD regime governed by the physics of confinement.

There is a possibility that the saturation regime was already reached in HERA - for example, the turnover of F_2 at small x and Q^2 may already indicate saturation. However, the results of HERA experiments are inconclusive. The investigations at THERA with larger energies and Q^2 will hopefully resolve the question whether the DIS at very small x is a domain of pQCD, non-perturbative QCD, or a high-density QCD.

3.1.2 High-energy asymptotics as a scattering from the shock-wave field

The amplitude of γp scattering is given by the matrix element

$$i\int d^4z d^4x e^{-ip_A\cdot x+ir\cdot z}\langle p'_B|T\{j_A(x+z)j'_A(z)\}|p_B\rangle = (2\pi)^4\delta(p_B-p'_B-r)T^{AA'}(s,t) \tag{3.1.1}$$

where $r = p_B - p'_B$, $p_B^2 = p'^2_B = m_N^2$. The DIS structure functions are given by the imaginary parts of the amplitude of forward scattering

$$W^{AA'} = \frac{1}{\pi} ImT^{AA'}(s,0) \tag{3.1.2}$$

where $x_B = \frac{p_A^2}{s}$, $p_A^2 = -Q^2$. The typical diagram is shown in Fig. 1 (recall that at small x_B the gluon exchanges are mandatory). It is convenient to start with the upper part of the diagram, i.e., to study how fast quarks move in an external gluon field. After that, functional integration over the slow gluon fields will reproduce us the Feynman diagrams of the type of Fig. 1:

The Regge limit $s \to \infty$ with p_A^2 fixed corresponds to the following rescaling of the virtual photon momentum:

$$p_A = \lambda p_1^{(0)} + \frac{p_A^2}{2\lambda p_1^{(0)} \cdot p_2} p_2, \tag{3.1.3}$$

with p_B fixed. This is equivalent to

$$p_1 = \lambda p_1^{(0)}, \quad p_2 = p_2^{(0)}, \tag{3.1.4}$$

where $p_1^{(0)}$ and $p_2^{(0)}$ are fixed light-like vectors so that λ is a large parameter associated with the center-of-mass energy ($s = 2\lambda p_1^{(0)} \cdot p_2^{(0)}$).

We study the asymptotics of high-energy $\gamma^*\gamma^*$ scattering from the fixed external field created by the nucleon

$$\int dx dz e^{-ip_A x + irz} \langle T\{j_\mu(x+z) j_\nu(z)\}\rangle_A. \tag{3.1.5}$$

Instead of rescaling of the incoming photon's momentum (3.1.3), it is convenient to boost the external field:

$$\int dx dz e^{-ip_A x + irz} \langle T\{j_\mu(x+z) j_\nu(z)\}\rangle_A \;=\; \int dx dz e^{-ip_A^{(0)} x + irz} \langle T\{j_\mu(x+z) j_\nu(z)\}\rangle_B, \tag{3.1.6}$$

where $p_A^{(0)} = p_1^{(0)} + \frac{p_A^2}{s_0} p_2$. The boosted field B_μ has the form

$$B_\circ(x_\circ, x_*, x_\perp) = \lambda A_\circ(\frac{x_\circ}{\lambda}, x_*\lambda, x_\perp), \quad B_*(x_\circ, x_*, x_\perp) = \frac{1}{\lambda} A_*(\frac{x_\circ}{\lambda}, x_*\lambda, x_\perp), \tag{3.1.7}$$

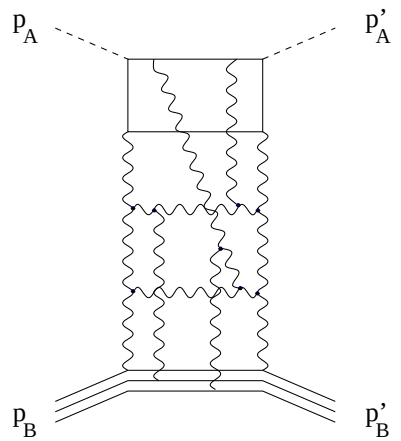

Figure 1: *A typical Feynman diagram for the nucleon structure function at small x_B.*

while the transverse components do not change: $B_\perp(x_\circ, x_*, x_\perp) = A_\perp(\frac{x_\circ}{\lambda}, x_*\lambda, x_\perp)$. Here I use the notations $x_\circ \equiv x^\mu p^{(0)}_{1\mu}$, $x_* \equiv x^\mu p_{2\mu}$ (and $x_\circ \equiv x^\mu p^{(0)}_{1\mu}$ later). The field

$$A_\mu(x_\circ, x_*, x_\perp) = A_\mu(\frac{2}{s_0}x_\circ p^{(0)}_1 + \frac{2}{s_0}x_* p_2 + x_\perp) \tag{3.1.8}$$

is the original external field in the coordinates independent of λ, therefore we may assume that the scales of $x_\circ, x_*$ (and $x_\perp$) in the function (3.1.8) are $O(1)$. First, it is easy to see that at large λ the field $B_\mu(x)$ does not depend on $x_\circ$. Moreover, in the limit of very large λ the field B_μ has a form of the shock wave. It is especially clear if one writes down the field strength tensor $G_{\mu\nu}$ for the boosted field. If we assume that the field strength $F_{\mu\nu}$ for the field A_μ vanishes at the infinity, we get

$$G_{\circ i}(x_\circ, x_*, x_\perp) \;=\; \lambda F_{\circ i}(\frac{x_\circ}{\lambda}, x_*\lambda, x_\perp) \to \delta(x_*)G_i(x_\perp) \tag{3.1.9}$$

while all other components of field strength tensor $G_{\mu\nu}$ vanish. The only component which survives the infinite boost exists only within the thin "wall" near $x_* = 0$. In the rest of the space the field B_μ is a pure gauge. Let us denote by Ω the corresponding gauge matrix and by B^Ω the rotated gauge field which vanishes everywhere except the thin wall:

$$B^\Omega_\circ = \lim_{\lambda\to\infty}\frac{\partial^i}{\vec{\partial}^2_\perp}G^\Omega_{i\circ}(0, \lambda x_*, x_\perp) \to \delta(x_*)\frac{\partial^i}{\vec{\partial}^2_\perp}G^\Omega_i(x_\perp),\;\; B^\Omega_* = B_\perp = 0. \tag{3.1.10}$$

To illustrate the method, consider at first the propagator of the scalar particle (say, the Faddeev-Popov ghost) in the shock-wave background. In Schwinger's notations we write down formally the propagator in the external gluon field $A_\mu(x)$ as

$$G(x,y) = \left(\!\!\left(x\left|\frac{1}{P^2+i\epsilon}\right|y\right)\!\!\right) = \left(\!\!\left(x\left|\frac{1}{(p+gA)^2+i\epsilon}\right|y\right)\!\!\right), \tag{3.1.11}$$

where $(\!(x|y)\!) = \delta^{(4)}(x-y)$,

$$(\!(x|p_\mu|y)\!) = -i\frac{\partial}{\partial y^\mu}\delta^{(4)}(x-y), \qquad (\!(x|A_\mu|y)\!) = A_\mu(x)\delta^{(4)}(x-y). \tag{3.1.12}$$

Here $|x)\!)$ are the eigenstates of the coordinate operator $\mathcal{X}|x)\!) = x|x)\!)$ normalized according to the second line in the above equation. (For details, see Appendix A in Ref. [31]). From Eq. (3.1.12) it is also easy to see that the eigenstates of the free momentum operator p are the plane waves $|p)\!) = \int d^4x\, e^{-ip\cdot x}|x)\!)$. The path-integral representation of a Green function of scalar particle in the external field has the form:

$$\left(\!\!\left(x\left|\frac{1}{\mathcal{P}^2}\right|y\right)\!\!\right) = -i\int_0^\infty dl\left(\!\!\left(x\left|e^{il\mathcal{P}^2}\right|y\right)\!\!\right) \tag{3.1.13}$$

$$= \;-i\int_0^\infty dl\mathcal{N}^{-1}\int_{x(0)=y}^{x(l)=x}\mathcal{D}x(t)e^{-i\int_0^l dt\frac{\dot{x}^2}{4}}Pexp\{ig\int_0^l dt(B^\Omega_\mu(x(t))\dot{x}^\mu(t)\},$$

where l is Schwinger's proper time. It is clear that all the interaction with the external field B_μ^Ω occurs at the point of the intersection of the path of the particle with the shock wave (see Fig. 2). Therefore, it is convenient to rewrite at first the bare propagator marking the point of the intersection of integration path with the plane $z_* = 0$. After some algebra (see the review [32]) we arrive at the following representation of the bare propagator (in the case of $x_* > 0,\ y_* < 0$):

$$\left(\!\!\left(x\left|\frac{1}{p^2+i\epsilon}\right|y\right)\!\!\right) = \frac{2}{s}\int dz_\bullet dz_\perp \frac{1}{4\pi^2(x-z)^2}\frac{y_*}{\pi^2(z-y)^4} \tag{3.1.14}$$

where $z = \frac{2}{s}z_\bullet p_2 + z_\perp$ is the point of the intersection of the path of the particle with the shock wave. Now let us recall that our particle moves in the shock-wave external field and therefore each path in the functional integral (3.1.13) is weighted with the additional gauge factor $Pe^{ig\int B_\mu dx_\mu}$. Since the external field exists only within the infinitely thin wall at $x_* = 0$ we can replace the gauge factor along the actual path $x_\mu(t)$ by the gauge factor along the straight-line path shown in Fig. 2. It crosses the plane $z_* = 0$ at the same point $(z_\circ, z_\perp)$ at which the original path does. Since the shock-wave field outside the wall vanishes we may formally extend the limits of this segment to infinity and write the corresponding gauge factor as $U^\Omega(z_\perp) = [\infty p_1 + z_\perp, -\infty p_1 + z_\perp]$. [1] The error brought by replacement of the original path *inside* the wall by the segment of straight line parallel to p_1 is $\sqrt{\frac{m^2}{s}}$. Indeed, the time of the transition of the particle through the wall is proportional to the thickness of the wall which is $\sim \frac{m^2}{s}$. It indicates that the particle can deviate in the perpendicular directions inside the wall only to the distances $\sqrt{\frac{m^2}{s}}$. Thus, if the particle intersects this wall at some point $(z_*, z_\perp)$ the

[1] We use the notation

$$[x,y] \equiv \mathrm{Pexp}\left\{ig\int_0^1 dv(x-y)^\mu A_\mu\big(vx+(1-v)y\big)\right\} \tag{3.1.15}$$

for the straight-line gauge link suspended between points x and y.

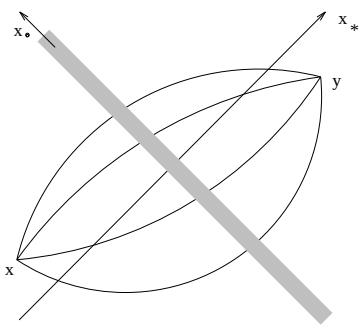

Figure 2: *Propagator in a shock-wave background.*

gauge factor $Pe^{ig\int B^{\Omega}_{\mu}dx_{\mu}}$ reduces to $U^{\Omega}(z_{\perp})$:

$$\left(\!\!\left(x\left|\frac{1}{\mathcal{P}^2}\right|y\right)\!\!\right) = \int dz\delta(z_*)\frac{1}{4\pi^2(x-z)^2}U^{\Omega}(z_{\perp})\frac{y_*}{\pi^2(z-y)^4} \tag{3.1.16}$$

(in the region $x_* > 0, y_* < 0$). It is easy to see that the propagator in the region $x_* < 0, y_* > 0$ differs from Eq. (3.1.16) by the replacement $U^{\Omega} \leftrightarrow U^{\Omega\dagger}$. Also, the propagator outside the shock-wave wall (at $x_*, y_* < 0$ or $x_*, y_* > 0$) coincides with the bare propagator. The final answer for the Green function of the scalar particle in the B^{Ω} background can be written down as:

$$\begin{aligned}\left(\!\!\left(x\left|\frac{1}{\mathcal{P}^2}\right|y\right)\!\!\right) &= \frac{i}{4\pi^2(x-y)^2}\theta(x_*y_*) + \int dz\delta(z_*)\frac{1}{4\pi^2(x-z)^2} \\ &\times \{U^{\Omega}(z_{\perp})\theta(x_*)\theta(-y_*) - U^{\Omega\dagger}(z_{\perp})\theta(y_*)\theta(-x_*)\}\frac{y_*}{\pi^2(z-y)^4}.\end{aligned} \tag{3.1.17}$$

We see that the propagator in the shock-wave background is a convolution of the free propagation up to the plane $z_* = 0$, instantaneous interaction with the shock wave described by the Wilson-line operator U^{Ω} ($U^{\dagger\Omega}$), and another free propagation from z to the final point (see Fig. 2)

In order to get the propagator in the original field B_{μ} we must perform back the gauge rotation with the Ω matrix. It is convenient to represent the result in the following form:

$$\begin{aligned}\left(\!\!\left(x\left|\frac{1}{\mathcal{P}^2}\right|y\right)\!\!\right) &= \frac{i}{4\pi^2(x-y)^2}[x,y]\theta(x_*y_*) + \int dz\delta(z_*)\frac{1}{4\pi^2(x-z)^2} \\ &\times \{U(z_{\perp};x,y)\theta(x_*)\theta(-y_*) - U^{\dagger}(z_{\perp};x,y)\theta(y_*)\theta(-x_*)\}\frac{y_*}{\pi^2(z-y)^4},\end{aligned} \tag{3.1.18}$$

where

$$\begin{aligned}&U(z_{\perp};x,y) = [x,z_x][z_x,z_y][z_y,y]\ , \\ &z_x \equiv (\frac{2}{s_0}z_{\circ}p_1^{(0)} + \frac{2}{s_0}x_*p_2 + z_{\perp}), \qquad z_y = z_x(x_* \leftrightarrow y_*)\end{aligned} \tag{3.1.19}$$

is a gauge factor for the contour made from segments of straight lines as shown in Fig. 3. Since the field B_{μ} outside the shock-wave wall is a pure gauge, the precise form of the contour does not matter as long as it starts at the point x, intersects the wall at the point z in the direction collinear to p_2, and ends at the point y. We have chosen this contour in such a way that the gauge factor (3.1.19) is the same for the field B_{μ} and for the original field A_{μ} (see Eq. (3.1.7)).

The quark propagator in a shock-wave background can be calculated in a similar way (see Ref. [33]),

$$\begin{aligned}\left(\!\!\left(x\left|\frac{1}{\mathcal{P}}\right|y\right)\!\!\right) &= -\frac{\not{x}-\not{y}}{2\pi^2(x-y)^4}[x,y]\theta(x_*y_*) + i\int dz\delta(z_*)\frac{\not{x}-\not{z}}{2\pi^2(x-z)^4} \\ &\times \{U(z_{\perp};x,y)\theta(x_*)\theta(-y_*) - U^{\dagger}(z_{\perp};x,y)\theta(y_*)\theta(-x_*)\}\frac{\not{z}-\not{y}}{2\pi^2(z-y)^4}.\end{aligned} \tag{3.1.20}$$

For the quark-antiquark amplitude in the shock-wave field (see Fig. 3) we get

$$\begin{aligned}
&\mathrm{Tr}\gamma_\mu\left(\left(x\left|\frac{1}{\not{\mathcal{P}}}\right|y\right)\right)\gamma_\nu\left(\left(y\left|\frac{1}{\not{\mathcal{P}}}\right|x\right)\right) \qquad (3.1.21)\\
&= \frac{\mathrm{Tr}\gamma_\mu(\not{x}-\not{y})\gamma_\nu(\not{y}-\not{x})}{4\pi^4(x-y)^8}\theta(x_*y_*) \;-\; \theta(-x_*y_*)\int dzdz'\delta(z_*)\delta(z'_*)\\
&\times\ \mathrm{Tr}\gamma_\mu\frac{\not{x}-\not{z}}{2\pi^2(x-z)^4}\not{p}_2\frac{\not{z}-\not{y}}{2\pi^2(z-y)^4}\gamma_\nu\frac{\not{y}-\not{z}'}{2\pi^2(y-z')^4}\not{p}_2\frac{\not{z}'-\not{x}}{2\pi^2(z'-x)^4}\mathrm{U}(z_\perp;z'_\perp),
\end{aligned}$$

where gauge factor $\mathrm{U}(z_\perp;z'_\perp) \equiv U(z_\perp;x,y)U^\dagger(z'_\perp;y,x)$ is a product of two infinite Wilson-lines operators connected by gauge segments at $\pm\infty$,

$$\mathrm{U}(z_\perp;z'_\perp) \;=\; U_z[z_\perp,z'_\perp]_-U^\dagger_{z'}[z'_\perp,z_\perp]_+. \qquad (3.1.22)$$

We use the space-saving notations

$$[x_\perp,y_\perp]_+ \equiv [\infty p_1+x_\perp,\infty p_1+y_\perp],\quad [x_\perp,y_\perp]_- \equiv [-\infty p_1+x_\perp,-\infty p_1+y_\perp] \qquad (3.1.23)$$

and

$$[un,vn]_x \equiv [un+x_\perp,vn+x_\perp]. \qquad (3.1.24)$$

As we mentioned above, the precise form of the connecting contour at infinity does not matter as long as it is outside the shock wave. We have chosen this contour in such a way that the gauge factor (3.1.22) is the same for the field B_μ and for the original field A_μ (see Eq. (3.1.7)). Now, substituting our result for quark-antiquark propagation (3.1.21) in the right-hand side of Eq. (3.1.5), one obtains

$$\begin{aligned}
&\int d^4x\int d^4z e^{-ip_Ax+irz}\langle T\{j_A(x+z)j'_A(z)\}\rangle_A\\
&\qquad = \;2\pi\delta(\alpha_r)\sum e_i^2\int\frac{d^2k_\perp}{4\pi^2}I^A(k_\perp,r_\perp)\mathrm{Tr}\{U(k_\perp)U^\dagger(r_\perp-k_\perp)\}, \qquad (3.1.25)
\end{aligned}$$

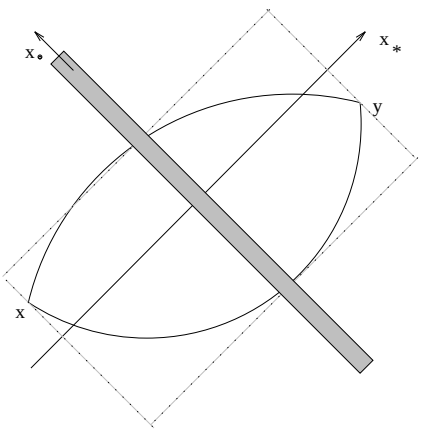

Figure 3: *Quark-antiquark propagation in the shock wave.*

where the impact factor I^A is an explicit function of Q^2 and $k_\perp, r_\perp$ [32]. (For brevity, we omit the end gauge factors (3.1.23).

Formula (3.1.25) describes fast quark and antiquark moving through an external gluon field. After integrating over gluon fields in the functional integral we obtain the amplitude (3.1.1) in the factorized form:

$$\begin{aligned}(2\pi)^2\delta(r_\perp - p'_{B\perp})2\pi\delta(\beta_r)T(s,t) \\ = \; i\frac{s}{2}\sum e_i^2 \int \frac{d^2k_\perp}{4\pi^2} I^A(k_\perp, r_\perp)\langle p'_B|\mathrm{Tr}\{\hat{U}(k_\perp)\hat{U}^\dagger(r_\perp - k_\perp)\}|p_B\rangle.\end{aligned} \tag{3.1.26}$$

where $U(k_\perp)$ denotes the Fourier transform $\int dx_\perp U(x_\perp)e^{-i(k,x)_\perp}$. The gluon fields in U and $U^\dagger$ have been promoted to operators, a fact which we signal by replacing U by $\hat{U}$, etc. It is easy to see that the δ-function of the transverse momenta is present in the r.h.s. of Eq. (3.1.26) as well, so we can cancel it from both sides of the equation. We obtain

$$2\pi\delta(\beta_r)T(s,t) \;=\; i\frac{s}{2}\sum e_i^2 \int \frac{d^2k_\perp}{4\pi^2} I^A(k_\perp, r_\perp)\int dx_\perp e^{-i(k,x)_\perp}\langle p'_B \mathrm{Tr}\{\hat{U}(x_\perp)\hat{U}^\dagger(0)\}|p_B\rangle. \tag{3.1.27}$$

This matrix element describes the propagation of the "color dipole" through the nucleon.

The remaining δ-function reflects the fact that the matrix element of the operator $U(x_\perp)U^\dagger(0)$ contains the unrestricted integration along p_1. It is convenient to define the reduced matrix element:

$$\langle p'_B|\mathrm{Tr}\{\hat{U}(x_\perp)\hat{U}^\dagger(0)\}|p_B\rangle = 2\pi\delta(\frac{s}{2}\beta_r)\langle\langle \mathrm{Tr}\{\hat{U}(x_\perp)\hat{U}^\dagger(0)\}\rangle\rangle \tag{3.1.28}$$

In the case of DIS (when $p'_B = p_B$) this matrix element is related to the non-integrated gluon distribution, see the discussion in Sect. 3.1.5.

3.1.3 Regularized Wilson-line operators

In the Regge limit (3.1.3) we have formally obtained the operators $\hat{U}$ ordered along the light-like lines. Matrix elements of such operators contain divergent longitudinal integrations which reflect the fact that light-like gauge factor corresponds to a quark moving with speed of light (i.e., with infinite energy). This divergency can be already seen at the one-loop level if one calculates the contribution to the matrix element of the two-Wilson-line operator $\hat{U}(x_\perp)\hat{U}^\dagger(y_\perp)$ between the "virtual photon states". As I mentioned above, the reason for this divergence is that we have replaced the fast-quark propagators in the "external field" represented by two gluons coming from the bottom part of the diagram in Fig. 4a by the light-like Wilson lines in Fig. 4b. The integration over rapidities of the gluon η_p in the matrix element of the light-like Wilson-line operator $\hat{U}(x_\perp)\hat{U}^\dagger(y_\perp)$ is formally unbounded , consequently we need some regularization of the Wilson-line operator which cuts off the fast gluons. As

demonstrated in Ref. [2], it can be done by changing the slope of the supporting line. If we wish the longitudinal integration stop at $\eta = \eta_0$, we should order our gauge factors U along a line parallel to $p_\zeta = p_1 + \zeta p_2$ where $\eta_0 = \ln\zeta$. [2] We define

$$\hat{U}^\zeta(x_\perp) \equiv [\infty p^\zeta + x_\perp, -\infty p^\zeta + x_\perp], \quad \hat{U}^{\dagger\zeta}(x_\perp) \equiv [-\infty p^\zeta + x_\perp, \infty p^\zeta + x_\perp]. \tag{3.1.29}$$

Matrix elements of these operators coincide with matrix elements of the operators $\hat{U}$ and $\hat{U}^\dagger$ calculated with the restriction $\alpha < \sigma = \sqrt{p_A^2 s\zeta}$ imposed in the internal loops (and external tails). Let us demonstrate this using the simple example of the matrix element of the operator $\hat{U}^\zeta(k_\perp)\hat{U}^{\dagger\zeta}(r_\perp - k_\perp)$ sandwiched between the "virtual photon" states. The contribution from the diagram shown in Fig. 4 has the form

$$-\frac{i}{2}g^6 \int \frac{d\alpha_p}{2\pi}\frac{d^4p'}{16\pi^4}\frac{[(\alpha_p - 2\alpha'_k)\beta'_k s - (\vec{k}+\vec{k}')_\perp^2]\Phi^B(k')}{(\zeta\alpha_p^2 s + \vec{k}_\perp^2 - i\epsilon)^2\,(\alpha'_k\beta'_k s - \vec{p}'^2_\perp + i\epsilon)^2}$$
$$\times \frac{1}{[-(\alpha_p - \alpha')(\alpha_p\zeta + \beta'_k)s - (\vec{k}-\vec{k}')_\perp^2 + i\epsilon]}, \tag{3.1.30}$$

where the numerator comes from the product of two three-gluon vertices $\Gamma^\lambda_{\mu\nu}(k,k') = (k+k')^\lambda g_{\mu\nu} + (k-2k')_\mu\delta^\lambda_\nu + (k'-2k)_\nu\delta^\lambda_\mu$:

$$4s^2\Gamma_{*\bullet}{}^\sigma(k,-k')\Gamma_{*\bullet\sigma}(k,-k') = (\alpha_k - 2\alpha'_k)\beta'_k s - (\vec{k}+\vec{k}')_\perp^2. \tag{3.1.31}$$

[2] The situation here is again quite similar to the usual OPE for DIS. Recall that when separating the Feynman integrals over loop momenta p into the coefficient functions (with $p^2 \gg \mu^2$) and matrix elements ($p^2 \ll \mu^2$) we expand hard propagators in powers of soft external fields. As a result of this expansion we formally obtain the expressions of the type $\bar{\psi}(\lambda e_1)[\lambda e_1, 0]\psi(0)$ with external fields lying exactly on the light cone. In operator language it corresponds to the matrix element of the same light-cone operator $\hat{\bar{\psi}}(\lambda e_1)[\lambda e_1, 0]\hat{\psi}(0)$ normalized at the point μ^2 in order to ensure the restriction that matrix elements of this operator do not contain virtualities larger than μ^2. Moreover, in principle we can regularize these light-cone operators for DIS by changing the slope of the supporting line (say, take $e = e_1 + \frac{\mu^2}{Q^2}e_2$). The only reason why we use the regularization by counterterms is that, unlike the regularization by the slope, counterterms are governed by renormalization-group equations.

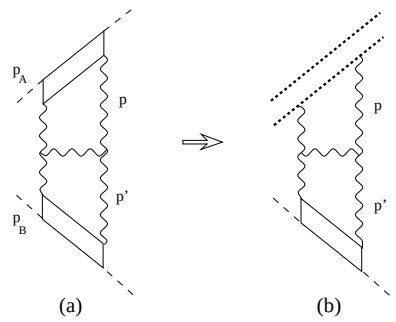

Figure 4: *A typical Feynman diagram for the $\gamma^*\gamma^*$ scattering amplitude (a) and the corresponding two-Wilson-line operator (b).*

As we shall see below, the logarithmic contribution comes from the region $\sqrt{\frac{m^2}{\zeta s}} \gg \alpha_k \gg \alpha'_k \sim \frac{m^2}{s}$, $1 \gg \beta'_p \gg \beta_p = -\zeta\alpha_k \sim \sqrt{\frac{m^2}{\zeta s}}$. In this region one can perform the integration over β'_k by taking the residue at the pole $\left[-(\alpha_p - \alpha')(\alpha_p\zeta + \beta'_k)s - (\vec{k} - \vec{k}')^2_\perp + i\epsilon\right]^{-1}$. The result is [3]

$$\frac{g^6}{s}\int\frac{d\alpha_k}{2\pi}\frac{d\alpha'_k}{2\pi}\int\frac{d^2k'_\perp}{4\pi^2}\left[\Theta(\alpha_k > \alpha'_k > 0 + \Theta(0 > \alpha'_k > \alpha_k)\right] \tag{3.1.32}$$
$$\times\ \frac{\left(\vec{k}^2_\perp + p'^2_\perp - \alpha_k^2\zeta s/2\right)\ \Phi^B\left(\alpha'_k p_1 - (\alpha_k\zeta + \frac{(\vec{k}-\vec{k}')^2_\perp}{\alpha_p s})p_2 + k'_\perp\right)}{|\alpha_p - \alpha'_k|\,(\zeta\alpha_p^2 s + \vec{k}^2_\perp - i\epsilon)^2\,[\frac{\alpha'_k}{\alpha_k}(\vec{k} - \vec{k}')^2_\perp + \vec{p}'^2_\perp + i\epsilon]^2}.$$

We see that the integral over α_p is logarithmic in the region $\sqrt{\frac{m^2}{\zeta s}} \gg \alpha_p \gg \alpha'_k \sim \frac{m^2}{s}$ (cf. Eq. (18)). The lower limit of this logarithmical integration is provided by the matrix element itself ($\beta_k \sim 1$ in the lower quark bulb) while the upper limit, at $\alpha_k^2 \sim m^2/\zeta s$ is enforced by the non-zero ζ and the result has the form

$$\langle\!\langle \mathrm{Tr}\hat{U}^\zeta(k_\perp)\hat{U}^{\dagger\zeta}(-k_\perp)\rangle\!\rangle_{\text{Fig. 4}} = \frac{g^6}{8\pi}\ln\left(\frac{s}{m^2\zeta}\right)\int\frac{d^2k'_\perp}{4\pi^2}\frac{\vec{k}^2_\perp + p'^2_\perp}{\vec{k}^4_\perp\vec{p}'^4_\perp}I^B(k'_\perp). \tag{3.1.33}$$

Similarly to the case of usual light-cone expansion, we expand the amplitude in a set of "regularized" Wilson-line operators $\hat{U}^\zeta$ (see Fig. 5):

$$A(p_A, p_B \Rightarrow p'_A, p'_B) = \sum\int d^2x_1...d^2x_n C(x_1, ...x_n : \zeta) \tag{3.1.34}$$
$$\times\ \langle p_B|\mathrm{Tr}\{\hat{U}^\zeta(x_1)\hat{U}^{\dagger\zeta}(x_2)...\hat{U}^\zeta(x_{n-1})\hat{U}^{\dagger\zeta}(x_n)|p'_B\rangle.$$

The coefficient functions in front of Wilson-line operators (impact factors) will contain logarithms $\sim g^2\ln 1/\sigma$ and the matrix elements $\sim g^2\ln\frac{s\sigma}{m^2}$. Similar to DIS, when we

[3] In the region we are investigating, we can neglect the β'_k dependence of the lower quark loop.

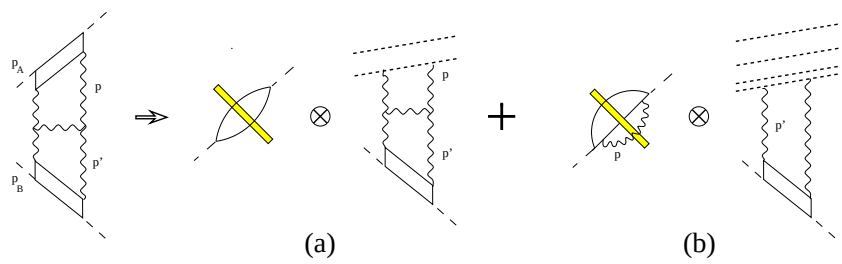

Figure 5: *Decomposition into product of coefficient function and matrix element of the two-Wilson-line operator for a typical Feynman diagram. (Double Wilson line corresponds to the fast-moving gluon.)*

calculate the amplitude, we add the terms $\sim g^2 \ln 1/\sigma$ coming from the coefficient functions (see Fig. 5b) to the terms $\sim g^2 \ln \frac{\sigma}{m^2/s}$ coming from matrix elements (see Fig. 5a) so that the dependence on the "rapidity divide" σ cancels resulting in the usual high-energy factors $g^2 \ln \frac{s}{m^2}$ which are responsible for the BFKL pomeron.

In the LLA, the light-like operators $\hat{U}$ and $\hat{U}^\dagger$ in Eq. (3.1.26) should be replaced by the Wilson-line operators $\hat{U}^\zeta$ and $\hat{U}^{\dagger\zeta}$ ordered along $n \parallel p_A$. Indeed, let us compare the matrix element (3.1.33) shown in Fig. 4b to the corresponding physical amplitude shown in Fig. 4a. The Feynman integral for this amplitude is similar to the one for the matrix element of the operator (3.1.33), except that there is now a factor of the upper quark bulb and the integral over $p_\perp$ (see Ref. [33] for details):

$$\sim \; i\frac{g^6}{4\pi} \ln\left(\frac{s}{m^2}\right) \int \frac{d^2k_\perp}{4\pi^2} \frac{d^2k'_\perp}{4\pi^2} \frac{\vec{k}_\perp^2 + \vec{p'}_\perp^2}{\vec{k}_\perp^4 \vec{p'}_\perp^4} I^A(k_\perp) I^B(k'_\perp) \tag{3.1.35}$$

The result (3.1.35) agrees with the with estimate Eq. (3.1.33) if we set $\zeta = \frac{p_A^2}{s}$. This corresponds to making the line in the path-ordered exponential collinear to the momentum of the photon.

3.1.4 One-loop evolution of Wilson-line operators

As we demonstrated in previous section, with the LLA accuracy, the improved version of the factorization formula Eq. (3.1.25) has the operators $\hat{U}$ and $\hat{U}^\dagger$ "regularized" at $\zeta \sim \frac{p_A^2}{s}$:

$$\begin{aligned} &\int d^4x \int d^4z \; e^{-ip_A\cdot x + irz_\perp} T\{j_A(x+z) j'_A(z)\} \\ &\quad = \; 2\pi\delta(\alpha_r) \sum_i e_i^2 \int \frac{d^2k_\perp}{4\pi^2} I^A(k_\perp, r_\perp) \mathrm{Tr}\{\hat{U}^{\zeta=\frac{m^2}{s}}(k) \hat{U}^{\dagger\zeta=\frac{m^2}{s}}(r-k)\}. \end{aligned} \tag{3.1.36}$$

In the next-to-leading order in α_s we will have the corrections $\sim \alpha_s \mathrm{Tr}\hat{U}(x_\perp)\hat{U}^\dagger(y_\perp)\mathrm{Tr}\hat{U}(y_\perp)\hat{U}^\dagger(z_\perp)$, see Fig. 5.

Next, we derive the equation for the evolution of these operators with respect to slope ζ (in the LLA). In order to find the behavior of the matrix elements of the operators $\hat{U}^\zeta(x_\perp)\hat{U}^{\dagger\zeta}(y_\perp)$ with respect to the slope ζ we must take the matrix element of this operator "normalized" at ζ_1 and integrate over the momenta with $\sigma_1 = \sqrt{\frac{m^2}{s\zeta_1}} > \alpha > \sigma_2 = \sqrt{\frac{m^2}{s\zeta_2}}$ (similar to the case of ordinary Wilson OPE where in order to find the dependence of the light-cone operator on the normalization point μ we integrate over the momenta with virtualities $\mu_1^2 > p^2 > \mu_2^2$). The result will be the operators $\hat{U}$ and $\hat{U}^\dagger$ "normalized" at the slope ζ_2 times the coefficient functions determining the kernel of the evolution equation. The calculation of the kernel is essentially identical to the calculation of the impact factor with the only difference of having initial gluons instead of quarks.

In the first order in α_s there are two one-loop diagrams for the matrix element of operator $\hat{U}(x_\perp)\hat{U}^\dagger(y_\perp)$ in external field (see Fig. 6). Let us start with the diagram shown in Fig. 6a. We will calculate the one-loop evolution of the operator $\hat{U}(x_\perp) \otimes \hat{U}^\dagger(y_\perp) \equiv \{\hat{U}(x_\perp)\}^i_j \{\hat{U}^\dagger(y_\perp)\}^k_l$ with the non-convoluted color indices.

Following Ref. [2], we use the gauge $A_* = 0$ for the calculations. In this gauge, the gluon propagator in the external field has the form[4]:

$$iG^{ab}_{\mu\nu}(x,y) = (\delta^\xi_\mu - \mathcal{P}_\mu \frac{e^\xi}{\mathcal{P}e}) \left[\frac{\delta_{\xi\eta}}{\mathcal{P}^2} - 2i\frac{1}{\mathcal{P}^2}F_{\xi\eta}\frac{1}{\mathcal{P}^2} + \mathcal{O}_{\xi\eta}\right](\delta^\eta_\nu - \frac{e^\eta}{\mathcal{P}e}\mathcal{P}_\nu) + \dots \tag{3.1.37}$$

where the operator $\mathcal{O}$ stands for

$$\begin{aligned} \mathcal{O}_{\mu\nu} &= 4\frac{1}{\mathcal{P}^2}F^\xi{}_\mu \frac{1}{\mathcal{P}^2}F_{\xi\nu}\frac{1}{\mathcal{P}^2} \\ &- \frac{1}{\mathcal{P}^2}(D^\alpha F_{\alpha\mu}\frac{p_{2\nu}}{p\cdot p_2} + \frac{p_{2\mu}}{p\cdot p_2}D^\alpha F_{\alpha\nu} - \frac{p_{2\mu}}{2p\cdot p_2}\mathcal{P}^\beta D^\alpha F_{\alpha\beta}\frac{p_{2\nu}}{2p\cdot p_2})\frac{1}{\mathcal{P}^2}. \end{aligned} \tag{3.1.38}$$

In the LLA, the slope p^ζ of the operators U can be replaced by p_1 so we need the $(\bullet\bullet)$ component of this propagator. It is easy to see that we may drop the terms proportional to $\mathcal{P}_\bullet$ in the parenthesis (they lead to the terms proportional to the integrals of total derivatives, see Ref. [32]) and obtain

$$\begin{aligned} \langle \hat{U}(x_\perp) \otimes \hat{U}^\dagger(y_\perp)\rangle_A &= -ig^2 \int du [\infty p_1, up_1]_x t^a [up_1, -\infty p_1]_x \\ \otimes \int dv [-\infty p_1, vp_1]_y t^b [vp_1, \infty p_1]_y &\left(\left(up_1 + x_\perp \middle| \mathcal{O}_{\bullet\bullet} \middle| vp_1 + y_\perp\right)\right)_{ab}. \end{aligned} \tag{3.1.39}$$

As in the calculation of the quark propagator, it is convenient to go to the rest frame of "fast" gluons. In this frame the "slow" gluons will form a thin pancake shown in Fig. 7. At first, we consider the case $x_* > 0$, $y_* < 0$. It is clear from the picture that we can rewrite Eq. (3.1.39) as follows:

$$\begin{aligned} \langle \hat{U}_x \otimes \hat{U}^\dagger_y\rangle_A &= -ig^2 t^a U_x \otimes t^b U^\dagger_y \\ &\times \int_0^\infty du \int_{-\infty}^0 dv \left(\left(up^{(0)}_A + x_\perp \middle| \mathcal{O}_{\bullet\bullet} \middle| vp^{(0)}_A + y_\perp\right)\right)_{ab} \end{aligned} \tag{3.1.40}$$

[4]It can be demonstrated that further terms in expansion in powers of gluon propagator beyond those given in Eq. (3.1.37) do not contribute in the LLA.

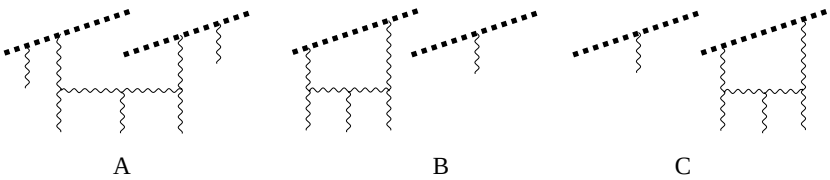

Figure 6: *One-loop diagrams for the evolution of the two-Wilson-line operator.*

Using the thin-wall approximation we obtain

$$\left(\!\!\left(x\middle|\mathcal{O}_{\bullet\bullet}\middle|y\right)\!\!\right) = \frac{s^2}{2}\int dz\delta(z_*)\frac{\ln(x-z)^2}{16\pi^2 x_*}\{2[FF](z_\perp)-i[DF](z_\perp)\}\frac{1}{4\pi^2(z-y)^2}, \tag{3.1.41}$$

where

$$\begin{aligned}
[DF](x_\perp) &\equiv \int du[\infty p_1, up_1]_x D^\alpha F_{\alpha\bullet}(up_1+x_\perp)[up_1,-\infty p_1]_x,\\
[FF](x_\perp) &\equiv \int du\int dv\Theta(u-v)[\infty p_1, up_1]_x F^\xi_\bullet(up_1+x_\perp)\\
&\times [up_1, vp_1]_x F_{\xi\bullet}(vp_1+x_\perp)[vp_1,-\infty p_1]_x.
\end{aligned} \tag{3.1.42}$$

It is easy to see that the operators in braces are in fact the total derivatives of U and $U^\dagger$ with respect to translations in the perpendicular directions,

$$\begin{aligned}
\vec{\partial}^2_\perp U_x &\equiv \frac{\partial^2}{\partial x_i\partial x_i}U_x = -i[DF](x_\perp)+2[FF](x_\perp),\\
\vec{\partial}^2_\perp U^\dagger_x &\equiv \frac{\partial^2}{\partial x_i\partial x_i}U^\dagger_x = i[DF](x_\perp)+2[FF](x_\perp),
\end{aligned} \tag{3.1.43}$$

(note that $\vec{\partial}^2_\perp U = -\partial^2 U$).

Technically it is simpler to find the derivative of the integral of gluon propagator in the right-hand side of Eq. (3.1.40) with respect to $x_\perp$. For this derivative, we obtain:

$$-ig^2\int du\int dv\left(\!\!\left(up^{(0)}_A+x_\perp\middle|p_i\mathcal{O}_{\bullet\bullet}\middle|vp^{(0)}_A+y_\perp\right)\!\!\right)_{ab} = \frac{g^2}{16\pi^4}\int dz_\perp \tag{3.1.44}$$
$$\times\int_0^\infty\frac{du}{u}dv\int dz_\bullet\frac{(x_\perp-z_\perp)_i[\vec{\partial}^2_\perp U(z_\perp)]_{ab}}{[u(u\zeta s-2z_\bullet)-(\vec{x}-\vec{z})^2_\perp-i\epsilon][v(v\zeta s+2z_\bullet)-(\vec{y}-\vec{z})^2_\perp-i\epsilon]}.$$

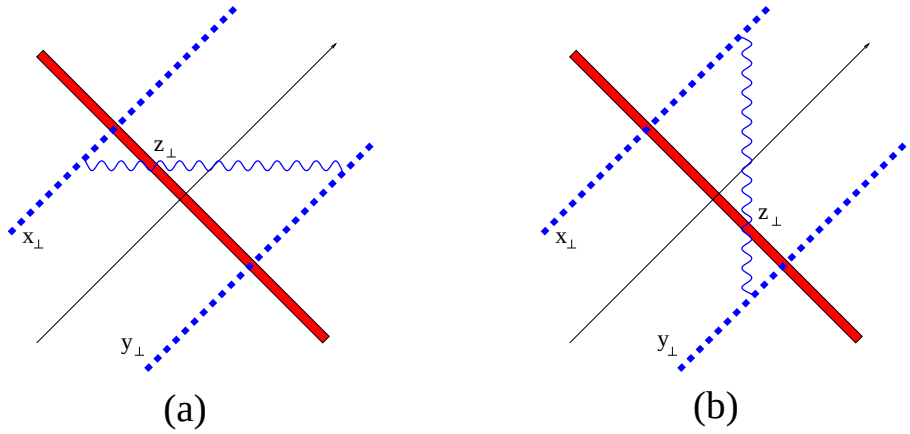

Figure 7: *Wilson-line operators in the shock-wave field background.*

The integration over $z_\bullet$ can be performed by taking the residue; the result is

$$-i\frac{g^2}{16\pi^3}\int dz_\perp \int_0^\infty \frac{du}{u}dv \frac{(x_\perp - z_\perp)_i[\vec{\partial}_\perp^2 U_z]_{ab}}{[(\vec{x}-\vec{z})_\perp^2 v + (\vec{y}-\vec{z})_\perp^2 v - uv(u+v)\zeta s + i\epsilon]}. \tag{3.1.45}$$

This integral diverges logarithmically when $u \to 0$ — in other words when the emission of quantum gluon occurs in the vicinity of the shock wave. (Note that if we had done integration by parts, the divergence would be at $v \to 0$, therefore there is no asymmetry between u and v). The size of the shock wave $z_* \sim m^{-1}\frac{\sigma_2}{\sigma_1}$ (where $1/m$ is the characteristic transverse size) serves as the lower cutoff for this integration and we obtain

$$\begin{aligned} -i\frac{g^2}{16\pi^3}\ln\frac{\sigma_1}{\sigma_2}\int dz_\perp \int_0^1 \frac{d\alpha}{\alpha}\frac{(x_\perp - z_\perp)_i[\vec{\partial}_\perp^2 U_z]_{ab}}{[(\vec{x}-\vec{z})_\perp^2\bar{\alpha} + (\vec{y}-\vec{z})_\perp^2\alpha]} \\ = -\frac{g^2}{16\pi^3}\ln\frac{\sigma_1}{\sigma_2}\left(\left(x_\perp\left|\frac{p_i}{\vec{p}_\perp^2}(\vec{\partial}_\perp^2 U)\frac{1}{\vec{p}_\perp^2}\right|y_\perp\right)\right)_{ab} \end{aligned} \tag{3.1.46}$$

($\bar{\alpha} \equiv 1-\alpha$). Thus, the contribution of the diagram in Fig. 7 in the LLA takes the form

$$\begin{aligned} \langle \hat{U}_x \otimes \hat{U}_y^\dagger\rangle_A &= -\left(\frac{g^2}{2\pi}\ln\frac{\sigma_1}{\sigma_2}\right)\left\{t^a U_x \otimes t^b U_y^\dagger\left(\left(x_\perp\left|\frac{1}{\vec{p}_\perp^2}(\vec{\partial}_\perp^2 U)\frac{1}{\vec{p}_\perp^2}\right|y_\perp\right)\right)_{ab}\right. \\ &+ \left. U_x t^b \otimes U_y^\dagger t^a\left(\left(x_\perp\left|\frac{1}{\vec{p}_\perp^2}(\vec{\partial}_\perp^2 U)\frac{1}{\vec{p}_\perp^2}\right|y_\perp\right)\right)_{ab}\right\}. \end{aligned} \tag{3.1.47}$$

where we have added the term coming from $x_* < 0, y_* > 0$ shown in Fig. 7b (note that $U^{\dagger\ ab} = U^{ba}$).

A corresponding result for the diagram shown in Fig. 8 can be obtained by com-

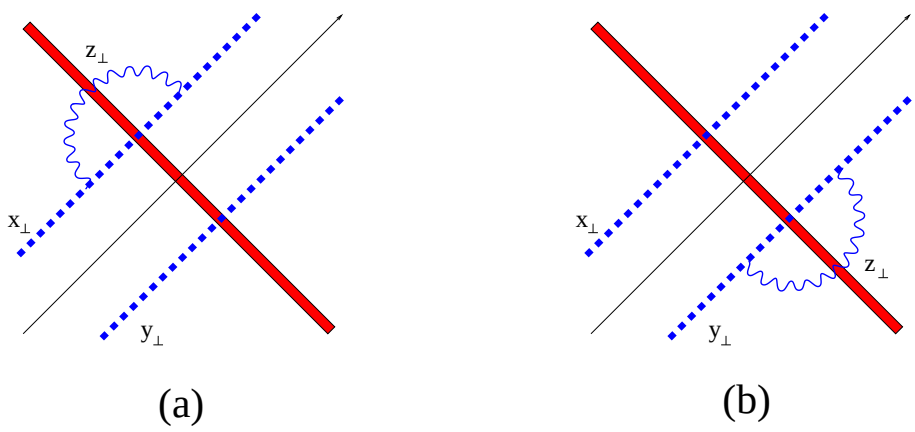

Figure 8: *Wilson-line operators in the shock-wave field background.*

paring the space-time picture Fig. 8a for this process with Fig. 7a,

$$\begin{aligned}\langle \hat{U}_x^\zeta \otimes \hat{U}_y^{\dagger\zeta}\rangle_A &= \left(\frac{g^2}{2\pi}\ln\frac{\sigma_1}{\sigma_2}\right)\left[t^a U_x t^b \otimes U_y^\dagger \left(\left(x_\perp\left|\frac{1}{\vec{p}_\perp^2}(\vec{\partial}_\perp^2 U)\frac{1}{\vec{p}_\perp^2}\right|x_\perp\right)\right)_{ab}\right.\\ &+ \left. U_x \otimes t^b U_y^\dagger t^a \left(\left(y_\perp\left|\frac{1}{\vec{p}_\perp^2}(\vec{\partial}_\perp^2 U)\frac{1}{\vec{p}_\perp^2}\right|y_\perp\right)\right)_{ab}\right]. \qquad (3.1.48)\end{aligned}$$

The total result for the one-loop evolution of two-Wilson-line operator is the sum of Eqs. (3.1.47) and (3.1.48).

3.1.5 BFKL pomeron from the evolution of Wilson-line operators

As we demonstrated in Sec. eq:bal:3.2, with the LLA accuracy the improved version of the factorization formula Eq. (3.1.25) has the operators U and $U^\dagger$ "regularized" at $\zeta \sim \frac{p_A^2}{s}$:

$$\begin{aligned}&\int d^4x d^4z\; e^{ip_A x + irz} T\{j_A(x+z) j_A'(z)\} \qquad (3.1.49)\\ &= 2\pi\delta(\alpha_r)\sum_i e_i^2 \int \frac{d^2k_\perp}{4\pi^2} I^A(k_\perp, r_\perp)\mathrm{Tr}\{U^{\zeta=\frac{m^2}{s}}(k_\perp)U^{\dagger\zeta=\frac{m^2}{s}}(r_\perp - k_\perp)\} + O(g^2).\end{aligned}$$

In the next-to-leading order in α_s we will have the corrections $\sim \alpha_s \mathrm{Tr}U(x_\perp)U^\dagger(y_\perp)\mathrm{Tr}U(y_\perp)U^\dagger(z_\perp)$, see Fig. 5. The matrix element of this operator $\langle\langle U^\zeta(x_\perp)U^{\dagger\zeta}(y_\perp)\rangle\rangle$ describes the gluon-photon scattering at large energies $\sim s$, see Eq. (3.1.25). (Hereafter we will wipe the label $(\hat{})$ from the notation of the operators). The behavior of this matrix element with energy is determined by the dependence on the "normalization point" ζ. From the one-loop results for the evolution of the Wilson-line operators (3.1.47) and (3.1.48) it is easy to obtain the following evolution equation [2]: [5]

$$\begin{aligned}\zeta\frac{\partial}{\partial\zeta}\mathcal{U}(x_\perp, y_\perp) &= -\frac{\alpha_s N_c}{4\pi^2}\int dz_\perp \Big\{\mathcal{U}(x_\perp, z_\perp) + \mathcal{U}(z_\perp, y_\perp) - \mathcal{U}(x_\perp, y_\perp)\\ &+ \mathcal{U}(x,z)\mathcal{U}(z,y)\Big\}\frac{(\vec{x}-\vec{y})_\perp^2}{(\vec{x}_\perp - \vec{z}_\perp)^2(\vec{z}_\perp - \vec{y}_\perp)^2}, \qquad (3.1.50)\end{aligned}$$

where

$$\mathcal{U}(x_\perp, y_\perp) \equiv \frac{1}{N_c}(\mathrm{Tr}\{U(x_\perp)[x_\perp, y_\perp]_- U^\dagger(y_\perp)[y_\perp, x_\perp]_+\} - N_c) \qquad (3.1.51)$$

[5] The double-log limit of this formula is known since 1983 as the GLR equation (it was conjectured in Ref. [21] and formally proved in Ref. [22]). The full LLA x result was first derived in Ref. [2] by the above method. After that, it was reobtained in Ref. [19] in the framework of the dipole model [5–8], in Ref. [34] by direct summation of relevant Feynman diagrams, and in Refs. [35, 36] by the semiclassical methods.

(cf. Eq. (3.1.22)). This equation describes the multiplication of pomerons due to the so-called "fan" diagrams. Note that right-hand side of this equation is both infrared (IR) and ultraviolet (UV) finite. [6] We see that as a result of the evolution, the two-line operator $\mathrm{Tr}\{UU^\dagger\}$ is the same operator (times the kernel) plus the four-line operator $\mathrm{Tr}\{UU^\dagger\}\mathrm{Tr}\{UU^\dagger\}$. The result of the evolution of the four-line operator will be the same operator times some kernel plus the six-line operator of the type $\mathrm{Tr}\{UU^\dagger\}\mathrm{Tr}\{UU^\dagger\}\mathrm{Tr}\{UU^\dagger\} + \mathrm{Tr}\{UU^\dagger UU^\dagger\}\mathrm{Tr}\{UU^\dagger\}$ and so on. Therefore it is instructive to consider at first the linearization of the Eq. (3.1.50) with the number of operators U conserved during the evolution.

The linear (BFKL) evolution of the two-line operator $\mathcal{U}(x_\perp, y_\perp)$ is governed by the first three terms in the r.h.s of Eq. (3.1.50). In the case of forward scattering (DIS) the matrix element $\langle\langle\mathcal{U}(x_\perp, y_\perp)\rangle\rangle$ (see Eq. (3.1.28)) depends only on $x - y$ so we get

$$\zeta\frac{\partial}{\partial\zeta}\langle\langle\mathcal{U}(x_\perp)\rangle\rangle = -\frac{\alpha_s}{4\pi^2}N_c\int dz_\perp[\langle\langle\mathcal{U}(x-z_\perp)\rangle\rangle + \langle\langle\mathcal{U}(z_\perp)\rangle\rangle - \langle\langle\mathcal{U}(x_\perp)\rangle\rangle]\frac{\vec{x}_\perp^2}{(\vec{x}-\vec{z})_\perp^2\vec{z}_\perp^2}, \tag{3.1.52}$$

where $\langle\langle\mathcal{U}(x_\perp)\rangle\rangle \equiv \langle\langle\mathcal{U}(x_\perp, 0)\rangle\rangle$. The eigenfunctions of this equation are powers $(x_\perp^2)^{-\frac{1}{2}+i\nu}$ and the eigenvalues are $-\frac{\alpha_s}{\pi}N_c\chi(\nu)$, where $\chi(\nu) = -\mathrm{Re}\ \psi(\frac{1}{2}+i\nu) - C$. Therefore, the evolution of the operator $\mathcal{U}$ takes the form:

$$\langle\langle\mathcal{U}^{\zeta_1}(x_\perp)\rangle\rangle = \int\frac{d\nu}{2\pi^2}(\vec{x}_\perp^2)^{\frac{1}{2}+i\nu}\left(\frac{\zeta_1}{\zeta_2}\right)^{-\frac{\alpha_s}{\pi}N_c\chi(\nu)}\int dz_\perp(\vec{z}_\perp^2)^{-\frac{3}{2}-i\nu}\langle\langle\mathcal{U}^{\zeta_2}(z)\rangle\rangle \tag{3.1.53}$$

We may proceed with this evolution as long as the upper limit of our logarithmic integrals over α, $\sqrt{\frac{p_A^2}{\zeta s}}$, is much larger than the lower limit $\frac{p_B^2}{s}$ determined by the lower quark bulb, see the discussion in Sec. eq:bal:3.eq:bal:3. It is convenient to stop evolution at a certain point ζ_0 such as

$$\zeta_0 = \sigma_0^2\frac{s}{m^2}, \quad \sigma_0 \ll 1, \quad g^2\ln\sigma_0 \ll 1, \tag{3.1.54}$$

The relative energy between the Wilson-line operators (parallel to $p_1 + \zeta_0 p_2 = \sigma_0 p_1 + \frac{p_A^2}{\sigma_0 s}p_2$) and the nucleon is then $s_0 = s\sigma_0$. Such intermediate energy is sufficiently large to apply our usual high-energy approximations (such as pure gluon exchange and substitution $g_{\mu\nu} \to \frac{2}{s_0}p_{2\mu}p_{1\nu}$) but small in a sense that one does not need take into account the difference between $g^2\ln\frac{s}{m^2}$ and $g^2\ln\frac{s}{m^2\sigma^2}$. Finally, the linear evolution of the color dipole operator takes the form:

$$\langle\langle\mathcal{U}^{\zeta=\frac{m^2}{s}}(x_\perp)\rangle\rangle = \int\frac{d\nu}{2\pi^2}(x_\perp^2)^{\frac{1}{2}+i\nu}(\frac{s}{m^2})^{\frac{2\alpha_s}{\pi}N_c\chi(\nu)}\int dz_\perp(z_\perp^2)^{-\frac{3}{2}-i\nu}\langle\langle\mathcal{U}^{\zeta_0}(z_\perp)\rangle\rangle. \tag{3.1.55}$$

[6] The IR finiteness is due to the fact that $\mathrm{Tr}UU^\dagger$ corresponds to the colorless state in t-channel, as a consequence the IR divergent parts coming from the diagrams in Figs. 7 and 8 cancel out. If we had the exchange by color state in t-channel, the result will be IR divergent (cf. Ref. [32])).

The nucleon matrix element of the two-Wilson-line operator can be parametrized as follows

$$\langle\langle \mathcal{U}(x_\perp)\rangle\rangle \;=\; 2sg^4 \int \frac{dp_\perp}{4\pi^2} e^{i(px)_\perp} \frac{1}{p_\perp^4} I^N(p_\perp) \tag{3.1.56}$$

The "nucleon impact factor" $I^B(p_\perp)$ defined in (3.1.56) is a phenomenological low-energy characteristic of the nucleon. At large $k_\perp$ it reduces to 1 (see the discussion in Ref. [37])

$$I^N(k_\perp) \overset{k_\perp^2 \gg m_N^2}{\to} 1 \tag{3.1.57}$$

For the BFKL evolution, the impact factor plays the role similar to that of nucleon structure function at low normalization point for the DGLAP evulution. In principle, it can be estimated using QCD sum rules or phenomenological models of nucleon.

Let us discuss how the nucleon impact factor (3.1.56) is related to the gluon structure function of the nucleon. The latter is defined as the matrix element of the gluon light-cone operator:

$$G(\omega,\mu) = -\frac{2}{s\omega\pi} \int du e^{-i\frac{s}{2}\omega u} \langle N|\mathrm{Tr}\{F^\xi_\bullet(up_1)[up_1,0]F_{\xi\bullet}[0,up_1]\}|N\rangle^\mu \tag{3.1.58}$$

where μ is the normalization point for the light-cone operator. (The unrenormalized operator $F(up_1)F(0)$ is UV divergent so we regularize it by counterterms just as for the local operator, see e.g. [31, 38]). The physical meaning of μ is the resolution in the transverse size of the gluon: $G(\omega,\mu)$ is the probability to find inside a nucleon the gluon carrying the fraction ω of the nucleon momentum with the transverse size μ^{-1}. Formally,

$$G(\omega,\mu) \simeq \int \frac{dp_\perp}{4\pi^2} \Theta(\mu^2 - p_\perp^2) G(\omega, p_\perp) \tag{3.1.59}$$

where $G(\omega,p_\perp)$ is the gluon distribution over transverse momentum $p_\perp$ and fraction of longitudinal momentum ωp_1:

$$G(\omega,p_\perp) \;=\; \int dx_\perp e^{-i(px)_\perp} G(\omega,x_\perp), \tag{3.1.60}$$

$$\begin{aligned} \omega G(\omega,x_\perp) \;=\; & -\frac{2}{s\pi} \int du e^{-i\frac{s}{2}\omega u} \langle p_B|\mathrm{Tr}\{F^\xi_\bullet(up_1+x_\perp) \\ & [up_1+x_\perp,0]F_{\xi\bullet}(0)[0,-\infty p_1+x_\perp]\}|p_B\rangle \end{aligned} \tag{3.1.61}$$

It is easy to relate impact factor to the gluon distribution. Indeed,

$$\begin{aligned} \frac{4g^2}{\pi p_\perp^2} I^N(p_\perp) \;=\; & -\frac{2}{\pi s} \int dx_\perp e^{-i(p,x)_\perp} \int du \langle p_B|\mathrm{Tr}\{[-\infty p^{\zeta_0}, up^{\zeta_0}]_x \\ & F^\xi_\bullet(up^{\zeta_0}+x_\perp)[up^{\zeta_0},-\infty p^{\zeta_0}]_x[-\infty p^{\zeta_0},0]F_{\xi\bullet}(0)[up^{\zeta_0},-\infty p^{\zeta_0}]_x\}|p_B\rangle \end{aligned} \tag{3.1.62}$$

The r.h.s.'s of eqs. (3.1.60) and (3.1.62) are identical up to a different cutoff in the longitudinal intergation in matrix elements: in the case of gluon distribution the integrals over the α component are restricted from above by $\frac{m^2}{\omega s}$ whereas for the matrix element (3.1.62) the cutoff is $\sqrt{\frac{m^2}{\zeta_0 s}} = \frac{m^2}{s\sigma}$, hence they coincide at $\sigma = \omega$ [7]. We get

$$\frac{4g^2}{\pi p_\perp^2} I^N(p_\perp) \;=\; \sigma G(\sigma, p_\perp) + O(g^2) \tag{3.1.65}$$

where the impact factor is determined by Wilson lines U and $U^\dagger$ parallel to $p_1 + \frac{s}{m^2}\sigma p_2 \parallel \sigma p_2 + \frac{m^2}{s} p_1$ and σm^2 plays the role of the relative energy between Wilson lines and nucleon.

The combination of Eqs. (3.1.57), (3.1.59), and (3.1.65) gives us the estimate of the gluon structure functions at moderately low x_B and small $x_\perp^2$

$$x_B G\big(x_B, \mu^2 = x_\perp^{-2}\big) = \frac{4\alpha_s}{\pi} \ln x_\perp^{-2}/m_0^2 \tag{3.1.66}$$

where m_0^2 an infrared cutoff in Eq. (3.1.59). As demonstrated in Ref. [39], m_0^2 is approximately $m^2/4$ (m is the nucleon mass).

3.1.6 Non-linear evolution of Wilson lines as functional integral

Unlike the linear evolution, the general picture is very complicated since the number of operators U and $U^\dagger$ increases after each evolution. At the time being, it is not known how to solve the non-linear evolution equation in an explicit form. [8] It is possible, however, to write down the solution of the non-linear equation (3.1.50) in the form of functional integral over the double set of the variables, $\pi(x_\perp, \eta) = t^a \pi^a(x_\perp, \eta)$ belonging

[7] For example, in the case of diagram in Fig. 4 the contribution to impact factor (3.1.62) is (cf.eq. (3.1.30)):

$$-\frac{is}{4}\int \frac{d\alpha_p}{2\pi}\frac{d\alpha'_p}{2\pi}\frac{d\beta'_p}{2\pi}\frac{dp'_\perp}{4\pi^2}\frac{g^6 N_c(N_c^2-1)p_\perp^2 \Gamma^\sigma_{*\bullet}(p,-p')\Gamma^\sigma_{*\bullet}(p,-p')\Phi^B_{\xi\eta}(p')}{(\zeta\alpha^2 s + p_\perp^2 - i\epsilon)^2(\alpha'_p\beta'_p s - p'^2_\perp + i\epsilon)^2[(\alpha-\alpha')(\beta-\beta')s - (p-p')^2 + i\epsilon]} \tag{3.1.63}$$

whereas the contribution to the gluon distribution defined by r.h.s. of eq. (3.1.60) has the form:

$$-\frac{is}{8}\int \frac{d\alpha_p}{2\pi}\frac{d\alpha'_p}{2\pi}\frac{d\beta'_p}{2\pi}\frac{dp'_\perp}{4\pi^2}\Big[\frac{1}{(\alpha\omega s - p_\perp^2 - i\epsilon)^2} + (\omega \leftrightarrow -\omega)\Big] \frac{g^6 N_c(N_c^2-1)p_\perp^2 \Gamma^\sigma_{*\bullet}(p,-p')\Gamma^\sigma_{*\bullet}(p,-p')\Phi^B_{\xi\eta}(p')}{(\alpha'_p\beta'_p s - p'^2_\perp + i\epsilon)^2[(\alpha-\alpha')(\beta-\beta')s - (p-p')^2 + i\epsilon]} \tag{3.1.64}$$

where Φ_B is the lower quark bulb in the diargam in Fig. 4. We see now that the only difference is the cutoff for the logarithmical integration over α

[8] An approximate methods were discussed in Refs. [18, 20, 34, 40].

to the Lie algebra of the SU(3) color group and $\Omega(x_\perp,\eta)$ belonging to the group itself:

$$
\begin{aligned}
&U^{\eta_A}(x_\perp)\otimes U^{\dagger\eta_A}(y_\perp) \qquad (3.1.67)\\
&= \int_{\Omega_{1,2}(\eta_0)=1}^{\pi_{1,2}(\eta_A)=0} D\pi_1(x_\perp,\eta)D\pi_2(x_\perp,\eta)D\Omega_1(x_\perp,\eta)D\Omega_2(x_\perp,\eta)\Omega_1^\dagger(x_\perp,\eta_A)U_x^{\eta_0}\Omega_2(x_\perp,\eta_A)\\
&\otimes\ \Omega_2^\dagger(y_\perp,\eta_A)U_y^{\dagger\eta_0}\Omega_1(y_\perp,\eta_A)\ \exp\left\{\int_{\eta_0}^{\eta_A} d\eta\int dz_\perp\Big[\frac{1}{g}\sum_{i=1,2}\pi_i^a(z_\perp,\eta)\Big(\Omega_i^\dagger(z_\perp,\eta)\right.\\
&\left.\times\ \frac{\partial}{\partial\eta}\Omega_i(z_\perp,\eta)\Big)^a-\frac{1}{4\pi}\int dz'_\perp\pi_1^a(z_\perp,\eta)\Big(\Big(z_\perp\Big|\frac{1}{\vec{\partial}_\perp^2}\Big(\hat\Omega_1^\dagger(\eta)\hat U^{\eta_0}\hat\Omega_2(\eta)\Big)^{ab}\frac{1}{\vec{\partial}_\perp^2}\Big|z'_\perp\Big)\Big)\pi_2^b(z'_\perp,\eta)\Big]\right\}
\end{aligned}
$$

Here $\left(\Omega^\dagger\frac{\partial}{\partial\eta}\Omega\right)^a\equiv 2\mathrm{Tr}\{t^a\Omega^\dagger\frac{\partial}{\partial\eta}\Omega\}$ and $\Big(\Big(x_\perp\Big|\hat{\mathcal{O}}(\eta)\Big|y_\perp\Big)\Big)\equiv\mathcal{O}(x_\perp,\eta)\delta(\vec{x}_\perp-\vec{y}_\perp)$. This is a phase-space functional integral for the non-local Hamiltonian

$$
\hat H(\pi_1,\pi_2,\Omega_1,\Omega_2)=\int dx_\perp dy_\perp\pi_1^a(x_\perp)\Big(\Big(x_\perp\Big|\frac{1}{\vec{\partial}_\perp^2}\vec{\partial}_\perp^2\Big(\hat\Omega_1^\dagger U^{\eta_0}\hat\Omega_2\Big)^{ab}\frac{1}{\vec{\partial}_\perp^2}\Big|y\Big)\Big)\pi_2^b(y_\perp). \qquad (3.1.68)
$$

with the rapidity η serving as the Euclidean "time" (cf. [35, 36, 40]).

We shall demonstrate that the perturbative expansion of the functional integral (3.1.67) reproduces the evolution of the color dipole $U(x_\perp)\otimes U^\dagger(y_\perp)$ in the LLA. To get the perturbative expansion, we substitute $\Omega(x_\perp,\eta)=e^{-ig\phi(x_\perp,\eta)}$:

$$
\begin{aligned}
U_x^{\eta_A}\otimes U_y^{\dagger\eta_A}\ &=\ \int_{\phi_{1,2}(\eta_0)=0}^{\pi_{1,2}(\eta_A)=0}\Pi_{i=1,2}D\pi_i(x_\perp,\eta)D\phi_i(x_\perp,\eta) \qquad (3.1.69)\\
&\times\ e^{ig\phi_1(x_\perp,\eta_A)}U_x^{\eta_0}e^{-ig\phi_2(x_\perp,\eta_A)}\otimes e^{ig\phi_2(y_\perp,\eta_A)}U_y^{\dagger\eta_0}e^{-ig\phi_1(y_\perp,\eta_A)}\\
&\times\ \exp\left\{\int_{\eta_0}^{\eta_A}d\eta\int dz_\perp\Big[\frac{1}{g}\sum_{i=1,2}\pi_i^a(z_\perp,\eta)\Big(e^{ig\phi_i(z_\perp,\eta)}\frac{\partial}{\partial\eta}e^{-ig\phi_i(z_\perp,\eta)}\Big)^a-\frac{1}{4\pi}\int dz'_\perp dz"_\perp\right.\\
&\left.\times\ \pi_1^a(z_\perp,\eta)\Big(\Big(z_\perp\Big|\frac{1}{\vec{\partial}_\perp^2}\Big|z'\Big)\Big)\vec{\partial}_\perp^2\Big(e^{ig\phi_1(z'_\perp,\eta)}U_{z'}^{\eta_0}e^{-ig\phi_2(z'_\perp,\eta)}\Big)^{ab}\Big(\Big(z'_\perp\Big|\frac{1}{\vec{\partial}_\perp^2}\Big|z"\Big)\Big)\pi_2^b(z"_\perp,\eta)\Big]\right\}
\end{aligned}
$$

Let us expand the r.h.s. of this equation in powers of g. The first nontrivial term

in this expansion is

$$
\begin{aligned}
U_x^{\eta_A} \otimes U_y^{\dagger\eta_A} &= \alpha_s \int_{\phi_{1,2}(\eta_0)=0}^{\pi_{1,2}(\eta_A)=0} \Pi_{i=1,2} D\pi_i(x_\perp,\eta) D\phi_i(x_\perp,\eta) \qquad (3.1.70)\\
&\times \Bigg[\Big(\phi_1(x_\perp,\eta_A)U_x^{\eta_0} - U_x^{\eta_0}\phi_2(x_\perp,\eta_A)\Big) \otimes \Big(\phi_2(y_\perp,\eta_A)U_y^{\dagger\eta_0} - U_y^{\dagger\eta_0}\phi_1(y_\perp,\eta_A)\Big)\\
&- \Big(\phi_1(x_\perp,\eta_0)U_x^{\eta_0}\phi_2(x_\perp,\eta_A)\Big) \otimes U_y^{\dagger\eta_0} + U_x^{\eta_0} \otimes \Big(\phi_2(y_\perp,\eta_A)U_y^{\dagger\eta_0}\phi_1(y_\perp,\eta_A)\Big)\Bigg]\\
&\times \int_{\eta_0}^{\eta_A} d\eta \int dz_\perp dz'_\perp dz"_\perp \pi_1^a(z_\perp,\eta) \left(\left(z_\perp \middle| \frac{1}{\vec{\partial}_\perp^2} \middle| z'\right)\right) \vec{\partial}_\perp^2 \left(e^{ig\phi_1(z'_\perp,\eta)} U_{z'}^{\eta_0} e^{-ig\phi_2(z'_\perp,\eta)}\right)^{ab}\\
&\times \left(\left(z'_\perp \middle| \frac{1}{\vec{\partial}_\perp^2} \middle| z"\right)\right) \pi_2^b(z"_\perp,\eta) \ \exp\left\{ -i \int_{\eta_0}^{\eta_A} d\eta \int dz_\perp \sum_{i=1,2} \pi_i^a(z_\perp,\eta) \frac{\partial}{\partial\eta} \phi_i^a(z_\perp,\eta)\right\}.
\end{aligned}
$$

The "propagators" for this phase-space functional integral are

$$
\begin{aligned}
&\langle \phi_i^a(x_\perp,\eta)\pi_j^b(y_\perp,\eta')\rangle = -i\delta_{ij}\delta^{ab}\delta(\vec{x}_\perp - \vec{y}_\perp)\theta(\eta-\eta'),\\
&\langle \phi_i^a(x_\perp,\eta)\phi_j^b(y_\perp,\eta')\rangle = 0, \quad \langle \pi_i^a(x_\perp,\eta)\pi_j^b(y_\perp,\eta')\rangle = 0 \qquad (3.1.71)
\end{aligned}
$$

With these propagators, the r.h.s of Eq. (3.1.70) reduces to

$$
\begin{aligned}
&-\alpha_s(\eta_A-\eta_0)\Bigg[\Big(t^aU_x^{\eta_0}\otimes t^bU_y^{\dagger\eta_0} + U_x^{\eta_0}t^b\otimes U_y^{\dagger\eta_0}t^a\Big)\left(\left(x_\perp\middle|\frac{1}{\vec{\partial}_\perp^2}\left[\vec{\partial}_\perp^2 U^{\eta_0}\right]\frac{1}{\vec{\partial}_\perp^2}\middle|y_\perp\right)\right)^{ab} - t^aU_x^{\eta_0}\\
&\times t^b\otimes U_y^{\dagger\eta_0}\left(\left(x_\perp\middle|\frac{1}{\vec{\partial}_\perp^2}\left[\vec{\partial}_\perp^2 U^{\eta_0}\right]\frac{1}{\vec{\partial}_\perp^2}\middle|x_\perp\right)\right)^{ab} - U_x^{\eta_0}\otimes t^bU_y^{\dagger\eta_0}t^a\left(\left(y_\perp\middle|\frac{1}{\vec{\partial}_\perp^2}\left[\vec{\partial}_\perp^2 U^{\eta_0}\right]\frac{1}{\vec{\partial}_\perp^2}\middle|y_\perp\right)\right)^{ab}\Bigg]
\end{aligned}
\qquad (3.1.72)
$$

which coincides with the sum of Eqs. (3.1.47) and (3.1.48)

To prove the Eq. (3.1.69) in all orders in g, we will use the formula

$$
\begin{aligned}
&\int_{\phi(\eta_0)=0}^{\pi(\eta_A)=0} D\pi(x_\perp,\eta)D\phi(x_\perp,\eta)\ \pi^{a_1}(x'_1,\eta'_1)\pi^{a_2}(x'_2,\eta'_2)...\pi^{a_n}(x'_n,\eta'_n)e^{ig\phi(x_1,\eta_1)}\\
&\otimes e^{-ig\phi(x_2,\eta_2)}\otimes ...e^{ig\phi(x_m,\eta_m)}\ \exp\left\{\int_{\eta_0}^{\eta_A} d\eta\int dz_\perp \frac{1}{g}\pi^a(z_\perp,\eta)\left(e^{ig\phi(z_\perp,\eta)}\frac{\partial}{\partial\eta}e^{-ig\phi(z_\perp,\eta)}\right)^a\right\}\\
&= \int_{\phi(\eta_0)=0}^{\pi(\eta_A)=0} D\pi D\phi\ \pi^{a_1}(x'_1,\eta'_1)\pi^{a_2}(x'_2,\eta'_2)...\pi^{a_n}(x'_n,\eta'_n)\ \mathrm{T}_+\left\{e^{ig\int_{\eta_0}^{\eta_1}\dot{\phi}(x_1,\eta)}\right\}\\
&\otimes \mathrm{T}_-\left\{e^{-ig\int_{\eta_0}^{\eta_2}\dot{\phi}(x_2,\eta)}\right\}\otimes ...\mathrm{T}_+\left\{e^{ig\int_{\eta_0}^{\eta_n}\dot{\phi}(x_n,\eta)}\right\}\ e^{-i\int_{\eta_0}^{\eta_A} d\eta\int dz_\perp \pi^a(z_\perp,\eta)\dot{\phi}^a(z_\perp,\eta)} \qquad (3.1.73)
\end{aligned}
$$

Here $\dot{\phi}\equiv\frac{\partial}{\partial\eta}\phi$ and T_+ means ordering of the operators according to the "time" η while T_- means the inverse ordering. This formula can be obtained by differentiation of the

identity

$$\int_{\phi(\eta_0)=0}^{\pi(\eta_A)=0} D\pi(x_\perp,\eta)D\phi(x_\perp,\eta)\ \Pi_{k=1}^m\ e^{\pm ig\phi(x_k,\eta_k)} \tag{3.1.74}$$
$$\times\ \exp\left\{\int_{\eta_0}^{\eta_A} d\eta\int dz_\perp\Big[\frac{1}{g}\pi^a(z_\perp,\eta)\Big(e^{ig\phi(z_\perp,\eta)}\frac{\partial}{\partial\eta}e^{-ig\phi(z_\perp,\eta)}\Big)^a - iJ^a(z_\perp,\eta)\pi^a(z_\perp,\eta)\Big]\right\}$$
$$=\int_{\phi(\eta_0)=0}^{\pi(\eta_A)=0} D\pi D\phi\ \Pi_{k=1}^m\ \mathrm{T}_\pm\left\{e^{ig\int_{\eta_0}^{\eta_1}\dot\phi(x_1,\eta)}\right\}\ e^{-i\int_{\eta_0}^{\eta_A}d\eta\int dz_\perp\left[\pi^a(z_\perp,\eta)\dot\phi^a(z_\perp,\eta)+J^a(z_\perp,\eta)\pi^a(z_\perp,\eta)\right]}$$

with respect to source J. [9]

Let us now prove the evolution equation for the r.h.s. of Eq. (3.1.69). First, we use the Eq. (3.1.73) to represent the r.h.s. of Eq. (3.1.69) in the form

$$\int_{\phi_{1,2}(\eta_0)=0}^{\pi_{1,2}(\eta_A)=0}\Pi_{i=1,2}D\pi_i(x_\perp,\eta)D\phi_i(x_\perp,\eta)[\eta_A,\eta_0]_xU_x^{\eta_0}\{\eta_0,\eta_A\}_x\otimes\{\eta_A,\eta_0\}_yU_y^{\dagger\eta_0}[\eta_0,\eta_A]_y$$
$$\times\ \exp\left\{\int_{\eta_0}^{\eta_A}d\eta\int dz_\perp\Big[-i\sum_{i=1,2}\pi_i^a(z_\perp,\eta)\dot\phi_i(z_\perp,\eta)-\frac{1}{4\pi}\int dz'_\perp dz"_\perp\pi_1^a(z_\perp,\eta)\right.$$
$$\left.\times\ \Big(\Big(z_\perp\Big|\frac{1}{\vec\partial_\perp^2}\Big|z'\Big)\Big)\vec\partial_\perp^2\Big([\eta_A,\eta_0]_zU_z^{\eta_0}\{\eta_0,\eta_A\}_z\Big)^{ab}\Big(\Big(z'_\perp\Big|\frac{1}{\vec\partial_\perp^2}\Big|z"\Big)\Big)\pi_2^b(z"_\perp,\eta)\Big]\right\} \tag{3.1.75}$$

where we introduced the notations

$$[\eta_1,\eta_2]_x\equiv\mathrm{T}_+\left\{e^{ig\int_{\eta_2}^{\eta_1}\dot\phi_1(x_\perp,\eta)}\right\},\quad \{\eta_1,\eta_2\}_x\equiv\mathrm{T}_+\left\{e^{ig\int_{\eta_2}^{\eta_1}\dot\phi_2(x_\perp,\eta)}\right\} \tag{3.1.76}$$

It is convenient to fix the boundary conditions for the integration over π at $\eta=\infty$. We get

$$\int_{\phi_{1,2}(\eta_0)=0}^{\pi_{1,2}(\infty)=0}\Pi_{i=1,2}D\pi_i(x_\perp,\eta)D\phi_i(x_\perp,\eta)\ [\eta_A,\eta_0]_xU_x^{\eta_0}\{\eta_0,\eta_A\}_x\otimes\{\eta_A,\eta_0\}_yU_y^\dagger[\eta_0,\eta_A]_y$$
$$\times\ e^{-i\int_{\eta_0}^\infty d\eta dz_\perp\sum_{i=1,2}\pi_i^a(z_\perp,\eta)\dot\phi_i(z_\perp,\eta)}\exp\left\{-\frac{1}{4\pi}\int_{\eta_0}^{\eta_A}d\eta\int dz_\perp dz'_\perp dz"_\perp\right.$$
$$\left.\times\ \pi_1^a(z_\perp,\eta)\Big(\Big(z_\perp\Big|\frac{1}{\vec\partial_\perp^2}\Big|z'\Big)\Big)\vec\partial_\perp^2\Big([\eta_A,\eta_0]_zU_z^{\eta_0}\{\eta_0,\eta_A\}_z\Big)^{ab}\Big(\Big(z'_\perp\Big|\frac{1}{\vec\partial_\perp^2}\Big|z"\Big)\Big)\pi_2^b(z"_\perp,\eta)\right\} \tag{3.1.77}$$

[9] The formula (3.1.74) is easily verified if one integrates over π fields. In the l.h.s. one obtains $\Pi_{z,\eta}\delta\Big(\frac{i}{g}e^{ig\phi(z_\perp,\eta)}\frac{\partial}{\partial\eta}e^{-ig\phi(z_\perp,\eta)}-J(z,\eta)\Big)$ and therefore $\Pi\ e^{\pm ig\phi(x_\perp,\eta)}$ in the integrand can be replaced by $\Pi\ \mathrm{T}_\pm\exp\Big\{ig\int_{\eta_0}^\eta d\eta' J(x_\perp,\eta')\Big\}$. In the r.h.s. of Eq. (3.1.74) one gets $\Pi_{z,\eta}\delta\Big(\dot\phi(z,\eta)-J(z,\eta)\Big)$ which leads to the same result $\Pi\ \mathrm{T}_\pm\exp\Big\{ig\int_{\eta_0}^\eta d\eta' J(x_\perp,\eta')\Big\}$.

It is easy to check that the propagator for the functional integral (3.1.77) is still given by Eq. (3.1.71) so the perturbative expansions for the Eq. (3.1.75) and Eq. (3.1.77) are identical.

Now we can prove the evolution equation (3.1.50). Let us differentiate the r.h.s. of Eq. (3.1.77) with respect to η_A. We get

$$
\begin{aligned}
& g\int_{\phi_{1,2}(\eta_0)=0}^{\pi_{1,2}(\infty)=0} \Pi_{i=1,2} D\pi_i(x_\perp,\eta) D\phi_i(x_\perp,\eta) \Bigg(\Big[i\dot{\phi}_1(x_\perp,\eta_A)[\eta_A,\eta_0]_x U_x^{\eta_0}\{\eta_0,\eta_A\}_x \\
& - i[\eta_A,\eta_0]_x U_x^{\eta_0}\{\eta_0,\eta_A\}_x \dot{\phi}_2(x_\perp,\eta_A)\Big] \otimes \{\eta_A,\eta_0\}_y U_y^{\dagger\eta_0}[\eta_0,\eta_A]_y + [\eta_A,\eta_0]_x U_x^{\eta_0} \\
& \times \{\eta_0,\eta_A\}_x \otimes \Big[i\dot{\phi}_2(y_\perp,\eta_A)\{\eta_A,\eta_0\}_y U_y^{\dagger\eta_0}[\eta_0,\eta_A]_y - i\{\eta_A,\eta_0\}_y U_y^{\dagger\eta_0}[\eta_0,\eta_A]_y \dot{\phi}_1(y_\perp,\eta_A)\Big] \\
& -\frac{1}{4\pi}[\eta_A,\eta_0]_x U_x\{\eta_0,\eta_A\}_x \otimes \{\eta_A,\eta_0\}_y U_y^{\dagger\eta_0}[\eta_0,\eta_A]_y \int dz_\perp dz'_\perp dz"_\perp \pi_1^a(z_\perp,\eta_A) \\
& \times \left(\left(z_\perp\middle|\frac{1}{\vec{\partial}_\perp^2}\middle|z'\right)\right)\vec{\partial}_\perp^2\Big([\eta_A,\eta_0]_z U_z^{\eta_0}\{\eta_0,\eta_A\}_z\Big)^{ab}\left(\left(z'_\perp\middle|\frac{1}{\vec{\partial}_\perp^2}\middle|z"\right)\right)\pi_2^b(z"_\perp,\eta_A)\Bigg) \\
& \times e^{-i\int_{\eta_0}^{\infty} d\eta dz_\perp \sum_{i=1,2}\pi_i^a(z_\perp,\eta)\dot{\phi}_i(z_\perp,\eta)} \exp\Bigg\{ -\frac{1}{4\pi}\int_{\eta_0}^{\eta_A} d\eta \int dz_\perp dz'_\perp dz"_\perp \pi_1^a(z_\perp,\eta) \\
& \times \left(\left(z_\perp\middle|\frac{1}{\vec{\partial}_\perp^2}\middle|z'\right)\right)\vec{\partial}_\perp^2\Big([\eta_A,\eta_0]_z U_z^{\eta_0}\{\eta_0,\eta_A\}_z\Big)^{ab}\left(\left(z'_\perp\middle|\frac{1}{\vec{\partial}_\perp^2}\middle|z"\right)\right)\pi_2^b(z"_\perp,\eta)\Bigg\}
\end{aligned}
\tag{3.1.78}
$$

It is easy to see that after performing the remaining contractions

$$
\begin{aligned}
\langle \dot{\phi}_i^a(x_\perp,\eta_A)\pi_j^b(z_\perp,\eta)\rangle &= -i\delta_{ij}\delta(\vec{x}_\perp-\vec{z}_\perp)\delta^{ab}\delta(\eta_A-\eta) \\
\langle \pi_1^a(z_\perp,\eta_A)[\eta_A,\eta_0]_x\rangle &= \frac{1}{2}\delta(\vec{x}_\perp-\vec{z}_\perp)t^a[\eta_A,\eta_0]_x, \\
\langle \pi_1^a(z_\perp,\eta_A)[\eta_0,\eta_A]_y\rangle &= -\frac{1}{2}\delta(\vec{x}_\perp-\vec{z}_\perp)[\eta_A,\eta_0]_y t^a, \\
\langle \pi_2^b(z_\perp,\eta_A)\{\eta_A,\eta_0\}_y\rangle &= \frac{1}{2}\delta(\vec{y}_\perp-\vec{z}_\perp)t^b\{\eta_A,\eta_0\}_y, \\
\langle \pi_2^b(z_\perp,\eta_A)\{\eta_0,\eta_A\}_x\rangle &= -\frac{1}{2}\delta(\vec{y}_\perp-\vec{z}_\perp)\{\eta_0,\eta_A\}_x t^b,
\end{aligned}
\tag{3.1.79}
$$

($\frac{1}{2}$ comes from $\theta(0) = \frac{1}{2}$, see the footnote [10]) we obtain:

$$
\begin{aligned}
&-\alpha_s \int_{\phi_{1,2}(\eta_0)=0}^{\pi_{1,2}(\infty)=0} \Pi_{i=1,2} D\pi_i D\phi_i \int dz_\perp \Bigg[\left(\left(x_\perp \middle| \frac{1}{\vec{\partial}_\perp^2} \middle| z_\perp \right) \right) \Big[t^a [\eta_A, \eta_0]_x U_x^{\eta_0} \{\eta_0, \eta_A\}_x \\
&\otimes t^b \{\eta_A, \eta_0\}_y U_y^{\dagger \eta_0} [\eta_0, \eta_A]_y + [\eta_A, \eta_0]_x U_x^{\eta_0} \{\eta_0, \eta_A\}_x t^b \otimes \{\eta_A, \eta_0\}_y U_y^{\dagger \eta_0} [\eta_0, \eta_A]_y t^a \Big] \\
&\times \left(\left(z_\perp \middle| \frac{1}{\vec{\partial}_\perp^2} \middle| y_\perp \right) \right) - \left(\left(x_\perp \middle| \frac{1}{\vec{\partial}_\perp^2} \middle| z_\perp \right) \right) t^a [\eta_A, \eta_0]_x U_x^{\eta_0} \{\eta_0, \eta_A\}_x t^b \left(\left(z_\perp \middle| \frac{1}{\vec{\partial}_\perp^2} \middle| x_\perp \right) \right) \\
&\otimes \{\eta_A, \eta_0\}_y U_y^{\dagger \eta_0} [\eta_0, \eta_A]_y - [\eta_A, \eta_0]_x U_x^{\eta_0} \{\eta_0, \eta_A\}_x \otimes \left(\left(y_\perp \middle| \frac{1}{\vec{\partial}_\perp^2} \middle| z_\perp \right) \right) t^b \{\eta_A, \eta_0\}_y \\
&\times U_y^{\dagger \eta_0} [\eta_0, \eta_A]_y t^a \left(\left(z_\perp \middle| \frac{1}{\vec{\partial}_\perp^2} \middle| y_\perp \right) \right) \Bigg] \vec{\partial}_\perp^2 \left([\eta_A, \eta_0]_z U_z^{\eta_0} \{\eta_0, \eta_A\}_z \right)^{ab} \\
&\times e^{-i \int_{\eta_0}^{\infty} d\eta dz_\perp \sum_{i=1,2} \pi_i^a (z_\perp, \eta) \dot{\phi}_i (z_\perp, \eta)} \exp \Bigg\{ -\frac{1}{4\pi} \int_{\eta_0}^{\eta_A} d\eta \int dz_\perp dz'_\perp dz"_\perp \pi_1^a (z_\perp, \eta) \\
&\times \left(\left(z_\perp \middle| \frac{1}{\vec{\partial}_\perp^2} \middle| z' \right) \right) \vec{\partial}_\perp^2 \left([\eta_A, \eta_0]_z U_z^{\eta_0} \{\eta_0, \eta_A\}_z \right)^{ab} \left(\left(z'_\perp \middle| \frac{1}{\vec{\partial}_\perp^2} \middle| z" \right) \right) \pi_2^b (z"_\perp, \eta) \Bigg\}
\end{aligned}
\tag{3.1.80}
$$

which is the functional integral corresponding to the sum of the r.h.s. of Eq. (3.1.47) and Eq. (3.1.48) (recall that $[\eta_A, \eta_0]_x U_x^{\eta_0} \{\eta_0, \eta_A\}_x = U_x^{\eta_A}$).

In conclusion we note that the integral over π variables in the Eq. (3.1.67) can be easily performed resulting in:

$$
\begin{aligned}
&U^{\eta_A}(x_\perp) \otimes U^{\dagger \eta_A}(y_\perp) \\
&= \int_{\Omega_{1,2}(\eta_0)=1} D\Omega_1(x_\perp, \eta) D\Omega_2(x_\perp, \eta)\ \Omega_1^\dagger(x_\perp, \eta_A) U^{\eta_0}(x_\perp) \Omega_2(x_\perp, \eta_A) \\
&\otimes \Omega_2^\dagger(y_\perp, \eta_A) U^{\dagger \eta_0}(y_\perp) \Omega_1(y_\perp, \eta_A)\ \exp \Bigg\{ -\frac{1}{4\pi} \int_{\eta_0}^{\eta_A} d\eta \int dz_\perp \vec{\partial}_\perp^2 \Big(i \Omega_1^\dagger (z_\perp, \eta) \\
&\times \frac{\partial}{\partial \eta} \Omega_1 (z_\perp, \eta) \Big)^a \left[\vec{\partial}_\perp^2 \left(\Omega_1^\dagger (z_\perp, \eta) U_z^{\eta_0} \Omega_2 (z_\perp, \eta) \right) \right]_{ab}^{-1} \vec{\partial}_\perp^2 \left(i \Omega_2^\dagger (z_\perp, \eta) \frac{\partial}{\partial \eta} \Omega_2 (z_\perp, \eta) \right)^b \Bigg\}.
\end{aligned}
\tag{3.1.81}
$$

Note that the action of this effective field theory is local and positive. This is our final result for the evolution of the color dipole in the LLA.

3.1.7 Nuclear structure functions

In the case of large nuclei it is possible to write initial conditions for the small-x evolution using the McLerran-Venugolalan model. To calculate the functional integral

[10] To avoid using this "formula", one should differentiate with respect to η_A *after* performing the necessary $\langle \phi \pi \rangle$ contractions. Then one gets the expressions of the type $i \frac{\partial}{\partial \eta_A} \langle \phi(\eta_A) \int_{\eta_0}^{\eta_A} d\eta \pi(\eta) \rangle = \frac{\partial}{\partial \eta_A} (\eta_A - \eta_0) = 1$ whereas in the formula (3.1.78) we obtain this as a sum $i \langle \dot{\phi}(\eta_A) \int_{\eta_0}^{\eta_A} d\eta \pi(\eta) \rangle + i \langle \phi(\eta_A) \pi(\eta_A) = \int_{\eta_0}^{\eta_A} d\eta \delta(\eta_A - \eta) + \theta(0)$ so we should use $\theta(0) = \frac{1}{2}$ to get the correct result

(3.1.67) for the small-x evolution, we need the average

$$\langle A|U_x^{\eta_0}U_y^{\dagger\eta_0}e^{\int dx_\perp \rho_{ab}(x_\perp)U_{ab}^{\eta_0}(x_\perp)}|A\rangle \tag{3.1.82}$$

where $\rho^{ab}(x_\perp) = \Omega_2^{am}(x_\perp,\eta_0)\left[\vec{\partial}_\perp^2\left(\pi_2^m(x_\perp,\eta_0),\pi_1^n(x_\perp,\eta_0)\right)\right]\Omega_1^{nb}(x_\perp,\eta_0)$.

The nuclear matrix element of the two-Wilson-line operator ("color dipole") is given by the Glauber formula [39, 41–44],

$$\int dz_\perp \langle A|\mathrm{Tr}U(x_\perp+z_\perp)U(z_\perp)|A\rangle = \langle A|A\rangle N_c \int d^2b\left[1-e^{-g^2c_F\mathcal{G}(x_\perp^2)L_b}\right] \tag{3.1.83}$$

illustrated in Fig. 9. Usually the nucleus state is normalized in the non-relativistic way so $\langle A|A\rangle = 1$. (Note that the normalization for the nucleon states used in Sect. 3.1.5 is relativistic: $\langle p_B'|p_B\rangle = 2p_{B0}(2\pi)^3\delta(\vec{p}_B'-\vec{p}_B)$). We assume that the size of the dipole $x_\perp$ is much smaller than the radius of the nucleus R so that the propagation length of the dipole located at the impact parameter b through the nucleus is $L_b \equiv 2\sqrt{R^2-b^2}$. In addition, $\rho = \frac{A}{4/3\pi R^3}$ is the nuclear density and

$$\mathcal{G}(x_\perp^2) \equiv \frac{\pi x_\perp^2}{4(N_c^2-1)}\rho\sigma_0 G(\sigma_0,\mu^2=\frac{1}{x_\perp^2}). \tag{3.1.84}$$

The Eq. (3.1.83) is derived under the assumption that the characteristic size of the dipole (the "saturation scale ") is smaller than the size of the nucleon [11]. In this case, the nucleon impact factor is reduced to 1 (see Eq. (3.1.57)), and therefore the quarks propagating along the straight light-like lines [12] interact by the instantaneous (in the

[11] This assumption is certainly true at $A\to\infty$. For real nuclei, one should find the saturation scale Q_s from the final result for the matrix element of the color dipole between the nuclear states, and verify that $Q_s \gg 1$GeV

[12] As we mentioned in Sect. 3.1.5, the energy $s\sigma_0$ should be high enough so we can replace the slope $p_1+\zeta_0 p_2$ by p_1 in the non-logarithmical expressions.

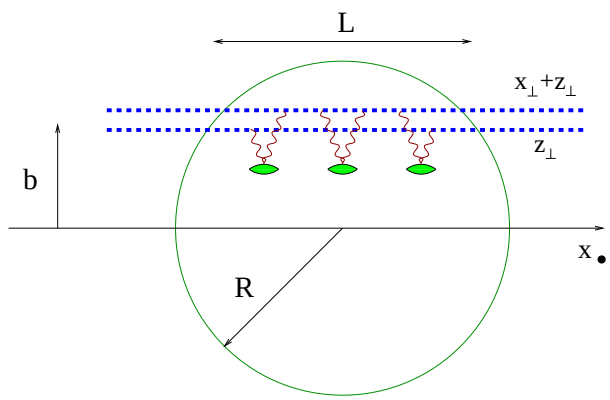

Figure 9: *Color dipole propagating through the nucleus.*

light-cone time $x_\bullet$) potential

$$\rho g^2 t^a \otimes t^a \int \frac{dp_\perp}{(2\pi)^2} \frac{g^2}{2p_\perp^4} \Big(e^{i(p,x-y)_\perp} - 1 \Big) = g^2 t^a \otimes t^a \rho \frac{\alpha_s}{8} (x-y)_\perp^2 \ln (x-y)_\perp^2 m_0^2 \tag{3.1.85}$$

where $m_0^2 \simeq \frac{m_N^2}{4}$ is the IR cutoff, see Eq. (3.1.66). It is worth noting that the factor -1 in the parenthesis in the l.h.s. comes from the diagrams with the two gluons attached to the same nucleon and the same Wilson line as shown in the middle of the Fig. 9. (We need the formula $\theta(0) = 1/2$ to get this result). Taking into account the color factors, one obtains the Eq. (3.1.83) with $x_B G\big(x_B, \mu^2 = x_\perp^{-2}\big) = \frac{4\alpha_s}{\pi} \ln x_\perp^{-2}/m_0^2$, see Eq. (3.1.66).

Similarly to Eq. (3.1.69), it is possible to represent this result as a functional integral over a double set of variables $\Lambda(x_\perp, l) \in SU(3)$ and $v^a(x_\perp, l) \in SU(3)$ algebra:

$$\int dz_\perp \langle A | U(x_\perp + z_\perp) U(z_\perp) | A \rangle = \tag{3.1.86}$$
$$\int d^2 b \int_{\Lambda(0,z_\perp)=1}^{v(L_b,z_\perp)=0} D v^a(y_\perp, l) D\Lambda(y_\perp, l)\ \Lambda(x_\perp + z_\perp, L_b) \Lambda^\dagger(z_\perp, L_b) e^{\int_0^{L_b} dl \mathcal{L}(v,\Lambda)}$$

and

$$\mathcal{L}(v^a(l, x_\perp), \Lambda(l, x_\perp)) = \tag{3.1.87}$$
$$\int dx_\perp v^a(l, x_\perp) \big(\Lambda^\dagger(l, x_\perp) \frac{\partial}{\partial l} \Lambda(l, x_\perp) \big)^a - \int dx_\perp dy_\perp v^a(l, x_\perp) \mathcal{G}\big((x-y)_\perp^2\big) v^a(l, y_\perp)$$

To prove this formula, we write $\Lambda(l, x_\perp) = e^{-igq(l,x_\perp)}$ (cf. Eq. (3.1.69)), use Eq. (3.1.73), and expand in powers of gq. The "propagator" for this functional integral is $\langle q^a(l, x_\perp) p^b(l', x_\perp) \rangle = -i\theta(l - l') \delta^{ab} \delta(x-y)_\perp$ (cf. Eq. (3.1.71), and it is easy to see that the expansion of the l.h.s. of Eq. (3.1.86) in powers of $\mathcal{G}$ reproduces the expansion of the exponent in r.h.s. of Eq. (3.1.83).

The matrix element (3.1.82) can be represented in a similar way:

$$\int dz_\perp \langle A | U_{x+z}^{\eta_0} U_z^{\dagger \eta_0} e^{\int dy_\perp \rho_{ab}(y_\perp) U_{ab}^{\eta_0}(y_\perp)} | A \rangle \ = \ \int d^2 b \int_{\Lambda(0,z_\perp)=1}^{v(L,z_\perp)=0} D v(y_\perp, l) D\Lambda(y_\perp, l)$$
$$\times\ \Lambda(x_\perp + z_\perp, L_b) \Lambda^\dagger(z_\perp, L_b)\ e^{\int dy_\perp \rho^{ab}(y_\perp) \Lambda^{ab}(L_b, y_\perp)} e^{\int_0^{L_b} dl \mathcal{L}(v,\Lambda)}. \tag{3.1.88}$$

(With our accuracy, all the produced dipoles are located on the same impact parameter b). For the gluon density given by Eq. (3.1.66) the integration over the auxiliary fields v^a yields:

$$\int dz_\perp \langle A | U_{x+z}^{\eta_0} U_z^{\dagger \eta_0} e^{\int dy_\perp \rho_{ab}(y_\perp) U_{ab}^{\eta_0}(y_\perp)} | A \rangle \tag{3.1.89}$$
$$= \int d^2 b \int_{\Lambda(0,y_\perp)=1} D\Lambda(y_\perp, l)\ \Lambda(x_\perp + z_\perp, L_b) \Lambda^\dagger(z_\perp, L_b) e^{\int dy_\perp \rho^{ab}(y_\perp) \Lambda^{ab}(L, y_\perp)}$$
$$\times\ \exp\Big\{ \frac{1}{2g^2\rho} \int_0^{L_b} dl \int dy_\perp \big(\Lambda(l, y_\perp) \frac{\partial}{\partial l} \Lambda(l, y_\perp) \big)^a (-\vec{\partial}_\perp^2 + m_0^2)^2 \big(\Lambda(l, y_\perp) \frac{\partial}{\partial l} \Lambda(l, y_\perp) \big)^a \Big\}$$

The final formula for the martix element of the color dipole operator at small x_B is obtained by combining the functional integrals (3.1.81) and (3.1.88):

$$\int dz_\perp \langle A|U^{\eta_A}(x_\perp+z_\perp)\otimes U^{\dagger\eta_A}(z_\perp)|A\rangle \tag{3.1.90}$$
$$= \int d^2b \int_{\Lambda(0,y_\perp)=1}\int_{\Omega_{1,2}(\eta_0,y_\perp)=1} D\Lambda(l,y_\perp)D\Omega_1(y_\perp,\eta)D\Omega_2(y_\perp,\eta)$$
$$\Omega_1^\dagger(x_\perp+z_\perp,\eta_A)\Lambda(L_b,x_\perp+z_\perp)\Omega_2(x_\perp+z_\perp,\eta_A)\otimes\Omega_2^\dagger(z_\perp,\eta_A)\Lambda^\dagger(L_b,z_\perp)\Omega_1(z_\perp,\eta_A)$$
$$\times\ \exp\Bigg\{-\frac{1}{2g^2\rho}\int_0^{L_b}dl\int dy_\perp\big(i\Lambda(l,y_\perp)\frac{\partial}{\partial l}\Lambda(l,y_\perp)\big)^a(m_0^2-\vec{\partial}^2)^2\big(i\Lambda(l,y_\perp)\frac{\partial}{\partial l}\Lambda(l,y_\perp)\big)^a$$
$$-\frac{1}{\alpha_s}\int_{\eta_0}^{\eta_A}d\eta\int dy_\perp\vec{\partial}_\perp^2\Big(i\Omega_1^\dagger(y_\perp,\eta)\frac{\partial}{\partial\eta}\Omega_1(y_\perp,\eta)\Big)^a$$
$$\times\ \Big[\vec{\partial}_\perp^2\Big(\Omega_2^\dagger(y_\perp,\eta)\Lambda^\dagger(L_b,y_\perp)\Omega_1(y_\perp,\eta)\Big)\Big]^{-1}_{ab}\vec{\partial}_\perp^2\Big(i\Omega_2^\dagger(y_\perp,\eta)\frac{\partial}{\partial\eta}\Omega_2(y_\perp,\eta)\Big)^b\Bigg\}.$$

where m_0 is approximately half of the nucleon mass, see Sect. 3.1.5. It is easy to see that the expression in the exponent is real and negative, hence this functional integral can be calculated by lattice methods. (The only restriction is that the lattice regularization should agree with the formula $\theta(0)=\frac{1}{2}$ which was used to get the functional integral (3.1.89) for the Glauber formula (3.1.83)). As we discussed in Sect. 3.1.5, the gluon structure function in the LLA is proportional to the matrix element of the dipole operator: $x_BG\big(x_B,\mu^2=\frac{1}{x_\perp^2}\big)=-\frac{2\pi}{s}\langle\langle \mathrm{Tr}U_i^{\eta_A}(x_\perp)U_i^{\eta_A}(0)\rangle\rangle$.

3.1.8 Conclusion

At high energies the particles move very fast and therefore their trajectories can be approximated by straight lines collinear to their velocities. (The rigorous argument is that if we produce two clusters of particles with different rapidities in a high-energy collision, they perceive each other as moving at a great speed along the straight lines). The propagator of a gluon (or a quark) moving along the straight line reduces to the Wilson-line operator – an infinite gauge link ordered along this line. Thus, we can replace the high-energy QCD of quarks and gluons by the effective field theory of Wilson lines $U(x_\perp,\eta)$ where $x_\perp$ stands for the impact parameter of the particle in the transverse plane and η is the rapidity determined by the velocity the particle. The dynamics of string-type Wilson-line variables in the imaginary "time" $=\eta$ is described by the Hamiltonian (3.1.68)). (The interactions of the particles inside each rapidity cluster, which cannot be described in terms of Wilson lines, give α_s corrections to the Hamiltonian (3.1.68)). The effective field theory of Wilson-line variables leads to the functional integral (3.1.81) for the small-x evoltuion of the color dipole. For large nuclei, we can go further and use the Glauber formula (3.1.82) for the initial conditions of the small-x evolution. Substituting these initial conditions into the functional integral (3.1.81), we have found an explicit expression for the small-x structure function of the

large nuclei in terms of the functional integral calculable by the lattice Monte-Carlo methods.

It should be emphasized that our formula (3.1.81) gives the evolution of the color dipole only in the LLA. In the case of large nucleus we have an additional parameter $A \gg 1$ so our LLA approximation based on the non-linear equation (3.1.50) has a window $\alpha_s^2 A^{1/3} \sim 1$, $\alpha_s \ln x_B \sim 1$ where it is justified even at moderately small x_B. In the case of nucleon, our $\alpha_s(Q_s) \ll 1$, $\alpha_s(Q_s) \ln x_B \sim 1$ approximation should be justified *a posteriori* after checking that the saturation does occur at sufficiently small x_B. If the saturation takes place at such low x that $\alpha_s(Q_s) \ln x_B \gg 1$, our LLA breaks down and we need to take into account the non-fan diagrams such as t-channel loops formed by BFKL pomerons. However, we hope that the non-linear equation (3.1.50) leads to the result for the structure function which does not violate unitarity (see the discussion in Refs. [18, 20, 25, 34, 45]) and therefore we should not expect the large discrepancy between the unitary LLA result and the exact amplitude at THERA energies.

Acknowledgements

The author is grateful to Y. Kovchegov and E. Levin for valuable discussions.

This work was supported by the US Department of Energy under contract DE-AC05-84ER40150.

References

[1] E.A. Kuraev, L.N. Lipatov and V.S. Fadin, Sov. Phys. JETP **45**, 199 (1977); I.I. Balitsky and L.N. Lipatov, Sov. J. Nucl. Phys. **28**, 822 (1978).

[2] I. Balitsky, Nucl. Phys. **B 463**, 99 (1996).

[3] O. Nachtmann, Ann. Phys. **209**, 436 (1991).

[4] J.C. Collins and R.K. Ellis, Nucl. Phys. **B 360**, 3 (1991).

[5] A.H. Mueller, Nucl. Phys. **B 415**, 373 (1994).

[6] A.H. Mueller and B. Patel, Nucl. Phys. **B 425**, 471 (1994).

[7] N.N. Nikolaev and B.G. Zakharov, Z. Phys. **C 49**, 607 (1991).

[8] N.N. Nikolaev and B.G. Zakharov, Z. Phys. **C 64**, 631 (1994).

[9] L.N. Lipatov, Phys. Reports **286**, 131 (1997).

[10] V.S. Fadin and L.N. Lipatov, Phys. Lett. **B 429**, 127 (1998).

[11] M. Ciafaloni and G. Camici, Phys. Lett. **B 430**, 349 (1998).

[12] Yu.V. Kovchegov and A.H. Mueller, Phys. Lett. **B 439**, 428 (1998).

[13] E. Levin, *The BFKL high-energy asymptotics in the next-to-leading approximation.* Preprint TAUP-2501-98 (hep-ph/9806228), 2000.

[14] I. Balitsky, Phys. Rev. Lett. **81**, 2024 (1998).

[15] L. McLerran and R. Venugopalan, Phys. Rev. **D 49**, 2233 (1994);
L. McLerran and R. Venugopalan, Phys. Rev. **D 49**, 3352 (1994).

[16] L. McLerran and R. Venugopalan, Phys. Rev. **D 50**, 2225 (1994).

[17] A.H. Mueller, Nucl. Phys. **B 558**, 285 (1999).

[18] E. Levin and K. Tuchin, Nucl. Phys. **B 573**, 833 (2000).

[19] Y.V. Kovchegov, Phys. Rev. **D 60**, 034008 (2000).

[20] Yu.V. Kovchegov, Phys. Rev. **D 61**, 074018 (2000).

[21] L.V. Gribov, E.M. Levin and M.G. Ryskin, Phys. Rept. **100**, 1 (1983).

[22] A.H. Mueller and J. Qiu, Nucl. Phys. **B 268**, 427 (1986).

[23] J. Jalilian-Marian et al., Nucl. Phys. **B 504**, 415 (1997).

[24] J. Jalilian-Marian et al., Phys. Rev. **D 59**, 014014 (1999).

[25] J. Jalilian-Marian et al., Phys. Rev. **D 59**, 034007 (1999).

[26] J. Jalilian-Marian, A. Kovner and H. Weigert, Phys. Rev. **D 59**, 014015 (1999).

[27] I. Balitsky, *Factorization and effective action for high-energy scattering in QCD.* Preprint hep-ph/9808215, 2001.

[28] I. Balitsky, Phys. Rev. **D60**, 014020 (1999).

[29] A. Kovner, J. G. Milhano and H. Weigert, Phys. Rev. **D 62**, 114005 (2000).

[30] A.L. Ayala, M.B. Gay Ducati and E.M. Levin, Nucl. Phys. **B 493**, 305 (1997).

[31] I. Balitsky and V.M. Braun, Nucl. Phys. **B 311**, 541 (1989).

[32] E. Levin, *Low-x physics.* Preprint hep-ph/0010272, 2000. Talk at *Diffraction 2000, Centraro, Italy.*

[33] I. Balitsky, *High-energy QCD and Wilson lines.* Preprint JLAB-THY-00-44 (hep-ph/0101042), 2001. To be published in the Boris Ioffe Festschrift "At the Frontier of Particle Physics/Handbook of QCD", edited by M. Shifman (World Scientific, Singapore, 2001).

[34] M.A. Braun, Eur. Phys. J. **C 16**, 337 (2000).

[35] E. Iancu, A. Leonidov and L. McLerran, *The renormalization group equation for the color glass condensate.* Preprint BNL-NT-01-3 (hep-ph/0102009), 2001.

[36] H. Weigert, *Unitarity at small Bjorken x.* Preprint NORDITA-2000-34-HE (hep-ph/0004044), 2000.

[37] I. Balitsky and E. Kuchina, Phys. Rev. **D62**, 074004 (2000).

[38] I. Balitsky and V.M. Braun, Nucl. Phys. **B 361**, 93 (1991).

[39] A.H. Mueller, Nucl. Phys. **B 335**, 115 (1990);
E. Levin and K. Tuchin, *New scaling in high energy DIS.* Preprint TAUP-2659-2000 (hep-ph/0012167), 2000;
E. Levin and K. Tuchin, *Nonlinear evolution and saturation for heavy nuclei in DIS.* Preprint TAUP-2664-2001 (hep-ph/0101275), 2001.

[40] E. Iancu and L. McLerran, *Saturation and universality in QCD at small x.* Preprint SACLAY-T01-026 (hep-ph/0103032), 2001.

[41] B.Z. Kopeliovich, L.I. Lapidus and A.B. Zamolodchikov, JETP. Lett. **33**, 595 (1981).

[42] E. Levin and M. Ryskin, Sov. J. Nucl. Phys. **47**, 889 (1988).

[43] J. Jalilian-Marian et al., Phys. Rev. **D 55**, 5414 (1997).

[44] Yu.V. Kovchegov and A.H. Mueller, Nucl. Phys. **B 529**, 451 (1998).

[45] A.H. Mueller, Nucl. Phys. **B 437**, 107 (1995).

3.2 Perturbative Evolution at Small x

G. Altarelli
Theory Division, CERN, CH-1211 Geneve 23, Switzerland

R.D. Ball
Dept. of Physics and Astronomy, University of Edinburgh, Edinburgh EH9 3JZ, Scotland

S. Forte
INFN, Sezione di Roma III, via della Vasca Navale 84, I-00146 Roma, Italy

Abstract

We review small x contributions to perturbative evolution equations for parton distributions, and their resummation. We emphasize in particular the resummation technique recently developed in order to deal with the apparent instability of naive small x evolution kernels and understand the empirical sucess of fixed–order perturbation theory. We give predictions for the gluon distribution and the structure functions $F_2(x, Q^2)$ and $F_L(x, Q^2)$ in an extended kinematic region, such as would be relevant for THERA or LEP+LHC ep colliders.

3.2.1 Introduction

Measurements of the inclusive structure functions $F_2(x, Q^2)$ and $F_L(x, Q^2)$ at HERA have shown that the scaling violations of structure functions are in extremely good agreement with the perturbative next-to-leading order (NLO) QCD prediction, down to the smallest values of x, and for all $Q^2 \gtrsim 1\,\mathrm{GeV}^2$ [1]. This agreement is surprising in that it is known that perturbative corrections beyond NLO in α_s are enhanced by powers of $\xi \equiv \ln(1/x)$, and thus one would expect higher order corrections to be sizable whenever $\alpha_s(Q^2)\xi \gtrsim 1$, i.e. in most of the HERA kinematic region. Whereas techniques for the inclusion of small x contributions to leading twist evolution equations have been known for some time [2, 3], only recently did a consistent picture of the general structure of these contributions and their resummation emerge. Indeed, considerable theoretical progress has been spurred by the determination [4] of next-to-leading corrections to the BFKL kernel, which allows the computation of the next-to-leading $\log(1/x)$ (NLLx) contributions to anomalous dimensions to all orders in α_s. Specifically, it is now understood that the inclusion of NLLx contributions leads to instability [5] of perturbative evolution, unless it is suitably combined with a resummation of the collinear singularities [6–8] which are resummed order by order in the standard QCD evolution equations. Furthermore, the NLLx perturbative corrections give rise to increasingly large contributions to high orders of perturbation theory [9, 10] that make

a nonsense of the perturbative expansion and call for an all-order resummation of the small-x behaviour of the anomalous dimensions [11, 12].

Practical methods to deal with these issues have been developed recently [7, 13], and lead to a resummation prescription which is amenable to numerical treatment and direct comparison with the data. It then appears that the observed smallness of perturbative higher order corrections at small x can be accommodated within the current knowledge of the general structure of anomalous dimensions, but it poses very stringent constraints on the form of the unknown higher order terms. Furthermore, even when these constraints are respected, so that, as required by the data, deviations of the behaviour of the observable structure functions from the fixed next-to-leading order prediction are very small, still non–negligible modifications of the fitted parton distributions at small x are found. This, because of ambiguities in the resummation procedure, entails larger uncertainties on parton distributions at small x. Likewise, these corrections have a sizable impact on the extraction of α_s from small x data, both on the central value and the estimates of overall theoretical uncertainties [13, 14].

In the wider kinematic region available at THERA the small differences between resummed and fixed–order predictions could be put to more stringent tests. This would allow one to pin down more precisely the ambiguities in the resummation procedure, thereby reducing the uncertainty on parton distributions at small x and on precision determinations of α_s at small x. Also, the possibility of reaching smaller values of x for given Q^2 would allow a test of resummed perturbation theory in a region where the relevant resummation parameter $\alpha_s\xi$ is large, and also to see whether the perturbative description of scaling violations remains satisfactory or starts to break down, as is often suggested [15].

Here we briefly review our current understanding of resummed perturbation theory at small x. We then give predictions for the gluon distribution and the structure functions F_2 and F_L in two different resummation scenarios, and compare these to fixed next–to–leading order results in the kinematic range which is relevant for THERA. This is essentially the same kinematic region accessible at a hypothetical lepton–hadron collider obtained combining LEP with the LHC, so our predictions would also be relevant at such a machine.

3.2.2 Duality of small x evolution

The basic result which allows the determination of contributions to anomalous dimensions which are logarithmically enhanced in x to all orders in the coupling, and thus their inclusion in evolution equations, is the *duality* of perturbative evolution [7, 16]: because leading–twist evolution of structure functions takes place both in x and Q^2, it admits a dual description in terms of equations for evolution in $t = \ln(Q^2/\mu^2)$ or evolution in $\xi = \ln(1/x)$. This property is easy to prove [16] when the coupling is fixed, and can be shown to remain valid when the coupling runs by explicit order–by–order perturbative computation [12].

Let us first consider for simplicity the case (relevant in the very small x limit) of a single parton distribution $G(\xi, t)$, identified with the dominant eigenvector of

perturbative evolution. The pair of dual evolution equations are then

$$\frac{d}{dt}G(\xi,t) = P(\xi,\alpha_s)\otimes G(\xi,t), \tag{3.2.1}$$

$$\frac{d}{d\xi}G(\xi,t) = K(t,\alpha_s)\otimes G(\xi,t), \tag{3.2.2}$$

The convolutions on the right–hand sides of the dual evolution equations (3.2.1-3.2.2) are with respect to ξ in the first equation ($P(\xi,\alpha_s)$ is the usual splitting function) and with respect to t in the second equation; $\alpha_s = \alpha_s(t)$ and is unaffected by convolutions. Duality means that the solutions to these equations coincide up to higher twist corrections provided the respective boundary conditions and kernels are suitably matched.

The detailed form of the matching of boundary conditions is irrelevant for our purposes, but it is important to notice that the matching is such that the boundary condition to (3.2.1) depends only on ξ (and not on t) and the boundary condition to (3.2.2) depends only on t (and not on ξ) as required by factorization. The matching of the kernels is given by the duality equation

$$\chi(\gamma(N,\alpha_s),\alpha_s) = N, \tag{3.2.3}$$

or equivalently its inverse

$$\gamma(\chi(M,\alpha_s),\alpha_s) = M. \tag{3.2.4}$$

Here γ is the usual anomalous dimension, related to the splitting function by Mellin transformation with respect to ξ:

$$\gamma(N,\alpha_s) = \int_0^\infty d\xi\, e^{-N\xi}\; P(\xi,\alpha_s). \tag{3.2.5}$$

The relation between $\chi(M,\alpha_s)$ and $K(t,\alpha_s)$ is somewhat more complicated because, upon Mellin transformation with respect to t the running coupling $\alpha_s(t)$ on the right–hand side of Eq. (3.2.1) becomes a differential operator. The relation between the evolution kernel $K(t,\alpha_s)$ and the dual kernel $\chi(M,\alpha_s)$ can nevertheless be determined order by order in perturbation theory [12]: defining

$$K(t,\alpha_s) = \alpha_s K_0(t) + \alpha_s^2 K_1(t) + \ldots, \tag{3.2.6}$$

$$\chi(M,\alpha_s) = \alpha_s \chi_0(M) + \alpha_s^2 \chi_1(M) + \ldots, \tag{3.2.7}$$

we get

$$\begin{aligned}\chi_0(M) &= \int_{-\infty}^{\infty} dt\, e^{-Mt}\; K_0(t);\\ \chi_1(M) &= \int_{-\infty}^{\infty} dt\, e^{-Mt}\; K_1(t) + \frac{\beta_0}{4\pi}\frac{1}{2}\frac{\chi_0(M)\chi_0''(M)}{{\chi_0'}^2(M)};\ldots,\end{aligned} \tag{3.2.8}$$

where $\beta_0 = \frac{11}{3}n_c - \frac{2}{3}n_f$ is the first coefficient of the QCD β function.

It follows from the form of the duality equation (3.2.3) that knowledge of the leading (next-to-leading, ...) term in the expansion of χ in powers of α_s at fixed M determines the leading (next-to-leading, ...) term in the expansion of γ in powers of α_s at fixed α_s/N: i.e. defining further

$$\gamma(N, \alpha_s) = \gamma_s(\tfrac{\alpha_s}{N}) + \alpha_s \gamma_{ss}(\tfrac{\alpha_s}{N}) + \dots , \tag{3.2.9}$$

then

$$\chi_0(\gamma_s(\tfrac{\alpha_s}{N})) = \frac{N}{\alpha_s}, \quad \gamma_{ss}(\tfrac{\alpha_s}{N}) = -\frac{\chi_1(\gamma_s(\frac{\alpha_s}{N}))}{\chi_0'(\gamma_s(\frac{\alpha_s}{N}))}, \dots . \tag{3.2.10}$$

Likewise, knowledge of the leading, next-to-leading, ... terms in the expansion of γ in powers of α_s at fixed N determines the leading, next-to-leading, ... terms in the expansion of χ in powers of α_s at fixed α_s/M: writing

$$\gamma(N, \alpha_s) = \alpha_s \gamma_0(N) + \alpha_s^2 \gamma_1(N) + \dots , \tag{3.2.11}$$

$$\chi(M, \alpha_s) = \chi_s(\tfrac{\alpha_s}{M}) + \alpha_s \chi_{ss}(\tfrac{\alpha_s}{M}) + \dots , \tag{3.2.12}$$

then

$$\gamma_0(\chi_s(\tfrac{\alpha_s}{M})) = \frac{M}{\alpha_s}, \quad \chi_{ss}(\tfrac{\alpha_s}{M}) = -\frac{\gamma_1(\chi_s(\frac{\alpha_s}{M}))}{\gamma_0'(\chi_s(\frac{\alpha_s}{M}))}, \dots . \tag{3.2.13}$$

It should be understood that the running coupling corrections Eq. (3.2.8) are always included in the definition of χ in the above equations.

Because the ξ evolution equation is essentially the same as the BFKL equation (up to factorization scheme and scale choices, which become relevant beyond leading order [4, 17]) the duality relation can be viewed as a consistency condition between this equation and the standard renormalization group equation for moments of structure functions in the region of their common validity (i.e. large Q^2 and small x). Hence, knowledge of the BFKL kernel $K(t, \alpha_s)$ (3.2.6) can be translated into information of χ (3.2.7), which in turn can be used to gain information on the logarithmically enhanced contributions γ_s, γ_{ss}, ... (3.2.9) to the anomalous dimension $\gamma(\alpha_s, N)$, and conversely. In fact, the leading-order equation in (3.2.10) has been known for a long time [18]; the new insight here is that this is just a consequence of a more general duality.

3.2.3 The Double–Leading expansion

Only the first two orders in the expansion of χ at fixed M and γ at fixed N are currently known. While the perturbative expansion of γ is well-behaved, in the sense that $\alpha_s\gamma_1$ is a small correction to γ_0 for reasonable values of the coupling constant, the perturbative expansion of χ is very poorly behaved, in that the NLO correction χ_1 completely changes the qualitative shape of the kernel. In particular (see Fig. 1), in the physical region $0 \leq M \leq 1$ the LO kernel has simple poles with positive residue at $M = 0$

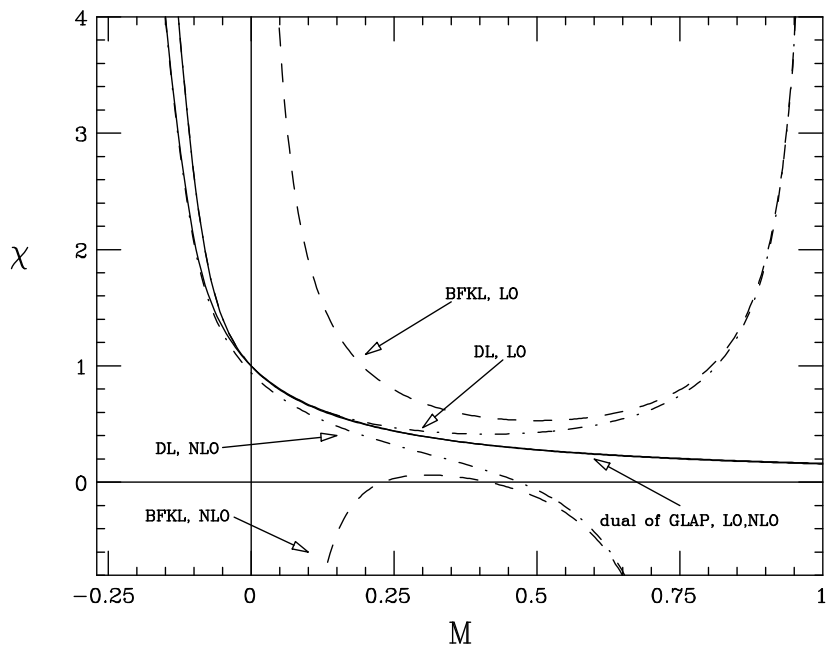

Figure 1: *Plots of different approximations to χ: the BFKL leading and next-to-leading order functions (3.2.7), $\alpha_s\chi_0$ and $\alpha_s\chi_0 + \alpha_s^2\chi_1$ (dashed); the LO and NLO dual $\alpha_s\chi_s$ and $\alpha_s\chi_s + \alpha_s^2\chi_{ss}$ (3.2.12) of the one and two loop anomalous dimensions (solid), and the double–leading functions at LO and NLO defined in Eq. (3.2.15) (dotdashed). All curves are computed with $\alpha_s = 0.2$.*

and $M = 1$ and a minimum in between. The NLO correction χ_1 instead has higher order poles with negative coefficient, and, for any realistic value of α_s (essentially, for all $\alpha_s \gtrsim 0.03$) the full NLO function has just a maximum (for smaller α_s it has a minimum and two maxima) [9]. It is easy to show that the solution to the evolution equation determined by a kernel with this shape displays unphysical oscillatory behaviour in the limit as $x \to 0$, and thus, in particular, leads to negative cross-sections [5].

Because the Mellin transform (3.2.8) of $t^k = \ln^k(Q^2/\mu^2)$ is $(k-1)!/M^{k-1}$, the presence of $1/M$ poles in the kernel χ is related to collinear singularities: indeed, according to Eq. (3.2.4) the coefficients of these singularities are determined by knowledge of the anomalous dimensions γ_0, γ_1, ... in the usual renormalization group equations, which resum collinear singularities. It is easy to understand [7] why these singularities lead to a series of poles in $M = 0$ with alternating signs. Indeed, recall that momentum conservation implies that the largest eigenvalue of the anomalous dimension matrix vanishes at $N = 1$, i.e. $\gamma(1, \alpha_s) = 0$, which by duality (3.2.3) implies $\chi(0, \alpha_s) = 1$. It follows that if, in the vicinity of $M = 0$, χ_s behaves as

$$\chi_s \underset{M\to 0}{\sim} \frac{\alpha_s}{\alpha_s + M} = \frac{\alpha_s}{M} - \frac{\alpha_s^2}{M^2} + \frac{\alpha_s^3}{M^3} + \dots \quad : \tag{3.2.14}$$

the series of poles in χ_s, χ_{ss}, ... actually sums up to the regular behaviour $\chi(0, \alpha_s) = 1$.

The poles in χ as $M \to 0$ are summed to all orders into χ_s, χ_{ss}, ... , and thus the undesirable behaviour of the expansion of χ can be removed by defining order by order an improved expansion. Namely, we define a *double leading expansion* where to each order in α_s both the terms present in the expansion in powers of α_s at fixed M and at fixed α_s/M are included:

$$\begin{aligned}\chi(M,\alpha_s) &= \left[\alpha_s\chi_0(M) + \chi_s\left(\tfrac{\alpha_s}{M}\right) - \tfrac{n_c\alpha_s}{\pi M}\right] \\ &\quad +\alpha_s\left[\alpha_s\chi_1(M) + \chi_{ss}\left(\tfrac{\alpha_s}{M}\right) - \alpha_s\left(\tfrac{f_2}{M^2} + \tfrac{f_1}{M}\right) - f_0\right] + \cdots \quad (3.2.15)\end{aligned}$$

In this expansion, in the vicinity of $M = 0$ the singularities of χ_0, χ_1, ... are resummed into χ_s, χ_{ss}, while the subtraction terms avoid double–counting of these contributions. Note (see Fig. 1) that at larger values of M the shape of χ_0, χ_1, ... is reproduced, but in most of the M range the kernel Eq. (3.2.15) coincides with the (dual of) the standard anomalous dimensions γ_0 and γ_1, consistent with the empirical smallness of small-x correction to perturbative evolution. This also has the significant implication that the double–leading expansion of χ is as stable as the usual expansion of γ at fixed N.

It is easy to show that the corresponding double leading expansion of γ,

$$\begin{aligned}\gamma(N,\alpha_s) &= \left[\alpha_s\gamma_0(N) + \gamma_s\left(\tfrac{\alpha_s}{N}\right) - \tfrac{n_c\alpha_s}{\pi N}\right] \\ &\quad +\alpha_s\left[\alpha_s\gamma_1(N) + \gamma_{ss}\left(\tfrac{\alpha_s}{N}\right) - \alpha_s\left(\tfrac{e_2}{N^2} + \tfrac{e_1}{N}\right) - e_0\right] + \cdots , \quad (3.2.16)\end{aligned}$$

is consistent with duality, in that χ (3.2.15) and γ (3.2.16) are dual to each other order by order in the double–leading expansion, up to higher order corrections. Hence, for practical applications we may directly use the double–leading anomalous dimension (3.2.16) in the usual evolution equation (3.2.1). This will ensure that collinear singularities are resummed according to the renormalization group in the usual way, while leading logs of $1/x$ are consistently included up to next–to–leading order.

For actual phenomenology, the full set of anomalous dimensions and coefficient functions are needed. It is easy to see that the double–leading expansion is consistent with diagonalization of the anomalous dimension matrix, in the sense that one may equivalently, up to subleading corrections, construct a two by two matrix of double–leading anomalous dimensions and diagonalize it, or else construct directly a double–leading expansion of eigenvalues and projectors. Because one of the two eigenvectors of γ is free of small–x singularities, so its double–leading expansion coincides with the standard expansion at fixed N, the latter procedure is in practice simpler. Hence, the double leading expansion can be fully defined in terms of the expansion of the large anomalous dimension eigenvalue, and of the quark–sector matrix elements which determine the projectors on the eigenvectors. Likewise, one can construct double–leading coefficient functions, and prove that the expansion transforms consistently upon changes of factorization scheme. Detailed proofs and results needed for a practical implementation are given in ref. [13].

3.2.4 Resummation

Even though the difference between the double–leading expansions of χ (3.2.15) and γ (3.2.16) is subleading, it can in practice be large when $M \gtrsim 0.25$. Indeed, recall that duality (3.2.3) implies $\chi = N$. It is clear from Fig. 1 that in the region $M \gtrsim 0.25$ the difference between the leading order and next-to-leading order double–leading curves is small for any fixed value of M, but it is quite large for a fixed value of $\chi = N$, because the curves are almost parallel to the M–axis: the LO BFKL curve has a minimum at $M = 1/2$. Since γ is a function of N, in this region the perturbative solution (3.2.10) of the duality relation (3.2.3) is not good and the expansion of γ is not well behaved.

A possible way out is to determine the double–leading γ (3.2.16) from the double–leading χ (3.2.15) by solving the duality relation (3.2.3) exactly (rather than perturbatively). This can be done for instance by numerical methods, or equivalently by differentiating with respect to t the solution of the evolution equation (3.2.2) determined using the double–leading χ kernel (3.2.15), as in ref. [8]. However, this approach, besides being cumbersome to implement in standard evolution codes, has the shortcoming that it hides a genuine perturbative ambiguity. Indeed, in this way the perturbative expansion of γ is in practice stabilized by assuming that in the region $M \approx 1/2$ the (large) subleading corrections to γ will be such as to reproduce the shape of χ, as computed to some fixed perturbative order, or possibly further improved according to a model of its behaviour at large $M \sim 1$ [8].

We instead prefer to use only the available perturbative information on γ, without making model–dependent assumptions. It can be shown [12] that the poor perturbative behavior of the expansion of γ at fixed α_s/N manifests itself in a rise of the associate splitting functions: $P_{ss}/P_s \underset{\xi\to\infty}{\sim} \alpha_s\xi$, $P_{sss}/P_s \underset{\xi\to\infty}{\sim} \alpha_s^2\xi^2$ and so on. This rise can be removed by simply subtracting at each order a suitable constant c_i from χ_i (computable order by order in perturbation theory as a function of χ_i and their derivatives at $M = 1/2$), and then determining $\gamma_{ss\ldots}$ from the subtracted χ_i. Thus, the expansion of γ (3.2.7) can be stabilized by just reorganizing the perturbative expansion of χ:

$$\chi(M,\alpha_s) = \alpha_s\chi_0(M) + \alpha_s^2\chi_1(M) + \ldots \tag{3.2.17}$$

$$= \alpha_s\tilde{\chi}_0(M) + \alpha_s^2\tilde{\chi}_1(M) + \ldots, \tag{3.2.18}$$

where

$$\alpha_s\tilde{\chi}_0(M,\alpha_s) \equiv \alpha_s\chi_0(M) + \Delta\lambda, \qquad \tilde{\chi}_i(M) \equiv \chi_i(M) - c_i, \tag{3.2.19}$$

for $i = 1, 2, \ldots$, and thus

$$\Delta\lambda \equiv \sum_{n=1}^{\infty} \alpha_s^{n+1} c_n. \tag{3.2.20}$$

If χ has a minimum, then its value at the minimum coincides [7] with the value of $\tilde{\chi}_0$ at its minimum $M = 1/2$, namely

$$\lambda \equiv \tilde{\chi}_0(\tfrac{1}{2}) = \chi_0(\tfrac{1}{2}) + \Delta\lambda. \tag{3.2.21}$$

Since the value of χ at its minimum determines the asymptotic behaviour of the structure function as $x \to 0$, this implies that in order to remove the perturbative instability it is necessary and sufficient to resum the asymptotic small x behaviour into the leading order kernel $\tilde{\chi}_0$. The perturbative instability signals the fact that the all–order asymptotic behaviour must be known to all orders.

Of course, we are free to use any particular truncation of $\Delta\lambda$ (3.2.20): for instance, we could simply take χ to coincide with its NLO form in the double–leading expansion. Eq. (3.2.18) then provides us with a stable perturbative expansion of γ, which at NLO is very close to the exact dual of χ, the large subleading corrections having been resummed in a minimal way. In this way Eq. (3.2.18) gives us a simple prescription which completely stabilizes the double–leading expansion of γ whenever the double–leading expansion of χ is also stable. Hence, any specific resummation of χ (such as that constructed in ref. [8]) can be accommodated in this formalism. Since however we prefer not to rely on such specific assumptions, we will consider λ (3.2.21) as a free parameter.

To NLO, the (resummed) expansion of γ obtained from Eq. (3.2.18) is related to the unresummed expansion obtained from Eq. (3.2.17) by

$$\tilde{\gamma}(N, \alpha_s) = \tilde{\gamma}_s\left(\tfrac{\alpha_s}{N}\right) + \alpha_s \tilde{\gamma}_{ss}\left(\tfrac{\alpha_s}{N}\right) + \ldots, \tag{3.2.22}$$

where

$$\begin{aligned} \tilde{\gamma}_s\left(\tfrac{\alpha_s}{N}\right) &= \gamma_s\left(\tfrac{\alpha_s}{N-\Delta\lambda}\right), \\ \tilde{\gamma}_{ss}\left(\tfrac{\alpha_s}{N}\right) &= \gamma_{ss}\left(\tfrac{\alpha_s}{N-\Delta\lambda}\right) - \frac{\chi_1(\frac{1}{2})}{\chi_0'\left(\gamma_s\left(\frac{\alpha_s}{N-\Delta\lambda}\right)\right)}. \end{aligned} \tag{3.2.23}$$

Since the resummation only involves formally subleading terms,

$$\gamma_s + \alpha_s \gamma_{ss} = \tilde{\gamma}_s + \alpha_s \tilde{\gamma}_{ss} + O(\alpha_s^3/N). \tag{3.2.24}$$

A resummed double–leading expansion can finally be constructed by combining the resummed anomalous dimension $\tilde{\gamma}$ (3.2.22) with the standard expansion of γ at fixed N. This gives a resummed double–leading expression for the large anomalous dimension eigenvector. It can further be shown [13] that resummed double–leading expressions for the full matrix of anomalous dimensions and for coefficient functions can be obtained by performing the replacement $N \to N - \Delta\lambda$ in all remaining quantities, i.e. the projectors and the coefficient functions.

The construction of the resummed double–leading expansion entails a further ambiguity in the treatment of the double counting subtractions in Eq. (3.2.16): because these terms are common to the fixed–N expansion γ_0, γ_1, ... and the fixed α_s/N expansion γ_s, γ_{ss}, ... , we are free to decide whether to leave them unaffected by the replacement $N \to N - \Delta\lambda$ or not. This defines a pair of resummation procedures, which of course only differ by subleading terms. Clearly, a variety of intermediate alternatives would also be possible. The main difference between these prescriptions is the nature of the small N singularities of the anomalous dimension, which control the

asymptotic small x behaviour. The resummed anomalous dimension always has a cut starting at $N = \lambda$ Eq. (3.2.21), which corresponds [13] to an $x^{-\lambda}$ behaviour of splitting functions at small x. If the subtractions are affected by the replacement, then γ_0 and γ_1 are the same as in the unresummed case (S–resummation), i.e. they have a simple pole at $N = 0$, which leads to a "double–scaling" [19] rise at small x. If the subtractions are unaffected, this pole is removed by the subtraction itself (R–resummation). It follows that if λ is positive, then the two resummations give similar results at small x, namely an $x^{-\lambda}$ power rise. If $\lambda \leq 0$, the S–resummation will display double scaling at small x, while the R–resummation will display a valence-like $x^{-\lambda}$ behaviour.

3.2.5 Predictions for THERA

A comparison of the resummation discussed in the previous sections to recent HERA data [20] was presented in ref. [13]. The best–fit results of that reference can be used to obtain predictions for THERA and discuss the study of small x scaling violations at such a facility. Because of the larger center–of–mass energy available at THERA, these predictions essentially amount to an extension of the current kinematic range of $1/x$ by about a decade for each value of Q^2. It is interesting to note that more or less the same center–of–mass energy would be available at a hypothetical lepton–hadron collider obtained combining LEP with the LHC.

The phenomenological analysis of ref. [13] is based on a fit to data for the reduced cross–section

$$\sigma_{red}(x, y, Q^2) = F_2(x, Q^2) + \frac{y^2}{2(1-y)+y^2} F_L(x, Q^2). \tag{3.2.25}$$

determined from structure functions F_2 and F_L computed to next–to–leading order in the double leading expansion with the R– and S–resummation prescriptions discussed in Sect. 3.2.4, by evolving parton distributions given at a scale $Q_0 = 2$ GeV. A standard unresummed next–to–leading order fit is also performed for comparison. The fits are performed in the parton scheme, so the quark distribution coincides by construction with F_2. The large–x shape of parton distributions is taken from a global fit, while the small x behaviour is parametrized by two free parameters λ_q and λ_g, which give the asymptotic small–x behaviour of the singlet quark and gluon distributions respectively as $x^{-\lambda_q}$, $x^{-\lambda_g}$. The resummation parameter λ Eq. (3.2.21) is also left as a free parameter. The strong coupling is fixed at $\alpha_s(M_z) = 0.119$.

Because at the initial scale Q_0 abundant data are available down to the smallest values of x, and F_2 coincides with the quark distribution, the quark exponent λ_q turns out to be the same in all fits, and gives the effective power rise of the $F_2(x, Q_0^2) \underset{x\to 0}{\sim} x^{-\lambda_q}$: $\lambda_q \approx 0.2$. The best–fit value of the gluon exponent is valence-like in all fits: in the two-loop fit it is $\lambda_g \approx -0.1$; while in the resummed fits it is significantly more valence-like, $\lambda_g \approx -0.2$ for both S– and R–resummation. The value of the resummation parameter λ instead varies significantly according to the resummation prescription which is adopted. For the S–resummation, any value $\lambda \leq 0$ gives a good fit, with the best fit around $\lambda \approx -0.25$. As discussed in Sect. 3.2.4 the S–resummation with vanishing or negative

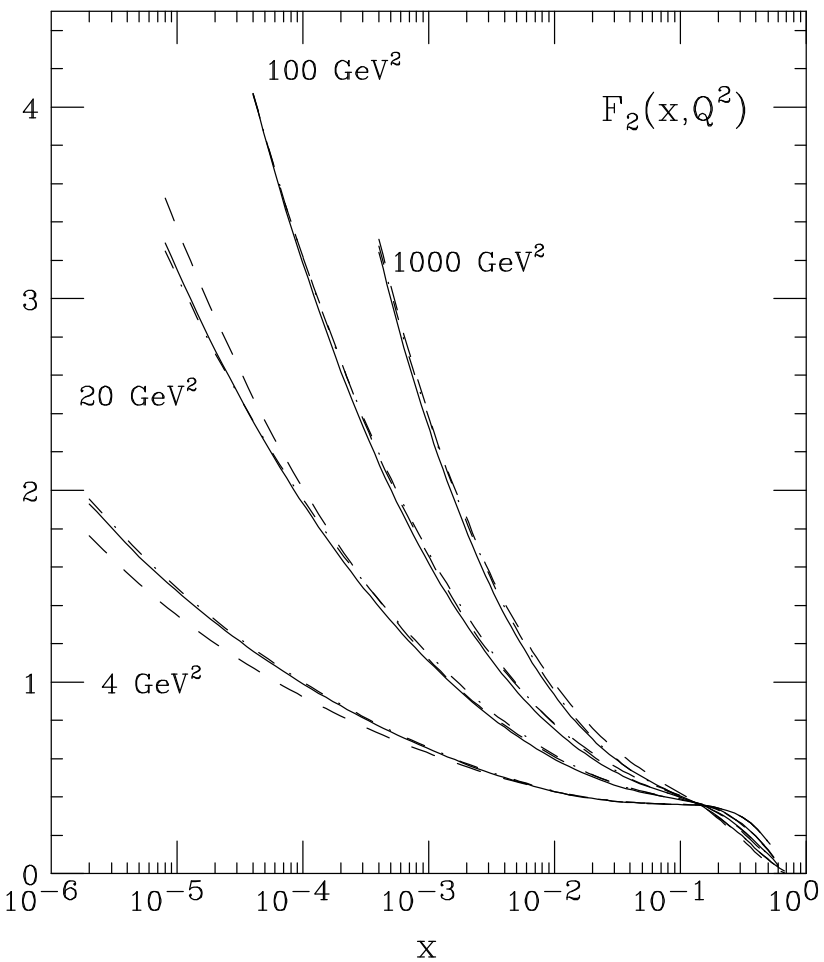

Figure 2: *The structure function $F_2(x, Q^2)$ obtained from a fit [13] to HERA data [20]. The prediction for THERA is the last decade in x for each value of Q^2. The solid curve is an unresummed fixed–order two loop fit, while the dot-dashed curve corresponds to the S–resummation and the dashed curve to the R–resummation discussed in Sect. 3.2.4.*

λ is closest to the unresummed fixed–order result. With the R–resummation, instead, only a fine–tuned value of $\lambda \approx 0.2$ gives a good fit. This value of λ turns out to be the same which one gets by fine–tuning the resummed anomalous dimension so that it be closest to the unresummed one in the HERA kinematic region [7]. Both resummed fits give a similar $\chi^2 \approx 52$ with 93 degrees of freedom, to be compared to the unresummed value $\chi^2 = 60$.

The structure function $F_2(x, Q^2)$ obtained in these fits is displayed in Fig. 2. It is apparent that, given the high precision of the HERA data, all curves, which give good fits to the data, are constrained to lie essentially on top of each other throughout the HERA region, except possibly at the smallest x values $x \lesssim 10^{-4}$ at the initial scale Q_0, where the R–resummation curve rises slightly less. In the THERA range it is still very difficult to tell the difference between various prescriptions at higher

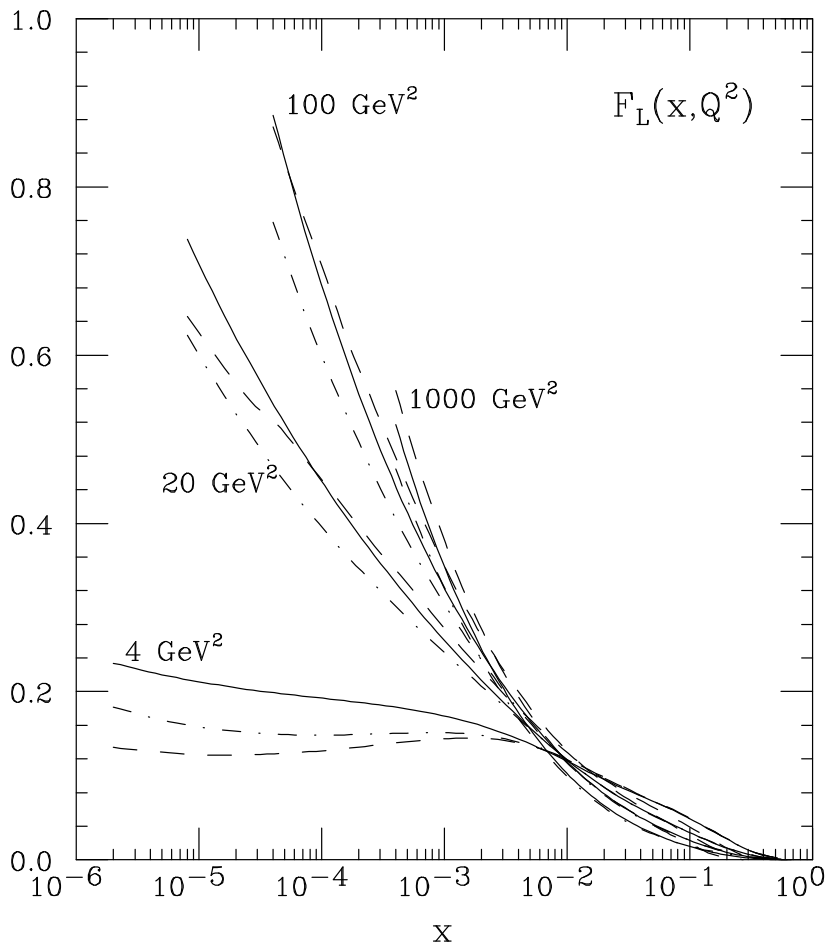

Figure 3: *Same as Fig. 2, but for the structure function $F_L(x, Q^2)$.*

scales $Q^2 \geq 100$ GeV^2, but at lower scales, while results in the S–resummation are still essentially indistinguishable from the two–loop ones, the R-resummation predicts a somewhat faster evolution.

The structure function F_L is displayed in Fig. 3. This structure function is not determined very accurately by the HERA data for the reduced cross section Eq. (3.2.25), essentially because of the scarcity of large–y data. The spread of the results is accordingly larger. Because F_L at small x has a large gluonic component, the behaviour of F_L is similar to that of the gluon distribution, displayed in Fig. 4. Both resummations give a rather softer behaviour than the fixed–order one at the initial scale Q_0: valence-like for the gluon, turned into a rise of F_L at very small x (well into the THERA range) by the rise of the coefficient function. The R-resummation, however, then leads to significantly more rapid evolution: as the scale increases, the resummed gluon overtakes the fixed–order one. This is essentially due to the fact that the R–resummation eventually generates an $x^{-\lambda}$ power behaviour of all parton distributions at small x, and here $\lambda = 0.2$ (power rise). The S–resummation, instead, leads to evolution dominated by double scaling, which is very similar to the fixed–order one, and thus both the gluon

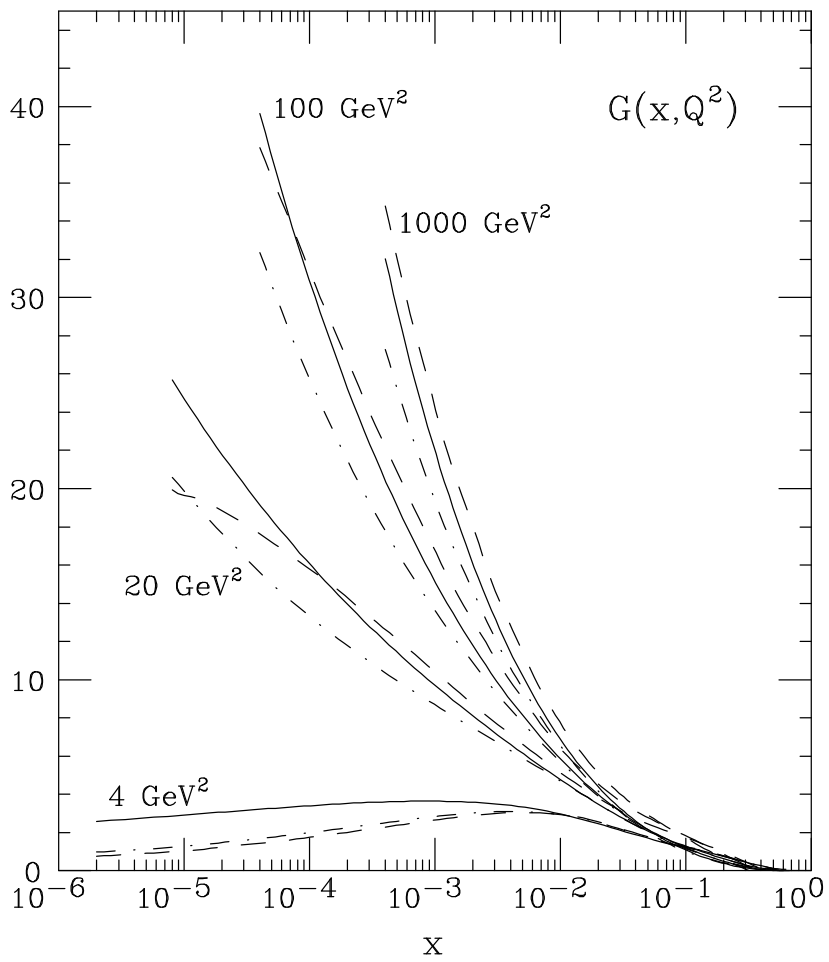

Figure 4: *Same as Fig. 2, but for the* $\overline{\mathrm{MS}}$ *gluon distribution* $G(x, Q^2) = xg(x, Q^2)$.

and F_L preserve the relative softness that they displayed at the initial scale.

Summarizing, it is clear that resummation effects, though very small, become increasingly important as x decreases. Deviations from the fixed–order behaviour appear, at least in a simultaneous determination of F_2 and F_L. At present, the deviations from the fixed order prediction are within the uncertainties of the resummation procedure: so, while it is clear that the resummed gluon distribution is softer than the unresummed one, it is hard to tell whether it will evolve faster or slower at small x. The underlying physics between these options is quite different: either the onset of a slow power-like rise (R-resummation), or persistence of the double–scaling rise (S–resummation). Both possibilities are consistent with present-day data, as well as with our current knowledge of anomalous dimensions. Understanding which (if any) of these possibilities is correct could be of considerable theoretical interest, and in particular, it could shed light on the running of the coupling in the high–energy limit [13, 16].

In conclusion, accurate data in the THERA region could reveal significant differences between the resummations procedures, and thus shed light on the structure of

unknown higher order contributions to perturbative anomalous dimensions, and on the underlying physics. The simultaneous measurement of F_2 and F_L in a wide range of Q^2 at small x would allow an accurate determination of structure functions at small x which are required e.g. for precise phenomenology of heavy quark production at future colliders.

Acknowledgements

This work was supported in part by EU TMR contract FMRX-CT98-0194 (DG 12 - MIHT).

References

[1] A. De Roeck, Nucl. Phys. **A666**, 129 (2000).

[2] R.D. Ball and S. Forte, Phys. Lett. **B351**, 313 (1995).

[3] R.K. Ellis, F. Hautmann and B.R. Webber, Phys. Lett. **B348**, 582 (1995).

[4] V.S. Fadin and L.N. Lipatov, Phys. Lett. **B429**, 127 (1998).

[5] D.A. Ross, Phys. Lett. **B431**, 161 (1998).

[6] G.P. Salam, JHEP **07**, 019 (1998).

[7] G. Altarelli, R.D. Ball and S. Forte, Nucl. Phys. **B575**, 313 (2000).

[8] M. Ciafaloni, D. Colferai and G.P. Salam, Phys. Rev. **D60**, 114036 (1999).

[9] R.D. Ball and S. Forte, *Corrections at small x*. Preprint hep-ph/9805315, 1998.

[10] J. Blümlein et al., *The unpolarized gluon anomalous dimension at small x*. Preprint hep-ph/9806368, 1998.

[11] Y.V. Kovchegov and A.H. Mueller, Phys. Lett. **B439**, 428 (1998).

[12] R.D. Ball and S. Forte, Phys. Lett. **B465**, 271 (1999).

[13] G. Altarelli, R.D. Ball and S. Forte, Nucl. Phys. **B599**, 383 (2001).

[14] R.D. Ball and S. Forte, Phys. Lett. **B358**, 365 (1995);
R.D. Ball and S. Forte, *Inclusive measurement of the strong coupling at HERA*. Preprint hep-ph/9607289, 1996.

[15] A.H. Mueller, *Small-x physics, high parton densities and parton saturation in QCD*. Preprint hep-ph/9911289, 1999;
R. Venugopalan, *Deeply inelastic scattering off nuclei at RHIC*. Preprint hep-ph/0102087, 2000.

[16] R.D. Ball and S. Forte, Phys. Lett. **B405**, 317 (1997).

[17] M. Ciafaloni and G. Camici, Phys. Lett. **B430**, 349 (1998).

[18] T. Jaroszewicz, Phys. Lett. **B116**, 291 (1982).

[19] A. De Rújula et al., Phys. Rev. **10**, 1649 (1974);
R.D. Ball and S. Forte, Phys. Lett. **B335**, 77 (1994).

[20] H1 Coll., C. Adloff et al., *Deep–inelastic inclusive ep scattering at low x and a determination of α_s*. Preprint hep-ex/0012053, 2000.

3.3 High Density QCD at THERA

E. Gotsman[a], E. Levin[a], M. Lublinsky[b], U. Maor[a], E. Naftali[a] and K. Tuchin[a]
[a] *HEP Department, School of Physics and Astronomy*
Tel Aviv University, Tel Aviv 69978, Israel
[b] *Department of Physics, Technion,*
Haifa, 32000, Israel

Abstract

These notes are a summary of our predictions for the new THERA project, related to deep inelastic scattering in the region of ultra low x ($x \to 10^{-7}$). We collect here predictions that satisfy two criteria (i) they do not depend on specific features of the model that we have to use to estimate a possible effect; and (ii) they do not contradict the HERA data.

3.3.1 Introduction: Our hopes and main goals at THERA

3.3.1.1 Three domains of QCD at low x

Deep inelastic scattering is a unique experiment which allows us to take 'snapshots' of the constituents inside a hadron at different moments of time with different resolutions. These 'snapshots' provide the possibility of finding the degrees of freedom (DOF) that are responsible for the interaction in QCD and generalize the theoretical approach from the well defined domain of perturbative QCD to the unknown non-perturbative (confinement) region, where the appropriate theoretical methods are still to be determined. DIS allows one to see the constituents of size $\approx 1/Q$, where Q is the photon virtuality, at the time $t \approx 1/mx$, where x is the Bjorken variable related to the energy (W) of the process ($x = Q^2/W^2$ at low x).

HERA data as well as theoretical studies suggest that hadrons have qualitatively diverse structure in the three different domains (see Fig. 1 and Fig. 2):

1. **Perturbative QCD domain** where the constituents are of small size and are distributed in a hadron with rather low density (packing factor of these constituents κ is small ($\kappa < 1$, see Fig. 3));

2. **High parton density QCD domain** in which the constituents are still small and we can use weak coupling methods, but their density is so large that their packing factor $\kappa > 1$, and so we cannot treat this system of partons using the established pQCD methods;

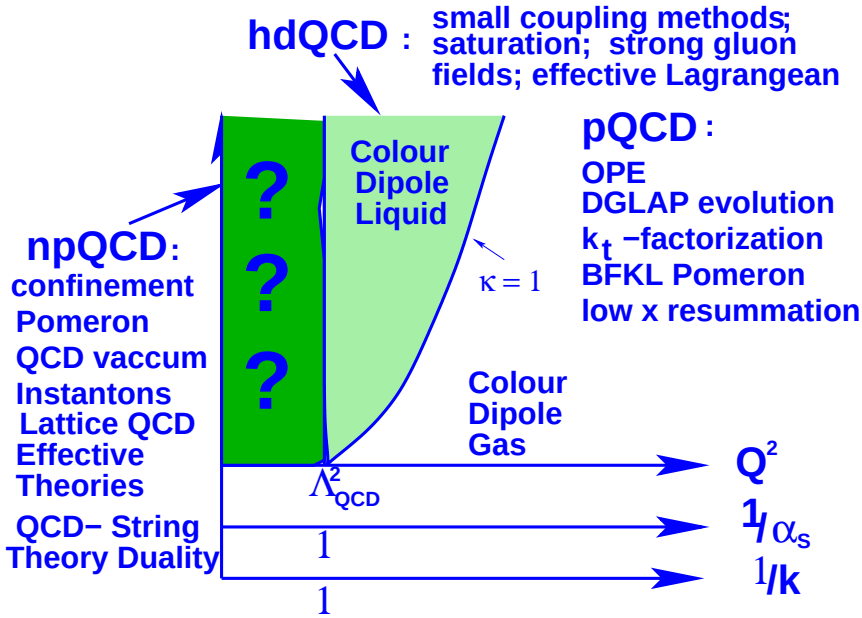

Figure 1: *Phase diagram of DIS. κ is the packing factor which is the number of constituents multiplied by its typical area and divided by the area of a hadron.*

3. **Non perturbative QCD domain** in which the QCD coupling is large, the confinement of quarks and gluons occurs, and new theoretical methods must be developed to explore this region.

Figure 2 illustrates these 'snapshots' of the constituents at different moments of time (different values of x). One can see three domains with different distributions of the constituents in the transverse plane. It should be stressed that the distributions do not depend on the reference frame, unlike time which differs in different reference frames.

Each of these domains has its own theoretical problems that can be clarified by THERA experiments. The key problems are shown in Fig. 1.

3.3.1.2 Brief summary of HERA data

Brief resume of HERA data: these data can be described by models including parton saturation, but they can also be described without assuming saturation. However, it turns out that all predictions of asymptotic hdQCD have already been seen in HERA data. This fact is so impressive and convincing that we, personally, think that HERA has reached a new regime of high density QCD [1]. However, the situation is still non-conclusive as is illustrated both in Fig. 3, which shows the value of the packing factor κ, and in Fig. 4, which shows the value of the saturation scale, in HERA and THERA kinematic region. One can see that $Q_s(x) \leq 1\,GeV$ for HERA. This low $Q_s(x)$ indicates that HERA data can be described by other approaches without saturation, for

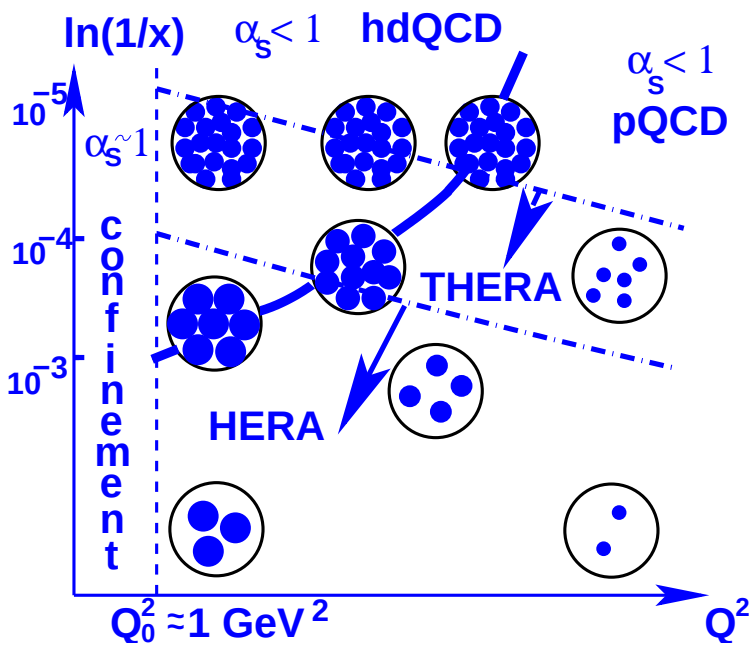

Figure 2: *'Snapshots' of the constituents of different size ($r \approx 1/Q$) at different values of x. Large circles indicate the hadron and small ones the constituents.*

example, by some models that include a smooth matching between "soft" and "hard" interactions. However, at THERA $Q_s(x)$ is larger and the hdQCD interpretation of the data will be cleaner. We illustrate this point with two figures that follow.

3.3.1.3 Main idea

As we have discussed, we face two challenging problems in the region of low x and low Q^2 which is now being investigated at HERA:

1. The matching of "hard" processes, which can be successfully described using perturbative QCD (pQCD), and "soft" processes, which should be described using non-perturbative QCD (npQCD);

2. Theoretical description of high density QCD (hdQCD). In this kinematic region we expect that the typical distances will be small, but the parton density will be so large that a new non perturbative approach needs to be developed for dealing with this system.

The main physical idea, on which our approach is based is [2]:

The above two problems are correlated and the system of partons always passes through the stage of hdQCD (at shorter distances) before it proceeds to non-perturbative QCD and which, in practice, we describe using Reggeon phenomenology.

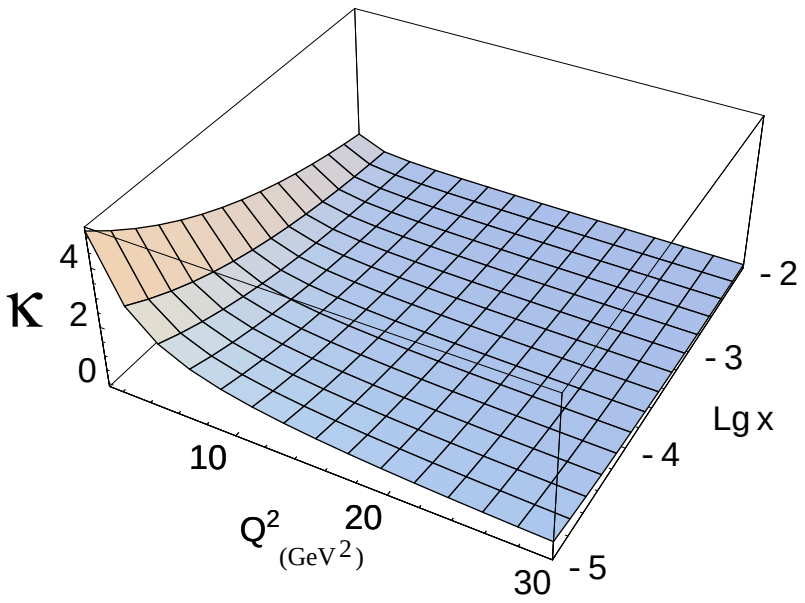

Figure 3: *The parton packing factor κ as function of Q^2 and Bjorken x in the GRV'98 parameterization of the solution to the DGLAP evolution equation. The GRV'98 parameterization describes all available data from HERA.*

3.3.1.4 Status of theory

Parton saturation as well as other collective phenomena typical of the high parton density system, is not an additional postulate of QCD, but follows from the QCD evolution equations in the kinematic region associated with high parton density. Therefore, it is very important to have a clear understanding what can be proven theoretically.

In DIS at low x, one can find a system of high density partons, which is a non-perturbative system due to high density of partons, although the running QCD coupling constant is still small ($\alpha_S(r_\perp) \ll 1$). Such a unique system can be treated theoretically [2]. It should be stressed that the theory of hdQCD is now in very good shape.

Two approaches have been developed for hdQCD. The first one [3] is based on pQCD (see GLR and Mueller and Qiu papers in Ref. [2]) and on dipole degrees of freedom [4]. This approach gives a natural description of the parton cascade in the kinematic region for $\kappa \leq 1$ and up to the transition region with $\kappa \approx 1$ (see Fig. 2).

The second method [5] uses the effective Lagrangian suggested by McLerran and Venugopalan [2], this is a natural framework to describe data in the deep saturation region, where $\kappa \gg 1$ (see Fig. 2). As a result of intensive work using these two approaches the non-linear evolution equation which has the following form has been

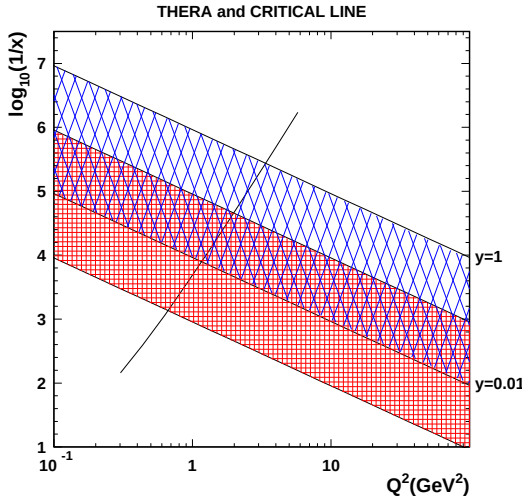

Figure 4: *The estimates for the saturation scale for HERA and THERA kinematic region.*

derived [6]

$$\frac{da^{el}(\mathbf{x_{01}}, b_t, y)}{dy} = -\frac{2\,C_F\,\alpha_s}{\pi}\,\ln\left(\frac{\mathbf{x_{01}^2}}{\rho^2}\right)\,a^{el}(\mathbf{x}, b_t, y) + \frac{C_F\,\alpha_s}{\pi}\cdot$$
$$\int_\rho d^2\mathbf{x_2}\,\frac{\mathbf{x_{01}^2}}{\mathbf{x_{02}^2}\mathbf{x_{12}^2}}\,\left(\,2\,a^{el}(\mathbf{x_{02}}, b_t, y) - a^{el}(\mathbf{x_{02}}, b_t, y)\,a^{el}(\mathbf{x_{12}}, b_t, y)\,\right), \quad (3.3.1)$$

where $a^{el}(r_\perp^2, b_t, x)$ is the elastic scattering amplitude for a dipole of size $r_\perp$ at energy $\propto 1/x$ and at impact parameter b_t. We assume that $b_t \leq x_{02}$ and/or x_{12}.

The dipole cross section is equal to $\sigma(r_\perp^2, x) = 2\int d^2b_t\,N(r_\perp^2, b_t, x)$, where $N = Ima^{el}$. The pictorial form of (3.3.1) is given in Fig. 5 which shows that the physics underlying this equation has a simple meaning: the dipole of size x_{10} decays in two dipoles of sizes x_{12} and x_{02}. These two dipoles interact with the target. The non-linear term which takes into account the Glauber corrections for such an interaction, (3.3.1) is the same as the GLR -equation [2] but here it is given in the coordinate representation. The coefficient in front of the non-linear term coincides in the double log with the one calculated in Ref. [7].

We wish to stress that this equation which includes the Glauber rescatterings , has definite initial conditions and has been derived by both methods (see Refs. [6, 8]). The model, which we will describe in the next section, provides both the correct initial conditions for (3.3.1) and also serves as a good first iteration. This iteration reproduces the main features of the solution, and it is only necessary to repeat the iteration procedure two or three times to obtain a correct solution for $x \leq 10^{-7}$.

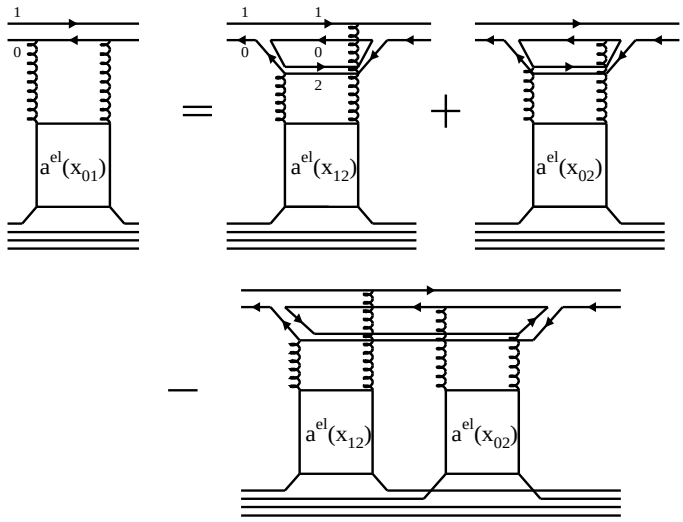

Figure 5: *The pictorial form of the non-linear evolution equation in the hdQCD kinematic region.*

3.3.2 Our model

3.3.2.1 General description

As was shown in Ref. [6], the correct initial condition for (3.3.1) is actually the Glauber-Mueller formula [10–12] for the rescattering of the colour dipole, namely

$$\sigma_{dipole}(r_\perp, x) \;=\; 2 \int d^2 b_t \, Im \, a^{el}(r_\perp, x; b_t) \;, \tag{3.3.2}$$

where

$$a^{el}(r_\perp, x; b_t) \;= i \left(1 \;-\; e^{-\frac{\Omega(r_\perp, x; b_t)}{2}} \right) \;, \tag{3.3.3}$$

The opacity $\Omega(r_\perp, x; b_t)$ is defined as

$$\Omega(r_\perp, x; b_t) \;=\; \frac{\pi^2 r_\perp^2}{3\pi R^2} \, x G^{DGLAP}(x, \frac{4}{r_\perp^2}; b_t) \;, \tag{3.3.4}$$

where $G^{DGLAP}(x, \frac{4}{r_\perp^2}; b_t) = G^{DGLAP}(x, \frac{4}{r_\perp^2}) \cdot S(b_t)$ and $G^{DGLAP}(x, \frac{4}{r_\perp^2})$ is the solution of the linear DGLAP evolution equation, and $S(b_t)$ is the profile function for the impact parameter distribution of the gluons in the target. The origin of this function is non-perturbative, and it is normalized in (3.3.4) by the condition $S(b_t = 0) = 1$.

For the solution of (3.3.1) one should fix the value of initial $x = x_0$ ($y = y_0$) and use $a^{el}(r_\perp, x = x_0; b_t)$ as a starting iteration of (3.3.1). In our model we suggest a different approach, namely we use (3.3.2) and (3.3.3) as the first iteration of the (3.3.1)

including their x-dependence. Therefore, the result of the second iteration of (3.3.1) can be written in the form:

$$a_2^{el}(r_\perp, y = \ln(1/x); b_t) = \frac{C_F\,\alpha_s}{\pi}\, r_\perp^2 \int^y dy' \int_{r_\perp} \frac{d^2 r'_\perp}{r'^4_\perp}\, \{\, 2\, a_1^{el}(r'_\perp, y'; b_t) \;-\; (\, a_1^{el}(r'_\perp, y'; b_t)\,)^2 \,\}\;, \quad (3.3.5)$$

where we assumed that $r'_\perp \gg r_\perp$. This assumption corresponds to the Leading Log Approximation of pertutbative QCD LLA, which has been used in the derivation of (3.3.2) and (3.3.3). Substituting (3.3.3) in (3.3.5) we obtain

$$a_2^{el}(r_\perp, y = \ln(1/x); b_t) \;=\; i\, r_\perp^2 \int^y dy' \int_{r_\perp^2} \frac{d\, r'^2_\perp}{r'^4_\perp} \left(1 \;-\; e^{-\frac{\Omega_G(r'_\perp, y'; b_t)}{2}}\right), \quad (3.3.6)$$

where $\Omega_G(r_\perp, y; b_t) \;=\; 2\Omega(r_\perp, y; b_t)$ of (3.3.4) [1]. The physical meaning of (3.3.6) is transparent. The dipole of size $r_\perp$ decays into two dipoles which interact with the target. Eq. 3.3.6 describes the rescatterings of these two dipoles. On the other hand, in pQCD this state is the $q\bar{q}G$ state. Since we assume the size of $q\bar{q}$ system to be much smaller than the size of the dipoles in the $q\bar{q}G$ state, (3.3.6) relates to the passage of the gluon through the target. Using the relation between the gluon-target cross section [2] and the gluon distribution

$$\sigma^G = 2 \int d^2 b_t\; N(r_\perp, y = \ln(1/x); b_t) = \frac{4\pi^2}{Q^2} \alpha_S(Q^2)\, x\, G(x, Q^2)$$

one obtains the Glauber-Mueller formula for the gluon distribution [12]

$$xG^{SC}(x, Q^2) \;=\; \frac{8}{\pi^4} \int_x^1 \frac{dx'}{x'} \int_{4/Q^2} \frac{d^2 r'_\perp}{r'^4_\perp} \int d^2\, b_t \left(1 \;-\; e^{-\frac{\Omega^G}{2}}\right). \quad (3.3.7)$$

Eq. 3.3.2 and (3.3.7) are the main formulae that we use in our estimates of the collective phenomena in DIS.

3.3.2.2 Advantages and disadvantages of the model

The main advantages of our model follow directly from the way it has been constructed. Our model reproduces the DGLAP limit for $r_\perp^2 \;<\; r^2_{saturation} \approx 1/Q_s^2$, gives a good approximation to the solution of (3.3.1) for $x \;\geq\; 10^{-6}$, and it preserves the relation between elastic, quasi-elastic (diffraction) scattering and multi particle production in DIS based on the AGK cutting rules [13] (see Ref. [1] for details).

The main problem relating to our model is the fact that the evolution equation (3.3.1) has only been proven in the leading ln(1/x) approximation of pQCD where we consider $\alpha_S \ln(1/x) \approx 1$ while $\alpha_S \ll 1$. This approximation does not insure the

[1] Actually, $\Omega_G/\Omega \;=\; 2N_c^2/(N_c^2 - 1) = 9/4(N_c = 3) \rightarrow 2(N_c \gg 1)$.

[2] In principle, the gluon - target cross sections can be measured using the graviton as a colouless probe.

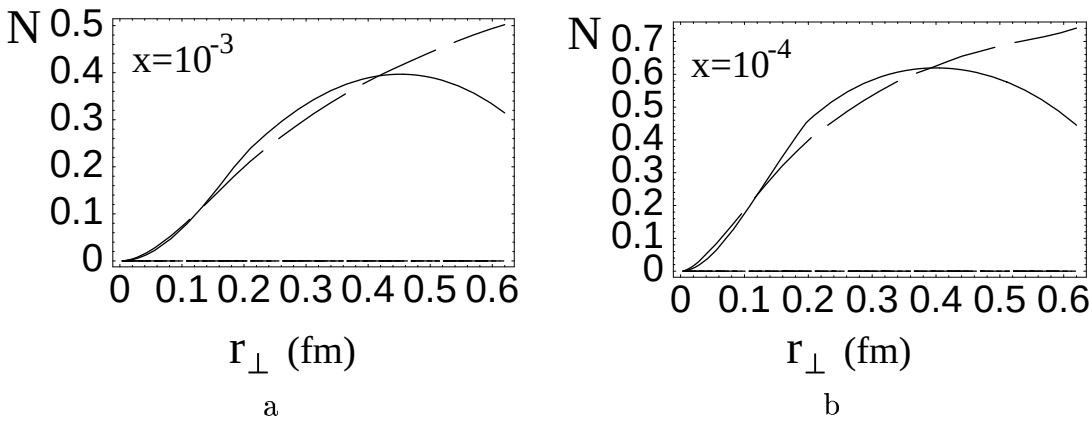

Figure 6: *The calculation for $N = Im\, a^{el}$ at $b_t = 0$ ($\sigma_{dipole} = \int d^2b_t\, N(x, r_\perp; b_t)$) in our model (full curve) and the solution to nonlinear equation (see (3.3.1)).*

accuracy of calculation for present accessible energies. On the other had, our model cannot be correct at low x and it is only suitable to describe DIS for $x \geq 10^{-6}$, where the model gives the second iteration of (3.3.1). For smaller values of x we require higher iterations.

In Ref. [14] we have already shown that our model gives a good approximation of (3.3.1). Figure 6 illustrates this point. Hence we can safely use our model for estimates of the collective phenomena even in THERA kinematic region.

Table 1 provides a guide for the different processes which we described in our model for kinematical range at HERA.

3.3.2.3 Phenomenological parameters of the model

Before discussing the applications at THERA we list the parameters that we use to fit the data at HERA.

$\mathbf{R^2}$ – size of the target

The size of the target enters the impact parameter profile of the target which we take in the Gaussian form:

$$S(b_t) \;=\; \frac{1}{\pi R^2}\, e^{-\frac{b_t^2}{R^2}} \;. \tag{3.3.8}$$

The HERA data for photo production of the J/Ψ - meson as well as CDF data on double parton cross section, leads to the value of $R^2 = 5 \div 10\ GeV^{-2}$. R^2 is a parameter fiied to describe of the experimental data. Note, that the value of $R^2 = 8.5\, GeV^{-2}$ was taken for all reactions that we have described.

$\mathbf{Q_0^2 = 1/r_{sep}^2}$ – separation parameter

As we have discussed we can only rely on our model for the saturation effect (see

Reaction	$Q^2\,(GeV^2)$	x	References
$\sigma_{tot}(\gamma^* p)$	$0 \div 65$	< 0.01	[15]
$F_2(x, Q^2)$	$1 \div 65$	< 0.01	[7, 17]
$xG(Q^2, x)$	$1 \div 65$	< 0.01	[7]
$dF_2/d\ln Q^2$	$1 \div 65$	< 0.01	[18, 23]
$\sigma_{tot}(\gamma\,\gamma^*)$	$0; 0 \div 20$	< 0.01	[19]
σ_{tot}^{diff}	$5 \div 65$	< 0.01	[20]
$\frac{\sigma_{tot}^{diff}}{\sigma_{tot}}$	$1 \div 65$	< 0.01	[21]
$\sigma(\gamma^* p \to J/\Psi + p)$	$0 \div 65$	< 0.01	[22, 23]
slope $B(\gamma^* p \to J/\Psi + p)$	$0 \div 65$	< 0.01	[22]
slope $B(\gamma^* p \to \rho + p)$	$5 \div 65$	< 0.01	[22]

Table 3.3.1: *The different processes which we described in our model for kinematical range at HERA*

(3.3.2) - (3.3.3)) at rather small distances ($r_\perp < r_\perp^{sep}$) or , in other words, at large virtualities of the incoming photon $Q^2 > Q_0^2$. We have commented on the value of $r_\perp^{sep}$, but in practice we used $Q_0^2 = 0.6 \div 1\ GeV^2$ and tried to estimate how our fit depends on the value of Q_0^2. Therefore, the result of our calculations should be read , as *"the shadowing corrections from short distances $r_\perp < 1/Q_0^2$ gives this or that ...."*.

Solution of the DGLAP evolution equations

We attempted to use all available parameterization of the solution of the DGLAP evolution equations [24, 25], but we prefer the GRV parameterization [26] . The reason for this is very simple: the theoretical formulae, that are the basis of our model, were derived in double log approximation of pQCD, and the GRV parameterization is the closest one to the DLA.

3.3.3 Predictions for THERA

3.3.3.1 The unitarity bound in THERA kinematic region

We start from the prediction which, in principle, does not depend on the exact form of the correct evolution equation and/or on the particular model, namely, from unitarity

bound for F_2 and $xG(x,Q^2)$ [27]. This bound stems from a simple formula for the DIS cross section [10–12]

$$\sigma(\gamma^* p) \;=\; \int_0^1 dz \int d^2 r_\perp |\Psi(z, r_\perp; Q^2)|^2 \; \sigma_{dipole}(x_B, r_\perp^2) \;, \tag{3.3.9}$$

where $\sigma_{dipole}(x_B, r_\perp^2)$ is the total cross section of the $q\bar{q}$ -dipole of size $r_\perp$ with the target; Ψ is the wave function of the $q\bar{q}$ -dipole in the virtual photon. This wave function is well known [12, 16] and for transverse polarised photon $|\Psi_T(z, r_\perp; Q^2)|^2$ is equal

$$|\Psi_T(z, r_\perp; Q^2)|^2 \;=\; \frac{\alpha^{em} N_c}{2\pi^2} \times \sum_1^{N_f} Z_f^2 \; [\, z^2 \,+\, (1-z)^2 \,]\; \tilde{Q}^2 \, K_1^2(\tilde{Q}\, r_\perp) \;, \tag{3.3.10}$$

where K_1 is the modified Bessel function, $\tilde{Q}^2 \;=\; z(1-z)\, Q^2$, N_f is the number of massless quarks and Z_f is the fraction of the charge carried by the quark.

It was shown in Ref. [12, 27] that in the DGLAP limit the essential $r_\perp$ in (3.3.9) are larger than $2/Q$ ($r_\perp \;>\; 2/Q$) and the integral over z can be taken, namely,

$$\int_0^1 dz |\Psi_T(z, r_\perp; Q^2)|^2 \;\to\; \frac{8}{3\, Q^2\, r_\perp^4} \;. \tag{3.3.11}$$

Finally, using the relation between the total cross section and F_2 structure function

$$\sigma(\gamma^* p) \;=\; \frac{4\,\pi^2\, \alpha^{em}}{Q^2}\, F_2(x_B, Q^2) \tag{3.3.12}$$

one obtains

$$F_2(x_B, Q^2) \;=\; \frac{N_c}{12\pi^3} \sum_1^{N_f} Z_f^2 \int_{\frac{1}{Q^2}}^{\infty} \frac{d\, r_\perp^2}{r_\perp^4} \;=\; \frac{N_c}{12\pi^3} \sum_1^{N_f} Z_f^2 \; 2 \int d^2 b_t \; Im\, a_{dipole}^{el}(x_B, r_\perp; b_t) \tag{3.3.13}$$

Taking the derivative with respect to $\ln Q^2$ and using the weak form of the unitarity constraint ($Im\;\; a_{dipole}^{el}(x_B, r_\perp; b_t) \;\leq\; 1$) we obtain

$$\frac{\partial F_2(x, Q^2)}{\partial \ln Q^2} \;\leq\; \frac{Q^2\, R^2}{3\pi^2} \;. \tag{3.3.14}$$

R^2 in (3.3.14) is the region of convergence for the integral over b_t in (3.3.14). In principle, R^2 grows with x but model estimates [27] as well as experimental data [28] show only mild x dependence.

Figure 7 shows that the F_2 slope approaches the unitarity bound at least in the GRV'98 parameterization of the solution to the DGLAP evolution equation. A violation of the unitarity bound in the DGLAP equation indicates that the shadowing corrections are unavoidable in the THERA kinematic region. The real size of these corrections is much larger than we can see from the violation of the unitarity bound, since the system starts becoming dense at densities lower than that which follows from the unitarity constraints. In other words, shadowing corrections lead to a considerable suppression in the deep inelastic structure function, at densities lower than originates from the unitarity constraints.

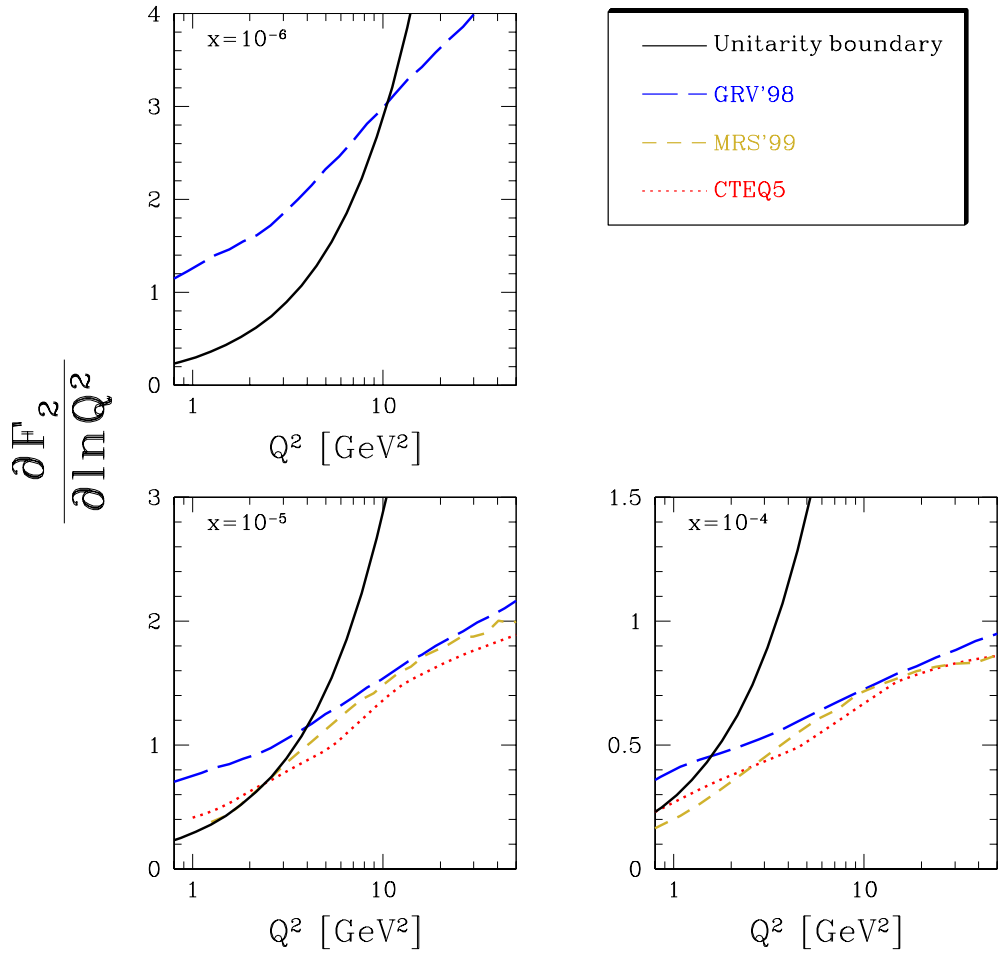

Figure 7: *The unitarity boundary and the DGLAP predictions for the F_2 - slope at different values of x.*

3.3.3.2 The unitarity bound for DIS with nuclei

Eq. 3.3.14 looks better for DIS with nuclei, since the radius of the nucleus is large and a shrinkage of the diffraction peak induced by SC will be very small and we can neglect it. We plot the $F_{2A} = AF_{2N}^{DGLAP}$ and unitarity bound in Fig. 8.

One can see that for DIS with nuclei we should see the collective phenomena at $x \approx 10^{-4}$ and at rather large value of $Q^2 \approx 3 \div 5\, GeV^2$.

3.3.3.3 Scaling violation in the F_2 slope

The careful analysis of the HERA data on the F_2- slope ($\frac{\partial F_2(x,Q^2)}{\partial \ln Q^2}$), given in Ref. [18], shows that (i) our saturation model as well as other models of this type (see [29]

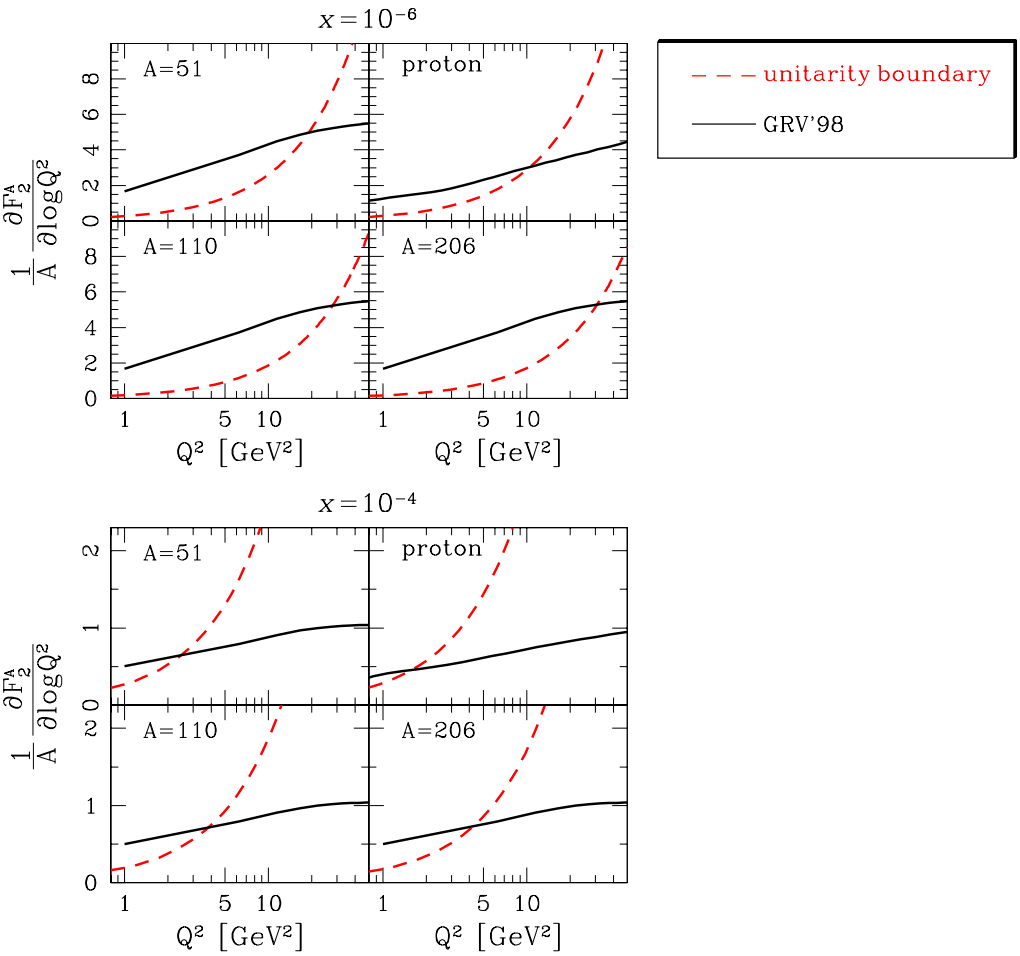

Figure 8: *The unitarity bound and the DGLAP predictions for the F_{2A} - slope at different values of x and atomic number A.*

for example) , are able to describe all experimental data ; and (ii) such a description cannot be very conclusive since other approaches are equally successful. The saturation hypothesis leads to $\frac{\partial F_2(x,Q^2)}{\partial \ln Q^2} \propto Q^2 R^2$ for $Q^2 \leq Q_s^2(x)$. The HERA data [30, 31] show such behaviour, but we cannot distingish this saturation behaviour from the vanishing of F_2 on the soft scale, which follows from the fact that the total photoproduction cross section is finite at $Q^2 \to 0$. There are two reasons for this uncertainty: (i) the soft scale is not so soft and typical transverse momentum in the soft Pomeron could be as large as $2\,GeV$ [32]; and (ii) the saturation scale is rather small $Q_s^2(x) = 1 \div 2\,GeV^2$ in HERA kinematic region.

One can see from Fig. 9 that THERA will allow us to distinguish between a mixture of soft and hard Pomerons (DL curve in Fig. 9) and our model for gluon saturation

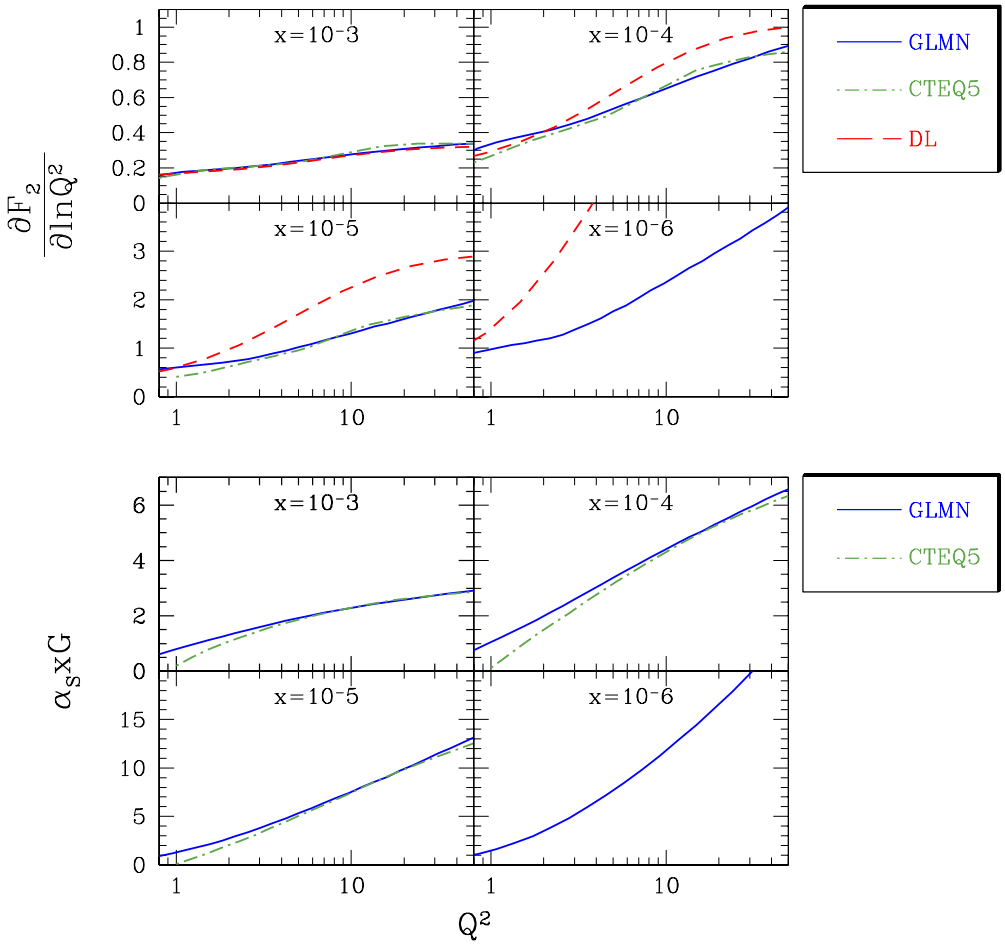

Figure 9: *Predictions for the different parameterizations at fixed low values of x.*

(GLMN curve in Fig. 9). The difference between the DGLAP approach (CTEQ5 curve in Fig. 9) and our predictions is concentrated in the region of small $Q^2 \approx 1 \div 2\,GeV^2$, but we recall that the corrections to the CTEQ5 parametrization due to high parton density effects reaches the value of about 30-40% at THERA energies. These estimates are an alternative way of saying, that at THERA energies we expect large SC theoretically, and a DGLAP approach can absorb these corrections in the initial nonperturbative gluon distributions at HERA energies, but it would be a more difficult task in THERA kinematic region.

3.3.3.4 Energy dependence of J/Ψ production

It was shown in [23, 33, 34] that the energy behaviour of the J/Ψ production is very sensitive to the value of the shadowing corrections. It turns out that the large uncer-

tainties due to our poor knowledge of the wave function of vector mesons contribute mostly in the normalization of the cross section, while the energy slope is still a source of the information on SC. In Refs. [23, 34] we showed that the shadowing corrections provide a natural explanation of the experimental energy behaviour for J/Ψ photo and deep inelastic production. However, the available data do not enable us to exclude explanations based on the mixture of soft and hard Pomerons, and the idea that this process is hard. Figure 10 gives our prediction for THERA kinematic region for three approaches: the SC calculations in our model (GRV98SC), the soft + hard Pomeron model (DL2P) [35] and the DGLAP approach based on the CTEQ parametrization (CTEQ5NSC).

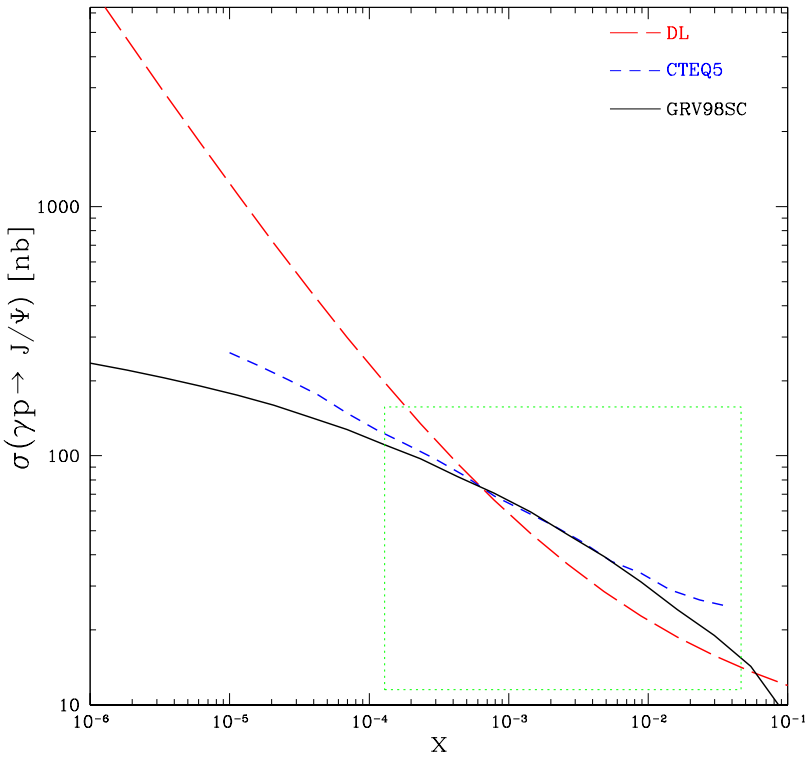

Figure 10: *A comparison between the energy dependence of different models (see text) for the integrated cross section of J/Ψ photoproduction. The available experimental data points are confined within the inner window.*

3.3.3.5 Shrinkage of diffraction peak for production of vector mesons

The experimentally observed shrinkage of the diffraction peak in photoproduction of J/Ψ [37] is a direct indication that this process is not a simple hard process that can be

described in the DGLAP approach . Indeed, one of the most well established properties of the hard processes is the fact that the t-dependence is independent of energy (x) (see for example Ref. [22]. There are two possible explanations: (i) the first one is the SC which lead to x-dependence of the t-slope [22] and (ii) the second is based on the contamination of the J/Ψ production by the soft processes for which the shrinkage of the diffraction peak is a phenomenon that is well established both theoretically and experimentally.

It should be stressed that the above two approaches have different predictions for the x-dependence: SC lead to the t-slope which increases at higher energies (lower x), since the contribution of SC grows with energy. For the mixture of soft and hard processes, the role of soft ones diminishes at higher energies, and as a result the value of effective α'_{eff} decreases [36].

In Fig. 11 one can see this effect for our model. This figure also shows that we cannot describe the ZEUS data regarding the value of the t-slope. The reason for this may be due to our under estimating the value of SC in our model. However, one lesson we can learn from Fig. 11: THERA will clarify the question which mechanism works. The important thing to emphasize once more is that the measurement of the shrinkage of the t-slope will provide reliable information on the deviation from the simple DGLAP approach.It is especially important to observe such shrinkage in the DIS diffraction production of J/Ψ and other vector mesons.

3.3.3.6 Maxima in ratios

Preparing this paper we tried to find improved observables which will be sensitive to the saturation scale. We study the Q^2 behaviour of the ratios:F_L/F_T and F_L^D/F_T^D for longitudinal and transverse structure function for inclusive DIS and for diffraction in DIS [38]. In Fig. 12 some examples of these ratios are plotted. We found that these ratios have maxima at $Q^2 = Q^2_{max}(x)$ which increases with x as $x \to 0$. It appears that $Q_{max}(x)$ is a simple function of the saturation scale $Q_s(x)$. In the THERA kinematic region $Q^2_{max}(x)$ is large $Q^2_{max}(x) \approx 6 \div 7\, GeV^2$. Such a large value of $Q^2_{max}(x)$ makes our calculation more reliable, and we expect that the measurement of this maxima in the THERA kinematic region will enable us to extract the value of the saturation scale from the experimental data.

3.3.3.7 Higher twist contribution

One of the most challenging problem of QCD is to understand the higher twist contributions. The present approach to DIS is based on two main ideas: (i) the DGLAP evolution equation for leading twist contributions and (ii) the firm belief that higher twist contributions are small in the whole kinematic region, when we start QCD evolution from the large value of $Q^2 = Q_0^2 \approx 1 - 4\, GeV^2$. In recent years it has been proven that there is no ground for such an assumption. It was found [39] that the anomalous dimension for the higher twists is much larger than for the leading one in the region of

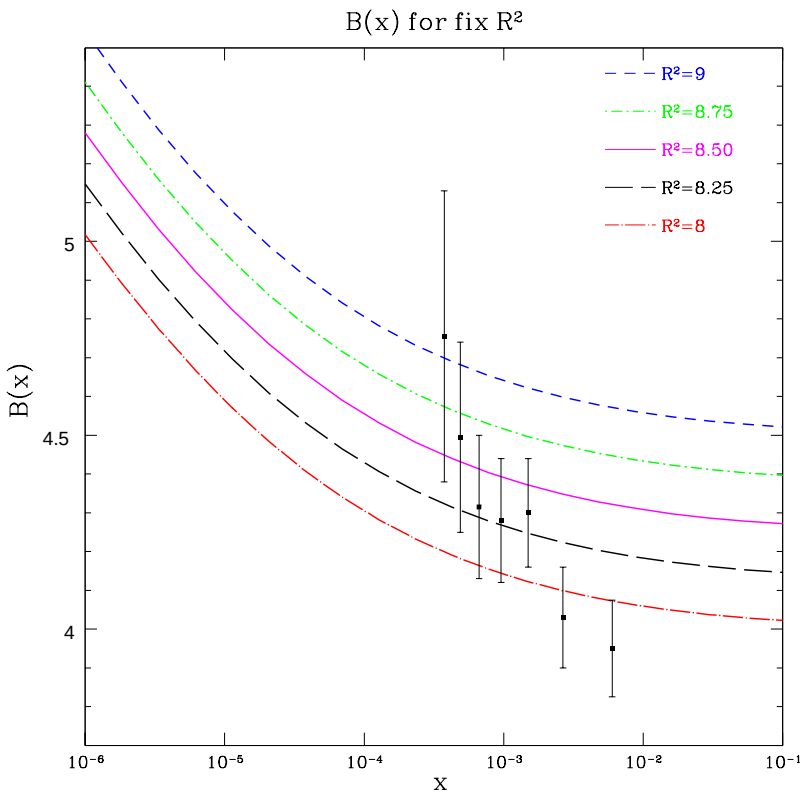

Figure 11: *The energy (x) dependence of the forward differential slope of J/Ψ photoproduction.ZEUS data [37] and our model calculation with several values of R^2. From this picture we chose the value of $R^2 = 8.5\,GeV^{-2}$ for the typical proton size in our model.*

low x. It turns out that if we write the deep inelastic structure function in the form

$$F_2(x,Q^2) \;=\; F_2^{LT}(x,Q^2) \;+\; \frac{M^2}{Q^2}\,F_2^{HT}(x,Q^2)$$

$F_2^{HT}(x,Q^2) \;\propto\; F_2^{LT}(x,Q^2) \times xG(x,Q^2)$ at $x \to 0$. Therefore, the experimental observation of the higher twist contribution, is one of the most challenging and important problems in DIS, as well as in QCD at large. The attractive feature of our model is the fact that it leads to higher twist contributions in accord with known theoretical information. Our calculations confirm the result of Ref. [40] that there is almost a full cancellation of the higher twist contributions in F_2 in spite of the fact that they give substantial contributions separately to F_L and F_T as well as to F^D. In the THERA kinematic region (at $x \approx 10^{-5}$) we expect the higher twist contributions to be of the same order as the leading twist at sufficiently high value of Q^2 (see Fig. 13) This high value of Q^2 insures us that our calculations are reliable. Therefore, we believe that THERA has a good chance to measure higher twist terms and a new era of DIS will open, that will include a systematic study of higher twist contributions.

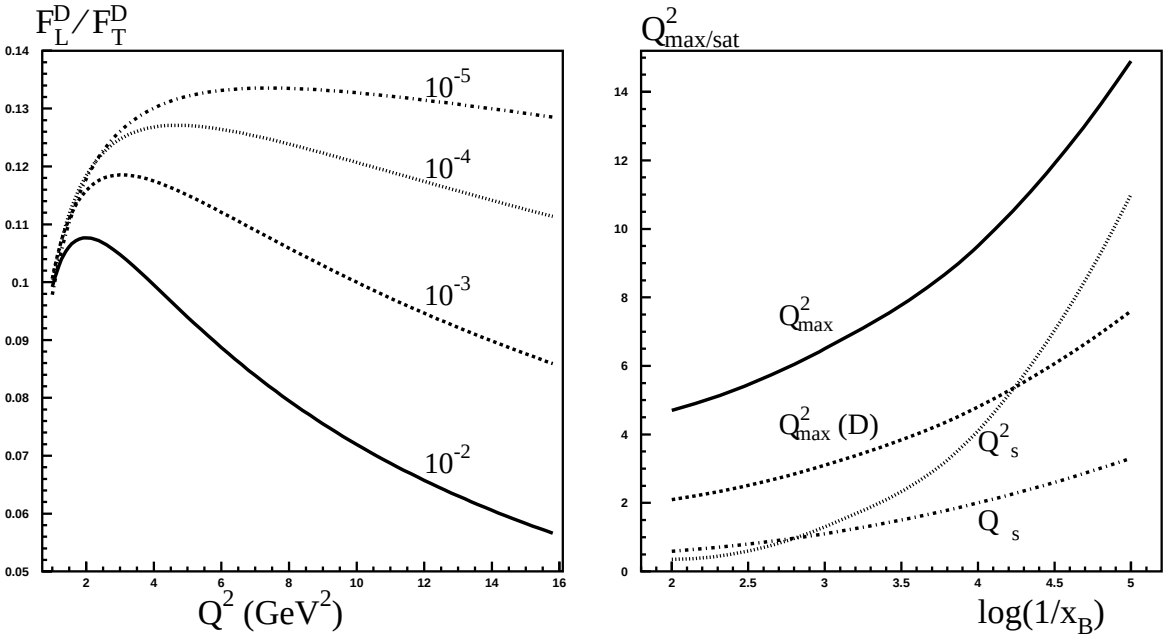

Figure 12: *The ratio of F_L^D/F_T^D as function of Q^2 at different values of x and the behavior of $Q^2_{max}(x)$ as function of x.*

3.3.4 Resume

We presented here our estimates for the possible manifestation of saturation in the THERA kinematic region. We believe that HERA has reached a new QCD regime: the high parton density QCD domain [1], where incorporating new collective phenomena is essential for understanding it's physics. We argue here that data from THERA will be able to show that we have reached this new regime, and will allow a systematic study of the QCD parton system with large parton density.

We hope that our estimates will help to plan the experimental strategy for the THERA project.

Acknowledgements

The authors are very much indebted to our coauthors and friends with whom we discussed our approach on a everyday basis Ian Balitsky, Jochen Bartels , Krystoff Golec Biernat, Larry McLerran, Dima Kharzeev, Yuri Kovchegov and Al Mueller for their help and fruitful discussions on the subject. E.G. , E. L., U.M. and K.T. thank BNL Nuclear Theory Group and DESY Theory group for their hospitality and creative atmosphere during several stages of this work.

This research was supported in part by the BSF grant # 9800276, by the GIF grant # I-620-22.14/1999 and by Israeli Science Foundation, founded by the Israeli Academy of Science and Humanities.

References

[1] E. Gotsman et al., *Has HERA reached a new QCD regime?*, DESY 00-19, TAUP-2649-200, hep-ph/001019.

[2] L.V. Gribov, E.M. Levin and M.G. Ryskin, Phys. Rep. **100**, 1 (1983);
A.H. Mueller and J. Qiu, Nucl. Phys. **B 268**, 427 (1986);
L. McLerran and R. Venugopalan, Phys. Rev. **D 49**, 2233,3352 (1994), **50**, 2225 (1994), **53**, 458 (1996), **59**, 094002 (1999).

[3] E. Levin and M.G. Ryskin, Phys. Rep. **189**, 267 (1990);
J.C. Collins and J. Kwiecinski, Nucl. Phys. **B 335**, 89 (1990);
J. Bartels, J. Blümlein and G. Schuler, Z. Phys. **C 50**, 91 (1991);
E. Laenen and E. Levin, Ann. Rev. Nucl. Part. Sci. **44**, 199 (1994) and references therein;
A.L. Ayala, M.B. Gay Ducati and E.M. Levin, Nucl. Phys. **B 493**, 305 (1997), **B510**, 355 (1990);
Ia. Balitsky, Nucl. Phys. **B 463**, 99 (1996);
Yu. Kovchegov, Phys. Rev. **D 54**, 5463 (1996), **D55**, 5445 (1997), **D60**, 034008 (2000), **61**, 074018 (2000);
A.H. Mueller, Nucl. Phys. **B 572**, 227 (2000), **B558**, 285 (1999);
Yu.V. Kovchegov and A.H. Mueller, Nucl. Phys. **B 529**, 451 (1998);
E. Levin and K. Tuchin, Nucl. Phys. **B 573**, 833 (2000).

[4] A.H. Mueller, Nucl. Phys. **B 415**, 373 (1994).

[5] J. Jalilian-Marian, et al., Phys. Rev. **D D55**, 5414 (1997);
H. Weigert, NORDITA-2000-34-HE, hep-ph/0004044;
J. Jalilian-Marian, A. Kovner and H. Weigert, Phys. Rev. **D 59**, 014015 (1999);
J. Jalilian-Marian et al., Phys. Rev. **D 59**, 014014,034007 (1999), Erratum Phys. Rev. **D 59**, 099903 (1999);
A. Kovner, J.Guilherme Milhano and H. Weigert, Phys. Rev. **D 62**, 114005 (2000);
H. Weigert, *Unitarity at small Bjorken x* NORDITA-2000-34-HE, hep-ph/0004044.

[6] Ia. Balitsky, Nucl. Phys. **B 463**, 99 (1996);
Yu. Kovchegov, Phys. Rev. **D 60**, 034008 (2000).

[7] A.L. Ayala, M.B. Gay Ducati and E.M. Levin, Nucl. Phys. **B 493**, 305 (1997), **B510**, 355 (1998).

[8] E. Iancy, A. Leonidov and L. McLerran, *Nonlinear Gluon Evolution in the Color Glass Condensate: I*, Saclay - T00/166, BNL-NT-00/24, hep-ph/0011241;
E. Iancy, A. Leonidov and L. McLerran, *The renormalization group equation for the color glass condensate*, BNL-NT-01-3, hep-ph/0102009.

[9] Yu.V. Kovchegov, Phys. Rev. **D 61**, 074018 (2000);
E. Levin and K. Tuchin, Nucl. Phys. **B 573**, 833 (2000);
M. Braun, Eur. Phys. J. **C 16**, 337 (2000).

[10] A. Zamolodchikov, B. Kopeliovich and L. Lapidus, JETP Lett. **33**, 595 (1981).

[11] E.M. Levin and M.G. Ryskin, Sov. J. Nucl. Phys. **45**, 150 (1987).

[12] A.H. Mueller, Nucl. Phys. **B 335**, 115 (1990).

[13] V.A. Abramovsky, V.N. Gribov and O.V. Kancheli, Sov. J. Nucl. Phys. **18**, 308 (1974).

[14] M. Lublinsky et al., *Nonlinear Evolution and Parton Distributions at LHC and THERA Energies*, `hep-ph/0102321`.

[15] E. Gotsman et al., Eur. Phys. J. **C 10**, 689 (1999);
E. Gotsman, E. Levin and U. Maor, Eur. Phys. J. **C 5**, 303 (1998).

[16] N.N. Nikolaev and B.G. Zakharov, Z. Phys. **C 49**, 607 (1991);
E.M. Levin et al., Z. Phys. **C 74**, 671 (1997).

[17] E. Gotsman, E. Levin and U. Maor, Phys. Lett. **B 379**, 186 (1990).

[18] E. Gotsman et al., Nucl. Phys. **B 539**, 535 (1999);
E. Gotsman, E. Levin and U. Maor, Phys. Lett. **B 425**, 369 (1998);
E. Gotsman et al., Phys. Lett. **B 500**, 87 (2001).

[19] E. Gotsman et al., Eur. Phys. J. **C 14**, 511 (2000).

[20] E. Gotsman, E. Levin and U. Maor, Nucl. Phys. **B 493**, 354 (1997).

[21] E. Gotsman et al., *Energy dependence of* $\frac{\sigma^{DD}}{\sigma_{tot}}$ *in DIS and shadowing corrections*, TAUP-2639-2000, Jul 2000, `hep-ph/0007261`.

[22] E. Gotsman, E. Levin and U. Maor, Phys. Lett. **B 403**, 120 (1997); Nucl. Phys. **B 464**, 251 (1996);
E. Gotsman et al., *Screening corrections in photo and DIS production of* J/Ψ, TAUP 2650-2000, `hep-ph/0101142`, Phys. Lett. **B** , ()(in press).

[23] E. Gotsman et al., *Screening corrections in DIS at low* Q^2 *and* x, Talk given at 30th International Conference on High-Energy Physics (ICHEP 2000), Osaka, Japan, 27 Jul - 2 Aug 2000, `hep-ph/0007274`.

[24] H.L. Lai et al., Eur. Phys. J. **C 12**, 37 (2000).

[25] A.D. Martin et al., Eur. Phys. J. **C 4**, 463 (1998).

[26] M. Glück, E. Reya and A. Vogt, Eur. Phys. J. **C 5**, 461 (1998).

[27] A.L. Ayala Filho, M.B. Gay Ducati and E.M. Levin, Phys. Lett. **B 388**, 188 (1996).

[28] H1 Coll., S. Aid et al., Nucl. Phys. **B 470**, 3 (1996); C. Adolf et al., Nucl. Phys. **B 497**, 3 (1997);
ZEUS Coll., M. Derrick et al., Z. Phys. **C 72**, 399 (1996);
J. Breitweg et al., Phys. Lett. **B 407**, 432 (1997); DESY-00-071, `hep-ex/0005018`;
A.M. Cooper-Sarkar, R.C.E. Devenish and A. De Roeck, Int. J. of Mod. Phys. **A 13**, 33 (1998);
H. Abramowicz and A. Caldwell, Rev. Mod. Phys. **71**, 1275 (1999).

[29] K. Golec-Biernat and M. Wüsthoff, Phys. Rev. **D 59**, 014017 (1999); **D60**, 114023 (1999);
K. Golec-Biernat, Talk at 8th International Workshop on Deep Inelastic Scattering and QCD (DIS 2000), Liverpool, England, 25-30 Apr 2000, `hep-ph/0006080`.

[30] M. Klein (H1 Coll.), *Structure Functions in Deep Inelastic Lepton-Nucleon Scattering* Talk at Lepton-Photon Symposium, Stanford, August 1999, `hep-ex/0001059`.

[31] B. Foster (ZEUS Coll.), Invited talk, Royal Society Meeting, London, May 2000;
ZEUS Coll., J. Breitweg et al., Phys. Lett. **B 487**, 53 (2000).

[32] D. Kharzeev and E. Levin, Nucl. Phys. **B 578**, 351 (2000);
Yu. Kovchegov, D. Kharzeev and E. Levin, *QCD instantons and the soft Pomeron*,BNL-NT-00-18, TAUP-2637-2000, Jul 2000, `hep-ph/0007182` ;
B.Z. Kopeliovich et al., Phys. Rev. Lett. **85**, 507 (2000).

[33] M.G. Ryskin et al., Z. Phys. **C 76**, 71 (1997).

[34] A.C. Caldwell and M.S. Soares, *Vector Meson Production in the Golec-Biernat Wusthoff Model*, `hep-ph/0101085`.

[35] A. Donnachie and P.V. Landshoff, Phys. Lett. **B 437**, 408 (1998); Phys. Lett. **B 470**, 243 (1999).

[36] M. McDermott et al., Eur. Phys. J. **C 16**, 641 (2000).

[37] ZEUS Coll., J. Breitweg et al., Eur. Phys. J. **C 14**, 213 (2000);
H1 Coll., C. Adloff et al., Phys. Lett. **B 483**, 36 (2000).

[38] E. Gotsman et al., *Higher twists and maxima for DIS on proton in high density QCD*, TAUP-2644-2000, BNL-NT-00-20, Aug 2000, `hep-ph/0008280`.

[39] J. Bartels, Phys. Lett. **B 298**, 204 (1993), Z. Phys. **C 60**, 471 (1993);
E.M. Levin, M.G. Ryskin and A.G. Shuvaev, Nucl. Phys. **B 387**, 589 (1992).

[40] B. Badelek and J. Kwiecinski, Phys. Lett. **B 418**, 229 (1998) and references therein;
J. Bartels, K. Golec-Biernat and K. Peters, Eur. Phys. J. **C 17**, 121 (2000).

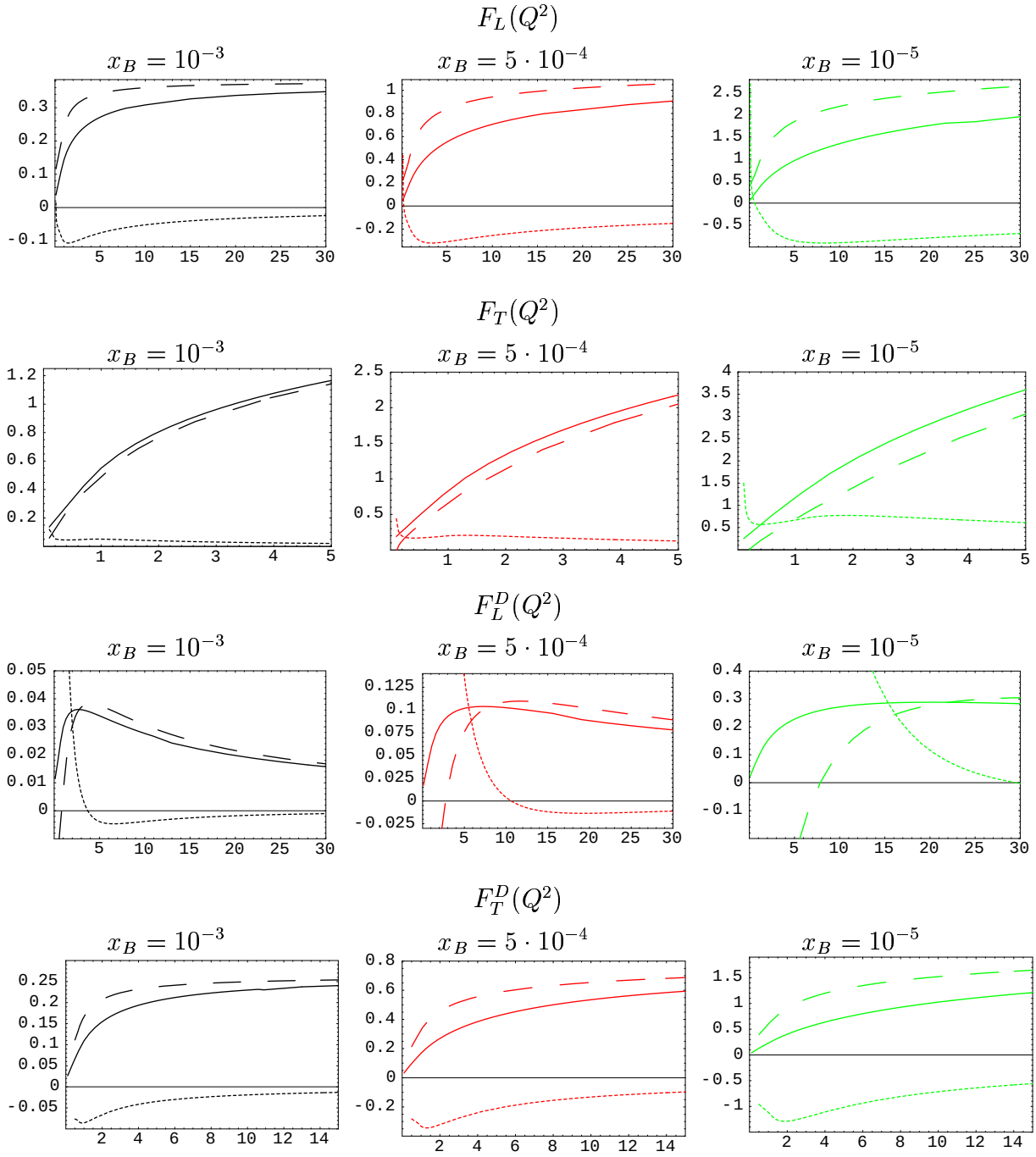

Figure 13: *Different twist contributions to the various structure functions for DIS on the proton: leading twist (at high Q^2) – dashed line, next-to-leading – dotted one, exact structure function – solid curve.*

3.4 Small x Physics and Forward Jet Production at THERA

H. Jung[1] and L. Lönnblad[2]
[1] *Department of Physics, Lund University, Sweden,*
jung@mail.desy.de

[2] *Department of Theoretical Physics, Lund University, Sweden,*
leif@thep.lu.se

Abstract

We discuss some aspects of forward jet production as a signature for small x physics at THERA energies.

3.4.1 Introduction

The evolution of the parton densities at small x is a very rich but complicated issue. The steep rise of the structure function F_2 at small x is explained by the presence of a huge gluon number density. The pure DGLAP [1, 2] evolution equations, meant to describe the evolution of the parton densities as a function of Q^2, are able to reproduce the rise of F_2 provided the input starting distributions are chosen properly.

Figure 1 shows the pattern of QCD initial-state radiation in a small-x DIS event, together with labels for the kinematics. The gluon splitting function P_{gg} is given by:

$$P_{gg}(z_i, k^2) = \bar{\alpha}_s \left(\frac{1}{z_i} - 2 + z_i(1 - z_i) + \frac{1}{1 - z_i} \right) \frac{1}{k^2}, \tag{3.4.1}$$

where $\bar{\alpha}_s = \alpha_s C_A/\pi$ and $z_i = x_i/x_{i-1}$ (see Fig. 1) is the ratio of the energy fractions of successive branchings in the gluon chain and k^2 is virtuality of the t-channel gluon with $k^2 \sim k_t^2$. In DGLAP the k^2 dependence of all emissions in the gluon chain are simplified by the observation that at not too small x the dominant part to the cross section comes from the region of phase space where k^2 is very small. However if x or z becomes very small, the collinear (small k_t^2) approximation of DGLAP may be inadequate. This region is treated by the BFKL [3, 4] evolution equation, which keeps the full k_t^2 integration but approximates the gluon splitting function with the asymptotic form

$$P_{gg} \sim \frac{1}{z} \frac{1}{k_t^2}.$$

From a detailed analysis of interference effects in a gluon chain, it was found [5] that the proper evolution variable is the angle of the emitted gluon, and not the virtuality

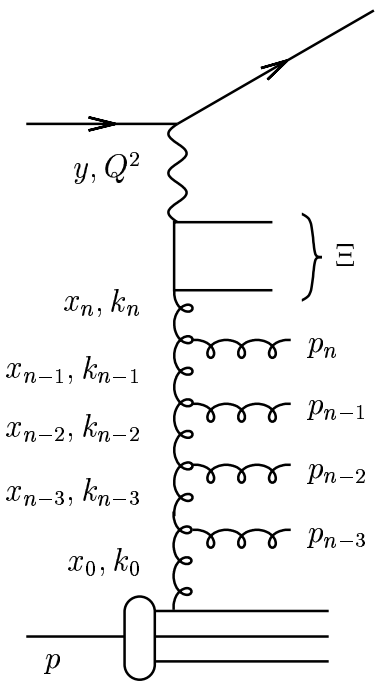

Figure 1: *Kinematic variables for multi-gluon emission. The t-channel gluon momenta are given by k_i and the gluons emitted in the initial state cascade have momenta p_i. The upper angle for any emission is obtained from the quark box, as indicated with Ξ.*

k^2 as in the DGLAP approximation, nor z as in the BFKL approximation. This angular ordering resulted in the new, and more complicated, CCFM evolution [5], which reproduces the BFKL and DGLAP approximations in the small and large x limits respectively. The CCFM equation naturally interpolates between the two extremes. However, in CCFM the gluon splitting function contains only the singular terms in z:

$$P_{gg} = \bar{\alpha}_s \left(\frac{1}{z} \Delta_{ns} + \frac{1}{1-z} \right),$$

with Δ_{ns} being the non-Sudakov form factor to regulate the $1/z$ singularity. The non singular terms of the splitting function (see eq.(3.4.1)) are not obtained within the CCFM approximation.

Whereas at HERA energies ($\sqrt{s} \sim 300$ GeV) the total cross section of deep inelastic scattering can be reasonably well described with the DGLAP evolution equations, measurements of specific features of the hadronic final state indicate clear deviations from a pure DGLAP scenario.

The cross section at low x and large Q^2 for a high E_T^2 jet in the proton direction (a forward jet) has been advocated as a particularly sensitive measure of small x parton dynamics [6, 7]. If the forward jet has large energy ($x_{jet} = E_{jet}/E_{proton} \gg x$) the evolution from x_{jet} to small x can be studied. When $E_T^2 \sim Q^2$ there is no room for Q^2 evolution left and the DGLAP formalism predicts a rather small cross section

in contrast to the BFKL/CCFM formalisms, which describe the evolution also in x. Measurements performed at HERA [8, 9] show that the prediction from the naive DGLAP formalism lies a factor ~ 2 below the data, whereas the data can be described by CCFM evolution equations [10].

3.4.2 Initial State QCD Cascade

The effect of new small x parton dynamics is most clearly seen if the contribution from typical DGLAP dynamics is suppressed. The forward jet production in deep inelastic scattering at small values of x is one example of such a process. However, the kinematics need to be investigated further. Typical event selection criteria at HERA are:

$$
\begin{aligned}
&Q^2 > 10 \text{ GeV}^2 \\
&E_{t\,jet} > 5 \text{ GeV} \\
&\eta_{jet} < 2.6 \\
&x_{jet} > 0.036 \\
&0.5 < E_T^2/Q^2 < 2
\end{aligned}
$$

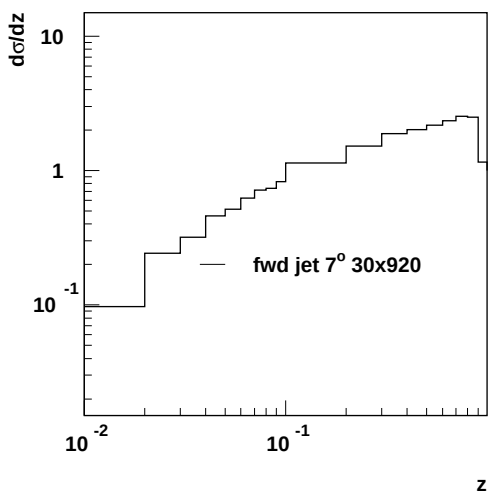

Figure 2: *The values of the splitting variable z for events satisfying the forward jet criteria, with $\theta = 7°$ at HERA energies.*

The range in x is typically $10^{-3} < x < 10^{-2}$. The evolution takes place from the large x_{jet} down to the small x with a typical range at HERA energies of $\Delta x = x/x_{jet} \sim 0.1 - 0.01$. In order to justify the use of an evolution equation (instead of a fixed order calculation) one would require at least 2 or more gluon emissions during the

evolution. To roughly estimate the energy fractions z_i of 3 gluon emissions between $10^{-3} < x < 10^{-1}$, one can assume that each gluon carries the same energy. Then the range of $\Delta x \sim 0.01$ results in $z \sim 0.2$, which is far from being in the very small z region, where the BFKL or CCFM approximations (treating only the $1/z$ terms in the gluon splitting function) are expected to be appropriate. In Fig. 2 we show the values of the splitting variable z in events satisfying the forward jet criteria at HERA energies obtained from the Monte Carlo generator CASCADE [10]. Since the values of the splitting variable z are indeed in the large z region (the majority has $z > 0.1$), it is questionable, whether the BFKL or CCFM evolution equations, including only the $1/z$ terms of the gluon splitting function, are already applicable. Whereas the measurement at HERA stops at $x \sim 10^{-3}$, the available phase space at THERA is enlarged by a factor of ~ 10. Therefore the gluons along the chain will presumably have smaller z values and the usage of the small x evolution equations might be more justified. In Fig. 3 we show the z values obtained from events satisfying the forward jet selection criteria at THERA energies ($\sqrt{s} = 959$ GeV) compared with the ones at HERA energies ($\sqrt{s} = 332$ GeV). The four plots correspond to different cuts on the minimum jet angle ($\theta = 1°, 3°, 5°, 7°$). One clearly can observe, that the distribution of z values becomes flat at small z at THERA energies and that the small z values are no longer suppressed as in the HERA kinematic region. This clearly shows, that the application of small x evolution equations at THERA energies are justified and unavoidable, although the sensitivity to the treatment of large z splittings does not completely go away.

At HERA the forward jet cross section could be reasonably well described by including a resolved virtual photon contribution, because the phase space for small z emissions at HERA energies was relatively small. The situation changes at THERA energies: the phase space for small z emissions is larger and effects from small x evolution become more visible. In Fig. 4 the cross section for forward jet production is shown as a function of x for standard DGLAP prediction (dotted), including in addition a contribution from resolved virtual photons (dashed-dotted) and the CCFM prediction (dashed). For comparison the prediction from ARIADNE [11][1] is shown, which implements a semi-classical soft radiation model in a dipole cascade, and which currently gives the best overall description of small-x HERA data. Since the the available phase space at THERA is enlarged by a factor of ~ 10, the difference between the standard DGLAP-based calculation and the CCFM calculation is increased. Moreover, at THERA the CCFM approach predicts a larger cross section than the model with resolved virtual photon contributions added, and smaller cross section than ARIADNE, while all three models give comparable results at HERA. This gives a unique opportunity, not only to distinguish between the different approaches, but also to study details of the QCD cascade in a regime, where the new small-x evolution equations should be appropriate.

In Fig. 5 the forward jet cross section is shown for different minimal jet angle cuts. On the experimental side this requires complete acceptance both in the electron and

[1] using the tuned parameters given by 'set2' in [12]

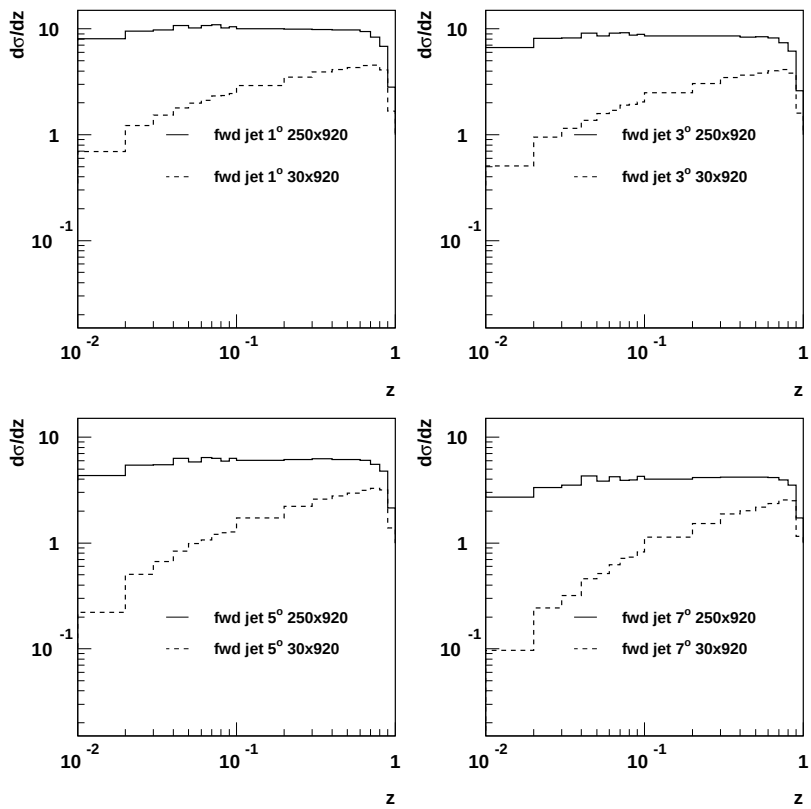

Figure 3: *The values of the splitting variable z for events satisfying the forward jet criteria, for different cuts on the minimum jet angle: a.* $\theta = 1°$, *b.* $\theta = 3°$, *c.* $\theta = 5°$, *d.* $\theta = 7°$. *The solid line corresponds to the prediction at THERA energies, the dashed line corresponds to HERA energies.*

proton direction down to the lowest possible angles. From the size of the cross section $d\sigma/dx$ one would like to reach at least $\theta \sim 3°$ for the forward jet measurement, but there are other reasons to ask even for $\theta \sim 1°$. On the other hand, the luminosities needed for such measurements are moderate so that this question can be settled within one year of running at THERA.

3.4.3 Conclusion

HERA has conclusively shown the need to go beyond the standard DGLAP evolution equations in order to explain the data on small-x final states. The reach in x is, however, not quite enough to really study details of the small-x evolution to be able to distinguish between different approaches, such as the CCFM evolution, resolved virtual photons and the dipole cascade model. With the increased kinematical region available

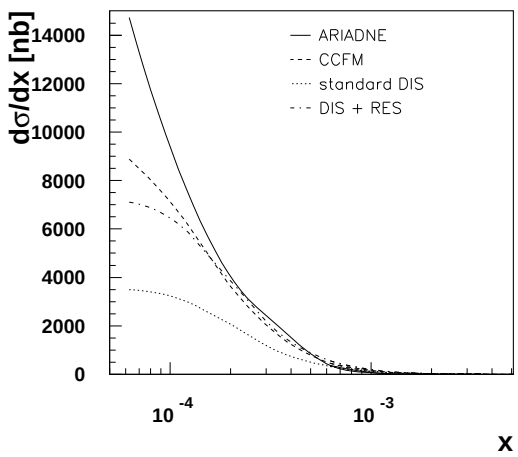

Figure 4: *Forward-jet cross section as a function of x in different models for* $0.5 < p_t^2/Q^2 < 2$ *and a minimum jet angle of* $1°$

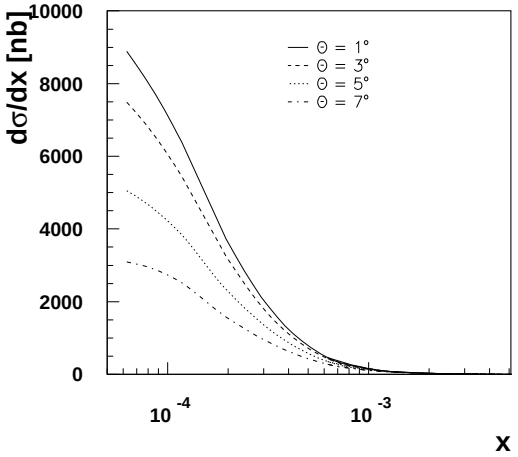

Figure 5: *Forward-jet cross section as a function of x obtained from CCFM for* $0.5 < p_t^2/Q^2 < 2$, *for different cuts on the minimum jet angle*

at THERA, this will become possible. The steeply rising cross section as x gets smaller means that such measurements can be done even with moderate luminosity. On the other hand the demands on the forward coverage of the detector is more critical — ideally it should be possible to measure jets down to an angle of $1°$.

Once a good understanding of the small-x evolution is obtained, it should be possible to use the underlying $k_\perp$-factorization theorem in BFKL/CCFM, where observables are described in terms of process–dependent off-shell matrix element and universal un-integrated parton densities, to make firm predictions of any other small-x measurement, just as normal DGLAP parton densities and matrix elements are used today at large Q^2. THERA will be the only place where these un-integrated parton densities can be measured.

References

[1] V.N. Gribov and L.N. Lipatov, Sov. J. Nucl. Phys. **15**, 438 (1972);
G. Altarelli and G. Parisi, Nucl. Phys. **B 126**, 298 (1977);
Yu.L. Dokshitzer, Sov. Phys. JETP **46**, 641 (1977).

[2] L.N. Lipatov, Sov. J. Nucl. Phys. **20**, 94 (1975).

[3] E.A. Kuraev, L.N. Lipatov and V.S. Fadin, Sov. Phys. JETP **44**, 443 (1976).

[4] E.A. Kuraev, L.N. Lipatov and V.S. Fadin, Sov. Phys. JETP **45**, 199 (1977);
I.I. Balitsky and L.N. Lipatov, Sov. J. Nucl. Phys. **28**, 822 (1978).

[5] M. Ciafaloni, Nucl. Phys. **B 296**, 49 (1988);
S. Catani, F. Fiorani and G. Marchesini, Phys. Lett. **B 234**, 339 (1990);
S. Catani, F. Fiorani and G. Marchesini, Nucl. Phys. **B 336**, 18 (1990);
G. Marchesini, Nucl. Phys. **B 445**, 49 (1995).

[6] A. Mueller, Nucl. Phys. **B** (Proc. Suppl) **18C**, 125 (1990).

[7] A. Mueller, J. Phys. **G 17**, 1443 (1991).

[8] H1 Coll., C. Adloff et al., Nucl. Phys. **B 538**, 3 (1999).

[9] ZEUS Coll., J. Breitweg et al., Eur. Phys. J. **C 6**, 239 (1999).

[10] H. Jung and G. Salam, Eur. Phys. J. **C 19**, 351 (2001).

[11] L. Lönnblad, Comp. Phys. Comm. **71**, 15 (1992).

[12] N.H. Brook et al., *A comparison of deep-inelastic monte carlo event generators*, in *Proceedings of the Workshop on Monte Carlo generators for HERA physics*, eds. A. Doyle and G. Grindhammer and G. Ingelman and H. Jung, p. 10. DESY, Hamburg, 1999.

3.5 Gluon Saturation and the Color Glass Condensate

E. Iancu
Service de Physique Théorique, CEA Saclay, 91191 Gif-sur-Yvette, France
e-mail: eiancu@cea.fr

L. McLerran
Physics Department, Brookhaven National Laboratory, Upton, NY 11973, USA
e-mail:mclerran@quark.phy.bnl.gov

3.5.1 Introduction

The problem of the gross properties of hadron interactions in the high energy limit has been a central problem of particle and nuclear physics for over fifty years. Remarkable progress in recent years has resulted from the observation that the gluon density of the small x part of the hadron wavefunction, the relevant piece for high energies, grows rapidly as x decreases [1–3]. When the gluon density increases, important non-linear phenomena are expected, which should eventually lead to *saturation* [4–13], that is, to a limitation of the maximum gluon phase-space density. At saturation, this density is expected to be of order $1/\alpha_s$ [4, 9, 12–15], since interactions among the gluons will cutoff further growth once the interaction energy is comparable to the kinetic energy. For such a large density, perturbation theory breaks down even if the coupling constant is small, because of strong non-linear effects.

In fact, linear evolution equations like BFKL [1, 2] or DGLAP [16], which do not take into account the rescattering among the produced partons, are well known to predict an exponential growth of the gluon distribution with $\ln(1/x)$. This leads to cross sections which in the high-energy limit violate the Froissart unitarity bound. If parton distributions saturate, then there is a natural resolution to this unitarity problem.

In what follows, we shall see that saturation arises indeed, at least within a well defined approximation scheme, when non-linear effects are included in the quantum evolution towards small x. The formalism that we shall rely on — an effective theory for QCD at small x — is intimately related to the physical picture of the saturation regime as a *Color Glass Condensate* (CGC) [17, 18], a concept to be explained below. This formalism provides us with a non-linear generalization of the BFKL evolution where the rescatterings among the produced gluons are included to all orders. The basic equation at work is a *functional* evolution equation: the equation satisfied by the effective action. This encompasses, in particular, the non-linear evolution equations previously derived by Balitsky [19] within perturbative QCD, and, independently, by Kovchegov [20, 21] within the dipole model of Mueller [22, 23]. There has been recent progress towards

solving these equations [24–26]. (See also the contributions by Balitsky, Kovchegov and Levin in this volume.) Thus, remarkably, various approaches, which involve quite different technical manipulations and rely on different physical pictures, appear to converge towards the same equations for the non-linear gluon evolution in QCD at small x. The effective theory approach that we shall follow here has nevertheless some clear advantages, that we emphasize now: It is associated with a clear physical picture, that of the Color Glass Condensate (cf. Sect. 3.5.2); it involves the elementary fields of QCD (the color fields and their sources), as opposed to the "BFKL pomeron" in other approaches [20, 21]; and, especially, it allows for a global perspective where all the n-point correlation functions — which are necessarily coupled by the non-linear effects — are treated on the same footing. As we shall see in Sect. 3.5.6, this greately simplifies the search for solutions in the non-linear regime.

3.5.2 The Color Glass Condensate

Before describing the quantum evolution towards small x, in the next sections, let us anticipate and qualitatively describe here the result of this evolution, the so-called Color Glass Condensate (CGC) [17, 18]. This is the matter made of gluons in the high-density regime at saturation. Quantum-mechanically, this corresponds to some complicated multiparticle gluonic state with high occupation numbers. But, at least in the weak coupling[1] regime $\alpha_s \ll 1$, it admits a simple description in terms of classical color fields and sources. The classical approximation is appropriate since, as we shall see, the saturated gluons have large occupation numbers $\sim 1/\alpha_s$, and can thus be described by classical color fields with large amplitudes $A^i \sim 1/g$.

The physical picture that we are going to describe is formulated in the infinite-momentum frame, that is, the frame where the hadron propagates almost at the speed of light, with four-momentum $P^\mu \simeq (P + M^2/2P, 0, 0, P)$ and $P \gg M$. Here, M is the hadron mass, and will be neglected in what follows. In this frame, we shall consider deep inelastic scaterring at small Bjorken's x, $x \ll 1$. The kinematics becomes simpler by using light-cone (LC) vector notations[2], in which $P^\mu \equiv (P^+, P^-, \mathbf{P}_\perp) = (\sqrt{2}P, 0, \mathbf{0}_\perp)$, with large P^+. By Lorentz contraction, the hadron appears to the external probe (the virtual photon in DIS) as strongly squeezed in the longitudinal direction: it looks like a "pancake" localized near $z = t$ (or $x^- = 0$) with a longitudinal extent $\Delta x^- = R/\gamma = 1/P^+$, where γ is the Lorentz factor and R is the hadron radius in its rest frame (and also the radius of the transverse disk in the infinite-momentum frame).

However, this cannot be the whole story. As a quantum system, the hadron involves quantum fluctuations with arbitrarily small longitudinal momenta $k^+ \ll P^+$, and therefore arbitrarily large longitudinal extent $\Delta x^- \sim 1/k^+$. These are virtual

[1] One can argue [6–9, 12] that it is the gluon density itself which sets the scale for the running of α_s; thus, $\alpha_s \ll 1$ if the density is high enough, or x is sufficiently small.

[2] These are as defined as follows: for an arbitrary 4-vector v^μ, we write $v^\mu = (v^+, v^-, \mathbf{v}_\perp)$, with $v^+ \equiv (1/\sqrt{2})(v^0 + v^3)$, $v^- \equiv (1/\sqrt{2})(v^0 - v^3)$, and $\mathbf{v}_\perp \equiv (v^1, v^2)$. The dot product reads: $p \cdot x = p^+x^- + p^-x^+ - p_\perp \cdot x_\perp$. p^- and p^+ are, respectively, the LC energy and longitudinal momentum; correspondingly, x^+ and x^- are the LC time and longitudinal coordinate.

fluctuations, with a short lifetime Δx^+. As we shall argue in Sect. 3.5.3, smaller is k^+, shorter is the lifetime Δx^+ of the fluctuations: $\Delta x^+ \propto k^+$. But these short-lived fluctuations are nevertheless important, since they are the modes probed in DIS at small x. Indeed, by kinematics, the Bjorken x variable of the virtual photon equals the longitudinal momentum fraction of the struck quark: $x = k^+/P^+$.

So, in what follows, we shall concentrate on the low–k^+, or "soft", component of the hadron wavefunction. Also, we shall consider only gluons, since the gluon density increases faster than the quark density when x decreases (since the gluons are bosons). Our ultimate goal is to construct a classical *effective theory* for the *soft* gluons with $k^+ = xP^+ \ll P^+$ by "integrating out" the (relatively) *fast* partons, with longitudinal momenta $k^+ \ll p^+ \leq P^+$. This strategy has the advantage that the quantum effects associated with the fast gluons can be computed in perturbation theory (in a strong background field though), while the non-linear effects expected at small x can be treated in the simpler setting of a classical field theory. The main result of this construction, to be described in the nextcoming sections, is that the fast partons can be replaced, as far as their effects on the soft gluon dynamics are concerned, by a *classical color source* whose gross features can be anticipated via simple kinematical arguments:

1. The fast partons move along the light-cone with large p^+ momenta. They can emit, or absorb, soft gluons, but in a first approximation they do not deviate from their LC trajectories at $z \simeq t$, or $x^- \simeq 0$ (*no recoil*, or *eikonal approximation*). Thus, they generate a color current only in the + direction: $J_a^\mu = \delta^{\mu+}\rho_a$.
2. The fast partons have relatively short longitudinal wavelengths $\lambda^- \sim 1/p^+$, and therefore appear to the soft gluons (with momenta $k^+ \ll p^+$, and therefore a poor longitudinal resolution) as *sharply localized* at the light cone, within a distance $\Delta x^- \ll 1/k^+$.
3. The dynamics of the fast partons takes place on time scales much larger than the typical lifetime $\Delta x^+ \propto k^+$ of the soft gluons. Indeed, the fast partons are nearly on-shell ($2p^+p^- \simeq p_\perp^2$), so they have relatively small energies $p^- \sim p_\perp^2/p^+$, and thus a slow dynamics. Therefore, the soft gluons can probe only the *equal-time* correlators of the fast partons, as generated by a *time-independent* color source $\rho_a(\vec{x})$ with $\vec{x} \equiv (x^-, \mathbf{x}_\perp)$.

To summarize, the soft color current due to the fast partons is expected to have the following structure:

$$J_a^\mu(x) = \delta^{\mu+}\rho_a(x^-, \mathbf{x}_\perp), \quad \partial^-\rho_a \equiv \frac{\partial \rho_a}{\partial x^+} = 0, \quad \text{supp}\,\rho_a = \{x^- | 0 \leq x^- \leq 1/k^+\}. \tag{3.5.1}$$

This current acts as a source for the Yang-Mills equations describing the soft gluon dynamics in the classical approximation (with $\vec{x} \equiv (x^-, \mathbf{x}_\perp)$) :

$$(D_\nu F^{\nu\mu})_a(x) = \delta^{\mu+}\rho_a(\vec{x}). \tag{3.5.2}$$

To have a gauge-invariant formulation, the source ρ_a must be treated as a *stochastic* variable with zero expectation value. This is also consistent with the physical interpretation of ρ_a as the instantaneous color charge of the fast partons "seen" by the shortlived soft gluons, at some arbitrary time. The spatial correlators of $\rho_a(\vec{x})$ are inherited from the (generally time-dependent) quantum correlations of the fast gluons, via the renormalization group equation to be presented in Sect. 3.5.4 below. They can

be summarized as a gauge-invariant weight function $W_\tau[\rho]$, which is the probability for having a color charge distribution with density $\rho_a(\vec{x})$, and is normalized as:

$$\int \mathcal{D}\rho\, W_\tau[\rho] \,=\, 1. \tag{3.5.3}$$

We have introduced here the momentum-space rapidity $\tau \equiv \ln(P^+/k^+) = \ln(1/x)$ to indicate the dependence of the weight function upon the soft scale k^+.

To conclude, in this effective theory, equal-time gluon correlation functions at the scale $k^+ = xP^+$ are obtained as:

$$\langle A^i_a(x^+,\vec{x})A^j_b(x^+,\vec{y})\cdots\rangle_\tau \,=\, \int \mathcal{D}\rho\, W_\tau[\rho]\, \mathcal{A}^i_a(\vec{x})\mathcal{A}^j_b(\vec{y})\cdots\,, \tag{3.5.4}$$

where $\mathcal{A}^i_a \equiv \mathcal{A}^i_a[\rho]$ is the solution to eq. (3.5.2) in the light-cone (LC) gauge $A^+_a = 0$, which is the gauge which allows for the most direct contact with the gauge-invariant physical quantities [12, 17]. For instance, the gluon distribution function ($\equiv$ the total number of gluons per unit of rapidity, as measured by an external probe with virtuality Q^2) is obtained as [12, 17]

$$xG(x,Q^2) \;=\; \frac{1}{\pi}\int \frac{d^2k_\perp}{(2\pi)^2}\,\Theta(Q^2-k_\perp^2)\left\langle |\mathcal{F}^{+i}_a(\vec{k})|^2\right\rangle_\tau . \tag{3.5.5}$$

where $\mathcal{F}^{+i}_a = \partial^+\mathcal{A}^i_a$ is the classical electric field, and $\vec{k} \equiv (k^+, \mathbf{k}_\perp)$ with $k^+ = xP^+ = P^+\mathrm{e}^{-\tau}$. However, to have explicit expressions for these classical fields, it is preferable to express the LC-gauge solution $\mathcal{A}^i_a[\rho]$ in terms of color source ρ in the covariant gauge $\partial^\mu\tilde{A}_\mu = 0$ (COV-gauge). This is possible since both the measure and the weight function in the functional integral (3.5.4) are gauge-invariant, so that the classical average can be done equally well by integrating over the source ρ in the COV-gauge. In terms of the latter, the classical solution $\mathcal{A}^\mu_a[\rho]$ is known explicitly [17], and reads: $\mathcal{A}^+_a = 0$ (the gauge condition), $\mathcal{A}^-_a = 0$, and (in matrix notations, with $\rho \equiv \rho_a T^a$, etc.)

$$\begin{aligned}
\mathcal{A}^i(\vec{x}) \;&=\; \frac{i}{g}\,U(\vec{x})\,\partial^i U^\dagger(\vec{x}),\\
U^\dagger(x^-,x_\perp) \;&=\; \mathrm{P}\exp\left\{ig\int_{-\infty}^{x^-} dz^-\,\alpha(z^-,x_\perp)\right\},\\
-\nabla^2_\perp\alpha(\vec{x}) \;&=\; \rho(\vec{x}).
\end{aligned} \tag{3.5.6}$$

This is the gauge-transform (with gauge function $U^\dagger$) of the corresponding solution in the COV-gauge, which has only one non-trivial component: $\tilde{\mathcal{A}}^\mu_a = \delta^{\mu+}\alpha(\vec{x})$. All the fields above are static, like the color source ρ_a itself. The LC-gauge field $\mathcal{A}^i$ is a two-dimensional pure-gauge (in the sense that $\mathcal{F}^{ij} = 0$), but not also a four-dimensional pure-gauge, since the associated electric field $\mathcal{F}^{+i} = \partial^+\mathcal{A}^i$ is non-vanishing. One rather has:

$$\mathcal{F}^{+i}_a(\vec{x}) \,=\, U^\dagger_{ab}(\vec{x})\tilde{\mathcal{F}}^{+i}_b(\vec{x}) \,=\, -U^\dagger_{ab}(\vec{x})\partial^i\alpha_b(\vec{x})\,, \tag{3.5.7}$$

where $\tilde{\mathcal{F}}_a^{+i} = -\partial^i \alpha_a$ is the electric field in the COV-gauge.

The structure of the effective theory displayed in the equations above will be confirmed by the quantum analysis in Sects. 3.5.3 and 3.5.4, which will also tell us how to construct the weight function $W_\tau[\rho]$ by integrating out the fast quantum modes, and what is the accuracy of this construction. But before going on with the quantum analysis, let us recall that, at a purely classical level, this theory has been originally proposed by McLerran and Venugopalan (MV) as a model for the gluon distribution in large nuclei [6–8]. (See also Refs. [14, 27–30] for applications and developments of this model.) In the MV model, eqs. (3.5.2) and (3.5.4) have been simply postulated, on the basis of the kinematical arguments alluded to before, and a Gaussian form for the weight function $W_\tau[\rho]$ has been conjectured. As we shall see later, in Sect. 3.5.6.1, that Gaussian form is indeed consistent with the quantum evolution, but only in a kinematical regime where the non-linear effects are not too important.

Remarkably, eqs. (3.5.2) and (3.5.4) are those for a glass (here, a *color* glass): There is an external random source, which is averaged over. This is entirely analogous to what is done for spin glasses when one averages over background magnetic fields [31]. We shall find later that, at saturation, the classical field has a typical strength of order $1/g$, corresponding to an occupation number of order $1/\alpha_s$ [12–15]. This is the maximal occupation number for a classical field, since larger occupation numbers are blocked by repulsive interactions of the gluon field. For weak coupling, this occupation number is large, and the gluons can be thought of as in some condensate. We are therefore led to conclude that the matter which describes the small x part of a hadron wavefunction is a *Color Glass Condensate*.

3.5.3 Quantum evolution and BFKL

In the hadron wave function, a soft gluon, with $k^+ = xP^+ \ll P^+$, is a shortlived excitation which is typically radiated by a fast parton (e.g., a valence quark) with a larger longitudinal momentum $p^+ \gg k^+$, and thus a longer lifetime. Indeed, by the uncertainty principle, the lifetime of the parton system in Fig. 1.a is:

$$\Delta x^+ = \frac{1}{\varepsilon_{p-k} + \varepsilon_k - \varepsilon_p} \simeq \frac{1}{\varepsilon_k} = \frac{2k^+}{k_\perp^2} \propto x, \tag{3.5.8}$$

where $\varepsilon_p \equiv p_\perp^2/2p^+$ is the LC energy of the on-shell excitation with momentum $\vec{p} = (p^+, \mathbf{p}_\perp)$, and we have used the fact that, for comparable transverse momenta $k_\perp$ and $p_\perp$, $\varepsilon_k \gg \varepsilon_p, \varepsilon_{p-k}$. To resume, softer partons have larger energies, and therefore shorter lifetimes.

The lowest-order process in Fig. 1.a is amended by radiative corrections enhanced by the large rapidity gap $\Delta\tau \equiv \ln(p^+/k^+) \sim \ln(1/x)$. (We assume here that $\ln(1/x) \gg 1$.) For instance, the probability for the emission of a second gluon with momentum p_1^+ in the range $p^+ > p_1^+ > k^+$ is (cf. Fig. 1.b) :

$$\Delta P \propto \alpha_s \int_{k^+}^{p^+} \frac{dp_1^+}{p_1^+} = \alpha_s \ln \frac{p^+}{k^+} \sim \alpha_s \ln \frac{1}{x}, \tag{3.5.9}$$

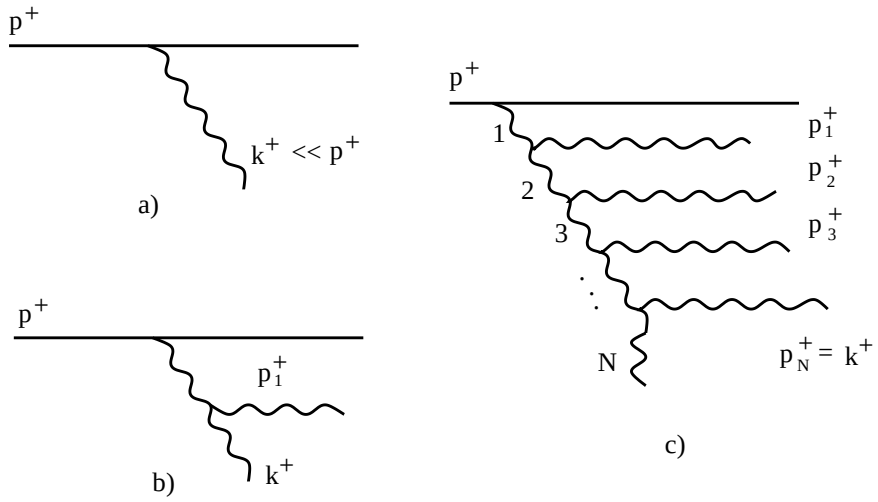

Figure 1: *a) Soft gluon emission by a fast parton; b) a second emission; c) a gluon cascade.*

and becomes of order one when $\ln(1/x) \sim 1/\alpha_s$. It is then highly probable that more gluons will be emitted along the way, thus giving birth to the gluon cascade depicted in Fig. 1.c. For a fixed number N of gluons in this cascade, the largest contribution, of order $(\alpha_s \ln(1/x))^N$, comes from the kinematical domain where

$$p^+ \equiv p_0^+ \gg p_1^+ \gg p_2^+ \gg \cdots \gg p_N^+ \equiv k^+. \tag{3.5.10}$$

Other momentum orderings give contributions which are suppressed by, at least, one factor of $1/\ln(1/x)$, and thus can be neglected to *leading logarithmic accuracy* (LLA). For the dominant contribution in eq. (3.5.10), the number of radiated gluons increases exponentially with $\Delta\tau$: $N(x) \sim \exp\{A\alpha_s \ln(1/x)\}$, with constant A. This is a coherence effect, consequence of the separation of scales in eq. (3.5.10), and of the bosonic nature of the gluons:

Indeed, because of its short lifetime, the soft gluon at the lower end of the cascade "sees" the N previous gluons as a frozen color charge distribution, with an average color charge $Q \equiv \sqrt{\langle Q_a Q_a \rangle} \propto N$. Thus, the Nth gluon is emitted *coherently* off the color charge fluctuations of the previously emitted gluons, with a differential probability (compare to eq. (3.5.9)) :

$$dP_N \propto \alpha_s N \, d\tau_N, \tag{3.5.11}$$

which implies that $N(\tau) \sim \mathrm{e}^{A\alpha_s \tau}$ (with $\tau \equiv \ln(1/x)$), as anticipated. Then, the gluon distribution

$$xG(x, Q^2) \equiv \frac{dN}{d\tau} \sim C\alpha_s \mathrm{e}^{A\alpha_s \tau} \tag{3.5.12}$$

grows exponentially as well. A more refined treatment, using the BFKL equation [1, 2], gives $A = 4N_c \ln 2/\pi$, and shows that the prefactor C in the r.h.s. of eq. (3.5.12) has a weak dependence on τ : $C \propto (\alpha_s \tau)^{-1/2}$.

Thus, the BFKL picture is that of an unstable growth of the color charge fluctuations as x becomes smaller and smaller. However, this evolution assumes the radiated gluons to behave as free particles, so it ceases to be valid at very low x, where the gluon density becomes so large that the radiated gluons overlap each other in the transverse plane and start interacting. This is the onset of saturation.

This is also the regime where the description in terms of the Colored Glass Condensate becomes appropriate: Because of the hierarchy of scales in eq. (3.5.10), the soft gluons "see" the fast partons as an effective color charge which is *static* (i.e., independent of x^+), and *localized* near the LC (i.e., at $x^- = 0$), with a *random* density $\rho_a(x^-, x_\perp)$. This is random since the gluons can belong to different cascades, and, moreover, the instantaneous configuration of the cascades inside the hadron is random. We thus recognize the main ingredients of the effective theory discussed in Sect. 3.5.2. The quantum evolution of the probability distribution $W_\tau[\rho]$ for $\rho_a(\vec{x})$ will be described in the next section. But it should be clear by now that, for consistency with perturbative QCD, this evolution should reduce to the BFKL equation in the low density limit.

3.5.4 The quantum evolution of the CGC

It has been first conjectured in Ref. [14] that the MV model could be promoted as an effective theory for QCD at small x. For this to be true, this model should be consistent with the quantum evolution towards small x, with the effects of the quantum corrections absorbed into a renormalization of the weight function $W_\tau[\rho]$. A decisive step towards proving this conjecture has been carried out in Ref. [32, 33] (see also Refs. [34–36]), where one has formulated a generic renormalization group equation (RGE) describing the evolution of $W_\tau[\rho]$ with the rapidity τ (i.e., with the separation scale $k^+ = P^+ \mathrm{e}^{-\tau}$ between fast and soft gluons). Still in Ref. [32, 33], one has proposed a gauge-invariant action describing the coupling between the quantum gluons and the classical color source, and one has verified that in the low-density, or weak-field, regime the RGE associated to this action reduces to the BFKL equation, as it should.

But a complete proof has been given only recently, via the thorough analysis in Refs. [17, 18], where the general non-linear RGE has been finally constructed. Specifically, it has been shown there, via a careful matching between classical and quantum correlations, that the quantum corrections can be indeed absorbed into a renormalization of the weight function, which is moreover governed by a RGE of the type proposed in Refs. [32, 33]. The coefficients in this equation have been computed explicitly, via an exact background field calculation.

To describe this quantum evolution, it is convenient to consider a sequence of two classical effective theories ("Theory I" and "Theory II") valid at the scales k^+ and bk^+, respectively, with $b < 1$ and such as $\alpha_s \ln(1/b) < 1$. Thus, corrections of order $\alpha_s \ln(1/b) < 1$ can be still controlled within perturbation theory. To the order of interest, the gluon correlations at the lower scale bk^+ can be computed in two ways: As classical correlations within Theory II (which is valid at this scale), or by allowing for quantum fluctuations in Theory I and integrating out the "semi-fast" quantum

gluons with longitudinal momenta in the strip

$$bk^+ \;<\; |p^+| \;<\; k^+ \,, \tag{3.5.13}$$

to leading order in $\alpha_s \ln(1/b)$ (since this is the accuracy to which holds the separation of scales assumed by the effective theory), but to *all* orders in the background field $\mathcal{A}^i$ created by the tree-level source ρ_a (since $\mathcal{A}^i \sim 1/g$ at saturation, so that the mean field effects cannot be expanded in perturbation theory). The difference $\Delta W \equiv W_{\tau+d\tau} - W_\tau$ [with $\tau \equiv \ln(P^+/k^+)$ and $d\tau \equiv \ln(1/b)$], and therefore the evolution equation for W_τ, can be then obtained by matching these two calculations [17]. Clearly, the resulting equation will be generally non-linear in the classical field $\mathcal{A}^i$, which is itself a non-linear functional of the source ρ_a (cf. eq. (3.5.6)). Via these classical non-linearities, the interactions among the soft gluons produced in the partons cascades (cf. Sect. 3.5.3) are included in the quantum evolution, to all orders.

The details of the quantum calculations are quite tedious, and will be omitted here (see Refs. [17, 18]). The final result, however — a functional RGE for the weight function $W_\tau[\rho]$ — has a relatively simple structure. It reads (in compact notations, where the sum (integral) over the repeated color indices (coordinate variables) is kept implicit) [17, 32, 33] :

$$\frac{\partial W_\tau[\rho]}{\partial \tau} \;=\; \alpha_s \left\{ \frac{1}{2} \frac{\delta^2}{\delta \rho^a_\tau(x) \delta \rho^b_\tau(y)} [W_\tau \chi^{ab}_{xy}] - \frac{\delta}{\delta \rho^a_\tau(x)} [W_\tau \sigma^a_x] \right\} \tag{3.5.14}$$

with the coefficients $\sigma^a_x \equiv \sigma_a(x_\perp)$ and $\chi^{ab}_{xy} \equiv \chi_{ab}(x_\perp, y_\perp)$ related to the 1-point and 2-point functions of the color charge $\delta\rho_a(x)$ of the semi-fast gluons via the following relations:

$$\alpha_s \ln \frac{1}{b} \, \sigma_a(x_\perp) \;\equiv\; \int dx^- \, \langle \delta\rho_a(x) \rangle \,, \tag{3.5.15}$$

$$\alpha_s \ln \frac{1}{b} \, \chi_{ab}(x_\perp, y_\perp) \;\equiv\; \int dx^- \int dy^- \, \langle \delta\rho_a(x^+, \vec{x}) \, \delta\rho_b(x^+, \vec{y}) \rangle \,, \tag{3.5.16}$$

where the brackets denote the average over the semi-fast quantum fluctuations in the background of the classical fields $\mathcal{A}^i_a$. [The meaning of the notation $\rho^a_\tau(x)$ in eq. (3.5.14) will be explained later.] The quantity $\langle \delta\rho_a(x) \rangle$ is the color source induced by the fields $\mathcal{A}^i_a$ when acting on the quantum gluons; thus, this is the quantum correction to the original source ρ_a. Similarly, $\langle \delta\rho_a(x) \, \delta\rho_b(y) \rangle$ is the quantum correction to the 2-point function of the classical source, which is one of the correlations encoded in the weight function $W_\tau[\rho]$. Thus, eq. (3.5.14) tells us how to include the quantum corrections to the 1-point and 2-point functions of ρ in a renormalization of the weight function. Higher-point correlations need not be included, since they are of higher order in α_s [17, 32, 33].

More precisely, eqs. (3.5.15)–(3.5.16) are complete as they stand provided the variable $\rho_a(\vec{x})$ in eq. (3.5.14) is the classical color source in the LC-gauge (where the quantum theory is a priori formulated [17, 32, 33]). In practice, however, it is more convenient to use the color source in the COV-gauge as the independent variable (since the field $\mathcal{A}^i_a$ is known explicitly only in terms of the COV-gauge ρ; cf. eq. (3.5.6)). In

that case, eq. (3.5.15) acquires an additional contribution due to the quantum evolution of the rotation from the LC-gauge to the COV-gauge [17]. In the final equation (3.5.20) below, this contribution will be implicitly included.

Some typical contributions to the correlations defining σ and χ read as follows (see [17, 32, 33] for the remaining contributions):

$$\langle \delta\rho_a(x)\rangle = gf^{abc}\langle(\partial^+ a_b^i(x))a_c^i(x)\rangle = g\mathrm{Tr}(T^a\partial_x^+ G^{ii}(x,y))\big|_{x=y}, \quad (3.5.17)$$

$$\langle \delta\rho_a(x)\,\delta\rho_b(y)\rangle = 4ig^2\,\mathcal{F}_{ac}^{+i}(\vec{x})\,G_{cd}^{ij}(x,y)\,\mathcal{F}_{db}^{+j}(\vec{y}), \quad (3.5.18)$$

and involve the LC-gauge propagator $iG_{ab}^{ij} = \langle a_a^i(x)a_b^j(x)\rangle$ of the semi-fast gluons a^μ in the presence of the background fields $\mathcal{A}^i$. This propagator can be computed exactly (i.e., to all orders in $\mathcal{A}^i$) by exploiting the special geometry of the background field [17]. In this construction, one meets with the ambiguity associated with the "axial" pole at $p^+ = 0$ in the LC-gauge propagator. Giving an $i\epsilon$ prescription for this pole is tantamount to chosing a gauge-fixing prescription for the residual gauge freedom in the LC-gauge[3]. This choice has non-trivial consequences as it influences the longitudinal structure of the induced source [17]. For consistency with the retarded boundary conditions (in x^-) imposed on the classical solution (3.5.6), we choose the same retarded $i\epsilon$ prescription for the axial pole in the LC-gauge propagator [4]. With this prescription, the induced source $\langle\delta\rho(\vec{x})\rangle$ has support only at positive x^-, with (typically) $1/k^+ \lesssim x^- \lesssim 1/bk^+$ [17, 18].

Thus, the quantum calculation predicts an interesting relation between the longitudinal structure of the classical source and the longitudinal momenta of the quantum gluons that have been integrated out to generate this source. This relation is most simply expressed in terms of the corresponding rapidities. Besides the momentum-space rapidity $\tau \equiv \ln(P^+/k^+) = \ln(1/x)$, let us introduce also the space-time rapidity $\mathrm{y} \equiv \ln(x^-/x_0^-)$, where $x_0^- \equiv 1/P^+$ is the minimal longitudinal size of the hadron. With these definitions, both τ and y are positive. Then, $1/k^+ = 1/(xP^+) = x_0^-\mathrm{e}^\tau$ and $1/(bk^+) = x_0^-\mathrm{e}^{\tau+d\tau}$, and the previous discussion shows that the induced source has support at space-time rapidities $\tau \lesssim \mathrm{y} \lesssim \tau + d\tau$. Thus, the two rapidities are identified by the quantum evolution: The classical source

$$\rho_{\mathrm{y}}^a(x_\perp) \equiv \rho^a(x^- = x_0^-\mathrm{e}^{\mathrm{y}}, x_\perp) \quad (3.5.19)$$

is constructed in layers of space-time rapidity, with the contribution in the rapidity bin $(\mathrm{y},\ \mathrm{y}+d\mathrm{y})$ obtained by integrating out the quantum gluons with longitudinal momenta in the momentum-rapidity bin $(\tau,\ \tau+d\tau)$ with $\tau = \mathrm{y}$ and $d\mathrm{y} = d\tau$. In particular, the total source created by the quantum evolution up to $\tau = \ln(1/x)$ has support at $0 \le \mathrm{y} \le \tau$, or $x_0^- \le x^- \le x_0^-\mathrm{e}^\tau$. This was anticipated in writing eq. (3.5.1).

[3] Recall that, even after imposing the LC-gauge condition $A^+ = 0$, one is still left with the possibility to perform x^-–independent gauge transformations, which preserve A^+.

[4] We have verified that the same results for χ and σ would be eventually obtained also by using an *advanced* prescription [17]. On the other hand, we have not been able to give a sense to calculations with principal value or Leibbrandt-Mandelstam prescriptions.

We are now in a position to explain the notation $\rho^a_\tau(x)$ in eq. (3.5.14): this is the classical source $\rho^a_{\rm y}(x_\perp)$, eq. (3.5.19), evaluated at y $=\tau$. According to eq. (3.5.14), the quantum evolution of the weight function proceeds exclusively via the variation of the color source ρ_a in the highest bin of space-time rapidity.

We now present the final result for the RGE [18]. This is most conveniently written as an equation for $W_\tau[\alpha]$ (recall that α and ρ are linearly related, cf. eq. (3.5.6)), and reads (with $\alpha^a_\tau(x_\perp)\equiv\alpha_a(x^-=x_0^-\mathrm{e}^\tau,x_\perp)$)

$$\frac{\partial W_\tau[\alpha]}{\partial\tau} = \alpha_s\left\{\frac{1}{2}\frac{\delta^2}{\delta\alpha^a_\tau(x_\perp)\delta\alpha^b_\tau(y_\perp)}[W_\tau\eta^{ab}_{xy}] - \frac{\delta}{\delta\alpha^a_\tau(x_\perp)}[W_\tau\nu^a_x]\right\}, \tag{3.5.20}$$

where the new coefficients η and ν are trivially related (via factors of $1/\nabla^2_\perp$) to the coefficients χ and σ in eq. (3.5.14), and read:

$$g\nu^a(x_\perp) = 2i\int\frac{d^2z_\perp}{(2\pi)^2}\frac{1}{(x_\perp-z_\perp)^2}\,\mathrm{Tr}\Big(T^aV^\dagger_xV_z\Big), \tag{3.5.21}$$

and

$$g^2\eta^{ab}(x_\perp,y_\perp) = 4\int\frac{d^2z_\perp}{(2\pi)^2}\frac{(x^i-z^i)(y^i-z^i)}{(x_\perp-z_\perp)^2(y_\perp-z_\perp)^2}\Big\{1+V^\dagger_xV_y-V^\dagger_xV_z-V^\dagger_zV_y\Big\}^{ab} \tag{3.5.22}$$

In these equations, V and $V^\dagger$ are the Wilson lines of eq. (3.5.6) evaluated at asymptotically large x^-:

$$V^\dagger_x \equiv U^\dagger(x^-\to\infty,x_\perp) = \mathrm{P}\exp\left\{ig\int_{-\infty}^{\infty}dx^-\,\alpha(x^-,x_\perp)\right\}. \tag{3.5.23}$$

The integral over x^- in eq. (3.5.23) runs effectively from $x^-_{min}=x_0^-$ up to $x^-_{max}=x_0^-\mathrm{e}^\tau$, since the field α vanishes outside this interval.

Eq. (3.5.20) is a functional Fokker-Planck equation with "time" τ. It depicts the quantum evolution towards small x as the diffusion of the probability density $W_\tau[\alpha]$ in the functional space spanned by $\alpha_a(x^-,x_\perp)$. Since the r.h.s. of this equation is a total derivative with respect to α, this flow automatically preserves the correct normalization of the weight function, cf. eq. (3.5.3). By using the following, remarkable, relation between the coefficients in this equation:

$$\frac{1}{2}\int d^2y\,\frac{\delta\eta^{ab}(x_\perp,y_\perp)}{\delta\alpha^b_\tau(y_\perp)} = \nu^a(x_\perp), \tag{3.5.24}$$

the RGE can be brought into a Hamiltonian form:

$$\frac{\partial W_\tau[\alpha]}{\partial\tau} = \frac{\alpha_s}{2}\int d^2x\int d^2y\,\frac{\delta}{\delta\alpha^a_\tau(x_\perp)}\left(\eta^{ab}_{xy}\frac{\delta W_\tau}{\delta\alpha^b_\tau(y_\perp)}\right) \equiv -H_\tau W_\tau, \tag{3.5.25}$$

with the following, τ-dependent and manifestly positive definite, Hamiltonian

$$\begin{aligned} H_\tau &= \int\frac{d^2z_\perp}{2\pi}\,J^i_a(z_\perp)\,J^i_a(z_\perp),\\ J^i_a(z_\perp) &\equiv \int\frac{d^2x_\perp}{2\pi}\,\frac{z^i-x^i}{(z_\perp-x_\perp)^2}\,(1-V^\dagger_zV_x)_{ab}\,\frac{i\delta}{\delta\alpha^b_\tau(x_\perp)}. \end{aligned} \tag{3.5.26}$$

Solutions to this RGE will be investigated in Sect. 3.5.6.

3.5.5 Recovering some known results

The RGE (3.5.20) is a functional equation, but it can be used to derive ordinary evolution equations for all the observables which are related to α (like the gluon distribution function (3.5.5)). If $O(\alpha)$ is any such an operator, then its average over the hadron wavefunction at the rapidity scale τ is obtained, within the present formalism, as an average over α with weight function $W_\tau[\alpha]$ (compare with eq. (3.5.4)):

$$\langle O(\alpha)\rangle_\tau = \int \mathcal{D}\alpha\, W_\tau[\alpha]\, O(\alpha)\,. \tag{3.5.27}$$

This quantity obeys the following evolution equation

$$\frac{\partial}{\partial\tau}\langle O(\alpha)\rangle_\tau = \alpha_s \left\langle \frac{1}{2}\,\eta^{ab}_{xy}\,\frac{\delta^2 O}{\delta\alpha^a_\tau(x)\delta\alpha^b_\tau(y)} + \nu^a_x\,\frac{\delta O}{\delta\alpha^a_\tau(x)}\right\rangle_\tau, \tag{3.5.28}$$

which is obtained by multiplying eq. (3.5.20) with $O(\alpha)$, integrating over α, and performing some integrations by parts in the r.h.s.

By appropriately chosing the operator $O(\alpha)$, one can make contact with other evolution equations previously proposed in the literature. First, as already mentioned, eq. (3.5.28) generates the BFKL equation in the weak field (or low density) limit. This has been already verified in Ref. [32, 33], where the coefficients η and ν in this equation have been computed to lowest order in α.

More interestingly, in the general non-linear case eq. (3.5.28) generates the evolution equations for Wilson line operators previously derived by Balitsky [19] and Kovchegov [20, 21] by different technics. Let us verify this on the example of the 2-point function $O(\alpha) = \mathrm{tr}(V_x^\dagger V_y)$. Following Refs. [19–21], the Wilson lines $V_x^\dagger$ and V_y are taken in the *fundamental* representation (that is, they are defined by eq. (3.5.23) with $\alpha \equiv \alpha_a t^a$). The functional derivatives in eq. (3.5.28) are then computed by using:

$$\frac{\delta V^\dagger(x_\perp)}{\delta\alpha^a_\tau(z_\perp)} = igt^a V^\dagger(x_\perp)\,\delta(x_\perp - z_\perp), \qquad \frac{\delta V(y_\perp)}{\delta\alpha^a_\tau(z_\perp)} = -igV(y_\perp)t^a\delta(y_\perp - z_\perp). \tag{3.5.29}$$

This gives:

$$\frac{\partial}{\partial\tau}\langle \mathrm{tr}(V_x^\dagger V_y)\rangle_\tau = \alpha_s \left\langle g^2\Big(\eta^{ab}_{xy} - \frac{1}{2}\eta^{ab}_{xx} - \frac{1}{2}\eta^{ab}_{yy}\Big)\mathrm{tr}\big(t^a V_x^\dagger V_y t^b\big) + ig\big(\nu^a_x - \nu^a_y\big)\mathrm{tr}\big(t^a V_x^\dagger V_y\big)\right\rangle_\tau .$$

After inserting eqs. (3.5.21) and (3.5.22), the color traces are computed by repeatedly using the Fierz identity (with N the number of colors)

$$t^{ij}_a\, t^{kl}_a = \frac{1}{2}\,\delta^{il}\delta^{jk} - \frac{1}{2N}\,\delta^{ij}\delta^{kl}\,. \tag{3.5.30}$$

One finally obtains:

$$\frac{\partial}{\partial\tau}\langle \mathrm{tr}(V_x^\dagger V_y)\rangle_\tau = \frac{\alpha_s}{2\pi^2}\int d^2z \frac{(x_\perp - y_\perp)^2}{(x_\perp - z_\perp)^2(y_\perp - z_\perp)^2}\left\langle \mathrm{tr}(V_x^\dagger V_z)\mathrm{tr}(V_z^\dagger V_y) - N\mathrm{tr}(V_x^\dagger V_y)\right\rangle_\tau , \tag{3.5.31}$$

which coincides indeed with the corresponding equation by Balitsky [19]. This equation relates a 2-point function to a 4-point function, and is only the first equation in an infinite hierarchy of coupled equations. However, in the large N limit, the 4-point function in the r.h.s. factorizes:

$$\left\langle \mathrm{tr}(V_x^\dagger V_z)\,\mathrm{tr}(V_z^\dagger V_y)\right\rangle_\tau \longrightarrow \left\langle \mathrm{tr}(V_x^\dagger V_z)\right\rangle_\tau \left\langle \mathrm{tr}(V_z^\dagger V_y)\right\rangle_\tau \quad \text{for } N\to\infty, \tag{3.5.32}$$

and eq. (3.5.31) reduces to a closed equation for the quantity $\mathcal{N}(x_\perp, y_\perp) \equiv \langle \mathrm{tr}(1 - V_x^\dagger V_y)\rangle_\tau$ (which physically represents the forward scattering amplitude of a color dipole with the hadron [20, 21]):

$$\frac{\partial}{\partial\tau}\mathcal{N}_{xy} = \frac{\alpha_s}{2\pi^2}\int d^2z \frac{(x_\perp - y_\perp)^2}{(x_\perp - z_\perp)^2(y_\perp - z_\perp)^2}\left\{N\Big(\mathcal{N}_{xz} + \mathcal{N}_{zy} - \mathcal{N}_{xy}\Big) - \mathcal{N}_{xz}\mathcal{N}_{zy}\right\} \tag{3.5.33}$$

This coincides with the evolution equation obtained by Kovchegov [20, 21] within the framework of Mueller's dipole model [22, 23].

More generally, Balitsky's whole set of coupled evolution equations for the n-point functions of the Wilson lines follows from the functional RGE (3.5.14). This can be verified either case be case, as we have done above for the 2-point function, or by noticing that the Hamiltonian (3.5.26) is actually the same as the Hamiltonian which generates Balitsky's equations, as rewritten in functional form by Weigert [26].

3.5.6 Solving the RGE: Saturation and Universality

After having developed all this heavy formalism, we finally come at the more exciting point where we look for solutions to the renormalization group equation [13, 37]. In doing this, we shall first assume, and a posteriori check, the existence of an intrinsic momentum scale $Q_s(\tau)$ ("the saturation momentum") which controls both the transverse correlation length in the problem, and the onset of the non-linear regime. That is, the typical variation scale for the Wilson line $V(x_\perp)$ is $1/Q_s$, and the non-linear effects become important at transverse momenta of order Q_s or less. Physically, this is the scale below which the non-linear effects are expected to slow down and eventually saturate the increase of the gluon density with $1/k_\perp^2$ [6–9, 12–15]. As we shall see, this momentum scale is introduced by the initial conditions (note that there is no explicit scale in the evolution equation (3.5.25)–(3.5.26)), and increases with τ, because of the quantum evolution.

Below, we shall find approximate solutions to eq. (3.5.25) in two different kinematical regimes: $k_\perp \gg Q_s(\tau)$ and $k_\perp \ll Q_s(\tau)$, where $k_\perp$ is the transverse momentum at which we measure the correlation functions (i.e., the transverse resolution of the external probe). No attempt will be made to describe the intermediate behaviour at $k_\perp \sim Q_s$, and thus the onset of saturation. Because of that, the saturation scale itself will be not exactly determined, but only estimated via a study of the onset of non-linearity in the high momentum regime, and also via the matching between the two limiting solutions, at low $k_\perp$ and large $k_\perp$, respectively. These two estimates for Q_s will be seen to agree with each other.

3.5.6.1 The high momentum regime

When the external momentum is large, $k_\perp^2 \gg Q_s^2(\tau)$, we are probing the system on transverse scales much shorter than its correlation length, and we are sensitive only to the short-ranged fluctuations of the color field, which are relatively weak: $\mathcal{F}_a^{+i} \sim \mathcal{O}(1)$. This allows us to perform a short-distance expansion in the Hamiltonian (3.5.26), and also to linearize the Wilson lines there with respect to α :

$$1 - V_z^\dagger V_x \approx (z^j - x^j)(\partial^j V^\dagger)_x V_x \approx ig(z^j - x^j)\partial^j \alpha(x_\perp), \tag{3.5.34}$$

where (with the notation $\hat{\alpha}_{\rm y}^a(x_\perp) \equiv x^- \alpha^a(x^-, x_\perp)$ for $x^- = x_0^- {\rm e}^{\rm y}$)

$$\alpha^a(x_\perp) \equiv \int_{x_0^-}^{\infty} dx^- \alpha^a(x^-, x_\perp) = \int_0^\tau d{\rm y}\, \hat{\alpha}_{\rm y}^a(x_\perp). \tag{3.5.35}$$

With these approximations, the Hamiltonian (3.5.26) can be brought in the form:

$$H \approx \frac{g^2}{2\pi} \int d^2x_\perp \int d^2y_\perp \, \langle x_\perp | \frac{1}{\nabla_\perp^4} | y_\perp \rangle \, \partial^i \alpha^{ab}(x_\perp) \, \frac{\delta}{\delta \alpha_\tau^b(x_\perp)} \, \partial^i \alpha^{ac}(y_\perp) \, \frac{\delta}{\delta \alpha_\tau^c(y_\perp)}. \tag{3.5.36}$$

The RGE associated to this Hamiltonian is still non-linear, and we have not been able to solve it exactly. To make progress, we perform a mean field approximation in which we replace, within eq. (3.5.36),

$$\partial^i \alpha^{ab}(x_\perp) \, \partial^i \alpha^{ac}(y_\perp) \to \langle \partial^i \alpha^{ab}(x_\perp) \, \partial^i \alpha^{ac}(y_\perp) \rangle_\tau \equiv N \delta^{bc} \nabla_x^2 \xi_\tau(x_\perp - y_\perp), \tag{3.5.37}$$

where the expectation value in the r.h.s. is defined as in eq. (3.5.4), and we have assumed homogeneity in the transverse plane, for simplicity. (The color structure in the r.h.s. follows from gauge invariance.) After this approximation, the RGE becomes linear and can be solved by a Gaussian weight function. The correlation function ξ_τ in eq. (3.5.37) can be then computed in terms of the width of this Gaussian, which, as we shall see, entails a self-consistency condition describing the evolution of the width with τ.

Specifically, by using (3.5.37) together with $k_\perp^2 \alpha_\tau(k_\perp) = \rho_\tau(k_\perp)$ (cf. eq. (3.5.6)), the Hamiltonian (3.5.36) is finally rewritten as (with $\alpha_s = g^2/4\pi$):

$$\begin{aligned} H_{{\rm high}-k_\perp} &= -\frac{1}{2} \int \frac{d^2k_\perp}{(2\pi)^2} \, \mathcal{G}_\tau(k_\perp) \, \frac{\delta^2}{\delta \rho_\tau^a(k_\perp) \delta \rho_\tau^a(-k_\perp)}, \\ \mathcal{G}_\tau(k_\perp) &\equiv 4\alpha_s N \int^{k_\perp} \frac{d^2p_\perp}{(2\pi)^2} \, p_\perp^2 \xi_\tau(p_\perp) \, . \end{aligned} \tag{3.5.38}$$

Thus, in this high-momentum regime, the solution to the RGE is most naturally written as a Gaussian in $\rho_a(\vec{x})$. The only subtle point about this solution refers to its longitudinal structure. To understand this structure, note that the two functional derivatives in eq. (3.5.38) act at the same point x^-, namely at $x^- = x_\tau^- \equiv x_0^- {\rm e}^\tau$. This

implies that the correlations generated by the RGE are local in x^-. We thus search for a solution $W_\tau[\rho]$ of the form:

$$W_\tau[\rho] \;=\; \mathcal{N}_\tau \exp\left\{-\frac{1}{2}\int_0^\infty dy \int \frac{d^2k_\perp}{(2\pi)^2}\,\hat{\rho}^a_{\rm y}(k_\perp)\lambda_\tau^{-1}({\rm y},k_\perp)\hat{\rho}^a_{\rm y}(-k_\perp)\right\}, \qquad (3.5.39)$$

which is the kind of Gaussian Ansatz that has been postulated in the original MV model [6–8, 12, 14, 15, 28]. In writing eq. (3.5.39), we have used the space-time rapidity y to indicate the x^-–dependence of the various functions, and have defined

$$\hat{\rho}^a_{\rm y}(x_\perp) \;\equiv\; x^-\rho^a(x^-,x_\perp) \qquad \text{for} \quad x^- = x_0^-{\rm e}^{\rm y}. \qquad (3.5.40)$$

The overall factor $\mathcal{N}_\tau$ follows from the normalization condition (3.5.3) as (up to some irrelevant, τ-independent, factor):

$$\mathcal{N}_\tau \;=\; [\det\lambda_\tau({\rm y},k_\perp)]^{-1/2} \;=\; \prod_{k_\perp}\prod_{\rm y}[\lambda_\tau({\rm y},k_\perp)]^{-(N^2-1)/2}, \qquad (3.5.41)$$

where in writing the second equality we have considered a lattice version of the 3-dimensional configuration space (i.e., the transverse plane and the space-time rapidity), with discrete points $k_\perp$ and y.

It is now straightforward to verify that the functional (3.5.39) satisfies the RGE associated to $H_{{\rm high}-k_\perp}$ provided the width $\lambda_\tau({\rm y},k_\perp)$ obeys the following equation:

$$\frac{\partial\lambda_\tau({\rm y},k_\perp)}{\partial\tau} \;=\; \delta(\tau-{\rm y})\mathcal{G}_\tau(k_\perp), \qquad (3.5.42)$$

which shows that the evolution of the width with the *momentum-space* rapidity τ takes place at the *space-time* rapidity ${\rm y}=\tau$, that is, at the end point of the color charge distribution produced at the previous steps. The solution to eq. (3.5.42) is immediate:

$$\lambda_\tau({\rm y},k_\perp) \;=\; \theta(\tau-{\rm y})\,\mathcal{G}_{\rm y}(k_\perp) \;+\; \delta({\rm y})\mu_0(k_\perp), \qquad (3.5.43)$$

where we have anticipated that the initial condition at $\tau=0$ is:

$$\lambda_0({\rm y},k_\perp) \;=\; \delta({\rm y})\mu_0(k_\perp). \qquad (3.5.44)$$

The δ-function in eq. (3.5.44) expresses the fact that, as $\tau\equiv\ln(1/x)\to 0$ (or $x\to 1$), the color source is created exclusively by the valence quarks localized within $\Delta x^- \sim 1/P^+$, which is the shortest longitudinal distance in the problem. Thus, this is effectively a *surface* color charge density in the transverse plane at $x^- = x_0^-$, or ${\rm y}=0$. The quantity μ_0 is the color charge squared of the valence quarks per unit transverse aria (see also eqs. (3.5.49) and (3.5.57)).

According to eqs. (3.5.39) and (3.5.43), the width of the Gaussian is the *inverse* of a θ-function. This means that the weight function $W_\tau[\rho]$ is identically zero for all the functions $\rho^a_{\rm y}(x_\perp)$ having support at rapidities ${\rm y}>\tau$. This is the mathematical expression of the fact that the color source created by the quantum evolution up to

τ has support at $0 \leq \mathrm{y} \leq \tau$. Thus, in the functional integral (3.5.4) one can freely integrate over all the functions $\rho^a_{\mathrm{y}}(x_\perp)$, without any restriction on their support (other than $\mathrm{y} > 0$); the restriction to $\mathrm{y} \leq \tau$ will be automatically implemented by the weight function.

Eq. (3.5.39) gives the following 2-point functions:

$$\begin{aligned} \langle \hat{\rho}^a_{\mathrm{y}}(x_\perp)\, \hat{\rho}^b_{\mathrm{y}'}(y_\perp)\rangle_\tau &= \delta^{ab}\delta(\mathrm{y}-\mathrm{y}')\, \lambda_\tau(\mathrm{y}, x_\perp - y_\perp), \\ \langle \hat{\alpha}^a_{\mathrm{y}}(x_\perp)\, \hat{\alpha}^b_{\mathrm{y}'}(y_\perp)\rangle_\tau &= \delta^{ab}\delta(\mathrm{y}-\mathrm{y}')\, \gamma_\tau(\mathrm{y}, x_\perp - y_\perp), \end{aligned} \tag{3.5.45}$$

with

$$\gamma_\tau(\mathrm{y}, k_\perp) \;=\; (1/k_\perp^4)\, \lambda_\tau(\mathrm{y}, k_\perp)\,. \tag{3.5.46}$$

At this point, one should recall that the correlation function ξ_τ, eq. (3.5.37), and thus the function $\mathcal{G}_\tau(k_\perp)$ in eq. (3.5.38), are expectation values with the weight function (3.5.39), and thus functionals of λ_τ. Thus, eqs. (3.5.42) or (3.5.43) imply self-consistency conditions, to be made explicit now. To this aim, it is convenient to introduce the quantity:

$$\mu_\tau(k_\perp) \;\equiv\; \int_0^\infty d\mathrm{y}\, \lambda_\tau(\mathrm{y}, k_\perp) \;=\; \mu_0(k_\perp) \;+\; \int_0^\tau d\mathrm{y}\, \mathcal{G}_{\mathrm{y}}(k_\perp)\,, \tag{3.5.47}$$

which is the same as the solution to the following equation

$$\frac{\partial \mu_\tau(k_\perp^2)}{\partial \tau} \;=\; \mathcal{G}_\tau(k_\perp), \tag{3.5.48}$$

with the initial condition $\mu_{\tau=0}(k_\perp) = \mu_0(k_\perp)$. Eqs. (3.5.45) and (3.5.47) imply:

$$\begin{aligned} \langle \rho_a(k^+, x_\perp)\rho_b(-k^+, y_\perp)\rangle_\tau &\equiv \int dx^- \int dy^- \mathrm{e}^{ik^+(x^- - y^-)} \langle \rho_a(x^-, x_\perp)\rho_b(y^-, y_\perp)\rangle_\tau \\ &= \delta^{ab} \int_0^\infty d\mathrm{y}\, \lambda_\tau(\mathrm{y}, x_\perp - y_\perp) = \delta^{ab}\, \mu_\tau(x_\perp - y_\perp) \end{aligned} \tag{3.5.49}$$

showing that, physically, $\mu_\tau(k_\perp)$ is the unintegrated gluon distribution (in the present weak field regime). To see this, note that, to lowest order in ρ,

$$\mathcal{F}_a^{+j}(\vec{k}) \;\simeq\; ik^j \alpha_a(\vec{k}) \;=\; i(k^j/k_\perp^2)\rho_a(\vec{k})\,, \tag{3.5.50}$$

so that eq. (3.5.5) becomes

$$\begin{aligned} xG(x, Q^2) &\simeq \frac{1}{\pi} \int \frac{d^2k_\perp}{(2\pi)^2} \frac{\Theta(Q^2 - k_\perp^2)}{k_\perp^2} \left\langle |\, \rho_a(\vec{k})|^2 \right\rangle_\tau \\ &= \frac{(N^2-1)R^2}{4\pi} \int_0^{Q^2} \frac{dk_\perp^2}{k_\perp^2}\, \mu_\tau(k_\perp^2), \end{aligned} \tag{3.5.51}$$

where R is the hadron radius, and we have used eq. (3.5.49).

From eqs. (3.5.37), (3.5.45) and (3.5.47), one obtains

$$\xi_\tau(k_\perp) = \int_0^\infty dy\, \gamma_\tau(\mathrm{y}, k_\perp) = (1/k_\perp^4) \int_0^\infty dy\, \lambda_\tau(\mathrm{y}, k_\perp) = (1/k_\perp^4)\mu_\tau(k_\perp), \quad (3.5.52)$$

which, together with eqs. (3.5.38) and (3.5.48), provides an *evolution equation* for $\mu_\tau(k_\perp^2)$:

$$\frac{\partial \mu_\tau(k_\perp^2)}{\partial \tau} = \frac{\alpha_s N}{\pi} \int_0^{k_\perp^2} \frac{dp_\perp^2}{p_\perp^2}\, \mu_\tau(p_\perp^2)\,. \quad (3.5.53)$$

By also using eq. (3.5.51), this can be recognized as the evolution equation for the gluon distribution function in the double logarithmic approximation (DLA) [16] :

$$\frac{\partial^2}{\partial \tau\, \partial \ln Q^2}\, xG(x, Q^2) = \frac{\alpha_s N}{\pi}\, xG(x, Q^2). \quad (3.5.54)$$

Given the approximations that we have performed, this is indeed the expected limit of the evolution equation [37]. The solution to eq. (3.5.54) is well known [16] : if one holds α_s fixed (independent of Q^2), the solution grows like:

$$xG(x, Q^2) \propto \exp\left\{2\sqrt{\frac{\alpha_s N}{\pi}\, \tau\, \ln(Q^2/Q_0^2)}\right\}, \quad (3.5.55)$$

where Q_0 is some arbitrary scale of reference. For our purposes here, what really matters is that the initial condition $\mu_0(k_\perp^2)$ to eq. (3.5.53) introduces a momentum scale in the problem, while there was no such a scale in the RGE by itself. For instance, in a simple valence-quark model, which should be a reasonable approximation near $x \sim 1$ (or $\tau \sim 0$), one has [12] (with $C_F = (N^2 - 1)/2N$)

$$xG(x, Q^2) \simeq \frac{\alpha_s N\, C_F}{\pi} \ln \frac{Q^2}{\Lambda_{QCD}^2} \quad \text{for} \quad x \sim 1\,, \quad (3.5.56)$$

where Λ_{QCD}^2 enters naturally as an infrared cutoff when taking into account the over all color neutrality of the hadron on scale sizes of order $1/\Lambda_{QCD}$ [30]. Thus, for $\tau \sim 0$,

$$\mu_0(k_\perp^2) \sim 2\alpha_s/R^2, \quad (3.5.57)$$

which for a proton is a relatively small momentum scale to start with, but which at low x is enhanced by the quantum evolution described by eq. (3.5.53).

When τ, and therefore μ_τ, are sufficiently large, the fluctuations of the color field described by eq. (3.5.39) become large as well, and the non-linear effects start to play a role. To study the onset of non-linearity, and verify the approximations performed in eq. (3.5.34), it is useful to consider the 2-point function $\langle V_x^\dagger V_y \rangle_\tau$. This is easily computed by expanding the path-ordered exponentials within the Wilson lines, performing the contractions of the fields α with the help of eq. (3.5.45), and then recognizing

the result as the expansion of an ordinary exponential. (See Refs. [14, 15] for similar calculations.) The final result can be written as:

$$\begin{aligned}\langle V^\dagger(x_\perp)V(0_\perp)\rangle_\tau &= \exp\left\{-g^2N\int_0^\infty dy\Big[\gamma_\tau(\mathrm{y},0_\perp)-\gamma_\tau(\mathrm{y},x_\perp)\Big]\right\}\\ &= \exp\left\{-g^2N[\xi_\tau(0_\perp)-\xi_\tau(x_\perp)]\right\}\,,\end{aligned}\tag{3.5.58}$$

with (cf. eq. (3.5.52))

$$\xi_\tau(0_\perp)-\xi_\tau(x_\perp) = \int\frac{d^2p_\perp}{(2\pi)^2}\frac{\mu_\tau(p_\perp^2)}{p_\perp^4}\left[1-\mathrm{e}^{ip_\perp\cdot x_\perp}\right].\tag{3.5.59}$$

Since $\mu_\tau(p_\perp^2)$ is rather slowly varying as a function of $p_\perp$, the integral in eq. (3.5.59) is dominated by small momenta $p_\perp^2 \ll 1/x_\perp^2$, where we can approximate

$$\int\frac{d^2p_\perp}{(2\pi)^2}\frac{1}{p_\perp^4}\left[1-\mathrm{e}^{ip_\perp\cdot x_\perp}\right] \simeq \int^{1/x_\perp^2}\frac{d^2p_\perp}{(2\pi)^2}\frac{1}{p_\perp^4}\frac{(p_\perp\cdot x_\perp)^2}{2} \simeq \frac{x_\perp^2}{16\pi}\ln\frac{1}{x_\perp^2\Lambda_{QCD}^2}\tag{3.5.60}$$

(This is valid to leading logarithmic accuracy, since the corresponding contribution of the hard momenta, $p_\perp^2 \gg 1/x_\perp^2$, is not enhanced by a large logarithm.) By performing a similar approximation on eq. (3.5.59), one obtains:

$$\langle V^\dagger(x_\perp)V(0_\perp)\rangle_\tau \simeq \exp\left\{-\frac{\alpha_sN}{4}x_\perp^2\int^{1/x_\perp^2}\frac{dp_\perp^2}{p_\perp^2}\mu_\tau(p_\perp^2)\right\}.\tag{3.5.61}$$

By inspection of this equation, it should be clear that, as anticipated, it is the same scale $Q_s^2 \sim 1/x_\perp^2$ which controls both the non-locality and the onset on non-linearity: this is the scale for which the exponent in eq. (3.5.61) is of order 1. This implies the following estimate (actually, an equation) for the saturation scale:

$$Q_s^2(\tau) \simeq \frac{\alpha_sN}{4}\int^{Q_s^2}\frac{dp_\perp^2}{p_\perp^2}\mu_\tau(p_\perp^2)\,.\tag{3.5.62}$$

For $k_\perp \gg Q_s$, the approximations in eq. (3.5.34) are justified, and the Gaussian (3.5.39) is the correct solution to the RGE within the mean field approximation. But this solution cannot be extended at low momenta $k_\perp \lesssim Q_s$. This shows the inconsistency of some previous calculations within the classical MV model, where the Gaussian weight function (3.5.39) has been used at *all* momenta, including in the saturation regime [14, 15].

Eqs. (3.5.51) and (3.5.62) imply that the saturation momentum is proportional to the gluon distribution function at saturation,

$$R^2Q_s^2(\tau) \simeq \frac{\pi\alpha_sN}{N^2-1}xG(x,Q_s^2),\tag{3.5.63}$$

in agreement with other estimates in the literature [5, 9, 24]. If we combine this with eq. (3.5.55), one obtains an estimate for the τ-dependence of Q_s in the DLA which will be useful later (with $\bar{\alpha}_s \equiv \alpha_s N/\pi$) :

$$Q_s^2(\tau) \propto xG(x, Q_s^2) \sim \exp\left\{2\sqrt{\bar{\alpha}_s \tau \ln(Q_s^2/Q_0^2)}\right\}, \quad \text{or} \quad Q_s^2(\tau) \propto \mathrm{e}^{4\bar{\alpha}_s \tau}. \quad (3.5.64)$$

This estimate may be slightly improved by using the BFKL approximation [9] (which is also contained in our general equation (3.5.25)) rather than the DLA. But getting a really precise result for Q_s would require solving the RGE in the non-linear regime at $k_\perp \sim Q_s$.

3.5.6.2 The low momentum regime: Gluon saturation

We now turn to the more interesting regime at small momenta, $k_\perp \ll Q_s(\tau)$, when the hadron is probed over distances large compared to the correlation length $1/Q_s(\tau)$ (but still small as compared to $1/\Lambda_{QCD}$). In addition to being relatively rapidly varying, the electric fields in this regime are also expected to have large amplitudes, of order $1/g$ (see eq. (3.5.77) below). In this regime, operators like $V_z^\dagger V_x$ are rapidly averaging to zero. Thus, in a first approximation, we shall simply ignore all the Wilson lines in the Hamiltonian (3.5.26). We shall verify a posteriori that this is a consistent approximation, by computing the expectation value $\langle V_x^\dagger V_y\rangle_\tau$ with the resulting weight function.

In this "random phase approximation" (RPA), the Hamiltonian reads simply:

$$H_{\text{low}-k_\perp} \approx -\frac{1}{2\pi}\int d^2x_\perp \int d^2y_\perp \, \langle x_\perp|\frac{1}{-\nabla_\perp^2}|y_\perp\rangle \, \frac{\delta^2}{\delta\alpha_\tau^a(x_\perp)\delta\alpha_\tau^a(y_\perp)}, \quad (3.5.65)$$

and does not involve the coupling constant at all. Thus, this is formally like a free theory, although it has been obtained in a strong field regime where $g\alpha \sim 1$. In fact, this is not really a free theory, since the classical fields whose correlators are needed are highly non-linear functionals of $g\alpha$, cf. eq. (3.5.6). However, as we shall shortly see, these classical non-linear effects are not essential for getting saturation.

To determine the weight function $W_\tau[\alpha]$, one has to integrate the RGE (3.5.25) over all rapidities τ' with $0 \le \tau' \le \tau$. Clearly, the RPA leading to the Hamiltonian (3.5.65), which requires $k_\perp \ll Q_s(\tau')$, is not appropriate for all such intermediate τ'. Let $\bar{\tau}(k_\perp)$ be the rapidity at which the saturation momentum becomes equal to the external momentum[5] :

$$Q_s^2(\bar{\tau}(k_\perp)) = k_\perp^2. \quad (3.5.66)$$

Then eq. (3.5.65) applies at $\tau' > \bar{\tau}(k_\perp)$, while for $0 \le \tau' \le \bar{\tau}(k_\perp)$ we are rather in the high-momentum regime. This suggests the following approximation:

$$W_\tau[\alpha] \approx W_{\bar{\tau}}^{\text{high}}[\alpha]\, W_{\bar{\tau}\to\tau}^{\text{low}}[\alpha], \quad (3.5.67)$$

[5] We are grateful to Al Mueller for pointing us the importance of the separation scale $\bar{\tau}(k_\perp)$.

where $W_{\bar\tau}^{\rm high}[\alpha]$ is the weight function in the high-momentum regime, eq. (3.5.39), evaluated at $\bar\tau(k_\perp)$ (this is the initial condition for the evolution described by $H_{{\rm low}-k_\perp}$), and $W_{\bar\tau\to\tau}^{\rm low}[\alpha]$ is obtained by integrating the RGE with Hamiltonian (3.5.65) from $\bar\tau(k_\perp)$ up to τ.

A crude estimate for the separation scale $\bar\tau(k_\perp)$ can be obtained by using the solution in the high-momentum regime. Eq. (3.5.64) implies $Q_s^2(\tau)\propto {\rm e}^{c\bar\alpha_s\tau}$, where $c=4$ in the DLA but will be kept here as a free parameter, to partially account for our ignorance of the true dynamics at $k_\perp\sim Q_s$. This, together with eq. (3.5.66), implies

$$\tau\,-\,\bar\tau(k_\perp)\;=\;\frac{1}{c\bar\alpha_s}\,\ln\frac{Q_s^2(\tau)}{k_\perp^2}\,, \tag{3.5.68}$$

which shows that, when $k_\perp\ll Q_s(\tau)$, we have also $\tau\gg\bar\tau(k_\perp)$. Physically interesting correlation functions like the gluon distribution (3.5.5) involve generally an integral over all rapidities $0\le {\rm y}\le\tau$. In the regime where $\tau\gg\bar\tau(k_\perp)$, the dominant contributions to such correlations come from the interval $\bar\tau(k_\perp)\le {\rm y}\le\tau$, and are therefore determined by the piece $W_{\bar\tau\to\tau}^{\rm low}[\alpha]$ of the weight function (3.5.67). Given the simplicity of the Hamiltonian (3.5.65), this is easily obtained as [37] :

$$W_{\bar\tau\to\tau}^{\rm low}[\alpha]\;=\;\mathcal{N}_\tau\exp\left\{-\frac{1}{2}\int_{\bar\tau(k_\perp)}^{\infty}d{\rm y}\int d^2x_\perp\;\partial^i\hat\alpha_{\rm y}^a(x_\perp)\,\zeta_\tau^{-1}({\rm y})\,\partial^i\hat\alpha_{\rm y}^a(x_\perp)\right\}, \tag{3.5.69}$$

with the following width:

$$\zeta_\tau({\rm y})\;=\;(1/\pi)\theta(\tau-{\rm y}). \tag{3.5.70}$$

This implies (for $\bar\tau(k_\perp)\le {\rm y},\,{\rm y}'\le\tau$)

$$\langle\hat\alpha_{\rm y}^a(x_\perp)\,\hat\alpha_{\rm y'}^b(y_\perp)\rangle_\tau\;=\;(1/\pi)\delta^{ab}\delta({\rm y}-{\rm y}')\,\langle x_\perp|\frac{1}{-\nabla_\perp^2}|y_\perp\rangle, \tag{3.5.71}$$

$$\left\langle\partial^i\hat\alpha_{\rm y}^a(x_\perp)\,\partial^i\hat\alpha_{\rm y'}^b(y_\perp)\right\rangle_\tau\;=\;(1/\pi)\delta^{ab}\delta({\rm y}-{\rm y}')\,\delta^{(2)}(x_\perp-y_\perp), \tag{3.5.72}$$

showing that the probability distribution for the COV-gauge electric field $\tilde{\mathcal{F}}^{+i}=-\partial^i\alpha$ is local and homogeneous both in the transverse space and in space-time rapidity (within the interval $\bar\tau(k_\perp)\le {\rm y}\le\tau$). This is consistent with our assumption that transverse correlations in the system are over a typical scale $1/Q_s$, and thus cannot be resolved when the hadron is probed with a much lower resolution. But this also shows that the transverse δ-function in eq. (3.5.72) must be taken with a grain of salt: this is really delocalized over the correlation length $1/Q_s({\rm y})$.

It is now possible to compute the gluon distribution function in this low momentum regime. Since the fields are strong, we have to use the fully non-linear expression for the classical field in eq. (3.5.6). Eq. (3.5.5) involves the following 2-point function:

$$\langle\mathcal{F}_a^{+i}(k^+,x_\perp)\mathcal{F}_a^{+i}(-k^+,y_\perp)\rangle_\tau\;=\;\int dx^-\int dy^-{\rm e}^{ik^+(x^--y^-)}\langle\mathcal{F}_a^{+i}(x^-,x_\perp)\mathcal{F}_a^{+i}(y^-,y_\perp)\rangle_\tau,$$

which we compute as follows (cf. eq. (3.5.7)):

$$\begin{aligned}\langle \mathcal{F}_a^{+i}(\vec{x})\mathcal{F}_a^{+i}(\vec{y})\rangle_\tau &= \left\langle \left(U^\dagger_{ab}\partial^i\alpha^b\right)_{\vec{x}} \left(U^\dagger_{ac}\partial^i\alpha^c\right)_{\vec{y}} \right\rangle_\tau \\ &= \left\langle \partial^i\alpha^b(\vec{x})\partial^i\alpha^c(\vec{y})\right\rangle_\tau \left\langle U^\dagger_{ab}(\vec{x})U_{ca}(\vec{y})\right\rangle_\tau , \end{aligned} \tag{3.5.73}$$

where, as indicated in the second line, the two COV-gauge electric fields $\partial^i\alpha$ can be contracted only together (mainly because of the path ordering in the Wilson lines, which forbids other contractions [14, 15, 37]). By also using eq. (3.5.72), one obtains:

$$\langle \mathcal{F}_a^{+i}(k^+,x_\perp)\mathcal{F}_a^{+i}(-k^+,y_\perp)\rangle_\tau \approx \frac{N^2-1}{\pi}\int_{\bar\tau(k_\perp)}^{\tau} d\mathrm{y}\,\delta^{(2)}(x_\perp-y_\perp)\left\langle U^\dagger_{\mathrm{y}}(x_\perp)U_{\mathrm{y}}(y_\perp)\right\rangle_\tau . \tag{3.5.74}$$

The transverse δ-function in the r.h.s. of eq. (3.5.74) imposes $x_\perp = y_\perp$, and therefore $\langle U^\dagger_{\mathrm{y}}U_{\mathrm{y}}\rangle \to 1$. More precisely, this δ-function is spread over a distance

$$|x_\perp - y_\perp| \sim 1/Q_s(\mathrm{y}),$$

which is precisely the correlation length for the 2-point function $\langle U^\dagger_{\mathrm{y}}(x_\perp)U_{\mathrm{y}}(y_\perp)\rangle$. Over such a distance, the latter decreases by a factor b, with $b > 1$ but not much larger (typically, $b \sim e$). We thus obtain:

$$\langle \mathcal{F}_a^{+i}(k^+,x_\perp)\mathcal{F}_a^{+i}(-k^+,y_\perp)\rangle_\tau = \frac{N^2-1}{\pi b}\,\delta^{(2)}(x_\perp-y_\perp)\Big(\tau-\bar\tau(k_\perp)\Big). \tag{3.5.75}$$

Up to the global factor $1/b$, this is the same result that would have been obtained in the linearized, or weak field, approximation $\mathcal{F}_a^{+i} \simeq -\partial^i\alpha_a$. All the non-linear effects — which were a priori encoded in the 2-point function of the Wilson lines — have dropped out from the gluon distribution because of the locality of the propagator (3.5.72).

By using eqs. (3.5.5) and (3.5.75), one can compute the number of gluons per unit of transverse phase space in this low-momentum regime. One obtains ($b_\perp$ is the impact parameter) :

$$\begin{aligned}\frac{d^2(xG)}{d^2k_\perp\,d^2b_\perp} &\equiv \int \frac{d^2x_\perp}{4\pi^3}\,\mathrm{e}^{-ik_\perp\cdot x_\perp}\langle \mathcal{F}_a^{+i}(k^+,x_\perp)\mathcal{F}_a^{+i}(-k^+,0_\perp)\rangle_\tau \\ &= \frac{N^2-1}{4\pi^4}\,\frac{1}{b}\Big(\tau-\bar\tau(k_\perp)\Big), \end{aligned} \tag{3.5.76}$$

or, after also using eq. (3.5.68),

$$\frac{d^2(xG)}{d^2k_\perp\,d^2b_\perp} = \frac{N^2-1}{4\pi^4 a}\,\frac{1}{\bar\alpha_s}\,\ln\frac{Q_s^2(\tau)}{k_\perp^2}, \tag{3.5.77}$$

where the two unknown constants b and c have been combined into $a = bc$.

Eq. (3.5.77) is an important result of our approach. It shows *marginal saturation* (when $k_\perp^2$ decreases, the gluon density still increases, but only logarithmically[6]), and is consistent with the *unitarity* bounds: at fixed $k_\perp^2$, the gluon density increases only linearly with τ (this is most obvious on eq. (3.5.76)), and so does also the associated distribution function $xG(x,Q^2)$ for $Q^2 \ll Q_s^2$. The latter is easily obtained from eq. (3.5.77) as (with $\int d^2b_\perp = \pi R^2$) :

$$\begin{aligned} xG(x,Q^2) &= \frac{N^2-1}{4\pi^2 a}\frac{1}{\bar{\alpha}_s} R^2Q^2\left[\ln(Q_s^2(\tau)/Q^2)+1\right] \\ &= \frac{N^2-1}{4\pi a N}\frac{1}{\alpha_s} R^2Q^2\Big[c\bar{\alpha}_s(\tau\,-\,\bar{\tau}(Q))+1\Big]. \end{aligned} \tag{3.5.78}$$

If extrapolated up to $Q \sim Q_s$, this agrees quite well with the corresponding result at high momenta, as given in eq. (3.5.63). Converserly, this shows that the same estimate (3.5.62) for Q_s would have been obtained also by matching our results for the gluon distribution function at high and, respectively, low momenta (i.e., eqs. (3.5.51) and, respectively, (3.5.78)), which is an important self-consistency check.

According to eq. (3.5.77), the gluon density at saturation is of order $1/\alpha_s$, which corresponds to color fields as strong as $\mathcal{F}^{+i} \sim 1/g$. Still, as the above analysis clearly shows, the non-linear effects leading to saturation are not those in the classical field, but rather those in the quantum evolution, which led to the local weight function (3.5.69). In other terms, the saturation is built-in in the effective action at low momenta. In this respect, our conclusions differ from those in Refs. [14, 15], although the final results found there for the gluon density are formally similar to our eq. (3.5.77).

On the other hand, our results are consistent with some recent analyses of the non-linear gluon evolution by Mueller [9] and Levin and Tuchin [24]. In Ref. [24], Levin and Tuchin have obtained approximate solutions to the Balitsky-Kovchegov equation for $\langle V^\dagger(x_\perp)V(y_\perp)\rangle_\tau$ [19–21], and then used these solutions to estimate the gluon distribution function. Their result is consistent with our eq. (3.5.78) provided one takes $c=4$, as predicted by the DLA (cf. eq. (3.5.64)).

As a check of the self-consistency of the RPA, let us compute the 2-point function $\langle V^\dagger(x_\perp)V(0_\perp)\rangle_\tau$ for $x_\perp^2 = 1/k_\perp^2 \gg 1/Q_s^2(\tau)$. This is again given by eq. (3.5.58) where the integral over y is now decomposed into two pieces: $0 < \mathrm{y} < \bar{\tau}(x_\perp)$ and $\bar{\tau}(x_\perp) < \mathrm{y} < \tau$, with $\bar{\tau}(x_\perp) \equiv \bar{\tau}(k_\perp^2 = 1/x_\perp^2)$ (cf. eq. (3.5.66)). The first rapidity interval gives an attenuation factor $b \sim e$, while in the second interval we can use the propagator in eq. (3.5.71), namely:

$$\gamma_\tau(\mathrm{y}, x_\perp - y_\perp) \;=\; (1/\pi)\langle x_\perp|\frac{1}{-\nabla_\perp^2}|y_\perp\rangle\theta(\tau-\mathrm{y})\theta(\mathrm{y}-\bar{\tau}(x_\perp)). \tag{3.5.79}$$

This gives (for $\bar{\tau}(x_\perp) \le \mathrm{y} \le \tau$)

$$\gamma_\tau(\mathrm{y},0_\perp) - \gamma_\tau(\mathrm{y},x_\perp) \;=\; \frac{1}{\pi}\int\frac{d^2p_\perp}{(2\pi)^2}\frac{1}{p_\perp^2}\left[1-\mathrm{e}^{ip_\perp\cdot x_\perp}\right] \;\simeq\; \frac{1}{4\pi^2}\ln\Big(Q_s^2(\mathrm{y})x_\perp^2\Big), \tag{3.5.80}$$

[6]By contrast, at high momenta, eq (3.5.51) shows that $(d^2\,xG/d^2k_\perp d^2b_\perp)$ increases like $1/k_\perp^2$ when $k_\perp$ decreases, a well known perturbative result [12].

where the scale $Q_s(\mathrm{y})$ has been introduced to cut off an ultraviolet divergence. It can be shown, via an analysis of eq. (3.5.31), that this is indeed the natural UV cutoff introduced by the non-linear effects [37]. Since (cf. eq. (3.5.68)):

$$\ln(Q_s^2(\mathrm{y})x_\perp^2) \;=\; c\bar{\alpha}_s(\mathrm{y}-\bar{\tau}(x_\perp)), \tag{3.5.81}$$

we finally obtain:

$$\begin{aligned}\langle V^\dagger(x_\perp)V(0_\perp)\rangle_\tau \;&\simeq\; \frac{1}{b}\exp\Big\{-c\bar{\alpha}_s^2\int_{\bar{\tau}(x_\perp)}^{\tau} d\mathrm{y}(\mathrm{y}-\bar{\tau}(x_\perp))\Big\} \propto \exp\Big\{-\frac{c}{2}\,\bar{\alpha}_s^2(\tau-\bar{\tau}(x_\perp))^2\Big\}\\ &\propto\; \exp\left\{-\frac{1}{2c}\left[\ln(Q_s^2(\tau)x_\perp^2)\right]^2\right\}.\end{aligned} \tag{3.5.82}$$

Once again, this coincides with the corresponding result in [24] provided one takes $c=4$. Eq. (3.5.82) shows that the correlator of the Wilson lines is rapidly decreasing when $Q_s^2(\tau)x_\perp^2 \gg 1$, so that the RPA is indeed justified, at least as a mean field approximation.

Note finally that, in contrast to the weight function at high momenta, eq. (3.5.39), the width of the Gaussian in eq. (3.5.69) does not involve any mass scale. Thus, the weight function at low momenta is *scale invariant* and *universal* (in the sense of being insensitive to the initial conditions, and thus the same for all hadrons). These properties transmit to the correlation functions computed with this weight function, up to logarithmic corrections which enter via the lower rapidity limit $\bar{\tau}(k_\perp)$ (which depends logarithmically on $k_\perp^2$) and via the ultraviolet cutoff $Q_s(\tau)$. Thus, the correlation functions at saturation are functions of $\ln(Q_s^2(\tau)/k_\perp^2)$, as manifest on eqs. (3.5.77) and (3.5.82).

More general solutions to the RGE (3.5.25) are currently under investigation [37].

Acknowledgements

The authors gratefully acknowledge conversations and correspondence with Ian Balitsky, Jean-Paul Blaizot, Mikhail Braun, Yuri Dokshitzer, Elena Ferreiro, Jamal Jalilian-Marian, Al Mueller, Eugene Levin, Yuri Kovchegov, Alex Kovner, Raju Venugopalan, and Heribert Weigert.

References

[1] L.N. Lipatov, Sov. J. Nucl. Phys. **23**, 338 (1976).

[2] E.A. Kuraev, L.N. Lipatov and V.S. Fadin, Sov. Phys. JETP **45**, 199 (1977); I.I. Balitsky and L.N. Lipatov, Sov. J. Nucl. Phys. **28**, 822 (1978).

[3] ZEUS Coll., J. Breitweg et al., Eur. Phys. J. **C 6**, 43 (1999).

[4] L.V. Gribov, E.M. Levin and M.G. Ryskin, Phys. Rept. **100**, 1 (1983).

[5] A.H. Mueller and J. Qiu, Nucl. Phys. **B 268**, 427 (1986).

[6] L. McLerran and R. Venugopalan, Phys. Rev. **D 49**, 2233 (1994);
L. McLerran and R. Venugopalan, Phys. Rev. **D 49**, 3352 (1994).

[7] L. McLerran and R. Venugopalan, Phys. Rev. **D 50**, 2225 (1994).

[8] L. McLerran and R. Venugopalan, Phys. Rev. **D 59**, 094002 (1999).

[9] A.H. Mueller, Nucl. Phys. **B 558**, 285 (1999).

[10] K. Golec-Biernat and M. Wüsthoff, Phys. Rev. **D 59**, 014017 (1999).

[11] K. Golec-Biernat and M. Wüsthoff, Phys. Rev. **D 60**, 114023 (1999).

[12] A.H. Mueller, *Small-x physics, high parton densities and parton saturation in QCD.* Preprint hep-ph/9911289, 1999. Lectures at *Int. Summer School on Particle Production Spanning MeV and TeV Energies*, Nijmegen.

[13] E. Iancu and L. McLerran, *Saturation and universality in QCD at small x.* Preprint SACLAY-T01-026 (hep-ph/0103032), 2001.

[14] J. Jalilian-Marian et al., Phys. Rev. **D 55**, 5414 (1997).

[15] Yu.V. Kovchegov and A.H. Mueller, Nucl. Phys. **B 529**, 451 (1998).

[16] V.N. Gribov and L.N. Lipatov, Sov. J. Nucl. Phys. **15**, 438 (1972);
G. Altarelli and G. Parisi, Nucl. Phys. **B 126**, 298 (1977);
Yu.L. Dokshitzer, Sov. Phys. JETP **46**, 641 (1977).

[17] E. Iancu, A. Leonidov and L. McLerran, *Nonlinear gluon evolution in the color glass condensate. I.* Preprint SACLAY-T00-166 (hep-ph/0011241), 2000;
E. Ferreiro et al., *Nonlinear gluon evolution in the color glass condensate. II.* Preprint in preparation.

[18] E. Iancu, A. Leonidov and L. McLerran, *The renormalization group equation for the color glass condensate.* Preprint SACLAY-T01-021 (hep-ph/0102009), 2001.

[19] I. Balitsky, Nucl. Phys. **B 463**, 99 (1996).

[20] Y.V. Kovchegov, Phys. Rev. **D 60**, 034008 (2000).

[21] Y.V. Kovchegov, Phys. Rev. **D 61**, 074018 (2000).

[22] A.H. Mueller, Nucl. Phys. **B 415**, 373 (1994).

[23] A.H. Mueller, Nucl. Phys. **B 437**, 107 (1995).

[24] E. Levin and K. Tuchin, Nucl. Phys. **B 573**, 833 (2000);
E. Levin and K. Tuchin, *New scaling at high energy DIS.* Preprint TAUP-2659-2000 (hep-ph/0012167), 2000;
E. Levin and K. Tuchin, *Nonlinear evolution and saturation for heavy nuclei in DIS.* Preprint TAUP-2664-2001 (hep-ph/0101275), 2001.

[25] M. Braun, Eur. Phys. J. **C 16**, 337 (2000).

[26] H. Weigert, *Unitarity at small Bjorken x.* Preprint NORDITA-2000/34 HE (hep-ph/0004044), 2000.

[27] A. Kovner, L. McLerran and H. Weigert, Phys. Rev. **D 52**, 6231 (1995).

[28] Y.V. Kovchegov, Phys. Rev. **D 54**, 5463 (1996);
Y.V. Kovchegov, Phys. Rev. **D 54**, 5445 (1997).

[29] A. Krasnitz and R. Venugopalan, Phys. Rev. Lett. **84**, 4309 (2000);
A. Krasnitz and R. Venugopalan, Phys. Rev. Lett. **86**, 1717 (2001).

[30] C.S. Lam and G. Mahlon, Phys. Rev. **D 62**, 114023 (2000).

[31] G. Parisi and N. Sourlas, Phys. Rev. Lett. **43**, 744 (1979).

[32] J. Jalilian-Marian et al., Nucl. Phys. **B 504**, 415 (1997).

[33] J. Jalilian-Marian et al., Phys. Rev. **D 59**, 014014 (1999).

[34] J. Jalilian-Marian, A. Kovner and H. Weigert, Phys. Rev. **D 59**, 014015 (1999).

[35] J. Jalilian-Marian et al., Phys. Rev. **D 59**, 034007 (1999).

[36] A. Kovner, J. G. Milhano and H. Weigert, Phys. Rev. **D 62**, 114005 (2000).

[37] E. Iancu and L. McLerran. Preprint in preparation.

TAUP

3.6 Saturation at low x

E. Levin
HEP Department, School of Physics,
Tel Aviv University
Ramat Aviv, 69978, ISRAEL
email: leving@post.tau.ac.il

Fighting prejudices

3.6.1 Introduction

At low values of x, QCD evolution, both DGLAP [1] and BFKL [2] , predict a striking increase of the parton densities which violate unitarity constraints [3]. Therefore, interactions between partons in the parton cascade, omitted in QCD evolution equations, should become essential to slow down the growth of the parton densities. We expect that these interactions will create an equilibrium -like system of partons with a definite value for the average transverse momentum, which we call a saturation scale ($Q_s(x)$). In other words, we expect a picture of a hadron as shown in Fig. 1 [3–6].

This talk is an attempt to review all our knowledge on saturation at low x both theoretical and experimental, to stimulate a search for saturation effects at THERA. In spite of the fact that the high density QCD phase was only briefly discussed in the THERA Contribution to the TESLA TDR, everybody knows that **if saturation effects are seeen at THERA it will be the machine, while if not, it will remain one of many**. The main goals of this presentation are

- To discuss an intuitive picture of the deep inelastic scattering that leads to the saturation of the parton densities;
- To show that the saturation hypothesis has solid theoretical proof;
- To report on the theoretical progress that has been made over the past two years in high parton density QCD, and on the property of the saturation phase that emerges from the theory that has been developed;
- To collect all that we know theoretically and experimentally about the saturation scale $Q_s(x)$.

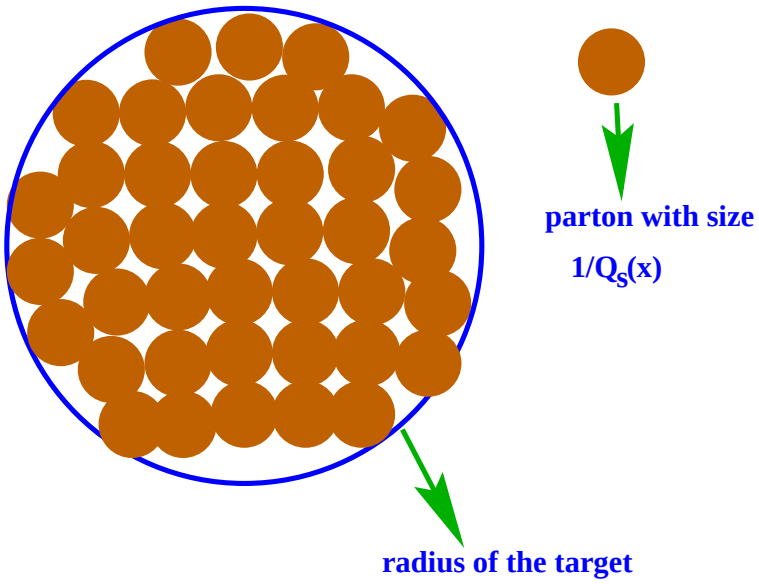

Figure 1: *Picture of a hadron in the saturation region.*

Thera are two different ways to reach a high parton density phase: the first, is DIS at low x, the second is deep inelastic scattering on a nuclear target in which we have a rather large parton density from the beginning, due to a large number of nucleons in a nucleus. The best avenue to investigate the high density phase is to use both paths and to measure DIS on nuclei at low x. This is one of the THERA options and we will also discuss saturation phenomena for such a reaction.

3.6.2 Qualitative Picture of Interaction in DIS at low x

3.6.2.1 Bjorken frame:

It is well known that deep inelastic scattering is most clearly visualized in a space-time picture in the Bjorken frame where the virtual photon has zero energy [7]. Therefore, in the Bjorken frame the electro-magnetic field is a standing wave with wavelength of the order of $1/q_z$ for a photon with four momentum $q_\mu = (0, q_z, 0, 0,)$ (see Fig. 2). In this frame the fast hadron decays into a system of partons. Each parton has a longitudinal momentum $p_{i,z} = x_i P$, where x_i is a fraction of the energy of incoming hadron carried by the parton, and a transverse momentum $p_{i,t}$. Due to the uncertainty principle each parton is localized in $\Delta z_i \approx 1/(x_i P)$ and, therefore, only partons with $x_i P \approx q_z$ can interact with the photon, since for all other partons the overlap integral is very small. In other words, the parton which interacts with the photon has $x_i \approx q_z/P$. Using the energy and momentum conservation for the parton - photon interaction one can easily obtain[1] that $x_i P = q_z/2$ which gives $x_i = q_z/2P = q_z^2/2Pq_z = Q^2/2(P \cdot q) = Q^2/s =$

[1]Energy conservation gives that the energy of the parton i and the recoiled energy are equal $(E_i = E_i')$, the conservation of the longitudinal moment leads to $p_{i,L} = q_z - p'_{i,L}$. $p'_{i,L} = p_{i,L}$ and

x_{Bj} at low x.

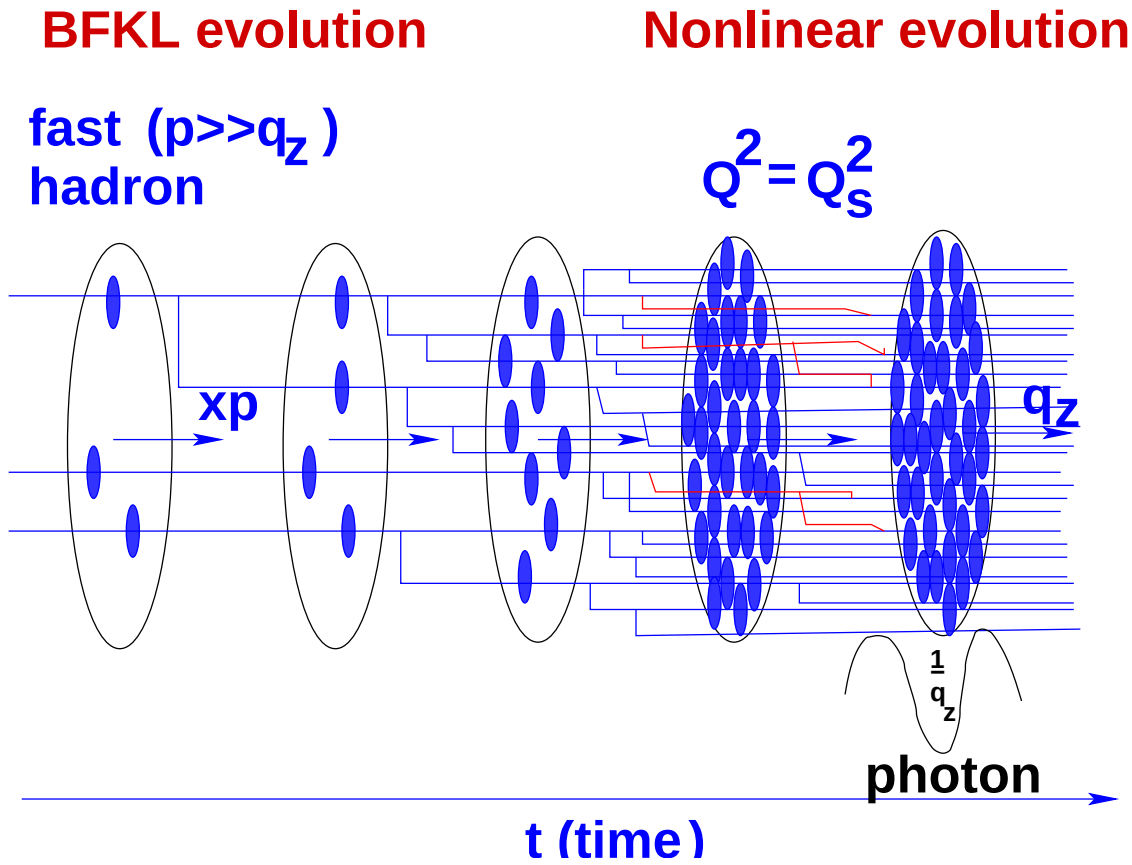

Figure 2: *Parton cascade in the Bjorken frame.*

The lifetime of the i-th parton is of the order of $\tau = \tau_{r.f.}\gamma = \frac{E_i}{p_{i,t}^2} = \frac{x_i P}{p_{i,t}^2}$ where the lifetime in the rest frame of the i-parton $\tau_{r.f.} = \frac{1}{p_{i,t}}$ and $\gamma = \frac{E_i}{p_{i,t}}$. The parton that interacts with the photon lives for a short time $\approx 1/q_z$ and because of this the interaction cannot change the parton distribution, and destroys only the coherence of the partons in the incoming hadron.

Over a long period of time every parton can decay into a large number of partons. Theoretically we can only control the emission of the partons with large values of the transverse momenta, as the QCD coupling is small for them, and we can safely use the developed methods of perturbative QCD. Fig. 2 shows the evolution of the partons with definite transverse momenta ($p_t = Q \gg 1/R$) (with definite size $r_t = 1/Q \ll R$) in time (so called the BFKL evolution). R is the size of the hadron. The first stage of the evolution for partons with $x_i \approx 1$ is not under theoretical control and only non-perturbative QCD will be able to give us information on probability ($P_h^i(x_i, p_{i,t} = Q \ll 1/R$) to find several partons with $p_{i,t} = Q$ and $x_i \approx 1$ in the hadron. The BFKL

$p_{i,L} = q_z/2$.

evolution takes into account the emission of partons with $p_t = Q \gg 1/R$. Fig. 2 shows that it is natural to expect that this emission leads to a considerable increase of the number of partons. The number of partons that can interact with the target (virtual photon) can be written in the form of the convolution $F^{BFKL}(\frac{x}{x_i}, Q^2) \bigotimes P_h^I(x_i, Q)$. We can obtain the result of the DIS experiment by taking the convolution (overlapping integral) with the photon wave function. In other words, the deep inelastic structure function is equal to

$$F_2(x, Q^2) = P_{\gamma^*}(\frac{x_{Bj}}{x}, Q) \bigotimes F^{BFKL}(\frac{x}{x_i}, Q^2) \bigotimes P_h^I(x_i, Q) \ , \tag{3.6.1}$$

where $P_{\gamma^*}(\frac{x_{Bj}}{x}, Q) = |\Psi_{\gamma^*}(\frac{x_{Bj}}{x}, Q)|^2$ and Ψ_{γ^*} is the wave function of the virtual photon.

Recalling that $\sigma(\gamma^*, h) = \frac{4\pi^2}{Q^2} F_2(x_{Bj}, Q^2)$ one can see that the unitarity constraint $\sigma(\gamma^*, h) \leq \pi R^2$ leads to a conclusion that the increase of the parton densities due to the BFKL (or DGLAP) emission should be tamed [3]. The simple idea how such taming can occur is clear from Fig. 2. Indeed, if the parton cascade has been measured at early time (at rather high x) the density of the partons in the transverse plane (see Fig. 2) is not large, and we have to take into account emission, since emission is proportional to the density (ρ) of partons (**emission** $\propto \rho$). However, the density of partons increase due to emission and at some value of x the system becomes so dense that partons cover the hadron disc. In such a situation the interactions of the partons start to be essential. These interactions are proportional to the square of the parton density since two partons have to meet in one point for this interaction (**annihilation** $\propto$ $(\alpha_{\mathbf{S}}/\mathbf{Q^2}) \cdot \ \rho^{\mathbf{2}}$, where α_S/Q^2 is the typical cross section of two parton annihilation in the parton cascade) and they cause the number of particles to diminish. Therefore, we expect there to be an equilibrium between emission and annihilation in the dense system of partons which can be described by simple equation:

$$\frac{d\rho}{d\ln(1/x)} \ = \ \frac{N_c\,\alpha_S}{\pi} \left(K^{BFKL} \bigotimes \rho \ - \ \frac{\gamma\,\alpha_S}{Q^2} \times \rho^2 \right) \ . \tag{3.6.2}$$

The first term of this equation gives the BFKL evolution at low x while the second one provides a taming of the density increase. Of course, all coefficients in the equation cannot be calculated in framework of such oversimplified approach, including numerical coefficient γ.

The principle prediction of this equation is the saturation of the parton density, namely, the fact that the parton density stops increasing. It should be stressed that at any value of Q^2, even a very large value, there exists a small value of x at which we face saturation (see Fig. 3). $\kappa \propto \rho$ in Fig. 3 is a packing factor for the partons and we will discuss its value later.

3.6.2.2 Laboratory frame:

The Bjorken frame is the frame which is best suited for the discussion of DIS in the parton (QCD) approach, since both pictures Fig. 2 and Fig. 3 give the parton distributions in a hadron, or, in other words, term , $F^{BFKL}(\frac{x}{x_i}, Q^2) \bigotimes P_h^I(x_i, Q)$ in Eq. 3.6.1.

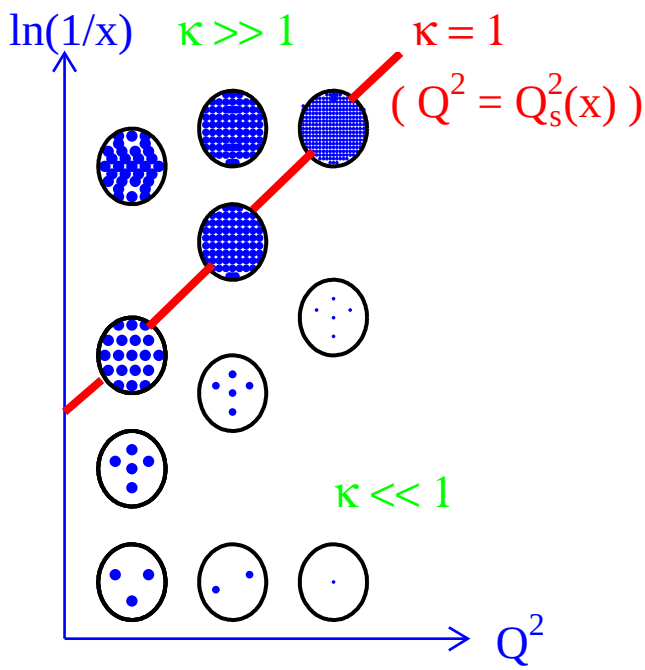

Figure 3: *Parton distribution in transverse plane and saturation in the Bjorken frame.*

However, it turns out that some properties of the high density parton system are clearer in the laboratory frame where the hadron is at rest. As we will see below, the fact that our partons are colour dipoles is easy to demonstrate in this frame. The time-space picture of DIS in this frame is shown in Fig. 4.

In the lab. frame the fast virtual photon decays into a quark-antiquark pair (two partons in Fig. 4). Quark (antiquark) has transverse momentum larger than Q and exists for a sufficiently long time ($\tau \approx 1/mx$)[2]. If the time τ is long enough, quarks (antiquarks) radiate gluons (as shown in Fig. 4) which create a dense parton system in the same way as in the Bjorken frame.

At first sight pictures Fig. 2 and Fig. 4 look quite different. Of course, the final result of the measurement (the total photon-hadron cross section) given by Eq. 3.6.1 , remains the same in both frames, but only part of Eq. 3.6.1 is shown in Fig. 4, namely, $P_{\gamma^*}(\frac{x_{Bj}}{x}, Q) \bigotimes F^{BFKL}(\frac{x}{x_i}, Q^2)$.

Therefore, the main difference between these two figures, Fig. 2 and Fig. 4 is the following: Fig. 2 shows all partons which can interact with the photon target, while the system of partons that has interacted with the virtual photon is depicted in Fig. 4. One can see that the Bjorken frame is much better for describing the parton densities,

[2]The estimates for τ we can easily obtain using the uncertainty principle:$\Delta E\,\tau \approx 1$ where ΔE is the difference in energy between initial and final states. For the virtual photon decay we have $\Delta E = q_0 - p_{1,0} + p_{2,0} \approx q_0 - q_z = mx$, where $p_{i,0}$ is the energy of produced quark (antiquark).

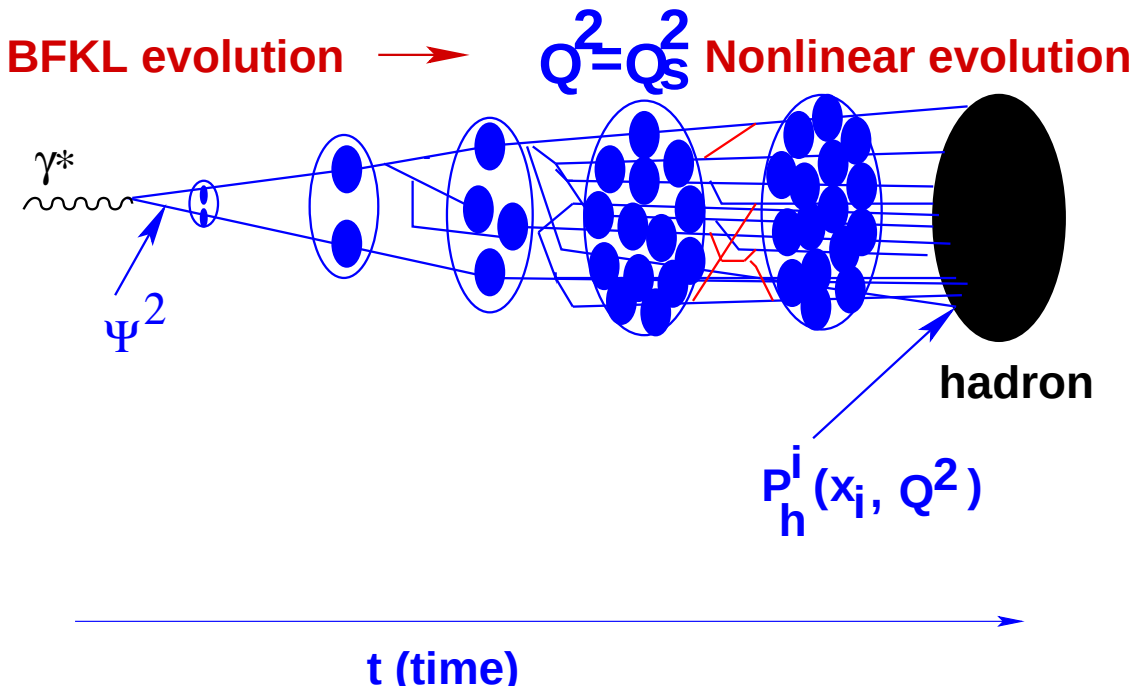

Figure 4: *Parton cascade in the laboratory frame.*

we will show in the next section the laboratory frame is very useful in answering the question: What are these partons in QCD.

3.6.2.3 Colour Dipoles = Partons:

The advantage of the lab. frame becomes clear if we want to understand how the produced quark -antiquark pair(which is a colour dipole) interacts with the target. The main observation is that the size ($r_\perp$ in Fig. 5) of the colour dipole or , in other words, the transverse distance between the quark and antiquark, is a good degree of freedom, which is preserved by the high energy QCD interaction [9–11]. Indeed, while the colour dipole is traversing the target, the distance $r_\perp$ between the quark and antiquark can vary by an amount $\Delta r_\perp \propto R\frac{k_\perp}{E}$, where E denotes the energy of the dipole in the lab. frame and R is the size of the target (see Fig. 5). Due to the uncertainty principle the quark transverse momentum is $k_\perp \propto \frac{1}{r_\perp}$. Therefore,

$$\Delta r_\perp \propto R\frac{k_\perp}{E} \approx R\frac{1}{r_\perp E} \ll r_\perp , \tag{3.6.3}$$

if

$$r_\perp^2\, 2mE \gg 2\, m\, R$$

. Since $r_\perp^2 \approx 1/Q^2$, and recalling the definition of the Bjorken x one can see that

$$\frac{\Delta r_\perp}{r_\perp} \ll 1 \quad \text{at} \quad x \ll \frac{1}{2mR}. \tag{3.6.4}$$

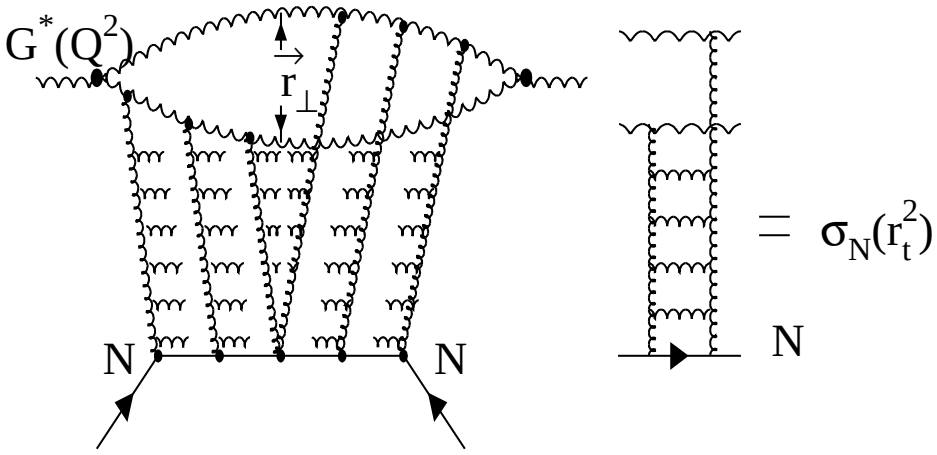

Figure 5: *Interaction of a colour dipole with the target (Glauber-Mueller formula) in the laboratory frame.*

A. Mueller proved two results [11, 12] which really showed that the colour dipoles are the correct degrees of freedom in QCD at high energies. First, he showed that the gluon structure function can be viewed as the interaction of the colour dipole with the target as shown in Fig. 5. Secondly, he proved that the BFKL evolution can be rewritten as a decay of one dipole into two dipoles for large N_c, as one can see in Fig. 6.

Therefore, we can discuss the high energy (low x) DIS in terms of colour dipoles which interact with themselves and with the target.

3.6.2.4 Glauber-Mueller formula:

It turns out that for an interaction with the target we can obtain the simple Glauber-Mueller formula which reads [9–11, 13][3]

[3]Giving credit to the authors of Refs. [9, 10, 13] we refer to this formula as the Glauber-Mueller formula because A. Mueller was the first who proved that the gluon structure function can be described as rescatterings of a dipole. This result changed the whole approach to DIS by creating a transparent picture of the interaction in QCD at high energies.

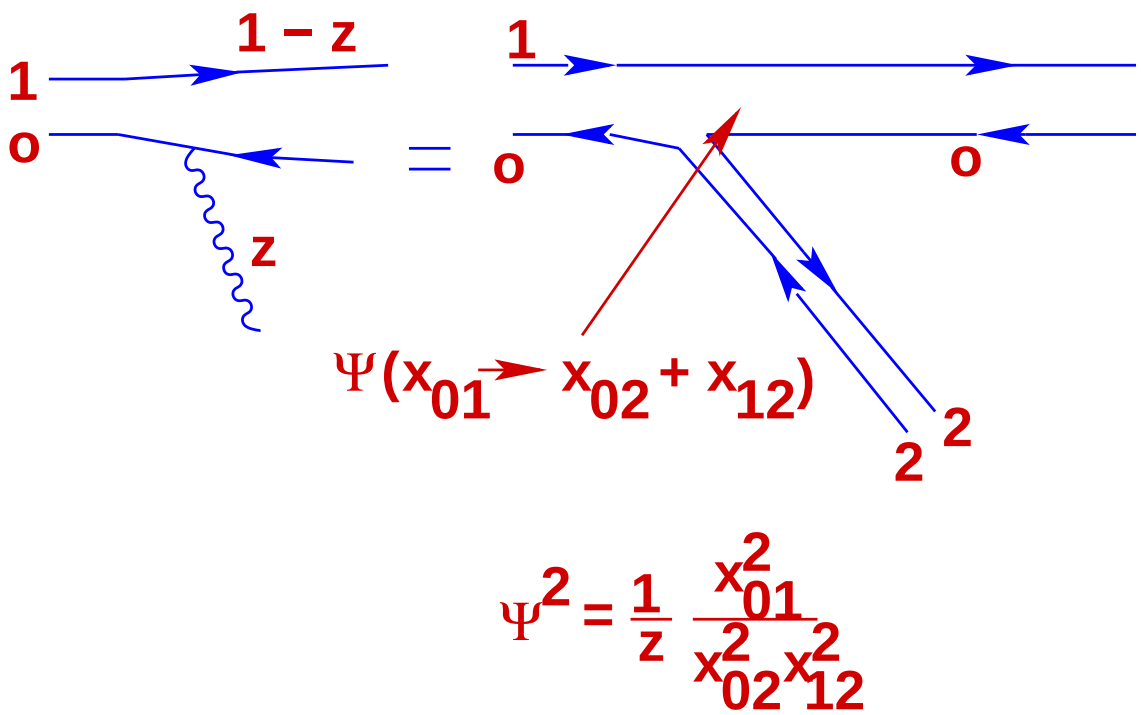

Figure 6: *BFKL gluon emission as a colour dipole decay.*

$$\sigma_{dipole}(x, r_\perp) = 2 \int d^2 b_t \left(1 \; - \; e^{-\frac{\Omega(x, r_\perp; b_t)}{2}} \right) \tag{3.6.5}$$

with opacity

$$\Omega \; = \; \frac{\alpha_S(\frac{4}{r_\perp^2})}{3} \, \pi^2 \, r_\perp^2 \, \left(x \, G^{DGLAP}(\frac{4}{r_\perp^2}, x) \right) \, S(b_t) \; , \tag{3.6.6}$$

where $S(b_t)$ is the target profile function. In the case of a nucleon target we can use the Gaussian form of $S(b_t) = (1/\pi R^2) \, exp{-}b_t^2/R^2$ while for nuclei we use the Wood-Saxon parameterization for $S_A(b_t)$.

Eq. 3.6.5 is a solution to the s-channel unitarity constraint for the dipole-target amplitude

$$2 \, Im \, a_{dipole}(x, r_\perp; b_t) \; = \; |a_{dipole}(x, r_\perp; b_t)|^2 \; + \; G_{in}(x, r_\perp; b_t) \tag{3.6.7}$$

The inelastic cross section is equal to

$$\sigma_{dipole}^{in} \; = \; \int d^2 \, b_t \, \left(1 \; - \; e^{-\Omega(x, r_\perp; b_t)} \right) \; . \tag{3.6.8}$$

Opacity Ω describes the interaction of one parton shower with the target as one can see in Fig. 5.

As has been mentioned the real breakthrough was the proof by A. Mueller that the gluon structure function can be calculated using a similar formula for the colour dipole rescatterings, namely [11]

$$x\,G(x,Q^2) \;=\; \frac{8}{\pi^3}\int_x^1 \frac{dr_\perp^2}{r_\perp^4}\int d^2b_t\,\left(1\;-\;e^{-\frac{(9/4)\Omega(x,r_\perp;b_t)}{2}}\right)\;. \tag{3.6.9}$$

3.6.2.5 Packing factor:

Eqs. 3.6.5, 3.6.8 and 3.6.9 allow us to introduce a packing factor for colour dipoles in the parton cascade. This factor is equal to

$$\kappa \;=\; (9/4)\,\Omega(x,r_\perp;b_t=0) \;=\; \frac{3\alpha_S(\frac{4}{r_\perp^2})}{4}\,\frac{\pi^2 r_\perp^2}{\pi R^2}\left(x\,G^{DGLAP}(\frac{4}{r_\perp^2},x)\right)\;. \tag{3.6.10}$$

The physical meaning of κ is very simple: $\kappa = \sigma_{dipole}/\pi R^2 = \sigma_{dipole}(BA)xG(x,Q^2)/\pi R^2 = \sigma_{dipole}(BA)\cdot\rho$. Therefore, κ is the size of the parton (or preferable to say its typical cross section) multiplied by the density of gluons in the transverse plane.

3.6.2.6 Observables:

It should be stressed that all our observables can be calculated if we know the dipole amplitude. Indeed, the main obsevables such as the total photon-hadron cross section , the gluon density and single diffraction production inclusive cross section, have a very simple relation with the dipole amplitude, namely,

$$\sigma(\gamma^* p) \;=\; \int_0^1 dz\int d^2r_\perp|\Psi(z,r_\perp;Q^2)|^2\;\sigma_{dipole}(x_B,r_\perp^2)\;; \tag{3.6.11}$$

$$xG(x,Q^2) \;=\; \frac{4}{\pi^3}\int_x^1\frac{dx'}{x'}\int_{4/Q^2}^\infty\frac{dr_\perp^2}{r_\perp^4}\,\sigma_{dipole}(x',2\,r_\perp^2)\;; \tag{3.6.12}$$

$$\sigma^{SD}(\gamma^* p) \;=\; \int_0^1 dz\int d^2r_\perp|\Psi(z,r_\perp;Q^2)|^2\int d^2b_t|a_{dipole}(x,r_\perp;b_t)|^2\,. \tag{3.6.13}$$

Eq. 3.6.11 was proven in Refs. [9–11, 13], while Eq. 3.6.12 was first written in Ref. [11] and was discussed in detail in Ref. [13]. The formula for the total diffractive production in DIS was suggested in Ref. [15].

The argument $2r_\perp^2$ in Eq. 3.6.12 reflects the fact that actually the rescattering of gluon corresponds to rescatterings of two dipoles of the same size, which works effectively as the interaction of one dipole but with a size which is $\sqrt{2}$ larger (for $N_c \gg 1$). Ψ was calculated in Refs. [11, 14].

3.6.3 Non-linear Evolution

3.6.3.1 The equation:

Using the colour dipole picture of an interaction and, in particular, the fact that the BFKL emission can be viewed as a decay of one colour dipole into two (see Fig. 6) we

can easily obtain the nonlinear equation for the imaginary part of the elastic dipole-target amplitude $N(x, r_\perp; b_t) = Im\, a^{el}_{dipole}(x, r_\perp; b_t)$. This equation can be written in the form (see also Fig. 7:

$$\frac{dN(\mathbf{x_{01}}, b_t, y)}{dy} = -\frac{2\, C_F\, \alpha_S}{\pi} \ln\left(\frac{\mathbf{x_{01}^2}}{\rho^2}\right) N(\mathbf{x}, b_t, y) + \frac{C_F\, \alpha_S}{\pi} \int_\rho d^2\mathbf{x_2} \frac{\mathbf{x_{01}^2}}{\mathbf{x_{02}^2}\, \mathbf{x_{12}^2}} \cdot \left(2\, N(\mathbf{x_{02}}, b_t, y) - N(\mathbf{x_{02}}, b_t, y)\, N(\mathbf{x_{12}}, b_t, y) \right) , \quad (3.6.14)$$

where $y = \ln(1/x)$ and we assume that that $b_t \leq x_{02}$ or/and x_{12}.

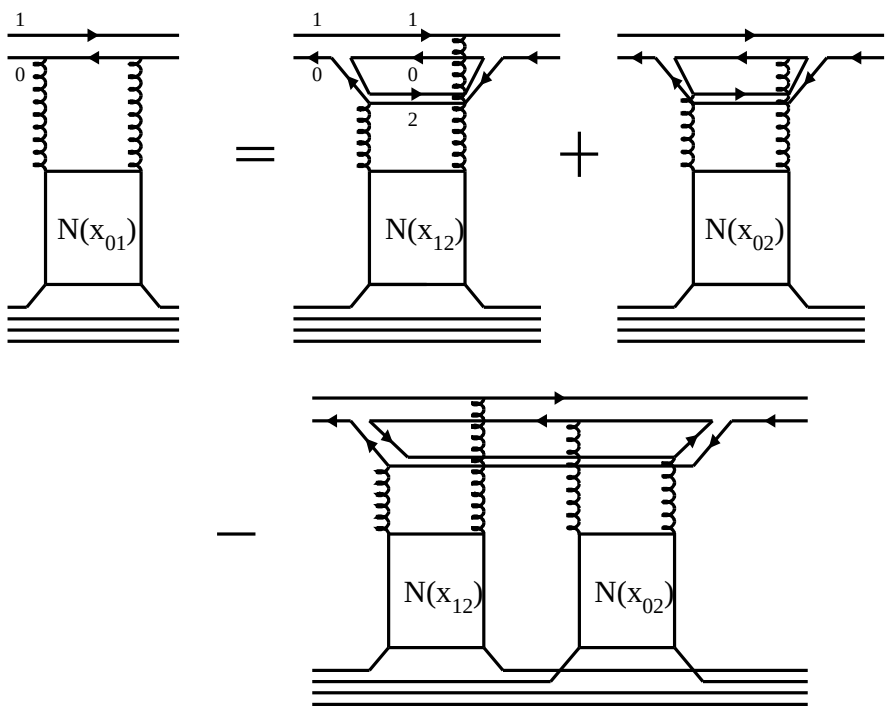

Figure 7: *The pictorial form of non-linear evolution equation.*

Eq. 3.6.14 has a very simple meaning and actually describes the fact that the dipole of the size x_{01} decays into two dipoles of sizes x_{02} and x_{12} with probability $\Psi|^2 = \frac{x_{01}^2}{x_{02}^2\, x_{12}^2}$ as it is shown in Fig. 6. These two dipoles then interact with the target. They can interact separately and this interaction leads to the linear term in Eq. 3.6.14. However, two produced dipoles can interact with the target simultaneously generating the non-linear term in the equation. From Fig. 7 one can see that this non-linear term takes into account the Glauber correction for the two dipole interaction.The minus

sign in front of the non-linear term reflects the well known fact that we overestimate the value of cross section considering it as a sum of two independent collision, since sometimes one dipole happens to be in the shadow of the second one. The linear term in Eq. 3.6.14 is the BFKL evolution, which describes the evolution of the multiplicity of the fixed size colour dipoles with respect to rapidity y. At first sight the linear term sums the leading twist contribution while the non-linear one is related to higher twist contributions. However, this is not true. The first term (the BFKL equation) has also higher twist contributions but with the same anomalous dimension as the leading twist ones. On the other hand, as was pointed out by Mueller and Qiu [4] the non-linear part contributes mostly to the leading twist. The beauty of the equation is that it sums both leading and higher twist contributions in a unique fashion and claims that at any fixed Q^2 (at any short distance), the higher twist contribution will dominate at sufficiently low x.

3.6.3.2 Brief review of the theoretical approaches:

Eq. 3.6.14 shows that the problem of high density QCD has been solved from first principles and we think that it is instructive to give a brief review of the theoretical approaches that all converge to this equation.

1981 - 1983 GLR pointed out the new phase of QCD-high density QCD, developed picture of parton interaction in the Bjorken frame (see above), proposed the hypothesis of parton saturation and suggested first non-linear equation which sums the "fan" diagrams of Fig. 8-a and which is actually Eq. 3.6.14 in momentum space [3].

1986 Mueller and Qiu [4] proved the GLR equation in the double log approximation of perturbative QCD.

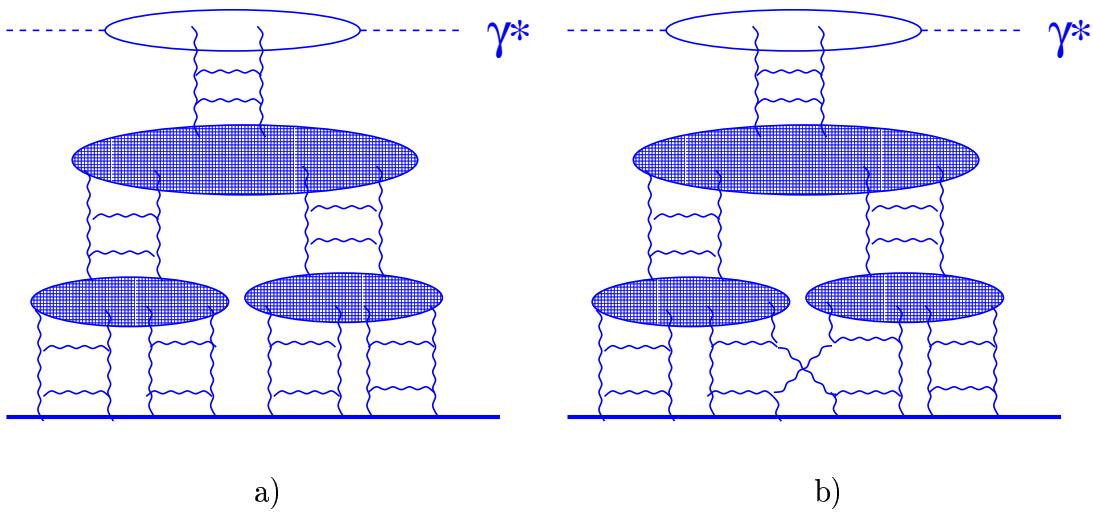

Figure 8: *"Fan" diagrams (a) and $1/N_c$ corrections to them (b).*

1992 - 1995 J.Bartels [16] showed that the non-linear equation can be correct only in large N_c approximation since $1/N_c$ corrections (see Fig. 8-b) lead to the inter-

action of two ladders in the "fan" diagrams (see also Ref. [17]. Laenen and Levin based on Ref. [18] generalized the non-linear equation, taking into account $1/N_c$ corrections in double log approximation [19]. It turns out that $1/N_c$-approximation works quite well in this problem and can be treated using the generating function formalism.

1994 L. McLerran and R. Venugopalan [5] noticed that at high density the gluonic fields are strong ($G_{\mu\nu} \approx 1/g$ where $\alpha_s = g^2/4\pi$) and, therefore, one can approach the high density QCD using the semiclassical gluon fields. Based on the space-time structure of the parton cascade at low x, they built the effective Lagrangian for high density QCD.

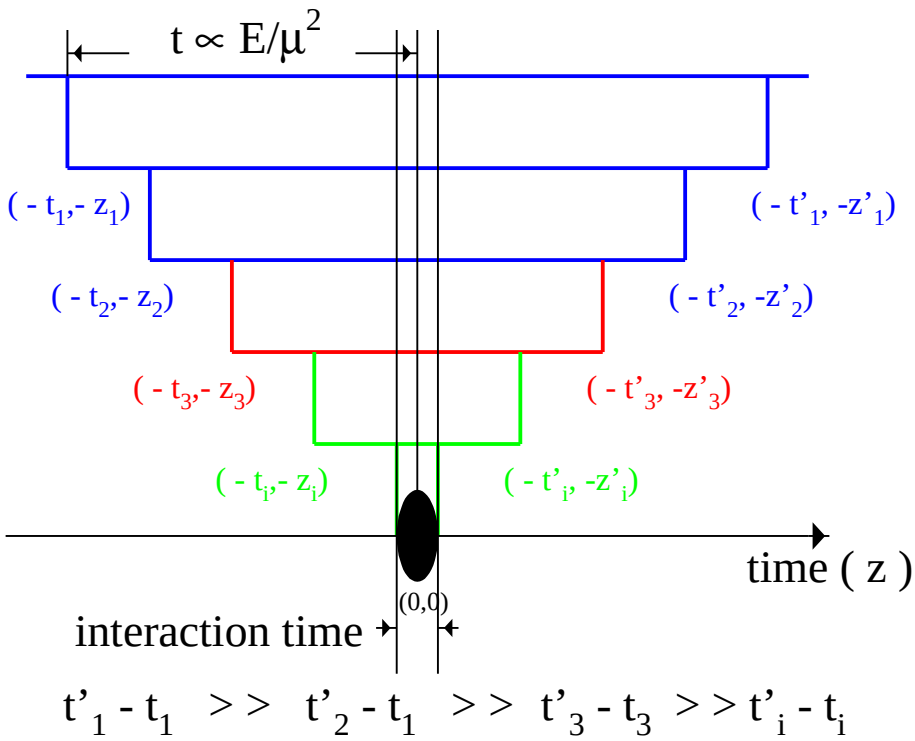

Figure 9: *The space-time structure of the parton cascade at low x.*

Indeed, the main and very important feature of the parton cascade, shown in Fig. 9, is the fact that a parton with higher energy in the cascade lives much longer than a parton with lower energy. We follow the parton emitted at time t'_2. This parton lives a much shorter time than all partons emitted before. Therefore, all these partons will have enough time to form a current which depends on their density. Since the density is large we expect that the current is a classical current. Finally, the Lagrangian of the interaction for the parton emitted at time t'_2 can be written as

$$L(\rho) \; + \; j_\mu \cdot A_\mu \; + \; L(A) \; ,$$

where A is the field of a parton emitted at t'_2. However, we can consider a parton

emitted at $t = t'_3$ and include the previous one in the system with density ρ. The form of the Lagrangian should be the same. This is a strong condition (equation) on the form of the effective Lagrangian, so called Wilson renormalization group approach. This is the beautiful idea of the McLerran and Venugopalan which leads to Eq. 3.6.14, as we will show below.

1996 I. Balitsky [20] proved the non-linear equation in Wilson Loop Operator Expansion at high energies developed by him. Unfortunately, his paper was not noticed by the experts in the field including me. It should be stressed that he also gave an operator proof of the BFKL equation.

1997 Ayla, Ducati and Levin suggested non-linear equation [13] which differs from that of Eq. 3.6.14. They used the double log approximation but summed two DLA contributions $((\alpha_s \ln(1/x) \ln(Q^2/\Lambda^2))^n$ and $(\alpha_s \ln(1/x) \ln(Q_s^2(x)/Q^2))^n$. It turns out that their equation is just the same equation as Eq. 3.6.14 but written for the opacity Ω instead of $N = (1 - exp(-\frac{\Omega}{2}))$. AGL determined all numerical coefficients and discussed the initial condition of Eq. 3.6.14 which we will consider later.

1999 -2000 Yu. Kovchegov [21] proved Eq. 3.6.14 in the colour dipole approach [12]. It should be stressed that he not only gave the derivation which we have discussed, but he found a correct observable which enters the equation (N) and he suggested an initial condition that we will discuss below.

2000 M. Braun [22] calculated the "fan" diagrams of Fig. 8-a in the BFKL kinematic region, using the triple ladder vertex of Refs. [23].

2001 E. Iancu, A. Leonidov and L. McLerran [24] (see also Ref. [25]) proved Eq. 3.6.14 in the effective Lagrangian approach. Their proof is based on long and successive development of the effective Lagrangian approach exploited in Refs. [26]

3.6.4 Initial conditions:

One can see that Eq. 3.6.14 does not depend on the target and the dependence on the target comes from the initial conditions at some initial value of $x = x_0$. For a target nucleus it was argued [13, 21] that the initial conditions should be taken in the Glauber - Mueller form (see Eq. 3.6.5), namely,

$$N(x_{01}, x = x_0, b_t) \;=\; N^{GM}(x_{01}, x = x_0, b_t) = 1 \;-\; e^{-\frac{\Omega(x_{01}, x = x_0, b_t)}{2}} \;. \qquad (3.6.15)$$

The value of x_0 is chosen in the interval

$$e^{-\frac{1}{\alpha_S}} \;\leq\; x_0 \;\leq\; \frac{1}{2\,m\,R}\;,$$

where R is the radius of the target. In this region the value of x_0 is small enough to use the low x approximation, but the production of the gluons (color dipoles) is still suppressed as $\alpha_S \ln(1/x) \;\leq\; 1$. Therefore, in this region we have the instantaneous exchange of the classical gluon fields. Hence, an incoming color dipole interacts separately with each nucleon in a nucleus (see Ref. [27]).

For the hadron we have no proof that Glauber-Mueller formula is correct. As far as we understand the only criteria in this problem (at the moment) is the correct

description of the experimental data. We described [28] almost all available HERA data using Eq. 3.6.5, and we feel confident using Eq. 3.6.5 as the initial condition for Eq. 3.6.14. It should be stressed that the experimental data on $dF_2/d\ln Q^2$ provides direct information on the integral over b_t for N since [29]

$$\frac{d\,F_2(x,Q^2)}{d\ln Q^2} \;=\; \frac{Q^2}{3\pi^3}\int d^2\,b_t\,N(x,4/Q^2,b_t) \;+\; O(1/lnQ^2)\;. \tag{3.6.16}$$

Choosing $x_0 = 10^{-2}$ we can make the initial condition practically independent of the parameterization of the xG^{DGLAP} since all available parametrizations give the same prediction, even for the gluon density in this x - range.

3.6.5 Saturation scale $\mathbf{Q_s(x)}$

3.6.5.1 Simple estimates:

The simplest estimates for the saturation scale come from the equation that the packing factor κ is of the order of 1 [11, 13, 28]. Fig. 10 shows the solution of the equation

$$\kappa(x,Q_s^2(x)) \;=\; 1 \tag{3.6.17}$$

As one can see Q_s can be rather large even in HERA region. However, this estimate depends crucially on the value of xG^{DGLAP}.

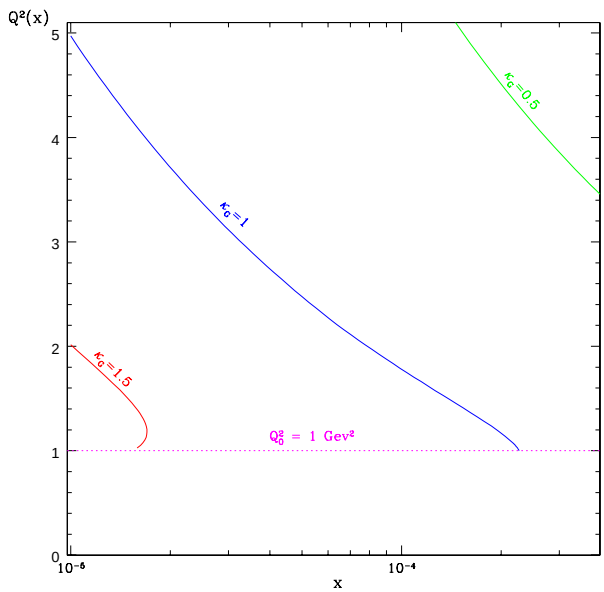

Figure 10: *The simplest estimate for the saturation scale $Q_s(x)$ from equation $\kappa(x,Q_s^2(x)) = 1,\ 1.5\ 0.5$.*

3.6.5.2 Analytic solution of the non-linear equation:

Eq. 3.6.14 has been solved analytically with the simplified version of the BFKL kernel [25, 30, 31], namely, in Mellin transform $\chi(f)$ was taken as $\frac{1}{f}+\frac{1}{1-f}$ instead of $\chi(f) =$

$2\psi(1) - \psi(f) - \psi(1-f)$, where ψ is the derivative of the log of Euler gamma function. In terms of s-channel resummation Eq. 3.6.14 with this kernel sums two kinds of double logs: $(\alpha_S \ln(1/x)\ \ln(Q^2/\Lambda^2))^n$ for $Q^2 > Q_s^2(x)$ and $(\alpha_S \ln(1/x)\ \ln(Q_s^2(x)/Q^2))^n$ for $Q^2 < Q_s^2(x)$. For large Q^2 Eq. 3.6.14 can be reduced to the linear equation and can be solved using the trajectory (characteristics) method [3, 32]. The structure of the trajectories both for linear and nonlinear equation is shown in Fig. 11.

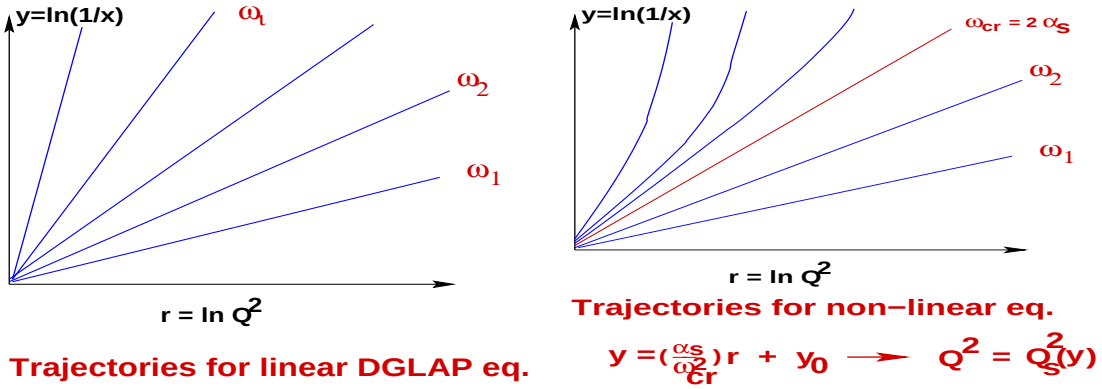

a) b)

Figure 11: *Trajectories for linear (a) and non-linear (b) equations.*

The idea is to interpret the last linear trajectory (line with $\omega_{cr} = 2\,\alpha_S$ in Fig. 11-b) of the linear equation which can be treated without nonlinear corrections, as the saturation scale. Doing so, we obtain [25, 30] the following expression for the saturation scale

$$Q_s^2(x) \;=\; Q_s^2(x = x_0) \cdot \left(\frac{x_0}{x}\right)^{\frac{4N_c\alpha_S}{\pi}} \tag{3.6.18}$$

where $Q_s^2(x = x_0))$ is a saturation scale in our initial condition.

Therefore, we expect power-like rise of the saturation scale at low x.

3.6.5.3 Phenomenological saturation scale:

Golec-Biernat and Wüsthoff [33] suggested one could extract the value of $Q_s(x)$ from HERA data assuming that the saturation region has been reached at HERA. Surprizingly they managed to describe almost all HERA data using a simple parameterization for the saturation scale, namely,

$$Q_s^2(x) \;=\; (1\ GeV^2) \cdot \left(\frac{x_0}{x}\right)^{\lambda} \tag{3.6.19}$$

with $\lambda = 0.288$ and $x_0 = 3.04 \times 10^{-4}$.

3.6.5.4 Saturation scale from numerical solution of the non-linear equation:

In Ref. [34] an attempt was made to solve the non-linear equation numerically (see also Ref. [22]), starting from initial $x = x_0 = 10^{-2}$. Defining the saturation scale as a value of $r_\perp^2 = 4/Q_s^2(x)$ at which the imaginary part of the elastic amplitude for the dipole-target scattering is equal to 1/2

$$N(r_\perp = 2/Q_s, x) = \frac{1}{2}$$

the saturation scale shown in Fig. 12 was calculated.

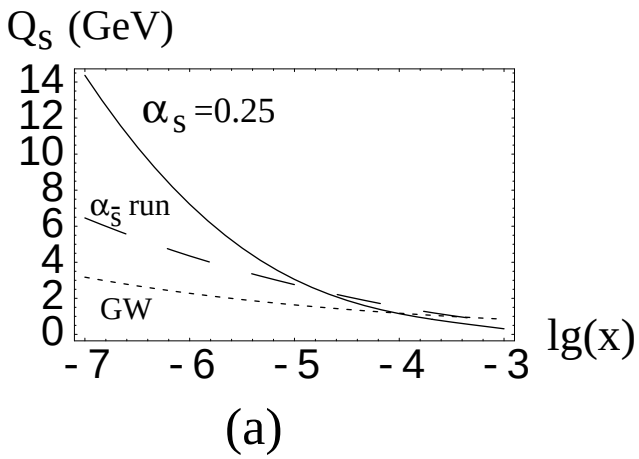

Figure 12: *The saturation scale $Q_s(x)$ plotted as a function of $lgx = log_{10}(x)$. GW denotes the saturation scale from Eq. 3.6.19*

One can see that the saturation scale reaches a sufficiently large value of the order of $Q_s(x) \approx 14\,GeV$ at $x = 10^{-7}$. It should be stressed that even at $x = 10^{-5}$ which is in the typical range for THERA, the saturation scale is approximately $2 \div 3$ times larger than the Golec-Biernat and Wüsthoff estimates.

3.6.5.5 Saturation scale from DIS with nuclei:

The first estimates for the saturation scale in DIS on nuclei, presented in Fig. 13, shows that the nucleus target gives a promising avenue to increase the parton density without requiring a region of extremely low x. Comparing Fig. 13 with Fig. 12 we see that $Q_s(x)$ at $x = 10^{-3}$ for gold is almost twice larger than for a nucleon.

3.6.6 A new scaling in the saturation region.

The simple picture of the hadron in the saturation region shown in Fig. 1, leads to a new scaling phenomens in this saturation region. We expect that the parton densities as well as cross sections are not functions of two variables:x and Q^2, but they depend only on ratio $Q^2/Q_s^2(x)$ [3, 5, 15, 30, 35]. Stasto, Golec-Biernat and Kwiecinski [36] found that this scaling is valid for HERA data at $x < 0.01$. Fig. 14 summarizes the situation and, here, I would like to comment on the theoretical arguments for such a new scaling scheme.

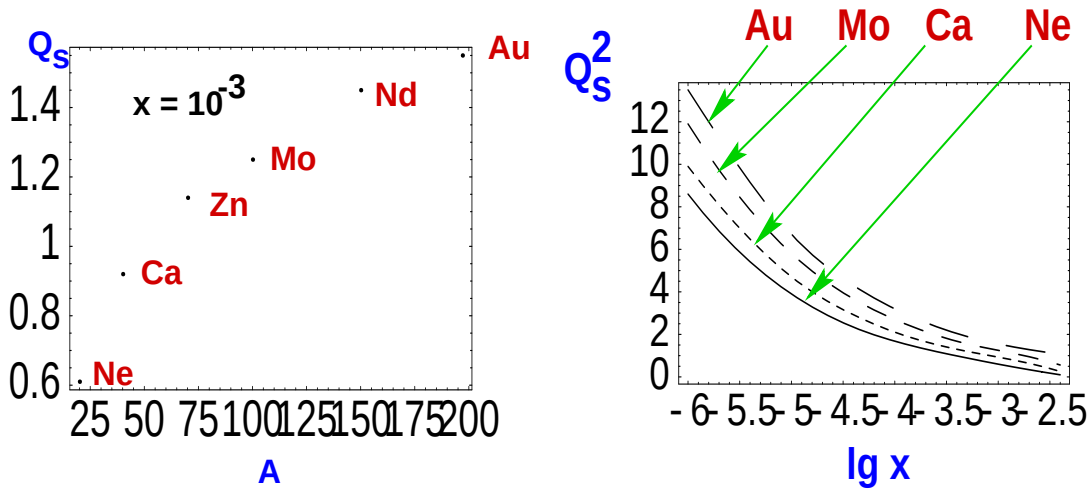

a) b)

Figure 13: *Saturation scale for DIS with nuclei: A (a) and x (b) dependencies .*

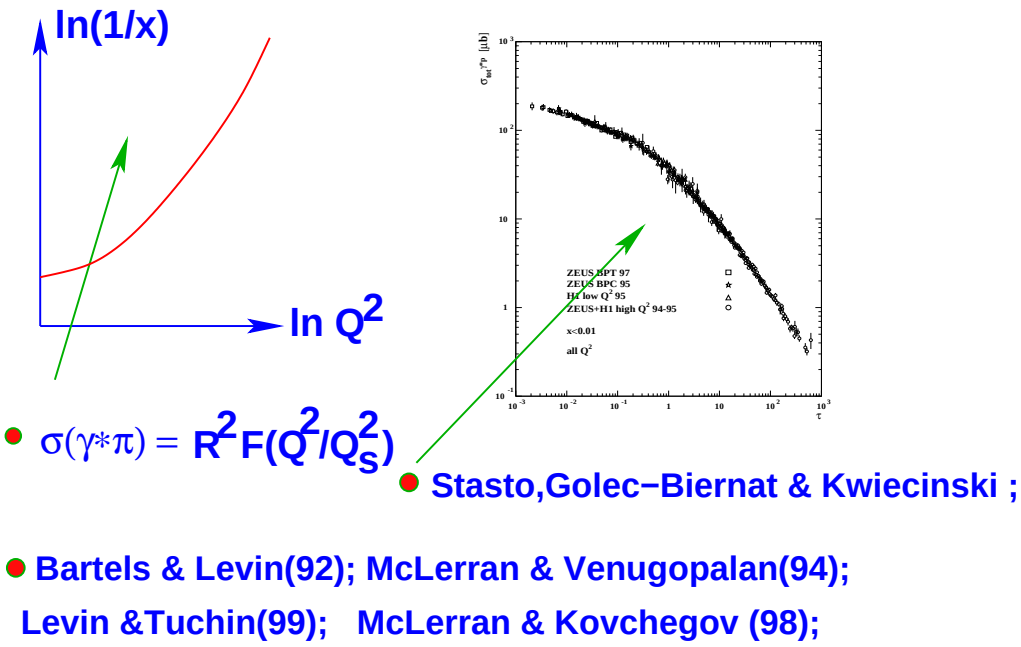

Figure 14:

3.6.6.1 Simple arguments for a new scaling:

Let us rewrite Eq. 3.6.14 in momentum space where it looks simpler

$$\frac{dN(Q,y,b_t)}{dy} = \bar{\alpha}_S \left(\int K(Q,Q')N(Q',y;b_t) - N^2(Q,y;b_t) \right) \quad . \tag{3.6.20}$$

For moments $N(\omega, Q) = N(\omega, Q_0)\, e^{\gamma(\omega)\ln Q^2}$ Eq. 3.6.20 can be reduced to the form

$$\omega e^{\gamma(\omega) lnQ^2} = \chi(\gamma) e^{\gamma(\omega) lnQ^2} - N(\omega, Q_0) \int d\omega' e^{(\gamma(\omega') + \gamma(\omega - \omega') lnQ^2} \tag{3.6.21}$$

The integral over ω' in Eq. 3.6.21 can be evaluated by saddle point method

$$\int d\omega' e^{(\gamma(\omega') + \gamma(\omega - \omega') lnQ^2} \quad \Longrightarrow \quad e^{2\gamma(\omega/2) lnQ^2}$$

Therefore, we can see two different regions in the solution to Eq. 3.6.20: large Q^2, where the non-linear term is small and can be neglected, and low Q^2 where linear and nonlinear terms should be of the same order. It gives [35]

$$\gamma(\omega) = 2\gamma(\omega/2) \qquad \rightarrow \quad \gamma(\omega) = C\omega \tag{3.6.22}$$

Using Eq. 3.6.22 we obtain for $N(y, Q^2)$

$$N(y, Q^2) = \int d\omega\, e^{-\omega y + \gamma(\omega)\ln Q^2} = \int d\omega e^{\omega(-y + C\ln Q^2)}\ , \tag{3.6.23}$$

which means that $N(y, Q^2)$ depends only on one variable [35]

$$-y + C\ln Q^2 = \ln(Q_s^2(x)/Q^2) = \xi\ . \tag{3.6.24}$$

It turns out that $C = \frac{\pi}{4N_c\alpha_S}$ in double log approximation [25, 35].

3.6.6.2 Scaling solution:

Eq. 3.6.24 gives the equation for the critical line $Q^2 = Q_s^2(x)$ in Fig. 3.A more refined approach to the solution of the master non-linear equation, allows us to understand how far we have to move from the critical line to see this new scaling. It turns out that the scaling is not applicable [30] only in a narrow (at low x) band along the critical line with the width $\ln(Q_s^2(x)/Q^2) \approx 1/4\alpha_S\ \ln(1/x) \ll 1$ for $\alpha_S\ \ln(1/x) \gg 1$.

It should be stressed that two quite different approaches: one is the analytic solution of the master equation [30] and the second is the solution of Wilson renormalization group equation for generating function [25], lead to the same answer and the same picture for the new scaling. The scaling solution is given in Fig. 15. the difference between $N(z, b_t = 0)$ and σ is due to the integration over impact parameter b_t.

3.6.6.3 Scaling violation:

The question which we wish to address is how large is the scaling violation for $Q^2 > Q_s^2(x)$. In Ref. [30] one can find first estimates of this scaling violation (see Fig. 16

One can see that at all reasonable values of $y = \ln(1/x)$ and $\xi = \ln(Q_s^2(x)/Q^2)$ the violation is less than 30%. It means that if we want to have a tool to measure $Q_s^2(x)$ as a value of Q^2 at which we see a scaling violation, we have to establish a scale to an accuracy of less than 10%. We think that it is instructive to examine Fig. 17 from this point of view. One can see from this figure that the accuracy of new scaling phenomena in HERA data is low, and we cannot use these data to measure the value of the saturation scale.

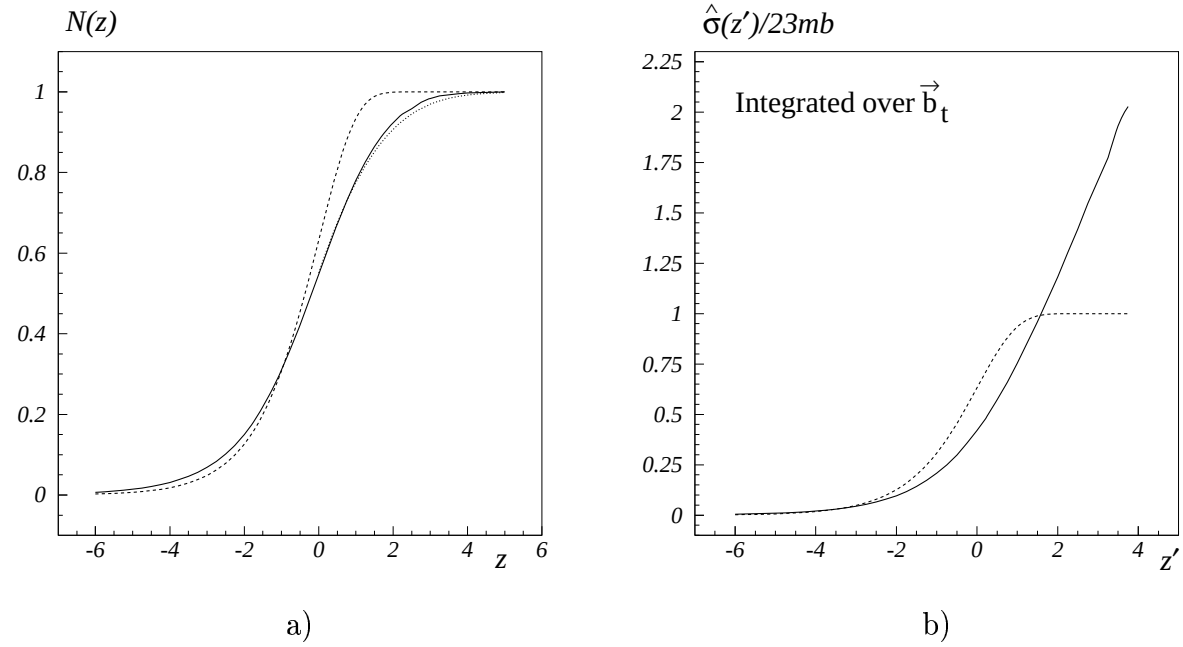

Figure 15: *(a) Dipole – target scattering amplitude $N(z)$ at $b_t = 0$ and (b) dipole – target cross section $\hat{\sigma}(z')$ in the scaling approximation versus scaling variable (a) $z = \ln(r_\perp^2\, Q_s^2(x))$ and (b) $z' = \ln(Q_s^2(x)/Q^2)$: Solid line is the scaling solution of the master equation, dashed line is a Golec-Biernat – Wüsthoff model as explained in text and dotted line is the $z \gg 1$ asymptotic calculated in the first paper of Ref [30].*

3.6.7 Parton densities at THERA and LHC energies

3.6.7.1 Analytic estimates:

All three theoretical analyses [6, 25, 30] of the master equation give the same result for the dipole-target amplitude $N(x, r_\perp; b_t)$, namely in the region of low x $N(x, r_\perp; b_t) \longrightarrow 1$ in accordance with the unitarity constraint. Eq. 3.6.12 leads to gluon structure function which can be calculated as follows

$$\begin{aligned} xG(x,Q^2) &= \frac{8}{\pi^3}\int_x^1 \frac{dx'}{x}\int_{4/Q^2}^{\infty}\frac{dr_\perp^2}{r_\perp^4}\int d^2\, b_t\, N(x', r_\perp; b_t) \\ &\longrightarrow \frac{2}{\pi^2}\, Q^2\, R^2 \int_y^{y_{cr}} dy' \,, \end{aligned} \tag{3.6.25}$$

where y_{cr} is the solution of the equation $Q_s^2(y_{cr}) = Q^2$ and R is the size of the target. Therefore, the answer for the asymptotic is clear, and it can be rewritten in the form [6, 25, 30]:

$$xG(x,Q^2) \longrightarrow \frac{N_c^2-1}{4\pi N_c}\,\frac{1}{\alpha_S}\, R^2\, Q^2\, \ln(Q_s^2(x)/Q^2)\,. \tag{3.6.26}$$

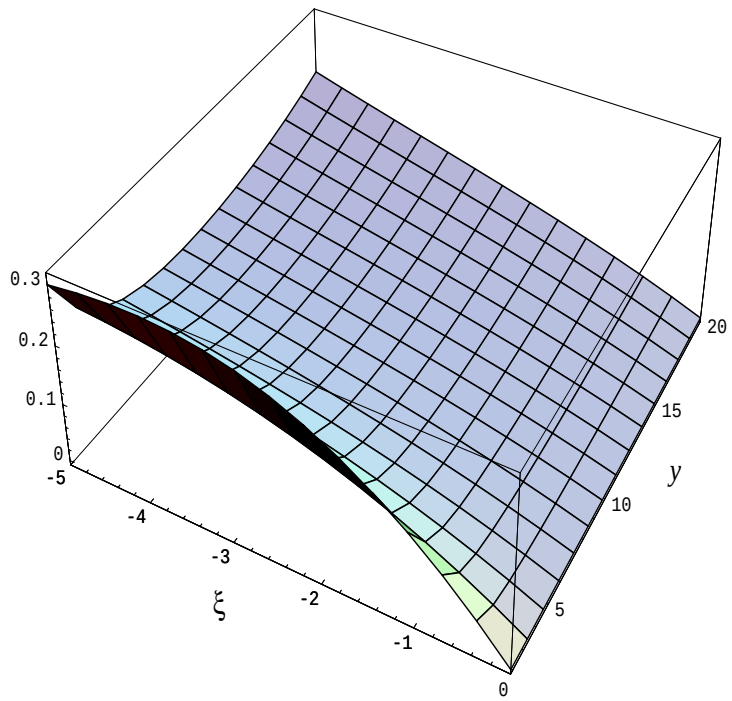

Figure 16: *The ratio* $\delta N(y,\xi)/N(\xi)$.

In Eq. 3.6.26 we assumed that the b_t -distribution does not depend on x. Actually this is not correct and we have some shrinkage of the diffraction peak [30]. All numerical coefficients in Eq. 3.6.26 are fixed in the double log approximation and have to be checked to a better accuracy.

3.6.7.2 Numerical results:

The analytic approach leads to an understanding, but also gives a certain check of a numerical procedure for solving the master equation. At the moment, we have two attempts to solve the equation numerically [22, 34] which can illustrate the effect that the non-linear evolution will have for the extrapolation of HERA data to higher energies (lower x). (see Fig. 18.

We can learn at least two lessons: first, the approximate models cannot be used for the predictions at higher energies; and second, the saturation phenomenon could be rather strong both at THERA and LHC energies. Such a strong modification of the $r_\perp$ - behaviour due to non-linear corrections reflects in Q^2 and x behaviour of gluon density as one can see in Fig. 19

Fig. 19 shows that the taming of the parton densities growth included in the master equation can easily reduce the value of the gluon density at THERA and LHC energies by $2\div 3$ times, at different values of Q^2.

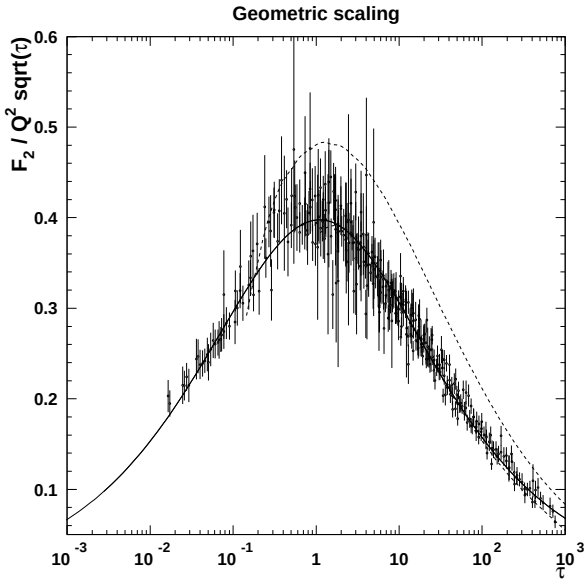

Figure 17: *The HERA data, plotted as a function of* $\tau = Q^2/Q_s^2(x)$. *The solid curve is the prediction of the Wüsthoff and Golec-Biernat saturation model, which was calculated by K. Golec-Biernat specially for THERA WS. The two dashed curves give the prediction of the DGLAP evolution (parameterization GRV'98) for the THERA kinematic region.*

3.6.8 Summary

3.6.8.1 From the first principles:

The main message that I want to deliver in this presentation is very simple: *Due to the hard work of number of experts, the theory of high parton density QCD has been established*, and this theory includes the proof of :

- The nonlinear evolution equation for the dipole-target amplitude at fixed b_t ($Im\, a(x, r_\perp; b_t) = N(x, r_\perp; b_t)$);
- The saturation of the parton densities as $x \to 0$ which means that $N(x, r_\perp; b_t) \longrightarrow 1$ at low x;
- The new scaling phenomena $N(x, r_\perp; b_t) = N(r_\perp^2 \cdot Q_s^2(x), b_t)$ for $Q^2 < Q_s^2(x)$;
- The sharp increase of the saturation scale $Q_s^2(x)$ in the region of low x;
- The importance of the saturation effects in taming the growth of the gluon density at THERA and LHC energies.

We would like to stress that during past two decades we have developed the perturbative QCD methods [21], based on the correct degrees of freedom: colour dipoles at high

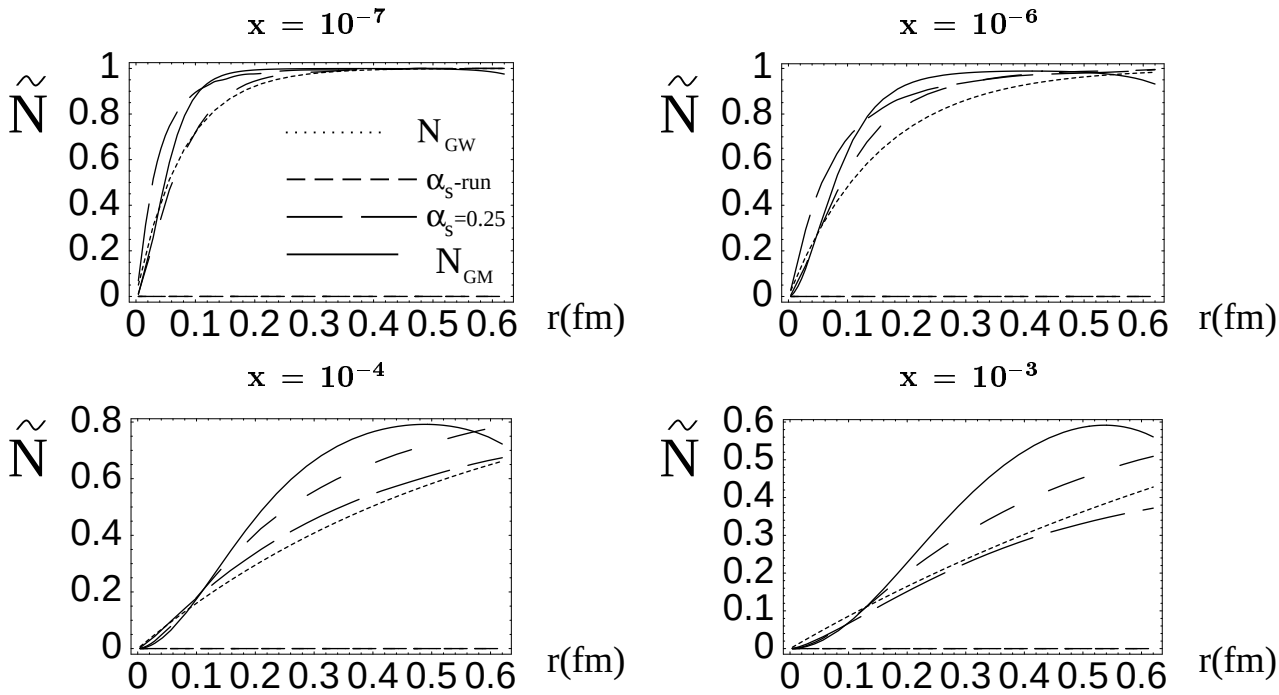

Figure 18: *The comparison between the solutions $\tilde{N}$, Glauber-Mueller formula [28], and Golec-Biernat and Wüsthoff (GW) model. The four curves correspond to two different solutions $\tilde{N}_{\alpha_S=0.25}$ (large dashes), $\tilde{N}_{\alpha_S-running}$(small dashes), N_{GM} (continuous line), and N_{GW} of the GW model (dots).*

energies [11] and created new operator methods of tackling this problem, such as the Wilson Loop Operator Expansion [20] and the effective Lagrangian approach [5, 24, 25]. My personal feeling is that the future is in the operator methods since they provide a possibility to describe the matching of the high density QCD with real non-perturbative QCD with large coupling constant in a unique way. However, I would like to emphasize the positive aspects of the pQCD approach : a clear physical picture in the pQCD calculations and, because of this picture, the transparent understanding of the meanings of observables which we calculate in pQCD.

The whole development of this new area of theory I consider as a triumph of approach of my teacher, Prof. Gribov, to high energy physics, which could be formulated as **"Physical picture - first, mathematics - after if ever"** [37]. Indeed, I am very certain that the remarkable progress, that we see now, was possible only, because the picture that has been discussed in the first section, was correct from the beginning.

3.6.8.2 Our prejudices:

I decided to finish my paper listing the prejudices (some of them) that I have fought during the two decades:

- The DGLAP evolution equation is more fundamental and has better proof than

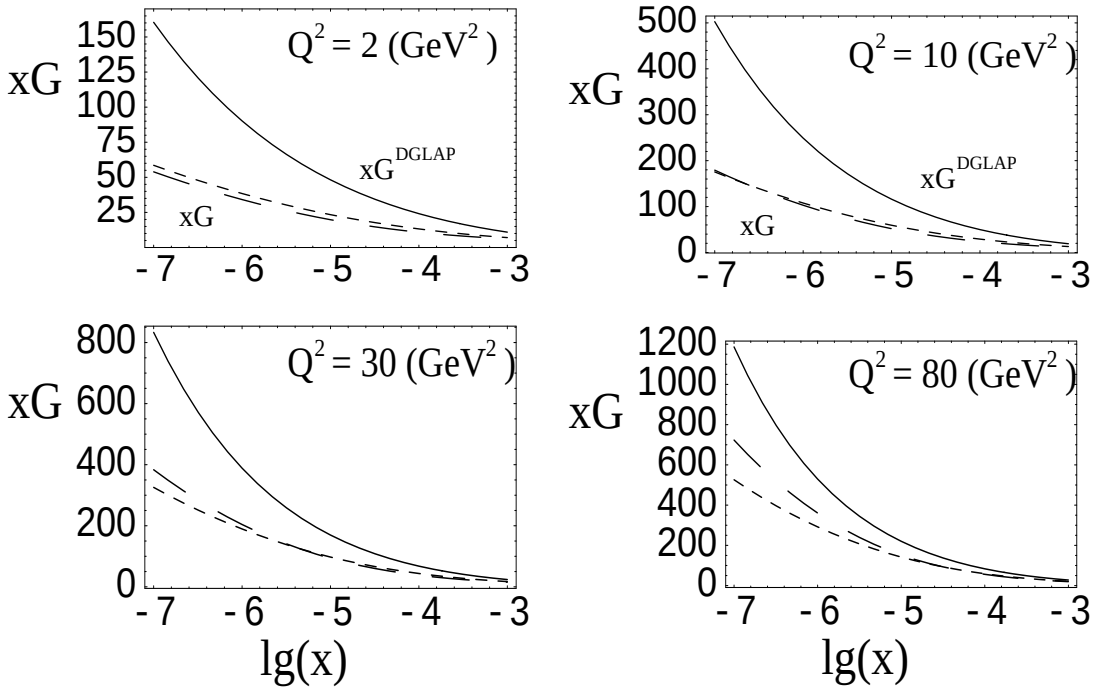

Figure 19: *The function xG is plotted versus* $\lg(x)$. *The small dashes correspond to the solution with the running α_S, while the large dashes are used for the constant $\alpha_S = 0.25$. The continuous line is the GRV parameterization.*

non-linear one. It is not true because

- The GLAP equation yields the parton densities which violate the unitarity constraints;
- It does not contain any proof of why the higher twist contribution is smaller, than the leading twist one, which has been incorporated in these equations;
- These equations demand initial conditions which we do not know how to treat theoretically or extract experimentally.

- By choosing the initial value for the DGLAP evolution Q_0^2 to be large enough, we can claim that the higher twists contributions are small. It was shown that the anomalous dimension of the higher twists is much larger that the leading one [16, 17] and at any value of Q^2 at low x, the higher twist will exceed the leading twist (DGLAP) contribution. Therefore, the practical procedure of solving the DGLAP evolution equation cannot be considered to be free of justified criticism ;

- The calculation of higher order corrections of pQCD will improve our descriptions of the experimental data. The pQCD series are the asymptotic series and they have intrinsic accuracy, which cannot be improved by calculating additional

orders in α_S, and this accuracy is rather poor in the region of low x. To evaluate errors we have to use the next order calculation in pQCD as an error, but with the same initial conditions.

Acknowledgments :

I would like to thank all participants of low x WG at THERA WS . Hot and useful discussions with them on high density QCD problems provided a stimulus for writing this presentation. I am very grateful for illuminating discussions to comrades in arms: Ian Balitsky, Jochen Bartels, Mikhail Braun, Asher Gotsman, Krystoff Golec-Biernat, Edmond Iancu, Dima Kharzeev, Boris Kopeliovich, Yura Kovchegov, Alex Kovner, Ian Kwiecinski, Uri Maor, Larry McLerran with his Minnesota-BNL team, Al Mueller and Heribert Weigert. I equally thank my students Mikhael Lublinsky, Eran Naftali and Kirill Tuchin for being good friends and labourers in the hard work on low x problems.

I would also like to express a deep acknowledgment to my opponents for keeping me in a fighting mood. The present status of high density QCD is a challenge to them and , I hope, they will scrutinize and criticize our approach on the same professional level as it has been proven. I am sure that such a criticism will give a new impetus for further development.

I wish to thank all HERA experimentalists for their beautiful data and the deep interest in low x problems. I have expressed my point of view on HERA data in different publication and, here, I wanted to give a review of the theoretical scene for them. I am very much indebted to them because HERA data revived a question on Pomeron structure , my first and strongest love which will never pass.

This research was supported in part by the BSF grant # 9800276, by the GIF grant # I-620-22.14/1999 and by Israeli Science Foundation, founded by the Israeli Academy of Science and Humanities.

References

[1] V.N. Gribov and L.N. Lipatov,Sov. J. Nucl. Phys. **15** (1972) 438;
L.N. Lipatov, Yad. Fiz. **20**(1974) 181;
G. Altarelli and G. Parisi, Nucl. Phys. **B 126** (1977) 298;
Yu.L. Dokshitser, Sov. Phys. JETP **46**(1977) 641.

[2] E.A. Kuraev, L.N. Lipatov and V.S. Fadin, Sov. Phys. JETP **45** (1978) 199;
Ya.Ya. Balitsky and L.N. Lipatov, Sov. J. Nucl. Phys. **28** (1978) 22.

[3] L.V. Gribov, E.M. Levin and M.G. Ryskin, Phys. Rep **100** (1983) 1.

[4] A.H. Mueller and J. Qiu, Nucl. Phys. **B 268** (1986) 427.

[5] L. McLerran and R. Venugopalan,Phys. Rev. **D 49** (1994) 2233,3352; **50** (1994) 2225; **53** (1996) 458; **59** (1999) 094002.

[6] A.H. Mueller, Nucl. Phys. **B 558** (1999) 285.

[7] R.P. Feyman, Photon - Hadron Interaction, Benjamin, NY,1972;
J.D. Bjorken, J. Kogut and D.E. Soper, Phys. Rev. **D 3** (1971) 1382;
J.D. Bjorken, Phys. Rev. **D 1** (1970) 1376;
J.D. Bjorken and E.A. Paschos, Phys. Rev. **185** (1969) 1975.

[8] J. Bartels and H. Kowalski, Diffraction at HERA and the Confinement Problem, DESY-00-154,`hep-ph/0010345`.

[9] A. Zamolodchikov, B. Kopeliovich and L. Lapidus, JETP Lett. **33** (1981) 595.

[10] E.M. Levin and M.G. Ryskin, Sov. J. Nucl. Phys. **45** (1987) 150.

[11] A.H. Mueller, Nucl. Phys. **B 335** (1990) 115.

[12] A.H. Mueller, Nucl. Phys. **B 415** (1994) 373.

[13] A.L. Ayala, M.B. Gay Ducati and E.M. Levin, Nucl. Phys.**B 493**(1997) 305; **B 511** (1998) 355.

[14] N.N. Nikolaev and B.G. Zakharov, Z. Phys. **C 49** (1991) 607;
E.M. Levin et al., Z. Phys. **C 74** (1997) 671.

[15] Yu.V. Kovchegov and L. McLerran, Phys. Rev. **D 60** (1999) 054025.

[16] J. Bartels, Z.Phys. **C 60** (1993) 471, Phys. Lett. **B 298** (1993) 204.

[17] E.M. Levin, M.G. Ryskin and A.G. Shuvaev, Nucl. Phys. **B 387** (1992) 589.

[18] E. Laenen, E. Levin and A.G. Shuvaev, Nucl. Phys. **B 419** (1994) 39.

[19] E. Laenen and E. Levin, Nucl. Phys. (1995) 207.

[20] I. Balitsky, Nucl. Phys. **B 463** (1996) 99, High energy QCD and Wilson lines, `hep-ph/0101042` ,JLAB-THY-00-44.

[21] Yu.V. Kovchegov, Phys. Rev. **D 60** (2000) 034008.

[22] M. Braun, Eur. Phys.J. **C 16** (2000) 337.

[23] A. Mueller and B. Patel, Nucl. Phys. **B 425** (1994) 471;
J. Bartels and M. Wüsthoff, Z. Phys. **C 66** (1995) 157.

[24] E. Iancu, A. Leonidov and L. McLerran, Nonlinear Gluon Evolution in the Color Glass Condensate, BNL-NT-00/24,`hep-ph/0011241`; The renormalization group equation for the color glass condensate, BNL-NT-01-3, `hep-ph/0102009`.

[25] E. Iancu and L. McLerran, Saturation and Universality in QCD at small x, SACLAY-T01-026, `hep-ph/0103032`.

[26] J. Jalilian-Marian et al., Phys. Rev.**D 55**(1997) 5414;
J. Jalilian-Marian, A. Kovner and H. Weigert, Phys. Rev. **59**(1999) 014015;
J. Jalilian-Marian et al., Phys. Rev. **59**(1999) 014014,034007;
A. Kovner, J.Guilherme Milhano and H. Weigert, Phys. Rev. **D 62**(2000) 114005;
H. Weigert, Unitarity at small Bjorken x NORDITA-2000-34-HE, `hep-ph/0004044`.

[27] Yu.V. Kovchegov and A.H. Mueller, Nucl. Phys. **B 529** (1998) 451.

[28] E. Gotsman et al. Has HERA reached a new QCD regime?, DESY-00-149, `hep-ph/0010198`.

[29] A.L. Ayala, M.B. Gay Ducati and E.M. Levin, Phys. Lett. **B 388** (1996) 188.

[30] E. Levin and K. Tuchin, Nucl. Phys. **B 573** (2000) 833; New scaling aty high energy DIS, TAUP-2659-2000,`hep-ph/0012167` ; *Nonlinear evolution and saturation for heavy nuclei in DIS*, TAUP-2664-2001,`hep-ph/0101275`.

[31] Yu.V. Kovchegov, Phys. Rev. **D 61** (2000) 074018.

[32] J.C. Collins and J. Kwiecinski, Nucl. Phys. **B 335** (1990) 89;
J. Bartels, J. Blümlein and G. Schuler, Z. Phys. **C 50** (1991) 91.

[33] K. Golec-Biernat and M. Wüsthoff, Diffractive parton distributions from the saturation model,DESY-00-180,`hep-ph/0102093`; *Phys.Rev.* **D 60** (1999) 114023;**D 59** (1999) 014017.

[34] M. Lublinsky et al., Non-linear evolution and parton distributions at LHC and THERA energies, TAUP-2667-2000,`hep-ph/0102321`.

[35] J. Bartels and E. Levin, Nucl.Phys. **B 387** (1992) 617.

[36] A. Stasto, K. Golec-Biernat and J. Kwiecinski,PPhys.Rev.Lett. **86** (2001) 596.

[37] Yu. Dokshitzer, V,N. Gribov: 1930 -1997, `physics/9801025`.

NT@UW-01-03

3.7 Saturation and Unitarity of Hadronic Structure Functions

Yu.V. Kovchegov
Department of Physics, University of Washington, Box 351560
Seattle, WA 98195-1560, USA
email: yuri@phys.washington.edu

3.7.1 "Phase Diagram" of High Energy QCD

At very small values of Bjorken x the growth of the hadronic structure functions with decreasing x is expected to slow down. This effect is known as saturation of structure functions and has a very interesting and profound underlying physics.

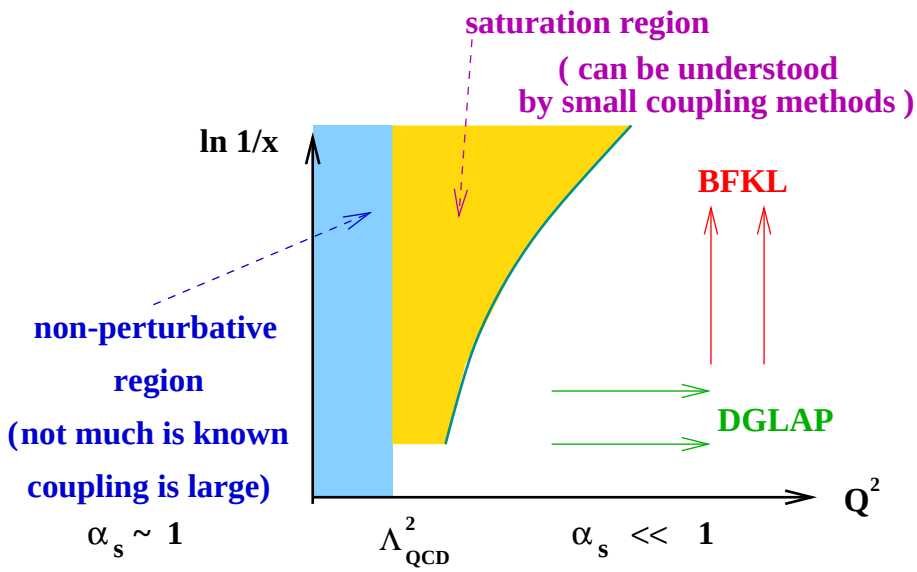

Figure 1: *"Phase diagram" of high energy QCD.*

The majority of the HERA data shows that the proton's structure functions at large Q^2 and not very small x can be described by the DGLAP evolution equation [1], which is a linear equation. It is convenient to present different properties of hadronic structure functions in terms of a "phase diagram" in Q^2 and $\ln 1/x$ plane (see Fig.

1). The DGLAP physics corresponds to the lower right section of the plane, where Q^2 is large and x is not too small. As one goes towards smaller x in the same region of Q^2 the hadronic structure functions rise. Most of the data in that region can be explained in terms of either small-x limit of DGLAP equation or, alternatively and more interestingly, by the BFKL equation [2], which is also a linear equation but could be responsible for evolving the system towards a higher gluonic density regime. However, the DIS cross sections can not rise forever as powers of center of mass energy s. This, for instance, would violate unitarity [3]. That means that at some very small x the hadronic structure functions have to undergo a significant qualitative change of behavior, becoming a much slower varying functions of x. The slow down of the growth of hadronic structure functions is usually associated with non-linear effects in the quark and gluon dynamics, such as parton recombination, which eventually balances the parton splitting process. Therefore the partons in the hadronic wave function reach the state of *saturation*. The region of saturation of the structure functions is represented in yellow in Fig. 1. The scale Q^2 corresponding to the transition to the saturation region is different for different values of Bjorken x, increasing with decreasing x (increasing energy). This scales is usually refereed to as the *saturation scale* $Q_s^2(x)$. If $Q_s^2(x) \gg \Lambda_{QCD}^2$ than the coupling constant inside the saturation region would still be small allowing us to perform analytical calculations inside of the saturation region [4, 5]. The gluon fields within the saturation region are strong, $A_\mu \sim 1/g$ which leads to a number of interesting nonlinear effects.

It is possible that the recent experimental data obtained at HERA [6] contains evidence of saturation transition in DIS on a proton at $x \approx 10^{-3} - 10^{-4}$ and $Q^2 \approx 2 - 4\,\mathrm{GeV}^2$. This implies that in the kinematic region of energies to be explored at THERA saturation scale would be even larger unambiguously distinguishing saturation physics from non-perturbative effects and allowing us to explore the physics deep inside of the saturation region.

The discussion in this chapter is going to be based on [7–9].

3.7.2 Qualitative Picture of Saturation

The Balitsky, Fadin, Kuraev and Lipatov (BFKL) [2] equation resums all leading logarithms of Bjorken x for hadronic cross sections and structure functions. The solution of the BFKL equation grows like a power of center of mass energy s, therefore violating the unitarity bound at very high energies [3]. This is one of the major problems of small x physics, since the Froissart bound [3] states that the total cross section should not raise faster than $\ln^2 s$ at asymptotically high energies. There is a general belief that the unitarity problem could be cured by resumming all multiple BFKL pomeron exchanges in the total cross section, or, equivalently, in the structure function.

As was argued by Mueller in [10] multiple pomeron exchanges become important at the values of rapidity of the order of

$$Y_U \sim \frac{1}{\alpha_P - 1} \ln \frac{1}{\alpha^2}, \tag{3.7.1}$$

with α the strong coupling constant, which is assumed to be small, and $\alpha_P - 1 = \frac{4\alpha N_c}{\pi}\ln 2$ is the intercept of the BFKL pomeron. This result could be obtained if one notes that one pomeron contribution to the total cross section of, for instance, onium–onium scattering, is parametrically of the order of $\alpha^2 \exp[(\alpha_P - 1)Y]$ and the contribution of the double pomeron exchange is $\alpha^4 \exp[2(\alpha_P - 1)Y]$. Since multiple pomeron exchanges become important when the single and double pomeron exchange contributions become comparable, we recover Eq. (3.7.1) by just equating the two expressions.

After completion of the calculation of the next–to–leading order corrections to the kernel of the BFKL equation (NLO BFKL) by Fadin and Lipatov [11], and, independently, by Camici and Ciafaloni [12], it was shown in [13, 14] that due to the running coupling effects these corrections become important at the rapidities of the order of

$$Y_{NLO} \sim \frac{1}{\alpha^{5/3}}. \tag{3.7.2}$$

One can see that $Y_U \ll Y_{NLO}$ for parametrically small α. That implies that the center of mass energy at which the multiple pomeron exchanges become important is much smaller, and, therefore, is easier to achieve, than the energy at which NLO corrections start playing an important role. That is multiple pomeron exchanges are probably more relevant than NLO BFKL to the description of current experiments [6]. Also multiple pomeron exchanges are much more likely to unitarize the total hadronic cross section. Here we are going to present a solution to the problem of resummation of multiple pomeron exchanges and show how the BFKL pomeron unitarizes.

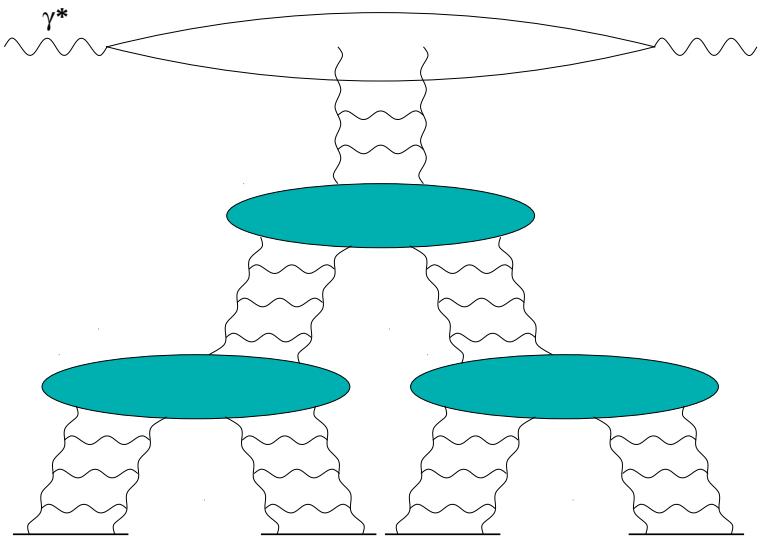

Figure 2: *An example of the pomeron "fan" diagram. Each ladder interacts with the proton at rest independently.*

We will to consider deep inelastic scattering (DIS) of a virtual photon on a hadron and will resum all multiple pomeron exchanges contributing to the F_2 structure function

of the hadron in the leading longitudinal logarithmic approximation in the large N_c limit. The first step in that direction in PQCD was a conjecture by Gribov, Levin and Ryskin (GLR) [15] of an equation describing the fusion of two pomeron ladders into one, which was proven in the double logarithmic limit by Mueller and Qiu [16]. The resulting equation resums all pomeron "fan" diagrams (see Fig. (2)) in the double logarithmic approximation. An extensive work on resumming the multiple pomeron exchanges in the gluon distribution function in the leading $\ln(1/x)$ approximation (i.e. without taking the double logarithmic limit) both in the framework of effective field theories and employing alternative approaches has been pursued in [17–25].

Let us consider a deep inelastic scattering (DIS) of a virtual photon on a hadron. An incoming photon splits into a quark–antiquark pair and then the $q\overline{q}$ pair rescatters on the target hadron. In the rest frame of the hadron all QCD evolution should be included in the wave function of the incoming photon. That way the incoming photon develops a cascade of gluons, which then scatter on the hadron at rest. We want to calculate this gluon cascade in the leading longitudinal logarithmic ($\ln 1/x$) approximation and in the large N_c limit. This is exactly the type of cascade described by Mueller's dipole model [26–29]. In the large N_c limit the incoming gluon develops a system of color dipoles and each of them independently rescatters on the hadron. The forward amplitude of the process is shown in Fig. 3. The double lines in Fig. 3 correspond to gluons in large N_c approximation being represented as consisting of a quark and an antiquark of different colors. The color dipoles are formed by a quark from one gluon and an antiquark from another gluon. In Fig. 3 each dipole, that was developed through the QCD evolution, later interacts with the hadron by a series of Glauber–type multiple rescatterings on the sources of color charge. The assumption about the type of interaction of the dipoles with the hadron is not important for the evolution. It could also be just two gluon exchanges. The important assumption is that each dipole interacts with the target independently of the other dipoles, which is done in the spirit of the large N_c limit and is valid for a model of a large dilute target proton.

For this case of a dilute target proton independent dipole interactions with the target proton are enhanced by some factors of the number of sources of color charge in the proton compared to the case when several dipoles interact with the same parton in the proton [4, 5]. This allowed us to assume that the dipoles interact with the proton independently. The summation of these contributions corresponds to summation of the pomeron "fan" diagrams of Fig. 2. However, in general there is another class of diagrams, which we will call pomeron loop diagrams. In a pomeron loop diagram a pomeron first splits into two pomerons, just like in the fan diagram, but then the two pomerons merge back into one pomeron. In other words the graphs containing pomerons not only splitting, but also merging together will be referred to as pomeron loop diagrams. In a dilute proton these pomeron loop diagrams could be considered small, since they would be suppressed by powers of color charge density. At very high energies this approximation becomes not very well justified even in the dilute proton case for the following reason. The contribution of each additional pomeron in a fan diagram on a hadron is parametrically of the order of $\alpha^2\rho^2 e^{(\alpha_P-1)Y}$ with ρ the color

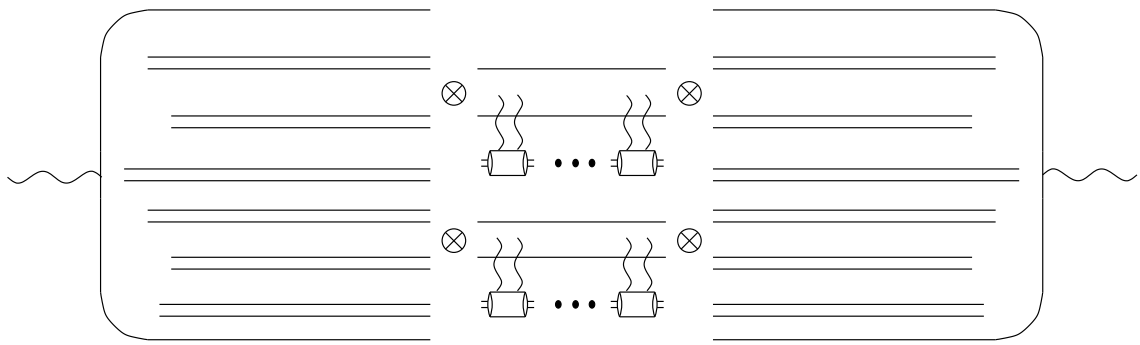

Figure 3: *Dipole evolution in the deep inelastic scattering process as pictured in Ref.[1]. The incoming virtual photon develops a system of color dipoles, each of which rescatters on the hadron (only two are shown).*

charge density (see [4, 5]), which is large at the rapidities of the order of Y_U given by Eq. (3.7.1). The contribution of an extra pomeron in a pomeron loop diagram is of the order of $\alpha^2 e^{(\alpha_P - 1)Y}$, which is not enhanced by powers of ρ and is, therefore, suppressed in the dilute proton case. However, one can easily see that at extremely high energies, when $\alpha^2 e^{(\alpha_P - 1)Y}$ becomes greater than or of the order of one, pomeron loop diagrams become important, still being smaller than the fan diagrams. Resummation of pomeron loop diagrams in a dipole wave function seems to be a very hard technical problem, possibly involving NLO BFKL or, even, next-to-next-to-leading order BFKL kernel calculations [30]. Nevertheless, it is the author's belief that these pomeron loop diagrams are not going to significantly change the high energy behavior of the structure functions.

3.7.3 Evolution equation from the dipole model

We start by considering a deep inelastic scattering process. The incoming virtual photon with a large q_+ component of the momentum splits into a quark–antiquark pair which then interacts with the proton at rest. We model the interaction by no more than two gluon exchanges between each source of color charge and the quark–antiquark pair. This is done in the spirit of the quasi–classical approximation used previously in [31, 32]. The interactions are taken in the eikonal approximation. Then, as could be shown in general, i.e., including the leading logarithmic QCD evolution, the total cross–section, and, therefore, the F_2 structure function of the proton can be rewritten as a product of the square of the virtual photon's wave function and the propagator of the quark–antiquark pair through the proton. The expression reads

$$F_2(x, Q^2) = \frac{Q^2}{4\pi^2 \alpha_{EM}} \int \frac{d^2\mathbf{x}_{01} dz}{2\pi} \left[\Phi_T(\mathbf{x}_{01}, z) + \Phi_L(\mathbf{x}_{01}, z)\right] d^2 b_0 \; N(\mathbf{x}_{01}, \mathbf{b}_0, Y), \quad (3.7.3)$$

where the incoming photon with virtuality Q splits into a quark–antiquark pair with the transverse coordinates of the quark and antiquark being $\tilde{\mathbf{x}}_0$ and $\tilde{\mathbf{x}}_1$ correspondingly,

such that $\mathbf{x}_{10} = \tilde{\mathbf{x}}_1 - \tilde{\mathbf{x}}_0$. The coordinate of the center of the pair is given by $\mathbf{b}_0 = \frac{1}{2}(\tilde{\mathbf{x}}_1 + \tilde{\mathbf{x}}_0)$. Y is the rapidity variable $Y = \ln s/Q^2 = \ln 1/x$. The square of the light cone wave function of $q\overline{q}$ fluctuations of a virtual photon is denoted by $\Phi_T(\mathbf{x}_{01}, z)$ and $\Phi_L(\mathbf{x}_{01}, z)$ for transverse and longitudinal photons correspondingly, with z being the fraction of the photon's longitudinal momentum carried by the quark. At the lowest order in electromagnetic coupling (α_{EM}) $\Phi_T(\mathbf{x}_{01}, z)$ and $\Phi_L(\mathbf{x}_{01}, z)$ are given by [[33] and references therein]

$$\Phi_T(\mathbf{x}_{01}, z) = \frac{2N_c\alpha_{EM}}{\pi}\left\{a^2\ K_1^2(x_{01}a)\ [z^2 + (1-z)^2]\right\}, \tag{3.7.4}$$

$$\Phi_L(\mathbf{x}_{01}, z) = \frac{2N_c\alpha_{EM}}{\pi}\ 4Q^2z^2(1-z)^2\ K_0^2(x_{01}a), \tag{3.7.5}$$

with $a^2 = Q^2z(1-z)$. We consider massless quarks having only one flavor.

The quantity $N(\mathbf{x}_{01}, \mathbf{b}_0, Y)$ has the meaning of the forward scattering amplitude of the quark–antiquark pair on a hadron. At the lowest (classical) order not including the QCD evolution in rapidity it is given by

$$N(\mathbf{x}_{01}, \mathbf{b}_0, 0) = -\gamma(\mathbf{x}_{01}, \mathbf{b}_0) \equiv \left\{1 - \exp\left[-\frac{C_F}{N_c}\frac{\mathbf{x}_{01}^2\tilde{v}(x_{01})R}{2\lambda}\right]\right\}, \tag{3.7.6}$$

with $\tilde{v}$ as defined in [32] and λ being the mean free path of a gluon in a hadronic medium, as defined in [32]. In the logarithmic approximation for large Q^2 (small x_{01}) Eq. (3.7.6) can be rewritten as

$$N(\mathbf{x}_{01}, \mathbf{b}_0, 0) = -\gamma(\mathbf{x}_{01}, \mathbf{b}_0) \approx \left\{1 - \exp\left[-\frac{\alpha\pi^2}{2N_cS_\perp}\mathbf{x}_{01}^2 xG(x, 1/\mathbf{x}_{01}^2)\right]\right\}. \tag{3.7.7}$$

$\gamma(\mathbf{x}_{01}, \mathbf{b}_0)$ is the propagator of the $q\overline{q}$ pair through the hadron. The propagator could be easily calculated, similarly to [31, 32], giving the Glauber multiple rescattering formula (3.7.7). Here and throughout the paper we assume for simplicity that the proton is a cylinder, which appears as a circle of radius R in the transverse direction and has a constant length $2R$ along the longitudinal z direction. Therefore its transverse cross–sectional area is $S_\perp = \pi R^2$. In formula (3.7.7) α is the strong coupling constant and $xG(x, 1/\mathbf{x}_{01}^2)$ is the gluon distribution of the hadron, taken at the lowest order in α, similarly to [32].

Eq. (3.7.7) resums all Glauber type multiple rescatterings of a $q\overline{q}$ pair on a hadron. As was mentioned before, since each interaction of the pair with a source of color charge in the hadron is restricted to the two gluon exchange, the formula (3.7.7) effectively sums up all the powers of the parameter $\alpha^2\rho^2$. Or, looking at the power of the exponent in (3.7.7) we conclude that since $x_{01} \sim 1/Q$, it resums all the powers of $\frac{\alpha^2\rho^2}{Q^2}$. This is the definition of quasi–classical limit, a more detailed discussion of which could be found in [34].

Since the proton is at rest in order to include the QCD evolution of F_2 structure function, we have to develop the soft gluon wave function of the incoming virtual

photon. In the leading longitudinal logarithmic approximation ($\ln 1/x$) the evolution of the wave function is realized through successive emissions of small–x gluons. The $q\overline{q}$ pair develops a cascade of gluons, which then scatter on the hadron. In order to describe the soft gluon cascade we will take the limit of a large number of colors, $N_c \to \infty$. Then, this leading logarithmic soft gluon wavefunction will become equivalent to the dipole wave function, introduced by Mueller in [26–29]. The physical picture becomes straightforward. The $q\overline{q}$ pair develops a system of dipoles (dipole wave function), and each of the dipoles independently scatters on the hadron. Since the proton is assumed to have many sources of color charge in it we may approximate the interaction of a dipole (quark–antiquark pair) with the hadron by $\gamma(\mathbf{x}, \mathbf{b})$ given by Eq. (3.7.7), with $\mathbf{x}$ and $\mathbf{b}$ being the dipole's transverse separation and impact parameter. That means that each of the dipoles interacts with several sources of color charge (Glauber rescattering) in the hadron independent of other dipoles.

To construct the dipole wave function we will heavily rely on the techniques developed in [26–29]. Following [26–29] we define the generating functional for dipoles $Z(\mathbf{b}_0, \mathbf{x}_{01}, Y, u)$ (see formulae (16) and (17) in [26]). The generating functional then obeys the equation (see Eq. (12) in [28])

$$Z(\mathbf{b}_0, \mathbf{x}_{01}, Y, u) = u(\mathbf{b}_0, \mathbf{x}_{01}) \exp\left[-\frac{4\alpha C_F}{\pi} \ln\left(\frac{x_{01}}{\rho}\right) Y\right] +$$

$$+\frac{\alpha C_F}{\pi^2} \int_0^Y dy \exp\left[-\frac{4\alpha C_F}{\pi} \ln\left(\frac{x_{01}}{\rho}\right)(Y-y)\right]$$

$$\times \int_\rho d^2\tilde{x}_2 \frac{x_{01}^2}{x_{02}^2 x_{12}^2} Z(\mathbf{b}_0 + \frac{1}{2}\mathbf{x}_{12}, \mathbf{x}_{02}, y, u)\, Z(\mathbf{b}_0 - \frac{1}{2}\mathbf{x}_{20}, \mathbf{x}_{12}, y, u), \tag{3.7.8}$$

where $\mathbf{x}_{20} = \tilde{\mathbf{x}}_0 - \tilde{\mathbf{x}}_2$, $\mathbf{x}_{21} = \tilde{\mathbf{x}}_1 - \tilde{\mathbf{x}}_2$ and the integration over $\tilde{x}_2$ is performed over the region where $x_{02} \geq \rho$ and $x_{12} \geq \rho$. This ρ serves as an ultraviolet cutoff in the equation and disappears in the physical quantities. $\mathbf{b}_0 = \frac{1}{2}(\mathbf{x}_0 + \mathbf{x}_1)$ is the position of the center of the initial dipole in the transverse plane [28]. $C_F = N_c/2$ in the large N_c limit. The generating functional is defined such that $Z(\mathbf{b}_0, \mathbf{x}_{01}, Y, u = 1) = 1$ [see [26]].

Eq. 3.7.8 is illustrated in Fig. 4. There the blob represents complicated dipole evolution which is included in the generating functional Z. In one step of the evolution a gluon is emitted in a dipole, splitting the parent dipole into two dipoles. The consecutive evolution can continue in either of the two dipoles. Thus the right hand sife of Eq. (3.7.8) is quadratic in Z.

Analogous to [27, 28] we now define the dipole number density by

$$\frac{1}{2\pi x^2} n_1(x_{01}, Y, |\mathbf{b} - \mathbf{b}_0|, x) = \frac{\delta}{\delta u(\mathbf{b}, \mathbf{x})} Z(\mathbf{b}_0, \mathbf{x}_{01}, Y, u)|_{u=1}. \tag{3.7.9}$$

$n_1(x_{01}, Y, |\mathbf{b} - \mathbf{b}_0|, x)$ convoluted with the virtual photon's wave function gives the number of dipoles of transverse size x at the impact parameter $|\mathbf{b} - \mathbf{b}_0|$ with the

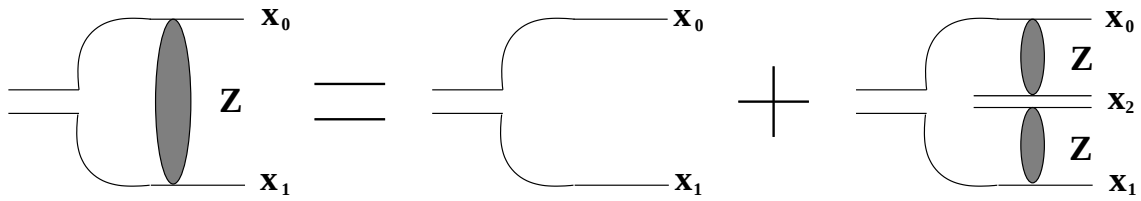

Figure 4: *A diagrammatic representation of the dipole evolution equation (3.7.8).*

smallest light cone momentum in the pair greater or equal to $e^{-Y}q_+$. Similarly to the dipole number density we can introduce dipole pair density [27, 28] for a pair of dipoles of sizes x_1 and x_2 at the impact parameters $|\mathbf{b}_1 - \mathbf{b}_0|$ and$|\mathbf{b}_2 - \mathbf{b}_0|$ by

$$\frac{1}{2\pi x_1^2}\frac{1}{2\pi x_2^2} n_2(x_{01}, Y, |\mathbf{b}_1 - \mathbf{b}_0|, x_1, |\mathbf{b}_2 - \mathbf{b}_0|, x_2) =$$

$$= \frac{1}{2!}\frac{\delta}{\delta u(\mathbf{b}_1, \mathbf{x}_1)}\frac{\delta}{\delta u(\mathbf{b}_2, \mathbf{x}_2)} Z(\mathbf{b}_0, \mathbf{x}_{01}, Y, u)|_{u=1}. \tag{3.7.10}$$

Our notation is different from the conventional approach of [27, 28] by the factor of a factorial, for reasons which will become obvious later. Generalizing the definition (3.7.10) to k dipoles of sizes $x_1, \ldots, x_n$ situated at the impact parameters $|\mathbf{b}_1 - \mathbf{b}_0|, \ldots, |\mathbf{b}_k - \mathbf{b}_0|$ we easily obtain:

$$\prod_{i=1}^{k} \frac{1}{2\pi x_i^2} n_k(x_{01}, Y, |\mathbf{b}_1 - \mathbf{b}_0|, x_1, \ldots, |\mathbf{b}_k - \mathbf{b}_0|, x_k) = \frac{1}{k!}\prod_{i=1}^{k} \frac{\delta}{\delta u(\mathbf{b}_i, \mathbf{x}_i)} Z(\mathbf{b}_0, \mathbf{x}_{01}, Y, u)|_{u=1}. \tag{3.7.11}$$

One can now see that in order to include all the multiple pomeron exchanges one has to sum up the contributions of different numbers of dipoles interacting with the hadron. Namely we should take the dipole number density $n_1(x_{01}, Y, \mathbf{b}, x)$ and convolute it with the propagator of this one dipole in the hadron $\gamma(\mathbf{x}, \mathbf{b})$. Then we should take the dipole pair density $n_2(x_{01}, Y, \mathbf{b}_1, x_1, \mathbf{b}_2, x_2)$ and convolute it with two propagators $\gamma(\mathbf{x}_1, \mathbf{b}_1)$ and $\gamma(\mathbf{x}_2, \mathbf{b}_2)$, etc. That way we obtain an expression for $N(\mathbf{x}_{01}, \mathbf{b}_0, Y)$:

$$-N(\mathbf{x}_{01}, \mathbf{b}_0, Y) = \int n_1(x_{01}, Y, \mathbf{b}_1, \mathbf{x}_1)\left(\gamma(\mathbf{x}_1, \mathbf{b}_1)\frac{d^2x_1}{2\pi x_1^2}d^2b_1\right) +$$

$$+\int n_2(x_{01}, Y, \mathbf{b}_1, \mathbf{x}_1, \mathbf{b}_2, \mathbf{x}_2)\left(\gamma(\mathbf{x}_1, \mathbf{b}_1)\frac{d^2x_1}{2\pi x_1^2}d^2b_1\right)\left(\gamma(\mathbf{x}_2, \mathbf{b}_2)\frac{d^2x_2}{2\pi x_2^2}d^2b_2\right) + \ldots =$$

$$= \sum_{i=1}^{\infty}\int n_i(x_{01}, Y, \mathbf{b}_1, \mathbf{x}_1, \ldots, \mathbf{b}_i, \mathbf{x}_i)\left(\gamma(\mathbf{x}_1, \mathbf{b}_1)\frac{d^2x_1}{2\pi x_1^2}d^2b_1\right)\ldots$$

$$\ldots \left(\gamma(\mathbf{x}_i, \mathbf{b}_i) \frac{d^2 x_i}{2\pi x_i^2} d^2 b_i \right), \tag{3.7.12}$$

where we put the minus sign in front of N to make it positive, since γ is negative. Eq. (3.7.12) clarifies the physical meaning of N as a total cross–section of a $q\overline{q}$ pair interacting with a hadron. One can understand now the factorials in the definitions of the dipole number densities (3.7.9), (3.7.10) and (3.7.11): once the convolutions with the propagators γ are done then the dipoles become "identical" and we have to include the symmetry factors.

In order to write down an equation for $N(\mathbf{x}_{01}, \mathbf{b}_0, Y)$ we have to find the equations for n_i's first. Following the techniques introduced in [26–29] we have to differentiate the equation for the generating functional (3.7.8) with respect to $u(\mathbf{x}, \mathbf{b})$ putting $u = 1$ at the end, keeping in mind that $Z(\mathbf{b}_0, \mathbf{x}_{01}, Y, u = 1) = 1$. Differentiating formula (3.7.8) once we obtain an equation for $n_1(x_{01}, Y, \mathbf{b}_1, \mathbf{x}_1)$:

$$n_1(x_{01}, Y, \mathbf{b}_1, \mathbf{x}_1) = \delta^2(\mathbf{x}_{01} - \mathbf{x}_1)\, 2\pi \mathbf{x}_1^2\, \delta^2(\mathbf{b}_1) \exp\left[-\frac{4\alpha C_F}{\pi} \ln\left(\frac{x_{01}}{\rho}\right) Y \right] +$$

$$+ \frac{\alpha C_F}{\pi^2} \int_0^Y dy \, \exp\left[-\frac{4\alpha C_F}{\pi} \ln\left(\frac{x_{01}}{\rho}\right) (Y - y) \right]$$

$$\times \int_\rho d^2\tilde{x}_2 \frac{x_{01}^2}{x_{02}^2 x_{12}^2}\, 2\, n_1(x_{02}, y, \overline{\mathbf{b}}_1, \mathbf{x}_1), \tag{3.7.13}$$

where, following [28], we have defined $\overline{\mathbf{b}}_i = \mathbf{b}_i - \mathbf{b}_0 - \frac{1}{2}\mathbf{x}_{12}$.

Differentiating Eq. (3.7.8) twice we obtain an equation for $n_2(x_{01}, Y, \mathbf{b}_1, \mathbf{x}_1, \mathbf{b}_2, \mathbf{x}_2)$

$$n_2(x_{01}, Y, \mathbf{b}_1, \mathbf{x}_1, \mathbf{b}_2, \mathbf{x}_2) = \frac{\alpha C_F}{\pi^2} \int_0^Y dy \, \exp\left[-\frac{4\alpha C_F}{\pi} \ln\left(\frac{x_{01}}{\rho}\right) (Y - y) \right]$$

$$\times \int_\rho d^2\tilde{x}_2 \frac{x_{01}^2}{x_{02}^2 x_{12}^2} [2\, n_2(x_{02}, y, \overline{\mathbf{b}}_1, \mathbf{x}_1, \overline{\mathbf{b}}_2, \mathbf{x}_2) + n_1(x_{02}, y, \overline{\mathbf{b}}_1, \mathbf{x}_1)\, n_1(x_{12}, y, \tilde{\mathbf{b}}_2, \mathbf{x}_2)], \tag{3.7.14}$$

where $\tilde{\mathbf{b}}_i = \mathbf{b}_i - \mathbf{b}_0 + \frac{1}{2}\mathbf{x}_{20}$. Now higher order differentiation of Eq. (3.7.8) becomes apparent, and could be easily done yielding the following equation for the number density of i dipoles:

$$n_i(x_{01}, Y, \mathbf{b}_1, \mathbf{x}_1, \ldots, \mathbf{b}_i, \mathbf{x}_i) = \frac{\alpha C_F}{\pi^2} \int_0^Y dy \, \exp\left[-\frac{4\alpha C_F}{\pi} \ln\left(\frac{x_{01}}{\rho}\right) (Y - y) \right]$$

$$\times \int_\rho d^2\tilde{x}_2 \frac{x_{01}^2}{x_{02}^2 x_{12}^2} [2\, n_i(x_{02}, y, \overline{\mathbf{b}}_1, \mathbf{x}_1, \ldots, \overline{\mathbf{b}}_i, \mathbf{x}_i) +$$

$$+\sum_{j+k=i} n_j(x_{02}, y, \overline{\mathbf{b}}_1, \mathbf{x}_1, \ldots, \overline{\mathbf{b}}_j, \mathbf{x}_j)\, n_k(x_{12}, y, \tilde{\mathbf{b}}_{j+1}, \mathbf{x}_{j+1}, \ldots, \tilde{\mathbf{b}}_i, \mathbf{x}_i)], \qquad (3.7.15)$$

where we anticipate the integration over the dipole sizes and treat the dipoles as identical objects. In principle Eq. (3.7.15) should contain the permutations of the arguments of the gluon densities in the product on the right hand side, but for the above mentioned reason we do not write this terms explicitly.

Multiplying formula (3.7.15) by

$$\left(\gamma(\mathbf{x}_1, \mathbf{b}_1)\frac{d^2x_1}{2\pi x_1^2}d^2b_1\right)\ldots\left(\gamma(\mathbf{x}_i, \mathbf{b}_i)\frac{d^2x_i}{2\pi x_i^2}d^2b_i\right),$$

integrating over the dipole sizes and impact parameters, and summing all such equations, i.e. summing over i from 1 to ∞ in (3.7.15) one obtains the equation for $N(\mathbf{x}_{01}, \mathbf{b}_0, Y)$ [7]

$$N(\mathbf{x}_{01}, \mathbf{b}_0, Y) = -\gamma(\mathbf{x}_{01}, \mathbf{b}_0)\, \exp\left[-\frac{4\alpha C_F}{\pi}\ln\left(\frac{x_{01}}{\rho}\right)Y\right]$$

$$+\frac{\alpha C_F}{\pi^2}\int_0^Y dy\, \exp\left[-\frac{4\alpha C_F}{\pi}\ln\left(\frac{x_{01}}{\rho}\right)(Y-y)\right]$$

$$\times\int_\rho d^2\tilde{x}_2\frac{x_{01}^2}{x_{02}^2x_{12}^2}\,[2\,N(\mathbf{x}_{02}, \mathbf{b}_0+\frac{1}{2}\mathbf{x}_{12}, y)$$

$$-N(\mathbf{x}_{02}, \mathbf{b}_0+\frac{1}{2}\mathbf{x}_{12}, y)\,N(\mathbf{x}_{12}, \mathbf{b}_0-\frac{1}{2}\mathbf{x}_{20}, y)]. \qquad (3.7.16)$$

Equation (3.7.16), together with equations (3.7.3), (3.7.4) and (3.7.5), provide us with the leading logarithmic evolution of the F_2 structure function of a hadron including all multiple pomeron exchanges in the large–N_c limit.

Throughout the preceding calculations we never made an assumption that Q^2 is large. Of course it should be large enough for the perturbation theory to be applicable. The only assumption about the incoming photon's momentum that we made was that its light–cone component q_+ is large, therefore we could neglect the inverse powers of q_+. This is eikonal approximation, which is natural for leading $\ln(1/x)$ calculation. However if the inverse power of q_+ comes with an inverse power of q_-, forming something like $1/2q_+q_- \sim 1/Q^2$ we do not neglect these terms, therefore resumming all the inverse powers of Q^2 ("higher twist terms"). That way we proceed to conclude that equation (3.7.16) sums up in the leading logarithmic approximation all diagrams that include the effects of multiple pomeron exchanges, with pomeron ladders together with pomeron splitting vertices being incorporated in the dipole wave function. In terms of conventional (not "wave functional") language Eq. (3.7.16) resums the so called

"fan" diagrams (see Fig. 2) which were summed up by conventional GLR-MQ equation [15, 16]. The difference between our equation and GLR is that Eq. (3.7.16) does not assume leading transverse logarithmic (large Q^2) approximation.

Eq. (3.7.16) can also be derived directly from Eq. (3.7.8) by putting $u(\mathbf{x}_{01}, \mathbf{b}_0) = \gamma(\mathbf{x}_{01}, \mathbf{b}_0) + 1$ in it and noticing that $N = 1 - Z$. That way we have a method of resumming all multiple pomeron exchanges for any higher order corrections to the dipole kernel. If one calculates the dipole kernel, say, at the next-to-lowest order, then we can write down an equation for generating functional Z, similar to Eq. (3.7.8). Though the next-to-lowest order equation will in addition have cubic terms in Z on the right hand side. Then, putting $u = \gamma + 1$ and $Z = 1 - N$ one would easily obtain an equation resumming multiple pomeron exchanges in the subleading logarithmic approximation. Therefore dipole model provides us with a relatively straightforward way of taking into account the multiple pomeron exchanges once the one–pomeron exchange contribution has been calculated. In other words if the dipole kernel is known at any order in the coupling constant one can easily generalize the resulting equation for generating functional to include the multiple pomeron exchanges on a proton.

3.7.4 Double Logarithmic Limit

In order to reconcile our approach with traditional results in this section we will take the large Q^2 limit of Eq. (3.7.16) and show that in this double logarithmic approximation Eq. (3.7.16) reduces to the GLR equation [15, 16]. We consider a scattering of a virtual photon, characterized by large momentum scale Q, on a hadron at rest characterized by the scale Λ_{QCD}. The $Q^2 \gg \Lambda^2_{QCD}$ limit implies that the dipoles produced at each step of the evolution in the dipole wave function must be of much greater transverse dimensions than the dipoles off which they were produced. Basically, since in the double logarithmic approximation the transverse momentum of the gluons in the dipole wave function should evolve from the large scale Q to the small scale Λ_{QCD}, than the transverse sizes of the dipoles should evolve from the small scale $1/Q$ to the large scale $1/\Lambda_{QCD}$.

In the limit when the produced dipoles are much larger than the dipole by which they were produced (large Q^2 limit), the kernel of Eq. (3.7.16) becomes

$$\int_\rho d^2\tilde{x}_2 \frac{x_{01}^2}{x_{02}^2 x_{12}^2} \to x_{01}^2 \pi \int_{x_{01}^2}^{1/\Lambda^2_{QCD}} \frac{dx_{02}^2}{(x_{02}^2)^2}, \tag{3.7.17}$$

where $x_{02} \approx x_{12} \gg x_{01}$, and the upper cutoff of the x_{02} integration is given by the inverse momentum scale characterizing the hadron, $1/\Lambda^2_{QCD}$. Since this integration is done in the region of large transverse sizes the ultraviolet cutoff ρ is no longer needed. One can easily see that including virtual corrections would bring in the exponential factor $e^{-\frac{\alpha C_F}{\pi} Y}$ in the Eqs. (3.7.8) and (3.7.16) instead of $\exp\left[-\frac{4\alpha C_F}{\pi} \ln\left(\frac{x_{01}}{\rho}\right) Y\right]$. In the double logarithmic approximation $\alpha Y \ln(Q^2/\Lambda^2_{QCD}) \geq 1$ and $\ln(Q^2/\Lambda^2_{QCD}) \gg 1$, therefore $\alpha Y \leq 1$. That way the factor of $e^{-\frac{\alpha C_F}{\pi} Y}$ can be neglected. The resulting

limit of Eq. (3.7.16) is

$$N(\mathbf{x}_{01}, \mathbf{b}_0, Y) = -\gamma(\mathbf{x}_{01}, \mathbf{b}_0) + \frac{\alpha C_F}{\pi} x_{01}^2 \int_0^Y dy \int_{x_{01}^2}^{1/\Lambda_{QCD}^2} \frac{dx_{02}^2}{(x_{02}^2)^2} [2\, N(\mathbf{x}_{02}, \mathbf{b}_0, y)$$

$$-N(\mathbf{x}_{02}, \mathbf{b}_0, y)\, N(\mathbf{x}_{02}, \mathbf{b}_0, y)],$$

which after differentiation with respect to Y yields

$$\frac{\partial N(\mathbf{x}_{01}, \mathbf{b}_0, Y)}{\partial Y} = \frac{\alpha C_F}{\pi} x_{01}^2 \int_{x_{01}^2}^{1/\Lambda_{QCD}^2} \frac{dx_{02}^2}{(x_{02}^2)^2} [2\, N(\mathbf{x}_{02}, \mathbf{b}_0, Y)$$

$$-N(\mathbf{x}_{02}, \mathbf{b}_0, Y)\, N(\mathbf{x}_{02}, \mathbf{b}_0, Y)], \tag{3.7.18}$$

where, for simplicity, we suppressed the difference in the impact parameter dependence of N on the left and right hand sides of Eq. (3.7.18). This is done in the spirit of the large cylindrical proton approximation. Also one should keep in mind that for this double logarithmic limit in the definition of $N(\mathbf{x}_{01}, \mathbf{b}_0, Y)$ given by Eq. (3.7.12) the integration over the dipole's transverse sizes should be also done from x_{01}^2 to $1/\Lambda_{QCD}^2$.

Now we have to make a connection between $N(\mathbf{x}_{01}, \mathbf{b}_0, Y)$ and the gluon distribution function $xG_A(x, Q^2)$ of a hadron. $N(\mathbf{x}_{01}, \mathbf{b}_0, Y)$ is a forward scattering amplitude of a $q\overline{q}$ pair on a proton and is a well–defined physical quantity. However there is some freedom in the definition of the gluon distribution. If one makes use of the general definition of the gluon distribution as a matrix element of leading twist operator, then an attempt to take into account higher twist operators would lead only to renormalization of their matrix elements. The evolution equation for xG would be linear, with all the non-linear saturation effects included in the initial conditions. The goal of the GLR type of approach is to put these non-linear effects in the evolution equation. Therefore in the double logarithmic approach one usually defines the gluon distribution function through a cutoff operator product expansion, i.e., as a matrix element of the $A_\mu A_\mu$ operator, with Q^2 an ultraviolet cutoff imposed on the operator (see the discussion on pp. 442-443 of [16]). In the spirit of this approach we define the gluon distribution by

$$N(\mathbf{x}_{01}, \mathbf{b}_0, Y) = \frac{\alpha \pi^2}{2 N_c S_\perp} \mathbf{x}_{01}^2 x G_A(x, 1/x_{01}^2), \tag{3.7.19}$$

with the coefficient fixed by the two gluon exchange between the quark–antiquark pair and the proton (in the large N_c limit). Substituting Eq. (3.7.19) into Eq. (3.7.18) one obtains

$$\frac{\partial x G_A(x, 1/x_{01}^2)}{\partial Y} = \frac{\alpha C_F}{\pi} \int_{x_{01}^2}^{1/\Lambda_{QCD}^2} \frac{dx_{02}^2}{x_{02}^2} [2\, x G_A(x, 1/x_{02}^2) -$$

$$-x_{02}^2 \frac{\alpha \pi^2}{2 N_c S_\perp} [x G_A(x, 1/x_{02}^2)]^2].$$

Differentiating the resulting equation with respect to $\ln(1/x_{01}^2\Lambda_{QCD}^2)$ and using $x_{01} \sim 2/Q$, which is valid in the double logarithmic limit, we end up with

$$\frac{\partial^2 x G_A(x,Q^2)}{\partial \ln(1/x)\,\partial \ln(Q^2/\Lambda_{QCD}^2)} = \frac{\alpha N_c}{\pi} x G_A(x,Q^2) - \frac{\alpha^2 \pi}{S_\perp}\frac{1}{Q^2}[x G_A(x,Q^2)]^2, \qquad (3.7.20)$$

which exactly corresponds to the GLR equation [15, 16], with the factors matching those corresponding to cylindrical proton case in reference [24, 25].

One has to note that the problems with the definition of the gluon distribution function outlined above bear no consequence on Eq. (3.7.16). This equation describes the evolution of $N(\mathbf{x}_{01}, \mathbf{b}_0, Y)$ in the leading $\ln(1/x)$ and does not assume collinear factorization or impose transverse momentum cutoffs, therefore posing no problems like the mixing of operators of different twists.

3.7.5 Approximate Solution of the Nonlinear Evolution Equation

3.7.5.1 Perturbative Solution of the Evolution Equation

Assuming that the typical size of the dipole wave function $x_\perp \ll R$, where R is the proton's radius, we can rewrite Eq. (3.7.16) as

$$\frac{\partial N(\mathbf{x}_{01},Y)}{\partial Y} = \frac{2\alpha C_F}{\pi^2}\int_\rho d^2x_2 \left[\frac{x_{01}^2}{x_{02}^2 x_{12}^2} - 2\pi\delta^2(\mathbf{x}_{01}-\mathbf{x}_{02})\ln\left(\frac{x_{01}}{\rho}\right)\right] N(\mathbf{x}_{02},Y)$$

$$-\frac{\alpha C_F}{\pi^2}\int d^2x_2 \frac{x_{01}^2}{x_{02}^2 x_{12}^2} N(\mathbf{x}_{02},Y)\, N(\mathbf{x}_{12},Y). \qquad (3.7.21)$$

Let us perform a Fourier transform

$$N(x_\perp,Y) = x_\perp^2 \int \frac{d^2k}{2\pi} e^{i\mathbf{k}\cdot\mathbf{x}} \tilde{N}(k,Y) = x_\perp^2 \int_0^\infty dk\, k\, J_0(k x_\perp)\, \tilde{N}(k,Y). \qquad (3.7.22)$$

We note that the inverse of this transformation is

$$\tilde{N}(k,Y) = \int \frac{d^2x}{2\pi x_\perp^2} e^{-i\mathbf{k}\cdot\mathbf{x}} N(x_\perp,Y) = \int_0^\infty \frac{dx_\perp}{x_\perp} J_0(k x_\perp)\, N(x_\perp,Y). \qquad (3.7.23)$$

Since $N(x_\perp,Y)$ does not depend on the direction of $\mathbf{x}_\perp$, $\tilde{N}(k,Y)$ does not depend on the direction of the relative transverse momentum of the $q\bar{q}$ pair $\mathbf{k}_\perp$. That allowed us to simplify the integrations in Eqs. (3.7.22) and (3.7.23). Now Eq. (3.7.21) becomes

$$\frac{\partial \tilde{N}(k,Y)}{\partial Y} = \frac{2\alpha N_c}{\pi}\chi\left(-\frac{\partial}{\partial \ln k}\right)\tilde{N}(k,Y) - \frac{\alpha N_c}{\pi}\tilde{N}^2(k,Y), \qquad (3.7.24)$$

where

$$\chi(\lambda) = \psi(1) - \frac{1}{2}\psi\left(1-\frac{\lambda}{2}\right) - \frac{1}{2}\psi\left(\frac{\lambda}{2}\right) \qquad (3.7.25)$$

is the eigenvalue of the BFKL kernel [2] with $\psi(\lambda) = \Gamma'(\lambda)/\Gamma(\lambda)$. In Eq. (3.7.24) the function $\chi(\lambda)$ is taken as a differential operator with $\lambda = -\partial/\partial \ln k$ acting on $\tilde{N}(k, Y)$. We also put $N_c/2$ instead of C_F everywhere in the spirit of the large N_c approximation. The details of obtaining Eq. (3.7.24) from Eq. (3.7.21) could be found in [8].

We want to find a solution of Eq. (3.7.24) satisfying the initial condition given by the BFKL pomeron contribution at relatively "small" rapidity $Y \sim 1/\alpha$. Unfortunately finding an exact analytical solution of Eq. (3.7.24) seems to be a very difficult task, partly because Eq. (3.7.24) is non–linear, partly because of a complicated structure of the BFKL kernel $\chi(\lambda)$. Instead we are going to construct a series resulting from the perturbative solution of Eq. (3.7.24), which, in the region where it is convergent, provides us with the *exact* solution of Eq. (3.7.24). As we will show below the region of convergence of that series corresponds to the regime when the DIS cross sections and structure functions are *not* saturated. In the saturation regime the series diverges, but allows us to construct an asymptotic solution by analytical continuation.

Let us start by assuming that at $Y \sim 1/\alpha$ the function $\tilde{N}$ is very small, $\tilde{N} \ll 1$. This allows us to neglect the quadratic term in Eq. (3.7.24), since it would be of higher order in $\tilde{N}$. Then Eq. (3.7.24) becomes

$$\frac{\partial \tilde{N}_1(k, Y)}{\partial Y} = \frac{2\alpha N_c}{\pi} \chi\left(-\frac{\partial}{\partial \ln k}\right) \tilde{N}_1(k, Y), \tag{3.7.26}$$

which corresponds to the usual BFKL equation. The solution of Eq. (3.7.26) in the saddle point approximation is given by

$$\tilde{N}_1(k, Y) = C_{-1} \frac{\Lambda}{k} \frac{\exp[(\alpha_P - 1)Y]}{\sqrt{14\alpha N_c \zeta(3) Y}} \exp\left(-\frac{\pi}{14\alpha N_c \zeta(3) Y} \ln^2 \frac{k}{\Lambda}\right) \equiv P_1(k, Y), \tag{3.7.27}$$

a factor usually associated with the zero momentum transfer single hard pomeron exchange, which we denoted by P_1. C_{-1} is determined from initial conditions. If the initial conditions are given by the two gluon exchange approximation, then $C_{-1} \sim \alpha^2$. That way, parametrically, when $Y \sim 1/\alpha$, the amplitude $\tilde{N}_1 \sim \alpha^2 \ll 1$, and our assumption of the smallness of $\tilde{N}$ at $Y \sim 1/\alpha$ is justified.

The scale Λ in Eq. (3.7.27) is a typical scale characterizing the hadron at not very small x. That is this scale should be taken form the initial conditions to our evolution equation given by Eq. (3.7.7). Therefore this scale is the saturation scale at larger values of Bjorken x, when the quantum (BFKL) evolution has not yet become important. This regime corresponds to the quasi–classical approximation and is discussed in [32, 34] more detail.

Eq. (3.7.27) provides us with the usual single BFKL pomeron solution. Now we are going to find corrections to this expression resulting from Eq. (3.7.24). Rewriting $\tilde{N} = \tilde{N}_1 + \tilde{N}_2$, substituting it back into Eq. (3.7.24), neglecting non–linear terms in $\tilde{N}_2$ and employing Eq. (3.7.26) we obtain

$$\frac{\partial \tilde{N}_2(k, Y)}{\partial Y} = \frac{2\alpha N_c}{\pi} \chi\left(-\frac{\partial}{\partial \ln k}\right) \tilde{N}_2(k, Y) - \frac{\alpha N_c}{\pi} \tilde{N}_1(k, Y)^2, \tag{3.7.28}$$

where $\tilde{N}_1$ is known. Eq. 3.7.28 can in its turm be solved to find $\tilde{N}_2$. The procedure could be continued at the end yielding us with the following series in powers of the single pomeron exchange P_1 [8]

$$\tilde{N}(k,Y) = \sum_{n=1}^{\infty} f_n \, P_1(k,Y)^n, \tag{3.7.29}$$

where the coefficients of the series should be determined from the relationship

$$f_n = a_n \sum_{m=1}^{n-1} f_m \, f_{n-m}, \qquad f_1 = 1, \tag{3.7.30}$$

with

$$a_n = \begin{cases} -\frac{1}{2}\, n\, a(k,Y)\{1 + n\, a(k,Y)\,[n\, 2\,\ln 2 - \psi(1) + \psi(n/2)]\}^{-1}, & \text{even } n, \\ \\ -\frac{1}{2}\,\{n\, 2\,\ln 2 - \psi(1) + \psi(n/2)\}^{-1}, & \text{odd } n. \end{cases} \tag{3.7.31}$$

Here

$$a(k,Y) = \frac{\pi \ln(k/\Lambda)}{7\alpha N_c \zeta(3) Y}. \tag{3.7.32}$$

Eqs. (3.7.29), (3.7.30) and (3.7.31) provide us with the exact solution of Eq. (3.7.24) in the kinematic region where the series of Eq. (3.7.29) is convergent. To obtain Eq. (3.7.31) we had to assume that $n\, a(k,Y) \ll 1$ (as $a(k,Y) \ll 1$) and expand the χ functions in the denominators to the first non-singular terms in $a(k,Y)$. Eq. (3.7.29) represents an expansion of the amplitude in terms of multiple hard pomeron exchanges, the nth term in the series corresponding to the n-pomeron exchange contribution.

After analyzing the convergence of the perturbative series in Eq. (3.7.29) we conclude that the constructed perturbation series is convergent as long as [8]

$$\frac{P_1(k,Y)}{r\, 4\,\ln 2} < 1. \tag{3.7.33}$$

where $r \approx 1.4$ is a constant found numerically. Outside the region specified by the condition of Eq. (3.7.33) the series in Eq. (3.7.29) is not convergent anymore. Multiple pomeron exchange contributions corresponding to large values of n become much larger and, consequently, more important than the one- or two-pomeron exchanges. Defining the saturation momentum scale Q_s by the following condition

$$\frac{P_1(Q_s,Y)}{r\, 4\,\ln 2} = 1 \tag{3.7.34}$$

we obtain (for not very large Q_s)

$$Q_s(Y) = Q_s(0)\, \frac{C_{-1}}{r\, 4\,\ln 2}\, \frac{\exp[(\alpha_P - 1)Y]}{\sqrt{14\alpha N_c \zeta(3) Y}}, \tag{3.7.35}$$

where we have denoted $Q_s(0) = \Lambda$. Eq. 3.7.35 describes the saturation scale generated by Eq. (3.7.16) which defines the border between the non-linear saturation region and the region of linear evolution equations plotted in Fig. 1. One can also explicitly see in Eq. (3.7.35) that when energy is not very high and x is not too small ($Y = 0$) the saturation scale reduces back to the saturation scale of the quasi–classical approximations of [32, 34].

3.7.5.2 Inside the Saturation Region

We can assume that in the saturation region $\tilde{N}(k, Y)$ ceases to depend on Y. Then Eq. (3.7.24) reduces to

$$2\,\chi\left(-\frac{\partial}{\partial \ln k}\right)\,\tilde{N}(k,Y) - \tilde{N}^2(k,Y) = 0. \tag{3.7.36}$$

To find the most general solution of Eq. (3.7.36) we represent $\tilde{N}$ as a series

$$\tilde{N}(k,Y) = \sum_{n,m=0}^{\infty} c_{nm}\left(\frac{k}{Q_s}\right)^n \ln^m \frac{Q_s}{k} \tag{3.7.37}$$

and substitute it into Eq. (3.7.36) in order to find the unknown coefficients c_{nm}. One can show that [8]

$$2\,\chi\left(-\frac{\partial}{\partial \ln k}\right)\left[\left(\frac{k}{Q_s}\right)^n \ln^m \frac{Q_s}{k}\right] = \begin{cases} \frac{2}{m+1}\left(\frac{k}{Q_s}\right)^n \ln^{m+1}\frac{Q_s}{k}, & \text{even } n, \\ 2\,\chi(-n)\left(\frac{k}{Q_s}\right)^n \ln^m \frac{Q_s}{k}, & \text{odd } n. \end{cases} \tag{3.7.38}$$

With the help of Eq. (3.7.38) one can show that in order for the series of Eq. (3.7.36) to satisfy Eq. (3.7.36) all of its coefficients must be zero with the exception of $c_{01} = 1$. Thus we proved that the most general energy independent solution of Eq. (3.7.24) is given by [8]

$$\tilde{N}(k,Y) = \ln\frac{Q_s}{k}. \tag{3.7.39}$$

Now that we know the solution for $\tilde{N}(k, Y)$ outside of the saturation region given by Eqs. (3.7.29), (3.7.30) and (3.7.31) and the high energy asymptotics inside the saturation region given by Eq. (3.7.39), one might want to construct the solution in coordinate space ($N(x_\perp, Y)$) using the Fourier transformation of Eq. (3.7.22). To do that one would have to integrate over all values of the transverse momentum k from 0 to ∞. If $x_\perp < 1/Q_s$ then the transverse momentum, which in Eq. (3.7.22) is effectively cut off by the Bessel function and , therefore, varies approximately from 0 to $1/x_\perp > Q_s$, will go through a range of values both above and below Q_s. For the first case one would have to use the perturbation series which we constructed as $\tilde{N}$, while for the second case one might use the asymptotic value of $\tilde{N}$ given by Eq. (3.7.39) ,

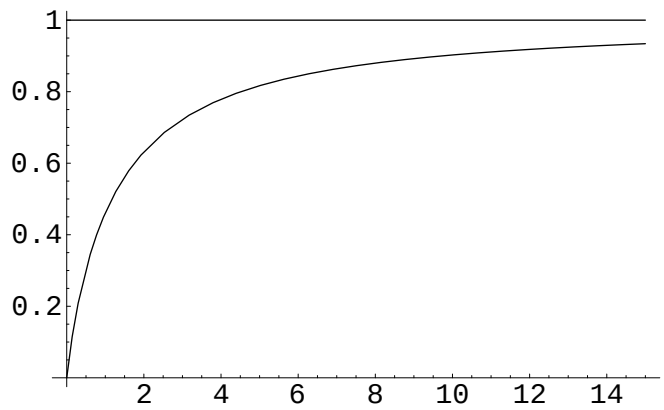

Figure 5: *Plot of the qualitative behavior of the forward $q\overline{q}$ pair scattering amplitude on a hadron, $N(x_\perp, Y)$, as a function of $x_\perp Q_s(Y)$ (one BFKL pomeron exchange contribution). At small values of $x_\perp Q_s$ the structure function is linear in $x_\perp Q_s$, reproducing BFKL pomeron. As energy increases the forward amplitude N saturates to a constant.*

although a perturbative expansion around it would be more accurate. The result would be a complicated combination of special function and we are not going to list it here.

If $x_\perp > 1/Q_s$ then the transverse momentum in Eq. (3.7.22) simply gets cut off by $1/x_\perp < Q_s$ and always stays within the saturation region. Thus one could just perform a Fourier transformation of formula (3.7.39) using Eq. (3.7.22). The result is

$$N(x_\perp, Y) \approx 1, \qquad Y \geq \frac{1}{\alpha_P - 1} \ln \frac{1}{\alpha^2}. \tag{3.7.40}$$

This corresponds to the blackness of the total cross section of the quark–antiquark pair on the target proton, since it is given by

$$\sigma^{tot}_{q\overline{q}A} = 2 \int d^2 b_0 \, N(x_\perp, b_0, Y) \approx 2\pi R^2 \tag{3.7.41}$$

for $N = 1$ and for a cylindrical proton of radius R as described above. That way the total cross section is independent of energy at asymptotically high energies and is completely unitary. It reaches its "geometrical" limit (3.7.41) which could be predicted even from quantum mechanics.

That way we have shown that $N(x_\perp, Y)$ given by the solution of Eq. (3.7.24) behaves like a single BFKL pomeron exchange contribution at moderately high energies ($Y \sim 1/\alpha$), which follows from the perturbation series we have constructed, and as energy increases to very high quantities ($Y \geq \frac{1}{\alpha_P - 1} \ln \frac{1}{\alpha^2}$), saturates to a constant independent of energy. A qualitative sketch of $N(x_\perp, Y)$ as a function of $x_\perp Q_s(Y)$ (one pomeron contribution) is shown in Fig. 5.

3.7.6 Asymptotic Behavior of the F_2 Structure Function

The F_2 structure function is given by

$$F_2(x, Q^2) = \frac{Q^2 R^2}{8\pi^2 \alpha_{EM}} \int d^2x_{01}\, dz\, \Phi(x_{01}, z)\, N(x_{01}, Y), \tag{3.7.42}$$

which follows from Eq. (3.7.3). We can rewrite Eq. (3.7.42) in momentum space using Eq. (3.7.22)

$$F_2(x, Q^2) = \frac{Q^2 R^2}{4\pi \alpha_{EM}} \int d^2k\, dz\, \tilde{\Phi}(k, z)\, \tilde{N}(k, Y), \tag{3.7.43}$$

where

$$\tilde{\Phi}(k, z) = \int \frac{d^2x_{01}}{(2\pi)^2}\, e^{i\mathbf{k}\cdot\mathbf{x}_{01}}\, x_{01}^2\, \Phi(x_{01}, z). \tag{3.7.44}$$

Employing Eqs. (3.7.4) and (3.7.5) we obtain

$$\tilde{\Phi}(k, z) = \frac{\alpha_{EM} N_c}{\pi^2} \left\{ [z^2 + (1-z)^2]\, \frac{2}{3a^2}\, {}_2F_1\left(2, 3, 2.5, -\frac{k^2}{4a^2}\right) + \right.$$

$$+4\, Q^2\, z^2 (1-z)^2\, \frac{1}{15a^6} \left[5\, a^2\, {}_2F_1\left(2, 2, 2.5, -\frac{k^2}{4a^2}\right) \right.$$

$$\left. \left. -2\, k^2\, {}_2F_1\left(3, 3, 3.5, -\frac{k^2}{4a^2}\right) \right] \right\}, \tag{3.7.45}$$

where ${}_2F_1$ is a hypergeometric function.

Eq. (3.7.43) shows that in order to write down an expression for the F_2 structure function one has to know $\tilde{N}(k, Y)$ in the areas above and below saturation. The situation is similar to the Fourier transformation of the previous section. The wave function $\tilde{\Phi}(k, z)$ given by Eq. (3.7.45) becomes very small for transverse momenta $k > a = Q\sqrt{z(1-z)}$, effectively providing an upper cutoff on the k integration. Thus if $Q > Q_s$ the integral over k includes $k < Q_s$ and $k > Q_s$ and to calculate it we have to use the solution for $\tilde{N}$ both inside and outside of the saturation region. We can again propose the approximation outlined in Sect. II for calculation of F_2, which consists of using perturbation series of Eq. (3.7.29) outside saturation region and approximating the solution inside that region by Eq. (3.7.39). The result would also include a complicated list of special functions which we are not going to list here. We have to admit that numerical solution of Eq. (3.7.16) could give a more precise results for F_2. Here we can just point out that at moderately high energies the behavior of the F_2 structure function will be dominated by single BFKL pomeron exchange, providing

us with the following formula which could be obtained by substituting the first term in the series of Eq. (3.7.29) into Eq. (3.7.43)

$$F_2(x,Q^2) = \frac{11}{256} S_\perp N_c Q \Lambda \frac{C_{-1}}{4 \ln 2} \frac{\exp[(\alpha_P - 1)Y]}{\sqrt{14 \alpha N_c \zeta(3) Y}}, \qquad Y \sim \frac{1}{\alpha}, \tag{3.7.46}$$

where we have neglected the transverse momentum diffusion term in the exponent of Eq. (3.7.9) and $S_\perp = \pi R^2$. Eq. (3.7.46) is valid only for moderately high energies, when the saturation momentum Q_s is small and we can neglect the k integration in Eq. (3.7.43) below that scale.

When $Q < Q_s$ or the energy gets very high to sufficiently increase Q_s the integral over k in Eq. (3.7.43) is limited to $k < Q < Q_s$, so that we can use Eq. (3.7.39) for $\tilde{N}(k,Y)$. The result yields

$$F_2(x,Q^2) = \frac{Q^2 R^2 N_c}{3\pi^2} \left(\ln \frac{Q_s}{Q} + \frac{13}{12} \right), \qquad Q < Q_s. \tag{3.7.47}$$

As energy becomes very large, corresponding to $Y \sim \frac{1}{\alpha_P - 1} \ln \frac{1}{\alpha^2}$, $\ln \frac{Q_s}{Q}$ becomes approximately equal to $(\alpha_P - 1)Y$. Therefore

$$F_2(x,Q^2) \approx \frac{Q^2 R^2 N_c}{3\pi^2} (\alpha_P - 1) Y, \qquad Y \geq \frac{1}{\alpha_P - 1} \ln \frac{1}{\alpha^2}. \tag{3.7.48}$$

We conclude that $F_2 \sim \ln s$ at asymptotically high energies. This conclusion may seem to be a little unusual, so we will reproduce the same result using more conventional coordinate space language. As was shown in the previous section the forward amplitude of the $q\overline{q}$ pair scattering on a hadron is $N(x_\perp, Y) = 1$, when $x_\perp > 1/Q_s$. When $x_\perp < 1/Q_s$ one could argue that the amplitude is roughly proportional to some positive power of $x_\perp$, at least $N(x_\perp, Y) \sim x_\perp$, as given by one pomeron exchange. Thus, for $Q < Q_s$ we can neglect the part of the integral with $x_{01} < 1/Q_s$ in Eq. (3.7.42), since the wave function Φ in Eq. (3.7.42) behaves like $\frac{1}{x_{01}^2}$ and is not singular enough to make that portion of the integral significant. That way, expanding the modified Bessel functions in Φ of Eq. (3.7.4) and integrating over z we obtain

$$F_2(x,Q^2) \approx \frac{Q^2 R^2 N_c}{3\pi^2} \int_{1/Q_s}^{1/Q} \frac{dx_{01}}{x_{01}}. \tag{3.7.49}$$

The upper cutoff on the x_{01} integration in Eq. (3.7.49) is provided by the fact that the modified Bessel functions fall off exponentially at the large values of the argument. Integrating over x_{01} in Eq. (3.7.49) we arrive at Eq. (3.7.48).

That way we have shown that the F_2 structure function given by the solution of Eq. (3.7.16) is proportional to the single BFKL pomeron exchange contribution (3.7.46) at moderately high energies with $Y \sim 1/\alpha$, and, as energy increases the F_2 structure function unitarizes, becoming linearly proportional to $\ln s$ (3.7.48). We stress again that even though the cross section of the quark–antiquark pair of a fixed transverse size $x_\perp$ scattering on a hadron saturates to a constant at large Y, the integral over $x_\perp$ makes F_2 depend on Y, such that $F_2 \sim Y$ at very large Y.

3.7.7 Diffractive Dissociation Including Multiple Pomeron Exchanges

Now we are going to study the cross section of the single diffractive dissociation. The physical picture of the process we are going to consider is the following: in DIS the virtual photon interacts with the proton breaking up into hadrons and jets in the final state. At the same time the target proton remains intact. The particles produced as a result of virtual photon's breakup do not fill the whole rapidity interval, leaving a rapidity gap between the target and the "slowest" produced particle.

Below we are going to employ the techniques of Mueller's dipole model [26–29], similarly to the way they were applied above, to construct a cross section of the single diffractive dissociation in DIS which would include the effects of multiple pomeron exchanges.

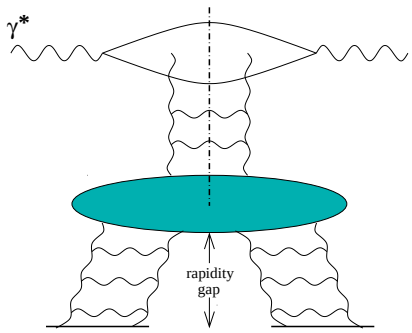

Figure 6: *Traditional description of single diffractive dissociation. Dash-dotted line represents the final state.*

In the traditional description of the single diffractive dissociation one usually considers triple pomeron vertex [35–37], where the pomeron above the vertex is cut, and the two pomerons below the vertex are on different sides of the cut, thus producing a rapidity gap, as shown in Fig. 6. That way the particles are produced by the cut pomeron in the rapidity interval adjacent to the virtual photon's fragmentation region and no particles are produced with rapidities close to the final state of the target due to uncut pomerons. In this paper we want to enhance this picture by including multiple pomeron exchange diagrams. We would like to understand the behavior of the diffractive dissociation at very high energies, which may include some effects of saturation of hadronic structure functions.

An example of a graph in the usual Feynman diagram language which we will consider below is given in Fig. 7. Dash-dotted line corresponds to the final state, i.e., to the cut. As one can see in Fig. 7 some of the pomerons are cut, some remain uncut. In the region of rapidity where pomerons are cut we have particles being produced. In the notation of Fig. 7 this corresponds to the interval in rapidity from $Y - Y_0$ to Y. In the region where the pomerons are uncut (rapidity interval from 0 to Y_0) nothing

is produced, which corresponds to a rapidity gap. That way Fig. 7 demonstrates a generalization of the traditional picture of Fig. (6), in which the cut pomeron splits into two pomerons, which later branch into two uncut pomerons each. Our goal here is to resum all the diagrams where the cut pomeron can split into any number of cut pomerons via fan diagrams, and the cut pomerons in turn split into uncut pomerons, which can also branch into any number of uncut pomerons interacting with the target below.

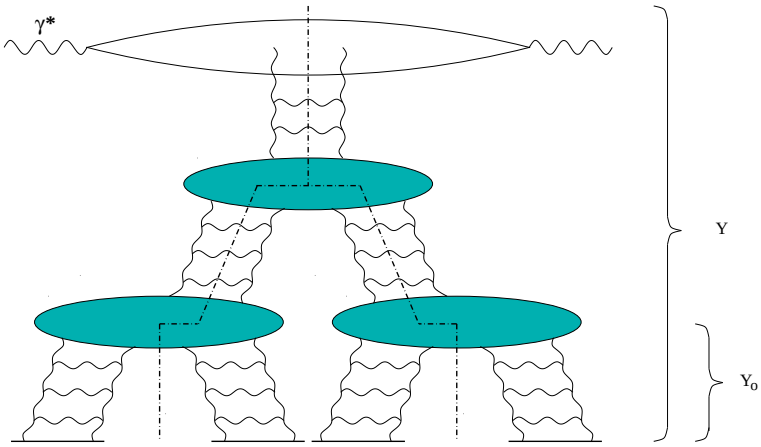

Figure 7: *A diagram contributing to the diffractive dissociation with rapidity gap* Y_0 *as considered in the text.*

Let us denote by $N^D(\mathbf{x}_\perp, \mathbf{b}, Y, Y_0)$ the cross section of single diffractive dissociation of a dipole of transverse size $\mathbf{x}_\perp$, rapidity Y and impact parameter $\mathbf{b}$ on a target hadron. The process has a rapidity gap covering a rapidity interval adjacent to the target (see Fig. 7) which could be greater or equal than Y_0. The corresponding diffractive structure function, similarly to Eq. (3.7.3), is

$$F_2^{SD}(x, Q^2, Y_0) = \frac{Q^2}{4\pi^2 \alpha_{EM}} \int \frac{d^2\mathbf{x}_{01} dz}{4\pi} \Phi(\mathbf{x}_{01}, z)\ d^2b\ N^D(\mathbf{x}_{01}, \mathbf{b}, Y, Y_0). \tag{3.7.50}$$

If one wishes to obtain a cross section of diffractive dissociation of the dipole with a fixed rapidity gap Y_0 one has to differentiate N^D with respect to Y_0, as will be discussed later (see Eq. (3.7.57)). When $Y = Y_0$ the rapidity gap fills out the whole rapidity interval, turning the process of dipole's dissociation into an elastic scattering. We obtain an initial condition for the evolution of N^D [9]

$$N^D(\mathbf{x}_\perp, \mathbf{b}, Y = Y_0, Y_0) = N^2(\mathbf{x}_\perp, \mathbf{b}, Y_0). \tag{3.7.51}$$

One can see that when the energy is not very high we can effectively put $Y = Y_0 = 0$ in Eq. (3.7.51) and using Eq. (3.7.7) we would recover the usual expression for elastic scattering in the quasi-classical approximation [38].

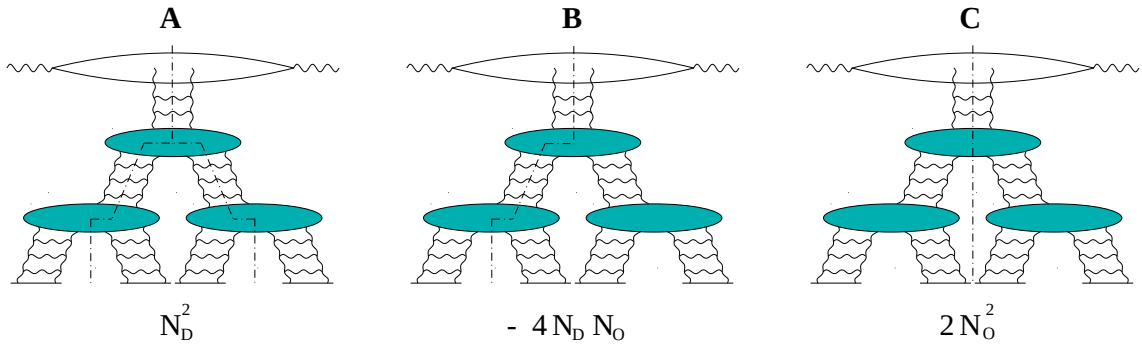

Figure 8: *Different pomeron cuts contributing to the cross section of diffractive dissociation which lead to different terms on the right hand side in Eq. (3.7.52).*

The evolution equation for the cross section of diffractive dissociation N^D has been derived in the language of dipole model in [9]. In terms of the traditional pomeron exchange language it is illustrated in Fig. 8, where N_0 denotes the uncut amplitude N of Eq. (3.7.16). The equation reads

$$N^D(\mathbf{x}_{01}, \mathbf{b}, Y, Y_0) = N^2(\mathbf{x}_{01}, \mathbf{b}, Y_0)\, e^{-\frac{4\alpha C_F}{\pi} \ln\left(\frac{x_{01}}{\rho}\right)(Y-Y_0)} + \frac{\alpha C_F}{\pi^2} \int_{Y_0}^{Y} dy$$

$$\times \int_\rho d^2x_2 \frac{x_{01}^2}{x_{02}^2 x_{12}^2}\, e^{-\frac{4\alpha C_F}{\pi} \ln\left(\frac{x_{01}}{\rho}\right)(Y-y)}\, [2\, N^D(\mathbf{x}_{02}, \mathbf{b} + \frac{1}{2}\mathbf{x}_{12}, y, Y_0)$$

$$+ N^D(\mathbf{x}_{02}, \mathbf{b} + \frac{1}{2}\mathbf{x}_{12}, y, Y_0)\, N^D(\mathbf{x}_{12}, \mathbf{b} + \frac{1}{2}\mathbf{x}_{02}, y, Y_0) - 4\, N^D(\mathbf{x}_{02}, \mathbf{b} + \frac{1}{2}\mathbf{x}_{12}, y, Y_0)$$

$$\times N(\mathbf{x}_{12}, \mathbf{b} + \frac{1}{2}\mathbf{x}_{02}, y) + 2\, N(\mathbf{x}_{02}, \mathbf{b} + \frac{1}{2}\mathbf{x}_{12}, y)\, N(\mathbf{x}_{12}, \mathbf{b} + \frac{1}{2}\mathbf{x}_{02}, y)]. \qquad (3.7.52)$$

Eq. (3.7.52) describes the small-x evolution of the cross section of the single diffractive dissociation for DIS N^D.

Let us define the following object

$$\mathcal{F}(\mathbf{x}_{01}, \mathbf{b}, Y, Y_0) = 2\, N(\mathbf{x}_{01}, \mathbf{b}, Y) - N^D(\mathbf{x}_{01}, \mathbf{b}, Y, Y_0)\, \theta(Y - Y_0), \qquad (3.7.53)$$

which has the meaning of the cross section of the events with rapidity gaps less than Y_0. The theta-function that multiplies N^D in Eq. (3.7.53) insures the trivial fact that the rapidity gap can not be larger than the total rapidity interval. One can see that differentiating Eq. (3.7.52) with respect to Y and employing Eq. (3.7.53) we can write the following equation for $\mathcal{F}$ (when $Y_0 \leq Y$)

$$\frac{\partial \mathcal{F}(\mathbf{x}_{01}, \mathbf{b}, Y, Y_0)}{\partial Y} = \frac{2\alpha C_F}{\pi^2} \int_\rho d^2x_2 \left[\frac{x_{01}^2}{x_{02}^2 x_{12}^2} - 2\pi\delta^2(\mathbf{x}_{01} - \mathbf{x}_{02}) \ln\left(\frac{x_{01}}{\rho}\right)\right]$$

$$\times \mathcal{F}(\mathbf{x}_{02}, \mathbf{b} + \frac{1}{2}\mathbf{x}_{12}, Y, Y_0) - \frac{\alpha C_F}{\pi^2} \int d^2x_2 \, \frac{x_{01}^2}{x_{02}^2 x_{12}^2} \, \mathcal{F}(\mathbf{x}_{02}, \mathbf{b} + \frac{1}{2}\mathbf{x}_{12}, Y, Y_0)$$

$$\times \mathcal{F}(\mathbf{x}_{12}, \mathbf{b} + \frac{1}{2}\mathbf{x}_{02}, Y, Y_0), \tag{3.7.54}$$

with the initial condition

$$\mathcal{F}(\mathbf{x}_{01}, \mathbf{b}, Y = Y_0, Y_0) = 2\, N(\mathbf{x}_{01}, \mathbf{b}, Y_0) - N^2(\mathbf{x}_{01}, \mathbf{b}, Y_0). \tag{3.7.55}$$

Eq. 3.7.54 is identical to Eq. (3.7.21), except for different initial conditions. Since we could not solve Eq. (3.7.21) exactly we can not find an exact analytical solution of Eq. (3.7.54) either. However we may understand the qualitative predictions of Eq. (3.7.54) by employing the following toy model for it [9]

$$\frac{\partial \mathcal{F}(Y)}{\partial Y} = (\alpha_P - 1)\, \mathcal{F}(Y) - (\alpha_P - 1)\, \mathcal{F}(Y)^2. \tag{3.7.56}$$

In order to obtain the toy equation (3.7.56) we have substituted all integral kernels in Eq. (3.7.54) by $\alpha_P - 1$.

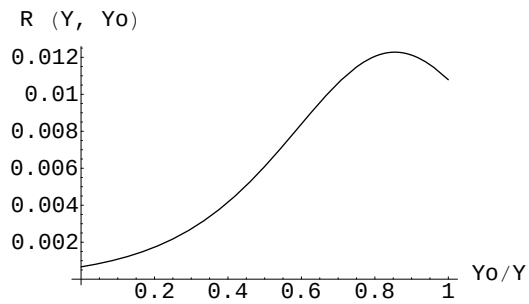

Figure 9: *The cross section of diffractive dissociation in units of πR^2 at fixed Y as a function of Y_0, which is scaled by Y. The elastic contribution is not included.*

Defining the cross section of single diffractive dissociation with the fixed rapidity gap Y_0 by [9]

$$R(\mathbf{x}_{01}, \mathbf{b}, Y, Y_0) = -\frac{\partial N^D(\mathbf{x}_{01}, \mathbf{b}, Y, Y_0)}{\partial Y_0}$$

$$= \frac{\partial \mathcal{F}(\mathbf{x}_{01}, \mathbf{b}, Y, Y_0)}{\partial Y_0} + \delta(Y - Y_0) N^2(\mathbf{x}_{01}, \mathbf{b}, Y_0) \tag{3.7.57}$$

we can find it using the solution of the toy model equation (3.7.56). We demonstrate the qualitative behavior of the cross section of diffractive dissociation $R(Y, Y_0)$ by plotting

the toy model prediction as a function of the size of rapidity gap Y_0 for a fixed center of mass rapidity Y excluding the elastic cross section (delta-function) contribution. This is equivalent to plotting the cross section as a function of the invariant mass of the particles produced in the virtual photon's decay, since $Y_0 = Y - \ln M_X^2/Q^2$. The plot is shown in Fig. 9 and is taken from [9].

Fig. 9 demonstrates that the cross section increases with the size of the rapidity gap over most of the rapidity interval. This is what one would expect from the lowest order diagram with one triple pomeron vertex. Also that implies that it is more advantageous to produce particles with smaller invariant mass M_X^2. However at some very large size of the rapidity gap the cross section $R(Y, Y_0)$ reaches a maximum and starts decreasing. This is a distinct effect of saturation physics and can not be obtained by triple pomeron vertex graphs.We can conclude that experimental observation of the maximum of the cross section of diffractive dissociation at certain size of the rapidity gap would signify the presence of saturation effects in the hadronic structure function.

Acknowledgements

I would like to thank Genya Levin for collaboration on one of the papers that contributed to the above presentation. This work has been supported in part by the U.S. Department of Energy under Grant No. DE-FG03-97ER41014.

References

[1] V.N. Gribov and L.N. Lipatov, Sov. J. Nucl. Phys. **15**, 438 (1972);
G. Altarelli and G. Parisi, Nucl. Phys. **B 126**, 298 (1977);
Yu.L. Dokshitzer, Sov. Phys. JETP **46**, 641 (1977).

[2] E.A. Kuraev, L.N. Lipatov and V.S. Fadin, Sov. Phys. JETP **45**, 199 (1977);
I.I. Balitsky and L.N. Lipatov, Sov. J. Nucl. Phys. **28**, 822 (1978).

[3] M. Froissart, Phys. Rev. **123**, 1053 (1961).

[4] L. McLerran and R. Venugopalan, Phys. Rev. **D 49**, 2233 (1994);
L. McLerran and R. Venugopalan, Phys. Rev. **D 49**, 3352 (1994).

[5] L. McLerran and R. Venugopalan, Phys. Rev. **D 50**, 2225 (1994).

[6] ZEUS Coll., J. Breitweg et al., Eur. Phys. J. **C 7**, 609 (1999).

[7] Y.V. Kovchegov, Phys. Rev. **D 60**, 034008 (2000).

[8] Yu.V. Kovchegov, Phys. Rev. **D 61**, 074018 (2000).

[9] Yu.V. Kovchegov and E. Levin, Nucl. Phys. **B 577**, 221 (2000).

[10] A.H. Mueller, Phys. Lett. **B 396**, 251 (1997).

[11] V.S. Fadin and L.N. Lipatov, Phys. Lett. **B 429**, 127 (1998).

[12] M. Ciafaloni and G. Camici, Phys. Lett. **B 430**, 349 (1998).

[13] Yu.V. Kovchegov and A.H. Mueller, Phys. Lett. **B 439**, 428 (1998).

[14] E. Levin, *The BFKL high-energy asymptotics in the next-to-leading approximation.* Preprint TAUP-2501-98 (hep-ph/9806228), 2000.

[15] L.V. Gribov, E.M. Levin and M.G. Ryskin, Phys. Rept. **100**, 1 (1983).

[16] A.H. Mueller and J. Qiu, Nucl. Phys. **B 268**, 427 (1986).

[17] J. Jalilian-Marian et al., Nucl. Phys. **B 504**, 415 (1997).

[18] J. Jalilian-Marian et al., Phys. Rev. **D 59**, 014014 (1999).

[19] J. Jalilian-Marian et al., Phys. Rev. **D 59**, 034007 (1999).

[20] J. Jalilian-Marian, A. Kovner and H. Weigert, Phys. Rev. **D 59**, 014015 (1999).

[21] A. Kovner, J. G. Milhano and H. Weigert, Phys. Rev. **D 62**, 114005 (2000).

[22] E. Iancu, A. Leonidov and L. McLerran, *Nonlinear gluon evolution in the color glass condensate. I.* Preprint SACLAY-T00-166 (hep-ph/0011241), 2000.

[23] I. Balitsky, Nucl. Phys. **B 463**, 99 (1996).

[24] A.L. Ayala, M.B. Gay Ducati and E.M. Levin, Nucl. Phys. **B 493**, 305 (1997).

[25] A.L. Ayala, M.B. Gay Ducati and E.M. Levin, Nucl. Phys. **B 511**, 355 (1998).

[26] A.H. Mueller, Nucl. Phys. **B 415**, 373 (1994).

[27] A.H. Mueller and B. Patel, Nucl. Phys. **B 425**, 471 (1994).

[28] A.H. Mueller, Nucl. Phys. **B 437**, 107 (1995).

[29] Z. Chen and A.H. Mueller, Nucl. Phys. **B 451**, 579 (1995).

[30] Y.V. Kovchegov, A.H. Mueller and S. Wallon, Nucl. Phys. **B 507**, 367 (1997).

[31] A.H. Mueller, Nucl. Phys. **B 335**, 115 (1990).

[32] Yu.V. Kovchegov and A.H. Mueller, Nucl. Phys. **B 529**, 451 (1998).

[33] N.N. Nikolaev and B.G. Zakharov, Z. Phys. **C 49**, 607 (1991).

[34] Yu.V. Kovchegov, Phys. Rev. **D 54**, 5463 (1996);
Yu.V. Kovchegov, Phys. Rev. **D 55**, 5445 (1997).

[35] A.H. Mueller, Phys. Rev. **D 2**, 2963 (1970).

[36] A.H. Mueller, Phys. Rev. **D 4**, 150 (1971).

[37] V.A. Abramovskii, V.N. Gribov and O.V. Kancheli, Sov. J. Nucl. Phys. **18**, 308 (1974).

[38] Yu.V. Kovchegov and L. McLerran, Phys. Rev. **D 60**, 054025 (1999).

3.8 Diffractive Production of Neutral Vector Mesons

James A. Crittenden [1]
Deutsches Elektronen-Synchrotron
Notkestraße 85, 22603 Hamburg, Germany
James.Crittenden@desy.de

Abstract

We consider the contribution to our understanding of vacuum-exchange processes to be made by investigations at the proposed electron-proton collider THERA. Recent results have highlighted the value of such studies for testing quantum chromodynamical descriptions of both long-range and short-range strong interactions. Stringent quantitative constraints have been provided by exploiting the opportunity to correlate scaling behaviour with helicity selection in exclusive and semi-exclusive vector-meson production. After reviewing the progress achieved by the measurement programs presently being carried out by the H1 and ZEUS collaborations at HERA, we discuss the performance criteria imposed by such investigations on the THERA accelerator complex and on the detector design. We conclude that the study of vector-meson production will form an essential component of the THERA physics program beginning with the early turn-on stage of the machine and continuing throughout the achievement of its full high-luminosity potential.

3.8.1 Introduction

Investigations of vector-meson production at THERA will confront our understanding of strong interaction dynamics, meson and baryon partonic structure, confinement mechanisms, flavour symmetries, scaling laws and helicity selection rules with detailed and multi-various extensions of the wealth of information obtained from the HERA programs presently being carried out by the H1 and ZEUS collaborations. Along with an unprecedented ability for detailed investigations of elastic and total photon-proton cross sections in the Regge limit of high energy, the electron-proton collider experimental strategy has established the research field of short-distance vacuum-exchange processes, or "hard diffraction", as a subject of essential importance to studies of Quantum Chromodynamics. While many of these research topics have built on a foundation of knowledge derived from decades of measurements, many others are completely new and only beginning to receive theoretical attention. All the topics have stimulated widespread theoretical and phenomenological interest, confirming existing theoretical prejudices in some cases, and clearly guiding theoretical approaches in others. The experimental opportunity presented by the THERA accelerator design directly addresses

[1] On leave from the Physikalisches Institut, University of Bonn, Nußallee 12, 53115 Bonn, Germany

the need for an extension of the energy range both for approaches based on Regge phenomenology and for those based on perturbative and nonperturbative QCD. Even more importantly, THERA will extend the kinematic reach in momentum transfer by more than an order of magnitude, providing clean and detailed test of quantitative perturbative calculations of strong vacuum-exchange processes.

There are several simple reasons for the extraordinary variety of theoretical physics concepts addressed by the study of diffractive vector-meson production in electron-proton interactions. Even at a fixed electron-proton centre-of-mass energy, a broad range of energies in the photon-proton centre-of-mass system is available for investigation. Such a broad range of energy is of essential importance for studies of the weak energy dependence of soft diffractive processes. The corresponding access to the low-x region means that the coherence length of the virtual photons in the proton rest frame is much longer than the diameter of the proton [1], resulting in an unambiguous definition of virtual-photon/proton cross sections and hence the opportunity to study their scaling behaviour and helicity-transfer characteristics. Figure 1 shows the energy dependence of this cross section measured at HERA.

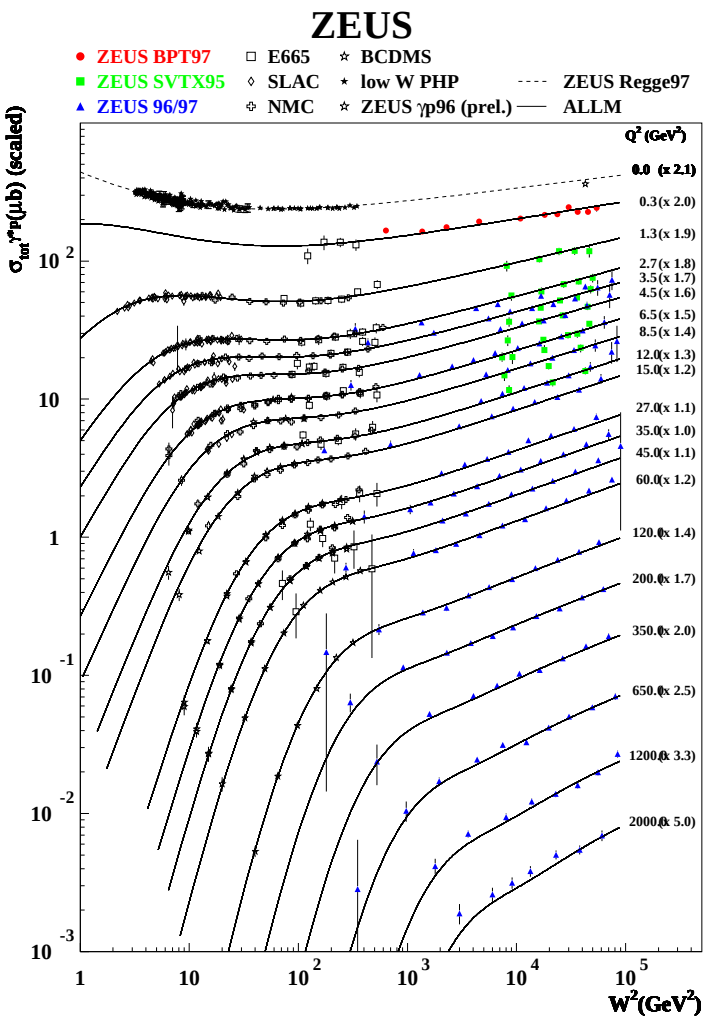

Figure 1: *The photon–proton cross section $\sigma_{tot}^{\gamma^* p}$ as a function of the squared centre–of–mass energy for various values of Q^2. The curves represent calculations using the ALLM parton distribution function parameterisations [2].*

The remarkably steep energy dependence at high photon virtuality reflects the steep rise in the F_2 structure function at low x. Such high energies and wide rapidity ranges provide access to the kinematic region of diffractive processes, where the momentum transfers are much smaller than the kinematic limit. In the context of Regge phenomenology, recent investigations interpret the Q^2 dependence exhibited in the photon-proton cross section as evidence for the discovery of a second, "hard" Pomeron [3]. HERA results also show that accurate measurements can be made at momentum transfers far exceeding the hadronic confinement scale yet also fulfilling this diffractive condition. The analysis of exclusive and semi-exclusive vector-meson production (see Fig. 2) in the photon-dissociation region ensures the selection of vacuum-

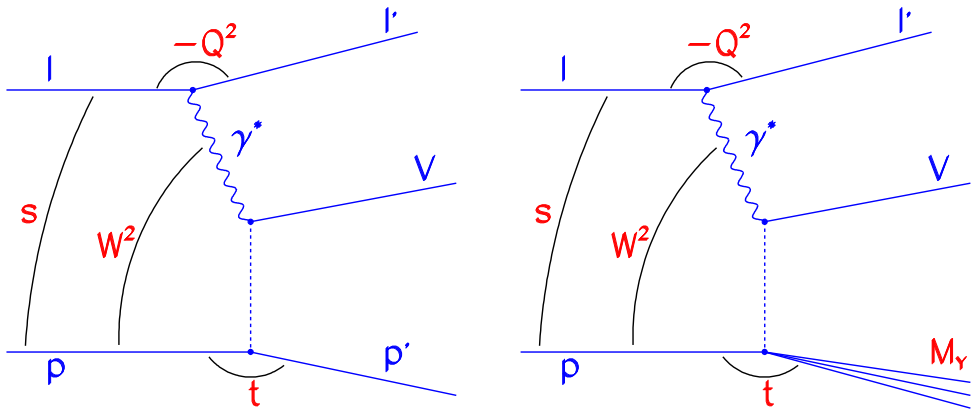

Figure 2: *Schematic diagrams of a) exclusive and b) semi-exclusive electroproduction of vector mesons. Such processes permit the study of vacuum-exchange processes in perturbative and nonperturbative kinematic domains, including the correlation of the helicity-transfer structure with the observed power-law scaling with momentum transfer for momentum transfers exceeding the hadronic confinement scale. The proton-dissociative process can be studied in both the nucleon-resonance and high-mass regions, providing information on Regge factorisation and on proton structure.*

exchange processes [4]. Since this selection can be done with little influence on the kinematics of the reaction, general questions concerning its characteristics can be addressed, in particular the momentum-transfer scaling behaviour. At low momentum transfer, this permits investigation of phenomena described by Regge theory, such as the Pomeron trajectory and unitarity [5]. At high momentum transfer, such experimental studies address the strong interaction dynamics of vacuum exchange on distance scales much smaller than the confinement scale, presently a subject of active theoretical speculation. Particular to these studies of the production of phase-space-isolated vector mesons is the clean experimental environment allowing exploitation of the two-charged-particle decays to measure spin-density matrices with high accuracy. Quantitative assessment of helicity-violating amplitudes provides information on the partonic structure of the vector meson [6]. Since the momentum-transfer scaling behaviour is correlated to the helicity structure of the interaction [7, 8], these measurements provide

strict constraints on field theoretical approaches and the associated power-law scaling features. The proton-dissociative process can be studied in both the nucleon-resonance and high-mass regions, providing information on Regge factorisation and on proton structure.

This highly varied phenomenology provides an extraordinarily rich experimental laboratory for testing new theoretical ideas. We will see in the following that the proposed THERA project is particularly well adapted for tests of quantum chromodynamical descriptions of this high-energy domain.

3.8.2 Lessons from HERA

Experimental investigations of vector-meson production at HERA [9–12] (see [13] for a review) have provided a wide variety of insights into the dynamics of both soft and hard diffractive processes. The high flux of quasi-real photons from the electron beam permitted detailed measurements of both elastic and proton-dissociative photoproduction of ρ^0, ω, ϕ, J/ψ, and Υ mesons. Power-law scaling with the photon-proton centre-of-mass energy, $W_{\gamma p}$, was observed for the J/ψ, as is illustrated by Fig. 3.

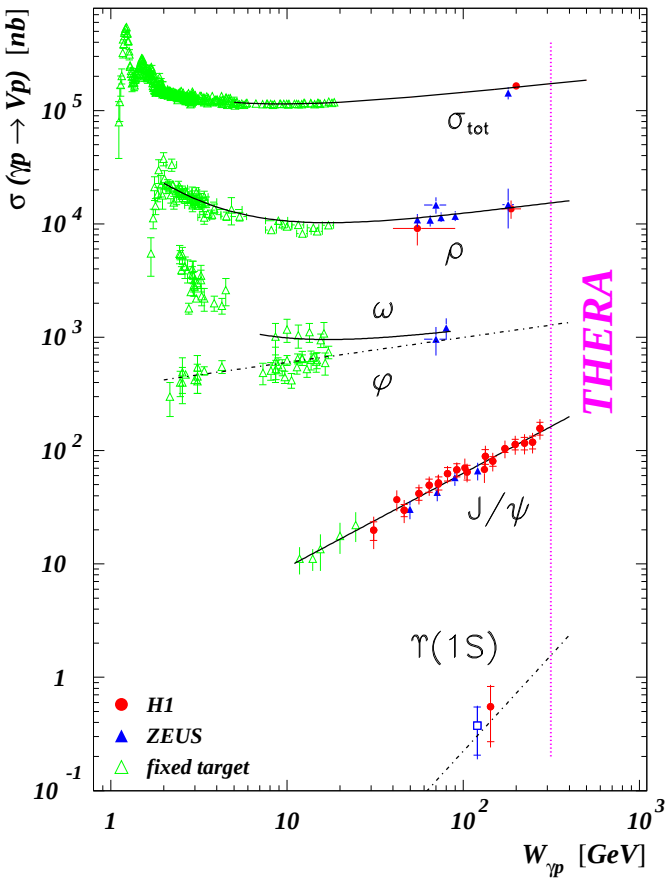

Figure 3: *Energy dependence of vector-meson photoproduction cross sections for ρ^0, ω, ϕ, J/ψ, and Υ mesons [14].*

It is instructive to compare the energy dependence of these vector-meson production cross sections to the photon-proton cross sections shown in Fig. 1, where the steep en-

ergy dependence arises from the x dependence of the gluon density in the proton. The steep energy dependence measured for J/ψ mesons encouraged a number of theoretical approaches based on perturbative QCD [15]. Figure 4 shows a diagram illustrating this

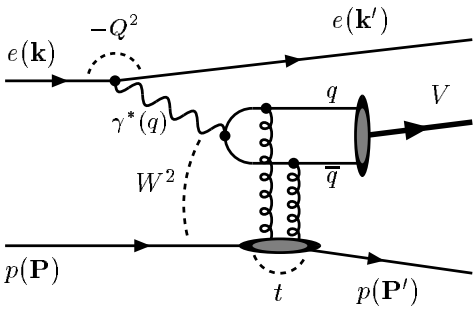

Figure 4: *Schematic diagram illustrating exclusive vector-meson production as mediated by the exchange of a gluon pair in a colour-singlet state*

approach. Salient features of such calculations are an energy dependence determined by the gluon density in the proton, flavour symmetry and the predominance of the longitudinal cross section for the light vector mesons at high momentum transfer. The HERA measurement of Υ photoproduction resulted in theoretical investigations [16] which predict a very strong energy dependence into the THERA region, with a large contribution from the off-diagonal gluon density. The phenomenological success of these calculations supports the view that the factorisation scale can be related to quark mass. Factorisation theorems have also been the object of theoretical investigations invoking the photon virtuality [8, 17, 18] and the momentum transferred to the proton [19] as hard scales in the production of vector mesons. These calculations demonstrated remarkable sensitivity to the gluon density in the proton, since the forward cross sections were shown to be proportional to its square. Measurements at HERA of ρ^0, ω, ϕ electroproduction and high-t photoproduction have served as testing grounds for these calculations. Of particular interest is the experimental access to the helicity structure of these processes via analysis of decay-angle distributions, since these reflect not only the helicity selection rules but also meson structure [6]. Figure 5 compares the ZEUS measurement of the differential cross section $\mathrm{d}\sigma_{\mathrm{L}}^{\gamma^\star \mathrm{p}}/\mathrm{d}|t|\Big|_{t=0}$ for ρ^0 production to the results of QCD calculations [10], illustrating the degree of consistency. The H1 collaboration has shown a remarkably consistent scaling behaviour common to the ρ^0, ω, ϕ, and J/ψ mesons by plotting the production cross sections as a function of $\mathrm{Q}^2 + \mathrm{M}_{\mathrm{V}}^2$, as shown in Fig. 6 [9]. This smooth behaviour is surprising from the point of view of the QCD models, given that the helicity analyses have shown the relative contributions of the longitudinal and transverse cross sections to depend strongly on Q^2, and the QCD models predict very different scaling behaviour for these two contributions. An investigation into high-t ρ^0 and ϕ photoproduction by the ZEUS collaboration [24] has recently turned up another surprise. This first measurement of vector-meson photoproduction at momentum transfers far exceeding the hadronic confinement scale, extending into a region where power-law scaling is observed, permits an accurate determination of the power. It was found that the ϕ/ρ^0 ratio reaches the SU(3) symmetric value in the same region of momentum transfer where the power-law scaling takes over from

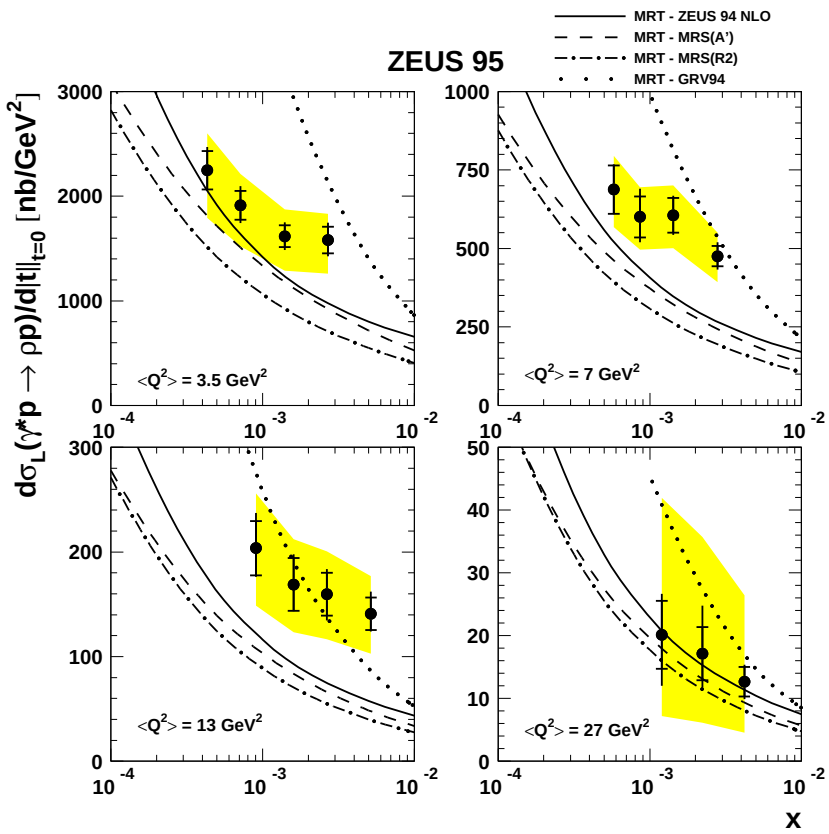

Figure 5: *The measured forward longitudinal cross section,* $\mathrm{d}\sigma_{\mathrm{L}}^{\gamma^\star \mathrm{p}}/\mathrm{d}|t|\Big|_{t=0}$, *as a function of* x *for* ρ^0 *electroproduction [10]. The inner error bars represent statistical uncertainties; the outer error bars indicate the quadratic sum of statistical and systematic uncertainties. The shaded areas indicate additional normalisation uncertainties due to the proton dissociation background subtraction as well as the measured values of the* $R = \sigma_{\mathrm{L}}^{\gamma^\star \mathrm{p}}/\sigma_{\mathrm{T}}^{\gamma^\star \mathrm{p}}$ *ratio and the t-slope parameter b. The curves show the predictions by Martin, Ryskin and Teubner [18] and correspond to various gluon parameterisations, indicated as follows: full lines – ZEUS 94 NLO [20], dashed lines – MRSA′ [21], dashed-dotted lines – MRSR2 [22], and dotted lines – GRV94 [23].*

the exponential dependence observed at low t. The measurements of the decay-angle distributions showed the vector mesons to be transverse. This result, together with the extremely hard spectrum observed in the t distribution (see Fig. 7) [25], appears to be at odds with the QCD helicity selection rules [19].

These studies of exclusive vector-meson production have shown that the transition region from the domain of applicability of perturbation theory to the domain where long-distance strong-interaction dynamics applies can be scanned in photon virtuality and in the momentum transfer at the proton vertex. Such measurements have led to detailed theoretical consideration of the interaction size scaling with energy [26, 27] and the relationship of diffraction to the mechanism of confinement [28].

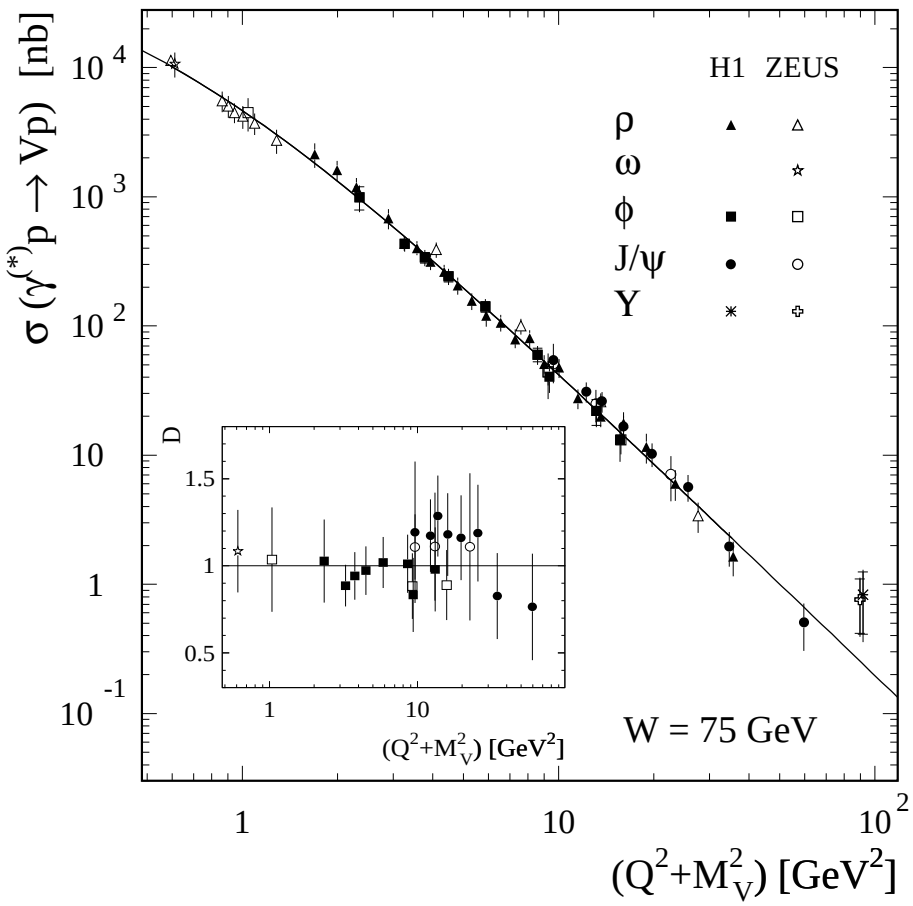

Figure 6: *H1 and ZEUS measurements of the cross sections $\sigma(\gamma^* \to Vp)$ as a function of $(Q^2 + \mathrm{M}_\mathrm{V}^2)$ for elastic ρ^0, ω, ϕ, J/ψ and Υ production at the fixed value $W = 75$ GeV. The cross sections were scaled by SU(5) factors according to the quark charge content of the vector mesons. The error bars show statistical and systematic uncertainties added in quadrature. The curve corresponds to a fit to the H1 and ZEUS ρ^0 data, and the ratio, D, of the scaled ω, ϕ and J/ψ cross sections to this parameterisation is presented in the insert.*

3.8.3 Requirements on the performance of machine and detector

Measurements of vector-meson production at THERA will benefit not only from the extended kinematic reach to low x (high energy, wider rapidity range) and high Q^2, but also from the improved coverage of the THERA detector at small angles and from tagging systems in both the proton and electron flight directions designed with forethought and the benefit of the experience obtained at HERA. This experience has made clear the importance of careful design and close interaction with the THERA machine group. In the forward direction, the lack of high-t acceptance in the proton spectrom-

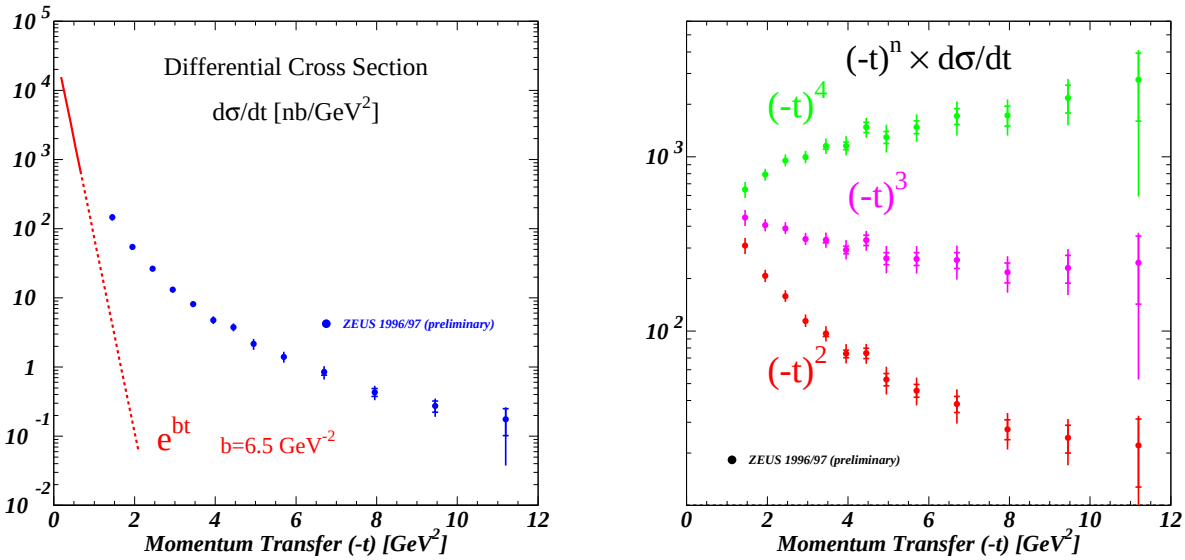

Figure 7: *a) Differential cross section* $\frac{d\sigma}{dt}$ *for the process* $\gamma + p \to \rho^0 + Y$*, where* Y *is a dissociated proton state. The line shows the* t *dependence measured for this process* $\gamma + p \to \rho^0 + Y$ $(\propto e^{6.5 \cdot t})$ *[11] at low* $|t|$ *(solid line) and its extrapolation to higher* $|t|$ *(dashed line) for comparison. b) Differential cross section* $\frac{d\sigma}{dt}$ *multiplied by (-t)*^{n}*, where n=2, 3, 4.*

eters prevents HERA studies of essential importance to QCD descriptions of exclusive processes. A lack of instrumentation in the the region of proton dissociation has resulted in the dominant source of systematic uncertainties for the measurement of elastic cross sections being the subtraction of this background. At THERA, improvement will come from requirements on the detector geometry independent of those imposed by studies vector-meson production [29], but further instrumentation of the low-M_Y region must also be taken into careful consideration. In the rear direction, a series of photoproduction taggers with associated bending magnets to select off-beam-momentum electrons will provide full coverage of the available range in W. The additional tracking coverage in the rear direction required by the investigations of inclusive processes at low-x will enable precise measurements of the vector-meson decay products, and so permit accurate reconstruction of t and and the decay-angles at high W. This is particularly important for the light vector mesons, since the hadronic decays used for their identification, together with the limited rear tracking in the H1 and ZEUS detectors result in a limitation to the W range of $W \lesssim 150$ GeV.

The program of measurements described above has been performed with an integrated luminosity corresponding to that estimated for less than one year's running time at THERA. The weak energy dependence of the diffractive cross sections at low momentum transfer for the light vector mesons ensures a high data rate during the early

THERA running, making vector-meson production a principal contribution to the early physics program, just as was the case at HERA. However, many of the HERA studies of vector-meson production will remain statistics-limited. In particular, multiply differential studies of the perturbative region of photon virtuality and momentum transfer to the proton require high integrated luminosity. Another example of investigations requiring stable accelerator performance at high luminosity are those of diffractive J/ψ and Υ photoproduction. Elastic electroproduction of Υ mesons, where effects of the off-diagonal parton densities are dominant, await THERA operation. The helicity analyses of vector-meson production benefit from the longitudinal electron polarisation of the electron beam at THERA, since the spin-density matrix elements arising from circular photon polarisation are otherwise inaccessible [30]. The high cross sections at low momentum transfer and the need for high statistics in the kinematic region of applicability of perturbative calculational techniques mean that the study of vector-meson production will play an important rôle in the THERA physics program beginning with the early turn-on stage of the machine and continuing throughout the achievement of its full high-luminosity potential.

3.8.4 Conclusions

The proposed THERA accelerator complex is conceived in the interest of extending the energy frontier in our understanding of electron-proton interactions. Simple extrapolation from the experience gained during the first nine years of HERA operation yield the reliable conclusion that THERA will make essential contributions to our understanding of the dynamics of strong interactions and, in particular, to the application of Quantum Chromodynamics as a means to achieve this understanding. The theoretical descriptions of the short-distance vacuum-exchange processes under investigation at HERA remain in their infancy; the discovery potential remains high. The parameters of the THERA machine directly address limitations to the present investigations of vector-meson production at HERA. The broad kinematic ranges in energy and momentum transfer accessible to the experimental investigation of diffractive vector-meson production ensure that such studies will make essential contributions to the THERA physics program throughout the entire duration of its operation.

Acknowledgements

The author thanks B. Surrow for providing Fig. 1. This work was supported by the Federal Ministry for Education and Research of Germany.

References

[1] B.L. Ioffe, V.A. Khoze and L.N. Lipatov, Hard Processes, Vol. 1. North Holland, Amsterdam, 1984.

[2] H. Abramowicz et al., Phys. Lett. **B269**, 465 (1991).

[3] A. Donnachie and P.V. Landshoff, hep-ph/0105088, 2001.

[4] J.A. Crittenden for the H1 and ZEUS collaborations, in *Newport News 1999, Exclusive and Semi-exclusive Processes at High Momentum Transfer*, eds. C. Carlson and A. Radyuskin, p. 89. World Scientific, Singapore, 1999, hep-ex/9910068.

[5] Y. Kovchegov, contributed to the THERA Book, DESY-LC-REV-2001-062 (2001).

[6] D.Yu. Ivanov and R. Kirschner, Phys. Rev. **D58**, 114026 (1998);
I. Royen and J.R. Cudell, Nucl. Phys. **B 545**, 505 (1999);
I.P. Ivanov and N.N. Nikolaev, JETP Lett. **69**, 294 (1999).

[7] S.J. Brodsky and G.P. Lepage, Phys. Rev. **D22**, 2157 (1980);
V.L. Chernyak and A.R. Zhitnitsky, Phys. Rep. **112**, 173 (1984).

[8] J.C. Collins, L. Frankfurt and M. Strikman, Phys. Rev. **D56**, 2982 (1997).

[9] H1 Coll., C. Adloff et al., Phys. Lett. **B483**, 360 (2000).

[10] ZEUS Coll., J. Breitweg et al., Eur. Phys. J. **C6**, 603 (1999).

[11] ZEUS Coll., J. Breitweg et al., Eur. Phys. J. **C2**, 247 (1998).

[12] H1 Coll., C. Adloff et al., Eur. Phys. J. **C13**, 371 (2000);
H1 Coll., C. Adloff et al., Phys. Lett. **B483**, 23 (2000);
H1 Coll., C. Adloff et al., Eur. Phys. J. **C10**, 373 (1999);
H1 Coll., C. Adloff et al., Phys. Lett. **B421**, 385 (1998);
H1 Coll., C. Adloff et al., Z. Phys. **C75**, 607 (1997);
H1 Coll., S. Aid et al., Nucl. Phys. **B472**, 3 (1996);
H1 Coll., S. Aid et al., Nucl. Phys. **B468**, 3 (1996);
H1 Coll., S. Aid et al., Nucl. Phys. **B463**, 3 (1996);
H1 Coll., S. Aid et al., Phys. Lett. **B338**, 507 (1994);
ZEUS Coll., J. Breitweg et al., Phys. Lett. **B487**, 273 (2000);
ZEUS Coll., J. Breitweg et al., Eur. Phys. J. **C12**, 393 (2000);
ZEUS Coll., J. Breitweg et al., Eur. Phys. J. **C14**, 213 (2000);
ZEUS Coll., J. Breitweg et al., Phys. Lett. **B437**, 432 (1998);
ZEUS Coll., J. Breitweg et al., Z. Phys. **C76**, 599 (1997);
ZEUS Coll., J. Breitweg et al., Z. Phys. **C75**, 215 (1997);
ZEUS Coll., M. Derrick et al., Z. Phys. **C73**, 253 (1997);
ZEUS Coll., M. Derrick et al., Phys. Lett. **B380**, 220 (1996);
ZEUS Coll., M. Derrick et al., Phys. Lett. **B377**, 259 (1996);
ZEUS Coll., M. Derrick et al., Z. Phys. **C73**, 73 (1996);
ZEUS Coll., M. Derrick et al., Z. Phys. **C69**, 39 (1995);
ZEUS Coll., M. Derrick et al., Phys. Lett. **B356**, 601 (1995);
ZEUS Coll., M. Derrick et al., Phys. Lett. **B350**, 120 (1995).

[13] J.A. Crittenden, *Exclusive Production of Neutral Vector Mesons at the Electron-Proton Collider HERA*, in Springer Tracts in Modern Physics, Vol. 140. (Springer, Berlin Heidelberg, 1997).

[14] P. Merkel, *Diffractive Photoproduction of Heavy Vector Mesons at HERA*. Ph.D. Thesis, University of Hamburg, 1999.

[15] M.G. Ryskin, Z. Phys. **C57**, 89 (1993);
M.G. Ryskin et al., Z. Phys. **C76**, 231 (1997);
L. Frankfurt, W. Koepf and M. Strikman, Phys. Rev. **D57**, 512 (1998).

[16] A. D. Martin, M. G. Ryskin and T. Teubner, Phys. Lett. **B454**, 339 (1999);
L.L. Frankfurt, M.F. McDermott and M. Strikman, JHEP **9902**, 2 (1999). (hep-ph/9812316).

[17] S.J. Brodsky et al., Phys. Rev. **D50**, 3134 (1994).

[18] A.D. Martin, M.G. Ryskin, and T. Teubner, Phys. Rev. **D55**, 4329 (1997);
L. Frankfurt, W. Koepf and M. Strikman, Phys. Rev. **D 54**, 3194 (1996);
J. Nemchik et al., Phys. Lett. **374**, 199 (1996).

[19] D.Yu. Ivanov et al., Phys.Lett. **B**478, 101 (2000); erratum-ibid. **B**498, 295 (2001);
D.Yu. Ivanov, Phys. Rev. **D53**, 3564 (1996);
I.F. Ginzburg and D.Yu. Ivanov, Phys. Rev. **D54**, 5523 (1996);
S.J. Brodsky et al., Phys. Lett. **B449**, 306 (1999);
J.R. Forshaw and M.G. Ryskin, Z. Phys. **C68**, 137 (1995);
J. Bartels et al., Phys. Lett. **B375**, 301 (1996).

[20] ZEUS Coll., M. Derrick et al., Z. Phys. **C72**, 399 (1996).

[21] A.D. Martin, W.J. Stirling and R.G. Roberts, Phys. Lett. **B 354**, 155 (1995).

[22] A.D. Martin, R.G. Roberts and W.J. Stirling, Phys. Lett. **B 387**, 419 (1996).

[23] M. Glück, E. Reya and A. Vogt, Z. Phys. **C67**, 433 (1995).

[24] ZEUS Coll., J. Breitweg et al., Paper 442 submitted to the XXX Int. Conf. on High Energy Physics, 27 July - 2 August, 2000, Osaka, Japan.

[25] J.A. Crittenden, in *Proceedings of DPF2000: The Meeting of the Division of Particles and Fields*. American Physical Society, Columbus, Ohio, USA, 2000, hep-ex/0010079.

[26] E. Gotsman et al., hep-ph/0010198, contributed to the THERA Book, DESY-LC-REV-2001-062 (2001).

[27] A. Levy, Phys. Lett. **B424**, 191 (1998).

[28] J. Bartels and H. Kowalski, hep-ph/0010345, 2000.

[29] J.A. Crittenden et al., *A Detector for THERA*, contributed to the THERA Book, DESY-LC-REV-2001-062 (2001).

[30] K. Schilling and G. Wolf, Nucl. Phys. **B61**, 381 (1973).

4 Proton Structure and Quantum Chromodynamics

4.1 Heavy Quark Production Measurements at THERA

L. Gladilin
Weizmann Institute, Department of Particle Physics,
Rehovot, Israel
on leave from Moscow State University
gladilin@mail.desy.de

I. Redondo
Universidad Autónoma de Madrid,
Departamento de Física Teórica, Madrid, Spain
redondo@mail.desy.de

Abstract

The total cross sections of charm and beauty production at a future high–energy *ep* collider, THERA, are expected to increase by factors of three and five, respectively, as compared to HERA. Heavy quarks can be measured at THERA in wide ranges of transverse momenta and Q^2 values, thereby providing a solid basis for testing the perturbative QCD calculations. The charm and beauty contributions to the proton structure can be probed at THERA at ~ 1 order of magnitude smaller Bjorken x values with respect to those at HERA. Charm production in the process of photon–gluon fusion at THERA can serve for the determination of the gluon structure of the proton in the as yet unexplored kinematic range $10^{-5} < x_g < 10^{-4}$. The cross section of charm production in charged current at THERA is ~ 1 order of magnitude larger than that at HERA.

4.1.1 Introduction

Heavy quarks are produced copiously at HERA which provides collisions between electrons or positrons with energy $E_e = 27.5$ GeV and protons with energy $E_p = 920$ GeV [1]. The total charm and beauty cross sections at HERA are of the order of 1 μb and 10 nb, respectively [1]. In photoproduction processes at HERA, a quasi-real photon with virtuality $Q^2 \sim 0$ is emitted by the incoming electron and interacts with the proton. At leading order (LO) in QCD two types of processes are responsible for the production of heavy quarks: the direct photon processes, where the photon participates as a point-like particle, and the resolved photon processes, where the photon acts as a source of partons. The dominant direct photon process is photon–gluon fusion (PGF) where the photon fuses with a gluon from the incoming proton. In resolved photon processes, a parton from the photon scatters off a parton from the proton. Charm and beauty quarks present in the parton distributions of the photon, as well as of the proton, lead to processes like $cg \to cg$ and $bg \to bg$, which are called heavy flavour excitation processes. In next-to-leading order (NLO) QCD only the sum of direct and resolved processes is unambiguously defined. The resolved photon processes are suppressed in deep inelastic scattering (DIS) at HERA because the virtuality of the exchanged photon is typically selected to be $Q^2 > 1\,\mathrm{GeV}^2$.

Charm production at HERA has been studied by the H1 and ZEUS collaborations in both the photoproduction and DIS regimes [2–5]. A description of the charm photoproduction cross sections is rather problematic for present perturbative QCD (pQCD) calculations. The fixed-order NLO calculations [6] are generally below the measured cross sections, in particular in the forward (proton) direction [3, 5]. The fixed-order approach assumes that gluons and light quarks (u,d,s) are the only active partons in the structure functions of the proton and the photon. In this approach there is no explicit heavy flavour excitation component and heavy quarks are produced only dynamically in hard pQCD processes. The resummed NLO calculations [7–9] treat charm as an additional active parton in the structure functions. These calculations are valid only if the heavy quark transverse momentum is much larger than $M_{c,b}$, where $M_{c,b}$ is the charm or beauty quark mass. The resummed NLO predictions of [7, 8] are rather close to the measured cross sections [3].

The fixed-order or three flavour Fixed Flavour Number Scheme (FFNS) calculations for charm production in DIS [10] agree with the cross sections measured at HERA [2, 4]. These calculations are expected to be less reliable when $Q^2/M_c^2 \gg 1$. In this range the $\ln(Q^2/M_c^2)$ terms should be resummed and absorbed into the charm distribution function in the proton [11–13].

The first measured beauty photoproduction cross sections at HERA [14, 15] lie above the fixed-order NLO QCD predictions [6, 16]. The preliminary value of the beauty production cross section in the DIS regime at HERA, reported recently by the H1 collaboration [17], exceeds the FFNS prediction [10].

Future THERA collider will utilize proton beam from HERA and electron beam prepared with one or both arms of the TESLA e^+e^- linear collider. Using only one arm

[1] The proton energy was 820 GeV from 1992 to 1997.

of the electron accelerator, electron energies of 250 GeV and 400 GeV can be reached in the first and second stages of TESLA, respectively. The electron energy can be as large as 800 GeV employing both TESLA arms. An increase of the centre-of-mass energy of *ep* collisions from about 300 GeV at HERA to $\sim$ 1 TeV at THERA will result in quite significant increase of the total heavy quark production cross sections. Tables 4.1.1 and 4.1.2 show LO estimations of the cross sections in direct and resolved photon processes, respectively. The estimations were obtained with the LO Monte Carlo program HERWIG [18].

Collider	charm [μb]	beauty [nb]	top [fb]
HERA, $E_e = 27.5$ GeV	0.6	4.3	–
THERA, $E_e = 250$ GeV	1.6	17	6.9
THERA, $E_e = 400$ GeV	1.9	22	26
THERA, $E_e = 800$ GeV	2.4	32	$1.2 \cdot 10^2$

Table 4.1.1: *Cross sections of charm, beauty and top production in direct photon processes at HERA and THERA estimated with the LO Monte Carlo program HERWIG.*

Collider	charm [μb]	beauty [nb]	top [fb]
HERA, $E_e = 27.5$ GeV	0.3	1.4	–
THERA, $E_e = 250$ GeV	1.2	14	0.2
THERA, $E_e = 400$ GeV	1.6	21	0.6
THERA, $E_e = 800$ GeV	2.5	38	1.9

Table 4.1.2: *Cross sections of charm, beauty and top production in resolved photon processes at HERA and THERA estimated with the LO Monte Carlo program HERWIG.*

The total charm and beauty production cross sections at THERA with E_e = 250 GeV are larger than those at HERA by factors $\sim$ 3 and $\sim$ 5, respectively. They grow further with the increase of the electron beam energy. The growth is larger for heavy quark production in the resolved photon processes. The total cross sections of top quark production at THERA with E_e = 250 GeV and E_e = 800 GeV are of the order of 10 fb and 100 fb, respectively.

4.1.2 Heavy quark photoproduction and proton gluon structure

Charm and beauty production in *ep* collisions is dominated by photoproduction with $Q^2 \sim 0$. In this regime both direct and resolved photon contributions are sizable. Prospects for investigations of heavy quark production in resolved photon processes at THERA are discussed elsewhere in this book [19]. In this section we will discuss charm and beauty photoproduction in direct photon processes and its sensitivity to the gluon structure of the proton.

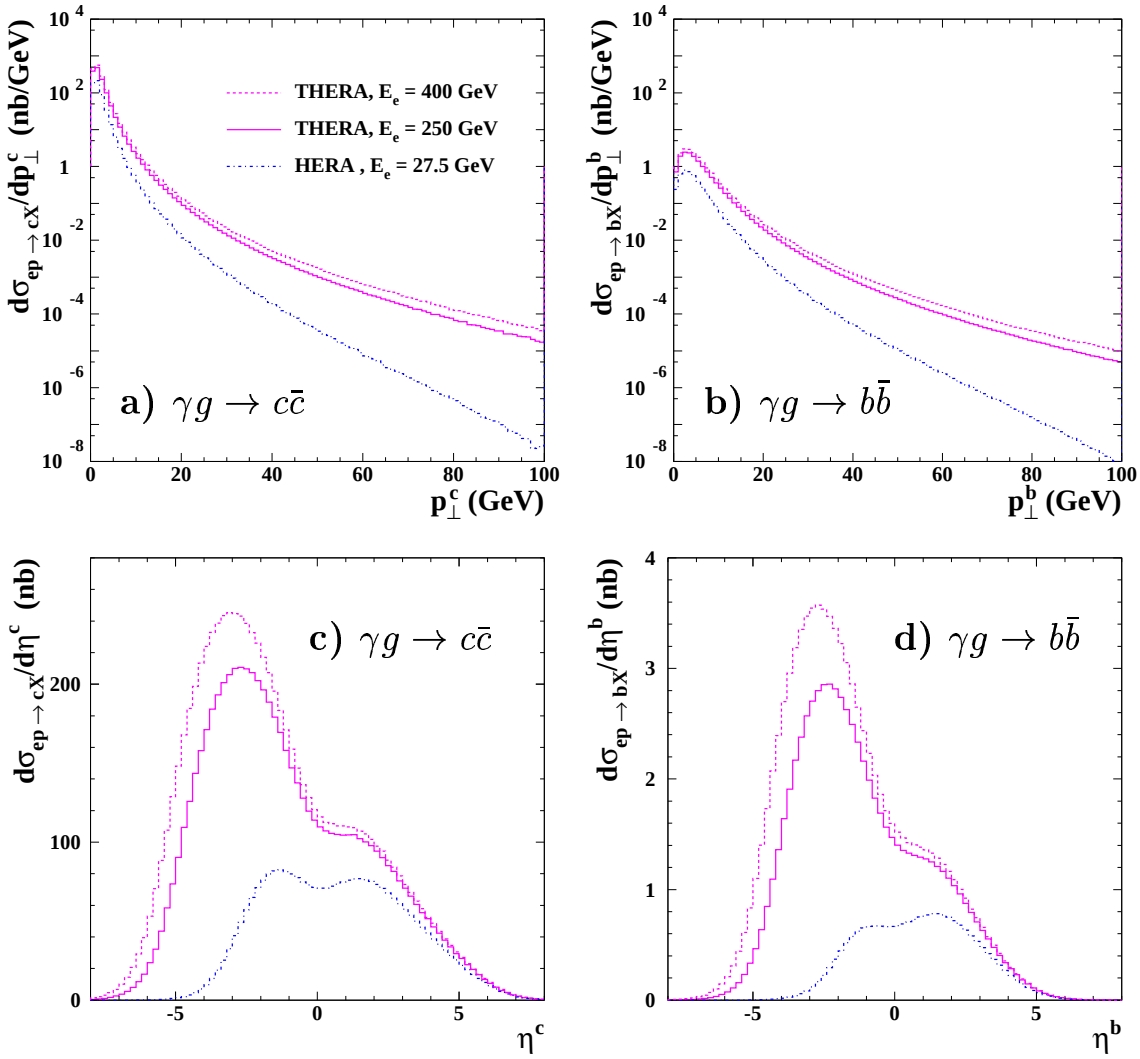

Figure 1: *The contribution of photon–gluon fusion to the differential cross sections $d\sigma/dp_\perp$ and $d\sigma/d\eta$ for charm ((a) and (c)) and beauty ((b) and (d)) production calculated in NLO QCD for $Q^2 < 1\,GeV^2$. The solid and dashed magenta curves show the predictions for THERA operation with an electron energy of 250 GeV and 400 GeV, respectively, and $E_p = 920\,GeV$. The predictions for the HERA case are indicated by the dash-dotted blue curves.*

Fig. 1 shows the contributions of photon–gluon fusion to the differential cross sections $d\sigma/dp_\perp^{c,b}$ and $d\sigma/d\eta^{c,b}$ ($p_\perp^{c,b}$ and $\eta^{c,b}$ denoting the quark transverse momentum and pseudorapidity [2]) at HERA and THERA, calculated within NLO QCD [16] for $Q^2 < 1\,\mathrm{GeV}^2$. The difference between the heavy quark production cross sections at THERA and HERA increases with increasing $p_\perp^{c,b}$, thereby creating the opportunity to measure charm and beauty quarks at THERA in a wider transverse momentum range.

[2]The pseudorapidity η is defined as $-\ln(\tan\frac{\theta}{2})$, where the polar angle θ is taken with respect to the proton beam direction.

Such measurements will provide a solid basis for testing the fixed-order, resummed, and k_t-factorization [20] pQCD calculations. One has to note that the heavy quark pseudorapidity distributions are shifted to backward (electron) direction at THERA with respect to those at HERA. To measure charm and beauty hadronization products

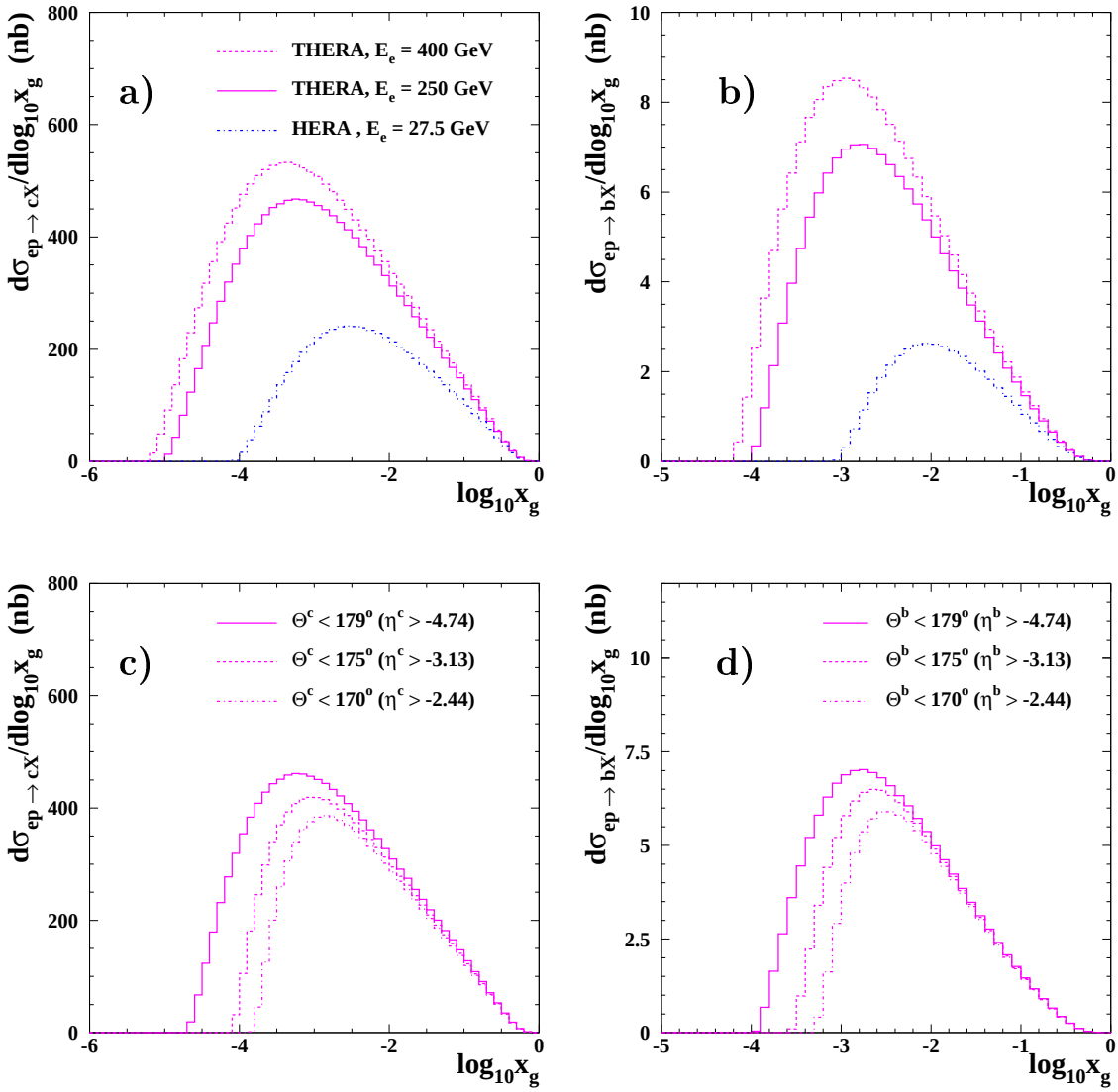

Figure 2: *The differential cross sections $d\sigma/d\log_{10} x_g$ for charm ((a) and (c)) and beauty ((b) and (d)) produced in the process of photon–gluon fusion. The cross sections were calculated within NLO QCD for $Q^2 < 1\,GeV^2$. In (a) and (b), the solid and dashed magenta curves show the predictions for THERA operation with an electron energy of $250\,GeV$ and $400\,GeV$, respectively, and $E_p = 920\,GeV$. The predictions for the HERA case are indicated by the dash-dotted blue curves. In (c) and (d), the predictions for THERA with $E_e = 250\,GeV$ are shown with additional cuts $\theta^{c,b} < 179°$ (solid curves), $\theta^{c,b} < 175°$ (dashed curves) and $\theta^{c,b} < 170°$ (dash-dotted curves).*

a detector for THERA should be equiped with special tracking and muon identification devices in the backward direction.

Measurements of the heavy quarks produced in the process of photon–gluon fusion can be used for the direct reconstruction of the gluon structure of the proton [2]. Fig. 2 shows the differential cross sections $d\sigma/d\log_{10} x_g$ (x_g denoting the gluon fractional momentum in the proton) for charm and beauty produced in PGF at HERA and THERA. The cross sections were calculated within NLO QCD [16] for $Q^2 < 1\,\mathrm{GeV}^2$. The increase of the electron beam energy will provide an opportunity to probe at THERA one order of magnitude smaller x_g values with respect to those at HERA. The kinematic limits of the x_g measurements at THERA are 10^{-5} and 10^{-4} for charm and beauty production, respectively. However, to be sensitive to the x_g values around the kinematic limits one will need to tag heavy quarks in the very backward direction at THERA. Plots (c) and (d) in Fig. 2 show the predictions for THERA with $E_e = 250\,\mathrm{GeV}$ imposing additional cuts $\theta^{c,b} < 179°$, $\theta^{c,b} < 175°$ and $\theta^{c,b} < 170°$. Only charm quarks with $\theta^c > 175°$ demonstrate sensitivity to the as yet unexplored range $10^{-5} < x_g < 10^{-4}$.

4.1.3 Heavy quark production in neutral current DIS

Electron–proton scattering at $\sqrt{s} \sim 1\,\mathrm{TeV}$ will open new regions for heavy quark production in DIS never measured before. One of the legacies of HERA is the experimental confirmation that charm electroproduction in the HERA regime is dominated by PGF [2, 4]. It is, therefore, a direct probe of the gluon in the proton.

A NLO QCD Monte Carlo program HVQDIS [10] was used to study the sensitivity for charm and bottom production at THERA with respect to that at HERA focusing in the increased reach at small Bjorken x values. The HVQDIS program produces fully differential distributions in the heavy quark momenta. It implements three flavour FFNS matrix elements to order α_s^2 calculated previously in [21], and gives a fair description of charm electroproduction at HERA [4].

It was assumed that scattered electrons will be measurable down to very low angles allowing sizable acceptance for DIS events with $Q^2 > 1\,\mathrm{GeV}^2$. Fig. 3 shows the scattered electron angle and energy constant lines for HERA and THERA. The angle line corresponding to the current ZEUS detector limit (177.5 degrees) excludes most of the region bellow $Q^2 = 100\,\mathrm{GeV}^2$ at THERA. Thus, to measure scattered electrons in the low Q^2 DIS range one will need a special low angle detector at THERA.

Minimum cuts on the $p_\perp$ and η of the heavy quarks were imposed to take into account the detector acceptance for the heavy quark tagging. The choices made here are an educated guess, which can be considered optimistic.

The following kinematic range was selected:

- $Q^2 > 1\,\mathrm{GeV}^2$
- $p_\perp^{c,b} > 3\,\mathrm{GeV}$
- $\mid \eta^{c,b} \mid < 5$

HVQDIS was run with the following settings unless otherwise stated:

- $E_e = 250\,\mathrm{GeV}$ and $E_p = 1\,\mathrm{TeV}$ for THERA
- parton densities in the proton: GRV98 [22]
- renormalization scale = factorization scale = $\sqrt{Q^2 + 4M_{c,b}^2}$
- $M_c = 1.4$; $M_b = 4.5\,\mathrm{GeV}$

Fig. 4 displays the differential cross sections $d\sigma/d\log_{10} Q^2$ and $d\sigma/d\log_{10} x$ for charm and beauty production at THERA and HERA in the kinematic region defined above. The most prominent difference is the increase of the cross sections for both charm and beauty at low x. The cross sections are experimentally measurable at values as low as 10^{-6}. The effect of increasing the energy of the electron beam to 400 GeV is shown in Fig. 6.

Fig. 7 illustrates the extension of the kinematic range of the $F_2^{c\bar{c}}$ measurement from HERA to THERA. $F_2^{c\bar{c}}$ at Q^2 values between 1.8 and $600\,\mathrm{GeV}^2$ is plotted as a function of x. The $F_2^{c\bar{c}}$ values measured by the ZEUS collaboration [4] are shown as an illustration. The expected extension is plotted as vertical shaded (yellow) bands. The bands have been produced from the difference of the THERA and HERA low x limits obtained with HVQDIS. The curves in Fig. 7 correspond to the three flavour FFNS NLO QCD calculation [21] using the parton distributions from the ZEUS NLO QCD fit [23]. The figure shows a gain of ~ 1 order of magnitude in x for all Q^2 values. And, since $F_2^{c\bar{c}}$ and the gluon density at larger Q^2 values increase steeper towards small x, the gain in the accepted x range produces an increase of the ratio between THERA and HERA cross sections with Q^2. This ratio rises from $\sim$3(3.5) at low Q^2 to $\sim$5(5.5) at $\log_{10}(Q^2)$=3.5 for charm (beauty) production. Of course, to benefit from the rise and to improve substantially HERA results in the high Q^2 region, THERA luminosity should be of the same order as the final HERA luminosity ($\sim 1\,\mathrm{fb}^{-1}$).

The gain in the acceptance to low x values will be marginal if it will be impossible to measure DIS with Q^2 below $10\,\mathrm{GeV}^2$ at THERA. Fig. 4.1.3 shows the differential cross sections for charm quark production at THERA (solid curve) and HERA (dashed curve). The effect of the $Q^2 > 10\,\mathrm{GeV}^2$ requirement for the THERA case is shown by the dash-dotted curve. THERA sensitivity to low x values depends also on the η range of the heavy quark tagging. The dotted curve shows the THERA cross section with the cut $|\,\eta^c\,|<3$ used instead of $|\,\eta^c\,|<5$. Relaxing the minimum $p_\perp^c$ cut leads to a gain in the accepted THERA cross section but not in the low x reach.

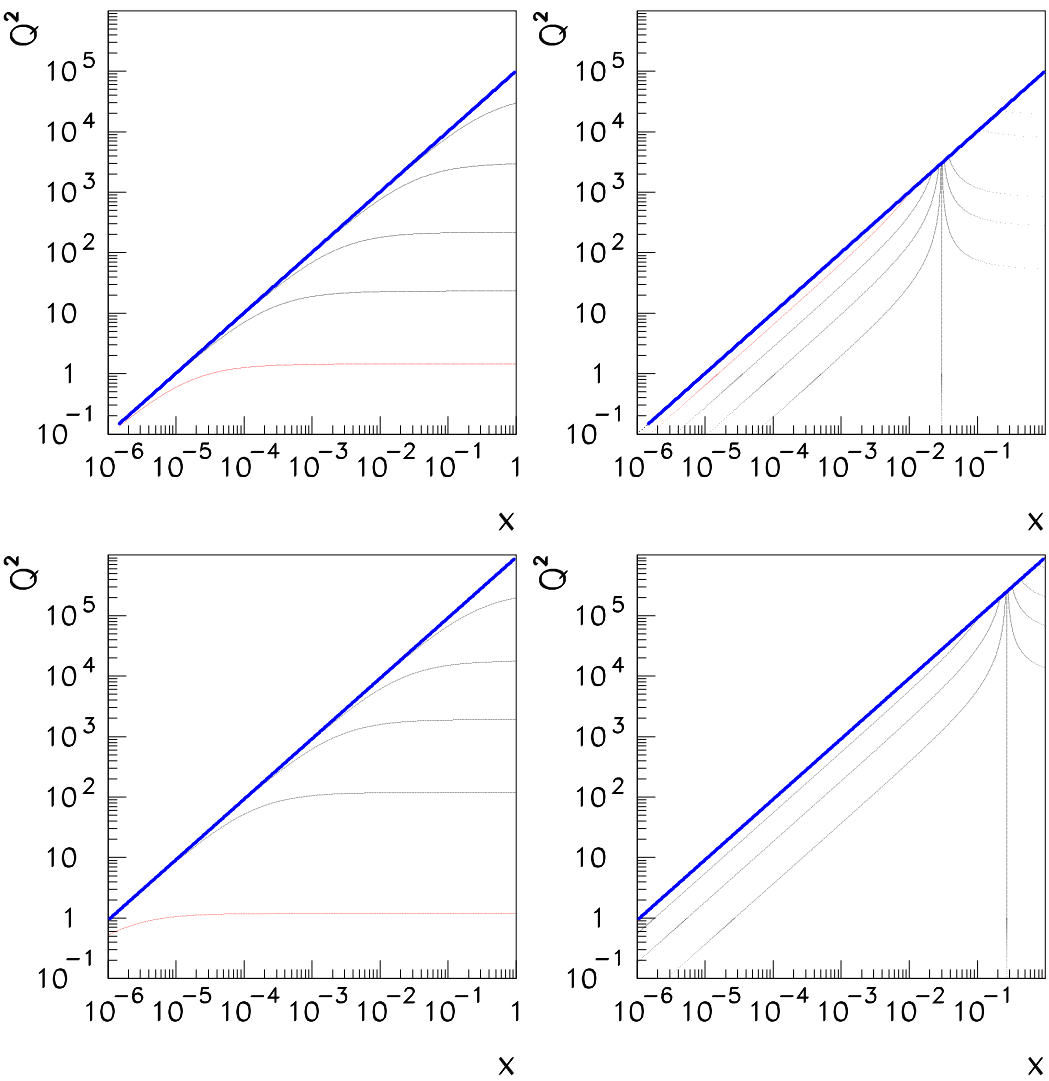

Figure 3: *The scattered electron angle (left) and energy (right) constant lines in the Q^2 and x plane. Top (bottom) plots are for HERA (THERA) kinematics. Thick (blue) diagonal lines are the kinematic limits. The values of constant angle and energy lines plotted for HERA(THERA) kinematics are 177.5, 170, 150, 90, 30 (179.75, 177.5, 170, 150, 90) degrees and 10, 20, 25, 27, 27.5, 28, 30, 35, 100, 200 (10, 100, 200, 240, 250, 260, 300, 400, 500) GeV. The 10 GeV line is indistinguishable from the kinematic limit in the case of THERA.*

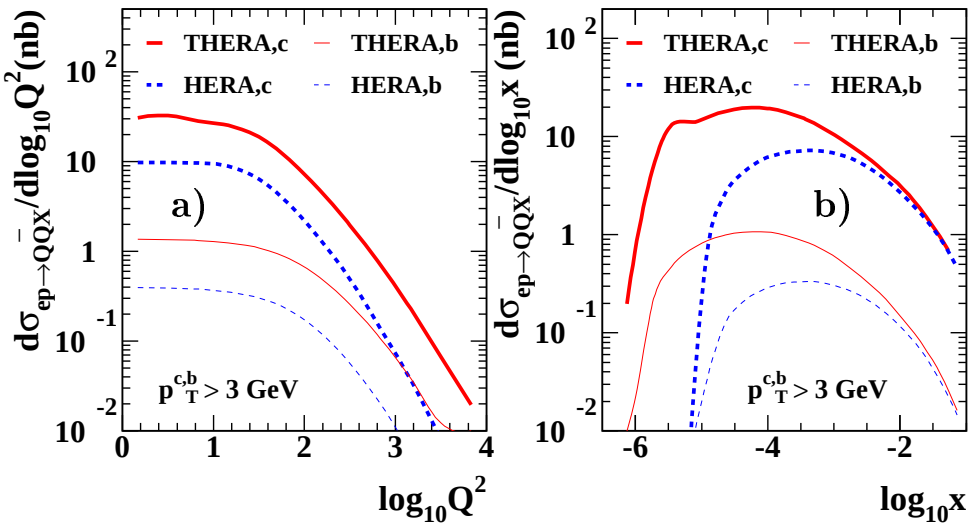

Figure 4: *The differential cross sections for charm (thick curves) and beauty (thin curves) production in neutral current DIS calculated in NLO QCD, (a)* $d\sigma/d\log_{10}Q^2$ *and (b)* $d\sigma/d\log_{10}x$*. The cross sections at THERA (solid red curves) and HERA (dashed blue curves) are compared.*

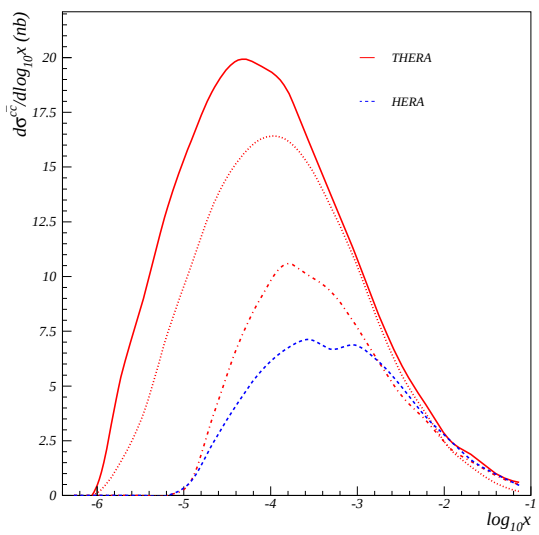

Figure 5: *The differential cross sections* $d\sigma/d\log_{10}x$ *for charm quark production at THERA (solid red curve) and HERA (dashed blue curve). The dash-dotted and dotted red curves show the cross sections for THERA with the additional cuts* $Q^2 > 10\,GeV^2$ *and* $|\eta^c| < 3$*, respectively.*

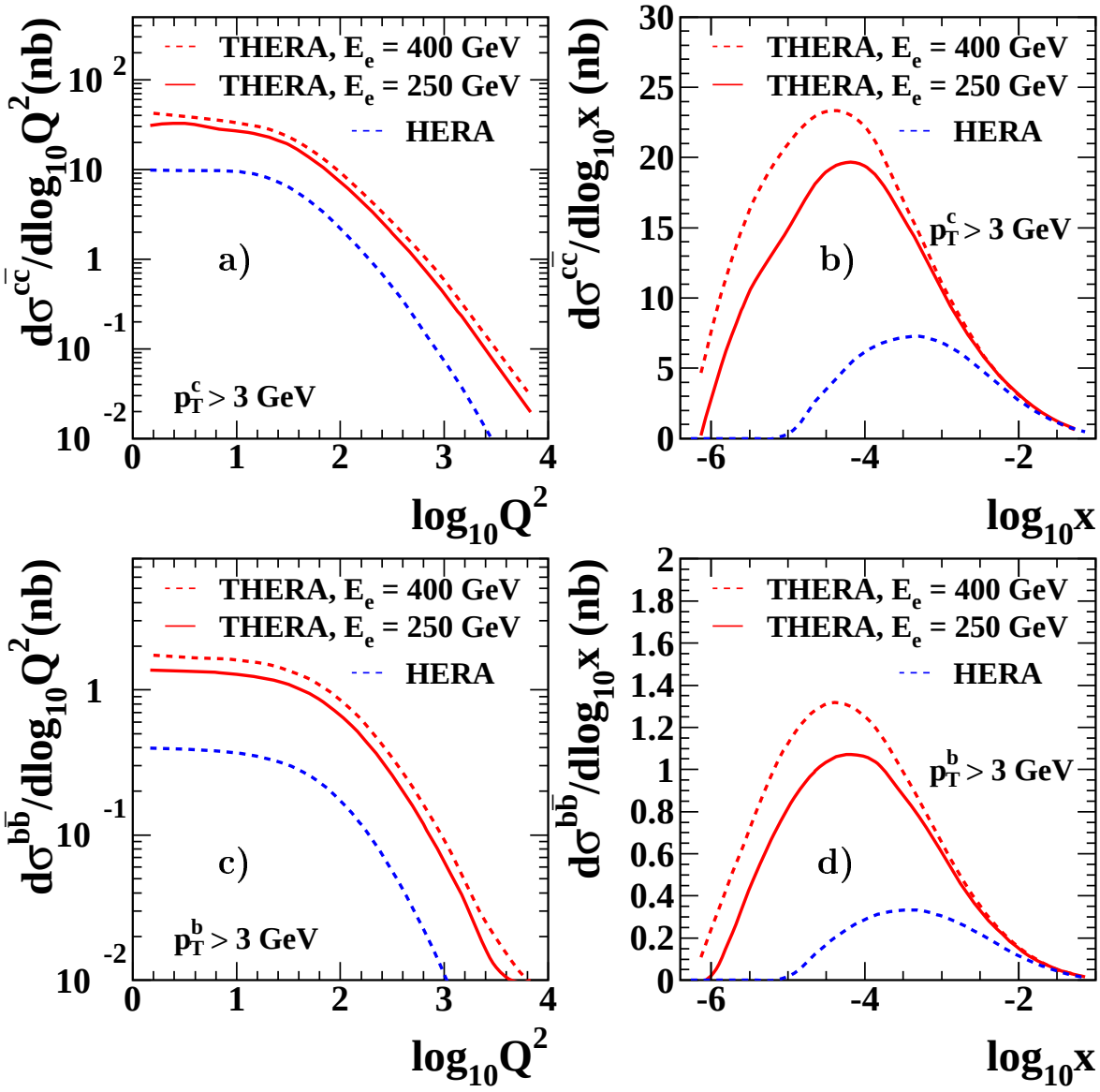

Figure 6: *The differential cross sections* $d\sigma/d\log_{10}Q^2$ *((a) and (c)) and* $d\sigma/d\log_{10}x$ *((b) and (d)) for charm ((a) and (b)) and beauty ((c) and (d)) production at THERA (solid curves) and HERA (lower dashed curves). The upper dashed curves correspond to THERA operation with* $E_e = 400$ *GeV.*

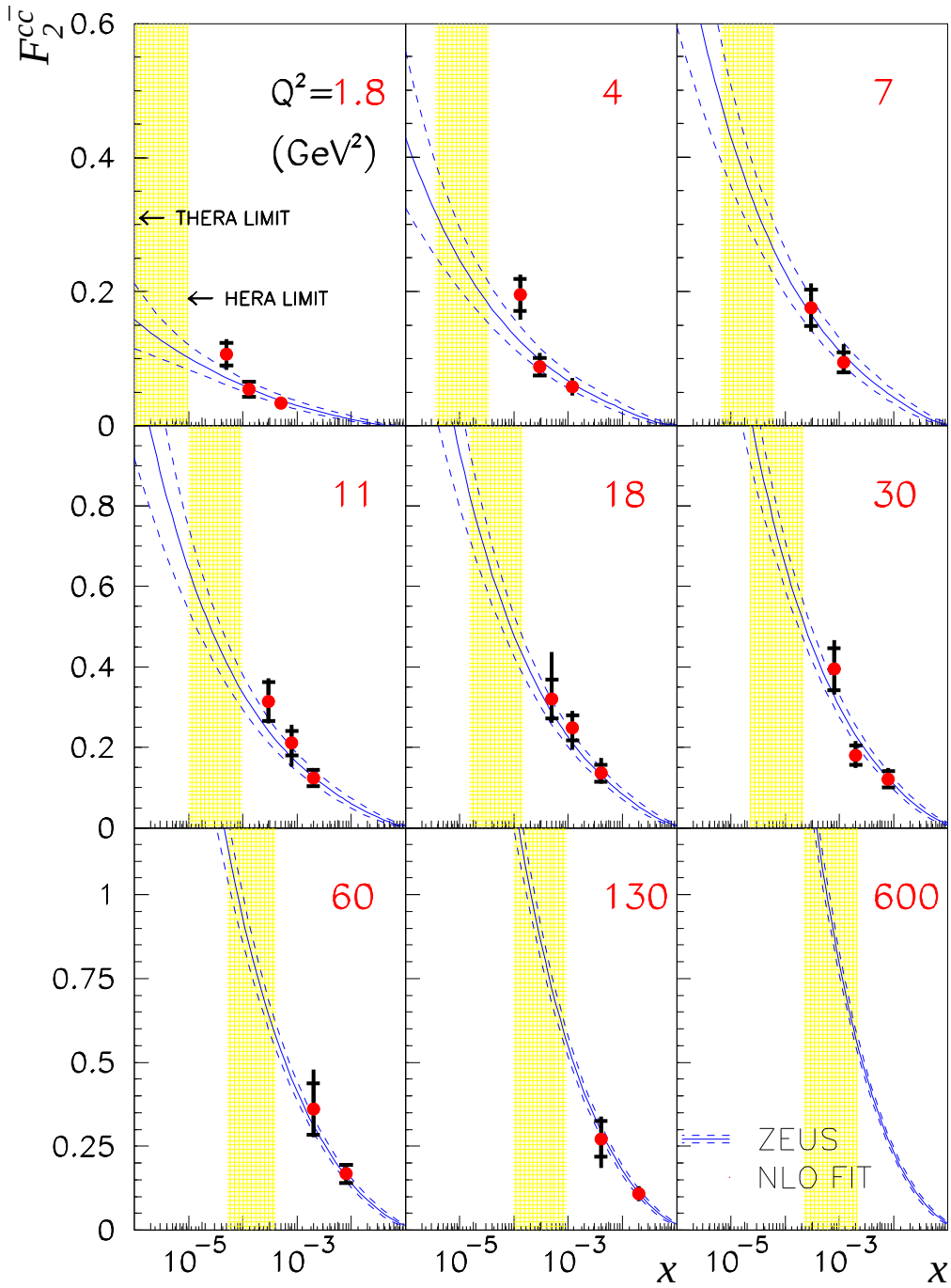

Figure 7: $F_2^{c\bar{c}}$ *at* Q^2 *values between 1.8 and* $600\,GeV^2$ *as a function of* x*. The curves correspond to the three flavour FFNS NLO QCD calculation using the parton distributions from the ZEUS NLO fit. The solid curves correspond to the central values and the dashed curves give the uncertainty due to the parton distributions from the ZEUS NLO fit. The vertical shaded (yellow) bands show the small* x *extension from HERA to THERA for every* Q^2*. The* $F_2^{c\bar{c}}$ *values measured by the ZEUS collaboration are shown as an illustration.*

4.1.4 Charm production in charged current DIS

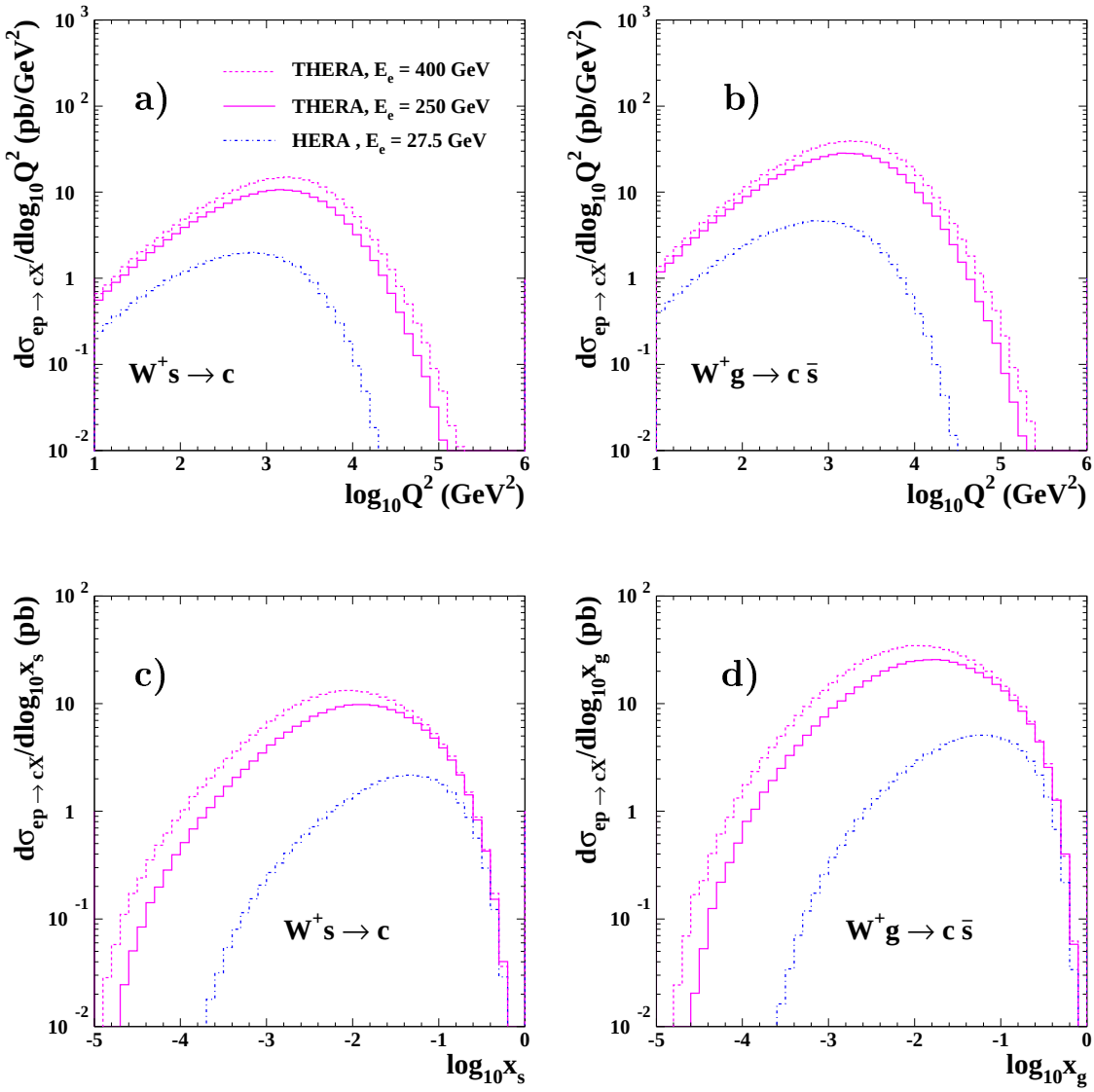

Figure 8: *The differential cross sections $d\sigma/d\log_{10}Q^2$ and $d\sigma/d\log_{10}x_{s,g}$ for charm production in charged current DIS from the strange sea ((a) and (c)) and from boson–gluon fusion ((b) and (d)), calculated with the LO Monte Carlo generator HERWIG. The solid and dashed magenta curves show the predictions for THERA operation with an electron energy of 250 GeV and 400 GeV, respectively, and $E_p = 920$ GeV. The predictions for the HERA case are indicated by the dash-dotted blue curves.*

The theoretical description of charm production in charged current (CC) DIS is challenging [24]. The special interest in this process is caused by its sensitivity to

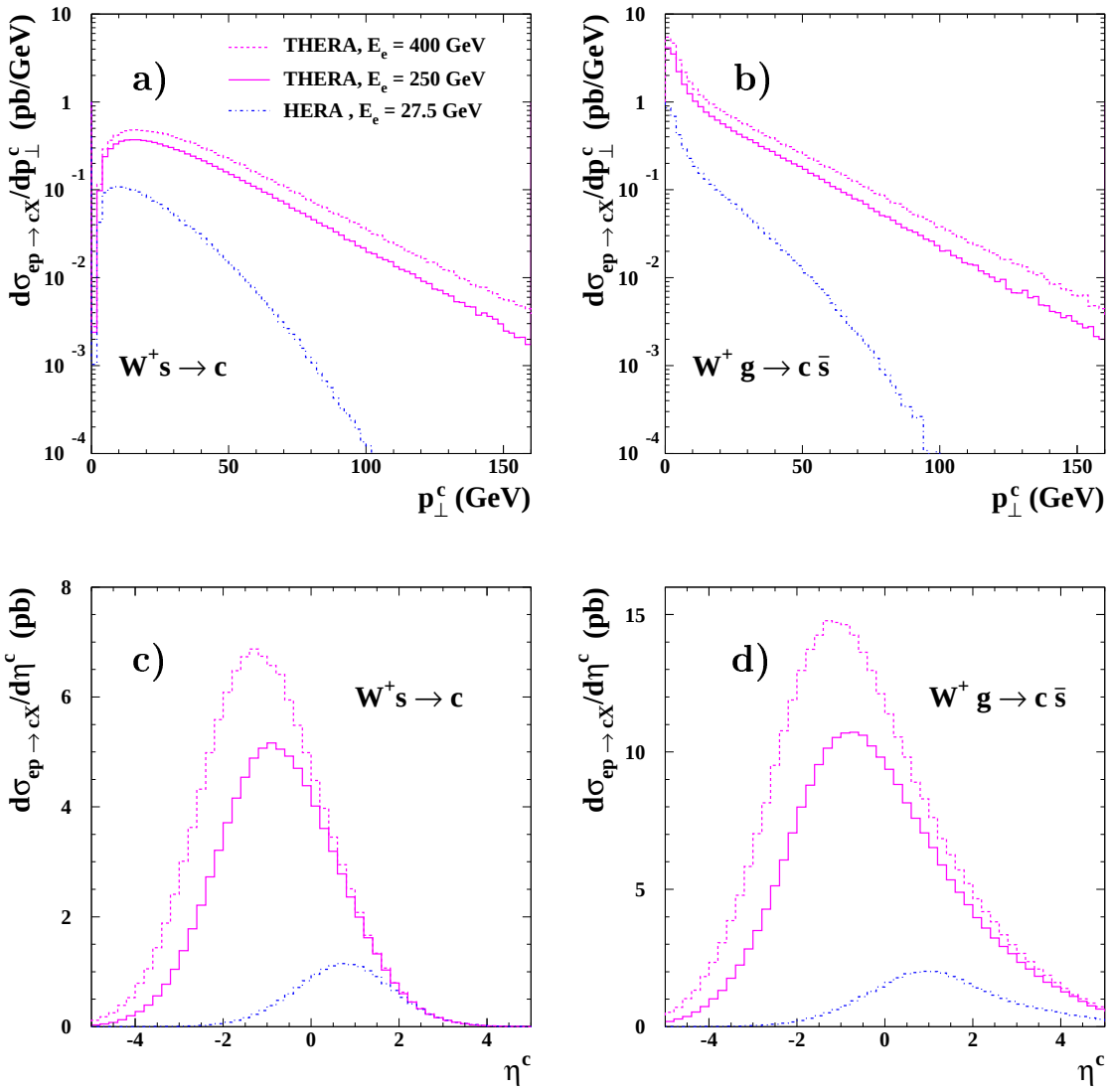

Figure 9: *The differential cross sections $d\sigma/dp_\perp^c$ and $d\sigma/d\eta^c$ for charm production in charged current DIS from the strange sea ((a) and (c)) and from boson–gluon fusion ((b) and (d)), calculated with the LO Monte Carlo generator HERWIG. The solid and dashed magenta curves show the predictions for THERA operation with an electron energy of 250 GeV and 400 GeV, respectively, and $E_p = 920$ GeV. The predictions for the HERA case are indicated by the dash-dotted blue curves.*

the proton strange-quark density which is rather poorly known [25]. However, no measurements of CC charm production have been performed at HERA so far due to the small process cross section (~ 10 pb). According to the LO Monte Carlo HERWIG calculation, the cross sections for both LO CC charm production processes, $W^+ s \to c$ and $W^+ g \to c\bar{s}$, will be more than 6 times larger at THERA than at HERA. The

differential cross sections $d\sigma/d\log_{10}Q^2$ and $d\sigma/d\log_{10}x_{s,g}$ ($x_{s,g}$ denoting the parton fractional momenta in the proton) for CC charm production are shown in Fig. 8. The THERA cross sections are shifted towards larger Q^2 with respect to those at HERA. They are one order of magnitude larger than the HERA cross sections at large Q^2 values, thereby creating the opportunity to study charm production in CC DIS at THERA. Fig. 8 shows also that charm production in CC at THERA is sensitive to much wider ranges in $x_{s,g}$ with respect to those at HERA.

The separation of the strange see contribution to the charm production in CC will require a special experimental procedure. It could utilize the different kinematics of $W^+s \to c$ and $W^+g \to c\bar{s}$ processes. Fig. 9 shows the differential cross sections $d\sigma/dp_\perp^c$ and $d\sigma/d\eta^c$ for the processes at HERA and THERA. The pseudorapidity distributions are rather close for both processes while the $p_\perp^c$ distributions are remarkably different. The boson–gluon fusion component is a few orders of magnitude larger than the strange see component at small $p_\perp^c$ values. At large $p_\perp^c$ values both component contributions are similar. Tagging charm quarks with $p_\perp^c$ above a few GeV suppresses effectively the boson–gluon fusion component contribution. Further separation of the strange see contribution will probably require a selection of events with only one jet representing the charm quark.

4.1.5 Summary

The total cross sections of charm and beauty production at THERA are expected to increase by factors of three and five, respectively, as compared to HERA. Heavy quarks can be measured at THERA in wide ranges of their transverse momenta, thereby providing a solid basis for testing the pQCD calculations. The gluon structure of the proton can be probed at THERA in as yet unexplored ranges. The kinematic limits of the x_g measurements are 10^{-5} and 10^{-4} for charm and beauty production, respectively. The measurements will require the special tracking and muon identification devices in the backward (electron) direction.

THERA will open new regions for the heavy quark DIS production never measured before. For all Q^2 values the kinematic limit in x at THERA is ~ 1 order of magnitude smaller with respect to that at HERA. Measuring the extreme low x (10^{-5}–10^{-6}) regime is an experimental challenge. If the luminosity turns out to be comparable with final HERA numbers, beauty and charm production at high Q^2 values will benefit from the $3-5$ times larger cross sections at THERA.

The cross section of charm production in charged current at THERA is ~ 1 order of magnitude larger than that at HERA, thereby creating the opportunity to study the process.

Acknowledgments

We would like to thank S. Frixione and B. Harris for providing us with the programs for their NLO calculations.

References

[1] S. Frixione et al., Phys. Lett. **B 308**, 137 (1993).

[2] H1 Coll., C. Adloff et al., Nucl. Phys. **B 545**, 21 (1999).

[3] ZEUS Coll., J. Breitweg et al., Eur. Phys. J. **C 6**, 67 (1999).

[4] ZEUS Coll, J. Breitweg et al., Eur. Phys. J. **C 12**, 35 (2000).

[5] ZEUS Coll., J. Breitweg et al., Phys. Lett. **B 481**, 213 (2000).

[6] S. Frixione et al., Phys. Lett. **B 348**, 633 (1995);
S. Frixione et al., Nucl. Phys. **B 454**, 3 (1995).

[7] B.A. Kniehl et al., Z. Phys. **C 76**, 689 (1997).

[8] J. Binnewies et al., Phys. Rev. **D 58**, 014014 (1998).

[9] M. Cacciari et al., Phys. Rev. **D 55**, 2736 (1997);
M. Cacciari et al., Phys. Rev. **D 55**, 2736 (1997).

[10] B.W. Harris and J. Smith, Phys. Rev. **D 57**, 2806 (1998).

[11] M.A.G. Aivazis et al., Phys. Rev. **D 50**, 3102 (1994).

[12] J. Amundson et al., JHEP **0010**, 031 (2000). Also in hep-ph/0005221.

[13] A. Chuvakin, J. Smith and W.L. van Neerven, Phys. Rev. **D 61**, 096004 (2000).

[14] H1 Coll., C. Adloff et al., Phys. Lett. **B 467**, 156 (1999).

[15] ZEUS Coll., J. Breitweg et al., Eur. Phys. J. **C 18**, 625 (2001).

[16] S. Frixione et al., Nucl. Phys. **B 412**, 225 (1994);
M.L. Mangano, P. Nason and G. Ridolfi, Nucl. Phys. **B 373**, 295 (1992).

[17] H1 Coll., *Beauty production in deep inelastic scattering.* Presented by T. Sloan at XXXVIth Rencontres de Moriond: QCD, Les Arcs, France, March 2001.

[18] G. Marchesini et al., Comp. Phys. Comm. **67**, 465 (1992).

[19] P. Jankowski, M. Krawczyk and M. Wing, *Heavy quark production at THERA*, in *The THERA Book* [26].

[20] S.P. Baranov and N.P. Zotov, *Heavy quark production in the semihard approach at THERA*, in *The THERA Book* [26].

[21] E. Laenen et al., Nucl. Phys. **B 392**, 162 (1995);
B.W. Harris and J. Smith, Phys. Lett. **B 353**, 535 (1995).

[22] M. Glück, E. Reya and A. Vogt, Eur. Phys. J. **C 5**, 461 (1998).

[23] ZEUS Coll., J. Breitweg et al., Eur. Phys. J. **C 7**, 609 (1999).

[24] M. Buza and W.L. van Neerven, Nucl. Phys. **B 500**, 301 (1997);
R.S. Thorne and R.G. Roberts, *A variable number flavor scheme for charged current heavy flavor structure functions.* Preprint RAL-TR-2000-048 (hep-ph/0010344), 2000.

[25] V. Barone, C. Pascaud and F. Zomer, *A new global analysis of DIS data and the strange sea distribution*, in *Proc. Workshop on Light-Cone QCD and Nonperturbative Hadron Physics, Adelaide, Australia, 1999*, p. 167. 2000. Also in preprint hep-ph/0004268.

[26] *The THERA Book*, Report DESY-LC-REV-2001-062, 2001.
`http://www.desy.de/~lcnotes`.

4.2 High-p_T Jet Production

B. Pötter
Max-Planck-Institut für Physik, Föhringer Ring 6, D-80805 München
e-mail: poetter@mppmu.mpg.de

4.2.1 Introduction

Jet production in high-energy scattering is a classical testing ground for QCD. Not only can one measure typical QCD quantities, such as the strong coupling α_s or the parton distributions functions (PDF's), but also one has a handle to test perturbative QCD, including the factorization theorems. Furthermore, especially at THERA as an extension of HERA, forward jet production provides an insight into small-x physics. Finally, jet production processes can provide important backgrounds for the search of new physics. Therefore jet production has received much attention in theoretical calculations and impressive progress has been made in the last decade to describe jet production in the framework of perturbative QCD.

Most available calculations have been performed in next-to-leading order (NLO) accuracy. There are several reasons to perform these NLO calculations. First, the theoretical uncertainties due to unphysical renormalization and factorization scale dependences are reduced. Second, due to the emission of additional particles in the initial and final state, one becomes sensitive to jet algorithms, which is certainly the case in the experimental results. Third, for the same reason, calculations become more sensitve to detector limitations. Finally, the presence of infrared (IR) logarithms is clearly seen and regions where resummation is needed can be identified.

The reason to investigate processes involving high p_T and Q^2 is twofold. On the one hand, one hopes that the presence of a large scale reduces hadronization corrections and furthermore that theoretical uncertainties are smaller. On the other hand, the edges of the presently accessible phase space regions are of course those, where new and unexpected events can occur. In looking at theoretical errors, one should keep in mind also the selection of a stable jet algorithm to obtain reliable results [1].

In the following I will briefly review the present state-of-the-art for perturbative calculations for eP-scattering and then present some results for a THERA collider.

4.2.2 Next-to-leading order calculations

All presently available calculations are at most NLO. Two type of corrections enter these calculations, the real and virtual contributions. Both have typical divergences, which can, e.g., be handled in dimensional regularization. The UV poles from the virtual corrections are absorbed into the running coupling. All IR poles cancel in the

sum of real and virtual corrections, except for initial state singularities proportional to the splitting functions, which are absorbed into the PDF's.

To include the NLO calculations into flexible numerical fixed order Monte-Carlo (MC) programs, it is necessary to handle the IR regions of the real corrections separately. Here, basically two types of procedures have emerged, which are the phase-space-slicing and the subtraction method. In the first procedure the IR phase space regions are avoided by introducing a small cut-off parameter (y_{cut}) into the integrals. The IR regions are then calculated analytically, whereas the hard regions are calculated numerically. Of course, the cut-off dependence must cancel in the sum of these two contributions. The subtraction method identifies the IR poles from the start and subtracts these from the integrals, leaving a finite part which can be calculated numerically.

In eP-scattering, the interaction of the electron with the proton is mediated by a gauge boson ($\gamma, Z^0, W^\pm$) with virtuality $Q^2 \geq 0$. The region from $Q^2 = 0$ (photoproduction) up to the highest $Q^2 > 10^5$ GeV^2 (deep-inelastic scattering, DIS) is covered by the THERA collider. In the DIS region there are four programs which have been developed for eP-scattering at HERA, namely `DISENT` [2], `DISASTER++` [3], `MEPJET` [4] and `JetViP` [5], based on the calculations in [6]. These are summarized in Tab. 4.2.1 (taken from [7]). In the photoproduction limit $Q^2 \to 0$, the DIS matrix elements with a direct coupling of the photon to the partons from the proton show an additional initial state singularity on the photon leg, which has to be subtracted and absorbed into the photon PDF. Furthermore, one has to calculate a so-called resolved component, where the photon serves as a source of partons. These direct and resolved photon-proton scattering processes have been calculated by three groups in NLO QCD [8–10]. One of the main features of `JetViP` is the possibility to include a resolved virtual photon component in NLO. In this way the photoproduction limit can be taken. However, only MEPJET so far incorporates contributions from Z^0 and $W^\pm$ exchange in NLO, which become important at virtualities above $Q^2 > 2500$ GeV^2. Therefore, a detailed comparison of the existing fixed order MC's is necessary to see whether these contributions are reliably predicted (see [7]). It should be mentioned here that presently the limiting factor for higher precision measurements of QCD parameters are the systematic and theoretical uncertainties. Therefore, theoretical advances are in urge, such as NNLO calculations (see e.g. [11]).

One has to keep in mind that currently all NLO calculations are on the parton level, whereas the experiment obviously provide data on the hadron level. One usually looks into regions, where hadronization corrections are small, however it would be very nice to have NLO calculations that are directly comparable to the hadron level. Especially in the last year quite some theoretical activity developed in the field of combining matrix element calculations with parton shower algorithms and hadronization models [12–16]. This topic will be of even higher importance for the THERA collider.

4.2.3 Jet Production at THERA

One can distinguish three main topics that can be studied intensively in jet production at THERA. First, there are the high Q^2 dijet measurements, which allow precise

	MEPJET	DISENT	DISASTER++	JETVIP
version	2.2	0.1	1.0.1	2.1
method	PS slicing	subtraction	subtraction	PS slicing
1+1,2+1	NLO	NLO	NLO	NLO
3+1	LO	LO	LO	LO
4+1	LO	—	—	—
full event record	✓	✓	✓	✓
Quark Masses	LO	—	—	—
Resolved γ	—	—	—	NLO
Electroweak	NLO	—	—	—
Polarized e/P	NLO	—	—	—

Table 4.2.1: *Summary of $eP \to$ jets fixed order MCs*

determinations of α_s and the gluon density in the proton. Second, the low Q^2 region allows to explore the structure of real and virtual photons. Third, the much enlarged kinematic region of THERA allows to study forward jet production at very low x. In the following I will show some examples of jet cross sections at small and large Q^2 by directly comparing results for HERA and THERA. In all plots I have employed the CTEQ4M PDF's for the proton.

Starting with photoproduction, I show in Fig. 1 plots for THERA and HERA energies for virtualities integrated over $Q^2 < 5$ GeV^2 with an additional electron cut of $y > 0.1$. To ensure IR stability I employed an asymmetric jet cut of $p_{T_1}, p_{T_2} > 6, 4$ GeV. The rapidity range is restricted to $|\eta| < 2$. I chose renormalization and factorization scales to be equal to the largest p_T in the event. For the PDF's of the photon we employed the GRV higher order parametrizations. The cross sections are plotted as a function of the largest p_T jet. The full line gives the sum of direct and resolved contributions. The direct contribution is given by the dotted line, the resolved by the dash-dotted line. One observes that the THERA cross sections are much harder in p_T. Second, for THERA the resolved cross section is dominant over the whole p_T range whereas the direct is dominant for large p_T at HERA. Therefore, THERA gives an excellent opportunity to study the real photon structure at large p_T, especially because problems of underlying events and hadronization corrections are small. The much enlarged resolved cross section of course enhances very much the sensitivity of the jet cross section to the PDF's.

In a similar manner I have studied virtual photoproduction at THERA by choosing the cuts on the Q^2-range to be $Q^2 \in [.25, 6]$ GeV^2, leaving the cuts on the electron $y > 0.1$. The jet-cuts are $|\eta| < 2$ and asymmetric transverse momentum cuts of $p_{T_1}, p_{T_2} > 7, 5$ GeV. As renormalization and factorization scales I choose $\mu^2 = Q^2 + p_T^2$, taking the SaS1D PDFs for the virtual photon. The results are plotted in Fig. 2 as functions of the photon virtuality, thereby integrating out the transverse momenta. As before, the sum is given by the full line, whereas the direct is the dotted and the resolved the dash-dotted line. We see that at THERA the resolved component is dominant over

the whole Q^2 range whereas the direct component dominates for larger Q^2 at HERA. The conclusion is that THERA will allow detailed studies also of the virtual photon structure function, especially of the Q^2-dependence. This will help to pin down the virtuality region where the hadronic component in the virtual photon can be neglected and a transition of the photoproduction region to the DIS region can be observed.

As a last point I looked into the DIS region of large Q^2, which is studied in Fig. 3 as a function of x. I integrated over $Q^2 > 100$ GeV^2 with $y > 0.1$, $|\eta^{lab}| < 2$ and $E^{lab}_{T_1,2} > 10$ GeV. As scales I chose $\mu^2 = \xi Q^2$ and studied scale variations $\xi = 1, 10$ and $\xi = 0.1$. The full line gives the central scale, higher scales lower the cross sections and vice versa. The scale dependences both for THERA and HERA are small. As we see, the prominent feature of the THERA cross section is that it reaches down to much smaller x, which is due to the larger cms energy s, where we have $x = Q^2/(ys)$. Therefore THERA gives a good possibility to study small x physics. Especially forward jet production can be studied very well. At HERA it was not clear, whether BFKL dynamics was clearly observed at small x [17].

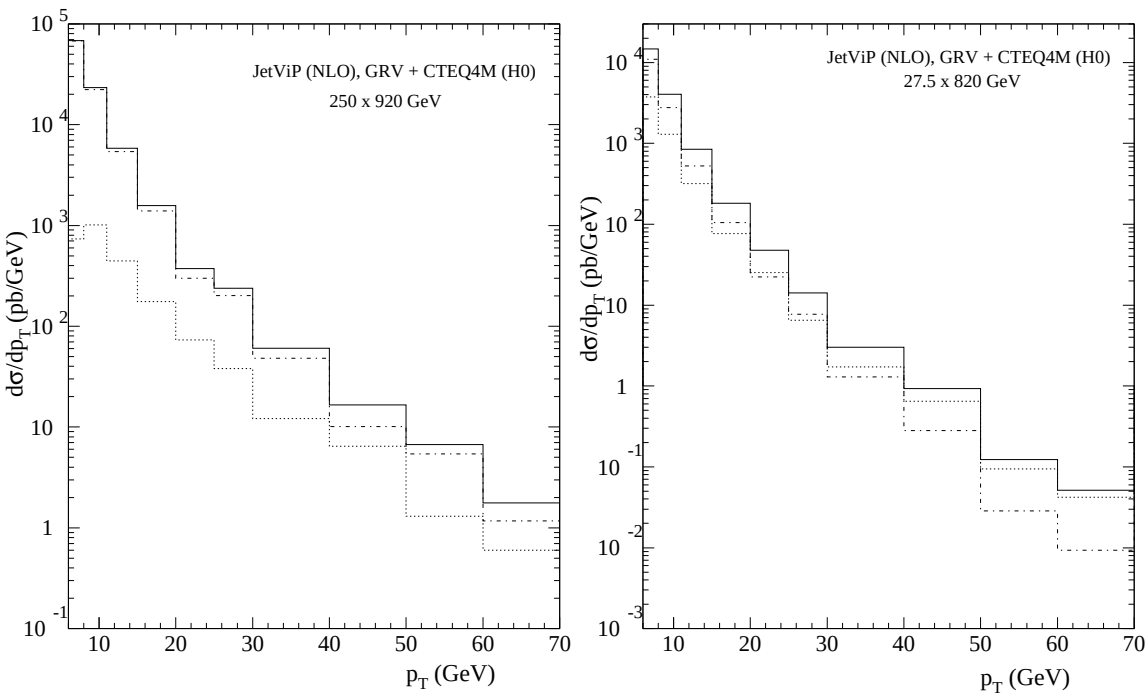

Figure 1: *Photoproduction cross section for $Q^2 < 5$ GeV^2, $|\eta| < 2$ and $y > 0.1$. The left shows the THERA curve, the right shows the equivalent HERA curve. The full line gives the sum of direct and resolved contributions. The direct contribution is given by the dotted line, the resolved by the dash-dotted line.*

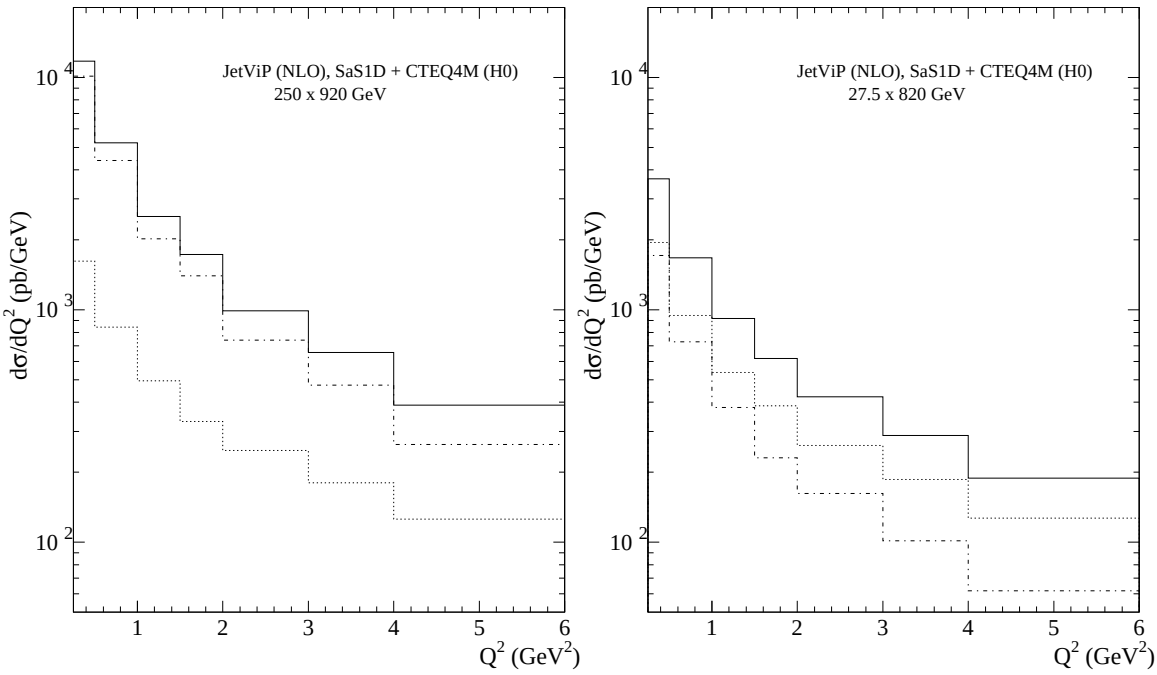

Figure 2: *Virtual Photoproduction cross section for* $0.25 < Q^2 < 6\ GeV^2$, $|\eta| < 2$ *and* $y > 0.1$. *The left shows the THERA curve, the right shows the equivalent HERA curve. The full line gives the sum of direct and resolved contributions. The direct contribution is given by the dotted line, the resolved by the dash-dotted line.*

4.2.4 Summary

We have studied jet production in eP-scattering at a THERA collider, covering most of the available phase-space in Q^2. In particular we have studied cross sections for photoproduction, deep-inelastic scattering and the intermediate region of small Q^2. We found the resolved photon component to play a dominant role in the cross sections, both for real and virtual photoproduction. This is true also at high jet transverse energies E_T, which allows to investigate the photon structure in a clean enviroment, where contributions from soft underlying events are small (for photoproduction, see also contribution by M. Klasen). For DIS, the available phase space in x is enhanced by an order of magnitude, which will allow important studies of the small x region in eP-scattering (see also contribution by H. Jung and L. Lönnblad).

References

[1] B. Pötter and M.H. Seymour, J. Phys. **G 25** (1999) 1473.

[2] S. Catani and M.H. Seymour, Phys. Lett. **B 378** (1996) 287; Nucl. Phys. **B 485** (1997) 291.

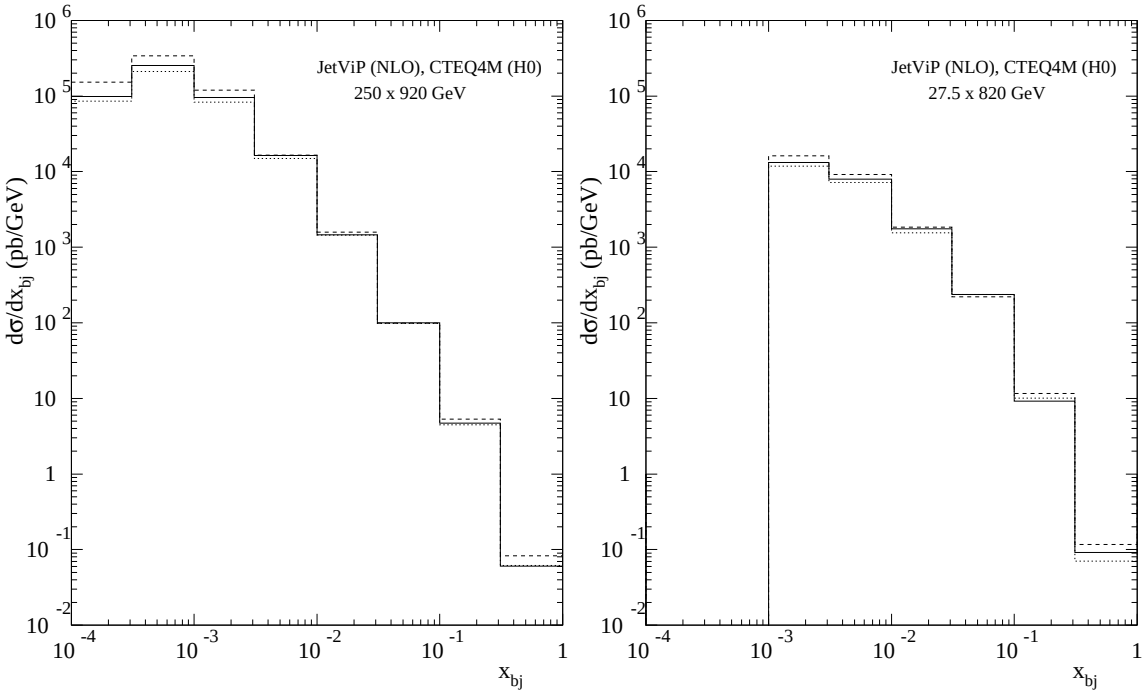

Figure 3: *Deep-inelastic scattering cross section for* $Q^2 > 100\ GeV^2$, $|\eta| < 2$ *and* $y > 0.1$. *The left shows the THERA curve, the right shows the equivalent HERA curve. The full line gives the sum of direct and resolved contributions. The direct contribution is given by the dotted line, the resolved by the dash-dotted line.*

[3] D. Graudenz, PSI-PR-97-20, hep-ph/9709240

[4] E. Mirkes and D. Zeppenfeld, Phys. Lett. **B 380** (1996) 23; Acta Phys. Polon. **B 27** (1996) 1392.

[5] B. Pötter, Comp. Phys. Comm. **119** (1999) 45;
B. Pötter, Comp. Phys. Comm. **133** (2000) 105.

[6] G. Kramer and B. Pötter, Eur. Phys. J. **C 5** (1998) 665;
B. Pötter, Eur. Phys. J. Direct **C 5** (1999) 1;
M. Klasen, G. Kramer and B. Pötter, Eur. Phys. J. **C 1** (1998) 261.

[7] C. Duprel et al., Proceedings of the Workshop on Monte Carlo Generators for HERA Physics Hamburg 1998/1999, ed. A. T. Doyle, G. Grindhammer, G. Ingelman, H. Jung, p. 142;
B. Pötter, hep-ph/9911221.

[8] S. Frixione, Nucl. Phys. **B 507** (1997) 205;
S. Frixione and G. Ridolfi, Nucl. Phys. **B 507** (1997) 315.

[9] B.W. Harris and J.F. Owens, Phys. Rev. **D 56** (1997) 4007; Phys. Rev. **D 57** (1998) 5555

[10] M. Klasen and G. Kramer, Z. Phys. **C 76** (1997) 67;
M. Klasen, T. Kleinwort and G. Kramer, Eur. Phys. J. Direct **C 1** (1998) 1.

[11] N. Glover, hep-ph/9805481.

[12] S. Mrenna, preprint UCD-99-4, hep-ph/9902471.

[13] C. Friberg and T. Sjöstrand in *Proceedings of the DESY Workshop on Monte Carlo Generators for HERA Physics*, A.T. Doyle, G. Grindhammer, G. Ingelman, and H. Jung (eds.), (DESY, Hamburg, 1999), hep-ph/9906316.

[14] J. Collins, JHEP **0005** (2000) 4.

[15] G. Corcella and M.H. Seymour, Nucl. Phys. **B 565** (2000) 227.

[16] B. Pötter, hep-ph/0007172, to appear in Phys. Rev. **D**.

[17] G. Kramer and B. Pötter, Phys. Lett. **B 453** (1999) 295.

4.3 Jet Photoproduction at THERA

DESY 01–031 ISSN 0418–9833
hep–ph/0103091
March 2001

M. Klasen
II. Institut für Theoretische Physik, Universität Hamburg,
Luruper Chaussee 149, 22761 Hamburg, Germany

Abstract

We demonstrate that a future high-energy electron-proton collider like THERA could largely extend the current HERA program in jet photoproduction of testing QCD and determining the partonic structure of the proton and the photon. Depending on the electron beam energy (250–500 GeV) and the collider mode (ep or γp), the range in the hard transverse energy scale of the jets could be increased by a factor of 2–3 and the reach in the momentum fraction x of the partons in the proton or photon by at least one order of magnitude. It would thus become possible to check the determinations of the gluon density in the proton obtained in deep–inelastic scattering experiments, to measure the gluon density in the photon down to low values of x, and to study the QCD dynamics in multi-jet events.

4.3.1 Motivation

In electron-proton collisions at the DESY HERA collider, the exchange of almost real photons is responsible for the largest fraction of the scattering events. In a subclass of these photoproduction events, hard jets are produced with large transverse energies. The presence of a hard scale then allows for a comparison of the data with predictions based on perturbative QCD.

Measurements of inclusive jets, dijets, and three jets have been performed by the H1 and ZEUS collaborations at HERA over the last nine years and were found to be in qualitatively good agreement with these predictions. They can also be used to extract the free parameters of the theory like the strong coupling constant or the parton densities in the colliding proton and photon. In the proton case, this information is complementary to determinations in deep-inelastic electron- or neutrino scattering or lepton pair production in hadronic collisions. The HERA deep-inelastic scattering data have been particularly useful to pin down the previously unknown gluon density at low values of the partonic momentum fraction x. However, it is important to test this determination in a second independent process like photoproduction. Information on the photonic parton densities is still very limited: Only the quark distributions have been constrained in deep-inelastic electron-photon scattering, and only at large x. Little is

known about the gluon density in the photon.

The determination of the parton densities in the proton and photon is thus an important research goal in the jet photoproduction experiments at HERA and also in photon-photon scattering at LEP2. Unfortunately, the experiments have so far been limited to transverse jet energies which may be too low to suppress the soft underlying event coming from the proton or photon remnants or the non-perturbative effects affiliated with hadronization. Furthermore, they are kinematically limited to relatively large values of x.

It is the aim of this paper to demonstrate that both of these restrictions can be overcome if the electron energy is raised and/or the exchanged photons are produced by laser backscattering. This may be possible at a facility where a high-energy electron beam from a future linear electron accelerator like TESLA is collided with a high-energetic proton beam like the one available at HERA. At such a 'THERA' collider it will thus be possible to reach smaller values of x and larger hard scales at the same time.

4.3.2 Dijet Cross Section

For the proton beam we choose an energy of $E_p = 920\,\mathrm{GeV}$, at which HERA is currently operating. For the electron beam, we start with the current HERA energy of $E_e = 27.5\,\mathrm{GeV}$. If only one arm of the future electron accelerator is used, 250 and 400 GeV can be reached in the first and second stages of TESLA, respectively. If both arms are used, the electron energy can be raised to as much as 500 GeV already in the first stage. Photoproduction events are selected by requiring that the electron scattering angle is less than 1° and that the photon momentum fraction lies within the range $0.2 < y < 0.85$. For the different electron beam energies, this maximum scattering angle corresponds to maximum photon virtualities of 0.18, 15, 39, and 61 GeV^2 at low y. The alternative approach of choosing a constant maximum virtuality of 1 GeV^2 leads to unrealistically small values of $\sim 0.1°$ at TESLA energies. Finally, we investigate the potential of a THERA γp collider where highly energetic real photons are produced by backscattering laser light off a 250 GeV electron beam.

In leading order of perturbative QCD, two partons with equal transverse energies are produced, corresponding to two hard jets. The dijet cross section is then given by

$$\frac{\mathrm{d}^3\sigma}{\mathrm{d}E_T^2\mathrm{d}\eta_1\mathrm{d}\eta_2} = \sum_{a,b} x_\gamma y f_{a/e}(x_\gamma y, \mu_f^2) x_p f_{b/p}(x_p, \mu_f^2) \frac{\mathrm{d}\sigma}{\mathrm{d}t}(ab \to p_1 p_2). \tag{4.3.1}$$

In next-to-leading order there may also be a third, softer jet. We can then use the average transverse energy $\overline{E}_T$ and the average rapidity $\overline{\eta}$ of the dijet system as observables and allow the two jets to differ in transverse energy by as much as $\Delta E_T < \overline{E}_T/2$. This choice, which allows for a full cancellation of infrared singularities and avoids

the sensitive region of two equal minimal E_T [1], has also been made in a recent H1 analysis [2]. The rapidity difference of the two jets $\Delta\eta$ is related to the center-of-mass scattering angle $\cos(\theta^*) = \tanh(\Delta\eta)/2$. While inclusive jet measurements yield higher statistics, only dijet analyses allow for a reconstruction of

$$x_p^{\rm obs} = \frac{E_{T,1}e^{+\eta_1} + E_{T,2}e^{+\eta_2}}{2E_p} \quad , \quad x_\gamma^{\rm obs} = \frac{E_{T,1}e^{-\eta_1} + E_{T,2}e^{-\eta_2}}{2yE_e} \tag{4.3.2}$$

which, in leading order, match exactly the momentum fractions of the partons in the proton x_p and photon x_γ, but neglect the contribution of a possible third jet. Jet photoproduction has been calculated in next-to-leading order QCD using three different phase space slicing methods [3–7] and the subtraction method [8]. The results were found to agree with each other within a few percent [7, 9]. In our next-to-leading order calculation [3, 4], jets are defined according to the k_T cluster algorithm with the parameter $R = 1$ [10, 11]. For the parton densities in the photon and proton, we choose the next-to-leading order set of GRV [12] and the latest CTEQ parameterization 5M [13] with the corresponding value of $\Lambda_{\overline{\rm MS}}^{\rm nf=5} = 226\,{\rm MeV}$. The strong coupling constant α_s is evaluated at two loops and at the scale $\mu = \mu_f = \max(E_{T,1}, E_{T,2})$. The sensitivity of a THERA collider to different photon parton densities has been analyzed in detail elsewhere [14].

With higher electron beam energies, the HERA center-of-mass energy $\sqrt{S}$ of 318 GeV can be increased to 959, 1213, or even 1357 GeV, approaching the 2 TeV regime of the Fermilab Tevatron in Run 2. At the Tevatron, jets with transverse energies in excess of 50 GeV are selected. Since THERA would operate at roughly half the Tevatron center-of-mass energy, we cut on $\overline{E}_T > 25\,{\rm GeV}$.

4.3.3 Results

Like hadronic jet cross sections, photoproduction jet cross sections drop steeply in transverse energy. It is therefore interesting to study the size of the dijet photoproduction cross section as a function of $\overline{E}_T$ as shown in Figure 1. At $\overline{E}_T = 40\,{\rm GeV}$, THERA with electron beam energies of 250 to 500 GeV produces cross sections which are larger than the HERA cross section by about a factor of 20-40. At a THERA photon collider, the cross section is even larger by a factor of 500. The larger cross sections result, of course, in a much extended range in $\overline{E}_T$. With an expected luminosity of 100 pb^{-1}/year, the range can be extended from 75 GeV at HERA to 150 GeV at THERA ep or 225 GeV at THERA γp, *i.e.* by a factor of 2-3.

Of course, these jets need not only be produced but also be measured in a detector. An important question in this context is the required coverage in rapidity. In Figure 2 we therefore show the average rapidity distribution of the produced dijet system with $\overline{E}_T > 25\,{\rm GeV}$. Jets at HERA are produced mostly in the proton (forward) direction $0 < \overline{\eta} < 3$, which has lead to the characteristic asymmetric designs of the H1 and ZEUS detectors. In contrast, jets at THERA will be produced centrally in the range

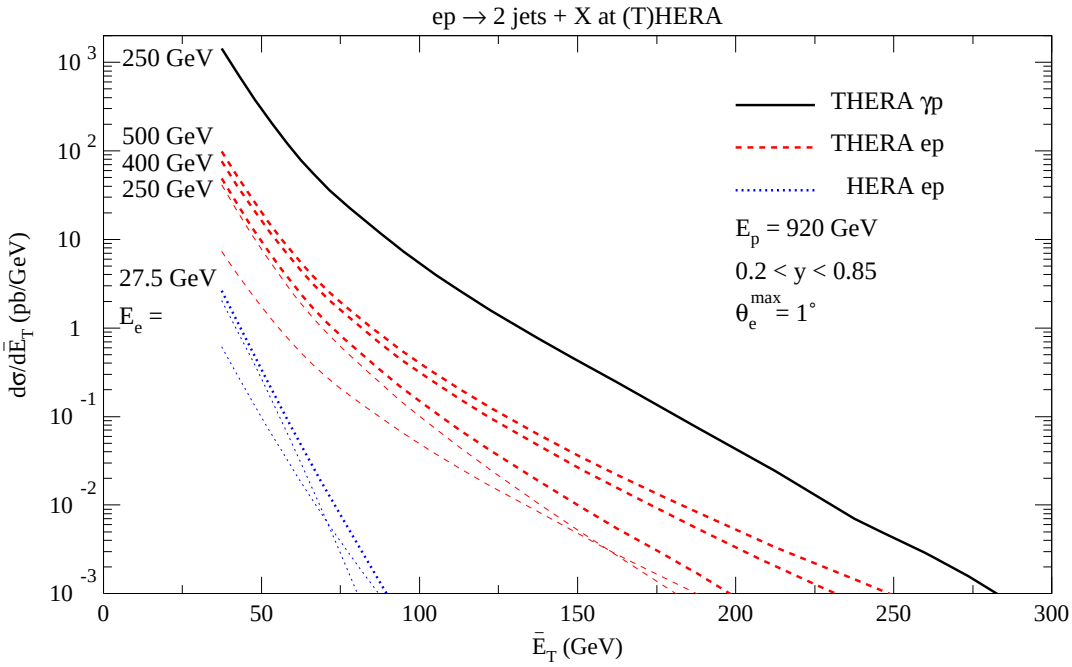

Figure 1: *Differential dijet photoproduction cross section as a function of the average transverse energy of the two jets $\overline{E}_T$. The thin lines show the separate contributions from the resolved (direct) processes for HERA and THERA with E_e =250 GeV, which dominate at small (large) $\overline{E}_T$.*

$-3 < \bar{\eta} < 3$, requiring a more symmetric detector design, closer to the design used at hadron colliders. Therefore, if the H1 and ZEUS detectors are to be used, some modifications will be necessary. However, an upgrade of the electron beam energy from 250 to 500 GeV will probably not necessitate additional changes, since the rapidity range is then only slightly extended.

The rapidity difference of the two jets or, equivalently, the cosine of the center-of-mass scattering angle $\cos(\theta^*)$ is related to the $2 \to 2$ Mandelstam variables of the underlying partonic subprocesses by

$$t = -\frac{1}{2}s(1 - \cos\theta^*) \quad , \quad u = -\frac{1}{2}s(1 + \cos\theta^*), \tag{4.3.3}$$

where $s = (p_a + p_b)^2 = x_\gamma y x_p S$ is the partonic center-of-mass energy squared. Most of the resolved (parton-parton) scattering processes are characterized by the exchange of

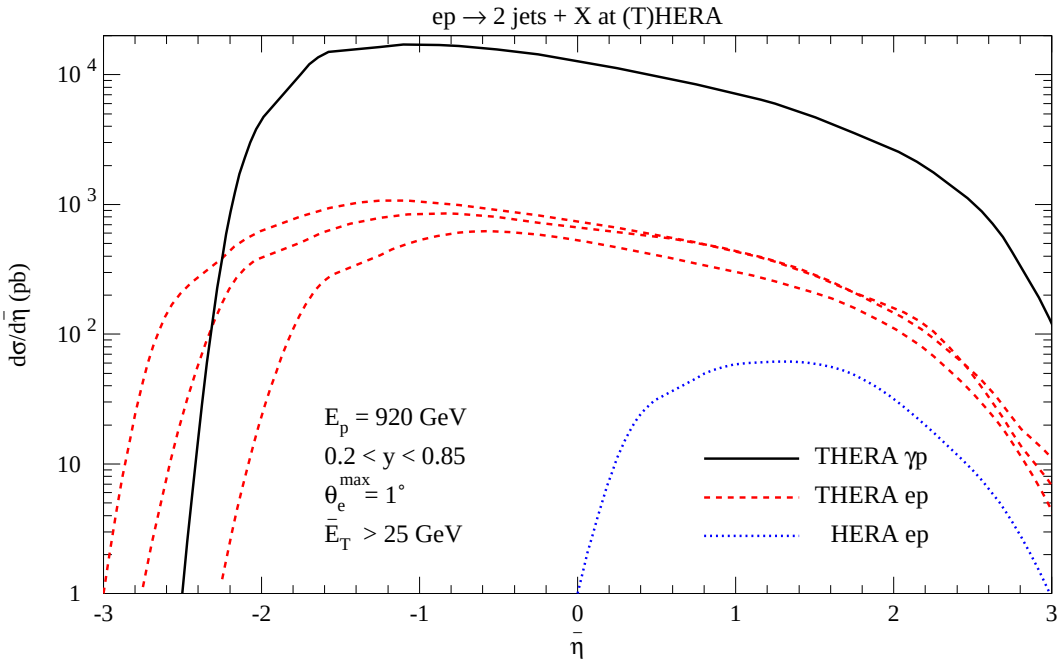

Figure 2: *Differential dijet photoproduction cross section as a function of the average rapidity of the two jets $\overline{\eta}$. For THERA ep we show results with three different electron beam energies E_e =250, 400, and 500 GeV.*

a massless vector boson in the t-channel

$$\overline{|\mathcal{M}|^2} \propto t^{-2} = \left[-\frac{1}{2}s(1-\cos\theta^*)\right]^{-2}, \tag{4.3.4}$$

whereas the direct processes proceed through a massless fermion exchange in the t-channel with less singular behavior,

$$\overline{|\mathcal{M}|^2} \propto t^{-1} = \left[-\frac{1}{2}s(1-\cos\theta^*)\right]^{-1} \tag{4.3.5}$$

or through s-channel contributions without any singular behavior. In Figure 3 we show the normalized dijet cross section as a function of $|\cos(\theta^*)|$. At HERA, the rather high cut on $\overline{E}_T > 25\,\mathrm{GeV}$ results in a $|\cos(\theta^*)|$ distribution which is mostly dominated by phase space. At THERA, the center-of-mass energies are larger: Phase space restrictions are unimportant, and the normalized distribution no longer depends on the electron beam energy or the collider mode (ep or γp), if the $\overline{E}_T$ cut is kept fixed. Therefore the expected singular behavior can now clearly be seen. The same distribution is valid if the HERA cut is scaled down to $\overline{E}_T > 318\,\mathrm{GeV}/959\,\mathrm{GeV} \times$

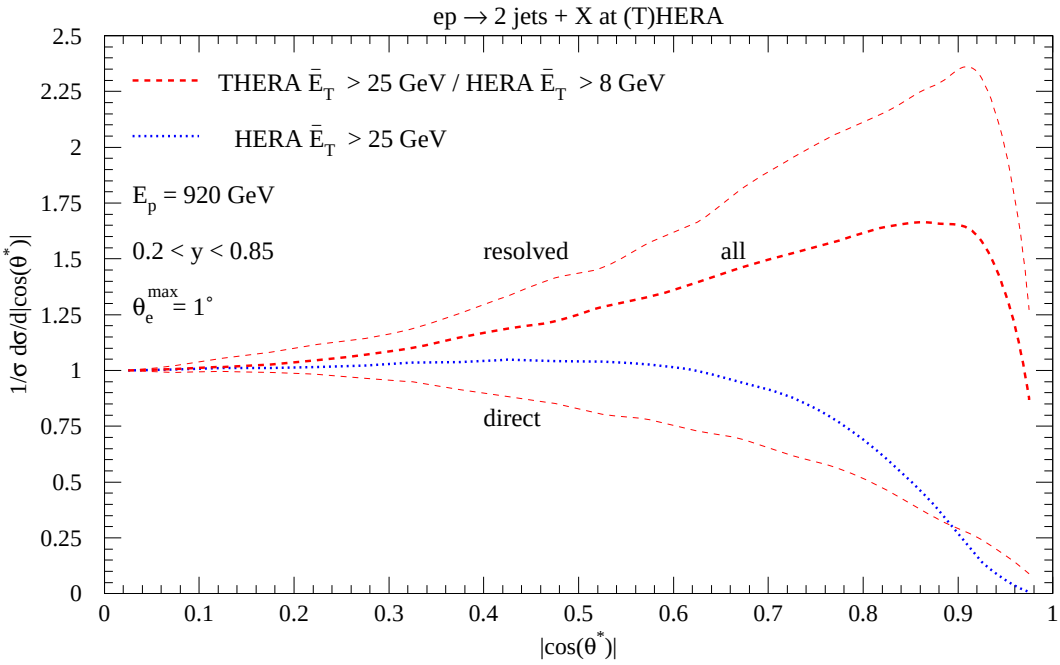

Figure 3: *Differential dijet photoproduction cross section as a function of the cosine of the center-of-mass scattering angle of the two jets* $|\cos(\theta^*)|$. *All curves have been normalized at* $|\cos(\theta^*)| = 0$.

25 GeV $\simeq$ 8GeV, which is similar to the cut $E_T > 6$ GeV used in a recent ZEUS analysis [15]. The ZEUS data were found to agree with next-to-leading order QCD predictions [5, 16]. In Figure 3 we also show results for direct and resolved photoproduction separately (thin curves). The resolved curve clearly shows the singular behavior in contrast to the direct contribution, which contributes only a small fraction to the total result (see also Figure 1).

For determinations of the partonic structure of protons and photons, distributions in the observed partonic momentum fractions are of great value. Figure 4 demonstrates that the range in $x_p^{\rm obs}$, in which the proton structure can be analyzed, is extended by at least one order of magnitude from 0.03 at HERA to 0.003–0.001 at THERA. Since the gluon dominates at values below 0.2, the low-x gluon determinations in deep-inelastic scattering could thus be tested in photoproduction for the first time.

Similarly, the range in $x_\gamma^{\rm obs}$ would be extended by at least one order of magnitude from 0.04 at HERA to 0.004–0.0025 at THERA. This can be seen in Figure 5. In the photon case, the gluon dominates below 0.25, so that HERA should already have the potential to constrain the gluon in the photon with photoproduced high-$\overline{E}_T$ jets in the region 0.04–0.25. THERA could, however, constrain the gluon down to much lower

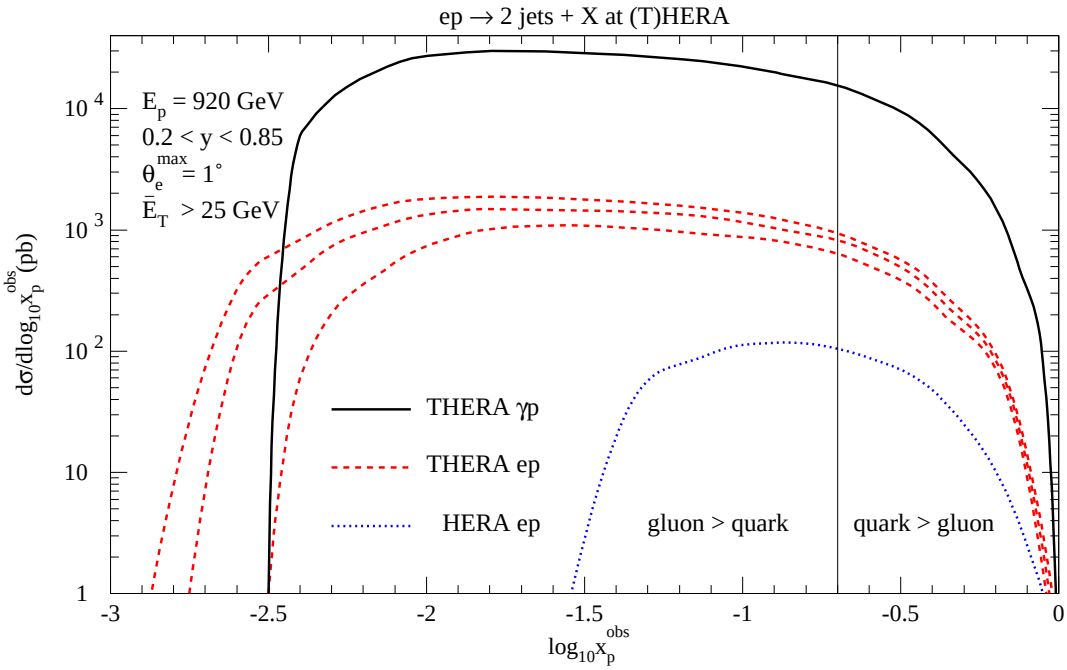

Figure 4: *Differential dijet photoproduction cross section as a function of the observed parton momentum fraction in the proton* $x_p^{\rm obs}$. *For THERA ep we show results with three different electron beam energies* E_e *=250, 400, and 500 GeV.*

values of $x_\gamma^{\rm obs}$. THERA *ep* cross sections with an electron beam energy of 250 GeV and different next-to-leading order parameterizations for the gluon density in the photon differ by 30–50% for $E_T > 29$ and 14 GeV [14].

4.3.4 Conclusion

Collisions of high-energy electrons from a future linear accelerator like TESLA with an existing proton beam in a 'THERA' *ep* machine offer great opportunities for jet photoproduction: They would naturally build on the current HERA program of testing QCD and determining the partonic structure of the proton and the photon. The range in the hard scale $\overline{E}_T$ could be extended by a factor of 2–3, which would reduce complications from the soft underlying event and hadronization. At the same time the range in the partonic momentum fractions x_p and x_γ could be extended by at least one order of magnitude. Determinations of the gluon in the proton at low x_p in deep inelastic scattering could then be tested, and the gluonic structure of the photon could be determined for the first time. Furthermore, event rates with three or more observed jets in the final state are expected to be larger at higher energies and could be compared

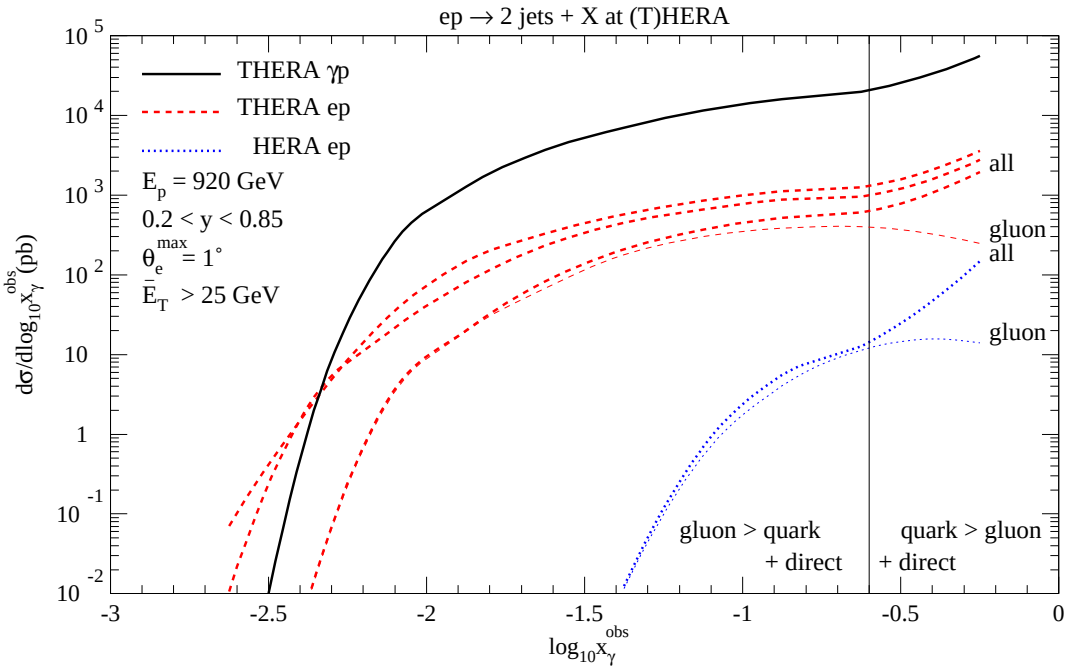

Figure 5: *Differential dijet photoproduction cross section as a function of the observed parton momentum fraction in the photon x_γ^{obs}. For THERA ep we show results with three different electron beam energies E_e =250, 400, and 500 GeV.*

to then-available higher order predictions to study the multi-particle QCD dynamics. The physics program of any future linear collider would thus greatly benefit from these additional opportunities.

Acknowledgments

The author thanks G. Kramer and H. Spiesberger for their encouragement and useful discussions and the Deutsche Forschungsgemeinschaft and the European Commission for financial support through Grants KL 1266/1-1 and ERBFMRX-CT98-0194.

References

[1] M. Klasen and G. Kramer, Phys. Lett. B **366** (1996) 385.

[2] H1 Coll., C. Adloff et al., Eur. Phys. J. C **1** (1998) 97.

[3] M. Klasen and G. Kramer, Z. Phys. C **76** (1997) 67.

[4] M. Klasen, T. Kleinwort and G. Kramer, Eur. Phys. J. direct C **1** (1998) 1.

[5] B.W. Harris and J.F. Owens, Phys. Rev. D **56** (1997) 4007.

[6] B.W. Harris and J.F. Owens, Phys. Rev. D **57** (1998) 5555.

[7] P. Aurenche et al., Eur. Phys. J. C **17** (2000) 413.

[8] S. Frixione and G. Ridolfi, Nucl. Phys. B **507** (1997) 315.

[9] B.W. Harris, M. Klasen and J. Vossebeld, Proc. of the Workshop on *Monte Carlo Generators at HERA Physics*, Hamburg, Germany, 1998, hep-ph/9905348.

[10] S. Catani et al., Nucl. Phys. B **406** (1993) 187.

[11] S.D. Ellis and D.E. Soper, Phys. Rev. D **48** (1993) 3160.

[12] M. Glück, E. Reya and A. Vogt, Phys. Rev. D **46** (1992) 1973.

[13] CTEQ Coll., H.L. Lai et al., Eur. Phys. J. C **12** (2000) 375.

[14] M. Wing, *The THERA Book*, DESY-LC-REV-2001-062 (2001).

[15] ZEUS Coll., M. Derrick et al., Phys. Lett. B **384** (1996) 401.

[16] M. Klasen, Eur. Phys. J. C **7** (1999) 225.

4.4 Precision Tests of Perturbative QCD at THERA

W.L.van Neerven[1]
Instituut-Lorentz, Universiteit Leiden, P.O. Box 9506, 2300 RA Leiden, The Netherlands.

Abstract

In this contribution we will point out that inclusive quantities like structure functions and sum rules, provided the latter are related to expectation values of (axial-) vector currents, are the best quantities to test perturbative QCD. This also holds for the heavy flavour component of the structure function which originates from the gluon-photon fusion process in deep inelastic lepton-hadron scattering. The principal reason is that all these observables receive their contributions from the light-cone region.

4.4.1 Introduction.

Calculations of higher order QCD corrections are very important for the following reasons

1. We need an accurate knowledge of the QCD background in order to find signatures of new physics like super-symmetry, lepto-quarks, compositeness etc. It might also be important for the Higgs search.
2. Analogous to the determination of the electro-weak constants we want to know the parameters in QCD like α_s, Λ_{QCD} and the heavy quark masses to a high degree of accuracy.

The last goal will be in particular achieved by studying the deep inelastic scattering process

$$l_1(k_1) + H(p) \to l_2(k_2) +' X' . \tag{4.4.1}$$

Here $'X'$ denotes any inclusive final hadronic state. The in and outgoing leptons are represented by l_1 and l_2 respectively and the hadron is denoted by H. On the Born level the reaction proceeds via the exchange of one of the vector bosons V of the standard model which are given by γ, Z and $W^{\pm}$. The kinematic variables are defined by

$$q = k_1 - k_2 , \qquad q^2 = -Q^2 < 0 , \qquad \nu = \frac{p \cdot q}{M} ,$$

$$x = \frac{Q^2}{2M\nu} , \quad 0 < x \leq 1 , \qquad y = \frac{p \cdot q}{p \cdot k_1} , \quad 0 < y < 1 . \tag{4.4.2}$$

[1]Work supported by the EC network 'QCD and Particle Structure' under contract No. FMRX–CT98–0194.

In lowest order of the electro-weak interaction one can compute the cross section

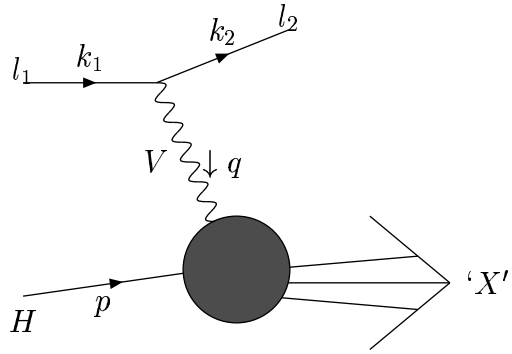

Figure 1: *Kinematics of deep inelastic lepton-hadron scattering.*

$d^2\sigma/dx\,dy$ of the process in Eq. (4.4.1) which provides us with the following observables

a. Unpolarised structure functions: F_1, F_2 (electromagnetism). Instead of the transverse structure function F_1 one can also choose the longitudinal structure function defined by $F_L = F_2 - 2xF_1$. For neutral or charged weak currents one gets access to F_3.

b. Polarised structure functions: g_1, g_2 (electromagnetism). In the case of neutral or charged weak currents one can in principle also measure g_3, g_4 and g_5.

One can also classify the structure functions according to their leading twist contributions.

a. Twist-two structure functions: F_1, F_2 (F_L), F_3, g_1, g_4 and g_5.

b. Twist-two and twist-three structure functions: g_2, g_3.

4.4.2 Light cone dominance and sum rules.

The reason why structure functions provides us with a better test of QCD, except for some totally integrated quantities like $\sigma_{tot}(e^+ + e^- \to \text{'}X')$, than any other process can be attributed to the property that the integrand of the Fourier transform

$$F(x, Q^2) = \frac{1}{4\pi M} \int d^4z\, e^{i\,q.z} \langle p \mid \Big[J(z), J(0)\Big] \mid p\rangle\,, \tag{4.4.3}$$

is dominated by the light-cone $z^2 \sim 0$ in the Bjorken limit $Q^2 \to \infty$ and $x = fixed$ with $x \neq 0$ and $x \neq 1$. Using the stationary phase argument where $q \cdot z = constant$ and causality which implies that

$$\Big[J(z), J(0)\Big] = 0 \qquad z^2 < 0\,, \tag{4.4.4}$$

one can show that all contributions to the integral are coming from the region $0 \leq z^2 < 1/Q^2$. This argument only holds when x is not too small. How small the value for x can be so that light-cone dominance still applies has to be determined by experiment. If the structure functions are dominated by the light-cone one can perform an operator production expansion (OPE) which can be written as

$$\Big[J(z), J(0)\Big] \underset{z^2 \sim 0}{=} \sum_{\tau} \sum_{N} C^{N,\tau}(z^2\mu^2) O^{N,\tau}(\mu^2, 0)\,, \tag{4.4.5}$$

where τ and N denote the twist and spin of the operator $O^{N,\tau}$ respectively. Both the coefficient function $C^{N,\tau}$ and the operator $O^{N,\tau}$ are understood to be re-normalised and μ denotes the re-normalisation scale which can be identified with the factorisation scale. Notice that the same arguments also apply to the cross section $\sigma_{tot}(e^+ + e^- \to \text{`}X')$ mentioned above, except for one thing namely that the latter is completely determined by perturbative QCD whereas the x-dependence of the structure function is due to non-perturbative effects which cannot be calculated yet. One can get rid of the x-dependence by computing sum rules which have the form $\int_0^1 dx\, \Delta F(x, Q^2)$. They can be classified as follows [1]

1. <u>Fundamental sum rules</u>

   They follow from quantum field theory from which one derives that the expression for $\int_0^1 dx\, \Delta F(x, Q^2)$ can be related to expectation values of conserved currents and partially conserved axial-vector currents sandwiched between hadronic states. These expectation values can be expressed into the quantum numbers of the hadron with respect to the underlying flavour group $SU(n)_F$. Examples are the Adler sum rule [2], the polarised [3] and unpolarised Bjorken [4] sum rules, The Gross Llewellyn-Smith [5] sum rule.

2. <u>phenomenological sum rules</u>

   In this case there does not exist a quantum field theoretical foundation so that the sum rules cannot be expressed into expectation values of the currents mentioned above. Mostly they depend on some assumptions made in parton models or are derived in the context of the Regge Pole model. An example of the former is the Gottfried sum rule [6] whereas the latter is represented by the Burkhardt-Cottingham sum rule [7]. The Ellis-Jaffe sum rule [8] is a special case. It can be related to expectation values of axial-vector currents among which the singlet axial-vector. However the latter is not conserved not even in the mass-less limit which is due to the Adler-Bell-Jackiw anomaly [9].

The sum rules of class 1 can be subdivided in two categories.

1a. This category of sum rules can be derived from equal time commutator (ETC) algebra [10]. They do not depend whether the (axial-) vector current consists of fermionic or bosonic fields. Therefore they even hold beyond QCD. An example

is the Adler sum rule [2] which in the case of $SU(4)_F$ is given by

$$\int_0^1 \frac{d\,x}{x}\left(F_2^{\bar{\nu}\mathrm{p}}(x,Q^2) - F_2^{\nu\mathrm{p}}(x,Q^2)\right) = 2 \tag{4.4.6}$$

Another property is that these sum rules do not receive any radiative corrections or power corrections of the type $(1/Q^2)^p$. This means that the result on the right hand side is independent of Q^2.

1b. These sum rules can be derived from a light-cone expansion of local currents where the coefficient function and the operators depend on the nature of the currents. In the case of QCD they consist out of quark fields. In the case of $SU(4)_F$ we have the following examples

unpolarised Bjorken sum rule [4]

$$\int_0^1 d\,x\left(F_1^{\bar{\nu}\mathrm{p}}(x,Q^2) - F_1^{\nu\mathrm{p}}(x,Q^2)\right) = 1 \tag{4.4.7}$$

Gross Llewellyn Smith sum rule [5]

$$\int_0^1 d\,x\left(F_3^{\bar{\nu}\mathrm{p}}(x,Q^2) + F_3^{\nu\mathrm{p}}(x,Q^2)\right) = 6 \tag{4.4.8}$$

Since the light-cone expansion is a series expansion in powers of $(1/Q^2)^p$ the sum rules of this category only hold in leading twist. Therefore the right hand side receives power corrections originating from higher twist operators and they become therefore Q^2 dependent. Moreover they also receive QCD corrections which have been calculated up to third order in α_s [11].

Besides the sum rules presented above one can derive similar ones which hold for neutral current reactions and polarised processes (see e.g. [1]). It would be interesting to measure them at THERA. Of course one also needs data from fixed target experiments to cover the whole x range. Hence the sum rules of class 1 which do not depend on any factorisation scale provide us with a very stringent test of QCD. The sum rules above are given by the first moment of the non-singlet structure function. One can also express the higher moments using the OPE in Eq. (4.4.5) into expectation values of higher spin operators as follows

$$\int_0^1 dx\, x^{N-1}\, F(x,Q^2) =$$

$$\sum_\tau \left(\frac{M^2}{Q^2}\right)^{\frac{\tau}{2}-1} A^{(N),\tau}(\mu^2)\mathcal{C}^{(N),\tau}\left(\frac{Q^2}{\mu^2}\right) . \tag{4.4.9}$$

Here N stands for the moment as well as the spin of the operator. The operator matrix element and the coefficient function are given by

$$A^{(N),\tau}(\mu^2) = \langle p \mid O^{N,\tau}(\mu^2,0) \mid p\rangle\,, \tag{4.4.10}$$

and

$$\mathcal{C}^{(N),\tau}\left(\frac{Q^2}{\mu^2}\right) = \int d^4z\, e^{iq.z} C^{N,\tau}(z^2\mu^2)\,, \tag{4.4.11}$$

If $F(x, Q^2)$ is known for the whole x-region (small extrapolations to regions where there are no data are allowed) one can extract $A^{(N),\tau}$ for finite N. In the future methods in lattice gauge theory will enable us to compute $A^{(N),\tau}$ with sufficient precision so that one compare the result with experiment. At this moment it is very hard to obtain the coefficient function at higher twist $\tau > 2$. However for $\tau = 2$ one can compute the coefficient functions and the anomalous dimensions of the operators $O^{N,2}(\mu^2, 0)$ up to a certain order in QCD in order to predict the Q^2-evolution of the structure function in Eq. (4.4.9). The measurement of the structure function at large Q^2 and large x is very important for

1 Determination of the strong coupling constant α_s and Λ_{QCD}.

2 Extraction of the quark densities $f_q(z, \mu^2)$ $(q = u, d, s)$ and the gluon density $f_g(z, \mu^2)$.

At this moment one can only analyse the structure functions up to next-to-leading order (NLO). However if one wants to determine the quantities above with high precision a next-to-next-to-leading order computation of the coefficient functions and the anomalous dimensions (splitting functions) is necessary. Since the early nineties one has achieved much progress. Let us enumerate the status.

1. Polarised and unpolarised coefficient functions are known up to order α_s^2 [12].

2. The three-loop anomalous dimensions $\gamma^{(N)}$ of the operators $O^{N,\tau}(\mu^2, 0)$ are known up to $N = 12$ [13].

In the near future one hopes to get the complete result for the three-loop anomalous dimension. However if the value of x is not too small one can already obtain from the first twelve moments and some additional theoretical input of the small x-behaviour a very good estimate of the splitting functions which is sufficient to determine the Q^2-evolution of the structure functions for $x > 10^{-4}$. The three-loop anomalous dimension is also important for the Drell-Yan process where the second order coefficient function is already known since about ten years. This enables us to obtain a full NNLO expression for the Drell-Yan cross section which can serve as a luminosity monitor for proton-antiproton and proton-proton collisions. One of the aims of the NNLO analysis is to remove the artificial factorisation scale dependence in the structure function which is purely artificial as we will show below. In order to facilitate our discussion we take the Mellin transform of the structure function. Choosing the non-singlet part as an example we can write

$$F^{(N)}(Q^2) = f_q^{(N)}(\mu_f^2, \mu_r^2)\, \mathcal{C}_q^{(N)}\left(\frac{Q^2}{\mu_f^2}, \frac{\mu_r^2}{\mu_f^2}\right) \tag{4.4.12}$$

where the non-singlet quark density is given by

$$f_q^{(N)}(\mu_f^2,\mu_r^2) = \left[1 + a_s(\mu_f^2)\left\{\frac{\gamma_{qq}^{(N),(1)}}{2\beta_0} - \frac{\beta_1\,\gamma_{qq}^{(N),(0)}}{2\beta_0^2}\right\}\right]\left[\frac{a_s(\mu_f^2)}{a_s(Q_0^2)}\right]^{\gamma_{qq}^{(N),(0)}/2\beta_0} f_q^{(N)}(Q_0^2)$$

$$\text{with} \qquad a_s(\mu_r^2) = \frac{\alpha_s(\mu_r^2)}{4\pi} \tag{4.4.13}$$

and the non-singlet quark coefficient function reads

$$\mathcal{C}_q^{(N)}\left(\frac{Q^2}{\mu_f^2},\frac{\mu_r^2}{\mu_f^2}\right) = \left[1 + a_s(Q^2)\left\{c_q^{(1)} + \frac{\gamma_{qq}^{(N),(1)}}{2\beta_0} - \frac{\beta_1\,\gamma_{qq}^{(N),(0)}}{2\beta_0^2}\right\}\right.$$

$$\left. -a_s(\mu_f^2)\left\{\frac{\gamma_{qq}^{(N),(1)}}{2\beta_0} - \frac{\beta_1\,\gamma_{qq}^{(N),(0)}}{2\beta_0^2}\right\}\right]\left[\frac{a_s(Q^2)}{a_s(\mu_f^2)}\right]^{\gamma_{qq}^{(N),(0)}/2\beta_0} \tag{4.4.14}$$

after multiplication one observes that the factorisation scale disappears in the order a_s expression which reads

$$F^{(N)}(Q^2) = \left[1 + a_s(Q^2)\left\{c_q^{(1)} + \frac{\gamma_{qq}^{(N),(1)}}{2\beta_0} - \frac{\beta_1\,\gamma_{qq}^{(N),(0)}}{2\beta_0^2}\right\}\right]\left[\frac{a_s(Q^2)}{a_s(Q_0^2)}\right]^{\gamma_{qq}^{(N),(0)}/2\beta_0} f_q^{(N)}(Q_0^2)$$

$$+a_s^2(\mu_f^2)\,F^{(2)}(Q^2,\mu_f^2) \tag{4.4.15}$$

where $F^{(2)}$ represents the second order term which is factorisation scheme and therefore factorisation scale dependent. This dependence is removed when one includes the corrections coming from the second order coefficient function $c_q^{(2)}$ and the three-loop anomalous dimension $\gamma_{qq}^{(N),(2)}$. Next we substitute

$$a_s(Q^2) = a_s(\mu_r^2)\Big[1 - a_s(\mu_r^2)\,\beta_0\,\ln\frac{Q^2}{\mu_r^2}\Big] \tag{4.4.16}$$

and truncate the perturbation series at order $a_s^2(\mu_r^2)$ so that it becomes factorisation scale independent. In this way we have removed the artificial dependence on μ_f and the perturbation series for the structure function has now the same characteristics as shown by the sum rules of class 1 and the ratio

$$R_{e^+e^-}(Q^2) = \frac{\sigma_{tot}(e^+ + e^- \to \text{`}X')}{\sigma_{tot}(e^+ + e^- \to \mu^+ + \mu^-)}$$

$$1 + a_s(\mu_r^2)\,c_1 + a_s^2(\mu_r^2)\Big[-\beta_0\,c_1\,\ln\frac{Q^2}{\mu_r^2} + c_2\Big] + \cdots \tag{4.4.17}$$

For the computation of the quantity above mass factorisation was not needed so that μ_f does not show up at the beginning. In order to get rid of the remaining normalisation

scale μ_r-dependence one very often uses improved perturbation theory. Examples of this method are the Principle of Minimal Sensitivity (PMS) [14], the Effective Charge Scheme [15] or Padé-methods. However in all procedures one needs at least a NNLO representation of the Physical quantities. Therefore it is necessary that the second order correction $F^{(2)}$ in Eq. (15) becomes completely known. Summarising our findings in this section we conclude that deep inelastic structure functions are one of the quantities which provides us with the best test of QCD. The reasons are

1. They are inclusive so that we do not have to deal with non-perturbative hadronisation effects which cannot be computed from first principles.

2. In the Bjorken limit only the light-cone region of the current-current correlation function contributes to the structure function. This statement is even valid beyond QCD.

3. In order to get rid of the non-perturbative x-dependence of the structure function one can compute sum rules which are a very stringent test of QCD. Some sum rules like the Adler sum rule are even valid beyond QCD.

Notice that apart from decay widths and the expression n Eq. (17) no other quantities satisfy the above properties. An example is the Drell-Yan process where the cross section can be written as

$$\begin{aligned} \frac{d\,\sigma}{d\,Q^2} &= \frac{4\pi\alpha^2}{Q^4}\,\tau\,W(\tau,Q^2) \qquad \tau = \frac{Q^2}{S} \qquad S = (p_1+p_2)^2 \\ W(\tau,Q^2) &= \frac{1}{4\pi}\int d^4z\,e^{i\,q\cdot z}\,\langle p_1,s_1;p_2,s_2 \mid J^\mu(z)\,J_\mu(0) \mid p_1,s_1;p_2,s_2\rangle \end{aligned} \tag{4.4.18}$$

Here the product of the two currents cannot be written as a commutator unlike we have seen in the case for the structure functions. Therefore when $Q^2 \to \infty$ the contribution to $W(\tau,Q^2)$ does not come from the light-cone only but also from other regions in position space. The same holds for all other deep inelastic or hard processes like jet production in hadron-hadron collisions, direct photon production, heavy flavour production etc.. Therefore these processes are theoretically less suitable to test QCD. There is one exception namely heavy flavour production in deep inelastic lepton-hadron scattering. here it turns out that the dominant production mechanism receives its contribution from the light-cone region only as we will discuss in the next section.

4.4.3 Heavy flavour production.

First we will discuss the theoretical and experimental problems characteristic of heavy flavour production in hadron-hadron collisions and photo-production which also show up in the case of jet-production, the Drell-Yan process and other reactions which do not receive their contributions from the light-cone region. Finally we address heavy flavour production in deep inelastic lepton-hadron scattering and show that that these processes are more promising as a test of QCD.

Hadron-hadron collisions

Examples are heavy flavour production like charm, bottom and top production in $p\bar{p}$ and $\pi - N$ (charm only) scattering. The main production mechanism is the gluon-gluon fusion process

$$g + g \to Q + \bar{Q} \tag{4.4.19}$$

which dominate $c\bar{c}$ and $b\bar{b}$ production. In the case of $t\bar{t}$ production also light quark anti-quark annihilation is important at least on the Born level

$$q + \bar{q} \to Q + \bar{Q} \tag{4.4.20}$$

The cross section can be schematically cast into the form

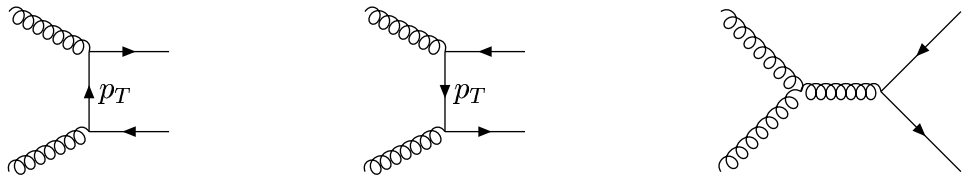

Figure 2: *Lowest order gluon-gluon fusion process* $g + g \to Q + \bar{Q}$.

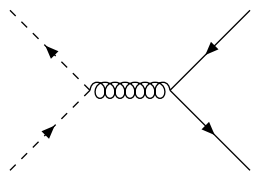

Figure 3: *Lowest order quark anti-quark process* $q + \bar{q} \to Q + \bar{Q}$.

$$d\sigma \sim \sum_{i,j=q,\bar{q},g} f_i^{H_1} \otimes f_j^{H_2} \otimes d\sigma_{ij} \tag{4.4.21}$$

where H_1 and H_2 are the incoming hadrons. The theoretical status is that the NLO partonic cross sections $d\sigma_{ij}$ are available [16], [17]. A re-summation is performed of the soft gluon contributions which dominate the threshold region $S \sim 4m^2$ [18]. Furthermore one also has re-summed the large logarithms of the form $\ln^k p_T/m$ which arise in the final state heavy quark fragmentation into hadrons [19]. The experimental status can be summarised as follows. A comparison of the reaction $\pi + N \to c + \bar{c} +' X'$ ($E_\pi = 500$ GeV, $E791 - data$) [20] shows that the NLO cross section agrees with the data but it has large theoretical uncertainties which is revealed by the variation of the factorisation and renormalisation scale. Furthermore to get agreement with D^0 production one needs a hard charm quark fragmentation function $D_c^{D^0}(x, k_T, \mu^2)$ with

a large intrinsic k_T of about 1 GeV. Therefore we think that the agreement between experiment and theory is fortuitous and that higher order corrections will completely change the picture. This becomes even clearer when we look at bottom production in the process $p + \bar{p} \to b + \bar{b} +' X'$ measured at the TEVATRON ($\sqrt{S} = 1.8$ TeV. The shape of the inclusive transverse momentum distribution agrees with the theoretical NLO prediction but the normalisation is off by roughly a factor of two [21] i.e.

$$\frac{d\ \sigma^{exp}/d\ p_T^b}{d\ \sigma^{NLO}/d\ p_T^b} \sim 2 \tag{4.4.22}$$

Resummation of the large logarithms in the heavy quark fragmentation process $\ln p_T/m_b$ [19] improves the situation a little bit at large p_T i.e. $p_T \gg m_b$ but hardly changes the normalisation in the region $p_T \sim m_b$. Another feature is that the ratio

$$\frac{d\ \sigma^{NLO}/d\ p_T^b}{d\ \sigma^{LO}/d\ p_T^b} \sim 2 \tag{4.4.23}$$

is quite big (a correction of about 100 %) which indicates that the perturbation series is unstable. Therefore we do not expect that NNLO contributions will improve the theoretical cross section because of Eq. (22) we need at least 100 % correction. If that happens one might then wonder about the N^3LO contribution. Finally we comment on top production. Since at this moment one has only a few events one can hardly draw any conclusion about the agreement between data and the NLO prediction for the total cross section. In the near future more data will be obtained. It will be very interesting to see whether the same discrepancy between theory and experiment also holds for the top quark cross section in particular as far as its normalisation is concerned.

Photon-hadron collisions

Here the main production mechanism is given by the photon-gluon fusion process

$$\gamma + g \to Q + \bar{Q} \tag{4.4.24}$$

Besides the reaction above, which is called the unresolved photon contribution, one

Figure 4: *Lowest-order photon-gluon fusion process* $\gamma + g \to Q + \bar{Q}$.

also has the resolved photon contribution which on the Born level is given by the processes in Figs. (2), (3). Here one of the gluons or the light (anti-) quark originates

from the real (on-shell) photon. The cross section can be written as

$$d\sigma \sim e_Q^2 \sum_{i=q,\bar{q},g} f_i^H \otimes d\sigma_i + \sum_{i,j=q,\bar{q},g} f_i^H \otimes f_j^\gamma \otimes d\sigma_{ij} \tag{4.4.25}$$

where $d\sigma_i$ and $d\sigma_{ij}$ are given by reactions (24) and (19),(20) respectively including higher order radiative corrections. Further f_i^γ denotes the parton density of the photon. From the theoretical view point we can say the following. Both partonic cross sections are known up to NLO [22] and a resummation of the large logarithms in the heavy quark fragmentation process $\ln p_T/m_b$ has been performed in [23]. The latter leads to an improved large p_T-distribution. Furthermore we have the same theoretical uncertainties as in hadron-hadron scattering like a considerable scale μ-dependence of $d\sigma^{NLO}$. Also the ratio $d\sigma^{NLO}/d\sigma^{LO}$ is large. Moreover one has to deal with large uncertainties in f_i^γ which is not well known in particular in the small x-region. As far as the experimental status is concerned one has measured the process $\gamma + p \to c + \bar{c} +' X'$ [24] from which one has obtained the distributions $d\sigma/dp_T^D$ and $d\sigma/d\eta_T^D$ where η^D is the rapidity of the D-meson. For $\eta^D > 0.1$ the shape of the cross section differs from the one given by the NLO prediction i.e.

$$\frac{d\ \sigma^{exp}}{d\ \eta^D} > \frac{d\ \sigma^{NLO}}{d\ \eta^D} \tag{4.4.26}$$

The discrepancy between theory and experiment becomes even more striking when one looks at bottom production $\gamma + p \to b + \bar{b} +' X'$ recently measured at HERA [25]. In the case of the total cross section one has found

$$\frac{\sigma_{tot}^{exp}}{\sigma_{tot}^{NLO}} \sim 1.6 \tag{4.4.27}$$

where the theoretical cross section has been obtained from [26]. which looks similar to

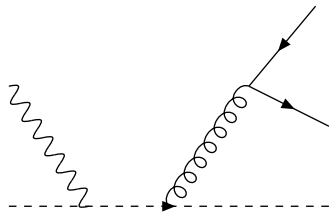

Figure 5: *Second-order Compton scattering process $\gamma^* + q \to Q + \bar{Q} + q$ contributing to the coefficient functions $L_{i,k}^{(2)}$.*

the observation made at the TEVATRON (see Eq. (23)).

Electro-production of heavy quarks.

In lowest order there is one production mechanism only provided one considers neutral

current processes. It is given by the photon-gluon fusion process in Eq. (24) where now the photon is highly virtual. In the case of charged current interactions one has in addition on the Born level the reaction

$$W + q \to Q \tag{4.4.28}$$

Notice that in our considerations above we have neglected intrinsic heavy quark production which would lead to the Born process $\gamma^* + Q \to Q$. We assume that the probability to find a heavy quark inside the hadron is very small. Limiting ourselves to virtual photon dominated reactions one can express the inclusive cross section into heavy quark structure functions denoted by $F_{i,Q}(x, Q^2, m^2)$ $(Q = c, b)$ similar to the deep inelastic process mentioned in the introduction. This structure function can be decomposed in two parts as

$$F_{i,Q} \sim e_Q^2 \sum_{k=g,q\bar{q}} f_k^H(\mu^2) \otimes H_{i,k}\left(\frac{Q^2}{m^2}, \frac{\mu^2}{m^2}\right) + \sum_{k=g,q\bar{q}} e_k^2 f_k^H(\mu^2) \otimes L_{i,k}\left(\frac{Q^2}{m^2}, \frac{\mu^2}{m^2}\right) \tag{4.4.29}$$

Each part originates from different production mechanisms. The first term, represented by the coefficient function $H_{i,k}$, is due to sub-processes where the virtual photon couples to the heavy quark with charge e_Q (see e.g. Fig. (4)) whereas the second term, represented by $L_{i,k}$, is determined by the processes where the virtual photon reacts with the light quark with charge e_k. The latter show up for the first time in second order (see Fig. (5)). Theoretical calculations show that $F_{i,Q}$ is dominated by the first term only whereas the second term is negligible over the whole phase space. The structure functions $F_{i,Q}$ $(i = 2, L)$ and the differential cross sections have been computed up to NLO on [27]. A soft gluon resummation which improves the threshold behaviour has also been performed in [28]. As is shown in [29] the NLO corrected structure function is much less sensitive to a variation in the factorisation/renormalisation scale than the NLO cross sections in hadron-hadron and photon-hadron production. As far as the experimental status is concerned at this moment we have data for charm quark production only from the reaction $\gamma^* + p \to c + \bar{c} +' X'$ [30], [31]. There exist good agreement between the NLO prediction of $F_{2,c}$ and the data in NLO, but not LO, over the whole x-range. This good agreement enables us to measure the gluon density $f_g(x, \mu^2)$ with high precision. The only uncertainty is the mass of the charm-quark. There exist also good agreement between the data and the differential distributions like $d\sigma/dp_T$ and $d\sigma/d\eta$ computed in [32] although the statistics is still rather low to draw definite conclusions. Anyhow it is interesting that the rapidity distribution is in better agreement with the data obtained in electro-production than in photo-production. At this moment there are no data for bottom quark electro-production. This will be possible at THERA which operates at larger energies than HERA. It will be interesting to see whether here the data are in better agreement with the NLO prediction than in the case of photo-production and hadron-hadron production.

4.4.4 Comparison between electro-production and photo- and hadro-production.

In this section we will give some arguments why electro-production of heavy quarks provides us with a better test of QCD than the other reactions which we have discussed above. Let us therefore look at the most simple physical quantities like total cross sections and structure functions since they are inclusive objects which are not affected by final state hadronisation mechanisms. The most striking difference between the structure function in electro-production on one hand and photo-production, hadron-hadron production on the other hand is that the former quantity depends on three scales whereas the latter on two scales only. Denoting $\sqrt{S}$ as the centre of mas energy of the (virtual) photon-hadron or hadron-hadron system the structure function can be written as $F_{i,Q}(S, Q^2, m^2)$ $(\gamma^* + H \to Q)$ whereas the total cross section is given by $\sigma_{tot}(S, m^2)$ $(\gamma + H \to Q,\ H1 + H2 \to Q)$. According to the principles of QCD perturbation theory is only possible if all kinematic scales are large and their mutual ratios are not too large but also not too small. This implies that for $\sigma_{tot}^{\gamma H}$ and σ_{tot}^{H1H2}, the CM energy should be in the region $S = O(m^2)$ which is unfortunately not satisfied by experiment in particular for charm production. In practice one has $S \gg m^2$. Calculations up to NLO reveal that the partonic cross sections behave for $s \gg m^2$ like

$$\begin{aligned}
\sigma_{tot}^{\gamma g} &\sim \alpha\, a_s \frac{1}{s}\left[c_{\gamma g}^{(0)} \ln\frac{s}{m^2} + a_s\, c_{\gamma g}^{(1)} \ln^3\frac{s}{m^2} + \cdots\right] \\
&\quad + \alpha\, a_s^2 \frac{1}{m^2}\left[d_{\gamma g}^{(0)} + a_s\, d_{\gamma g}^{(1)} \ln\frac{s}{m^2} + \cdots\right] \\
\sigma_{tot}^{gg} &\sim a_s^2 \frac{1}{s}\left[c_{gg}^{(0)} \ln\frac{s}{m^2} + a_s\, c_{gg}^{(1)} \ln^3\frac{s}{m^2} + \cdots\right] \\
&\quad + a_s^3 \frac{1}{m^2}\left[d_{gg}^{(0)} + a_s\, d_{gg}^{(1)} \ln\frac{s}{m^2} + \cdots\right]
\end{aligned} \tag{4.4.30}$$

where s is the partonic centre of mass energy squared which can be written as $s = x_1 S$ (photo-production) or $s = x_1 x_2 S$ (hadro-production). Here x_i denote the fractions of the hadronic H_i momenta carried away by the incoming partons. In the expressions above we observe two types of large corrections. The ones proportional to $1/m^2$ originate from soft gluon exchanges in the t-channel sub-processes and give rise to the so called small x-terms which can be re-summed in all orders of perturbation theory. However after convolution with the gluon density the contributions proportional to $1/m^2$ become suppressed. This is not the case for the first parts in Eq. (30). The large logarithms, which rise faster in power than those coming from the small x-terms in the second part, originate from the integration region $p_T \sim O(m) \to 0$ (see Figs. (2), (4)) so that the process ceases to be hard when $p_T \to 0$. Furthermore these large logarithms cannot be re-summed since mass factorisation is not applicable here. However this does not happen for $F_{i,Q}(S, Q^2, m^2)$. Since we have an additional scale Q^2 one can write for

$S \sim O(Q^2)$ and $Q^2 \gg m^2$

$$F_{i,Q} \quad \rightarrow \quad F_{i,Q}^{\text{asymp}} \sim e_Q^2 \sum_{k=1}^{\infty} a_s^k \ln^k \frac{Q^2}{m^2} \tag{4.4.31}$$

where we have limited ourselves for simplicity to the production mechanism corresponding to the first part of Eq. (29) only. The reason for this behaviour is very simple. The heavy quark structure function is dominated by the light-cone region in contrast to the quantities in Eq. (30). This is revealed by the behaviour of the Mellin transform of the heavy quark coefficient functions which for $Q^2 \rightarrow \infty$ behave in the same way as the Mellin transform of the structure function in Eq. 9.

$$H_{i,k}^{(N),\text{asymp}} \sim \sum_{k=1}^{\infty} a_s^k \sum_{l=0}^{k} \ln^l \frac{Q^2}{m^2} \ln^{k-l-1} \frac{\mu^2}{m^2} \quad k \geq l+1 \tag{4.4.32}$$

One can now apply mass factorisation and write

$$H_{i,k}^{(N),\text{asymp}} \left(\frac{Q^2}{m^2}, \frac{\mu^2}{m^2} \right) = A_{Qk}^{(N)} \left(\frac{\mu^2}{m^2} \right) \mathcal{C}_{i,q} \left(\frac{Q^2}{m^2} \right) \quad i = 2, L \tag{4.4.33}$$

with

$$A_{Qk}^{(N)} \left(\frac{\mu^2}{m^2} \right) = \langle k \mid O_Q^N(0, \mu^2) \mid k \rangle \quad k = g, q, \bar{q} \tag{4.4.34}$$

where O_Q^N represents the heavy quark operator of spin N. Furthermore $\mathcal{C}_{i,q}$ denotes the light quark coefficient function. The large logarithmic terms $\ln^k Q^2/m^2$ can be resummed via the renormalisation group equation because of the factorisation property in Eq. (33). Notice that this was not possible for the terms $\ln^k S/m^2$ appearing in the first part of Eq. (30) which moreover rise faster at increasing power in a_s than the logarithms $\ln^k Q^2/m^2$ in Eq. (31). The light-cone dominance of the structure function is a much stronger property than the mass factorisation of the initial state collinear divergences leading to the partonic cross sections in Eq. (30). Moreover it is possible that soft hadronic exchanges between the incoming hadrons or incoming (hadron-like) real photon and hadron cannot be ignored. They are excluded in the virtual photon case provided Q^2 is chosen large enough. This is maybe the reason why the theoretical description of heavy flavour production works much better for deep inelastic lepton-hadron scattering than for other reactions. The factorisation property in (33) also leads to another phenomenon namely a change in the number of light flavours for the description of the structure function. Choosing charm production as an example. For three flavours ($n_f = 3$) one can write

$$F_{i,Q}^{\text{asymp}} \sim e_Q^2 \left[f_g(3) \otimes H_{i,g}^{\text{asymp}} + \Big(f_u(3) + f_{\bar{u}}(3) + f_d(3) + f_{\bar{d}}(3) + f_s(3) + f_{\bar{s}}(3) \Big) \otimes H_{i,q}^{\text{asymp}} \right] \tag{4.4.35}$$

Using Eq. (33) one can write a four flavour number ($n_f = 4$) scheme representation for the charm structure function

$$F_{i,Q}^{\rm asymp} \sim e_Q^2 \Bigg[\Big(f_c(4) + f_{\bar{c}}(4) \Big) \otimes \mathcal{C}_{i,q}^{\rm NS} + f_g(4) \otimes \mathcal{C}_{i,g} + \Big(f_u(4) + f_{\bar{u}}(4) + f_d(4) + f_{\bar{d}}(4) + f_s(4) + f_{\bar{s}}(4) + f_c(4) + f_{\bar{c}}(4) \Big) \otimes \mathcal{C}_{i,q}^{\rm PS} \Bigg] \tag{4.4.36}$$

where PS denotes the purely singlet contribution. The charm quark density in the four flavour number scheme reads

$$f_c(4) + f_{\bar{c}}(4) = f_g(3) \otimes A_{Qg} + \Big(f_u(3) + f_{\bar{u}}(3) + f_d(3) + f_{\bar{d}}(3) + f_s(3) + f_{\bar{s}}(3) \Big) \otimes A_{Qq} \tag{4.4.37}$$

with similar expressions for $f_q(4) + f_{\bar{q}}(4)$ ($q = u, d, s$). All logarithms of the type $\ln^k \mu^2/m^2$ are absorbed in the heavy quark operator matrix elements A_{Qk} ($k = g, \bar{q}, q$) which enter the definition of the four flavour parton density. Using the renormalisation group one can re-sum these logarithms in all orders of the coupling constant a_s. A thorough analysis [33] reveals that the resummation does not cause a big effect with respect to the exact structure function provided it is calculated beyond LO. Notice that the procedure which changes the description of the structure function for n_f flavours into a function of $n_f + 1$ flavours is also applicable to other quantities carrying three scales even if they are not dominated by the light-cone. Examples are the transverse momentum distributions $d\sigma^{\gamma H}/dp_T$ and $d\sigma^{H_1 H_2}/dp_T$ for $p_T \gg m$ where the three scales are given by S, m^2 and p_T^2 with the condition $S \sim O(p_T^2)$ and $p_T \gg m$. From the considerations above we conclude

1. Electro-production of heavy flavours is one of the examples which provide us with a good test of QCD. This statement holds for charm quark production and it will be interesting to see whether our predictions are also correct for bottom production at THERA.

2. Because of the non-re-summable logarithmic terms $\ln^k S/m^2$ which occur in the total cross sections of photo-production and hadro-production, the higher order corrections will not lead to more reliable predictions in particular as far as the normalisation is concerned (too large K-factors).

3. Structure functions and other inclusive quantities which contributions are coming from the light-cone region are the best observables to test QCD.

References

[1] V. Ravindran and W.L. van Neerven, hep-ph/0102280.

[2] S.L. Adler, Phys. Rev. **143** (1966) 1144.

[3] J.D. Bjorken, Phys. Rev. **148** (1966) 1467, Phys. Rev. **D 1** (1970) 1376.

[4] J.D. Bjorken, Phys. Rev. **163** (1967) 1767.

[5] D.J. Gross and C.H. Llewellyn Smith, Nucl. Phys. **B 283** (1969) 337.

[6] K. Gottfried, Phys. Rev. Lett. **18** (1967) 1174.

[7] H. Burkhardt and W.N. Cottingham, Ann. Phys. (N.Y.) **56** (1970) 453.

[8] J. Ellis and R. Jaffe, Phys. Rev. **D 9** (1974) 1444, Erratum **D 10** (1974) 1669.

[9] S.L. Adler, Phys. Rev. **177** (1969) 2426; J.S. Bell and R. Jackiw, Nuovo Cim. **A 60** (1969) 47.

[10] M. Gell-Mann, Physics **1**, (1964) 63.

[11] S.A. Larin and J.A.M. Vermaseren, Phys. Lett. **B 259** (1991) 345.

[12] E.B. Zijlstra and W.L. van Neerven, Nucl. Phys. **B 383** (1992) 525, ibid. **B 417** (1994) 61, ibid. Erratum **B 426** (1994) 245, **B 501** (1997) 599.

[13] S.A. Larin, T. van Ritbergen and J.A.M. Vermaseren, Nucl. Phys. **B 427** (1994) 41;
S.A. Larin et al., Nucl. Phys. **492** (1997) 338;
J.A.M. Vermaseren and S. Moch, hep-ph/0004235;
A. Retey and J.A.M. Vermaseren, hep-ph/0007294.

[14] P.M. Stevenson, Phys. Rev, **D 23** (1981) 2916.

[15] G. Grunberg, Phys. Lett. **B 95** (1980) 70, Erratum ibid. **B 110** (1982) 501.

[16] P. Nason, S. Dawson and R.K. Ellis, Nucl. Phys. **B 303** (1988) 697; ibid. **B 327** (1989) 49, Erratum ibid. **B 335** (1990) 260.

[17] W. Beenakker et al., Phys. Rev. **D 40** (1989) 54;
W. Beenakker et al., Nucl. Phys. **B 351** (1991) 507.

[18] E. Laenen, J. Smith and W.L. van Neerven, Nucl. Phys. **B 369** (1992) 543.

[19] M. Cacciari and M. Greco, P. Nason, JHEP **9805** (1998) 007, hep-ph/9803400.

[20] E791 Coll., E.M. Aitala et al. Phys. Lett. **B 462** (1999) 225.

[21] CDF Coll., F. Abe et al. , Phys. Rev. Lett. **71** (1993) 2396, Phys. Rev. **D 53** (1996) 1051;
D0 Coll., S. Abachi et al. , Phys. Rev. Lett. **74** (1993) 3548, Phys. Lett. **B 370** (1996) 239.

[22] R.K. Ellis and P. Nason, Nucl. Phys. **B 312** (1989) 551;
J. Smith and W.L. van Neerven, Nucl. Phys. **B 374** (1992) 36;
S. Frixione et al., Nucl. Phys. **B 412** (1994) 225.

[23] B.A. Kniehl, G. Kramer and M. Spira, Z. Phys. **C 76** (1997) 689;
M. Cacciari, S. Frixione and P. Nason, hep-ph/0102134.

[24] H1 Coll., C. Adloff et al., Nucl. Phys. **B 545** (1999) 21.

[25] H1 Coll., C. Adloff et al. (H1-Collaboration), Phys. Lett. **B 467** (1999) 156.

[26] S. Frixione et al., Phys. Lett. **B 348** (1995) 633.

[27] E. Laenen et al., Nucl. Phys. **B 392** (1993) 162, 229;
S. Riemersma, J. Smith, W.L. van Neerven, Phys. Lett. **B 347** (1995) 143.

[28] E. Laenen and S.O. Moch, Phys. Rev. **D 59** (1999) 034027.

[29] M. Glück, E. Reya and M. Stratmann, Nucl. Phys. **B 422** (1994) 37;
A. Vogt, in *Deep Inelastic Scattering and Related Phenomena, DIS96*, edited by G.D. 'Agostini and A. Nigro, (World Scientific 1997), p. 254, hep-ph/9601352.

[30] H1 Coll., C. Adloff et al., Z. Phys. **C 72** (1996) 593; Nucl. Phys. **B 545** (1999) 21.

[31] ZEUS Coll., J. Breitweg et al., Phys. Lett. **B 407** (1997) 402; Euro. Phys. J. **C 12** (2000) 1, 35.

[32] B.W. Harris and J. Smith, Nucl. Phys. **B 452** (1995) 109; Phys. Lett. **353** (1995) 535; Phys. Rev. **D 57** (1998) 2806.

[33] A. Chuvakin, J. Smith and W.L. van Neerven, Phys. Rev. **D 61** (2000) 096004.

4.5 Heavy Quark Production in the Semihard QCD Approach at THERA

S.P. Baranov
P.N. Lebedev Physics Institute, Leninsky prosp. 53,
Moscow 117924, Russia

N.P. Zotov
D.V. Skobeltzyn Institute of Nuclear Pysics,
M.V. Lomonosov Moscow State University, Moscow 119899, Russia

Abstract

In the framework of the semihard (k_T factorization) QCD approach, we consider the photoproduction of $D^{*\pm}$ mesons associated with two hadron jets and the $D^{*\pm}$ production in DIS at THERA conditions with the emphasis on the BFKL and CCFM dynamics of gluon distributions. In the photoproduction of $D^{*\pm}$ mesons the attention is focused on the variable x_γ, which is the fraction of the photon momentum contributed to a pair of jets with largest p_T. We show that our theoretical results are sensitive to the BFKL type dynamics which may be investigated at THERA energies. We also discuss possible effect of J/ψ meson spin alignement, which is thought to be a vivid manifestation of gluon off-shellness.
PACS number(s): 12.38.-t, 13.60.-r, 13.87.Ce

Keywords: $D^{*\pm}$, J/ψ and jet production, semihard QCD approach, BFKL and CCFM unintegrated gluon distribution

4.5.1 Introduction

The experimental results on heavy flavour production processes obtained by the H1 [1] and ZEUS [2, 3] collaborations at HERA provide a strong impetus for further theoretical and experimental studies in a new energy region at THERA conditions.

In due time, the experimental data have been compared with next-to-leading order (NLO) perturbative QCD calculations using the 'massive' and 'massless' schemes. The measured cross sections generally lie above the predicted level, and an agreement between the theoretical and experimental results can only be achieved using some extreme parameter values. In particular, the production rates of $D^{*\pm}$ mesons in the NLO massive scheme [4] require as low quark mass as $m_c = 1.2$ GeV and as sharp charm fragmentation function as $\epsilon = 0.02$ (in the Peterson parametrization). However, even

within this set of parameters, the shapes of the $D^{*\pm}$ transverse momentum and rapidity distributions cannot be said well reproduced. A good agreement between the massless scheme [5] and the measured $p_T(D^*)$ (though not $\eta(D^*)$) spectrum was achieved upon introducing an additional charm excitation contribution assuming an incredibly large charm content in the photon structure functions [6]: $c(x) \approx u(x)$.

The so called k_T factorization, or the semihard approach (SHA) [7]- [10] can give reasonable explanations for many phenomena, and this fact becomes more and more commonly recognised. Its applications to a variety of photo-, lepto- and hadroproduction processes are widely discussed in the literature [11] - [15]. In many cases a remarkable agreement is found between the data and the theoretical calculations regarding the photo- [16] and electroproduction [17] of $D^{*\pm}$ mesons, forward jets [18], as well as for specific kinematical correlations observed in the associated $D^{*\pm}$ +jets photoproduction [19] at HERA and also the hadroproduction of beauty [20, 21], χ_c [22] and J/ψ [23] at Tevatron. The theoretical predictions made in ref. [24] has triggered a dedicated experimental analysis [25] of the J/ψ polarization (i.e., spin alignement) at HERA energies.

To some extent, the SHA based on the BFKL [26] gluon dynamics includes the relevant effects of higher order contributions [27, 28]. It has been also demonstrated in [19] that the SHA effectively imitates the anomalous coupling of the resolved photon and an ad hoc contribution from the resolved photon is no longer needed at least for the description of the x_γ distribution in $D^{*\pm}$ photoproduction at HERA energies.

In the present paper we use the semihard QCD approach to predict some features of the $D^{*\pm}$ and J/ψ production processes in the new energy region of THERA collider.

4.5.2 The semihard QCD approach

The production of J/ψ mesons and open-flavoured $c\bar{c}$ pairs is described in terms of the photon-gluon fusion mechanism. A generalization of the usual parton model to the k_T-factorization approach implies two essential steps. These are the introduction of unintegrated gluon distributions and the modification of the gluon spin density matrix in the parton-level matrix elements.

At first, we consider the relevant partonic subprocesses. Let k_1, k_2, k_3 and p_ψ be the momenta of the initial state photon, the initial state gluon, the final state gluon and the final state J/ψ, respectively, ϵ_1, ϵ_2, ϵ_3 and ϵ_ψ the polarization vectors, and $k{=}k_1{+}k_2$. The photon-gluon fusion matrix elements then read:

$$\begin{aligned}\mathcal{M}(\gamma g \to \psi g) = tr\{ \not\epsilon_1 \, (\not p_c - \not k_1 + m_c) \, \not\epsilon_2 \, (- \not p_{\bar{c}} - \not k_3 + m_c) \, \not\epsilon_3 \, J(\epsilon_\psi)\} \\ \times [k_1^2 - 2(p_c k_1)]^{-1} [k_3^2 + 2(p_{\bar{c}} k_3)]^{-1} \quad + 5 \text{ permutations}\end{aligned} \tag{4.5.1}$$

Similarly, for the production of an open-flavoured $c\bar{c}$ pair (see fig. 1b):

$$\begin{aligned}\mathcal{M}(\gamma g \to c\bar{c}) = \bar{u}(p_c)\{ \not\epsilon_1 \, (\not p_c - \not k_1 + m_c) \, \not\epsilon_2 \, [k_1^2 - 2k_1 p_c]^{-1} \\ + \not\epsilon_2 \, (\not p_c - \not k_2 + m_c) \, \not\epsilon_2 \, [k_2^2 - 2k_2 p_c]^{-1}\} u(p_{\bar{c}})\end{aligned} \tag{4.5.2}$$

In the expression (4.5.1), the projection operator [29] $J(\epsilon_\psi) = \not\epsilon_\psi\,(\not p_c + m_c)/\sqrt{m_\psi}$ guarantees the proper spin structure of the $c\bar{c}$ state, and the charmed quarks are assumed to each carry one half of the J/ψ momentum, $p_c = p_{\bar{c}} = p_\psi/2$, $m_c = m_\psi/2$. The formation of a meson from the $c\bar{c}$ pair is a nonperturbative process. Within the nonrelativistic approximation we are using, this probability reduces to a single parameter related to the meson wave function at the origin $|\Psi(0)|^2$, which is known for J/ψ and Υ families from the measured leptonic decay widths.

The evaluation of traces in (4.5.1)-(4.5.2) is straightforward and is done using the algebraic manipulation system FORM [30]. The complete set of matrix elements has been tested for gauge invariance by substituting the gluons momenta for their polarization vectors.

The multiparticle phase space $\prod d^3p_i/(2E_i)\,\delta^4(\sum p_{in} - \sum p_{out})$ is parametrized in terms of transverse momenta, rapidities and azimuthal angles: $\frac{d^3p_i}{2E_i} = \frac{\pi}{2} dp_{iT}^2 dy_i \frac{d\phi_i}{2\pi}$. Let ϕ_1 and ϕ_2 be the azimuthal angles of the initial photon and gluon, ϕ_3, ϕ_ψ, ϕ_c and $\phi_{\bar{c}}$ the azimuthal angles of the partonic subprocess products (i.e., of a J/ψ and a gluon, or a charmed quark and an antiquark, respectively) and y_3, y_ψ, y_c and $y_{\bar{c}}$ their rapidities. Then, the fully differential cross sections read:

$$d\sigma(ep \to \psi g X) = \frac{\alpha_s^2 \alpha e_c^2\,|\Psi(0)|^2}{4\,x_2\,s^2}\,\frac{1}{4}\sum_{\text{spins}}\frac{1}{8}\sum_{\text{colours}}|\mathcal{M}(\gamma g \to \psi g)|^2$$
$$\times \mathcal{F}_g(x_2, k_{2T}^2, \mu^2)\; dk_{1T}^2\, dk_{2T}^2\, dp_{\psi T}^2\, dy_3\, dy_\psi\, \frac{d\phi_1}{2\pi}\,\frac{d\phi_2}{2\pi}\,\frac{d\phi_\psi}{2\pi}, \tag{4.5.3}$$

$$d\sigma(ep \to c\bar{c}X) = \frac{\alpha_s \alpha e_c^2}{16\pi\,x_2\,s^2}\,\frac{1}{4}\sum_{\text{spins}}\frac{1}{8}\sum_{\text{colours}}|\mathcal{M}(\gamma g \to c\bar{c})|^2$$
$$\times \mathcal{F}_g(x_2, k_{2T}^2, \mu^2)\; dk_{1T}^2\, dk_{2T}^2\, dp_{cT}^2\, dy_c\, dy_{\bar{c}}\, \frac{d\phi_1}{2\pi}\,\frac{d\phi_2}{2\pi}\,\frac{d\phi_c}{2\pi}. \tag{4.5.4}$$

The phase space physical boundary is determined by the inequality

$$G(\hat{s}, \hat{t}, k_4^2, k_1^2, k_2^2, k_3^2) \le 0, \tag{4.5.5}$$

where k_3 and k_4 denote the final state partons' momenta, $\hat{s} = (k_1 + k_2)^2$, $\hat{t} = (k_1 - k_3)^2$, and G is the standard kinematical function [31].

When calculating the spin average of the matrix element squared, we substitute the full lepton tensor for the photon polarization matrix:

$$\overline{\epsilon_1^\mu \epsilon_1^{*\nu}} = 4\pi\alpha[8p_e^\mu p_e^\nu - 4(p_e k_1) g^{\mu\nu}]/(k_1^2)^2 \tag{4.5.6}$$

(including also the photon propagator factor and photon-lepton coupling). For the off-shell incoming gluon we take [7]

$$\overline{\epsilon_2^\mu \epsilon_2^{*\nu}} = k_{2T}^\mu k_{2T}^\nu / |k_{2T}|^2. \tag{4.5.7}$$

This formula converges to the usual $\sum \epsilon^\mu \epsilon^{*\nu} = -g^{\mu\nu}$ when $k_T \to 0$. The final state gluon in (4.5.1) is assumed on-shell, $\sum \epsilon_3^\mu \epsilon_3^{*\nu} = -g^{\mu\nu}$. The J/ψ polarization vector ϵ_ψ is

defined as an explicit four-vector. In the frame with z-axis along the J/ψ momentum, $p_\psi = (0,\, 0,\, |p_\psi|,\, E_\psi)$, it reads for different helicity states:

$$\epsilon_{\psi(h=\pm 1)} = (1,\, \pm i,\, 0,\, 0)/\sqrt{2}, \qquad \epsilon_{\psi(h=0)} = (0,\, 0,\, E_\psi,\, |p_\psi|)/m_\psi. \tag{4.5.8}$$

The initial photon and gluon momentum fractions x_1 and x_2 are calculated from the energy-momentum conservation laws in the light cone projections:

$$\begin{aligned} (k_1+k_2)_{E+p_{||}} = x_1\sqrt{s} &= m_{3T}\exp(y_3) \;+\; |m_{4T}|\exp(y_4), \\ (k_1+k_2)_{E-p_{||}} = x_2\sqrt{s} &= m_{3T}\exp(-y_3) + |m_{4T}|\exp(-y_4). \end{aligned} \tag{4.5.9}$$

The multidimensional integration in (4.5.3), (4.5.4) has been performed by means of Monte-Carlo technique, using the routine VEGAS [32].

Another important ingredient of the semihard approach is the so called unintegrated gluon distribution $\mathcal{F}(x, k_T^2, \mu^2)$, which determines the probability to find a gluon carrying the longitudinal momentum fraction x and transverse momentum k_T. In calculations we use two different sets of unintegrated gluon distributions. One of them is based on the approach of ref. [33] and is costructed as a leading-order perturbative solution of the BFKL equation. Technically, the unintegrated gluon density $\mathcal{F}_g(x, k_T^2, \mu^2)$ is calculated as a convolution of the ordinary gluon density $G(x, \mu^2)$ with universal weight factors:

$$\mathcal{F}_g(x, k_T^2, \mu^2) = \int_x^1 \mathcal{G}(\eta, k_T^2, \mu^2)\, \frac{x}{\eta}\, G(\frac{x}{\eta}, \mu^2)\, d\eta, \tag{4.5.10}$$

$$\mathcal{G}(\eta, k_T^2, \mu^2) = \frac{\bar{\alpha}_s}{\eta\, k_T^2}\, J_0(2\sqrt{\bar{\alpha}_s \ln(1/\eta)\ln(\mu^2/k_T^2)}), \qquad k_T^2 < \mu^2, \tag{4.5.11}$$

$$\mathcal{G}(\eta, k_T^2, \mu^2) = \frac{\bar{\alpha}_s}{\eta\, k_T^2}\, I_0(2\sqrt{\bar{\alpha}_s \ln(1/\eta)\ln(k_T^2/\mu^2)}), \qquad k_T^2 > \mu^2, \tag{4.5.12}$$

where J_0 and I_0 stand for Bessel functions (of real and imaginary arguments, respectively), and $\bar{\alpha}_s = \alpha_s/3\pi$. The LO GRV set [34] was used here for the boundary conditions. Another set of unintegrated gluon densities was extracted from a numerical simulution of the CCFM equations [35] and then tabulated in the form of a FORTRAN code [18]. Finally, the charm quarks were converted into $D^{*\pm}$ mesons using the Peterson fragmentation function [36].

In the paper [16] we used the standard GRV parametrization [34] for the collinear gluon density, from which the unintegrated gluon distribution was developed according to eqs. (4.5.10)-(4.5.12). Some other essential parameters were chosen as follows: the charm quark mass $m_c = 1.5$ GeV, the Peterson fragmentation parameter $\epsilon = 0.06$, the overall $c \to D^*$ fragmentation probability 0.26. The Pomeron intercept Δ was regarded as free parameter, and then the value $\Delta = 0.35$ has been extracted from a fit to the experimental $p_T(D^*)$ spectrum measured by the ZEUS collaboration [2]. Close estimates for Δ have also been obtained by many other authors, see, e.g. [37, 38]. Since the agreement with the data achieved within this set of parameters was really good [16, 17], we continue using it in the present calculations.

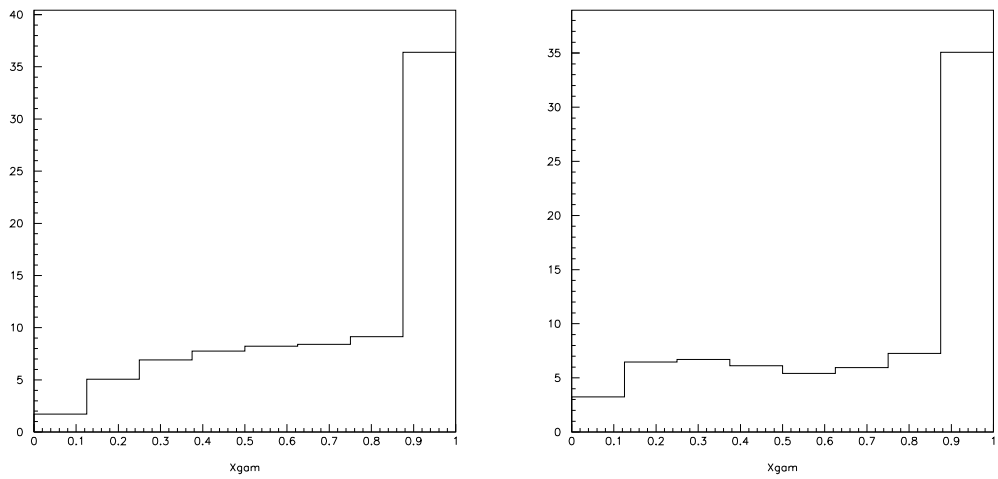

Figure 1: *The differential cross section $d\sigma/dx_\gamma$ (nb) for $Q^2 < 1$ GeV^2 with BFKL and CCFM unintegrated gluon distributions at THERA.*

4.5.3 Numerical results

4.5.3.1 $D^{*\pm}$ and dijet associated photoproduction at THERA

The ZEUS collaboration has measured the associated charm and dijet production [2] as a further test of the underlying parton dynamics. In these measurements, the quantity of interest is the fraction of the photon momentum contributing to the production of two jets with highest E_T, which is experimentally defined as

$$x_\gamma = [E_{1T}\exp(-\eta_1) + E_{2T}\exp(-\eta_2)]/(2E_e\, y) \tag{4.5.13}$$

with E_{iT} and η_i being the transverse energy and rapidity of these hardest jets.

In the ref. [19] the theoretical calculations have been made within the SHA with different unintegrated gluon distributions at HERA energies. In Fig.1 we present the results of similar theoretical calculations made within the semihard approach with BFKL and CCFM unintegrated gluon distributions at THERA energies. The simulation procedure consists in generating a photon-gluon fusion event using the off-shell matrix elements and the unintegrated gluon distribution functions described in Section 2.

The basic $2 \to 2$ partonic subprocess gives rise to two high-energy quarks, which can further evolve into hadron jets. Actually, as the matter of some reasonable approximation, the calculations were restricted to parton level, and so the produced quarks (with their known kinematical parameters) were taken to play the role of the final jets: $E_T(jet_{1,2}) = E_T(q, \bar{q})$.

The two quarks are accompanied by a number of gluons radiated in the course of the gluon evolution. It has been mentioned already that, on the average, the gluon transverse momentum decreases from the hard interaction block towards the proton.

As an approximation, we assume that the gluon closest to the quark block with its momentum k' compensates the whole transverse momentum of the virtual gluon participating in the hard interaction: $\vec{k'}_T \simeq -\vec{k}_T$, while all the other emitted gluons are collected together in the 'proton remnant', which is assumed to carry only a negligible transverse momentum compared to $\vec{k'}_T$. This gluon gives rise to a third hadron jet with $E_T = |\vec{k'}_T|$.

From among the three hadron jets represented by the quark, antiquark and gluon we choose the two carrying the largest transverse energies, and then calculate the quantity x_γ according to its definition given by equ. (4.5.13) [1].

In a significant fraction of events, the gluon radiated from the BFKL cascade appears to be harder than one or even both of the quarks produced in hard parton interaction [19]. In fact, the specified events are responsible for the wide plateau seen in the x_γ distribution in Fig. 1

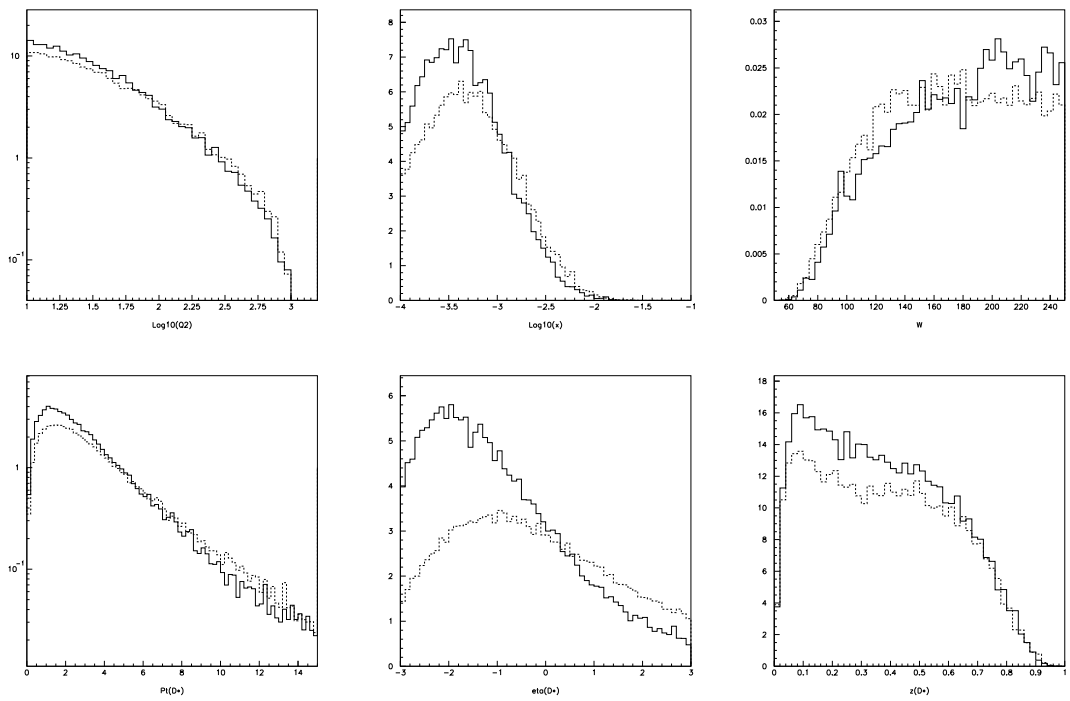

Figure 2: *Differential cross sections for deep inelastic $D^{*\pm}$ production with BFKL and CCFM unintegrated gluon distributions at THERA as functions of:* (*a*) $\log_{10} Q^2$, (*b*) $\log_{10} x$, (*c*) W, (*d*) $p_T(D^*)$, (*e*) $\eta(D^*)$ *and* (*f*) $z(D^*)$.

[1]The full FORTRAN code is available from the authors on request.

4.5.3.2 Deep inelastic $D^{*\pm}$ production at THERA

The process of deep inelastic $D^{*\pm}$ production at HERA is truly semihard because of the presence of two large scales: the virtuality of the exchanged photon (Q^2) and the charm mass (m_c^2), both being much larger than Λ_{QCD} but much smaller than s. Therefore, experimental data concerning the $D^{*\pm}$ production in DIS at THERA provide a strong impetus for further theoretical studies of this process.

In Fig. 2 the theoretical predictions on the differential cross sections of deep inelastic $D^{*\pm}$ production are shown for the THERA kinematical region: $1 < Q^2 < 1000$ GeV^2, $1.5 < p_T(D^{*\pm}) < 15$ GeV and $|\eta(D^{*\pm})| < 1.5$. Different curves in Fig. 2 correspond to the BFKL and CCFM unintegrated gluon distributions. At HERA energies the SHA calculations with BFKL unintegrated gluon distribution have shown [17] some shift to negative $\eta(D^*)$ with respect to the ZEUS data. When we have used the CCFM unintegrated gluon density from MC generator CASCADE [18] with JETSET based fragmentation function [39] implemented in, we obtain good agreement between our theoretical results and the ZEUS experimental data [3] also for $d\sigma/d\eta(D^*)$ [17].

4.5.3.3 J/ψ photoproduction at THERA

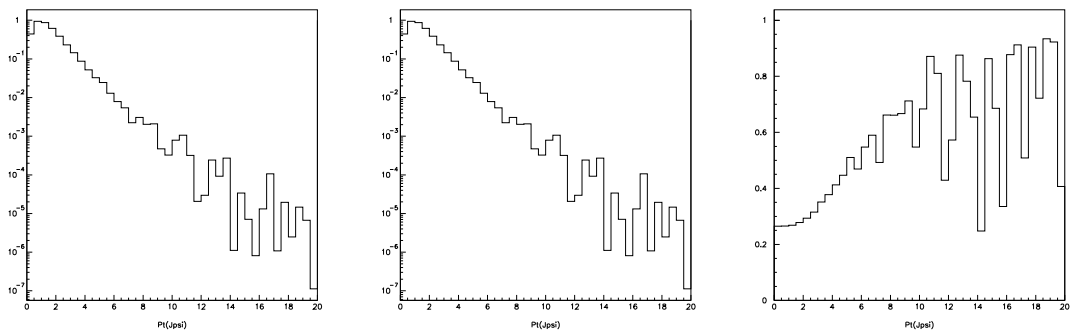

Figure 3: *Differential cross sections for inelastic J/Ψ photoproduction with BFKL unintegrated gluon distributions at THERA: (a) Inclusive J/Ψ transverse momentum distribution, (b) the same, but for J/Ψ zero helicity states only, (c) the fraction of J/Ψ mesons in helicity zero state (degree of spin alignement).*

The role of the gluon virtuality may be seen in Fig. 3, where we show the results of calculations for J/ψ photoproduction made with the BFKL unintegrated gluon distribution. The results correspond to THERA conditions, i.e. electron proton collisions at the energy $\sqrt{s} = 1000$ GeV, where no other cuts were applied except the photoproduction limit $Q^2 < 1$ GeV^2 and the inelasticity requirement $0.4 < z < 0.9$.

The effects of initial gluon off-shellness may be, best of all, seen in the transverse momentum spectra [24], because the gluon virtuality is proportional to its transverse momentum: $m^2 = -k_T^2/(1-x)$. In contrast with the conventional (massless) parton

model, the SHA shows that the fraction of J/ψ mesons in the helicity zero state increases with their transverse momentum p_T. A deviation from the parton model behaviour becomes well pronounced already from $p_T > 3$ GeV at HERA energies [24], and at $p_T > 6$ GeV the helicity zero polarization tends to be even dominant (Fig. 3c).

Qualitatively, the difference between the model predictions referes to different origins of the J/ψ transverse momentum. In the case of conventional parton model J/ψ mesons obtain their transverse momenta from the hard photon gluon interaction, while in the SHA there is also a large contribution from the initial gluon transverse momentum.

The degree of spin alignement can be measured experimentally since the different polarization states of J/ψ result in significantly different angular distributions of the $J/\psi \to l^+l^-$ decay leptons:

$$d\Gamma_{h=\pm 1}/dcos\Theta = 1 + cos^2\Theta, \qquad d\Gamma_{h=0}/dcos\Theta = 1 - cos^2\Theta \tag{4.5.14}$$

Here Θ is the angle between the lepton and J/ψ directions, measured in the J/ψ meson rest frame. Evidently, the most informative regions relate to $cos\Theta = \pm 1$.

4. Conclusions

In the framework of semihard QCD approach, we obtained some predictions for the cross sections of inclusive $D^{*\pm}$ meson production at THERA conditions using different unintegrated gluon distribution driven by the BFKL and CCFM evolution equations.

We have considered the photoproduction of $D^{*\pm}$ mesons associated with two hadron jets and also $D^{*\pm}$ production in DIS at THERA conditions, which may be a sensitive indicator of the underlying parton dynamics. The results of the simulations show that theoretical results are very sensitive to BFKL type dynamics in particular to the unintegrated gluon distribution in the proton.

We have considered also the effects of initial gluon off-shellness in SHA for J/ψ meson photoproduction at THERA energies. Gluon virtuality connected with its transverse momentum is one of the inherent properties of noncollinear (BFKL) parton evolution theory. Compared to traditional (collinear) parton model gluons are characterized by a different spin density matrix. The latter is found to affect the polarization of J/ψ mesons produced in ep collisions via photon gluon fusion subprocess. The effect is best pronounced at large J/ψ transverse momenta and can be detected experimentally by measuring the $J/\psi \to l^+l^-$ decay lepton angular distributions. We recommend the above process as a direct probe of the gluon virtuality, which can eventually testify for the validity of BFKL gluon evolution.

Thus the experimental and theoretical investigations in the new kinematic region of THERA collider will provide additional tests of the semihard (k_T factorization) approach and, in particular, of the "universality" of unintegrated gluon distribution.

Acknowledgments

The work was supported by Royal Swedish Academy of Sciences.

References

[1] H1 Coll., C. Adloff et al., Eur. Phys. J. **C 13**, 371 (2000); Contributed paper to the 30th International Conference on High-Energy Physics ICHEP2000, Osaka, Japan, July 2000, abstract 984.

[2] ZEUS Coll., J. Breitweg et al., Eur. Phys. J. **C 6**, 67 (1999).

[3] ZEUS Coll., J. Breitweg et al., Eur. Phys. J. **C 12**, 35 (2000).

[4] S. Frixione, P. Nason and G. Ridolfi, Nucl. Phys. **B 454**, 3 (1995).

[5] J. Binnewies, B.A. Kniehl and G. Kramer, Zeit. Phys. **C 76**, 677 (1997), Phys. Rev. **D 58**, 014014 (1998);
B.A. Kniehl, G.Kramer and M. Spira Zeit. Phys. **C 76**, 689 (1997);
M. Cacciari et al., Phys. Rev. **D 55**, 2736 (1997);
M. Cacciari and M. Greco *ibid.* , 7134 (1997).

[6] L.E. Gordon and J.K. Storrow, Zeit. Phys. **C 56**, 307 (1992).

[7] L.V. Gribov, E.M. Levin and M.G. Ryskin, Phys. Rep. **100**, 1 (1983);
E.M. Levin and M.G. Ryskin, Phys. Rep. **189**, 267 (1990).

[8] E.M. Levin et al., Sov. J. Nucl. Phys. **53**, 657 (1991).

[9] S. Catani, M. Ciafaloni and F. Hautmann, Phys. Lett. **B 242**, 97 (1990); Nucl. Phys. **B 366**, 135 (1991).

[10] J.C. Collins and R.K. Ellis, Nucl. Phys. **B 360**, 3 (1991).

[11] E.M. Levin et al., Sov. J. Nucl. Phys. **53**, 1059 (1991) , Sov. J. Nucl. Phys. **54**, 1420 (1991); M.G. Ryskin, Yu.M. Shabelski and A.G. Shuvaev, Zeit. Phys. **C 69**, 269 (1996).

[12] J.R. Forshaw and R.G. Roberts, Phys. Lett. **B 335**, 494 (1994).

[13] V. Del Duca, Sci. Acta 10 (1995) 91.

[14] V.A. Saleev and N.P. Zotov, Mod. Phys. Lett. **A 9**, 151 (1994); **A 11**, 25 (1996).

[15] A.V. Lipatov and N.P. Zotov, Mod. Phys. Lett. **A 15**, 695 (2000);
A.V. Lipatov, V.A. Saleev and N.P. Zotov, Mod. Phys. Lett. **A 15**, 1727 (2000).

[16] S.P. Baranov and N.P. Zotov, Phys. Lett. **B 458**, 389 (1999).

[17] S.P. Baranov, H. Jung and N.P. Zotov, in: Proc. Workshop on Monte Carlo Generators, A. Doyle, G. Grindhammer, G. Ingelman, H. Jung (Ed.), DESY, Hamburg, 1999, p. 484; hep-ph/9910210; S.P. Baranov, H. Jung and N.P. Zotov, in: Proc. Int. Workshop on Diffraction Phenomena, Cetraro, Italy, 2000 (to be published in Nucl. Phys.

[18] H. Jung, in: Proc. Workshop on Monte Carlo Generators, DESY, Hamburg, 1999, p. 75.

[19] S.P. Baranov and N.P. Zotov, Phys. Lett. **B 491**, 111 (2000).

[20] S.P. Baranov and M. Smižanská, Phys. Rev. **D 62**, 014012 (2000).

[21] Ph. Hägler et al., Phys. Rev. **D 62**, 071502 (2000).

[22] Ph. Hägler et al., hep-ph/0004263.

[23] Ph. Hägler, et al., hep-ph/008316;
F. Yuan and K.-T. Chao, hep-ph/0008302; 0009224.

[24] S.P. Baranov, Phys. Lett. **B 428**, 377 (1998).

[25] L. Gladilin, private communication.

[26] E.A. Kuraev, L.N. Lipatov and V.S. Fadin, Sov. Phys. JETP **45**, 199 (1977);
Ya. Balitsky and L.N. Lipatov, Sov. J. Nucl. Phys. **28**, 822 (1978).

[27] A.G. Ryskin, A.G. Shuvaev and Yu.M. Shabelski, hep-ph/9907507.

[28] B. Andersson, G. Gustafson and J. Samuelsson, Nucl. Phys. **B 467**, 443 (1996).

[29] R. Baier and R. Rückl, Phys. Lett. **B 102**, 364 (1981);
E.L. Berger and D. Jones, Phys. Rev. **D 23**, 1521 (1981).

[30] J.A.M. Vermaseren, Symbolic Manipulations with FORM, published by CAN (Computer Algebra Nederland), Kruislaan 413, 1098, SJ Amsterdaam 1991, ISBN 90-74116-01-9.

[31] E. Bycling and K. Kajantie, *Particle Kinematics*, John Wiley and Sons (Eds.), 1973.

[32] G.P. Lepage, J. Comp. Phys. **27**, 192 (1978).

[33] J. Blümlein, DESY preprint DESY 95-121 (1995).

[34] M. Glück, E. Reya and A. Vogt, Zeit. Phys. **C 67**, 433 (1995).

[35] M. Ciafaloni, Nucl. Phys. **B 296**, 49 (1988);
S. Catani, F. Fiorani and G. Marchesini, Phys. Lett. **B 234**, 339 (1990); Nucl. Phys. **B 336**, 18 (1990);
G. Marchesini, Nucl. Phys. **B 445**, 49 (1995).

[36] C. Peterson et al., Phys. Rev. **D 27**, 105 (1983).

[37] J. Kwiecinski, A.D. Martin and P.J. Sutton, Zeit. Phys. **C 71**, 585 (1996);
B. Andersson et al., Zeit. Phys. **C 71**, 613 (1996);
B.I. Ermolaev, M. Greco and S.I. Troyan, Preprint CERN-TH/99-155;
N.N. Nikolaev and V.R. Zoller, hep-ph/0001084.

[38] L3 Coll., M. Acciarri et al., Phys. Lett. **B 453**, 333 (1999);
M. Kienzle, talk given at the International Symposium on Evolution Equations and Large Order Estimates in QCD, Gatchina, May 2000.

[39] T. Sjöstrand, Comp. Phys. Comm. 82 (1994) 74.

4.6 Charged-current Deep Inelastic Scattering at THERA

K. Nagano
Institute of Particle and Nuclear Studies, KEK, Tsukuba, Japan
kunihiro.nagano@desy.de

4.6.1 Introduction

The charged-current (CC) DIS cross sections can be written as

$$\frac{d^2\sigma^{CC}(e^{\pm}p)}{dxdQ^2} = \frac{{G_F}^2}{2\pi x}\left(\frac{{M_W}^2}{{M_W}^2+Q^2}\right)^2 \times \phi_{\pm}^{CC}(x,Q^2), \quad (4.6.1)$$

$$\phi_{\pm}^{CC}(x,Q^2) = \frac{1}{2}\{Y_+F_2^{CC}(x,Q^2) \mp Y_-xF_3^{CC}(x,Q^2) - y^2F_L^{CC}(x,Q^2)\}, \quad (4.6.2)$$

where G_F is the Fermi constant, and M_W is the mass of the $W^{\pm}$ boson. At leading-order QCD, the structure function terms $\phi_{\pm}^{CC}$ can be written as

$$\phi_{+}^{CC}(x,Q^2) = x[(\overline{u}(x,Q^2)+\overline{c}(x,Q^2)) + (1-y)^2(d(x,Q^2)+s(x,Q^2))], \quad (4.6.3)$$

$$\phi_{-}^{CC}(x,Q^2) = x[(u(x,Q^2)+c(x,Q^2)) + (1-y)^2(\overline{d}(x,Q^2)+\overline{s}(x,Q^2))], \quad (4.6.4)$$

where $d(x,Q^2)$ is, for example, the parton density function (PDF) for the d-quark. The flavor-selecting nature of CC interaction is clearly seen; only down-type quarks (antiquarks) and up-type antiquarks (quarks) participate at leading order in e^+p (e^-p) CC DIS. The kinematic suppression factor $(1-y)^2$ is multiplied to quarks (antiquarks) in e^+p (e^-p) collisions.

In this study, we assume THERA will provide $200\,\mathrm{pb}^{-1}$ for each of e^- and e^+ beams. The beam energies are assumed to be 250 GeV and 920 GeV for $e^{\pm}$ and p, respectively. It is denoted "THERA-I" in this section. There is also a THERA upgrade plan of colliding $e^{\pm}$ of 800 GeV and p of 800 GeV. We denote this upgrade "THERA-II" with an assumption of $200\,\mathrm{pb}^{-1}$ of luminosities for each of e^- and e^+ beams. Monte Carlo events were generated using DJANGOH [1] generator with CTEQ5D PDF [2]. Detector responses were simulated using ZEUS detector simulation program based on GEANT [3]. The event-selection efficiency was evaluated by applying the algorithm used in the ZEUS analysis [4]. For comparison, we have made the same studies also for the HERA upgrade, "HERA-II", which runs during years from 2001 to 2005. The beam energies were assumed to be 27.5 GeV for $e^{\pm}$ and 920 GeV for p. A $500\,\mathrm{pb}^{-1}$ of luminosity was assumed for each of e^- and e^+ beams. For all studies in this section, beams are assumed to be un-polarised.

4.6.2 Double differential cross-section measurement

Measuring CC-DIS cross-section offers a flavor sensitive investigation of PDFs, which is a unique test of QCD. Thanks to the higher centre-of-mass energy, such flavor-specific investigation can be extended to lower-x and higher-Q^2 regions at THERA as compared to HERA-II.

Figure 1 shows the structure function term ϕ_+^{CC} expected to be measured at THERA-I in e^+ running. The errors are statistical only and are typically a few %. It is re-

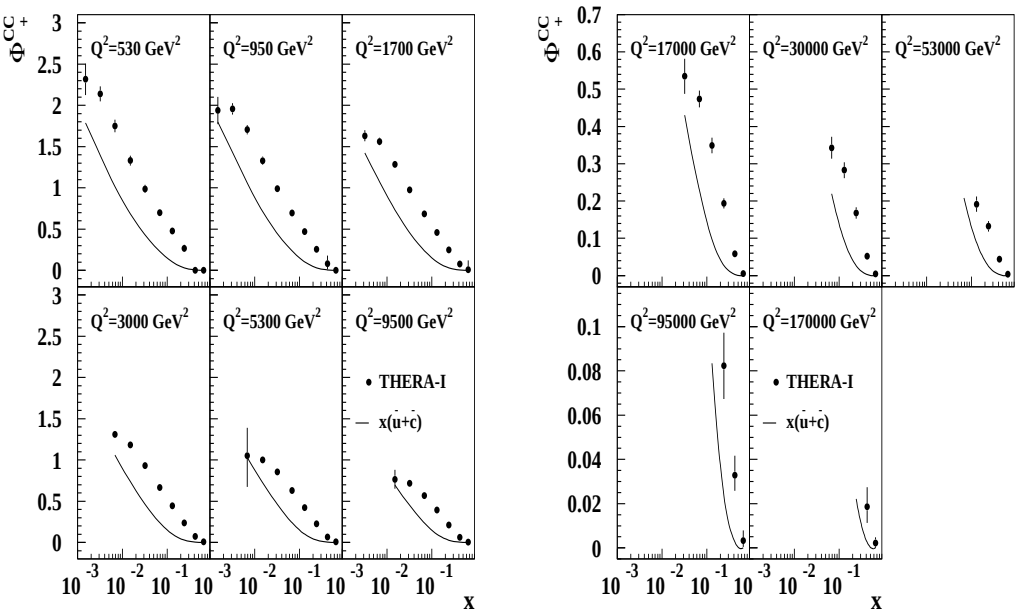

Figure 1: *The CC structure function term ϕ_+^{CC} as expected to be measured at THERA-I with e^+ beam. The errors are statistical only. The solid-lines indicate the anti-quark contributions ($\overline{u}$ and $\overline{c}$).*

markable that the measurement is extended to low-x region e.g. down to $x \sim 10^{-3}$ at $Q^2 \lesssim 3000\,\mathrm{GeV}^2$ (at HERA, the CC cross-section was measured only down to $x \sim 10^{-2}$ [4]). In such region, anti-quark densities, $\overline{u}$ and $\overline{c}$, dominate e^+ CC cross-section as indicated in the figure with the solid-lines. This allows a unique possibility to disentangle anti-quark densities at low-x.

The other advantage of the CC measurement at THERA, i.e. the extension to high-Q^2 region, can be impressively seen in the right side plot of the figure. The cross-sections can be measured with a few 10% of precision up to $Q^2 \sim 2 \cdot 10^5\,\mathrm{GeV}^2$ which is larger than the maximum reachable Q^2 at HERA-II and corresponds to be probing proton with spatial resolution of about 10^{-17} cm.

4.6.3 The d-quark density at high-x

One of the interesting topics of QCD is the ratio of d- to u-quark density at high-x. The e^+p CC-DIS provides a clean measurement of d-quark density at high-x. Notice that the d-quark density is currently only weakly constrained from deuteron-lepton fixed-target scattering data. Naively, deuteron structure function, F_2^D, is only proportional to the sum of u- and d-quark densities $F_2^D \propto x(u+d)$, while u-quark density can be strongly constrained by using proton structure function $F_2^p \propto x(4u+d)$. And also, there are some uncertainties in such fixed-target data e.g. in deuterium correction, target-mass and higher-twist effects etc, from which the CC measurement at THERA is free.

Figure 2 shows the x distribution for $Q^2 > 400\,\mathrm{GeV}^2$ expected to be observed at THERA-I and THERA-II with e^+ beam. For comparison, the same distribution

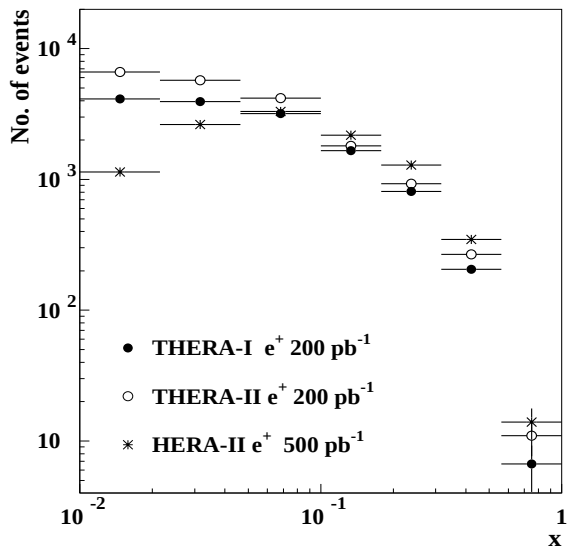

Figure 2: *The x distribution expected to be observed at THERA-I (closed circles), THERA-II (open circles) and HERA-II (asterisks) for $Q^2 > 400\,GeV^2$ with e^+ beam. The errors are statistical only.*

expected at HERA-II is also displayed in the figure. At the high-x region of $x \gtrsim 0.1$, the number of events at THERA was estimated to be similar to or smaller than that at HERA-II. Also, the figure shows that there is only a small gain of event rates at THERA-II compared to THERA-I. A reason is that the cross-section does not gain so drastically at high-x in spite of the higher centre-of-mass energy. This can be understood in the following way: the e^+p cross section σ is proportional to $(1-y)^2 d$ at high-x (see (4.6.1) and (4.6.3)). This results in: the cross-section ratio between different centre-of-mass energies $\frac{\sigma(s')}{\sigma(s)}$ is proportional to $\frac{s}{s'} \cdot \frac{xs'-Q^2}{xs-Q^2}$, which is close to unity at large-

	THERA-I	THERA-II	HERA-II
e^-	270 MeV	220 MeV	380 MeV
e^+	370 MeV	260 MeV	690 MeV

Table 4.6.1: *The precision of M_W determination expected to be obtained at THERA-I, THERA-II and HERA-II. The numbers are due only to statistical errors.*

x and small-Q^2. From these observations, it can be said that the sensitivity to d-quark density at THERA will be at most comparable to HERA-II.

4.6.4 Determination of the propagator mass

As indicated in (4.6.1), the Q^2 dependence of the CC-DIS cross-section is governed by the propagator term $\frac{{M_W}^2}{{M_W}^2+Q^2}$, hence by M_W. Extracting M_W from the CC-DIS is complementary to the direct measurements of M_W at LEP and TEVATRON experiments.

Figure 3 shows the Q^2 distribution expected to be observed at THERA with e^- beam. The curve of the Q^2 distribution reflects M_W. A χ^2 fit was performed to evaluate

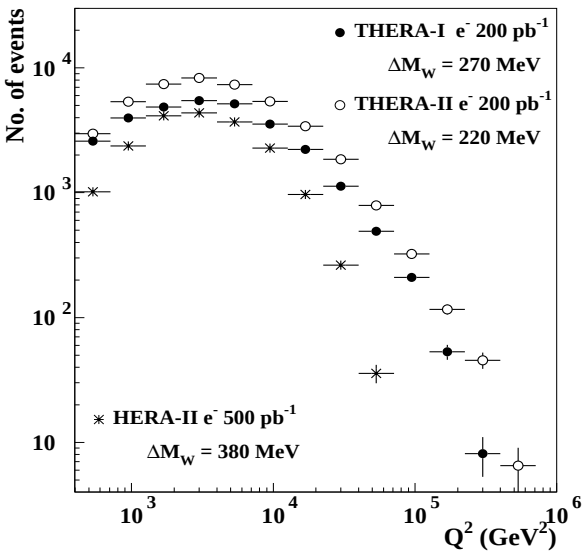

Figure 3: *The Q^2 distribution expected to be observed at THERA-I (closed circles), THERA-II (open circles) and HERA-II (asterisks) with e^- beam. The errors are statistical only.*

the precision of M_W obtained from such fit. The results are summarized in Tab. 4.6.1. These values of precision are due only to statistical errors. Since the CC-DIS cross

section is in general larger for e^- than for e^+ (see Sect. 4.6.1), the estimated precision of M_W is more precise in e^-. The M_W precision at HERA-II was also estimated and summarized in the table. From the numbers in the table, it can be said that THERA will give a better precision on M_W than HERA-II.

4.6.5 Summary

The main interesting topics of CC-DIS at THERA lie in the kinematic regions where only THERA can explore; i.e. low-x and high-Q^2 regions. The CC interaction provides a flavor specific investigation of PDFs in such new kinematic regions. For example, anti-quark densities at low-x can be measured in e^+ beam. The gain in Q^2 reach brings larger statistics in high-Q^2 region which determines the propagator $W^\pm$ mass. For the physics topics whose sensitivity lie mainly in the kinematic region where HERA can explore, the potential of THERA is marginal with limited amount of luminosity. The d/u ratio is such an example.

Acknowledgment

The author deeply thanks Masahiro Kuze for his helpful comments, suggestions and discussion on this study. For d/u and M_W, initial studies were made by him. The HERA-II numbers presented in this manuscript were estimated from Takahiro Fusayasu's analysis on ZEUS data. The author thanks him.

References

[1] K. Charchuła, G.A. Schuler and H. Spiesberger, Comp. Phys. Commun. **81**, 381 (1994); H. Spiesberger, DJANGO6 *version 2.4 – A Monte Carlo Generator for Deep Inelastic Lepton Proton Scattering Including QED and QCD Radiative Effects*, 1996, available on WWW:
`http://www.desy.de/~hspiesb/django6.html`.

[2] CTEQ Coll., H.L. Lai et al., Euro. Phys. J. **C 3**, 1 (1998).

[3] R. Brun et al., GEANT 3.13, CERN DD/EE/84-1.

[4] ZEUS Coll., J. Breitweg et al., Euro. Phys. J. **C 12**, 411 (2000).

5 Searches for New Particles or Phenomena

5.1 Contact Interactions, Large Extra Dimensions and Leptoquarks

A.F. Żarnecki
Warsaw University, Institute of experimental physics
Filip.Zarnecki@fuw.edu.pl

5.1.1 Contact Interactions

Four-fermion contact interactions are an effective theory, which allows us to describe, in the most general way, possible low energy effects coming from "new physics" at much higher energy scales. As very strong limits have been already placed on both scalar and tensor contact interactions [1], only vector contact interactions are considered in this analysis. The influence of the vector contact interactions on the *ep* NC DIS cross-section can be described as an additional term in the tree level $eq \to eq$ scattering amplitude [2, 3]:

$$M^{e_i q_j \to e_i q_j}(t) = -\frac{4\pi\alpha_{em} e_q}{t} + \frac{4\pi\alpha_{em}}{sin^2\theta_W \cdot cos^2\theta_W} \cdot \frac{g_i^e g_j^q}{t - M_Z^2} + \eta_{ij}^{eq} \qquad (5.1.1)$$

where $t = -Q^2$ is the Mandelstam variable describing the four-momentum transfer between the electron and the quark, e_q is the electric charge of the quark in units of the elementary charge, the subscripts i and j label the chiralities of the initial lepton and quark respectively ($i, j = L, R$), g_i^e and g_j^q are electroweak couplings of the electron and the quark, and η_{ij}^{eq} are the contact interaction couplings.

In the most general case, vector contact interactions are described by 4 independent couplings for every quark flavour. As *ep* scattering is sensitive predominantly to electron-up and electron-down quark couplings, 8 independent couplings should be considered. However, it is not be possible, in one experiment, to put significant constraints on all of these couplings simultaneously, without additional assumptions. Therefore, only one-parameter models, assuming fixed relations between the separate couplings, are considered in this paper. Relations between couplings assumed for different models

Model	η^{ed}_{LL}	η^{ed}_{LR}	η^{ed}_{RL}	η^{ed}_{RR}	η^{eu}_{LL}	η^{eu}_{LR}	η^{eu}_{RL}	η^{eu}_{RR}
q_{LL}	$+\eta$				$+\eta$			
q_{LR}		$+\eta$				$+\eta$		
q_{RL}			$+\eta$				$+\eta$	
q_{RR}				$+\eta$				$+\eta$
d_{LL}	$+\eta$							
d_{LR}		$+\eta$						
d_{RL}			$+\eta$					
d_{RR}				$+\eta$				
u_{LL}					$+\eta$			
u_{LR}						$+\eta$		
u_{RL}							$+\eta$	
u_{RR}								$+\eta$

Table 5.1.1: *Relations between couplings for contact interaction models with defined coupling chirality considered in this paper.*

are presented in Tab. 5.1.1 and 5.1.2. Listed in Tab. 5.1.1 are models with defined coupling chirality. Models in Tab. 5.1.2 fulfil the relation

$$\eta^{eq}_{LL} + \eta^{eq}_{LR} - \eta^{eq}_{RL} - \eta^{eq}_{RR} = 0$$

which is imposed to conserve parity, and to avoid strong limits coming from atomic parity violation measurements. In the presented contact interaction analysis it is also assumed that all up type and down type quarks have the same contact interaction couplings:

$$\begin{aligned} \eta^{eu}_{ij} &= \eta^{ec}_{ij} = \eta^{et}_{ij} \\ \eta^{ed}_{ij} &= \eta^{es}_{ij} = \eta^{eb}_{ij} \end{aligned}$$

Coupling η can be related to the effective mass scale of contact interactions Λ:

$$\eta = \pm\frac{g^2_{CI}}{\Lambda^2}$$

where the coupling strength of new interactions is by convention set to $g_{CI} = \sqrt{4\pi}$.

5.1.2 Large Extra Dimensions

Model proposed by Arkani-Hamed, Dimopoulos and Dvali [4, 5] assumes the space-time is $4+n$ dimensional. Standard Model particles, including strong and electroweak bosons are confined to 4 dimensions, but the gravity can propagate in the extra dimensions as well. With very large extra dimensions, the effective Plank scale M_S can be of

Model	η^{ed}_{LL}	η^{ed}_{LR}	η^{ed}_{RL}	η^{ed}_{RR}	η^{eu}_{LL}	η^{eu}_{LR}	η^{eu}_{RL}	η^{eu}_{RR}
VV	$+\eta$	$+\eta$	$+\eta$	$+\eta$	$+\eta$	$+\eta$	$+\eta$	$+\eta$
AA	$+\eta$	$-\eta$	$-\eta$	$+\eta$	$+\eta$	$-\eta$	$-\eta$	$+\eta$
VA	$+\eta$	$-\eta$	$+\eta$	$-\eta$	$+\eta$	$-\eta$	$+\eta$	$-\eta$
X1	$+\eta$	$-\eta$			$+\eta$	$-\eta$		
X2	$+\eta$		$+\eta$		$+\eta$		$+\eta$	
X3	$+\eta$			$+\eta$	$+\eta$			$+\eta$
X4		$+\eta$	$+\eta$			$+\eta$	$+\eta$	
X5		$+\eta$		$+\eta$		$+\eta$		$+\eta$
X6			$+\eta$	$-\eta$			$+\eta$	$-\eta$
U1					$+\eta$	$-\eta$		
U2					$+\eta$		$+\eta$	
U3					$+\eta$			$+\eta$
U4						$+\eta$	$+\eta$	
U5						$+\eta$		$+\eta$
U6							$+\eta$	$-\eta$

Table 5.1.2: *Relations between couplings for the parity conserving contact interaction models considered in this paper.*

the order of TeV. The graviton, after summing the effects of its excitations in the extra dimensions, couples to the Standard Model particles with an effective strength of $1/M_S$. At high energies, gravitation interaction can become comparable in strength to electroweak interactions. Virtual graviton exchange contribution to $eq \to eq$ scattering can be described by an effective contact interactions. Contribution to the scattering amplitude (5.1.1), equivalent to the cross-section formula given in [6], can be written as:

$$\begin{aligned} \eta^{eq}_{LL} &= \eta^{eq}_{RR} = -\frac{\pi\lambda}{2M_S^4}(4t+s) \\ \eta^{eq}_{LR} &= \eta^{eq}_{RL} = -\frac{\pi\lambda}{2M_S^4}(4t+3s) \end{aligned}$$

where t and s are the Mandelstam variables describing electron-quark scattering. By convention the coupling strength is set to $\lambda = \pm 1$.

5.1.3 Leptoquarks

In this paper a general classification of leptoquark states proposed by Buchmüller, Rückl and Wyler [7] will be used. The Buchmüller-Rückl-Wyler (BRW) model is based on the assumption that new interactions should respect the $SU(3)_C \times SU(2)_L \times U(1)_Y$ symmetry of the Standard Model. In addition leptoquark couplings are assumed to

be family diagonal (to avoid FCNC processes) and to conserve lepton and baryon numbers (to avoid rapid proton decay). Taking into account very strong bounds from rare decays [8] it is also assumed that leptoquarks couple either to left- or to right-handed leptons. With all these assumptions there are 14 possible states (isospin singlets or multiplets) of scalar and vector leptoquarks. Table 5.1.3 lists these states according to the so-called Aachen notation [9]. An S(V) denotes a scalar(vector) leptoquark and the subscript denotes the weak isospin. When the leptoquark can couple to both right- and left-handed leptons, an additional superscript indicates the lepton chirality. A tilde is introduced to differentiate between leptoquarks with different hypercharge. Listed in Tab. 5.1.3 are the leptoquark fermion number F, electric charge Q, and the branching ratio to an electron-quark pair (or electron-antiquark pair), β. The leptoquark branching fractions are predicted by the BRW model and are either 1, $\frac{1}{2}$ or 0. For a given electron-quark branching ratio β, the branching ratio to the neutrino-quark is by definition $(1-\beta)$. Also included in Tab. 5.1.3 are the flavours and chiralities of the lepton-quark pairs coupling to a given leptoquark type. In three cases the squark flavours (in supersymmetric theories with broken R-parity) with corresponding couplings are also indicated. Present analysis takes into account only leptoquarks which couple to the first-generation leptons (e, ν_e) and first-generation quarks (u, d). It is also assumed that one of the leptoquark types gives the dominant contribution, as compared with other leptoquark states and that the interference between different leptoquark states can be neglected. Using this simplifying assumption, different leptoquark types can be considered separately. Finally, it is assumed that different leptoquark states within isospin doublets and triplets have the same mass.

In the limit of heavy leptoquark masses ($M_{LQ} \gg \sqrt{s}$) the effect of leptoquark production or exchange is equivalent to a vector type $eeqq$ contact interaction. Contribution to the $eq \to eq$ scattering amplitude (5.1.1) does not depend on the process kinematics and can be written as

$$\eta_{ij}^{eq} \;=\; a_{ij}^{eq} \cdot \left(\frac{\lambda_{LQ}}{M_{LQ}}\right)^2 \quad ,$$

where M_{LQ} is the leptoquark mass, λ_{LQ} the leptoquark-electron-quark Yukawa coupling and the coefficients a_{ij}^{eq} are given in Tab. 5.1.4 [10].

For leptoquark masses comparable with the available ep center-of-mass energy u-channel leptoquark exchange process and the s-channel leptoquark production have to be considered separately. Corresponding diagrams for F=0 and F=2 leptoquarks are shown in Fig. 1. The leptoquark contribution to the scattering amplitude can be now described by the following formulae:

- for u-channel leptoquark exchange (F=0 leptoquark in e^-q or $e^+\bar{q}$ scattering, or $|F|$=2 leptoquark in e^+q or $e^-\bar{q}$ scattering)

$$\eta_{ij}^{eq}(s,u) \;=\; \frac{a_{ij}^{eq} \cdot \lambda_{LQ}^2}{M_{LQ}^2 - u} \quad ,$$

Model	Fermion number F	Charge Q	$BR(LQ \to e^{\pm}q)$ β	Coupling		Squark type
$S_\circ^L$	2	$-1/3$	1/2	$e_L u$	νd	$\tilde{d}_R$
$S_\circ^R$	2	$-1/3$	1	$e_R u$		
$\tilde{S}_\circ$	2	$-4/3$	1	$e_R d$		
$S_{1/2}^L$	0	$-5/3$	1	$e_L \bar{u}$		
		$-2/3$	0		$\nu \bar{u}$	
$S_{1/2}^R$	0	$-5/3$	1	$e_R \bar{u}$		
		$-2/3$	1	$e_R \bar{d}$		
$\tilde{S}_{1/2}$	0	$-2/3$	1	$e_L \bar{d}$		$\overline{\tilde{u}_L}$
		$+1/3$	0		$\nu \bar{d}$	$\overline{\tilde{d}_L}$
S_1	2	$-4/3$	1	$e_L d$		
		$-1/3$	1/2	$e_L u$	νd	
		$+2/3$	0		νu	
$V_\circ^L$	0	$-2/3$	1/2	$e_L \bar{d}$	$\nu \bar{u}$	
$V_\circ^R$	0	$-2/3$	1	$e_R \bar{d}$		
$\tilde{V}_\circ$	0	$-5/3$	1	$e_R \bar{u}$		
$V_{1/2}^L$	2	$-4/3$	1	$e_L d$		
		$-1/3$	0		νd	
$V_{1/2}^R$	2	$-4/3$	1	$e_R d$		
		$-1/3$	1	$e_R u$		
$\tilde{V}_{1/2}$	2	$-1/3$	1	$e_L u$		
		$+2/3$	0		νu	
V_1	0	$-5/3$	1	$e_L \bar{u}$		
		$-2/3$	1/2	$e_L \bar{d}$	$\nu \bar{u}$	
		$+1/3$	0		$\nu \bar{d}$	

Table 5.1.3: *A general classification of leptoquark states in the Buchmüller-Rückl-Wyler model. Listed are the leptoquark fermion number, F, electric charge, Q (in units of elementary charge), the branching ratio to electron-quark (or electron-antiquark), β and the flavours of the coupled lepton-quark pairs. Also shown are possible squark assignments to the leptoquark states in the minimal supersymmetric theories with broken R-parity.*

- for s-channel leptoquark production (F=0 leptoquark in e^+q or $e^-\bar{q}$ scattering, or $|F|$=2 leptoquark in e^-q or $e^+\bar{q}$ scattering)

$$\eta_{ij}^{eq}(s,u) \quad = \quad \frac{a_{ij}^{eq} \cdot \lambda_{LQ}^2}{M_{LQ}^2 - s - is\frac{\Gamma_{LQ}}{M_{LQ}}} \quad ,$$

Model	a^{ed}_{LL}	a^{ed}_{LR}	a^{ed}_{RL}	a^{ed}_{RR}	a^{eu}_{LL}	a^{eu}_{LR}	a^{eu}_{RL}	a^{eu}_{RR}
$S^L_\circ$					$+\frac{1}{2}$			
$S^R_\circ$								$+\frac{1}{2}$
$\tilde{S}_\circ$				$+\frac{1}{2}$				
$S^L_{1/2}$						$-\frac{1}{2}$		
$S^R_{1/2}$			$-\frac{1}{2}$				$-\frac{1}{2}$	
$\tilde{S}_{1/2}$		$-\frac{1}{2}$						
S_1	$+1$				$+\frac{1}{2}$			
$V^L_\circ$	-1							
$V^R_\circ$				-1				
$\tilde{V}_\circ$								-1
$V^L_{1/2}$		$+1$						
$V^R_{1/2}$			$+1$				$+1$	
$\tilde{V}_{1/2}$						$+1$		
V_1	-1				-2			

Table 5.1.4: *Coefficients a^{eq}_{ij} defining the effective contact interaction couplings $\eta^{eq}_{ij} = a^{eq}_{ij} \cdot \frac{\lambda^2_{LQ}}{M^2_{LQ}}$ for different models of scalar (upper part of the table) and vector (lower part) leptoquarks. Empty places in the table correspond to $a^{eq}_{ij} = 0$.*

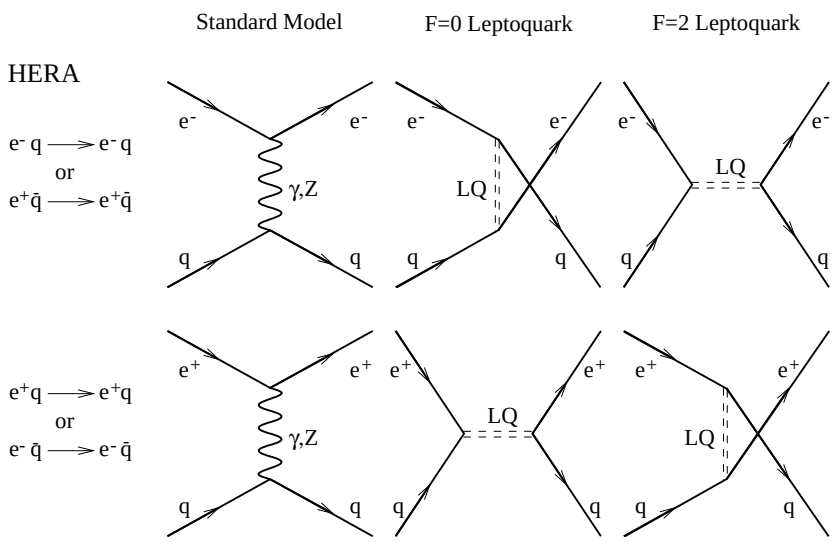

Figure 1: *Diagrams describing leading order Standard Model processes and leptoquark contributions coming from F=0 and F=2 leptoquarks, for NC $e^{\pm}p$ DIS at THERA.*

where Γ_{LQ} is the total leptoquark width. The partial decay width for every decay channel is given by the formula:

$$\Gamma_{LQ} = \frac{\lambda_{LQ}^2 M_{LQ}}{8\pi(J+2)} ,$$

where J is the leptoquark spin.

For leptoquark masses smaller than the available ep center-of-mass energy direct production of single leptoquarks can be considered. In the narrow-width approximation, the cross-section for single $F = 2$ leptoquark production in electron-proton scattering (via the electron-quark fusion) is given by:

$$\sigma^{ep\to LQ\ X}(M_{LQ}, \lambda_{LQ}) = (J+1) \cdot \frac{\pi\lambda_{LQ}^2}{4M_{LQ}^2} \cdot x_{LQ} q(x_{LQ}, M_{LQ}^2) \tag{5.1.2}$$

where $q(x, Q^2)$ is the quark momentum distribution in the proton and $x_{LQ} = \frac{M_{LQ}^2}{s}$.

5.1.4 Analysis method

The analysis method used has been described in details in the recently published papers [11, 12]. For all models considered, limits on the model parameters can be extracted from the measured Q^2 distribution of NC DIS events at THERA. The leading-order doubly-differential cross-section for electron-proton NC DIS ($e^-p \to e^-X$) can be written as

$$\begin{aligned}\frac{d^2\sigma^{LO}}{dxdQ^2} = \frac{1}{16\pi}\sum_q & q(x,Q^2)\left\{|M_{LL}^{eq}|^2 + |M_{RR}^{eq}|^2(1-y)^2\left[|M_{LR}^{eq}|^2 + |M_{RL}^{eq}|^2\right]\right\} + \\ & \bar{q}(x,Q^2)\left\{|M_{LR}^{eq}|^2 + |M_{RL}^{eq}|^2(1-y)^2\left[|M_{LL}^{eq}|^2 + |M_{RR}^{eq}|^2\right]\right\} ,\end{aligned}$$

where x is the Bjorken variable, describing the fraction of the proton momentum carried by the struck quark (antiquark), $q(x, Q^2)$ and $\bar{q}(x, Q^2)$ are the quark and antiquark momentum distribution functions in the proton and M_{ij}^{eq} are the scattering amplitudes of (5.1.1), which can include contributions from "new physics".

The cross-section integrated over the x and Q^2 range of an experimental Q^2 bin from Q_{min}^2 to Q_{max}^2 is

$$\sigma^{LO} = \int_{Q_{min}^2}^{Q_{max}^2} dQ^2 \int_{\frac{Q^2}{s\cdot y_{max}}}^{1} dx\, \frac{d^2\sigma^{LO}}{dxdQ^2} \tag{5.1.3}$$

where y_{max} is an upper limit on the reconstructed Bjorken variable y, $y = \frac{Q^2}{x\,s}$. In the presented analysis this limit is set to y_{max}=0.95. Eq. 5.1.3 is used to calculate numbers of expected events in Q^2 bins. Expected limits on model parameters, from high-Q^2 NC

$e^{\pm}p$ DIS at THERA, are calculated assuming that no deviations from the Standard Model predictions will be observed.

For every value of the model parameter η ($\pm 4\pi/\Lambda^2$ for the contact interaction models, $\pm 1/M_S^4$ for large extra dimensions, $(\lambda_{LQ}/M_{LQ})^2$ for leptoquark models in the high-mass limit[1]) the probability function describing the agreement between the model and the data is calculated:

$$\mathcal{P}(\eta) \sim \prod_i P_i(\eta)$$

The product runs over all Q^2 bins i (separately for e^-p and e^+p data). The probability P_i described by the Poisson distribution

$$P_i(\eta) \sim \frac{n(\eta)^N \cdot exp(-n(\eta))}{N!}, \tag{5.1.4}$$

where N and $n(\eta)$ are the measured and expected number of events in a given bin. This formula properly takes into account statistical errors in the measured event distributions. The systematic errors in the Standard Model expectations are assumed to be correlated to 100% between different Q^2 bins, and increase from 1% at $Q^2 = 1000\,\mathrm{GeV}^2$ to 5% at $Q^2 = 100000\,\mathrm{GeV}^2$. The method used to include systematic errors, as well as the migration corrections resulting from the assumed Q^2 measurement resolution of 5% are discussed in detail in [11].

To constraint leptoquark Yukawa coupling values, for leptoquark masses smaller than the available *ep* center-of-mass energy, direct production of single leptoquarks is also considered, as described by (5.1.2). Only the leptoquark signal in the electron-jet decay channel is taken into account. Expected signal from single leptoquark production, for given leptoquark mass M_{LQ} and Yukawa coupling λ_{LQ}, is compared with the observed number of events from the Standard Model background (NC DIS) in the $\pm 5\%$ mass window. The background is suppressed by applying a cut on the Bjorken variable y, which is optimised for every leptoquark type as a function of the leptoquark mass. After the y cut is imposed, probability function $\mathcal{P}(\lambda_{LQ}, M_{LQ})$ is calculated from the Poisson distribution (5.1.4). As $\mathcal{P}$ is not a probability distribution, it does not satisfy any normalisation condition. Instead it is convenient to rescale the probability function in such a way that for the Standard Model it has the value of 1:

$$\mathcal{P}(\eta = 0) = 1.$$

Using the probability function $\mathcal{P}(\eta)$ limits on the model parameters are calculated. Rejected are all models (parameter values) which result in

$$\mathcal{P}(\eta) < 0.05 \tag{5.1.5}$$

[1]For leptoquark masses comparable with the available center-of-mass energy, two parameter probability function $\mathcal{P}(\lambda_{LQ}, M_{LQ})$ is considered and limits on λ_{LQ} are calculated as a function of the leptoquark mass M_{LQ}.

This is taken as the definition of the 95% confidence level (CL) exclusion limit.[2] Exclusion limits presented in this paper are lower limits in case of mass scales Λ or M_S, leptoquark mass M_{LQ} or M_{LQ}/λ_{LQ}, and upper limits in case of λ_{LQ}. For leptoquark masses smaller than the available center-of-mass energy, both indirect (from $\frac{d\sigma}{dQ^2}$) and direct λ_{LQ} limits are calculated, and the stronger one is presented.

5.1.5 THERA running

Following THERA running scenarios are considered in this paper:

- For nominal electron beam energy of $E_e = 250\,\mathrm{GeV}$ and proton beam energy of $E_p = 1000\,\mathrm{GeV}$ integrated luminosity of about $40\,\mathrm{pb}^{-1}$ is expected in a year. Results presented for this option assume integrated luminosity of $100\,\mathrm{pb}^{-1}$ for e^-p and/or $100\,\mathrm{pb}^{-1}$ for e^+p collisions. It will be referred to as THERA-250.

- Using both arms of TESLA, electron beam energy can be increased to $E_e = 500\,\mathrm{GeV}$. Assumed integrated luminosity for this scenario is also $100\,\mathrm{pb}^{-1}$ for e^-p and/or $100\,\mathrm{pb}^{-1}$ for e^+p collisions. It will be referred to as THERA-500.

- With TESLA machine upgraded in power, electron energies as high as $E_e = 800\,\mathrm{GeV}$ are possible for THERA operation. In this case proton beam energy is lowered to $E_p = 800\,\mathrm{GeV}$, to provide maximum luminosity. Results presented for this option assume integrated luminosity of $200\,\mathrm{pb}^{-1}$ for e^-p and/or $200\,\mathrm{pb}^{-1}$ for e^+p collisions. It will be referred to as THERA-800.

5.1.6 Results

95% CL exclusion limits on the contact interaction mass scales Λ^- and Λ^+ (for negative and positive coupling signs) expected from the measurement of high-Q^2 NC DIS cross-sections at THERA, are presented in Tab. 5.1.5 and 5.1.6. Results presented are the mean values from 1000 MC experiments. Poisson fluctuations in the observed numbers of events can result in the statistical fluctuations in the limit values of the order of 10-20%. Current limits from the global contact interaction analysis [13][3] and from the global analysis of existing data in the large extra dimensions (ED) model [6] are included for comparison.

[2] For Gaussian shape of the probability function, condition (5.1.5) corresponds to $\pm 2.45\sigma$ limit. Mass scale limits presented in this paper would increase by 10 to 15%, if the definition more commonly used in the literature is used: $\mathcal{P}(\eta) = 0.147$ corresponding to $\pm 1.96\sigma$. However, this definition assumes the Gaussian shape of the probability function, which is not always the case. Therefore definition (5.1.5) is used as more "conservative". Same limit setting method has been used in the global analysis of existing data [12, 13].

[3] Numerical limit values presented in this paper differ slightly from limits presented in [13]. They have been recalculated using data on $eeqq$ interactions only. Data from neutrino scattering experiments and from charged current processes, which can be included in the analysis when assuming $SU(2)_L \times U(1)_Y$ symmetry of new interactions, were not used. This is because some of the considered models violate $SU(2)$ invariance.

Model	Current limits [TeV]		Expected 95% CL exclusion limits [TeV]																	
			THERA-250						THERA-500						THERA-800					
			e^-p		e^+p		$e^\pm p$		e^-p		e^+p		$e^\pm p$		e^-p		e^+p		$e^\pm p$	
	Λ^-	Λ^+	Λ^-	Λ^+	Λ^-	Λ^+	Λ^-	Λ^+	Λ^-	Λ^+	Λ^-	Λ^+	Λ^-	Λ^+	Λ^-	Λ^+	Λ^-	Λ^+	Λ^-	Λ^+
d_{LL}	23.3	8.4	5.6	4.7	5.0	4.2	6.3	5.5	7.3	6.0	6.5	5.6	8.1	7.1	8.8	7.4	7.8	6.8	9.8	8.7
d_{LR}	19.6	7.5	3.2	2.9	4.8	3.9	4.9	4.0	4.1	3.7	6.0	5.0	6.1	5.1	4.9	4.4	7.3	6.0	7.5	6.1
d_{RL}	7.4	20.4	2.7	3.3	3.9	4.8	3.9	4.9	3.5	4.3	5.0	6.0	5.0	6.2	4.2	5.1	6.0	7.4	6.0	7.5
d_{RR}	8.8	17.5	4.6	3.5	4.0	3.0	4.9	3.6	5.8	4.5	5.2	3.8	6.3	4.7	7.0	5.3	6.2	4.5	7.6	5.6
u_{LL}	14.7	11.3	7.9	8.3	5.6	5.9	8.5	8.8	9.8	10.3	7.0	7.6	10.5	10.9	12.2	12.7	8.7	9.2	13.0	13.5
u_{LR}	16.9	7.8	3.1	3.8	4.9	7.1	5.1	7.3	3.9	4.9	6.0	8.7	6.2	8.9	4.6	5.8	7.4	10.9	7.6	11.0
u_{RL}	7.1	18.3	3.2	3.4	4.7	6.2	4.9	6.3	4.0	4.5	6.0	7.7	6.2	7.8	4.7	5.3	7.3	9.4	7.4	9.6
u_{RR}	7.0	21.2	6.3	7.3	4.4	5.3	6.8	7.8	7.6	9.1	5.6	6.8	8.4	9.7	9.6	11.3	6.8	8.3	10.4	11.9
q_{LL}	26.1	10.9	4.2	7.2	3.5	4.8	4.3	7.3	5.3	8.8	4.6	6.1	5.5	9.0	6.4	10.9	5.4	7.4	6.6	11.2
q_{LR}	25.8	10.6	3.5	4.0	4.9	7.1	5.0	7.2	4.5	5.2	6.3	8.7	6.4	8.8	5.3	6.2	7.6	10.7	7.7	10.9
q_{RL}	10.2	27.3	3.4	4.1	5.1	7.0	5.2	7.2	4.4	5.4	6.5	8.7	6.6	8.9	5.2	6.4	7.8	10.7	8.0	10.9
q_{RR}	10.3	27.1	4.4	7.0	3.5	5.0	4.5	7.3	5.6	8.7	4.5	6.3	5.8	9.0	6.8	10.7	5.4	7.7	7.0	11.1

Table 5.1.5: *95% CL exclusion limits on the contact interaction mass scales Λ^- and Λ^+ (for negative and positive coupling signs respectively) expected from the measurement of high-Q^2 NC DIS cross-sections at THERA, for different running scenarios, as indicated in the table. Limits from the global analysis of existing data [11, 13] are included for comparison.*

Model	Current limits [TeV]		Expected 95% CL exclusion limits [TeV]																	
			THERA-250						THERA-500						THERA-800					
			e^-p		e^+p		$e^\pm p$		e^-p		e^+p		$e^\pm p$		e^-p		e^+p		$e^\pm p$	
	Λ^-	Λ^+	Λ^-	Λ^+	Λ^-	Λ^+	Λ^-	Λ^+	Λ^-	Λ^+	Λ^-	Λ^+	Λ^-	Λ^+	Λ^-	Λ^+	Λ^-	Λ^+	Λ^-	Λ^+
VV	8.3	14.5	7.6	9.9	7.2	10.3	9.8	11.9	8.7	12.3	8.5	12.5	11.3	14.6	11.3	15.2	10.6	15.6	14.4	18.1
AA	11.2	10.8	4.7	9.2	8.4	6.2	9.3	9.3	6.2	11.2	10.4	8.1	11.1	11.4	7.3	14.0	12.8	9.7	13.9	14.1
VA	5.8	6.3	6.3	6.7	7.3	7.2	7.7	7.7	8.2	8.5	9.3	9.1	9.8	9.9	9.7	10.3	11.3	11.0	11.8	11.9
$X1$	8.5	8.6	4.2	7.2	6.8	5.4	7.2	7.3	5.6	8.8	8.5	7.0	8.7	9.1	6.5	10.9	10.4	8.4	10.8	11.2
$X2$	6.7	10.8	4.5	7.6	5.2	7.8	6.1	9.0	5.7	9.5	6.7	9.6	7.4	11.1	6.9	11.6	8.1	11.9	9.2	13.6
$X3$	8.8	12.0	7.0	9.4	4.0	6.2	7.4	9.7	7.9	11.5	5.2	7.9	8.2	11.9	10.5	14.2	6.1	9.6	11.0	14.7
$X4$	6.2	10.0	4.0	5.0	5.9	9.1	6.1	9.2	5.2	6.6	7.5	11.1	7.7	11.3	6.1	7.8	9.1	13.7	9.2	13.9
$X5$	5.6	9.1	4.5	7.4	5.1	7.9	5.8	8.9	5.8	9.2	6.6	9.8	7.2	11.0	6.9	11.3	7.9	12.0	8.8	13.6
$X6$	6.8	5.4	6.9	4.4	5.5	6.7	7.1	6.9	8.6	5.7	7.1	8.4	9.0	8.6	10.5	6.8	8.6	10.3	10.9	10.5
$U1$	6.3	13.0	7.1	8.1	6.2	5.1	8.1	8.1	8.3	9.9	7.7	6.7	9.7	10.1	10.7	12.3	9.5	8.0	12.2	12.5
$U2$	7.3	15.6	8.1	8.5	6.6	7.9	9.1	9.7	9.9	10.6	8.1	9.9	11.1	12.1	12.3	13.1	10.0	12.1	13.8	14.9
$U3$	8.9	19.8	10.8	10.8	7.6	7.7	11.5	11.4	13.3	13.3	9.6	9.9	14.2	14.2	16.5	16.4	11.8	11.9	17.5	17.5
$U4$	5.2	8.4	3.8	4.5	6.2	8.7	6.5	8.9	4.7	5.9	7.3	10.6	7.6	10.8	5.5	7.0	9.0	13.2	9.3	13.3
$U5$	6.9	14.8	6.9	7.8	7.3	8.4	8.7	9.6	8.4	9.8	8.7	10.3	10.6	11.9	10.4	12.0	10.8	12.8	13.2	14.7
$U6$	11.9	5.8	7.3	5.3	5.5	5.7	7.6	6.8	9.1	6.3	7.1	7.2	9.5	8.3	11.2	8.1	8.6	8.8	11.6	10.4
ED		0.94	1.41	1.74	1.81	1.52	1.88	1.83	1.84	2.29	2.36	1.96	2.44	2.38	2.18	2.70	2.81	2.34	2.90	2.83

Table 5.1.6: *95% CL exclusion limits on the contact interaction mass scales Λ^- and Λ^+, and on the the effective Plank scales M_S^- and M_S^+ in the large extra dimensions (ED) model (for negative and positive coupling signs respectively) expected from the measurement of high-Q^2 NC DIS cross-sections at THERA, for different running scenarios, as indicated in the table. Limits from the global analysis of existing data [6, 11, 13] are included for comparison.*

For contact interaction models violating parity (models with defined coupling chirality; Tab. 5.1.5), current limits from global analysis are already of the order of 10-20 TeV. This is mainly due to very strong constraints from the atomic parity violation (APV) measurements in cesium [14–16]. THERA running with the nominal electron beam energy of 250 GeV (THERA-250) will be only sensitive to mass scales from about 3 to 9 TeV. With electron beam energy increased to 500 GeV (THERA-500), contact interaction mass scale limits improve on average by 20-30%. Another improvement by similar factor is observed when going from THERA-500 to THERA-800 option. Nevertheless, even for high electron beam energies (THERA-500 and THERA-800) improvement of existing limits will only be possible for selected models (mainly models coupling to the u quark only).

For contact interaction models conserving parity (Tab. 5.1.6), current limits from global analysis are, on average, lower than for parity violating models. At the same time THERA sensitivity increases. Already at THERA-250 mass scale limits can be improved for about half of the considered models, provided that both e^-p and e^+p data are collected. With increasing electron beam energy, most limits can be significantly improved. From combined e^-p and e^+p data at THERA-800 limits on the contact interaction mass scales up to about 18 TeV can be obtained.

For the model of large extra dimensions, THERA will improve existing limits in any configuration. This is because the graviton exchange contribution increases with the increasing center-of-mass energy. THERA-800 will be sensitive to the effective Plank scale M_S up to about 2.8 TeV.

In the limit of heavy leptoquark masses ($M_{LQ} \gg \sqrt{s}$) contact interaction model has been also used to set limits on the leptoquark mass to the coupling ratio M_{LQ}/λ_{LQ}. Expected 95% CL exclusion limits, for different leptoquark models and different THERA running scenarios are presented in Tab. 5.1.7. Current limits from the global analysis [12] are included for comparison. In most cases existing limits are already above THERA sensitivity, even in the highest electron energy option. Limits on M_{LQ}/λ_{LQ} can be only improved for $\tilde{V}_\circ$ and $\tilde{V}_{1/2}$ models.

For leptoquark masses comparable with the available center-of-mass energy, contact interaction approach has to be modified, as described in Sect. 5.1.3. Limits on λ_{LQ} are calculated as a function of the leptoquark mass M_{LQ} from the two-dimensional probability function $\mathcal{P}(\lambda_{LQ}, M_{LQ})$. For leptoquark masses smaller than the available center-of-mass energy ($M_{LQ} < \sqrt{s}$), limits are also set from the measurement of the direct leptoquark production. It turns out both approaches give similar results [12]. Measurement of the direct leptoquark production process results in better limits for low leptoquark masses ($M_{LQ} \ll \sqrt{s}$) and for leptoquark production involving valence quarks (production of F=2 leptoquarks in e^-p collisions or F=0 leptoquarks in e^+p collisions). $\frac{d\sigma}{dQ^2}$ measurement can results in slightly better limits (than expected from the direct production process) for leptoquark masses close to the center-of-mass energy and for leptoquark production from anti-quarks in the proton (F=0 leptoquarks in e^-p or F=2 in e^+p). For leptoquark masses $M_{LQ} < \sqrt{s}$ both kinds of limits are always calculated and the stronger one is taken.

Shown in Fig. 2, 3 and 4 are expected 95% CL exclusion limits in (λ_{LQ}, M_{LQ}), for

Model	Current limit [TeV]	Expected 95% CL exclusion limits on M_{LQ}/λ_{LQ} [TeV]								
		THERA-250			THERA-500			THERA-800		
		e^-p	e^+p	$e^\pm p$	e^-p	e^+p	$e^\pm p$	e^-p	e^+p	$e^\pm p$
$S_\circ^L$	3.7	1.7	1.2	1.7	2.1	1.5	2.2	2.5	1.8	2.7
$S_\circ^R$	3.9	1.5	1.1	1.5	1.8	1.4	1.9	2.2	1.6	2.4
$\tilde{S}_\circ$	3.6	0.7	0.6	0.7	0.9	0.8	0.9	1.1	0.9	1.1
$S_{1/2}^L$	3.5	0.6	1.0	1.0	0.8	1.2	1.2	0.9	1.5	1.5
$S_{1/2}^R$	2.1	0.7	1.0	1.0	0.9	1.3	1.3	1.0	1.6	1.6
$\tilde{S}_{1/2}$	3.8	0.6	1.0	1.0	0.8	1.2	1.2	1.0	1.5	1.5
S_1	2.4	1.4	1.0	1.4	1.7	1.2	1.7	2.1	1.5	2.1
$V_\circ^L$	8.1	1.6	1.4	1.8	2.1	1.8	2.3	2.5	2.2	2.8
$V_\circ^R$	2.3	1.3	1.1	1.4	1.7	1.4	1.8	2.0	1.7	2.1
$\tilde{V}_\circ$	1.9	1.8	1.2	1.9	2.1	1.6	2.4	2.7	1.9	2.9
$V_{1/2}^L$	2.1	0.8	1.1	1.1	1.0	1.4	1.4	1.2	1.7	1.7
$V_{1/2}^R$	7.5	1.2	2.0	2.0	1.5	2.5	2.5	1.8	3.0	3.1
$\tilde{V}_{1/2}$	2.1	1.1	2.0	2.1	1.4	2.5	2.5	1.6	3.1	3.1
V_1	7.3	2.6	1.5	2.8	3.1	1.9	3.3	3.9	2.3	4.2

Table 5.1.7: *95% CL exclusion limits on M_{LQ}/λ_{LQ} (in the limit of heavy leptoquark masses $M_{LQ} \gg \sqrt{s}$) expected from the measurement of high-Q^2 NC DIS cross-sections at THERA, for different running scenarios, as indicated in the table.*

different leptoquark models and THERA running with 250 GeV, 500 GeV and 800 GeV electron (positron) beam respectively. Limits expected from e^-p data and from e^+p data are compared. As expected, better limits on the F=2 leptoquark Yukawa coupling λ_{LQ}, for $M_{LQ} < \sqrt{s}$, are obtained from e^-p data, whereas e^+p data constrain better F=0 leptoquarks. Differences between limits expected from e^-p and e^+p data are smaller for scalar leptoquarks with $M_{LQ} > \sqrt{s}$. For high-mass vector leptoquarks it turns out that better limits can be obtained for "wrong" beam choice (e^-p for F=0 leptoquarks and e^+p for F=2 leptoquarks). Limits expected from combined e^-p and e^+p data, for different THERA running scenarios, are compared with existing limits [12] in Fig. 5. In all cases search for single leptoquark production at THERA significantly improves the existing limits.

In Fig. 6, 7, 8 and 9, limits on the leptoquark Yukawa coupling λ_{LQ} and mass M_{LQ} expected from THERA are compared with existing limits and limits expected from other future experiments [17], for $S_{1/2}^R$, S_1, $\tilde{V}_\circ$ and $V_{1/2}^L$ leptoquark models respectively.[4] Leptoquarks with masses up to about 2.0 TeV can be searched for at LHC,

[4]Selected models were shown to describe the existing experimental data better than the Standard Model [12].

independently of λ_{LQ}. THERA will not be able to improve any limits if LHC excludes leptoquark masses below 1.6 TeV. However, if any leptoquark type state is discovered at LHC, THERA will be the best place to study its properties, covering the widest range in (λ_{LQ}, M_{LQ}) space. Leptoquark mass, spin, fermion number and branching fraction (assuming leptoquark decays into $\nu + jet$ are reconstructed) can be determined. Yukawa coupling can be precisely measured down to the very small coupling values of the order of $\lambda_{LQ} \sim 10^{-2}$, not accessible at LHC.

5.1.7 Summary

The sensitivity of THERA to different contact interaction models has been studied in detail. For models conserving parity, scales up to about 18 TeV can be probed at THERA, extending considerably beyond the existing bounds. Significant improvement of existing limits is also expected for models with large extra dimensions. Effective Plank mass scales up to about 2.8 TeV can be probed. THERA will be the best machine to study leptoquark properties, for leptoquark masses up to about 1 TeV. It will be sensitive to the leptoquark Yukawa couplings down to $\lambda_{LQ} \sim 10^{-2}$.

References

[1] P. Haberl, F. Schrempp and H.U. Martyn, *Contact interactions and new heavy bosons at HERA: A model independent analysis*, in *Proc. Physics at HERA, vol. 2*, eds. W. Buchmüller and G. Ingelman, p. 1133. Hamburg, Germany, DESY, 1991.

[2] V. Barger et al., Phys. Rev. **D57**, 391 (1998).

[3] D. Zeppenfeld and K. Cheung, *New interactions in neutral current processes.* Preprint hep-ph/9810277, 1998.

[4] N. Arkani-Hamed, S. Dimopoulos and G. Dvali, Phys. Lett. **B 429**, 263 (1998); N. Arkani-Hamed, S. Dimopoulos and G. Dvali, Phys. Rev. **D 59**, 086004 (1999).

[5] I. Antoniadis et al., Phys. Lett. **B436**, 257 (1998).

[6] K. Cheung, Phys. Lett. **B460**, 383 (1999).

[7] W. Buchmüller, R. Rückl and D. Wyler, Phys. Lett. **B 191**, 442 (1987). Erratum in Phys. Lett. **B 448** 320 (1999).

[8] W. Buchmüller and D. Wyler, Phys. Lett. **B177**, 377 (1986).

[9] A. Djouadi et al., Z. Phys. **C 46**, 679 (1990).

[10] J. Kalinowski et al., Z. Phys. **C74**, 595 (1997).

[11] A.F. Żarnecki, Eur. Phys. J. **C11**, 539 (1999).

[12] A.F. Żarnecki, Eur. Phys. J. **C 17**, 695 (2000).

[13] A.F. Żarnecki, *Leptoquarks and contact interactions from a global analysis.* Preprint hep-ph/0006196, 2000. Contrib. to *DIS2000*, Liverpool.

[14] C.S. Wood et al., Science **275**, 1759 (1997).

[15] S.A. Blundell, J. Sapirstein and W.R. Johnson, Phys. Rev. **D45**, 1602 (1992).

[16] S.C. Bennett and C.E. Wieman, Phys. Rev. Lett. **82**, 2484 (1999).

[17] A.F. Żarnecki, *Leptoquark searches at future colliders.* Preprint hep-ph/0006335, 2000. Subm. to *ICHEP2000*, Osaka, Japan, abstract 193.

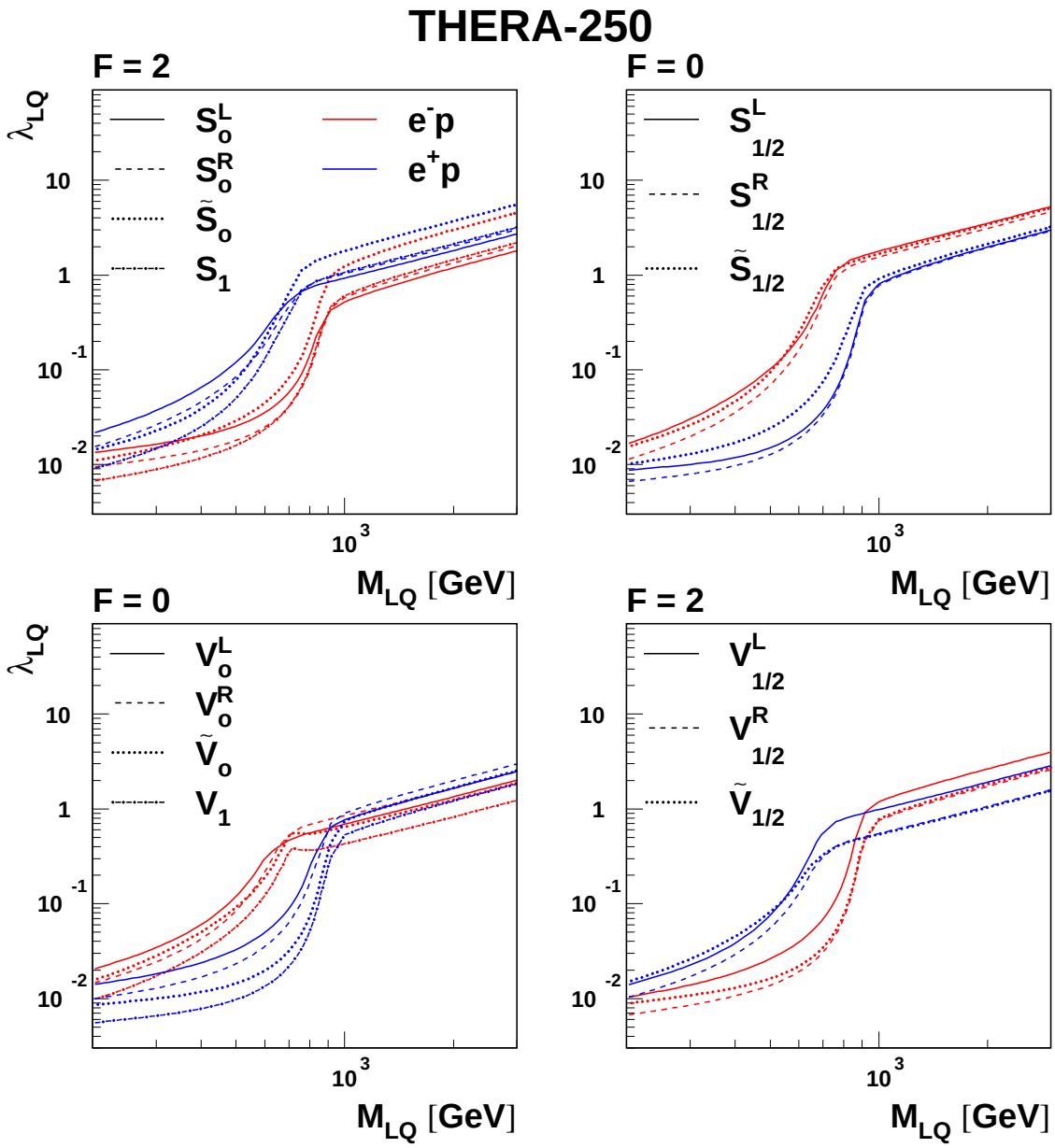

Figure 2: *Expected 95% CL exclusion limits in* (λ_{LQ}, M_{LQ}) *space, for different leptoquark models (as indicated in the plot), for* $100\,pb^{-1}$ *of* e^-p *data (red curves) and* $100\,pb^{-1}$ *of* e^+p *data (blue curves) collected at* 250 *GeV electron (positron) beam energy (THERA-250). Limits based on single leptoquark production and high-*Q^2 *NC DIS cross-section measurements.*

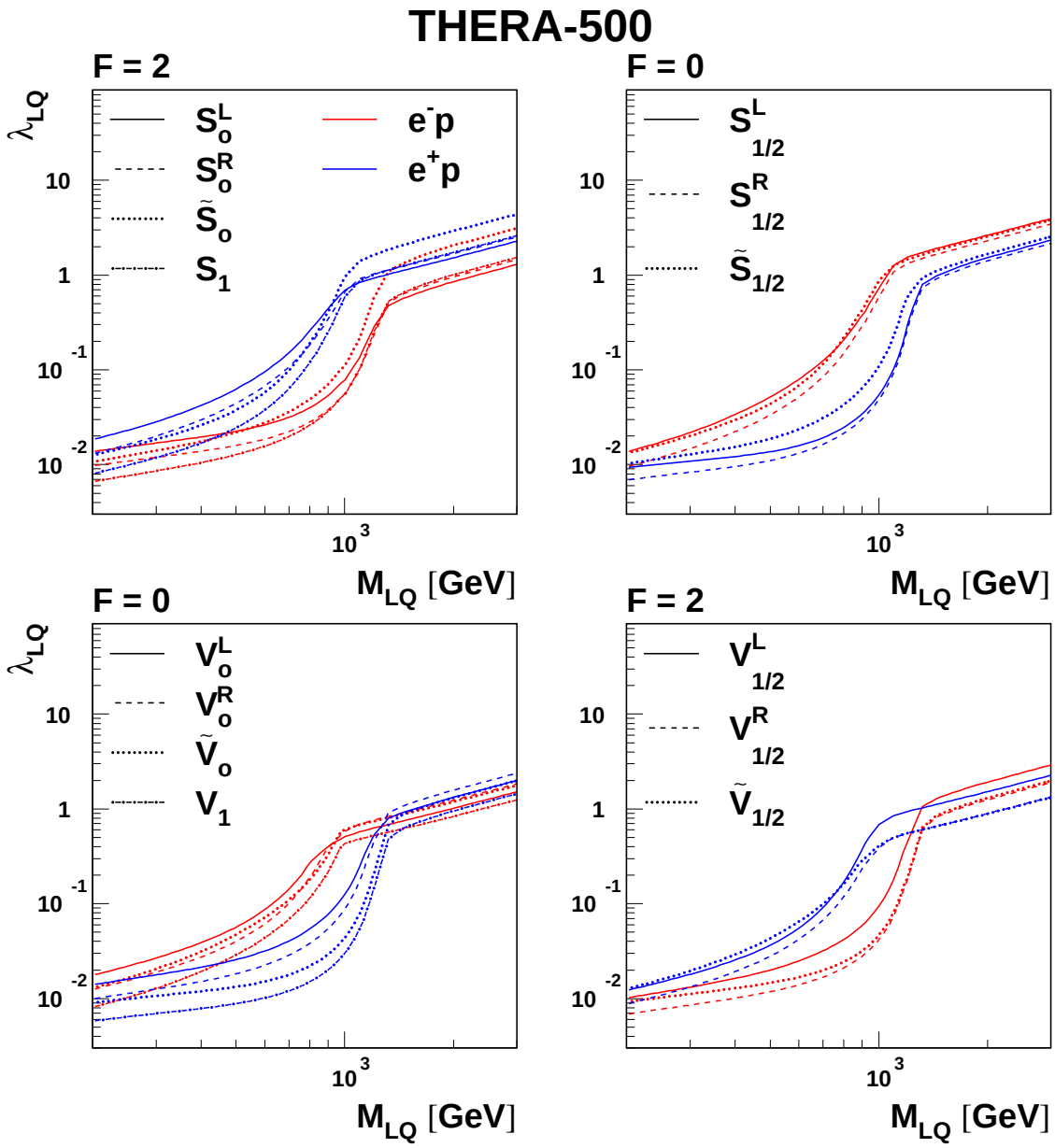

Figure 3: *Expected 95% CL exclusion limits in* (λ_{LQ}, M_{LQ}) *space, for different leptoquark models (as indicated in the plot), for* $100\,pb^{-1}$ *of* e^-p *data (red curves) and* $100\,pb^{-1}$ *of* e^+p *data (blue curves) collected at* 500 *GeV electron (positron) beam energy (THERA-500). Limits based on single leptoquark production and high-*Q^2 *NC DIS cross-section measurements.*

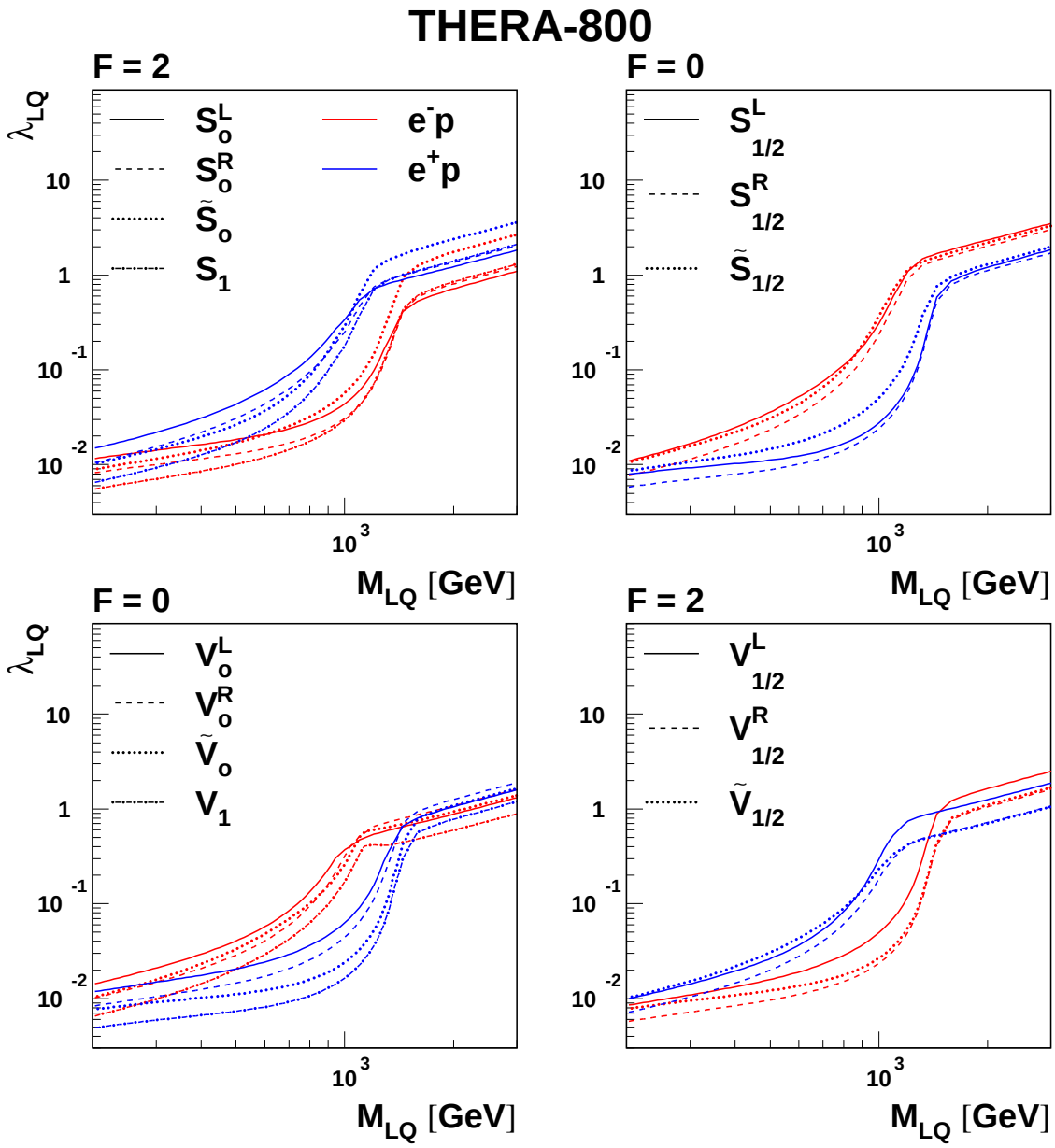

Figure 4: *Expected 95% CL exclusion limits in* (λ_{LQ}, M_{LQ}) *space, for different leptoquark models (as indicated in the plot), for* $200\,pb^{-1}$ *of* e^-p *data (red curves) and* $200\,pb^{-1}$ *of* e^+p *data (blue curves) collected at* 800 *GeV electron (positron) beam energy (THERA-800). Limits based on single leptoquark production and high-*Q^2 *NC DIS cross-section measurements.*

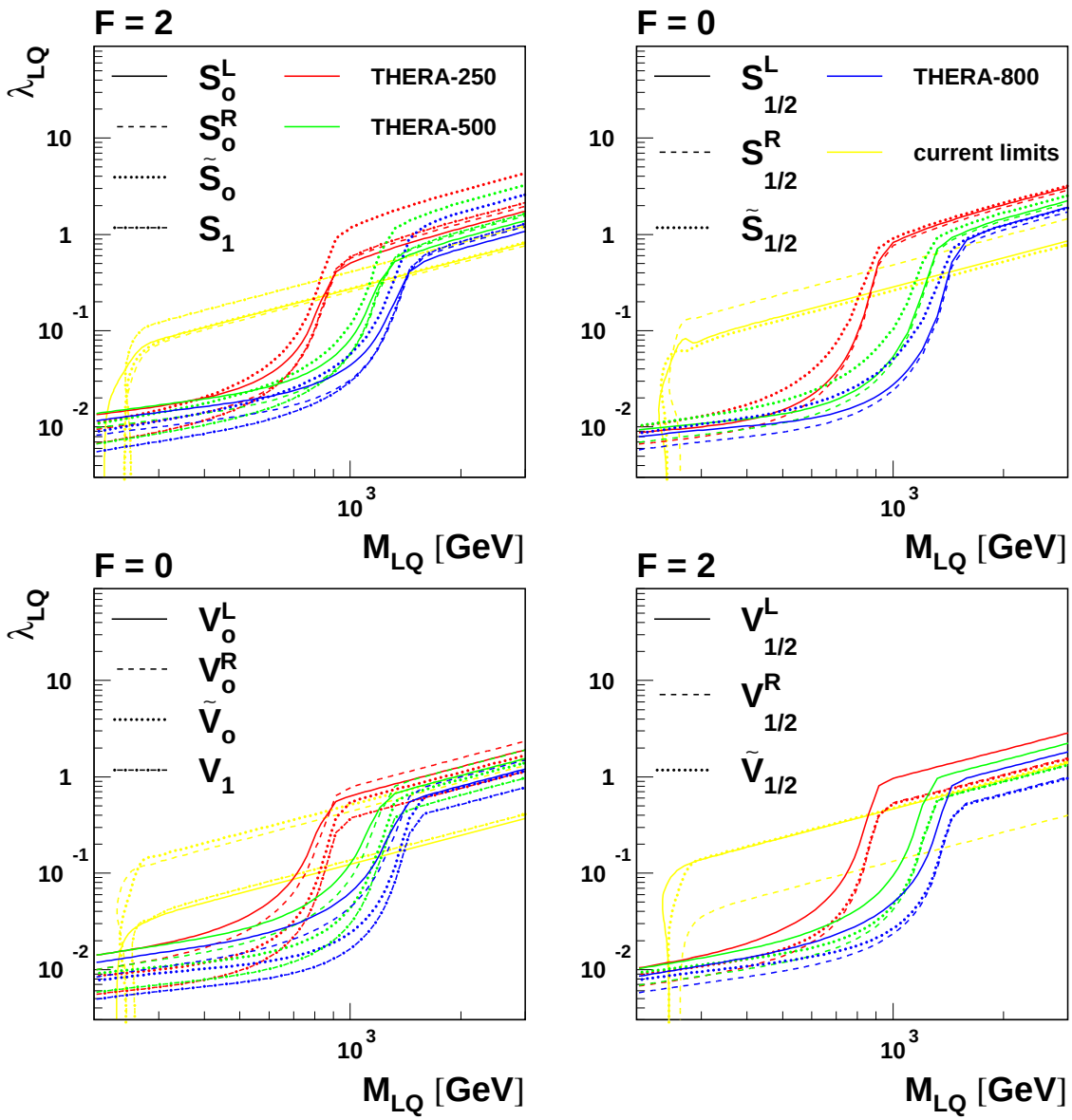

Figure 5: *Expected 95% CL exclusion limits in* (λ_{LQ}, M_{LQ}) *space, for different leptoquark models and for different THERA running scenarios (as indicated in the plot). Limits based on single leptoquark production and high-*Q^2 *NC DIS cross-section measurements from the combined* e^-p *and* e^+p *data. Indicated in yellow are existing limits from global analysis [12].*

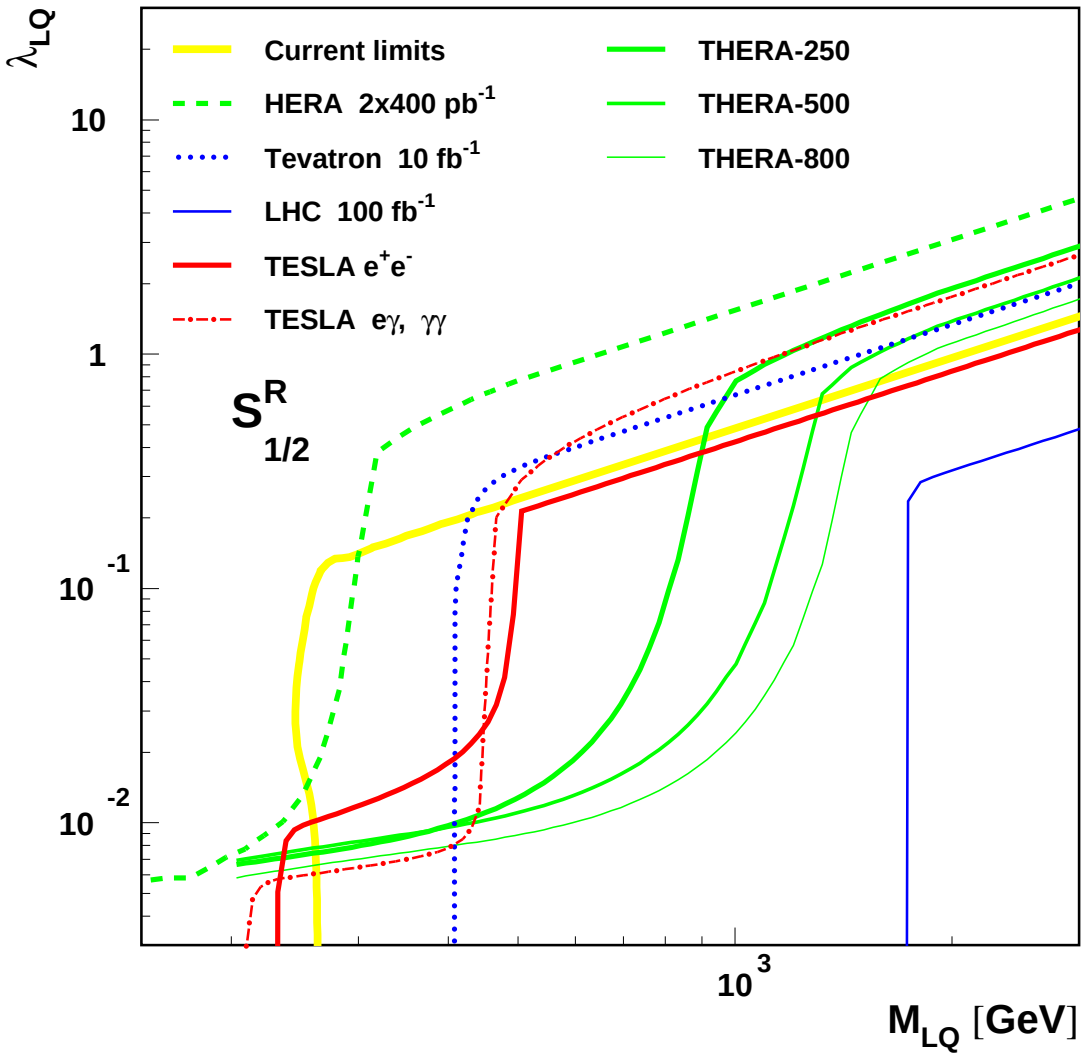

Figure 6: *Comparison of expected 95% CL exclusion limits in* (λ_{LQ}, M_{LQ}) *for* $S^R_{1/2}$ *leptoquark model, for different THERA running scenarios and other future experiments, as indicated in the plot. Presented limits correspond to* $2\times 400\,pb^{-1}$ *of* $e^{\pm}p$ *data at HERA* ($\sqrt{s}$ = 318 *GeV*), $2\times 100\,pb^{-1}$ *or* $2\times 200\,pb^{-1}$ *of* $e^{\pm}p$ *data at THERA* ($\sqrt{s}$=1.0,1.4 *and* 1.6 *TeV*), $10\,fb^{-1}$ *of* $p\bar{p}$ *data at the Tevatron* ($\sqrt{s}$ = 2 *TeV*), $100\,fb^{-1}$ *of pp data at the LHC* ($\sqrt{s}$ = 14 *TeV*) *and* $100\,fb^{-1}$ *of* e^+e^-, $e\gamma$ *and* $\gamma\gamma$ *data at TESLA* ($\sqrt{s_{ee}}$ = 500 *GeV*). *Also indicated are 95% CL exclusion limits from global analysis of existing data [12].*

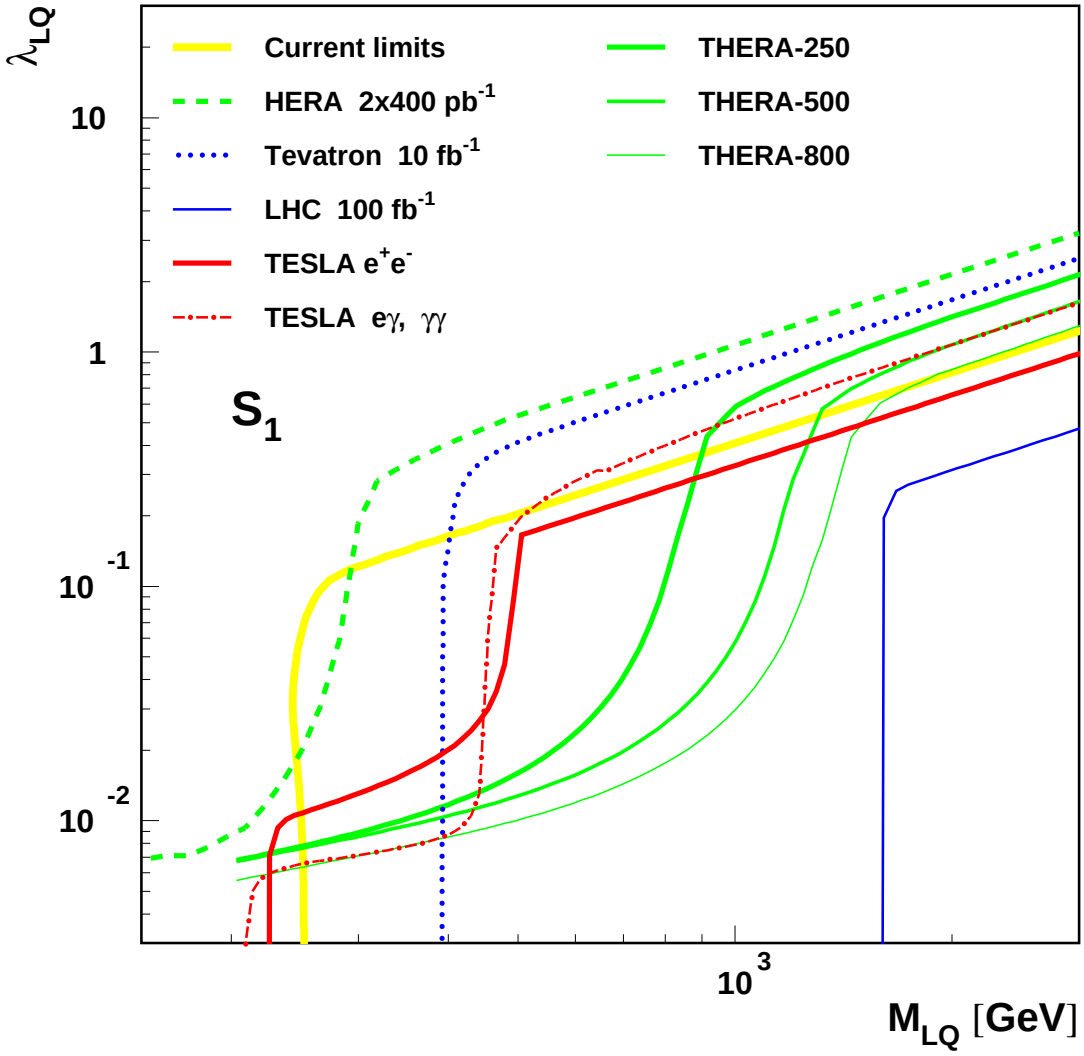

Figure 7: *Comparison of expected 95% CL exclusion limits in* (λ_{LQ}, M_{LQ}) *for* S_1 *leptoquark model, for different THERA running scenarios and other future experiments, as indicated in the plot. Presented limits correspond to* $2\times400\,pb^{-1}$ *of* $e^{\pm}p$ *data at HERA* ($\sqrt{s}$ = 318 *GeV*), $2\times100\,pb^{-1}$ *or* $2\times200\,pb^{-1}$ *of* $e^{\pm}p$ *data at THERA* ($\sqrt{s}$=*1.0,1.4 and 1.6 TeV*), $10\,fb^{-1}$ *of* $p\bar{p}$ *data at the Tevatron* ($\sqrt{s}$ = 2 *TeV*), $100\,fb^{-1}$ *of pp data at the LHC* ($\sqrt{s}$ = 14 *TeV*) *and* $100\,fb^{-1}$ *of* e^+e^-, $e\gamma$ *and* $\gamma\gamma$ *data at TESLA* ($\sqrt{s_{ee}}$ = 500 *GeV*). *Also indicated are 95% CL exclusion limits from global analysis of existing data [12].*

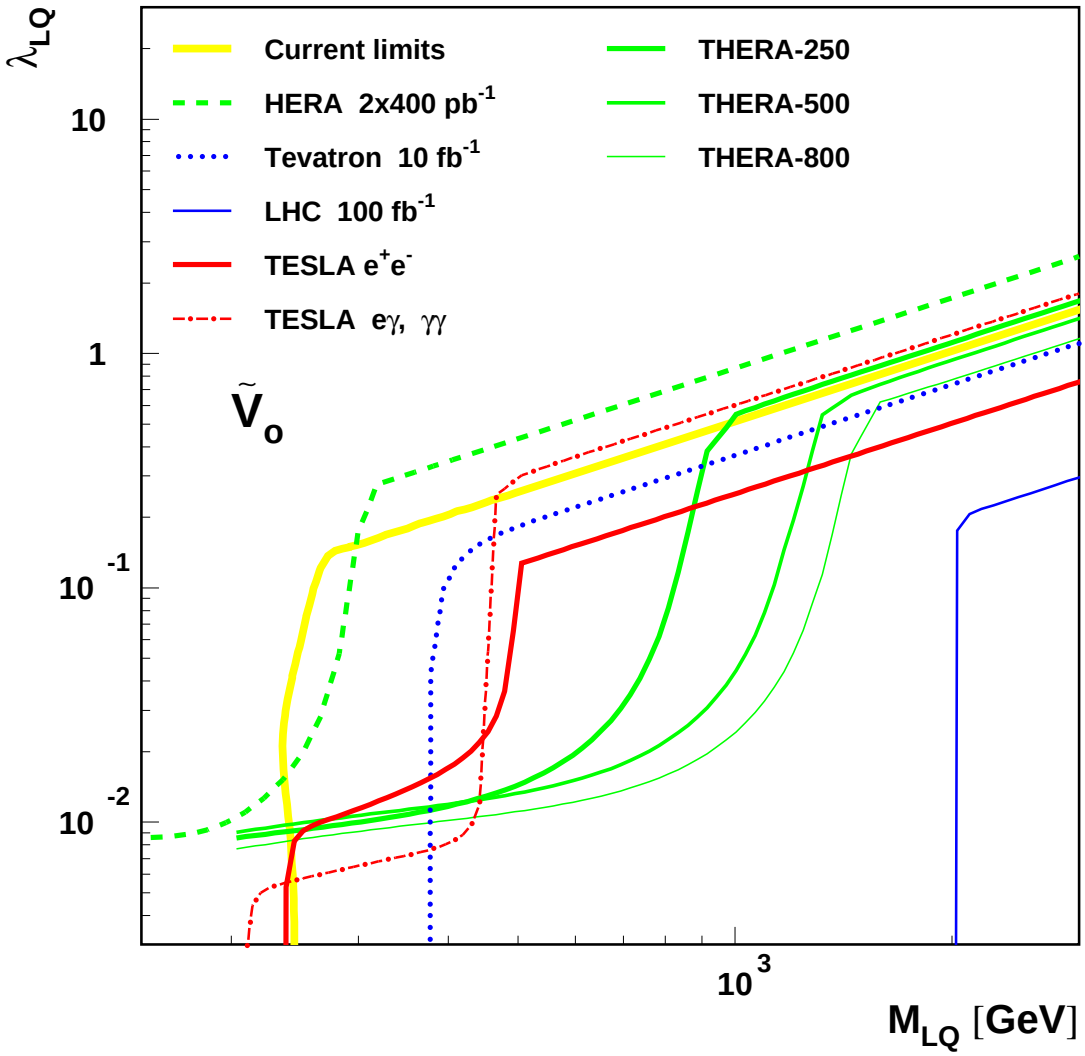

Figure 8: *Comparison of expected 95% CL exclusion limits in* (λ_{LQ}, M_{LQ}) *for* $\tilde{V}_\circ$ *leptoquark model, for different THERA running scenarios and other future experiments, as indicated in the plot. Presented limits correspond to* $2\times 400\,pb^{-1}$ *of* $e^{\pm}p$ *data at HERA* ($\sqrt{s}$ = 318 *GeV*), $2\times 100\,pb^{-1}$ *or* $2\times 200\,pb^{-1}$ *of* $e^{\pm}p$ *data at THERA* ($\sqrt{s}$=1.0,1.4 *and* 1.6 *TeV*), $10\,fb^{-1}$ *of* $p\bar{p}$ *data at the Tevatron* ($\sqrt{s}$ = 2 *TeV*), $100\,fb^{-1}$ *of pp data at the LHC* ($\sqrt{s}$ = 14 *TeV*) *and* $100\,fb^{-1}$ *of* e^+e^-, $e\gamma$ *and* $\gamma\gamma$ *data at TESLA* ($\sqrt{s_{ee}}$ = 500 *GeV*). *Also indicated are 95% CL exclusion limits from global analysis of existing data [12].*

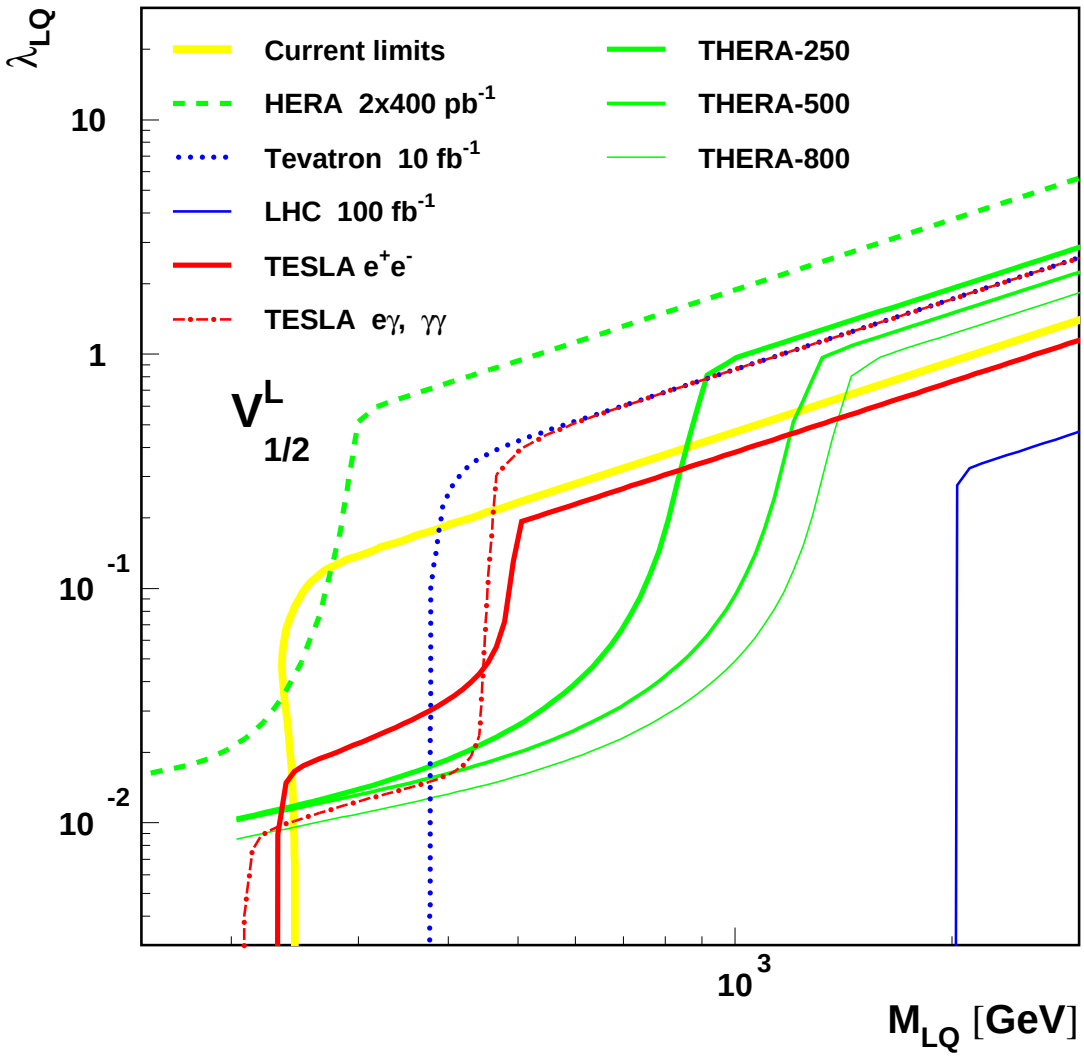

Figure 9: *Comparison of expected 95% CL exclusion limits in* (λ_{LQ}, M_{LQ}) *for* $V^L_{1/2}$ *leptoquark model, for different THERA running scenarios and other future experiments, as indicated in the plot. Presented limits correspond to* $2\times400\,pb^{-1}$ *of* $e^{\pm}p$ *data at HERA* ($\sqrt{s}$ = 318 *GeV*), $2\times100\,pb^{-1}$ *or* $2\times200\,pb^{-1}$ *of* $e^{\pm}p$ *data at THERA* ($\sqrt{s}$=1.0,1.4 *and* 1.6 *TeV*), $10\,fb^{-1}$ *of* $p\bar{p}$ *data at the Tevatron* ($\sqrt{s}$ = 2 *TeV*), $100\,fb^{-1}$ *of* pp *data at the LHC* ($\sqrt{s}$ = 14 *TeV*) *and* $100\,fb^{-1}$ *of* e^+e^-, $e\gamma$ *and* $\gamma\gamma$ *data at TESLA* ($\sqrt{s_{ee}}$ = 500 *GeV*). *Also indicated are 95% CL exclusion limits from global analysis of existing data [12].*

5.2 Pair Production of Supersymmetric Particles

M. Corradi
INFN Bologna
via Irnerio 46, 40126 Bologna, Italy
massimo.corradi@desy.de

5.2.1 Introduction

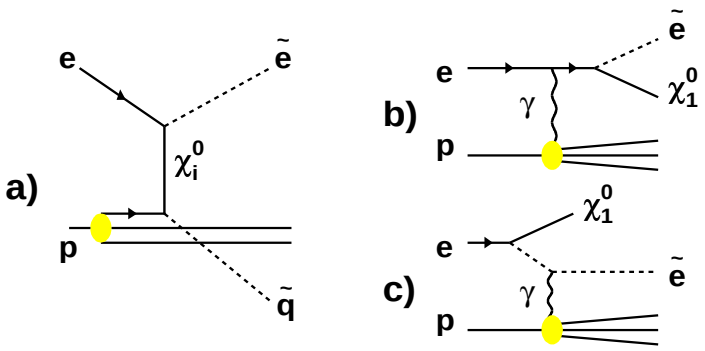

Figure 1: *Diagrams for R_p-conserving SUSY: a) $ep \to \tilde{e}\tilde{q}$, the amplitude is given by the sum of four such diagrams, one for each neutralino state; b), c) diagrams for $ep \to \tilde{e}\chi_1^0$.*

R-parity conserving Supersymmetry (SUSY) models, such as the Minimal Supersymmetric Standard Model (MSSM) and its constrained versions, probably are the most popular and most studied scenarios of physics beyond the Standard Model (SM) [1]. These models extend the SM by adding a supersymmetric partner to each SM particle, differing in spin by half a unit. The R-parity is a multiplicative quantity defined in such a way that $R_p = +1$ for "ordinary" SM particles and $R_p = -1$ for their supersymmetric partners. The conservation of R_p implies that the supersymmetric particles are always produced in pairs; that their decay products always contain an odd number of supersymmetric particles and that the lightest supersymmetric particle (LSP) is stable. To avoid cosmological constraints, the LSP is usually assumed to be neutral and only weakly interactive. Thus, in R-parity conserving models, the production of SUSY particles has the characteristic signature of large missing momentum carried away by (at least two) LSPs. In the MSSM, for a large portion of its parameter space, the LSP is the lightest neutralino (χ_1^0) i.e. the lightest mass eigenstate of the supersymmetric partners of the neutral gauge and Higgs bosons.

In the case of *ep* interactions, the lowest order process in which pairs of supersymmetric particles may be produced is

$$e^{\pm}p \to \tilde{e}^{\pm}\tilde{q}X,$$

namely the production of a squark ($\tilde{q}$, the scalar partner of the quark) and a selectron ($\tilde{e}$, the scalar partner of the electron). The potential of this process at THERA is analyzed in next section.

To occur at THERA at a detectable rate, $\tilde{e}\tilde{q}$ production requires a relatively light squark. On the other hand, many extensions of the MSSM predict the squark to be one of the heaviest states of the supersymmetric spectrum. Moreover the squarks can be very well constrained at hadronic colliders. Therefore last section considers a process in which potentially lighter and less constrained particles are produced, a selectron and the lightest neutralino: $ep \to \tilde{e}\tilde{\chi}_1^0 X$.

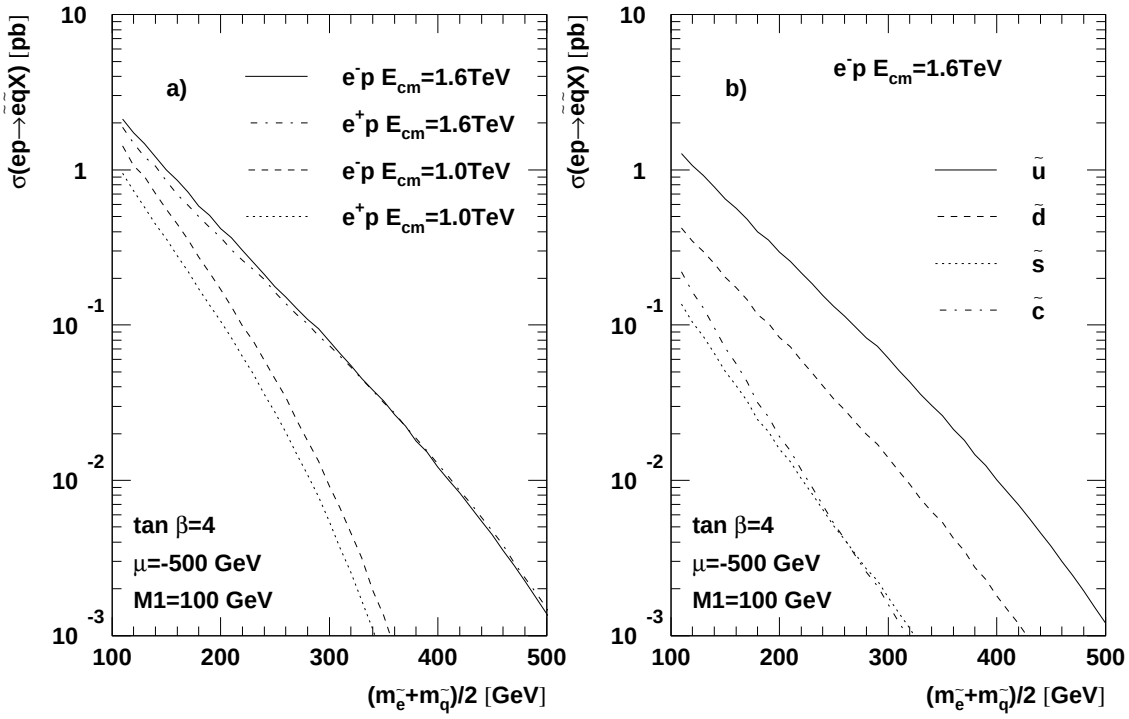

Figure 2: *Cross section for selectron-squark production as a function of* $(m_{\tilde{e}} + m_{\tilde{q}})/2$. *In a) for mass-degenerate squarks at* e^-p *and* e^+p *center of mass energies of* $E_{cm} = 1.0$ *and* 1.6 *TeV, in b) the cross section for the production of* $\tilde{u}, \tilde{d}, \tilde{s}$ *and* $\tilde{c}$ *squarks is reported for* e^-p *interactions at* $E_{cm} = 1.6$ *TeV.*

5.2.2 Selectron and Squark Production

The production of a selectron and squark occurs in the MSSM through neutralino exchange, as shown in Fig. 1 (a). This process has been already exploited at HERA to set limits on the MSSM [2, 3].

The cross section for $ep \to \tilde{e}\tilde{q}X$ has been evaluated using a Monte Carlo program based on [4] and already used in [3]. The cross section depends strongly on the sum of

the masses of the produced objects $(m_{\tilde{e}} + m_{\tilde{q}})$ due to the steep decrease of the parton densities in the proton at high x, while its dependence on other MSSM parameters, such as the masses and the mixing of the neutralinos, is weak. Figure 2(a) shows the cross section as a function of $(m_{\tilde{e}} + m_{\tilde{q}})/2$ for electron and positron beams and for two choices of the $e^{\pm}p$ center of mass energy and for the following values of the MSSM parameters: $\tan\beta = 4$, $\mu = -500\,\mathrm{GeV}$, $M_1 = 100\,\mathrm{GeV}$ that give a LSP mass $m_{\chi_1^0} = 102\,\mathrm{GeV}$. Left- and right- handed electrons and quarks have been considered to have the same mass $(m_{\tilde{e}_L} = m_{\tilde{e}_R};\ m_{\tilde{q}_L} = m_{\tilde{q}_R})$.

The simplest final state occurs when the $\tilde{e}$ $(\tilde{q})$ decays directly to e (q) and the LSP. In this case the typical signature is one electron, one jet and missing momentum from the two LSPs that escape detection. If the decays into gluinos, charginos or next-to-lightest neutralinos are open, more complex signals with ≥ 1 jets, ≥ 1 lepton and missing momentum are expected. The decay products are expected to be roughly distributed within ± 1 unit in rapidity around the rapidity of the $\tilde{e}\tilde{q}$ system which can be approximated by $y^{\mathrm{lab}}_{\tilde{e}\tilde{q}} \sim \ln \frac{(m_{\tilde{e}}+m_{\tilde{q}})}{2E_e}$, the positive rapidity being defined by the proton beam direction. In the case of THERA at $800 + 800$ GeV, it goes from $y^{\mathrm{lab}}_{\tilde{e}\tilde{q}} = -1.5$ at $(m_{\tilde{e}} + m_{\tilde{q}})/2 = 175$ GeV to $y^{\mathrm{lab}}_{\tilde{e}\tilde{q}} = 0$ at $(m_{\tilde{e}} + m_{\tilde{q}})/2 = 400\,\mathrm{GeV}$. Therefore the decay products are expected to be quite central, well within the acceptance of a typical detector for THERA.

Previous experience at HERA [3, 5] shows that a negligible background can be obtained with a sizeable acceptance in a hermetic detector with good resolution on the missing momentum. At THERA the main source of background is expected to come from W production. Events with leptonic decay $W \to e\nu$ in association with a jet are similar to $\tilde{e}\tilde{q}$ events, being characterized by one electron, one jet and missing momentum. Extrapolating the results of [6] for $\sqrt{1.3}\,\mathrm{TeV}$ (LEP-LHC), we found an expected cross section times branching ratio $\sigma(e^{\pm}p \to W^{\pm}X)\mathrm{B}(W^{\pm} \to e^{\pm}\nu)$ of the order of $3\,\mathrm{pb}$ and a fraction of events with an associated jet with $E_{\mathrm{t}}^{\mathrm{jet}} > 50\,\mathrm{GeV}$ around 20%. Requiring the transverse mass $M_{\mathrm{t}}^{\mathrm{eP_t}}$ from the electron and the missing-P_{t} system to be above the W mass should be effective in reducing this background down to a negligible level. The price is the loss of acceptance for the signal if the mass difference between the selectron and the LSP $\Delta_m = (m_{\tilde{e}} - m_{\chi_1^0})$ is below $M_W/2$, since in $\tilde{e}\tilde{q}$ events, for small $\Delta_m/m_{\tilde{e}}$, the average transverse mass is $\langle M_{\mathrm{t}}^{\mathrm{eP_t}} \rangle \sim 2\Delta_m$.

Assuming an acceptance of 25% for events with $\Delta_m > 50$ GeV in the case of zero observed events in an integrated luminosity $\mathcal{L} = 250\ \mathrm{pb}^{-1}$, it would be possible to set a final upper limit on the cross section $\sigma_{\mathrm{lim}} \sim 0.05$ pb , corresponding to the exclusion of masses up to $(m_{\tilde{e}} + m_{\tilde{q}})/2 \sim 330(220)\,\mathrm{GeV}$ at $\sqrt{s} = 1.6(1.0)$ TeV.

Therefore the phase space between the present limits on the selecron (~ 100 GeV) and on the squark mass (~ 200 GeV) and those obtainable at THERA is large but well inside the reach of LHC, that will probe squark masses up to 2-2.5 TeV.

Nevertheless, even if THERA is not well suited to discover R-parity supersymmetry, it can give a relevant contribution in the determination of the squark flavor, i.e. in identifying which SM quark is the "ordinary" partner of the squark. In e^+e^- and pp interactions the squarks are produced in pairs, independently of their generation.

Conversely, in ep collisions almost only first generation squarks are produced, as they come mostly from the u and d valence quarks of the proton. If a squark was discovered at the e^+e^- or pp colliders, it will be possible to identify it as a $\tilde{u}$, a $\tilde{d}$ or an higher generation squark from a crude measurement of the ep production cross section. The cross section for different squark flavours at $\sqrt{s} = 1.6\,\text{TeV}$ is shown in Fig. 2 (b). As an example, for $m_{\tilde{e}} = 150$ GeV and $\mathcal{L} = 250$ pb^{-1}, it could be possible to exclude a $\tilde{u}$ squark up to $m_{\tilde{q}} \sim 500\,\text{GeV}$ and a $\tilde{d}$ up to $m_{\tilde{q}} \sim 300\,\text{GeV}$.

5.2.3 Selectron and Neutralino Production

The MSSM production of a selectron and neutralino ($ep \to \tilde{e}\chi_1^0 X$) occurs through the diagrams shown in fig. 1(b,c). The cross section has been evaluated using the same program as in [7], based on the calculations of [8] that includes a relevant contribution from the "elastic" process $ep \to \tilde{e}\chi_1^0 p$. The result is that the cross section is negligible even for masses at the edge of present limits. For example, at $\sqrt{s} = 1.6$ TeV, for $m_{\tilde{e}} = 100$ GeV and $m_{\chi_1^0} = 50$ GeV, and in the favorable case of a photino-like LSP,

$$\sigma(ep \to \tilde{e}\chi_1^0 X) = 3.7 \times 10^{-2}\,\text{pb},$$

which drops to 5.6×10^{-2} pb at $m_{\tilde{e}} = 200$ GeV. It seems therefore unrealistic to expect a visible selectron-neutralino signal at THERA.

5.2.4 Conclusions

The production cross section for $\tilde{e}\tilde{u}$ ($\tilde{e}\tilde{d}$) pairs at $\sqrt{s} = 1.6\,\text{TeV}$ is small but should be measurable at THERA provided that the average mass $(m_{\tilde{e}}+m_{\tilde{q}})/2$ is below $\sim 300(200)$ GeV and assuming that ~ 250 pb^{-1} will be collected. Therefore THERA will not be competitive with LHC and TESLA for the first discovery of R-parity conserving SUSY. Nevertheless a measurement or a limit on $\tilde{e}\tilde{u}$ ($\tilde{e}\tilde{d}$) production can be crucial for the determination of the flavour structure of the squarks.

References

[1] H.E. Haber and G.L. Kane, Phys. Rept. **117**, 75 (1985);
Particle Data Group, D.E. Groom et al., Eur. Phys. J. **C 1-4**, 817 (2000).

[2] H1 Coll., S. Aid et al., Phys. Lett. **B 380**, 461 (1996).

[3] ZEUS Coll., J. Breitweg et al., Phys. Lett. **B 434**, 214 (1998).

[4] A. Bartl, H. Fraas and W. Majerotto, Nucl. Phys. **B 297**, 479 (1988);
H. Komatsu and R. Rückl, Nucl. Phys. **B 299**, 407 (1988);
T. Bartels and W. Hollik, Z. Phys. **C 39**, 433 (1988).

[5] P. Schleper, *Searches for minimal supersymmetry at HERA*, in *Proc. Workshop on Future Physics at HERA*, eds. G. Ingelman, A. De Roeck and R. Klanner, p. 275. Hamburg, Germany, DESY, 1996.

[6] U. Baur, J.A.M. Vermaseren and D. Zeppenfeld, Nucl. Phys. **B 375**, 3 (1992).

[7] M. Corradi, *Associated production of selectron neutralino pairs*, in *Proc. Workshop on Future Physics at HERA*, eds. G. Ingelman, A. De Roeck and R. Klanner, p. 289. Hamburg, Germany, DESY, 1996.

[8] G. Altarelli et al., Nucl. Phys. **B 262**, 204 (1985);
J.L. Lopez et al., Phys. Rev. **D 48**, 4029 (1993);
M. Drees and D. Zeppenfeld, Phys. Rev. **D 39**, 2536 (1989);
H. Tsutsui et al., Phys. Lett. **B 245**, 663 (1990).

5.3 Search for Excited Fermions at THERA

M. Kuze
Institute of Particle and Nuclear Studies, KEK, Tsukuba, Japan
masahiro.kuze@desy.de

5.3.1 Introduction

Existence of heavy excited states of fermions (leptons and quarks) would imply that they have substructures rather than being elementary, and thus provides a direct evidence for physics beyond the Standard Model. Searches for excited leptons and quarks are extensively carried out in current high-energy collider experiments. A simple study of investigating the sensitivity of THERA collider for excited electrons and neutrinos has been done, which is presented here.

The study is based on the theoretical framework of Hagiwara, Komamiya and Zeppenfeld [1] which assumes that excited fermions have spin and isospin 1/2, and both left- and right-handed components are in weak isodoublets. The Lagrangian for describing the magnetic transition between ordinary and excited fermions is described as [2]:

$$\mathcal{L}_{f^*f} = \frac{1}{2\Lambda}\bar{f}^*_R\sigma^{\mu\nu}\left[gf\frac{\vec{\tau}}{2}\vec{W}_{\mu\nu} + g'f'\frac{Y}{2}B_{\mu\nu} + g_s f_s\frac{\lambda^a}{2}G^a_{\mu\nu}\right]f_L + h.c., \tag{5.3.1}$$

where $\vec{W}_{\mu\nu}, B_{\mu\nu}$ and $G^a_{\mu\nu}$ are the field-strength tensors of the SU(2), U(1) and SU(3) gauge fields, $\vec{\tau}, Y$ and λ^a are the corresponding gauge-group generators, and g, g' and g_s are the gauge coupling constants, respectively. Λ is the compositeness scale and f, f' and f_s are weight parameters associated with the three gauge groups which are determined by the composite dynamics.

The production of excited electrons (neutrinos) in ep collisions at THERA takes place via t-channel $\gamma, Z(W)$ exchange as shown in Fig. 1. Once produced, excited leptons decay into a gauge boson and an ordinary lepton. This study concentrates on the photonic decay channels $e^* \to e\gamma$ and $\nu^* \to \nu\gamma$ which can be cleanly identified with small background contribution from Standard Model processes.

5.3.2 Results

As there are no dedicated Monte Carlo simulations for a detector at THERA, the results from ZEUS preliminary analysis [3] was simply extrapolated to obtain an estimated sensitivity for e^* and ν^* signals through their decay channels $e^* \to e\gamma$ and $\nu^* \to \nu\gamma$. Reconstruction efficiency of 80% is assumed for the signal events, and the background

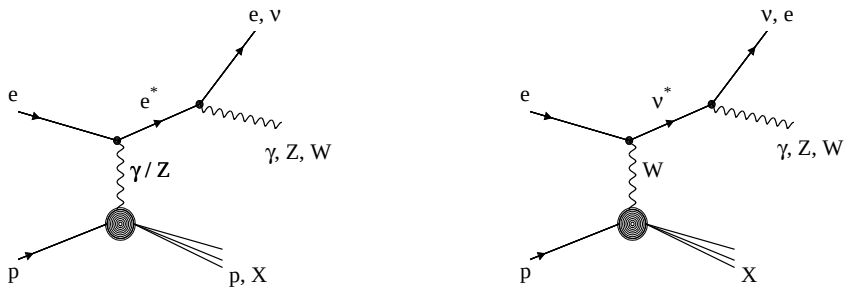

Figure 1: *Diagrams for excited electron (left) and neutrino (right) production and decay in ep interaction.*

from SM processes will be negligibly small at high mass. At large excited-fermions masses, the branching ratio for these photonic decay modes will be approximately constant at 30% under the assumption $f = f'(f = -f')$ for $e^*(\nu^*)$.

Putting together these numbers with the excited-fermion production cross sections calculated by HEXF [4] generator, expected 95% CL upper limits in case of no signal are illustrated in Fig. 2 for 30 pb^{-1} of e^-p data from THERA. It can be seen that the sensitivity will extend much beyond the kinematical limit of HERA, and and also improve the indirect limit on e^* from LEP using virtual effects in $e^+e^- \to \gamma\gamma$ process. For the assumption $f/\Lambda = 1/m_{e^*(\nu^*)}$, the lower bound of about 570 GeV (500 GeV) for $e^*(\nu^*)$ can be obtained from these data. If upgraded THERA (800 GeV electron and 800 GeV proton, 200pb^{-1} of data) is assumed, the corresponding exclusion limits will extend to approximately 1 TeV.

It is worth mentioning that *electron*-proton collision is the much preferred option for the excited-neutrino production due to the large u-quark density and the helicity nature of the charged-current interaction.

5.3.3 Conclusions

Sensitivity of THERA for excited electrons and neutrinos have been investigated based on experiences with the current HERA data. A large amount of coupling phase space will open above the HERA kinematical limit even with a modest amount of luminosity from THERA. Assuming $f/\Lambda = 1/m_{e^*(\nu^*)}$, lower bound of 570 GeV (500 GeV) in $e^*(\nu^*)$ mass can be obtained at 95% CL. These limits will increase to about 1 TeV for the case of upgraded THERA.

However, it should be noted that hadron colliders can in principle produce excited leptons with a large cross section [2]. The sensitivity of LHC is deemed to reach a few TeV in mass, although there seem to exist no dedicated studies involving experimental simulations.

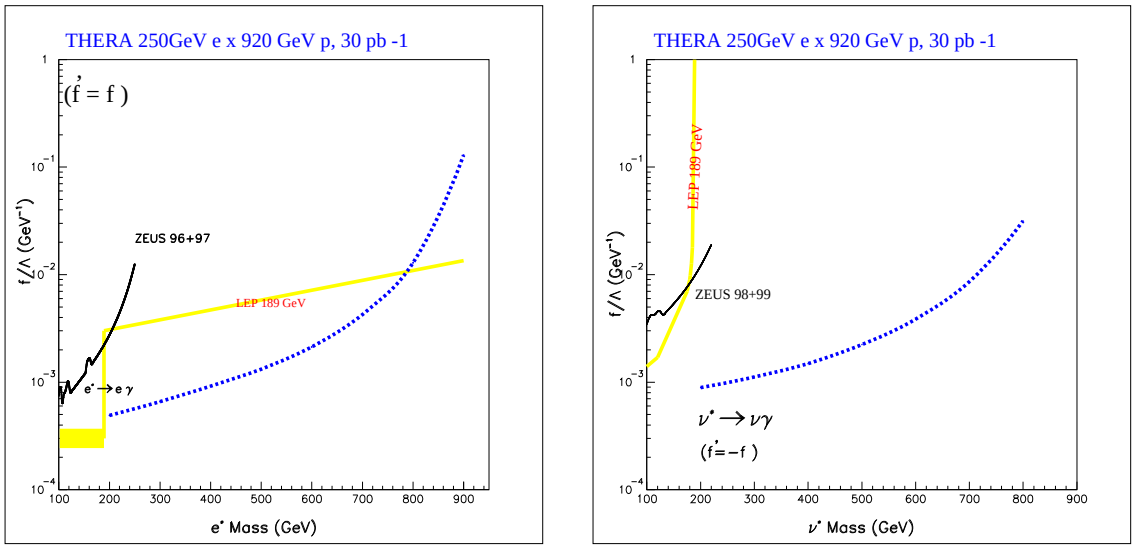

Figure 2: *Expected 95% CL upper limits on f/Λ as a function of excited-fermion mass for e^* (left) and ν^* (right) are illustrated by dotted curves, and compared with current limits from HERA (solid curves) and LEP (light-shaded band).*

References

[1] K. Hagiwara, D. Zeppenfeld and S. Komamiya, Z. Phys. **C 29**, 115 (1985).

[2] U. Baur, M. Spira and P.M. Zerwas, Phys. Rev. **D 42**, 815 (1990).

[3] ZEUS Coll., *Search for excited fermions in ep collisions at HERA.* Subm. to *EPS-HEP99*, Tampere, Finland, paper 555, 1999;
ZEUS Coll., *Search for excited fermions in ep collisions at HERA.* Subm. to *ICHEP2000*, Osaka, Japan, paper 454, 2000.

[4] H.J. Kim and S. Kartik, *A Monte Carlo generator for excited fermions at HERA - HEXF version 1.0.* Preprint LSUHE-145-1993, 1993.

6 Resolving the Partonic Structure of the Photon

6.1 Reach of Future Colliders in Probing the Structure of the Photon

M. Krawczyk
Institute of Theoretical Physics, University of Warsaw
Warsaw, Poland
krawczyk@fuw.edu.pl

S. Söldner-Rembold
CERN, Geneva
Switzerland
Stefan.Soldner-Rembold@cern.ch

M. Wing
McGill University, Montreal
Canada
wing@mail.desy.de

Abstract

A comparison of the potentials of ep and e^+e^- machines to probe the structure of the photon is performed. In particular, the kinematic reach of a proposed future ep facility, THERA, is compared with those of current colliders, LEP and HERA, and with the proposed linear collider, TESLA. THERA like HERA will use a proton beam of 920 GeV but with an increased electron beam energy of 250 GeV allowing higher scales, $\hat{Q}^2$, and lower values of parton momentum fraction in the photon, x_γ, to be probed.

6.1.1 Introduction

The photon - the gauge boson of QED - has, in high energy processes, a "hadronic structure". In deep inelastic scattering, $e\gamma \to e$ hadrons, the corresponding structure

function can be introduced, $F_2^\gamma(x, \hat{Q}^2)$, where $\hat{Q}^2$ is the scale at which the quasi-real photon is probed. At low Bjorken x this structure function is expected to behave like F_2^{p}, i.e. it increases towards lower x at sufficiently large $\hat{Q}^2$, where $\hat{Q}^2$ is the scale at which the quasi-real photon is probed. Unique expectations for the photon are the logarithmic rise of the structure function, F_2^γ, with the scale $\hat{Q}^2$ and a large quark density at large x ($\sim x_\gamma$). Observations of these phenomena are basic tests of QCD.

In deep-inelastic eγ scattering at $\mathrm{e^+e^-}$ colliders the scale $\hat{Q}^2$ is given by the virtuality Q^2 of the probing virtual photon whereas in the photoproduction regime ($Q^2 < 1$ GeV^2) in ep collisions and collisions of quasi-real photons, $\gamma\gamma$ scattering, in $\mathrm{e^+e^-}$ colliders it is usually given by the transverse momentum p_{T} of jets or final state particles.

The ep collider, THERA, would offer the opportunity to study the partonic structure of the photon extending the kinematic range in x_γ and $\hat{Q}^2$ over existing colliders (HERA and LEP) by approximately one order of magnitude. At lowest order, x_γ is equal to unity for "direct" processes (Fig. 1a), whereas "resolved" processes (Fig. 1a), where the photon interacts via its partonic content, are characterised by a smaller value of x_γ. In addition, the photoproduction of particles (hadrons or prompt photons) or jets at high p_{T} provides complementary information to that from deep-inelastic eγ on the partonic, in particular gluonic (Fig. 1b), content of the quasi-real photon. The photoproduction of dijets, heavy quarks and prompt photons have been studied [1–4], with the emphasis on the potential of THERA to yield information on the structure of the real photon. The possibility of studying the structure of the virtual photon at THERA has also been considered [5].

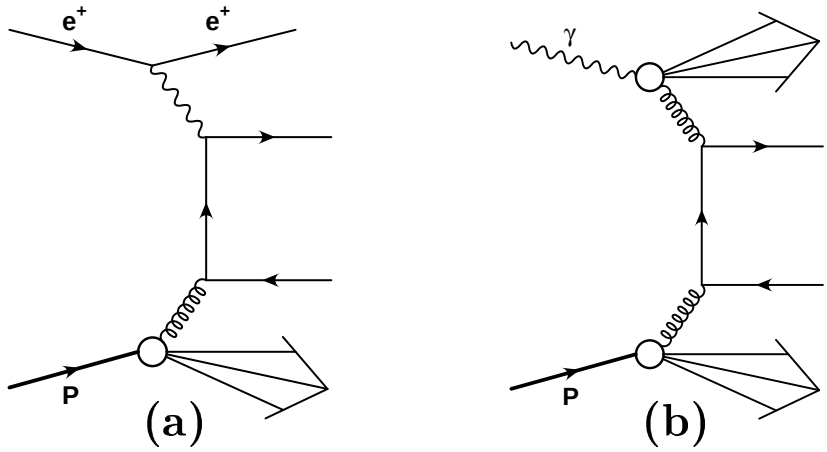

Figure 1: *Examples of lowest order (a) direct photon and (b) resolved photon processes in ep collisions.*

Good knowledge of the hadronic interactions of a fundamental particle - the photon - is essential for the future high energy physics programme. The present situation is not satisfactory as data for some processes, such as that for the photoproduction of dijets at HERA are not in agreement with existing next-to-leading (NLO) QCD

calculations [6, 7]. The agreement for processes involving resolved virtual photons is even more problematic. A proper description of the hadronic interaction of photons is also needed to calculate the Standard Model background in searches for the Higgs particle and other new phenomena at future colliders.

Initially a comparison is made of the kinematic regions accessible at various colliders where the structure of the photon can be tested: LEP, HERA and the future linear collider (TESLA) in the basic e^+e^- mode. The aim of this section is to show how THERA can enrich the potential of TESLA in its standard e^+e^- mode and so detailed comparisons with photon colliders ($\gamma\gamma$ or $e\gamma$ modes) are not considered. It is assumed that the energy of the electron beam is 250 GeV and that of the proton beam is 920 GeV.

6.1.2 The THERA kinematic region in comparison with other colliders

In considering the benefits of THERA for studying the structure of the photon, all current machines and those of the future are discussed for comparison. The kinematic reach of THERA ($\sqrt{s} \approx 1$ TeV) is compared with those of LEP ($\sqrt{s} \approx 200$ GeV), HERA ($\sqrt{s} \approx 300$ GeV) and a future linear e^+e^- collider, TESLA, ($\sqrt{s} \approx 500$ GeV), where $\sqrt{s}$ denotes the centre-of-mass energy of the colliding primary beams. The nominal ep and e^+e^- options are considered for THERA and TESLA, respectively; the corresponding γp and γe or $\gamma\gamma$ options cover a similar kinematic region with an increased cross section but lower luminosity. Of interest is to consider the minimum x_γ, the range of $\hat{Q}^2$ and the polar angle (rapidity) of the jets in resolved photon events. For comparison the following quantities are introduced, relevant for deep-inelastic $e\gamma$ scattering and resolved photon processes in e^+e^- and ep colliders:

$$Q^2_{\mathrm{max,min}}|_{e^+e^-} = \frac{W^2_{\mathrm{max,min}} x_\gamma}{1 - x_\gamma}, \qquad \hat{Q}^2|_{\mathrm{ep}} \equiv p_{\mathrm{T}}^2 = (y_{\mathrm{max}} E_{\mathrm{e}} e^{\eta_{\mathrm{max}}} x_\gamma)^2 \tag{6.1.1}$$

$$x|_{e^+e^-} = \frac{Q^2}{Q^2 + W^2}, \qquad x_\gamma^{\mathrm{min}}|_{e^+e^-} = \frac{p_{\mathrm{T}} e^{\pm\eta_{\mathrm{CM}}}}{2E_{\mathrm{e}} - p_{\mathrm{T}} e^{\mp\eta_{\mathrm{CM}}}}, \qquad x_\gamma^{\mathrm{min}}|_{\mathrm{ep}} = \frac{E_{\mathrm{p}} p_{\mathrm{T}} e^{-\eta_{\mathrm{LAB}}}}{2E_{\mathrm{e}} E_{\mathrm{p}} - E_{\mathrm{e}} p_{\mathrm{T}} e^{\eta_{\mathrm{LAB}}}}, \tag{6.1.2}$$

where W denotes the invariant mass of the hadronic final state. In Fig. 2a, the minimum photon momentum fraction, x_γ^{min}, is shown for a given transverse momentum, p_{T}, ($= E_{\mathrm{T}}$ for massless particles) of 10 GeV, as a function of the rapidity, η, of the jets in the laboratory frame for e^+e^- colliders (equivalent to the centre-of mass frame) and ep colliders. It can be seen that for a given rapidity, an order of magnitude smaller value of x_γ^{min} at THERA can be probed compared with HERA due to the increased electron beam energy, E_{e}. The minimum x_γ^{min} at TESLA would also extend the minimum possible at LEP and HERA. However, smaller values of x_γ^{min} can be reached at THERA than at TESLA in the very forward rapidity direction ($\eta_{\mathrm{LAB}}^{\mathrm{ep}} > 2$) reaching a minimum

for this transverse momentum at $\eta^{\rm ep}_{\rm LAB} \sim 4.6$. This demonstrates that good forward detectors are needed for THERA with the ability to accurately reconstruct jets up to the rapidities discussed here. Only the e^+e^- TESLA collider is considered. The kinematic reach of the e^+e^- TESLA collider depends very much on the minimum required for the energy $E_{\rm tag}$ and angle $\theta_{\rm tag}$ of the scattered electron. A much larger kinematic range could be covered with an $e\gamma$ collider based on TESLA [8]

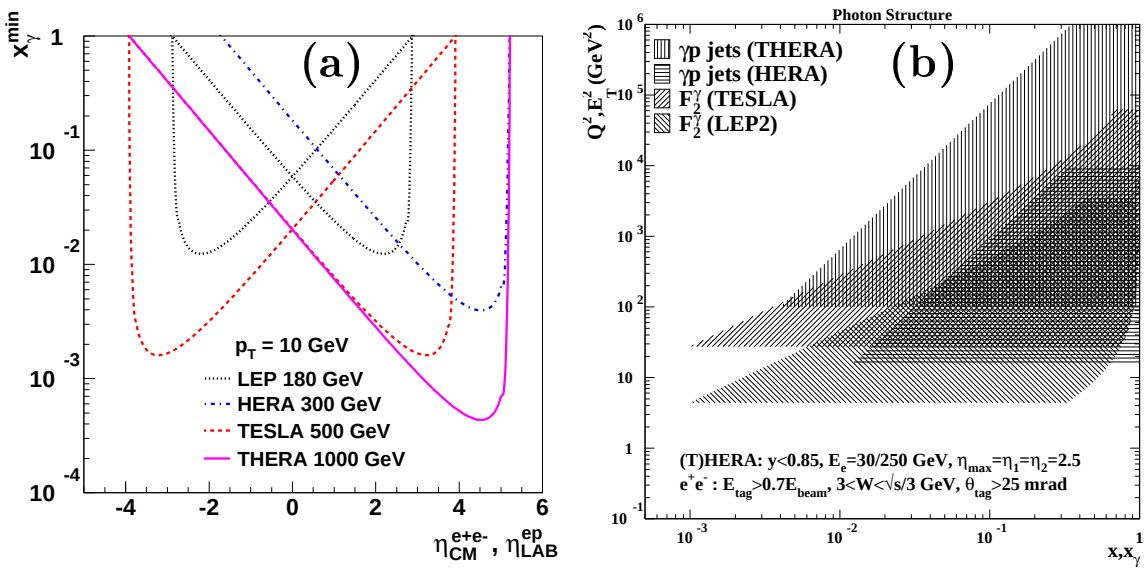

Figure 2: *(a) The minimum photon momentum fraction, $x_\gamma^{\rm min}$, versus the rapidity of the jets in the centre-of-mass frame for e^+e^- machines and laboratory frame for ep machines. (b) Range in $\hat{Q}^2$ (Q^2 for F_2^γ or $p_{\rm T}^2$ for γp jets) versus x_γ with realistic detector scenarios shown. The region for THERA is compared with that of TESLA, HERA and LEP.*

Considering some restrictions in the detector layout, the values of $\hat{Q}^2$ obtainable are shown versus x_γ in Fig. 2b. Detectable scenarios for LEP and HERA are described in Fig. 2b and the same for TESLA and THERA are also imposed, although it is hoped that the future experiments would have improved detectors in the very forward and backward regions. Here it can be seen that although the e^+e^- machines will yield the lowest values of x_γ, it is also apparent that the ep machines can probe a smaller value of x_γ for a given $\hat{Q}^2$. In particular, THERA will provide valuable additional information on the structure of the photon in the region, $x_\gamma > 0.01$, particularly at high-$p_{\rm T}$, complementing TESLA and the current experiments.

6.1.3 Summary

Photoproduction at THERA can further current knowledge of the structure of the photon, extending the current colliders, HERA and LEP and complementing the future linear e^+e^- collider program. The kinematic range can be extended, for quasi-real

photons, in x_γ and the hard scale, $\hat{Q}^2 \sim p_{\rm T}^2$. Also the structure of the virtual photon for larger square of its mass, Q^2, can be probed. Inclusive dijets, heavy quarks and prompt photons have been studied as tools to probe the structure of the quasi-real and virtual photon. The building of THERA will, therefore, enrich the field on the structure of a fundamental gauge boson - the photon.

Acknowledgements

We would like to thank the organisers for an interesting and productive series of workshops. One of us (MK) have been partly supported by the Polish State Committee for Scientific Research (grant 2P03B05119, 2000-2001). MK is also grateful to the European Commission 50th Framework Contract HPRN-CT-2000-00149 and DESY for financial support.

References

[1] M. Klasen, *Jet photoproduction at THERA*, in *The THERA Book* [9].

[2] M. Wing, *Inclusive dijet photoproduction and the resolved photon at THERA*, in *The THERA Book* [9].

[3] P. Jankowski, M. Krawczyk and M. Wing, *Heavy quark production at THERA*, in *The THERA Book* [9].

[4] M. Krawczyk and A. Zembrzuski, *Prompt photon production at THERA*, in *The THERA Book* [9].

[5] U. Jezuita-Dabrowska and M. Krawczyk, *On the importance of the interference terms and longitudinal virtual photon contribution at THERA*, in *The THERA Book* [9].

[6] ZEUS Coll., J. Breitweg et al., Euro. Phys. J. **C 11**, 35 (1999);
ZEUS Coll., *The structure of the photon and the dynamics of resolved-photon processes in dijet photoproduction.* Subm. to *ICHEP2000*, Osaka, Japan, paper 418, 2000;
ZEUS Coll., *Measurement of dijet photoproduction at high transverse energies at HERA.* Subm. to *EPS-HEP99*, Tampere, Finland, paper 540, 1999.

[7] M. Krawczyk, A. Zembrzuski and M. Staszel, *Survey of present data on photon structure functions and resolved photon processes.* Preprint IFT-99-15 (hep-ph/0011083), 2000. Subm. to Phys. Rept.

[8] A. Vogt, Nucl. Phys. Proc. Suppl. **82**, 394 (2000).

[9] *The THERA Book*, Report DESY-LC-REV-2001-062, 2001. `http://www.desy.de/~lcnotes`.

6.2 Inclusive Dijet Photoproduction and the Resolved Photon at THERA

M. Wing
McGill University, Montreal, Canada
wing@mail.desy.de

Abstract

A future *ep* facility, THERA, where electrons of 250 GeV and protons of 920 GeV are collided could provide valuable information on the structure of the photon. With an increase in the centre-of-mass energy of a factor of 3 and an extension of the minimum photon energy fraction carried by the interacting parton of a factor of 10 compared to HERA, a new kinematic regime in the study of the photon will be opened. Inclusive dijet production has been studied and the potential gains the new collider would bring are discussed. The differences between current parametrisations of the photon structure in this new kinematic region are shown to be up to 50%. Comparisons of THERA's capabilities are made with what HERA can currently produce and how it complements e^+e^- colliders addressed.

6.2.1 Introduction

Using the proton accelerator ring from HERA and the lepton accelerator chain for the proposed linear collider, TESLA, a centre-of-mass energy for *ep* collisions of ~ 1 TeV could be achieved [1]. The proposed facility, THERA, using protons of 920 GeV and leptons of 250 GeV would, due to the increase in lepton beam energy, greatly extend the kinematic regime currently accessible to HERA [1, 2].

The measurement of jet photoproduction in *ep* collisions allows the structure of the photon, emitted from the incoming lepton, to be probed. In Leading Order (LO) quantum chromodynamics (QCD), two types of processes contribute to jet photoproduction: the direct photon process, in which the photon itself interacts with a parton from the proton and the resolved photon process in which the photon acts as a source of partons, one of which interacts with a parton from the proton. Examples of these processes are shown in Fig. 1, where Fig. 1a shows the boson-gluon fusion direct process and Fig. 1b gluon-gluon fusion resolved process. As can be seen from Fig. 1, photoproduction processes depend on both the structure of the photon and proton; the cross-section, $d\sigma_{\gamma p\to cd}$ for the production of two partons being,

$$d\sigma_{\gamma p\to cd} = \sum_{ab} \int_{x_p} dx_p \int_{x_\gamma} dx_\gamma f_{p\to b}(x_p,\mu^2) f_{\gamma\to a}(x_\gamma,\mu^2) d\hat{\sigma}_{ab\to cd}, \tag{6.2.1}$$

where $f_{p\to b}(x_p, \mu^2)$ describes the proton parton density of a parton of momentum fraction, x_p, $f_{\gamma\to a}(x_\gamma, \mu^2)$ the photon parton density of a parton of momentum fraction, x_γ, both at some renormalisation and factorisation scale, μ^2, and $d\hat{\sigma}_{ab\to cd}$ is the perturbatively calculable short distance cross-section. As next-to-leading (NLO) order programs reasonably describe jet production, one can choose a region of phase space where the proton structure is well constrained and the only uncertainty, as can be seen in Eq. 6.2.1, is then the photon structure function. It is noted (although not studied further) that dijet production at HERA and THERA could also provide information on the proton structure using high transverse energy or (very) forward jets. This would provide information on the parton densities at high values of x_p at large scales, as in $p\bar{p}$ collisions, which are not well constrained by the F_2^p DIS measurements.

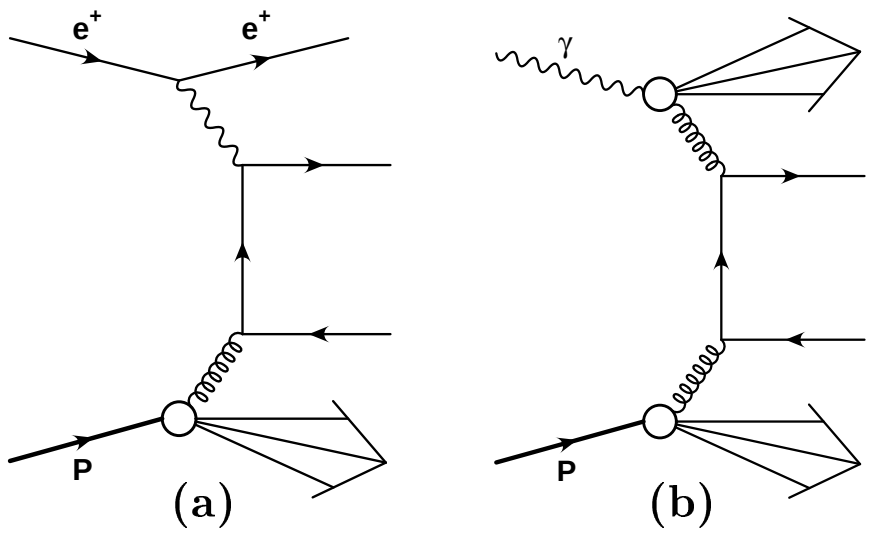

Figure 1: *Examples of LO (a) direct photon and (b) resolved photon processes in ep collisions.*

Measurements of the photon structure function, F_2^γ, at e^+e^- experiments have constrained the quark density in the region $10^{-3} < x_\gamma < 0.5$ [3]. Photoproduction can provide further constraints on the quark density at high x_γ and on the gluon density at all x_γ. In jet photoproduction, unlike in e^+e^- scattering, there is direct access to the gluon density in the photon at LO. The poorly constrained gluon density is expected to become more significant with decreasing x_γ. Measurements have been made at HERA, which probe these uncertain parts of the structure of the photon [4–6]. An electron beam energy of a factor of 10 higher for THERA than for HERA gives an extension in the minimum x_γ also by a factor of 10 [2]. THERA would lead to an extension of the kinematic range into a region where accurate measurements of the gluon density could be made and the rise in the structure function, F_2^γ, thoroughly tested.

6.2.2 Photoproduction from HERA to THERA

Currently at HERA, the highly asymmetric beam energies provide problems in measuring resolved photon processes. In general, there is a strong tendency for events to be very forward in the proton beam direction. This means that many events fall outside the acceptance of the current detectors or are mixed up with the proton remnant making their measurement difficult. This is particularly acute in the case of resolved photon processes in which jets are generally produced in the forward direction; direct photon processes generally being central. The reduced asymmetry THERA would provide will significantly change the topology of photoproduction events. Direct photon events would then be concentrated in the rear direction and resolved photon processes in the central and forward parts of the detector. This would then increase the acceptance for resolved photon events and hence improve the measurements.

Measurements of dijet photoproduction at HERA can be (somewhat artificially) categorised into those with low transverse energy jets, low$-E_T^{\rm jet}$, and those with high$-E_T^{\rm jet}$ which start at around 5 GeV and 10 GeV, respectively. The advantage of the low$-E_T^{\rm jet}$ measurements is the increased resolved photon cross section, in particular at low$-x_\gamma$. The measurements suffer, however, from a lack of understanding of soft underlying physics which either leads to results with large systematic uncertainties or inconclusive comparisons with theory. At high$-E_T^{\rm jet}$, the effect of soft underlying physics is greatly reduced, but so is the resolved cross section at low$-x_\gamma$. This can be seen by considering the observable $x_\gamma^{\rm obs}$, which is the fraction of the photon's energy producing the two jets of highest transverse energy [7];

$$x_\gamma^{\rm obs} = \frac{E_T^{\rm jet1}{\rm e}^{-\eta^{\rm jet1}} + E_T^{\rm jet2}{\rm e}^{-\eta^{\rm jet2}}}{2yE_e}, \tag{6.2.2}$$

where $\eta^{\rm jet}$ is the pseudorapidity of the jet and E_e is the electron energy and y the fraction of the electron's energy carried by the photon.

Recent results from HERA are shown for low$-E_T^{\rm jet}$ events ($E_T^{\rm jet} > 6$ GeV) in Fig. 2a and for high$-E_T^{\rm jet}$ events ($E_T^{\rm jet} > 14$ GeV) in Fig. 2b. Shown are the detector-level distributions for $x_\gamma^{\rm obs}$ compared to Monte Carlo (MC) models. In Fig. 2a, the data is compared to MC models with and without multiparton interactions (MPI). Here it can be seen that the MC without MPI greatly underestimates the data at low$-x_\gamma^{\rm obs}$, and that a significantly increased cross-section is observed in the MC with the inclusion of MPI. The data is, however, still poorly described by the MC at this low$-x_\gamma^{\rm obs}$ region for jets of low$-E_T^{\rm jet}$. In Fig. 2b, the data compares well, over the full $x_\gamma^{\rm obs}$ range, with MC models containing no MPI, due to the increased $E_T^{\rm jet}$. The significant decrease in the number of low$-x_\gamma^{\rm obs}$ events at high$-E_T^{\rm jet}$ is also apparent.

With the increased lepton beam energy THERA could provide the optimum scenario in which measurements could be made at relatively high$-E_T^{\rm jet}$ and low$-x_\gamma^{\rm obs}$.

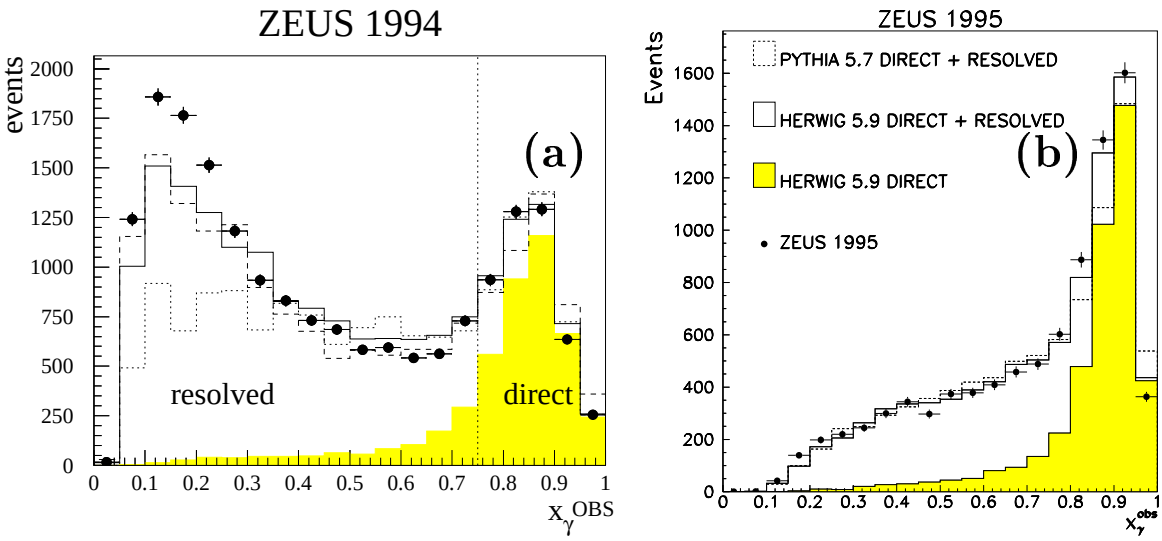

Figure 2: *Detector-level distributions of* $x_\gamma^{\rm obs}$ *at HERA for (a)* $E_T^{\rm jet} > 6$ *GeV and (b)* $E_T^{\rm jet} > 14$ *GeV. In (a), the data points are compared to* HERWIG *MC [8] with (solid line) and without (dotted line) multiparton interactions and* PYTHIA *MC [9] predictions also with multiparton interactions (dashed line). In (b), the data points are compared to* HERWIG *MC (solid line) and* PYTHIA *MC (dashed line) predictions, both without multiparton interactions. In both (a) and (b) the shaded histogram indicates the contribution from direct photon processes in* HERWIG.

6.2.3 Cross section definition

A realistic approach has been performed to evaluate the extent to which dijet production at THERA can yield new information on the structure of the photon. Therefore a kinematic range has been considered which could possibly be measured rather than choosing the full phase space. The kinematic region is based on a high$-E_T^{\rm jet}$ measurement from the ZEUS collaboration [5].

To define the region to be photoproduction, a value of the photon virtuality, Q^2, of less than 1 GeV^2 has been applied. Currently at HERA, the requirement that the scattered lepton is not seen in the calorimeter implicitly leads to the condition on the photon virtuality. To achieve the same Q^2 requirement with the increased lepton beam energy, the angle of scatter will be much smaller. This would mean that the calorimeter (or some other detector) would need to be positioned very close (in fact to within $\sim 0.5°$) to the beam-pipe in the rear direction to achieve the same Q^2 requirement using the anti-tag condition. The inelasticity, y, is chosen to be within the region, $0.2 < y < 0.85$, which corresponds to a photon-proton centre-of-mass energy of between 429 GeV and 884 GeV. The jets are required to have transverse energies, $E_T^{\rm jet1,2} > 14, 11$ GeV in the region of pseudorapidity, $-1 < \eta^{\rm jet} < 2$. Increasing the cut on the transverse energy was also considered. Allowing the jets to go more forward in pseudorapidity would increase the resolved photon cross section and would hopefully

be possible depending on the detector configuration. At HERA where the proton beam energy is very much greater than the lepton beam energy, there are very few jets with a pseudorapidity less than -1. At THERA the distribution of jets would be more symmetric in pseudorapidity and relaxing this cut to, say -2 or -2.5 would also be an option. For this analysis, the value of -1 is retained to try and enhance the (more forward going) resolved photon component in a part of phase space which could definitely be measured. Extension and modification of these requirements could be considered in future studies.

For studying the potential of ep collisions at $\sim$ 1 TeV, the cross sections were produced using NLO code from Frixione and Ridolfi [10, 11]. As the proton structure function is well constrained in the region of x_p under study (approximately $10^{-2} < x_p < 10^{-1}$), only the CTEQ-4M [12] parton distribution function was considered. The renormalisation and factorisation scales, μ, were set to be equal to $E_T^{\mathrm{jet}1}$. To test the sensitivity of the cross sections, three photon parton density parametrisations were used; GS96-HO [13], GRV-HO [14, 15] and AFG-HO [16]. Jets are defined using the longitudinally invariant k_T-clustering algorithm [17] in the inclusive mode [18].

6.2.4 Results

The kinematic requirements for the analysis performed at HERA restrict the minimum x_γ^{obs} to be $\sim$ 0.07, where both jets are of minimum transverse energy and have a pseudorapidity of 2. At THERA the minimum x_γ^{obs} is reduced by the same factor as the lepton beam energy is increased to $\sim$ 0.008. Figure 3a shows the cross-sections in x_γ^{obs} for HERA and THERA for the kinematic region stated. At HERA, the events are concentrated at high$-x_\gamma^{\mathrm{obs}}$ arising predominantly from direct photon events. At THERA, the events are concentrated at low$-x_\gamma^{\mathrm{obs}}$ characteristic of resolved photon events, with a very small cross-section at x_γ^{obs}>0.75 which is taken to be a direct photon enriched region. Having seen that THERA greatly improves the potential for studying the resolved photon, it is then interesting to see if the new kinematic region shows sensitivity to the current parametrisations of the structure of the photon. Results for the three different photon parton density parametrisations are shown in Fig. 3a and their relative difference in Fig. 3b. It can be seen that the prediction using the GS96-HO parametrisation gives the highest and using the AFG-HO parametrisation the lowest cross section. The prediction with GS96-HO is up to 35% higher than that of GRV-HO and 50% higher than that of AFG-HO at low$-x_\gamma^{\mathrm{obs}}$. The difference between the results based on the three parton density parametrisations decreases with increasing x_γ^{obs}. It should be noted that at the lowest values of x_γ^{obs} shown here, there exist no measurements from LEP at the scale considered ($\sim$ 200 GeV^2).

As can be seen from Eq. 6.2.2, the minimum x_γ^{obs} increases with increasing E_T^{jet}. The relative fraction of low to high$-x_\gamma^{\mathrm{obs}}$ and hence resolved photon to direct photon processes also decreases with increasing E_T^{jet}. Nevertheless, differences between the predictions with GS96-HO and AFG-HO are up still to 30% at a minimum cut-off in the transverse energy of the leading jet of 29 GeV.

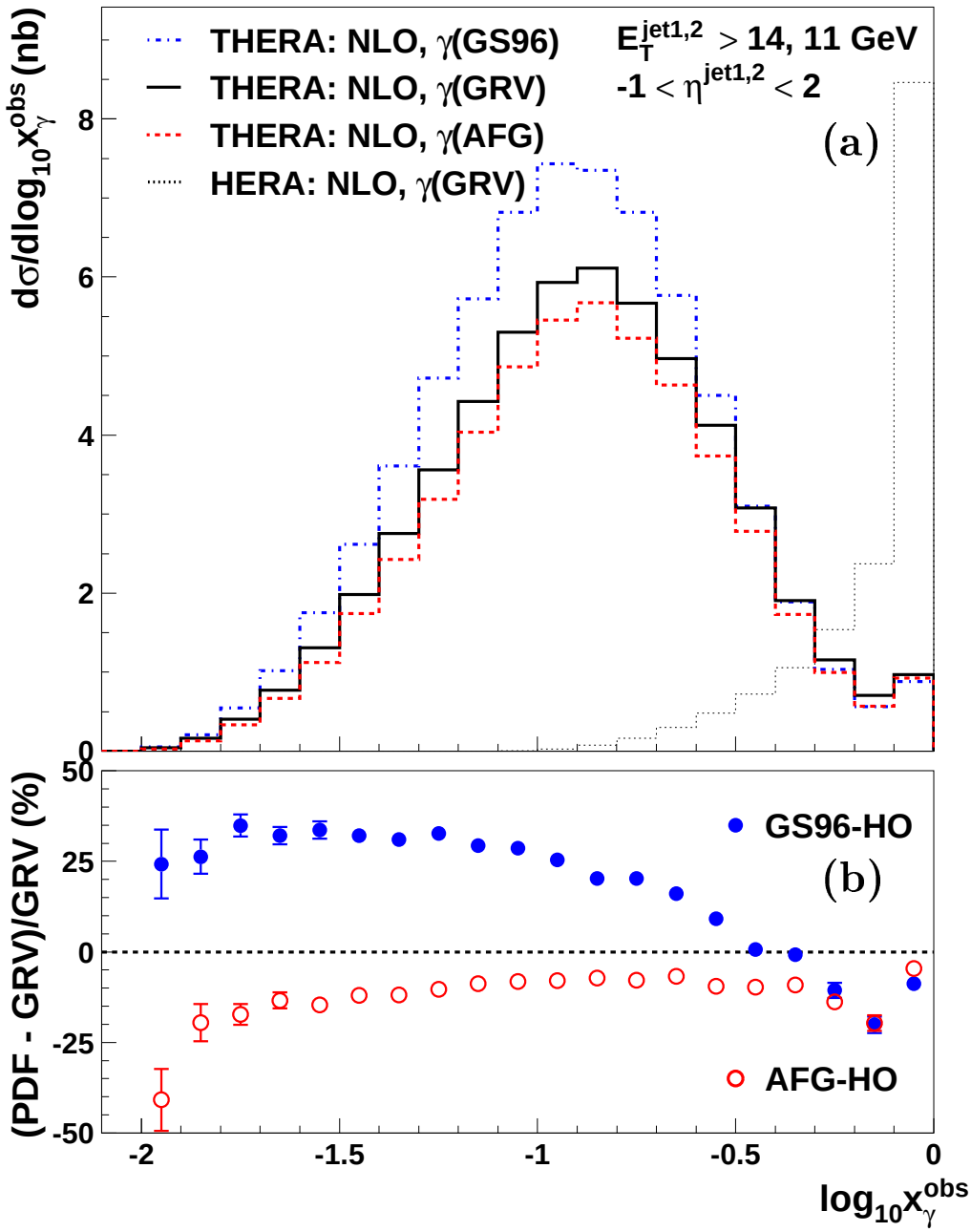

Figure 3: *(a) The differential cross section, $d\sigma/d\log_{10}x_\gamma^{\rm obs}$ for inclusive dijet photoproduction at HERA and THERA as predicted by a NLO calculation. For the kinematic range, $Q^2 < 1$ GeV^2, $0.2 < y < 0.85$ with two jets, $E_T^{\rm jet1,2} > 14, 11$ GeV and $-1 < \eta^{\rm jet} < 2$, the prediction for HERA using the GRV-HO photon parametrisation is shown as the dotted line. For THERA with the same kinematic cuts, three photon parton density parametrisations are shown; GS96-HO (dot-dashed line), GRV-HO (solid line) and AFG-HO (dashed line). In (b) the percentage differences in the cross-sections between the three predictions for THERA are shown as a function of $\log_{10}x_\gamma^{\rm obs}$. The relative difference of the predictions using GS96-HO (solid points) and AFG-HO (open points) with respect to GRV-HO is displayed.*

Cross-sections as a function of the transverse energy of the leading jet, $E_T^{\rm jet1}$, in different regions of pseudorapidity of the jets are shown in Fig. 4. It is shown that the differences between the three predictions are concentrated at low$-E_T^{\rm jet1}$ and forward pseudorapidity. At more central and rear values of pseudorapidity and higher transverse energies, the predictions converge.

The cross-section as a function of the pseudorapidity of the second jet, $\eta_2^{\rm jet}$, is expected to be sensitive to the structure of the photon [5]. In Fig. 5, this cross section is shown in three regions of pseudorapidity of the first jet, $\eta_1^{\rm jet}$. Again, it can be seen that the predictions differ most significantly, up to 50%, when both jets are forward. It can also be seen that in the region where both jets are forward the direct photon enriched region, $x_\gamma^{\rm obs} > 0.75$, is negligible. As for the cross section in $x_\gamma^{\rm obs}$, the predictions for the GRV-HO and AFG-HO parametrisation are very similar in shape and differ in magnitude by roughly 10%. At higher transverse energies, $E_T^{\rm jet1} > 29$ GeV, a difference of 30% persists when both jets are forward.

To assess the significance of the differences observed between the predictions with the three different parametrisations, the renormalisation and factorisation scale uncertainties were evaluated. The cross sections using the GRV-HO parametrisation were calculated with the scale doubled and halved. For the cross-sections as a function of $\eta_2^{\rm jet}$, the relative differences to the central values are shown. The differences are of the order of $10-15\%$, which is small compared with the differences between the parametrisations. A difference of 15% was also observed for the cross-section as a function of $x_\gamma^{\rm obs}$.

There exist many other calculations of jet photoproduction at HERA [19–27] all of which (including the one used in this article) have been shown to agree within $5-10\%$ [5, 28, 29]. From this and the estimation of the scale uncertainty, it can be seen that the differences in the photon parton denisty parametrisations are much larger than other uncertainties.

6.2.5 Discussion

The potential of THERA with respect to what can be done at HERA and at LEP in the field of the photon structure is as follows. For a given transverse energy, it can achieve lower values of x_γ than is accessible at either of the current facilities. THERA would have the potential to measure the structure of the photon in the region where the structure function is predicted to rise with decreasing x_γ. Indications for the rise have be seen at LEP and HERA although the measurements have large errors. THERA would, however, be able to make more precise measurements by being able to achieve the factor of 10 smaller in the minimum $x_\gamma^{\rm obs}$ for a given $E_T^{\rm jet}$ compared with HERA. It has also been shown elsewhere that the accessible maximum average transverse energy of a dijet system is 2-3 times larger at THERA than at HERA with roughly 150 GeV and 225 GeV being reachable at the ep and γp options, respectively [30].

Forward detectors would also be desirable for measurements of the proton structure function at high x_p. For studying values of $x_p > 0.5$, for example, jets of $E_T^{\rm jet}$ greater

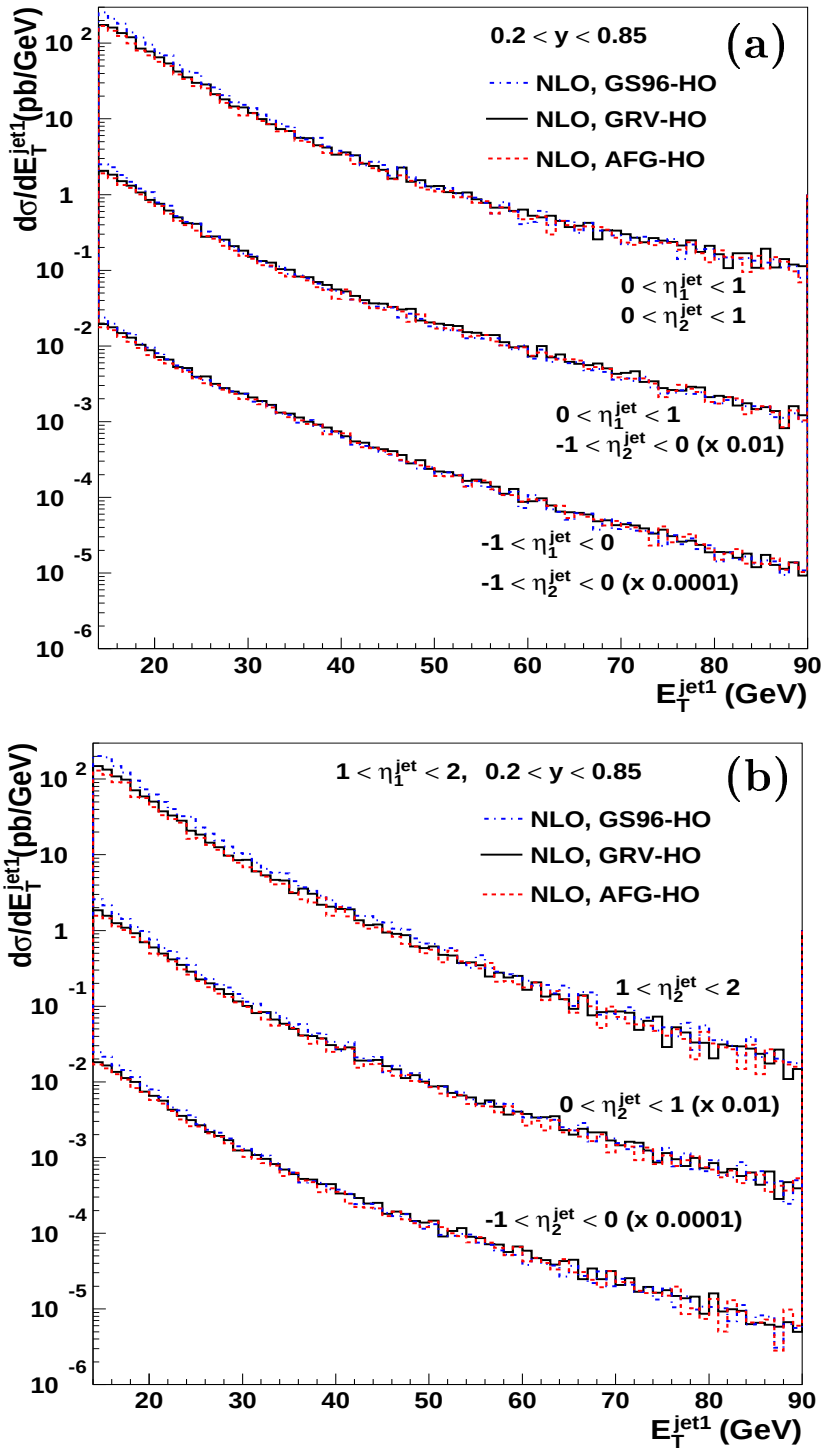

Figure 4: *(a) The differential cross section, $d\sigma/dE_T^{\mathrm{jet}\,1}$ for inclusive dijet photoproduction at THERA as predicted by a NLO calculation. For the kinematic range as in Fig. 3, the prediction for THERA using three photon parton density parametrisations are shown; GS96-HO (dot-dashed line), GRV-HO (solid line) and AFG-HO (dashed line). The three different sets of curves represent jets in different regions of pseudorapidity. (b) The differential cross section, $d\sigma/dE_T^{\mathrm{jet}\,1}$ for inclusive dijet photoproduction at THERA as predicted by a NLO calculation when one jet is in the region $1 < \eta^{\mathrm{jet}\,1} < 2$ and the other jet is in three different regions of pseudorapidity.*

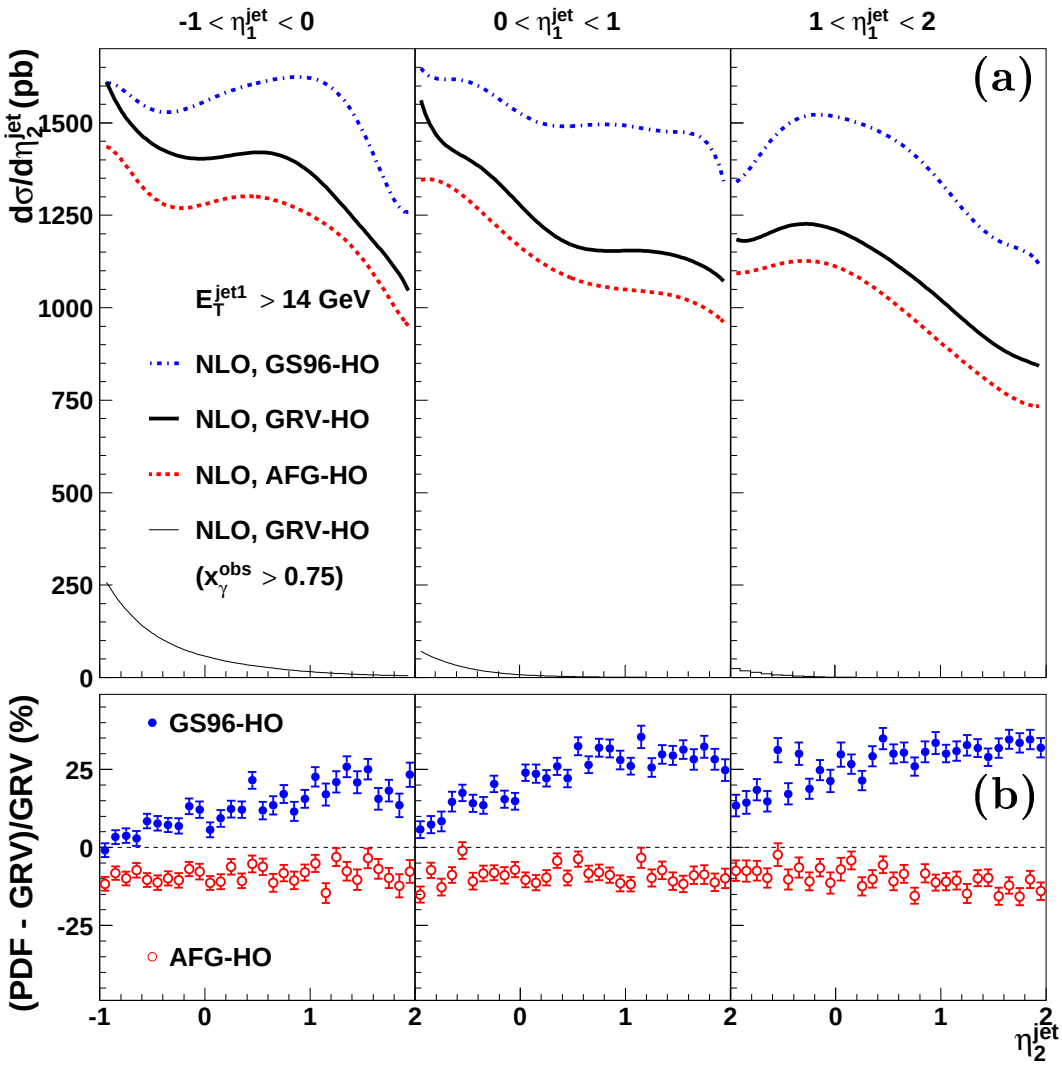

Figure 5: *(a) The differential cross section, $d\sigma/d\eta_2^{\rm jet}$ for inclusive dijet photoproduction at THERA as predicted by a NLO calculation. For the kinematic range, $Q^2 < 1$ GeV^2, $0.2 < y < 0.85$ with two jets, $E_T^{\rm jet\,1,2} > 14, 11$ GeV and $-1 < \eta^{\rm jet} < 2$, the prediction for THERA using three photon parton density parametrisations are shown; GS96-HO (dot-dashed line), GRV-HO (solid line) and AFG-HO (dashed line). One jet is restricted to be in a rear, central or forward direction. The prediction for $x_\gamma^{\rm obs} > 0.75$ is also shown as the thin solid line. In (b) the percentage differences in the cross-sections between the three predictions for THERA are shown as a function of $\eta_2^{\rm jet}$. The relative difference of the predictions using GS96-HO (solid points) and AFG-HO (open points) with respect to GRV-HO is displayed.*

than roughly 20 GeV would need to be detected at pseudorapidity values, $\eta^{\rm jet} = 3$. Jets of this energy would be produced copiously; considering those more central would require much larger energy.

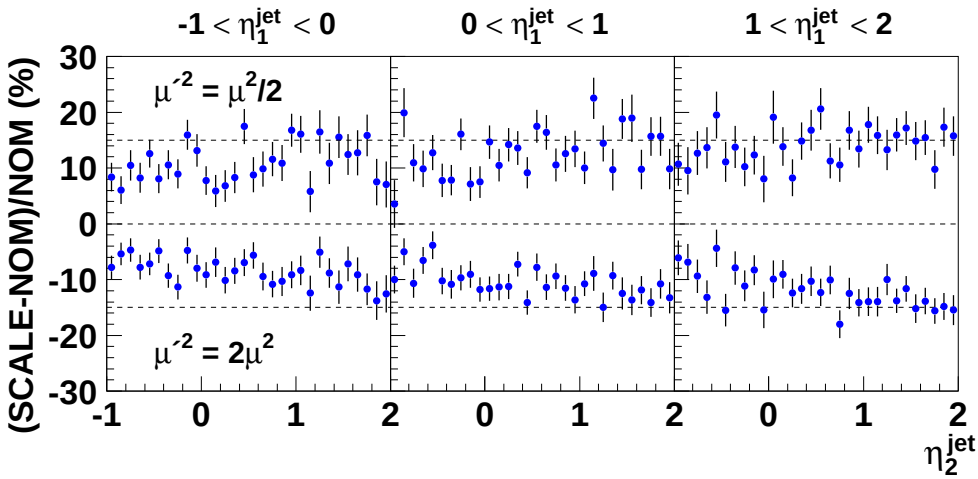

Figure 6: *The percentage differences in the cross-sections from Fig. 5 when varying the renormalisation and factorisation scales by a factor of 0.5 and 2. The photon parton density parametrisation used was GRV-HO. The dashed line indicates* $\pm 15\%$.

Heavy quarks in dijet production have also been studied as a tool for constraining the structure of the photon and are discussed in detail elsewhere [31].

With respect to the linear collider, TESLA, lower values of x_γ can also be reached at THERA but only at very forward values of pseudorapidity [2]. Development of a detector for THERA which can measure jets in the forward direction would therefore be very desirable. THERA would also complement a linear collider in the measurement of the structure of the photon in much the same way as HERA complements LEP; for example in directly constraining the gluon density and testing the universality of the parton distribution functions.

6.2.6 Summary

It has been shown that cross sections in the kinematic region open to THERA with a centre-of-mass energy of ~ 1 TeV have a large sensitivity to the structure of the photon. Three currently available parametrisations lead to cross sections which vary by up to 50% in certain regions of the phase space considered. THERA would provide a new kinematic region in the measurement of the structure of the photon and complement measurements from the proposed linear collider.

Acknowledgements

I would like to thank S. Frixione and G. Ridolfi for making their NLO code freely available on the web and in particular S. Frixione who answered many questions on how to use the code such that I could use it for this study.

References

[1] *The THERA Book*, Report DESY-LC-REV-2001-062, 2001. `http://www.desy.de/~lcnotes`.

[2] M. Krawczyk, S. Söldner-Rembold and M. Wing, *Kinematics of photoproduction at THERA*, in *The THERA Book* [1].

[3] S. Söldner-Rembold, *Experimentalists summary.* Talk at Photon 2000, Ambleside, UK, 2000. `http://lapg.lancs.ac.uk/p2kscan/talk69/index.html`.

[4] ZEUS Coll., J. Breitweg et al., Euro. Phys. J. **C 1**, 109 (1998).

[5] ZEUS Coll., J. Breitweg et al., Euro. Phys. J. **C 11**, 35 (1999);
ZEUS Coll., *The structure of the photon and the dynamics of resolved-photon processes in dijet photoproduction.* Subm. to *ICHEP2000*, Osaka, Japan, paper 418, 2000;
ZEUS Coll., *Measurement of dijet photoproduction at high transverse energies at HERA.* Subm. to *EPS-HEP99*, Tampere, Finland, paper 540, 1999.

[6] H1 Coll., C. Adloff et al., Phys. Lett. **B 483**, 36 (2000).

[7] ZEUS Coll., M. Derrick et al., Phys. Lett. **B 348**, 665 (1995).

[8] G. Marchesini et al., Comp. Phys. Comm. **67**, 465 (1992).

[9] H.-U. Bengtsson and T. Sjöstrand, Comp. Phys. Comm. **46**, 43 (1987).

[10] S. Frixione, Z. Kunszt and A. Signer, Nucl. Phys. **B 467**, 399 (1996);
S. Frixione, Nucl. Phys. **B 507**, 295 (1997).

[11] S. Frixione and G. Ridolfi, Nucl. Phys. **B 507**, 315 (1997).

[12] H.L. Lai et al., Phys. Rev. **D 55**, 1280 (1997).

[13] L.E. Gordon and J.K. Storrow, Nucl. Phys. **B 489**, 405 (1997).

[14] M. Glück, E. Reya and A. Vogt, Phys. Rev. **D 45**, 3986 (1992).

[15] M. Glück, E. Reya and A. Vogt, Phys. Rev. **D 46**, 1973 (1992).

[16] P. Aurenche, J.P. Guillet and M. Fontannaz, Z. Phys. **C 64**, 621 (1994).

[17] S. Catani et al., Nucl. Phys. **B 406**, 187 (1993).

[18] S.D. Ellis and D.E. Soper, Phys. Rev. **D 48**, 3160 (1993).

[19] P. Aurenche et al., *Dijet cross section in photoproduction at HERA.* Future Physics at HERA, 1996.

[20] P. Aurenche et al., Euro. Phys. J. **C 17**, 413 (2000).

[21] B.W. Harris and J.F. Owens, Phys. Rev. **D 56**, 4007 (1997).

[22] B.W. Harris and J.F. Owens, Phys. Rev. **D 57**, 5555 (1998).

[23] M. Klasen, and G. Kramer, Z. Phys. **C 76**, 67 (1997).

[24] M. Klasen, T. Kleinwort and G. Kramer, Euro. Phys. J. direct **C 1**, 1 (1998).

[25] B. Pötter, Euro. Phys. J. **C 5**, 1 (1998).

[26] G. Kramer and B. Pötter, Euro. Phys. J. **C 5**, 665 (1998).

[27] B. Pötter, Comp. Phys. Comm. **119**, 4 (1999).

[28] B.W. Harris, M. Klasen and J. Vossebeld, *Detailed comparison of next-to-leading order predictions for jet photoproduction at HERA.* Preprint hep-ph/9905348, 1998. Proceedings of the Workshop on "Monte Carlo Generators for HERA Physics".

[29] B. Pötter, Comp. Phys. Comm. **133**, 105 (2000).

[30] M. Klasen, *Jet photoproduction at THERA*, in *The THERA Book* [1].

[31] P. Jankowski, M. Krawczyk and M. Wing, *Heavy quark production at THERA*, in *The THERA Book* [1].

6.3 Heavy Quark Photoproduction at THERA

P. Jankowski, M. Krawczyk
Institute of Theoretical Physics, University of Warsaw
Warsaw, Poland
pjank@fuw.edu.pl, krawczyk@fuw.edu.pl

M. Wing
McGill University, Montreal
Canada
wing@mail.desy.de

Abstract

Measurements of heavy quark production at a possible future *ep* facility, THERA, would provide valuable information on the structure of the photon. QCD cross-section predictions are made at LO for both charm and beauty production and their sensitivity to current parametrisations of the photon parton densities is investigated.

6.3.1 Introduction

Heavy quark production can provide information on the structure of the real photon as well as provide stringent tests of QCD by itself. In this paper the potential of the possible future *ep* collider, THERA, to give new information on the real photon structure through charm and beauty quark photoproduction is studied. The potential of the collider is also compared with other existing or planned colliders.

Photoproduction processes are dominated by the exchange of quasi-real photons (virtuality of the photon $Q^2 \ll 1\text{GeV}^2$). Their energy distribution can be described by an effective (real) photon energy spectrum, i.e. using the Weizsäcker-Williams approximation. A hard scale is provided by a large transverse momentum or the mass of the produced heavy quark Q. In this paper the region $p_T \geq m_Q$ is studied. In LO QCD, two processes contribute to the photoproduction of heavy quarks: the direct process, in which the photon couples directly to a parton in the proton, and the resolved process, in which the photon acts as a source of partons, one of which scatters from a parton in the proton. Heavy quarks can be produced in the final state or they already exist in the initial state as partons in the photon and proton, depending on the scheme used in the calculations.

If not stated otherwise the computations were performed with the THERA electron and proton beams energies of 250 GeV and 920 GeV, respectively. In the first section results are presented on LO QCD calculations of inclusive charm quark production, $ep \to c/\bar{c}\, X$, at the THERA collider. In particular the possible information this process can reveal on the structure of the photon is discussed. The second section uses

MC expectations to investigate events where at least one heavy quark and two jets are produced. Further requirements on a final state muon from a semi-leptonic decay are also imposed and sensitivity to current parametrisations of the photon investigated.

6.3.2 Leading order QCD predictions of charm quark production

LO calculations were performed in two schemes which differ by the number of quark flavours which are considered to be part of the structure of the photon and proton, and can thus take part in the process as partons. The massive scheme, the so-called Fixed Flavour Number Scheme (FFNS), assumes that both the photon and proton consist of gluons and only light (u, d and s) quarks whilst heavy quarks are produced in the final state. The massless Variable Flavour Number Scheme (VFNS), considers heavy quarks as active flavours. Therefore such partonic processes, $Q + g \to Q + g$ or $Q+\bar{Q} \to Q+\bar{Q}$, with Q denoting a heavy quark, are also allowed. (Events in which the heavy quark is one of the active partons are also referred to as "flavour-excitation".) In the FFNS scheme the mass of the produced charm quark is always kept nonzero in the calculations while in the VFNS all flavours are treated as massless.

In the massive (FFNS) calculations the number of active flavours (N_f) is taken to be 3. In the massless (VFNS) scheme it varies from 3 to 4 depending on the value of the hard (factorisation and renormalisation) scale, μ. The charm quark is included in the computation provided that $\mu > m_c$ with the mass of the charm quark set to $m_c = 1.5$GeV. Also the QCD energy scale, Λ_{QCD}, which appears in the one loop formula for the strong coupling constant α_s is affected by the change of the number of active flavours, so is denoted as $\Lambda_{QCD}^{N_f}$. The scale is taken to be $\Lambda_{QCD}^3 = 232$ MeV and $\Lambda_{QCD}^4 = 200$ MeV as in the GRV[1] parametrisation of the photon [2]. If not stated otherwise μ is taken to be the transverse mass of the produced charm quark, $m_T = \sqrt{m_c^2 + p_T^2}$, and the differential cross-section, $d^2\sigma/d\eta dp_T^2$, with $p_T = 10$ GeV is calculated. This means that $\mu \sim p_T$ and therefore $N_f = 4$ in case of the VFNS calculations. The spectrum of the quasi-real photons taking part in the process is described by the Weizsäcker-Williams (EPA) formula,

$$f_{\gamma/e}(y) = \frac{\alpha}{2\pi}\left[\frac{1+(1-y)^2}{y}\ln\frac{Q^2_{max}}{Q^2_{min}} + 2m_e^2 y\left(\frac{1}{Q^2_{max}} - \frac{1}{Q^2_{min}}\right)\right], \tag{6.3.1}$$

where $Q^2_{max} = 4\text{GeV}^2$, $Q^2_{min} = m_e^2 y^2/(1-y)$ and y is the fraction of the electron's four-momentum carried by the photon ($y = E_\gamma/E_e$). No requirements were placed on y. Finally the LO CTEQ5L [3] and GRV [2] were used as the parton parametrisations of the proton and photon, respectively.

To show the power of the THERA collider for heavy quark physics it is useful to compare the cross-section for charm production that can be achieved in THERA with cross-sections expected for other existing or planned accelerators. In Fig. 1, a

[1]The old GRV('92) parametrisation was used in this analysis. It treats heavy quarks as massless above the heavy quark threshold region ($W \gg 2m_Q$), and moreover latest experimental results [1] indicate that its gluon distribution is closest to the data.

comparison with results from the ep HERA ($E_e = 27.5$ GeV, $E_p = 920$ GeV), LEP ($E_e = 90$ GeV), a Linear Collider (LC) and a Photon Collider (PC) both with $E_e = 250$ GeV are presented for two options of THERA, ep and γp. Real photons in the PC and γp THERA option can be achieved through the Compton backscattering laser photons from the electron beam [4–6] (the full theoretical spectrum for $0 < y < 0.83$ was used). It can be seen that THERA provides the largest cross-sections over the whole range in η and has the potential to probe regions kinematically inaccessible at other colliders.

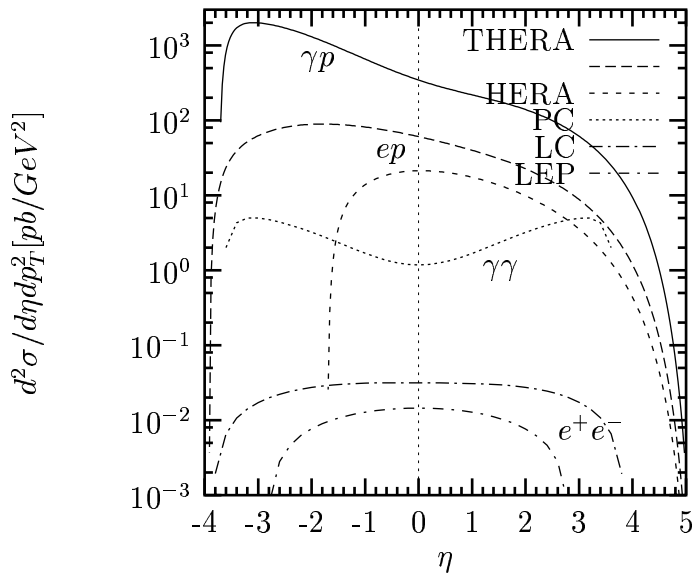

Figure 1: *Inclusive charm quark production in processes including real photon interactions calculated in the VFNS scheme for $p_T = 10$ GeV for five accelerators: THERA (ep and γp options) and HERA ($E_e = 27.5$ GeV, $E_p = 920$ GeV) ($ep \to c/\bar{c}\,X$) , LEP ($E_e = 90$ GeV) & LC ($E_e = 250$ GeV) ($e^+e^- \to e^+e^-\,c/\bar{c}\,X$) with quasi-real WW photons and PC ($e^+e^- \to e^+e^-\,c/\bar{c}\,X$) with real photons achieved through the Compton backscattering laser photons from the electron beam and $E_e = 250$ GeV [4–6]). CTEQ5L proton and GRV LO photon parton parametrisations were used.*

It has been demonstrated elsewhere [7], that there is a large dependence of the cross-section for heavy quark production on the choice of scheme for the case of HERA energies. It is also true for the THERA collider. Direct and resolved contributions to the cross-section for charm production obtained using the two discussed schemes clearly show this dependency, as displayed in Fig. 2. Note that the resolved and direct cross-sections are similar for the VFNS scheme whereas in the FFNS scheme, the resolved cross-section is small compared to that of the direct contribution. The small difference between the direct cross-sections for the two schemes is due to the mass term in the matrix elements and phase space integral. Figure 3 presents the cross-sections with their dependence on the choice of the μ varied from $1/2m_T$ to $2m_T$. The dependence

on the choice of scheme is most significant for resolved processes, varying by up to several orders of magnitude in the cross-section. In the case of direct processes the variation is relatively small and the subsequent total cross-section prediction variation is therefore dominated by the difference between the two schemes for the resolved process. The variation in the choice of scale leads to small effects in the cross-section in comparison with the scheme dependence as it only influences the value of α_s and the parton densities and not the set of allowed partonic processes.

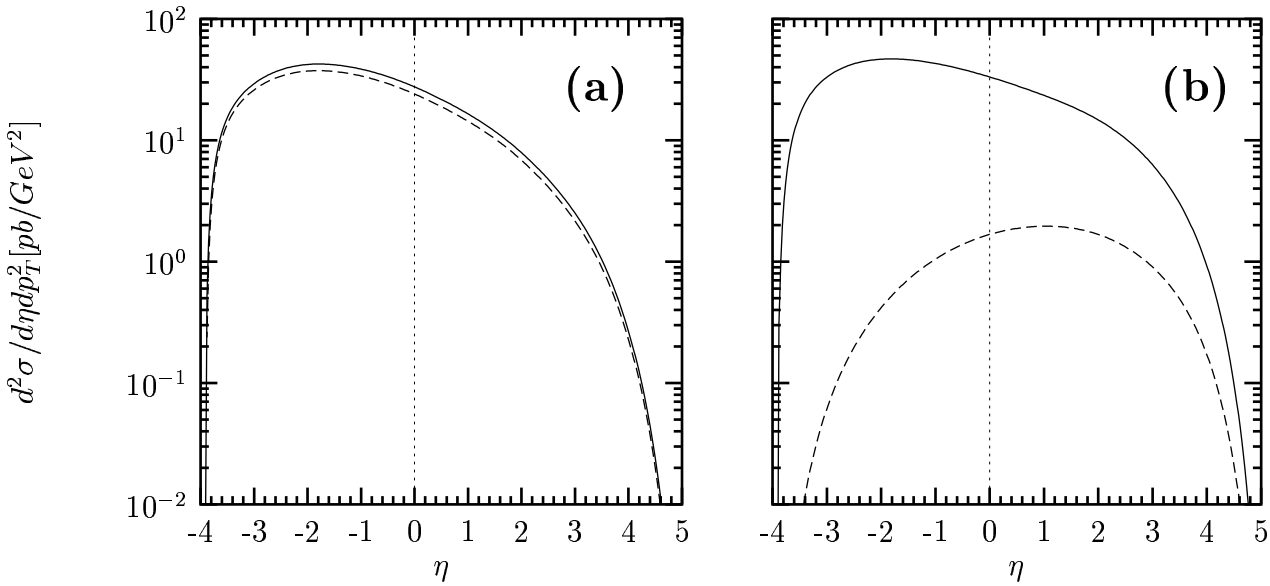

Figure 2: *THERA. (a) Direct and (b) resolved contributions to the differential cross-section of* $ep \to c/\bar{c}X$ *production calculated for* $p_T = 10$ *GeV in the VFNS (solid lines) and FFNS (dashed lines) schemes using the CTEQ5L and GRV LO parton parametrisations of the proton and photon, respectively.*

To test the sensitivity of inclusive charm production to the form of the parton densities in the photon, cross-sections for this process were computed with three different LO parton parametrisations of the photon: GRV [2], GS96 [8] and SaS1D [9]. Sensitivity to the form of the current parametrisations of the photon structure function at the THERA collider is larger than at HERA as shown in Fig. 4a (the results of the VFNS calculation). Note that the SaS1D and GRV parametrisations give similar results. Figure 4b shows the uncertainty resulting from the variation of the hard scale by a factor of two compared to the central value. Here it is demonstrated that the differences between the cross-sections obtained using three parton parametrisations of the photon are significant for GRV (or SaS1D) and GS96 in the region $-2.5 < \eta < 0$, despite this large theoretical uncertainty.

The differences between two current parton parametrisations of the photon, GRV and SaS1D, have previously been compared for LC and PC colliders [10]. More specifically, the relative difference $\frac{GRV-SaS1D}{GRV}$ of the cross-section, $d^2\sigma/d\eta dp_T^2(ep \to c/\bar{c}\,X)$,

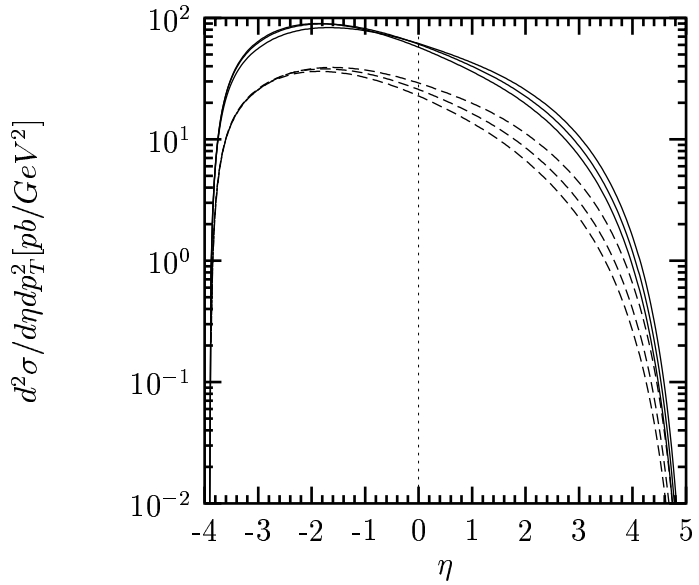

Figure 3: *THERA. Differential cross-section of* $ep \to c/\bar{c}\,X$ *production calculated for* $p_T = 10$ *GeV in the VFNS (solid lines) and FFNS (dashed lines) schemes with three different values of the hard scale;* $\mu = 1/2, 1$ *and* $2 \times m_T$*, using the CTEQ5L and GRV LO parton parametrisations of the proton and photon, respectively.*

was calculated in both VFNS and FFNS schemes. Values of $\sim 0.1 - 0.4$ were found with the PC having the larger value. Similar numbers (up to 0.3) to those for the LC and PC could be achieved at THERA in the forward η region. The massive FFNS gives the same results for the considered sensitivity as those of the massless VFNS scheme.

Sensitivity to the photon parton densities can be also tested through the ratio of the resolved to the direct photon contributions. This is shown in Fig. 5 for $d^2\sigma/d\eta dp_T^2$ in comparison with the results for the HERA collider. Again the results for THERA show a larger resolved cross-section and increased sensitivity to the form of the current parametrisations. The sensitivity is also large in the central η region where there is, experimentally, a large acceptance.

6.3.3 MC predictions of dijet production with charm and beauty quarks

The dijet system can be formed from the production of a heavy quark pair such as in the boson-gluon fusion process. When the heavy quark is an active parton in the photon then the dijet system is formed from one heavy quark and a gluon. The other heavy quark in the event is produced at low transverse energy and forms part of the photon remnant.

A natural variable to describe dijet production is the observable $x_\gamma^{\rm obs}$, which is the

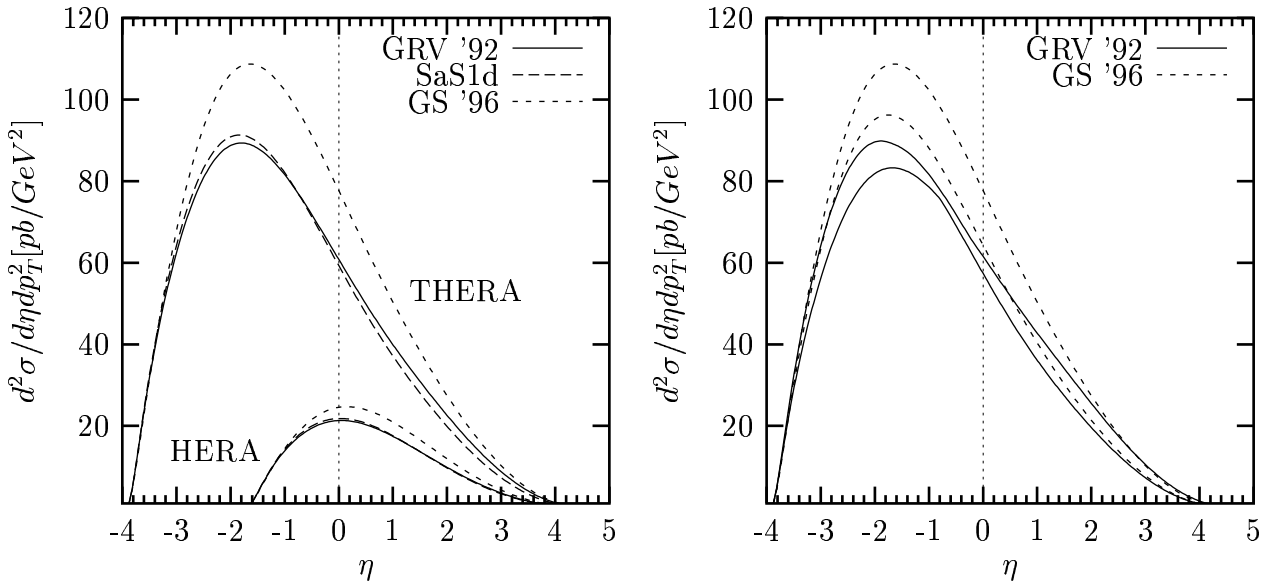

Figure 4: *Differential cross-section for $ep \to c/\bar{c}\,X$ for $p_T = 10$ GeV calculated with the CTEQ5L parton parametrisation of the proton and three various LO parton parametrisations of the photon in the massless (VFNS) scheme. A) Lower lines correspond to the HERA collider energies (27.5×920 GeV), while upper to the THERA collider energies. B) Lower and upper lines for each photon parametrisation show respectively the lowest and greatest values of the cross-section calculated with different values of the hard scale $\mu = 1/2, 1,$ & $2 \times m_T$ in the GRV case and $\mu = 1, 2 \times m_T$ in the GS96 case.*

fraction of the photon's energy producing the two jets of highest transverse energy [11];

$$x_\gamma^{\rm obs} = \frac{E_T^{\rm jet1} {\rm e}^{-\eta^{\rm jet1}} + E_T^{\rm jet2} {\rm e}^{-\eta^{\rm jet2}}}{2yE_e}, \tag{6.3.2}$$

where $\eta^{\rm jet}$ is the pseudorapidity of the jet and E_e is the electron energy and y the fraction of the electron's energy carried by the photon.

Due to the increase in the beam energy, there is a corresponding order of magnitude extension in the minimum $x_\gamma^{\rm obs}$. This is shown in Fig. 6 in which two THERA scenarios (with the electron beam energy $E_e = 250$ GeV and $E_e = 400$ GeV) are compared with HERA. A greatly increased cross-section possible at THERA over that at HERA for low$-x_\gamma^{\rm obs}$, particularly in beauty production, is seen. Realistic scenarios for the cuts on the jet quantities have been made of transverse energy $E_T^{\rm jet1,2} > 10{,}8$ GeV and pseudorapidity $\eta^{\rm jet} < 2.5$. The distribution is peaked at high-$x_\gamma^{\rm obs}$, consistent with direct photon processes, but has a significant cross-section at low-$x_\gamma^{\rm obs}$ arising from resolved photon events.

Charm and beauty production at a γp collider has also been considered and compared with the nominal ep scenario for THERA. The photon beam energy is assumed to be $0.8E_e$, i.e. 200 GeV assuming an electron beam of energy 250 GeV. The predictions for the ep and γp options with the same jet cuts are shown in Fig. 7. The

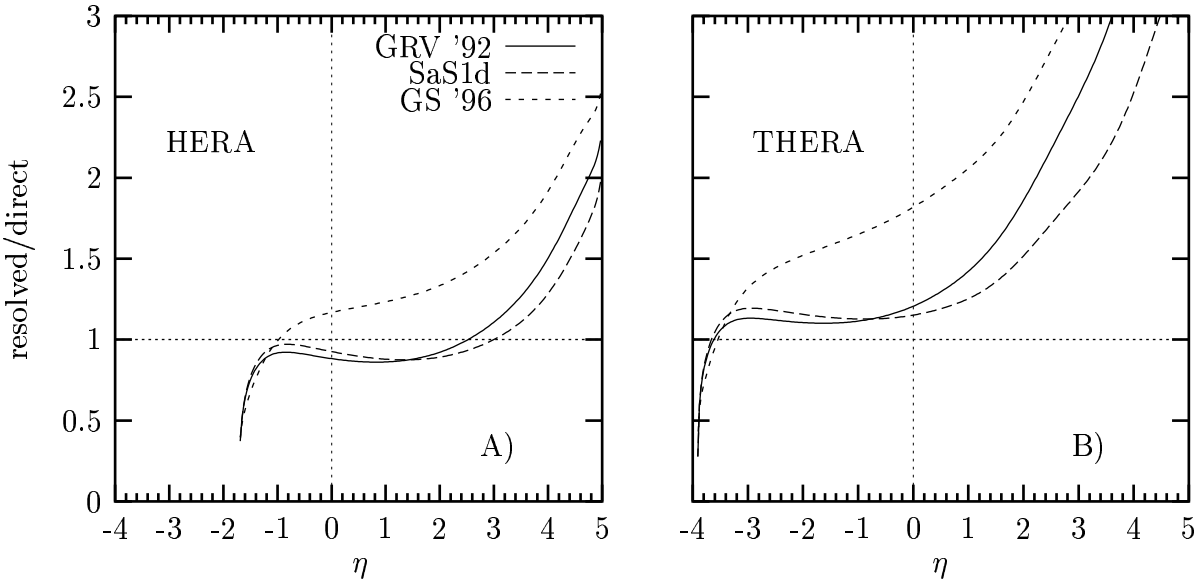

Figure 5: *The ratio of the resolved to the direct photon contribution of* $e^+e^- \to e^+e^- c/\bar{c}X$ *(for* $d^2\sigma/d\eta dp_T^2$*) for* p_T*=10 GeV calculated in LO with the CTEQ5L parton parametrisation of the proton and three various LO parton parametrisations of the photon in the massless (VFNS) scheme. A) HERA, B) THERA collider.*

cross-section prediction for the γp option is a factor of $\sim$ 25 higher than the nominal ep option. This factor arises simply from the Weizsäcker-Williams flux associated with the electron.

Further requirements can be made such that the kinematic range closely corresponds to what could be measured. Therefore the observation of a final state muon from the semi-leptonic decay of a beauty quark is imposed. The momentum and angular requirements imposed on the muon are typical of those at HERA. Considering jets of slightly lower transverse energy ($E_T^{\mathrm{jet1,2}} > 7{,}6$ GeV), the effect on the low-x_γ^{obs} component of pseudorapidity cut is shown in Fig. 8. It can be seen that for a pseudorapidity cut of $\eta^{\mathrm{jet}} > -1$, the direct peak at high-x_γ^{obs} is drastically reduced with respect to a cut of $\eta^{\mathrm{jet}} > -2$. This demonstrates that by applying a cut of $\eta^{\mathrm{jet}} > -1$ interactions of almost exclusively the resolved photon are being probed.

This rather tight restriction on the pseudorapidity of the jets of $-1 < \eta^{\mathrm{jet}} < 2$ is imposed and the sensitivity of the cross-section to the current parametrisations of the photon structure function investigated for THERA. In Fig. 9 predictions are shown for events where a beauty quark decays into a muon. Predictions are shown using both Herwig [12] and Pythia [13] MC generators for four different LO photon PDFs. At values of x_γ^{obs}=0.1, differences between the four parametrisations of up to 40% are seen. The predictions from GRV and GS96 generally have the largest cross-sections at low-x_γ^{obs} and also rise more quickly. The large difference in the Pythia and Herwig MC predictions comes mainly from the different default treatments of α_s, different scales and hadronisation and the use of massive matrix elements in Herwig and massless in

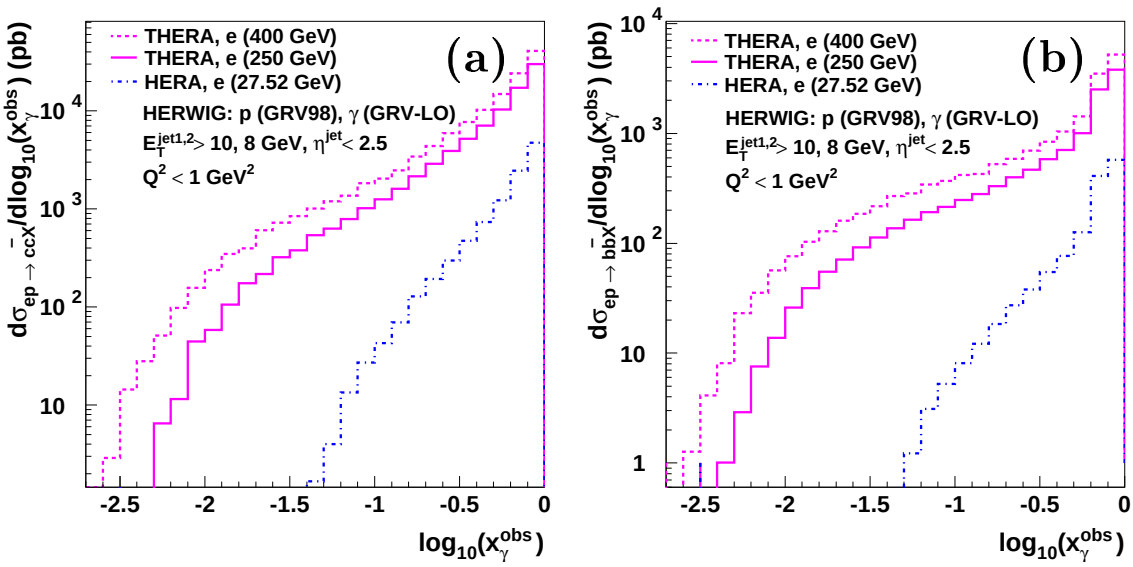

Figure 6: *The differential cross-section, $d\sigma/d\log_{10}x_\gamma^{\rm obs}$ for (a) charm and (b) beauty in dijet photoproduction at HERA and THERA as predicted by the* HERWIG *MC. The dashed and solid lines show THERA with an electron energy of 400 GeV and 250 GeV respectively and the dot-dashed lines indicate the expectation from HERA. The kinematic range is the same in all three cases, namely, $Q^2 < 1$ GeV^2, with two jets, $E_T^{\rm jet1,2} > 10, 8$ GeV and $\eta^{\rm jet} < 2.5$.*

PYTHIA for the generation of flavour-excitation processes.

6.3.4 Summary

It has been shown that the photoproduction of heavy quarks at THERA has a much increased cross-section relative to HERA. With the expected luminosity of about 100 pb^{-1}/year stringent tests of pQCD could be performed. It has also been shown that the cross-sections are sensitive to the structure of the photon, with the current parametrisations differing by significant amounts. The THERA collider also compares favourably with other current and planned machines studying heavy quark production, with the γp mode for THERA providing the largest cross-section.

Acknowledgements

Some of use (PJ and MK) have been partly supported by the Polish State Committee for Scientific Research (grant 2P03B05119, 2000-2001). MK is also grateful to the European Commission 50th Framework Contract HPRN-CT-2000-00149 and DESY for financial support.

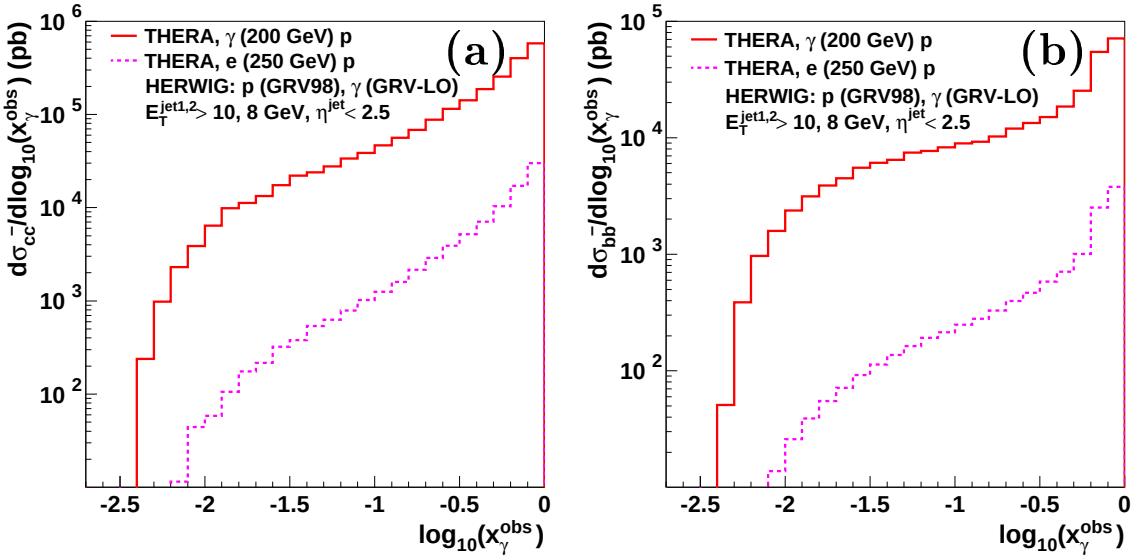

Figure 7: *The differential cross-section, $d\sigma/d\log_{10}x_\gamma^{\rm obs}$ for (a) charm and (b) beauty in dijet photoproduction at for γp and ep options at THERA as predicted by the* HERWIG *MC. The solid lines show THERA with an electron energy of 250 GeV and the dashed lines the expectation with an photon energy of 200 GeV. The kinematic range is the same in all three cases, namely, two jets, $E_T^{\rm jet1,2} > 10, 8$ GeV and $\eta^{\rm jet} < 2.5$.*

References

[1] H1 Coll., C. Adloff et al., Euro. Phys. J. **C 10**, 363 (1999).

[2] M. Glück, E. Reya and A. Vogt, Phys. Rev. **D 46**, 1973 (1992).

[3] CTEQ Coll., H.L. Lai et al., Eur. Phys. J. **C 12**, 375 (2000).

[4] I.F. Ginzburg et al., Nucl. Instrum. Meth. **205**, 47 (1983).

[5] I.F. Ginzburg et al., Nucl. Instrum. Meth. **A 219**, 5 (1984).

[6] V.I. Telnov, Nucl. Instrum. Meth **A 294**, 72 (1990).

[7] B.A. Kniehl et al., Phys. Lett. **B 356**, 539 (1995).

[8] L.E. Gordon and J.K. Storrow, Nucl. Phys. **B 489**, 405 (1997).

[9] G.A. Schuler and T. Sjöstrand, Z. Phys. **C 68**, 607 (1995).

[10] P. Jankowki, M. Krawczyk and A. De Roeck, *Heavy quark production at a linear e^+e^- and photon collider and its sensitivity to the gluon content of the photon.* Preprint hep-ph/0002169, 2000. In preparation and to be published in the

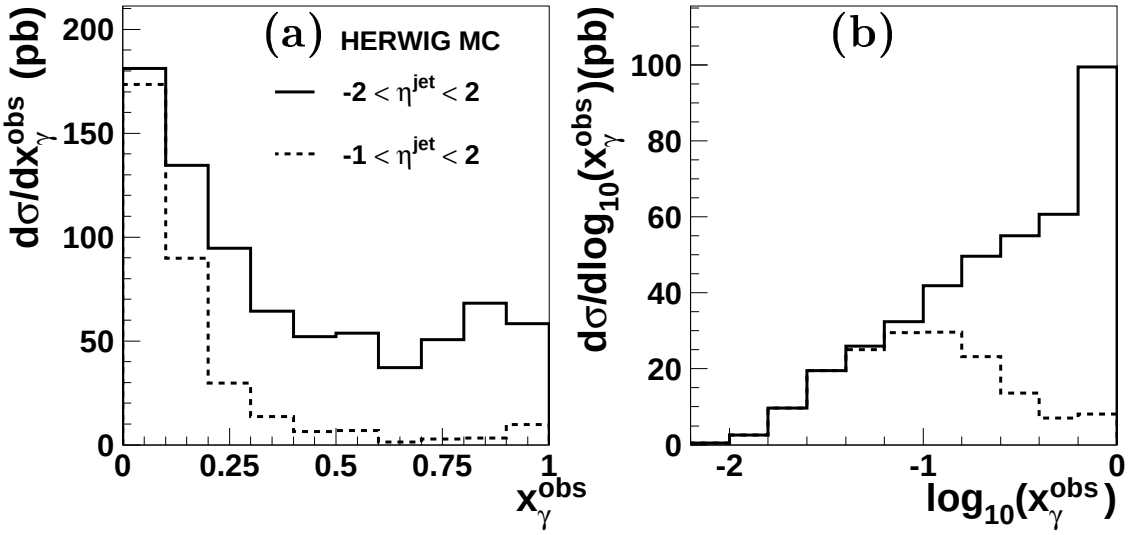

Figure 8: *The differential cross-sections, (a)* $d\sigma/dx_\gamma^{\rm obs}$ *and (b)* $d\sigma/d\log_{10}x_\gamma^{\rm obs}$ *for beauty in dijet photoproduction at THERA as predicted by the* HERWIG *MC. The events are selected in the range,* $Q^2 < 1$ GeV^2, $0.2 < y < 0.85$ *with two jets of transverse energy,* $E_T^{\rm jet\,1,2} > 7,6$ *GeV. The points represent when the jets are restricted to* $-1 < \eta^{\rm jet} < 2$ *and the solid lines when the jets are restricted to* $-2 < \eta^{\rm jet} < 2$. *A muon in the final state has also been required with transverse momentum,* $p_T^\mu > 2$ *GeV and* $|\eta^\mu| < 2$.

proceedings of Workshop on the Development of Future Linear Electron-Positron Colliders for Particle Physics Studies and for Research Using Free Electron Lasers, Lund, Sweden, 23-26 Sep 1999, Rolf Heuer, Francois Richard and Peter Zerwas Eds..

[11] ZEUS Coll., M. Derrick et al., Phys. Lett. **B 348**, 665 (1995).

[12] G. Marchesini et al., Comp. Phys. Comm. **67**, 465 (1992).

[13] H.-U. Bengtsson and T. Sjöstrand, Comp. Phys. Comm. **46**, 43 (1987).

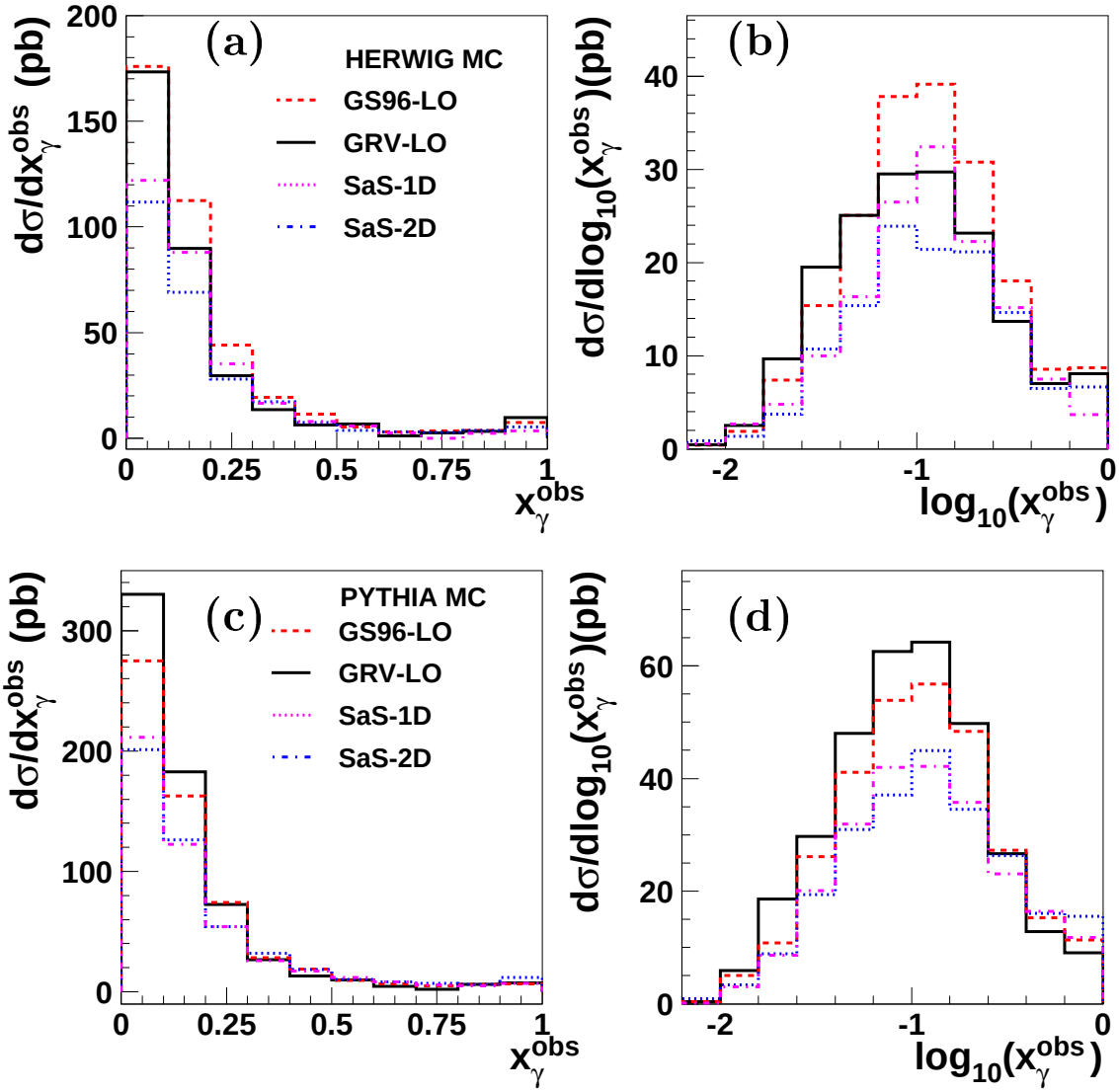

Figure 9: *The differential cross-sections, (a)* $d\sigma/dx_\gamma^{\rm obs}$ *and (b)* $d\sigma/d\log_{10}x_\gamma^{\rm obs}$ *for beauty in dijet photoproduction at THERA as predicted by the* HERWIG *MC. The differential cross-sections, (c)* $d\sigma/dx_\gamma^{\rm obs}$ *and (d)* $d\sigma/d\log_{10}x_\gamma^{\rm obs}$ *for beauty in dijet photoproduction at THERA as predicted by the* PYTHIA *MC. Predictions for four different PDFs are shown; GS96-LO (open circles), GRV-LO (solid circles), SaS-1D (stars) and SaS-2D (diamonds).*

6.4 The Prompt Photon Photoproduction at THERA

M. Krawczyk and A. Zembrzuski
Institute of Theoretical Physics, Warsaw University,
ul. Hoża 69, 00-681 Warsaw, Poland

Abstract

We present NLO QCD predictions for the prompt photon photoproduction at the THERA, and compare them with results for the HERA collider.

6.4.1 Introduction

Photoproduction of photons with large transverse momentum, $p_T \gg \Lambda_{QCD}$, in ep collisions, $ep \to e\gamma X$, is an important test of pQCD [1–12]. In particular it allows to probe the photonic content of the photon. This process, called also the prompt photon photoproduction or the Deep Inelastic Compton (DIC) scattering, was measured at the HERA collider by the ZEUS [13–15] and H1 [16] Collaborations. In this note we compare the potential of the THERA and HERA colliders in measuring the DIC process. The predictions of NLO QCD calculations for the photoproduction of *non-isolated* prompt photon at HERA and THERA energies are presented.

In the present experimental analyses of the prompt photon production at HERA the hadronic energy detected close to the final photon has been restricted, and therefore one can say that the final photon is *isolated*. The NLO calculations for the DIC process with isolated photon at the HERA collider [17–20] give reasonably good description of the ZEUS data for the p_T distribution [15]. For the rapidity distribution the results are in good agreement with data at rapidities $\eta_\gamma > 0.1$, however they lie below data at rapidities $\eta_\gamma < 0.1$ (the difference is $\sim 30\%$) [15]. For comparison with results for non-isolated photon discussed in this paper, we present also our predictions for isolated photon at HERA together with the ZEUS data [15].

6.4.2 The NLO cross section

The cross section for the photoproduction in the ep collision can be calculated using the equivalent photon approximation [21–23]:

$$d\sigma^{ep} = \int G_{\gamma/e}(y) d\sigma^{\gamma p} dy, \tag{6.4.1}$$

where $y = E_\gamma/E_e$ is (in the laboratory frame) a fraction of the initial electron energy taken by the photon. The (real) photon distribution in the electron we take in the

form:

$$G_{\gamma/e}(y) = \frac{\alpha}{2\pi}\{\frac{1+(1-y)^2}{y}\ln[\frac{Q^2_{max}(1-y)}{m_e^2 y^2}] - \frac{2}{y}(1-y-\frac{m_e^2 y^2}{Q^2_{max}})\}, \tag{6.4.2}$$

with m_e being the electron mass, and $Q^2_{max} = 1$ GeV^2 (used both for the HERA and THERA collider).

We consider now the production of a large-p_T photon in the $\gamma p \to \gamma X$ scattering. The lowest order (Born) contribution to the cross section comes from the Compton process on the quark, $\gamma q \to \gamma q$. In the NLO calculation one takes into account α_s corrections to the Born process: the virtual gluon exchange and real gluon emission, together with the subprocess $\gamma g \to \gamma q\bar{q}$. The collinear singularities, which appear in these corrections, are subtracted and shifted into corresponding parton densities or fragmentation function. The remaining corrections, without singularities, constitute the so called K-factor.

The initial photon may interact directly with the parton from the proton (as in the Born process) or may interact as the resolved one via its partons. Analogously, the observed final photon arise directly from hard partonic subprocesses (as in the Born process) or arise from fragmentation processes in which q or g 'decays' into γ.

The NLO cross section for the photon production in γp collision can therefore be written in the following form [1]:

$$E_\gamma \frac{d^3\sigma^{\gamma p\to\gamma X}}{d^3p_\gamma} =$$

$$= \sum_q \int dx f_{q/p}(x,\bar{Q}^2) E_\gamma \frac{d^3\sigma^{\gamma q\to\gamma q}}{d^3p_\gamma} + \sum_b \int dx f_{b/p}(x,\bar{Q}^2)\frac{\alpha_s(\bar{Q}^2)}{2\pi^2\hat{s}}K_b + \tag{6.4.3}$$

$$+\sum_{ab}\int dx_\gamma \int dx f_{a/\gamma}(x_\gamma,\bar{Q}^2) f_{b/p}(x,\bar{Q}^2) E_\gamma \frac{d^3\sigma^{ab\to\gamma d}}{d^3p_\gamma} + \tag{6.4.4}$$

$$+\sum_{bc}\int \frac{dz}{z^2}\int dx f_{b/p}(x,\bar{Q}^2) D_{\gamma/c}(z,\bar{Q}^2) E_\gamma \frac{d^3\sigma^{\gamma b\to cd}}{d^3p_\gamma} + \tag{6.4.5}$$

$$+\sum_{abc}\int \frac{dz}{z^2}\int dx_\gamma \int dx f_{a/\gamma}(x_\gamma,\bar{Q}^2) f_{b/p}(x,\bar{Q}^2) D_{\gamma/c}(z,\bar{Q}^2) E_\gamma \frac{d^3\sigma^{ab\to cd}}{d^3p_\gamma} + \tag{6.4.6}$$

$$+\int dx f_{g/p}(x,\bar{Q}^2) E_\gamma \frac{d^3\sigma^{\gamma g\to\gamma g}}{d^3p_\gamma}, \tag{6.4.7}$$

where x_γ (x) stands for the photon (proton) momentum fraction taken by the a (b)-parton, and z is the momentum fraction of the c-parton fragmenting into photon. The $f_{a/\gamma}$, $f_{b/p}$ and $D_{\gamma/c}$ are the parton densities in the photon, parton densities in the proton and parton fragmentation into photon, respectively.

[1] Note, that in our approach the parton densities in the photon and parton fragmentation into photon are treated as quantities of order α_{em} [20], while e.g. in [17–19] they are assumed to be of order α_{em}/α_s. This leads to different set of subprocesses included in NLO calculations in both approaches.

The first and the second term in (6.4.3) correspond to the Born contribution and to the K-factor, respectively. The three terms (6.4.4, 6.4.5, 6.4.6) are due to various resolved photon subprocesses, with resolved initial or/and final photon. The last term (6.4.7) stands for the contribution of the box diagram, $\gamma g \to \gamma g$. The box diagram is of NNLO-type (as the double resolved photon processes), nevertheless we take it into account in our NLO calculation, because it is known that the box process give a sizable contribution, see e.g. [20].

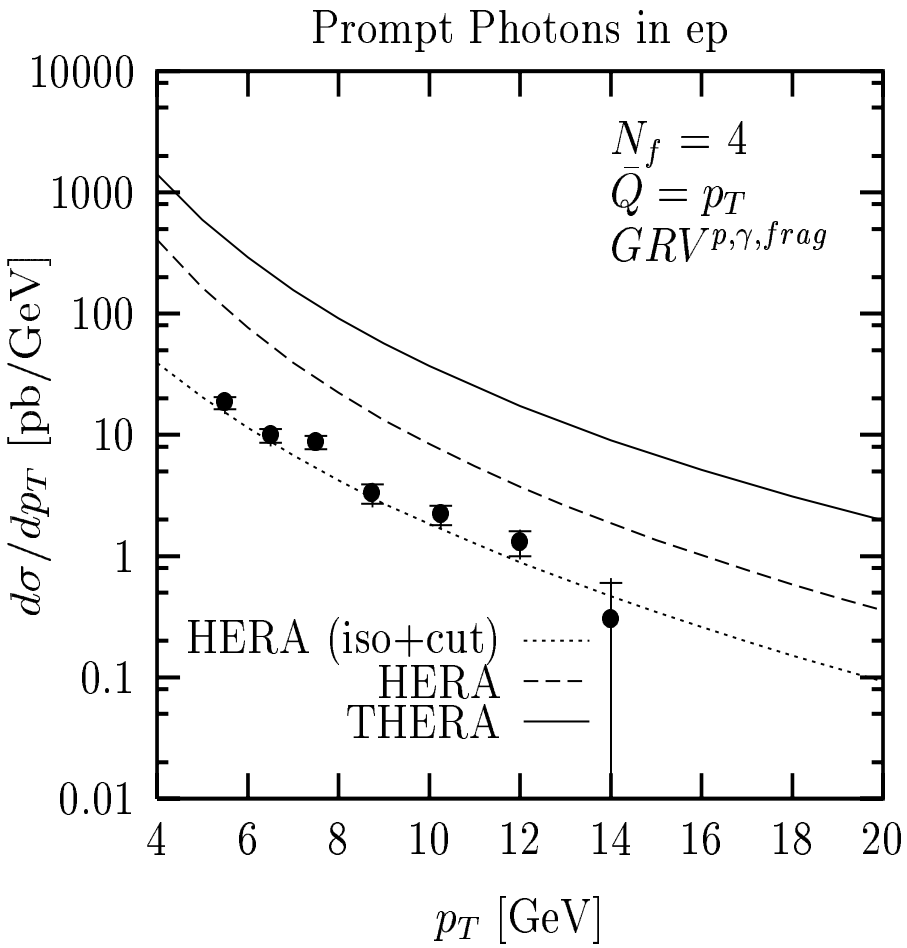

Figure 1: *The p_T distribution for the inclusive prompt photon production. The rapidity is taken in the range $-0.7 \leq \eta_\gamma \leq 0.9$. The NLO results for THERA (solid line) and HERA [20] (dashed line) are shown. For comparison also results for isolated photons with an additional cut ($0.2 \leq y \leq 0.9$) as measured by the ZEUS Collaboration [15] are plotted together with the NLO predictions [20] (dotted line).*

6.4.3 The results

We present NLO QCD results for the DIC cross section at HERA and THERA energies. For THERA we assume $E_e = 250$ GeV and $E_p = 920$ GeV. For HERA we take $E_e = 27.5$ GeV and $E_p = 820$ GeV [2] used in the ZEUS [13–15] and H1 [16] measurements. The GRV NLO parametrizations for the parton distributions in the proton [24] and photon [25], and parton fragmentation into photon [26] are used. The renormalization/factorization scale is assumed equal to the transverse momentum of the final photon, $\bar{Q} = p_T$. The calculations are performed for four massless quarks, $N_f = 4$, and $\Lambda_{QCD} = 320$ MeV.

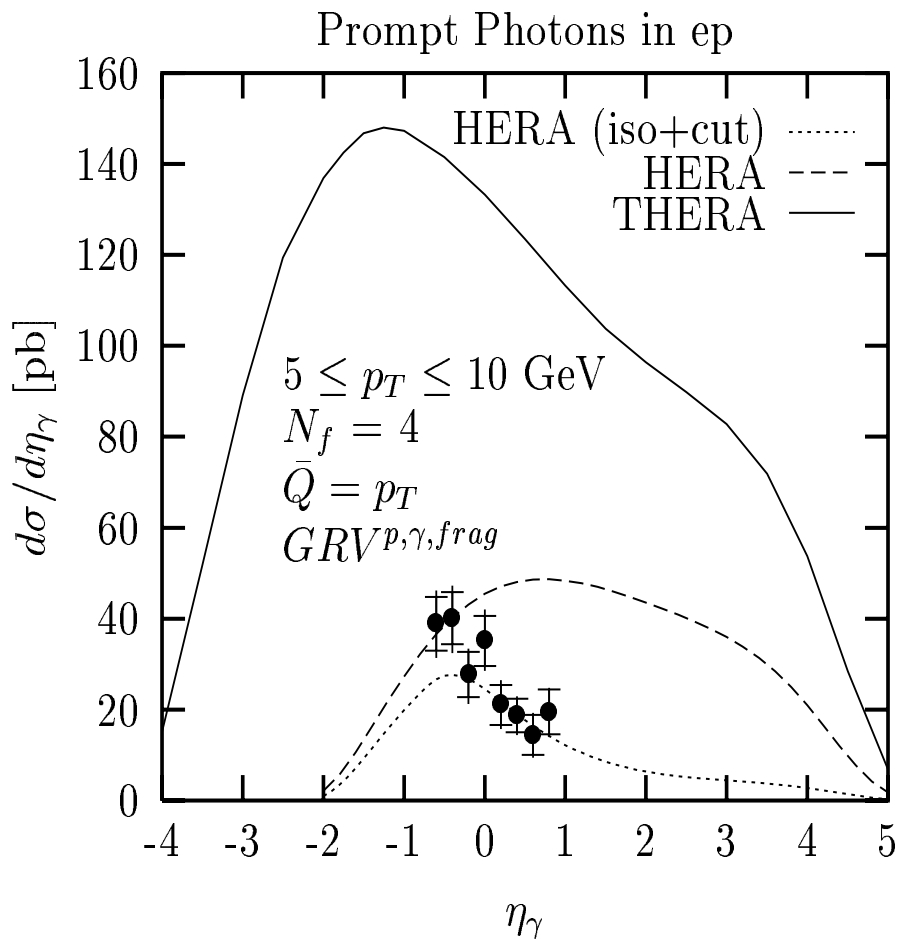

Figure 2: *The η_γ distribution for $5 \leq p_T \leq 10$ GeV. The NLO results for THERA (solid line) and HERA [20] (dashed line) are shown. For comparison the ZEUS Collaboration data [15] and the NLO predictions [20] (dotted line) for isolated photons with additional cuts ($0.2 \leq y \leq 0.9$, $-0.7 \leq \eta_\gamma \leq 0.9$) are presented.*

[2] not 920 GeV

In Fig. 1 the cross section $d\sigma/dp_T$ is presented for $4 \leq p_T \leq 20$ GeV and $-0.7 \leq \eta_\gamma \leq 0.9$. The results strongly depend on p_T: the cross section decreases by three orders of magnitude when the p_T increases from 4 to 20 GeV. The predictions for the THERA collider are larger than for HERA, 3.5 to 5.5 times for p_T from 4 to 20 GeV. Note that the isolation and additional cuts applied by the ZEUS group [15] at HERA reduce the cross section by a factor of 10 (4) at $p_T = 4$ (20) GeV.

The cross section $d\sigma/d\eta_\gamma$ for $5 \leq p_T \leq 10$ GeV is presented in Fig. 2. The range of accessible rapidities is extended and the value of the cross section is much higher for the THERA collider in comparison with predictions for HERA. In the central rapidity region, $-1 \leq \eta_\gamma \leq 1$, (where the ZEUS data [15] are shown) the results obtained for THERA are $\sim$ 2 - 5.5 times larger than for HERA.

6.4.4 Summary

We have presented results of NLO calculation for the non-isolated prompt photon photoproduction at the THERA and HERA colliders. The predictions for THERA are a few times larger than for HERA in a wide range of transverse momentum and rapidities. This can allow to perform much more precise measurements than the present ones and e.g. in testing the parton densities in the photon. For a comparison the current data and predictions for isolated photon at HERA are also shown.

Acknowledgements

Supported in part by Polish State Committee for Scientific Research, grant number 2P03B05119 (2000-2001), and by European Commision 50th framework contract HPRN-CT-2000-00149.

References

[1] J.D. Bjorken and E.A. Paschos, Phys. Rev. **185**, 1975 (1969).

[2] T. Tu, C. Wu, Nucl. Phys. **B 156**, 493 (1979).

[3] M. Fontannaz and D. Schiff, Z. Phys. **C 14**, 151 (1982).

[4] D. W. Duke and J.F. Owens, Phys. Rev. **D 26**, 1600 (1982). Erratum in Phys. Rev. **D 28**, 1227 (1983).

[5] P. Aurenche et al., Z. Phys. **C 24**, 309 (1984).

[6] M. Krawczyk, Acta Phys. Polon. **B 21**, 999 (1990).

[7] A.C. Bawa, M. Krawczyk and W.J. Stirling, Z. Phys. **C 50**, 293 (1991).

[8] A.C. Bawa and M. Krawczyk, Phys. Lett. **B 262**, 492 (1991).

[9] A.C. Bawa and M. Krawczyk, *Probing the structure of proton and photon in deep inelastic Compton process at HERA and LEP / LHC.* Preprint IFT-17-91, 1991.

[10] M. Krawczyk, *Structure of photon in deep inelastic Compton process at HERA.* Preprint IFT-17-92, 1992. Talk at *27th Rencontres de Moriond: QCD and High Energy Hadronic Interactions, Les Arcs, France, 1992.*

[11] P. Aurenche et al., Z. Phys. **C 56**, 589 (1992).

[12] L.E. Gordon and J.K. Storrow, Z. Phys. **C 63**, 581 (1994).

[13] ZEUS Coll., J. Breitweg et al., Phys. Lett. **B 413**, 201 (1997).

[14] ZEUS Coll., *Prompt photon processes in photoproduction at HERA.* Subm. to *29th International Conference on High-Energy Physics (ICHEP 98), Vancouver, Canada, 23-29 Jul 1998*, abstract 815, 2000.

[15] ZEUS Coll., J. Breitweg et al., Phys. Lett. **B 472**, 175 (2000).

[16] H1 Coll. Subm. to *the International Europhysics Conference on High Energy Physics, HEP97, Jerusalem, Israel, 1997*, abstract 265, 1997.

[17] L.E. Gordon and W. Vogelsang, Phys. Rev. **D 52**, 58 (1995).

[18] L.E. Gordon and W. Vogelsang, *Isolated prompt photon production at HERA.* Preprint hep-ph/9606457, 1996.

[19] L.E. Gordon, Phys. Rev. **D 57**, 235 (1998).

[20] M. Krawczyk and A. Zembrzuski, *NLO prediction for the photoproduction of the isolated photon at HERA.* Preprint hep-ph/9810253, 1998.

[21] C.F. von Weizsäcker, Z. Phys. **88**, 612 (1934).

[22] E.J. Williams, Phys. Rev. **45**, 729 (1934).

[23] E.J. Williams. *Kgl. Danske Vidensk. Selskab. Mat.-Fiz. Medd. 13 (1935) N4*, 1935.

[24] M. Glück, E. Reya and A. Vogt, Z. Phys. **C 67**, 433 (1995).

[25] M. Glück, E. Reya and A. Vogt, Phys. Rev. **D 46**, 1973 (1992).

[26] M. Glück, E. Reya and A. Vogt, Phys. Rev. **D 48**, 116 (1993).

6.5 On the Importance of the Contribution of the Longitudinal Virtual Photon and the Interference Terms in the ep Collisions

Urszula Jezuita-Dąbrowska and Maria Krawczyk
Institute of Theoretical Physics, Warsaw University,
ul. Hoża 69, 00-681 Warsaw, Poland

Abstract

The importance of the longitudinally polarised virtual photon γ_L^* in ep collisions is discussed. The numerical calculations for large p_T photon produced in the Compton process $ep \to e\gamma X$ are performed for the HERA and THERA colliders. For $p_T = 5\ GeV$ the $Q^2 \lesssim p_T^2$ range is studied in the Born approximation. In the rapidity distribution two terms, the cross section for the longitudinally polarised virtual photon, σ_L, and the interference term for the longitudinal and the transverse polarisation states for γ^*, τ_{LT}, almost cancel each other. As a result such cross section is strongly dominated by the transversely polarised intermediate photon, and therefore the γ_L^* contribution is not expected to play an significant role in hard ep processes, even for large Q^2.

Both σ_L and τ_{LT} terms for the Compton process can also be studied in the azimuthal angle distribution. In the special reference frame, the brick-wall (Breit) frame in which the four-momenta of the virtual photon and the proton are anti-parallel, we found relatively large sensitivity of $d\sigma/d\phi$ to the interference term τ_{LT} for this process both for the HERA and THERA colliders.

6.5.1 Introduction

Assuming that the one-photon exchange dominates in the deep inelastic lepton-nucleon collisions (DIS) a cross section for such process can be described in terms of two transverse (T) and one longitudinal (L) polarisation states of the intermediate virtual photon γ^*. The cross section for the unpolarised $lN \to lX$ process can be decomposed on two cross sections, describing the processes with the transversely and the longitudinally polarised γ^*, $\gamma_T^* N \to X$ $(d\sigma_T)$ and $\gamma_L^* N \to X$ $(d\sigma_L)$, respectively [1–6]. When the polarisation states of the initial lepton and/or nucleon are taken into account in a process $lN \to lX$, or a semi-inclusive process $lN \to laX$ is considered, the terms coming from the interference between the longitudinally and transversely polarised virtual photons (denoted by τ_{LT}) or between two different transverse states of γ^* (denoted by τ_{TT}) appear in addition [6]. Such interference terms may also occur in the cross sections for the two-photon exchange processes, in the e^+e^- collisions, as discussed in [6, 7].

The detailed study of relevance of various contributions, especially of the interference terms in the cross section for the process $e^+e^- \to e^+e^-\mu^+\mu^-$, has been performed in [8, 9] for the kinematical acceptance range of the PLUTO and LEP experiments. Here the two-photon exchange leading to the subprocess $\gamma^*\gamma^* \to \mu^+\mu^-$ was considered and large cross sections for processes containing at least one longitudinally polarised photon were found. In addition the interference terms were found to give large negative contribution. Both these contributions were found to vary strongly as a function of the kinematical variables. For special kinematical requirements one can obtain a cancelation between the cross sections for processes with one or two γ_L^* $(\sigma_{TL}, \sigma_{LT}, \sigma_{LL})$ and the interference contributions (τ_{TT}, τ_{LT}). Therefore both these types of terms have to be taken into account in the extraction of the leptonic (mionic) structure functions of the virtual photon (see also [10]). This is not the case in some of measurements of the structure functions, $F_2^{\gamma^*}$ and $F_L^{\gamma^*}$ where terms τ_{TT}, τ_{LT} and σ_{LL} are neglected, see [11, 12].

The question of the significance of the longitudinal polarisation state of the virtual photon in the ep or e^+e^- collisions leads to further question of the importance of the resolved γ_L^* contribution in the corresponding processes [13–22]. It was pointed out in [19], that in case of the dijet production in ep HERA collider and in case of the e^+e^- scattering at LEP, the contributions to the cross section coming from the longitudinally polarised photon are sizable and that in the description of such processes the partonic content of the γ_L^* should be taken into account.

However in our opinion the study of γ_L^* contribution to the cross section for the large p_T processes should be accompanying by a consideration of the interference terms. To get access to the interference between γ_L^* and γ_T^* term, $d\tau_{LT}$, and between two different transverse polarisation states of the virtual photon, $d\tau_{TT}$, it is useful to consider the azimuthal angle distributions of final state particle. Here the choice of the special reference frame - the brick-wall (Breit) frame allows to analyse individually the interference terms $d\tau_{LT}$ and $d\tau_{TT}$ [23–31]. Recently such azimuthal asymmetries for the charged hadrons production for neutral current deep inelastic e^+p scattering have been observed with ZEUS detector at the ep collider HERA [32].

The aim of this paper is to find out a significance of the contribution due to γ_L^* to the high-p_T prompt γ production at the HERA and the planned THERA colliders. In Sect. 6.5.2 a short derivation of the factorisation formulae for the inclusive and the semi-inclusive ep processes is presented. The relation of the interference terms to the contributions proportional to $\cos\phi$ and $\cos 2\phi$ in the azimuthal distribution for a final γ in the special reference frame is discussed in Sect. 6.5.3. Sect. 6.5.4 is devoted to the numerical studies of the different contributions to the cross section for the process $ep \to e\gamma X$ with unpolarised initial and final particles in the Born approximation. Some conclusions and remarks are presented in Sect. 6.5.5.

6.5.2 Factorisation of the one-photon exchange cross sections for the inclusive and semi-inclusive unpolarised lepton-nucleon scattering

6.5.2.1 Inclusive process $ep \to eX$ (DIS)

We start with the short description of the standard DIS process for the unpolarised ep collision (Fig. 1),

$$ep \to eX \ , \tag{6.5.1}$$

assuming that the one-photon exchange dominates. The corresponding differential cross section is denoted by $d\sigma^{ep\to eX}$, and we use the following notation for the kinematical variables: k^μ (p^μ) denotes the four-momentum of the initial electron (proton), q^μ - the four-momentum of the intermediate photon and $Q^2 = -q^2$ is the photon's virtuality. ε_i^μ ($i = T_1, T_2, L$) are the transverse and the longitudinal polarisation vectors of the exchanged virtual photon γ^*.

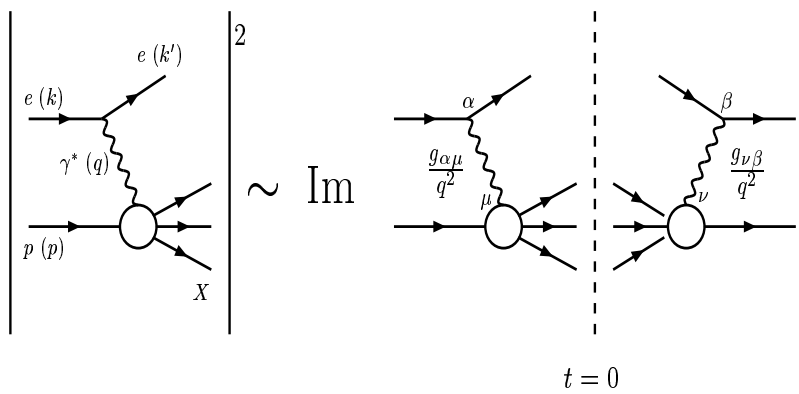

Figure 1: *Kinematics and notation for the unpolarised process $ep \to eX$ with the one-photon exchange. The optical theorem relation of the squared matrix element for $ep \to eX$ to the imaginary part of the amplitude for $ep \to ep$ at $t = 0$.*

For the considered process (6.5.1) the well known factorisation and separation formula holds [1–6]:

$$d\sigma^{ep\to eX} \ = \ d\sigma_T^{ep\to eX} \ + \ d\sigma_L^{ep\to eX} \ = \ \Gamma_T \ d\sigma_T^{\gamma^* p\to X} \ + \ \Gamma_L \ d\sigma_L^{\gamma^* p\to X} \ , \tag{6.5.2}$$

where $d\sigma_T^{\gamma^* p\to X}$ and $d\sigma_L^{\gamma^* p\to X}$ are the cross sections for the $\gamma^* p$ collision with the virtual photon polarised transversely and longitudinally, respectively. The functions Γ_T and Γ_L can be interpreted as the probabilities of the emission by the initial electron the

virtual photon in the transverse and the longitudinal polarisation states, respectively.

The above formula (6.5.2) can be obtained in various ways [1–6]. For example the cross section for process $ep \to eX$ (see fig. 1) can be expressed as the convolution of the leptonic tensor $L_e^{\mu\nu}(k,q)$ and the hadronic tensor $W_p^{\mu\nu}(p,q)$, both symmetric in the indexes μ and ν, namely

$$d\sigma^{ep\to eX} \sim \frac{1}{q^4} L_{e\,\mu\nu} W_p^{\mu\nu} . \tag{6.5.3}$$

Next by expressing the hadronic tensor $W_p^{\mu\nu}(p,q)$ in terms of the polarisation states of the exchanged photon, i.e.

$$W_p^{\mu\nu} = W_1 \sum_T \varepsilon_T^{*\,\mu} \varepsilon_T^{\nu} + \frac{W_2}{M^2}[p^2 - \frac{(pq)^2}{q^2}]\, \varepsilon_L^{*\,\mu} \varepsilon_L^{\nu} , \tag{6.5.4}$$

the factorisation and separation formula (6.5.2) can be derived easily.

Another way of obtaining the formula (6.5.2) is "the propagator decomposition method", see eg. [33] and references therein. In this method one represents the cross section for process (6.5.1) in the following form,

$$d\sigma^{ep\to eX} \sim L_e^{\alpha\beta} \frac{g_{\alpha\mu}}{q^2} \frac{g_{\nu\beta}}{q^2} W_p^{\mu\nu} . \tag{6.5.5}$$

Since $q^{\mu\nu}/q^2$ represents the propagator of the exchanged photon in the Feynman gauge one can decompose two propagators from eq.(6.5.5) by using the completeness relation:

$$-\frac{g^{\mu\nu}}{q^2} = \frac{\sum_T \varepsilon_T^{*\mu} \varepsilon_T^{\nu} - \varepsilon_L^{*\mu} \varepsilon_L^{\nu} - q^\mu q^\nu}{q^2} . \tag{6.5.6}$$

Due to the gauge invariance, i.e. $q_\mu L_e^{\mu\nu} = q_\mu W_p^{\mu\nu} = 0$, the term $q^\mu q^\nu/q^2$ from (6.5.6) can be omitted in further calculation of $d\sigma^{ep\to eX}$. Then in eq. (6.5.5) a separation between transversely and longitudinally polarised intermediate photon appears, namely $d\sigma^{ep\to eX} = d\sigma_T^{ep\to eX} + d\sigma_L^{ep\to eX}$. This method is especially useful in analysing the semi-inclusive processes, which we will discuss below.

6.5.2.2 Semi-inclusive process $ep \to e\gamma X$ (Compton process)

Let us now consider the semi-inclusive process $ep \to eaX$ where in comparison with DIS ($ep \to eX$) one additional particle in the final state is produced. In the following we choose the particular final state with the large p_T prompt photon, i.e. $a = \gamma$. We will study the factorisation of the cross section for the production of large p_T photon, assuming that it is emitted from the hadronic "vertex" (Fig. 2). The final photon in the ep collision can be emitted also from the electron line (the Bethe-Heitler process), for more details see the discussion in the beginning of Sect. 6.5.4.

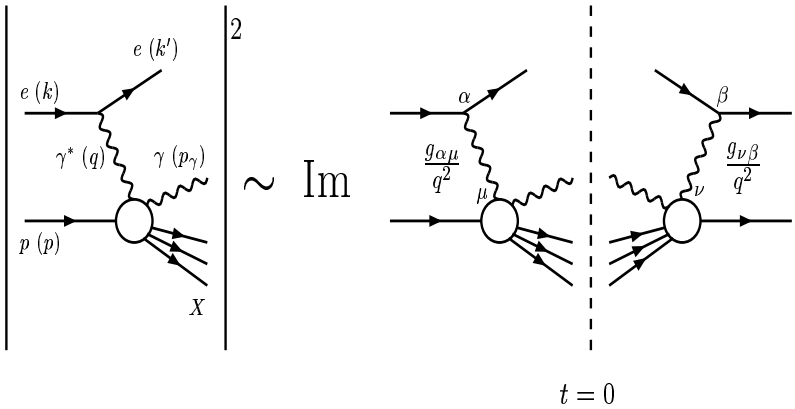

Figure 2: *Kinematics and notation for the unpolarised semi-inclusive process* $ep \to e\gamma X$ *with one-photon exchange. The optical theorem which relates* $\sigma(ep \to e\gamma X)$ *to the imaginary part of the forward amplitude for the process* $ep \xrightarrow{\gamma} ep$ *corresponding to* $\gamma^* p \xrightarrow{\gamma} \gamma^* p$ *is also shown.*

The invariant differential cross section for the unpolarised process

$$ep \to e\gamma X \ , \tag{6.5.7}$$

can be written as for the process (6.5.1), namely

$$d\sigma^{ep\to e\gamma X} \ \sim \ L_e^{\alpha\beta} \ \frac{g_{\alpha\mu}}{q^2} \ \frac{g_{\nu\beta}}{q^2} \ T^{\mu\nu} \ , \tag{6.5.8}$$

where the corresponding hadronic tensor $T^{\mu\nu}(p, q, p_\gamma)$ is introduced, (compare to (6.5.5)). The hadronic tensor $T^{\mu\nu}(p, q, p_\gamma)$ depends not only on the four-momenta of the intermediate photon and proton but also on the four-momentum of the final photon (p_γ). Consequently the interference between two contributions for different transverse (TT) or between the transverse and the longitudinal (LT) polarisation states of the exchanged photon may appear. Hence the invariant differential cross section for the considered process (6.5.7) contains $d\sigma_T$, $d\sigma_L$ and in addition two terms, called the interference terms (see eg. [33] and references therein):

$$d\sigma^{ep\to e\gamma X} \ = \ d\sigma_T + d\tau_{TT} \ + \ d\sigma_L \ + \ d\tau_{LT}. \tag{6.5.9}$$

These four terms are related via the optical theorem (see Fig.2) to the corresponding amplitudes as follows:

$$d\sigma_T \ \sim \ [\sum_{i=j=T_1,T_2} (\varepsilon_i^*)_\mu \ L^{\mu\nu} \ (\varepsilon_j)_\nu \ ] \cdot [\sum_{i=j=T_1,T_2} (\varepsilon_i)_\mu \ T^{\mu\nu} \ (\varepsilon_j^*)_\nu \ ] \ , \tag{6.5.10}$$

$$d\sigma_L \sim [\ (\varepsilon_L^*)_\mu\ L^{\mu\nu}\ (\varepsilon_L)_\nu\ ] \cdot [\ (\varepsilon_L)_\mu\ T^{\mu\nu}\ (\varepsilon_L^*)_\nu\ ]\ , \tag{6.5.11}$$

$$d\tau_{TT} \sim [\sum_{i,j=T_1,T_2;\ i\neq j} (\varepsilon_i^*)_\mu\ L^{\mu\nu}\ (\varepsilon_j)_\nu\ ] \cdot [\sum_{i,j=T_1,T_2;\ i\neq j} (\varepsilon_i)_\mu\ T^{\mu\nu}\ (\varepsilon_j^*)_\nu\ ]\ , \tag{6.5.12}$$

$$\tau_{LT} \sim [\sum_{j=T_1,T_2} (\varepsilon_L^*)_\mu\ L^{\mu\nu}\ (\varepsilon_j)_\nu + \sum_{i=T_1,T_2} (\varepsilon_i^*)_\mu\ L^{\mu\nu}\ (\varepsilon_L)_\nu\ ]\cdot$$

$$\cdot[\sum_{j=T_1,T_2} (\varepsilon_L)_\mu\ T^{\mu\nu}\ (\varepsilon_j^*)_\nu + \sum_{i=T_1,T_2} (\varepsilon_i)_\mu\ T^{\mu\nu}\ (\varepsilon_L^*)_\nu\ ]\ . \tag{6.5.13}$$

where ε_i denotes polarisation four-vectors of the virtual photon ($i = T_1, T_2$ and L).

It is worth noticing that the decomposition of the differential cross section $d\sigma^{ep\to e\gamma X}$ onto three components: $d\bar{\sigma}_T = d\sigma_T + d\tau_{TT}$, $d\sigma_L$ and $d\tau_{LT}$, does not depend on the choice of the basis of the polarisation vectors [33]. Note, that in the differential cross section $d\sigma^{ep\to e\gamma X}$ there are two independent terms related to the longitudinal polarisation state of the virtual photon, $d\sigma_L$ and $d\tau_{LT}$.

Obviously the above factorisation formula (6.5.9) holds for any semi-inclusive process with the one-photon exchange and with an arbitrary final particle a.

For a particular particle a integration over full phase space of this particle leads to the cross section from (6.5.2), so the interference terms vanish.

6.5.3 Azimuthal angle distribution for the semi-inclusive process

In studies of the process $lN \to laX$ (in particular $ep \to e\gamma X$) we can consider the differential cross section in form of the distribution of the azimuthal angle ϕ. This angle is defined as

$$\phi\ =\ \phi_l\ -\ \phi_a\ , \tag{6.5.14}$$

i.e. it is equal to the difference of the azimuthal angle of the final lepton (ϕ_l) and of the final particle a (ϕ_a). In general the ϕ-dependence of the differential cross section for the semi-inclusive lN collision can be written as [23–31]:

$$\frac{d\sigma^{lN\to laX}}{d\phi}\ =\ \sigma_0\ +\ \sigma_1\ \cos\phi\ +\ \sigma_2\ \cos 2\phi\ +\ \sigma_1'\ \sin\phi\ +\ \sigma_2'\ \sin 2\phi\ , \tag{6.5.15}$$

where the functions σ_0, σ_1, σ_2, σ_1' and σ_2' depend on kinematical variables, in particular on the angle ϕ [1].

[1] The functions σ_0, σ_1, σ_2, ... are denoted in some papers by A, B, C, ..., respectively.

The choice of the special reference frame - the brick-wall (Breit) frame in which the momenta of the virtual photon and the proton are anti-parallel[2] makes the cross section $d\sigma^{ln\to laX}/d\phi$ linear in $\cos\phi$, $\cos 2\phi$, $\sin\phi$ and $\sin 2\phi$, i.e. all σ_i are independent on ϕ. Moreover, for the cross sections calculated in the Born approximation the terms containing $\sin\phi$ and $\sin 2\phi$ vanish. Consequently the azimuthal distribution for the semi-inclusive ep process reduces in this particular frame and in the Born approximation to the following form:

$$\frac{d\sigma^{ep\to eaX}}{d\phi} = \sigma_0 + \sigma_1 \cos\phi + \sigma_2 \cos 2\phi \,. \tag{6.5.16}$$

One can find that in the chosen reference frame (the Breit frame) the functions σ_0, σ_1 and σ_2 are related to the four contributions, $d\sigma_T$, $d\sigma_L$, $d\tau_{LT}$ and $d\tau_{TT}$, discussed previously [3] (see Sect. 6.5.2.2). The term $\sigma_2 \cos 2\phi$ arises from the interference between two different transverse polarisation states of the exchanged photon ($\sim d\tau_{TT}$). The longitudinal-transverse interference ($\sim d\tau_{LT}$) gives rise to the term $\sigma_1 \cos\phi$. The function σ_0 consists of the remaining contributions, that it is due to the cross section of the virtual photon polarised transversely and longitudinally ($\sim (d\sigma_L + d\sigma_T)$) .

Hence in the brick-wall (Breit) frame the azimuthal angle distribution $d\sigma/d\phi$ is directly related to the interference terms. Consequently it may provides us the complementary information about τ_{LT} and τ_{TT}.

6.5.4 Numerical results

Below we present results of the calculation of the cross sections for the unpolarised Compton process $ep \to e\gamma X$. We analyse the emission of the prompt photon with a large p_T from the hadronic vertex at the Born level (i.e. we consider $\gamma^* q \to \gamma q$ process). The production of the prompt photon from the electron line (called the Bethe-Heitler process) and the interference between the Compton process and the Bethe-Heitler one should be included in the cross section for this process [34–36]. Both, Bethe-Heitler and interference, dominate the cross section for the photon's rapidity range $Y \lesssim 0$, for the greater values of the rapidity the Compton process dominates [33, 37].

We calculate the contributions to the cross section separately for different polarisation states of the virtual photon.

The cross section for the Compton process $ep \to e\gamma X$ is calculated for HERA and THERA colliders with energies: $E_e^{HERA} = 27.5$ GeV, $E_e^{THERA} = 250$ GeV and $E_p^{HERA} = E_p^{THERA} = 920$ GeV. We consider the cross section $d\sigma^{ep\to e\gamma X}/dY dp_T$ for $p_T = 5$ GeV as a function of the rapidity defined in the electron-proton center-of-mass frame. Of course the THERA rapidity range avaible for the final γ with $p_T = 5$ GeV

[2] In this frame ϕ is the angle between the electron scattering plane and the plane fixed by the momenta of the exchanged γ^* and the final photon.

[3] Here calculated in the same reference frame, i.e. the Breit frame.

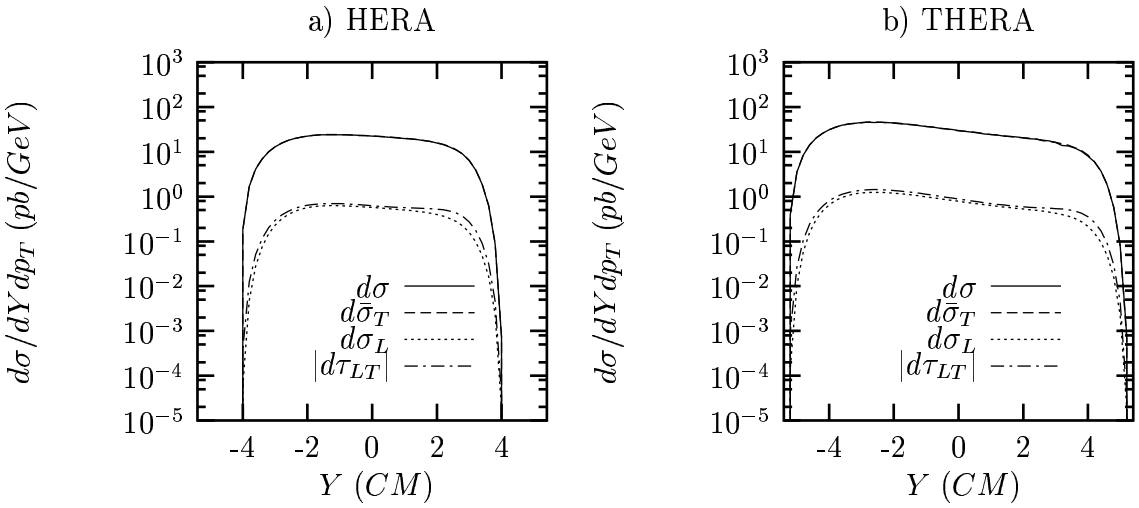

Figure 3: *Various contributions to the differential cross section for high-p_T photon production at a) HERA and b) THERA for $p_T = 5$ GeV. The contribution due to the transverse polarisation states: $d\bar{\sigma}_T = \sigma_T + \tau_{TT}$ (dashed line), due to the longitudinal polarisation state $d\sigma_L$ (dotted line) and the absolute value of the interference term: $|d\tau_{LT}|$ (dotted-dashed line), together with the sum of all terms $d\sigma$ (solid line) are shown. The CTEQ5L parton parametrization of the proton [38] with the hard scale equal to p_T was used.*

is wider than the HERA rapidity range, $|Y| < 5.2$ and $|Y| < 4$, respectively. Three different contributions to $d\sigma^{ep\to e\gamma X}/dYdp_T$ for $p_T = 5$ GeV, $d\bar{\sigma}_T$, $d\sigma_L$, $|d\tau_{LT}|$ together with the sum of these terms $d\sigma$, are presented in Fig. 3. The dependence on the rapidity is similar for all contributions and both colliders. The differential cross section for the Compton process at the Born level is dominated by the contribution due to transversely polarised intermediate photon $d\bar{\sigma}_T = d\sigma_T + d\tau_{TT}$. The $d\sigma_L$ contributes at the few percents level to the whole cross section and it's magnitude is very close to that of $d\tau_{LT}$ term. Moreover, $d\sigma_L$ is positive while $d\tau_{LT}$ is negative and these two contributions almost cancel each other. Therefore the resulting cross section $d\sigma^{ep\to e\gamma X}/dYdp_T$ in the considered kinematical range is basical described by $d\bar{\sigma}_T = d\sigma_T + d\tau_{TT}$ term only. The same effect was observed for more differential cross section $d\sigma^{ep\to e\gamma X}/dYdp_TdQ^2$ calculated for fixed values of virtuality Q^2 [33] (not shown). The magnitudes of the differential cross sections $d\sigma^{ep\to e\gamma X}/dYdp_T$ and the three contributions ($d\bar{\sigma}_T$, $d\sigma_L$ and $d\tau_{LT}$) shown in Fig. 3 are similar for HERA and THERA colliders.

The fact that the longitudinal γ^* gives negligible contributions to the considered cross section does not mean that this contribution does not grow with Q^2 (for $Q^2 \lesssim p_T^2$), as expected. This can be seen in the ratio of the contributions $d\sigma_L$ to $d\bar{\sigma}_T$, as a function of virtuality Q^2. The numerical results obtained for the Compton process at the ep THERA collider for the fixed rapidity ($Y = 0$) and chosen values of p_T equal to 2, 5 and 20 GeV are presented in Fig. 4. The magnitude of the cross sections ratio [$d\sigma_L/dYdp_TdQ^2$] / [$d\sigma_T/dYdp_TdQ^2$] for THERA collider grows with the virtuality

of the intermediate photon for $p_T^2 > Q^2$, with the maximum value reached at the virtuality $Q^2 \approx p_T^2$. Similar behavior, i.e. growth with Q^2, is observed for $|d\tau_{LT}|/d\sigma_T$ ratio. Analogous results hold also for HERA, see [33].

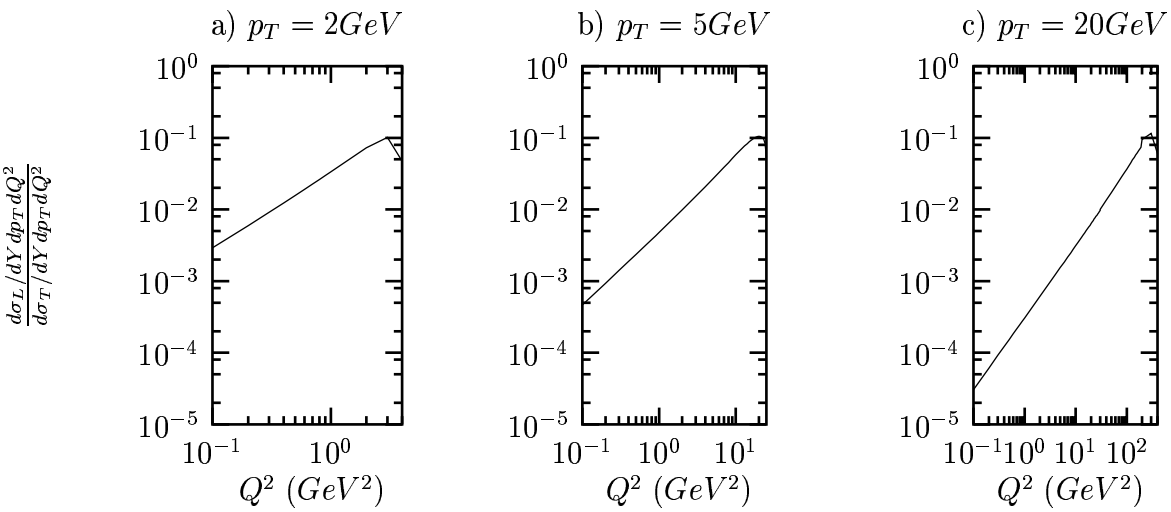

Figure 4: *The ratio* $[d\sigma_L/dYdp_TdQ^2]$ / $[d\sigma_T/dYdp_TdQ^2]$ *for high-*p_T *photon production in ep collision at THERA as a function of* Q^2 *at* $Y = 0$ *for a)* $p_T = 2$ *GeV, b)* $p_T = 5$ *GeV and c)* $p_T = 20$ *GeV is shown. The CTEQ5L parton parametrization of the proton [38] with the hard scale equal to* p_T *was used.*

Although the size of γ_L^* contribution grows with Q^2 (for $Q^2 \lesssim p_T^2$), as seen in Fig. 4, the above differential cross sections, $d\sigma/dYdp_T$ and $d\sigma/dYdp_TdQ^2$, can be described with a very good accuracy by $d\bar{\sigma_T}$ only due to the cancellation with the corresponding interference term. Therefore the measurements of such cross sections do not provide us the information about the magnitudes of the contributions due to the longitudinally polarised virtual photon: $d\sigma_L$ and $d\tau_{LT}$.

In order to study the sensitivity of the considered process to the interference terms we have analysed the azimuthal dependence of the cross section. We calculate $d\sigma^{ep\to e\gamma X}/d\phi = \sigma_0 + \sigma_1 \cos\phi + \sigma_2 \cos 2\phi$ in the brick-wall (Breit) frame. As discussed in Sect. 6.5.3, in this frame the functions σ_1, σ_2 and σ_0 are directly related to the interference terms $d\tau_{TT}$, $d\tau_{LT}$ and to the sum: $d\sigma_L + d\sigma_T$, respectively. (For more details see Sect. 6.5.3).

The numerical calculations are performed for HERA and THERA energies for the kinematical region[4] choosen as in experiment [32], namely 180 $GeV^2 < Q^2 <$

[4] y is a Bjorken scaling variables related to the energy of the exchanged photon: $y = (pq)/(pk)$ and z_γ is the Lorentz-invariant variable defined as $z_\gamma = (pp_\gamma)/(pq)$.

7220 GeV^2, $0.2 < y < 0.8$, $0.2 < z_\gamma < 1.0$ and the $(p_T)_{min} = 2\ GeV$[5], (Fig. 5). The contribution related to the interference between two transverse polarisation states of γ^* (the term proportional to $\sigma_2 \cos 2\phi$) gives a negligible effect, while the interference between the virtual photon polarised longitudinally and transversely (the term proportional to $\sigma_1 \cos\phi$) leads to the visible effect, both for HERA and THERA colliders. We have checked that the results obtained with other values of p_T cut: $(p_T)_{min} = 1$, 1.5 and 2 GeV (not shown) lead to similar conclusions.

Therefore we can conclude that from the measurements of the differential cross section in form of azimuthal distribution $d\sigma^{ep\to e\gamma X}/d\phi$ at the HERA and the THERA colliders the informations of the size of the TL interference contribution via $\sigma_1 \sim d\tau_{LT}$ term can be obtained, with an effect at the 30% level. While for $\sigma_2 \sim d\tau_{TT}$ the effect is to small to be observed.

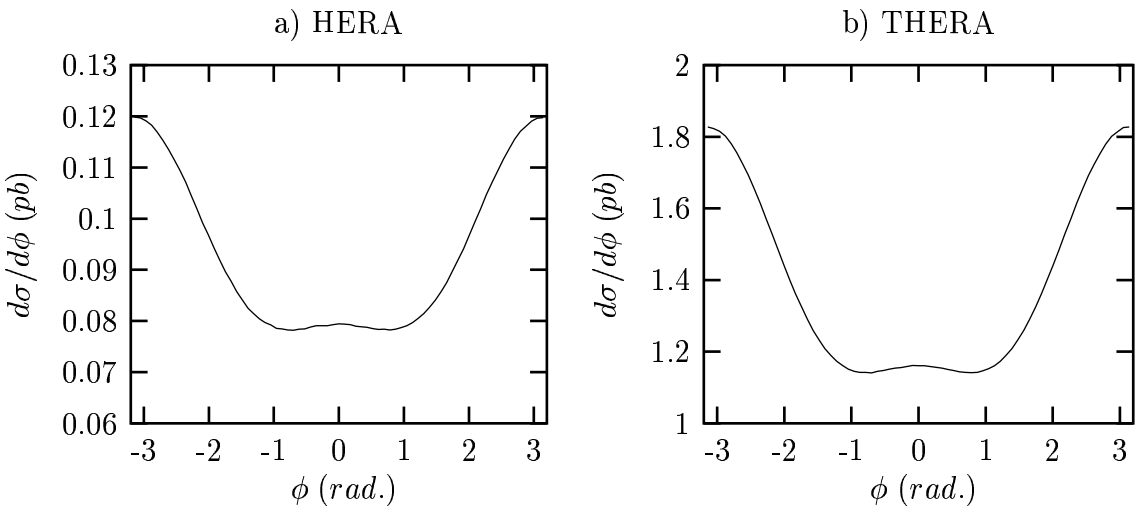

Figure 5: *The ϕ distributions obtained for the special reference frame (see text) in the kinematical region:* 180 $GeV^2 < Q^2 <$ 7220 GeV^2, $0.2 < y < 0.8$, $0.2 < z_\gamma < 1.0$ *and the* $(p_T)_{min} = 2.0$ *GeV for a) HERA and b) THERA energies. The CTEQ5L parton parametrization of the proton [38] with the hard scale equal to* p_T *was used.*

It is worthwhile to compare our results with the recent measurements of the azimuthal angle dependence of the cross section for the charged hadrons produced in the neutral current deep inelastic e^+p scattering by the ZEUS collaboration at HERA [32]. In the ϕ distributions, the term $\sigma_1 \cos\phi$ is clearly seen for four considered values of p_T cut: $(p_T)_{min} = 0.5$, 1, 1.5 and 2 GeV. At low $(p_T)_{min}$ the term $\sigma_2 \cos 2\phi$ gives a negligible effect, however this term becomes visible with the increasing value of $(p_T)_{min}$. This is different as compared to the Compton process discussed above, where σ_2 is found to be negligible small. This difference arises from the following fact. In case of the

[5]This p_T seems to be to small for the perturbative QCD, however in the considered process the virtuality Q^2 provides hard scale.

Compton process $ep \to e\gamma X$ calculated in the Born approximation only one subprocess, $\gamma^* q \to q\gamma$, contributes to the cross section. In the same approximation there are two subprocesses which contribute to the semi-inclusive charged hadrons production at HERA, namely $\gamma^* q \to qg$ and $\gamma^* g \to q\bar{q}$. Moreover the process $\gamma^* g \to q\bar{q}$ dominates in the $\sigma_2 \cos 2\phi$ term, while the contribution coming from the process $\gamma^* q \to gq$, analogous to our $\gamma^* q \to \gamma q$ process, dominates the term $\sigma_1 \cos \phi$.

6.5.5 Conclusions

In this paper we investigate the importance of the contribution of the longitudinal virtual photon and the interference terms in the ep collisions. As a particular process we choose the Compton process. For the unpolarised process $ep \to e\gamma X$ at HERA and THERA energies we analyse three contributions: the cross section $d\sigma_L$ related to the longitudinally polarised exchanged photon γ_L^*, $d\tau_{LT}$ coming from the interference between the longitudinal and the transverse polarisation states of γ^* and $d\bar{\sigma}_T$ the contribution due to the γ_T^*. The calculations are performed at the Born approximation. In the p_T and the rapidity distributions both contributions $d\sigma_L$ and $d\tau_{LT}$ are of similar size but due their opposite signs they almost cancel each other in the summed cross section. It means that the considered cross section is strongly dominates by contribution due to transversely polarised virtual photon. Our analysis shows that if the contribution $d\sigma_L$ is included then on the same footing the interference terms need to be included in a consistent analise.

The importance of the resolved γ_L^* in hard semi-inclusive ep collisions for HERA and THERA energies remains an open question. Although it is straightforward to estimate the contributions due to resolved γ_L^* unfortunetly the partonic content of γ_L^* for the interference terms can not be introduced. Somehow one should model this part of the cross section related to $d\tau_{LT}$. So a further study is needed in order to reach final conclusions, however the fact that the direct γ_T^* contribution dominates so strongly, it is hard to imagine that the resolved contribution related to γ_L^* will play a significant role.

Although our results are based on the Born term only, we think that this should already shed some light on the importance of contributions due to γ_L^*. For a full calculation the resolved photon subprocesses for γ_L^* should be included in addition, however for interference terms the concept of the partonic content of the virtual photon does not applied.

In any case it is interesting that from the studies of the azimuthal angle dependence of $d\sigma^{ep\to e\gamma X}/d\phi$ in the brick-wall (Breit) frame we can get access to the interference term τ_{LT}.

Appendix: The φ-dependence of the cross-section for the process $eq \to eq\gamma$ in the brick-wall (Breit) frame

The general factorisation formula for the electron-quark scattering with the photon in the final state has the following form (6.5.8):

$$d\sigma^{eq\to eq\gamma} \sim e^6 Q_q^4 \, Re\,[L_{\alpha\beta}\frac{g^{\alpha\mu}g^{\nu\beta}}{Q^4}\hat{T}_{\mu\nu}] = \frac{e^6 Q_q^4}{Q^4} Re\,[\sum_{i,j\,=\,L,T1,T2} \zeta_{ij} \underbrace{(L_{\alpha\beta}\varepsilon_i^{*\alpha}\varepsilon_j^{\beta})}_{\equiv L_{ij}} \underbrace{(\varepsilon_i^{\mu}\varepsilon_j^{*\nu}\hat{T}_{\mu\nu})}_{\equiv T_{ij}}] \,, \tag{6.5.17}$$

where: i, j denote the polarisation states of the virtual photon (L - the longitudinal, $T1, T2$ - the transverse polarisations) and $\zeta_{LT} = \zeta_{TL} = -1$, while in remaining cases $\zeta_{ij} = 1$. The tensors $L_{\mu\nu}$ and $\hat{T}_{\mu\nu}$ are related the emission of the virtual photon by the electron and to the collision of the virtual photon with the quark in which the photon in the final state is produced, respectively. In this paper, we consider the subprocess $\gamma^* q \to \gamma q$ at lowest order (LO).

The special reference frame - the brick-wall (Breit) frame (see also [26]) is defined by choosing the momenta of the exchanged photon and the electrons in forms:

$$q^\mu = \sqrt{Q^2}\,(0,\ 0,\ 0,\ 1)\,, \qquad -q^2 = Q^2\,; \tag{6.5.18}$$

$$k^\mu = \frac{1}{2}\sqrt{Q^2}\,(\cosh\psi,\ \sinh\psi\cos\varphi,\ \sinh\psi\sin\varphi,\ 1)\,, \qquad k^2 = 0\,; \tag{6.5.19}$$

$$k'^\mu = \frac{1}{2}\sqrt{Q^2}\,(\cosh\psi,\ \sinh\psi\cos\varphi,\ \sinh\psi\sin\varphi,\ -1)\,, \qquad k'^{\,2} = 0\,. \tag{6.5.20}$$

φ is the azimuthal angle between the electron scattering plane and a plane defined by the momenta of the intermediate photon and the final photon. The $\cos\varphi$ is defined by the relation:

$$\cos\varphi = \frac{\vec{k}\times\vec{k'}}{|\,\vec{k}\times\vec{k'}\,|}\cdot\frac{\vec{q}\times\vec{p_\gamma}}{|\,\vec{q}\times\vec{p_\gamma}\,|}\,. \tag{6.5.21}$$

The hyperbolic functions of angle ψ are related to the variables $y = qp/kp$ as follows:

$$\cosh\psi = \frac{1}{y}\,(2-y)\,, \tag{6.5.22}$$

$$\sinh\psi = \frac{2}{y}\sqrt{1-y}\,. \tag{6.5.23}$$

The momenta of the initial quark and the final photon are following:

$$p_q^\mu = (E_q,\ 0,\ 0,\ -E_q)\,, \qquad p_q^2 = 0 \tag{6.5.24}$$

and

$$p_\gamma^\mu \;=\; p_T\,(\frac{1}{\sin\theta_\gamma},\;1,\;0,\;\frac{\cos\theta_\gamma}{\sin\theta_\gamma})\;. \tag{6.5.25}$$

where E_q (E_p) is the energy of the initial quark (proton), p_T - the transverse momentum of the real photon (perpendicular to the momentum of the exchange photon) and θ_γ - the polar (scattering) angle between the direction of the initial electron and the direction of the final photon.

We take the circular polarisation vectors of the virtual photon with the momenta q^μ given by (6.5.18). These polarisation vectors can be interpreted as the helicities of the intermediate photon (λ) and have the following forms:

- the longitudinal polarisation vector ($\varepsilon_L^2 = 1$)

$$\varepsilon_L^\mu\,(\lambda=0) \;=\; (1,\;0,\;0,\;0)\;, \tag{6.5.26}$$

- the two transverse polarisation vectors ($\varepsilon_T^2 = -1$)

$$\varepsilon_{T1}^\mu\,(\lambda=+1) \;=\; \frac{1}{\sqrt{2}}\,(0,\;-1,\;-i,\;0) \tag{6.5.27}$$

and

$$\varepsilon_{T2}^\mu\,(\lambda=-1) \;=\; \frac{1}{\sqrt{2}}\,(0,\;1,\;-i,\;0)\;. \tag{6.5.28}$$

From the defined above four momenta and polarisation four vectors one can obtained the explicit forms of the coefficients L_{ij} and $\hat{T}_{ij}$. They can be treated as the elements of the matrices L and $\hat{T}$, respectively (ordering of rows and columns is $T1$ ($\lambda=+1$), L ($\lambda=0$), $T2$ ($\lambda=-1$)). The specific forms of these matrices calculated in the Born approximation related to the brick-wall (Breit) frame are following:

$$\mathbf{L} = \frac{1}{2}\begin{pmatrix} \cosh^2\psi+1 & \frac{1}{\sqrt{2}}\sinh 2\psi\; e^{-i\varphi} & -\sinh^2\psi\; e^{-2i\varphi} \\ \frac{1}{\sqrt{2}}\sinh 2\psi\; e^{i\varphi} & 2\sinh^2\psi & -\frac{1}{\sqrt{2}}\sinh 2\psi\; e^{-i\varphi} \\ -\sinh^2\psi\; e^{2i\varphi} & -\frac{1}{\sqrt{2}}\sinh 2\psi\; e^{i\varphi} & \cosh^2\psi+1 \end{pmatrix} \tag{6.5.29}$$

and

$$\hat{\mathbf{T}} = 2\frac{Q^2}{su}\begin{pmatrix} -U-2p_T^2 & 2\sqrt{2}p_T\hat{E} & -2p_T^2 \\ 2\sqrt{2}p_T\hat{E} & U-4[\hat{E}^2+E_q^2] & -2\sqrt{2}p_T\hat{E} \\ -2p_T^2 & -2\sqrt{2}p_T\hat{E} & -U-2p_T^2 \end{pmatrix}\;, \tag{6.5.30}$$

where $\hat{E} = E_q - E_\gamma$, $U = \frac{u^2+s^2}{Q^2} - 2t$ and s, t, u are the Mandelstam variables for the process $\gamma^* q \to \gamma q$ defined by:

$$s = (q+p)^2 , \qquad t = (q-p_\gamma)^2 , \qquad u = (p-p_\gamma)^2 , \tag{6.5.31}$$

with

$$q + p_q = p_\gamma + p'_q , \qquad s + t + u = q^2 . \tag{6.5.32}$$

The elements $\hat{T}_{ij}$, calculated in the first-order, are real. The matrix L contains $e^{\pm i\varphi}$ and $e^{\pm 2i\varphi}$. Consequently the cross-section (6.5.17) depend only on $\cos\varphi$ and $\cos 2\varphi$, namely:

$$\frac{d\sigma^{eq\to eq\gamma}}{d\phi} \sim \frac{e^6 Q_q^4}{Q^4} L^{\mu\nu} \hat{T}_{\mu\nu} = \sigma_0 + \sigma_1 \cos\varphi + \sigma_2 \cos 2\varphi . \tag{6.5.33}$$

The coefficients $\sigma_i, (i = 0,1,2)$ in formula (6.5.33) are strictly related to the four contributions to the differential cross section for the process $eq \to eq\gamma$ as follows:

$$d\sigma_T + d\sigma_L \sim \frac{e^6 Q_q^4}{Q^4} Re\,[\sum_{i=j=T1,T2,L} L_{ij}\hat{T}_{ij}] = \tag{6.5.34}$$

$$= -4e^6 Q_q^4 \frac{1}{su} [\,(\cosh^2\psi + 1)\, p_T^2 + 2\sinh^2\psi\,[\hat{E}^2 + E_q^2] + (\frac{u^2+s^2}{Q^2} - 2t)\,] \equiv \sigma_0 , \tag{6.5.35}$$

$$d\tau_{LT} \sim -\frac{e^6 Q_q^4}{Q^4} Re\,[\sum_{i=L\,,\,j=T1,T2} L_{ij}\hat{T}_{ij} + \sum_{i=T1,T2\,,\,j=L} L_{ij}\hat{T}_{ij}] = \tag{6.5.36}$$

$$= -8e^6 Q_q^4 \frac{1}{su} \sinh 2\psi\, p_T\, \hat{E}\, \cos\phi \equiv \sigma_1 \cos\phi, \tag{6.5.37}$$

$$d\tau_{TT} \sim \frac{e^6 Q_q^4}{Q^4} Re\,[\sum_{i=T1,T2\,,\,j=T1,T2\,,\,i\neq j} L_{ij}\hat{T}_{ij}] = \tag{6.5.38}$$

$$= 8e^4 Q_q^4 \frac{1}{su} \sinh^2\psi\, p_T^2 \cos 2\phi \equiv \sigma_2 \cos 2\phi. \tag{6.5.39}$$

Acknowledgements

We would like to acknowledge P.M. Zerwas for an interesting and fruitful discussion. This research has been partly supported by the Polish Committee for Scientific Research, Grant No 2P03B05119(2000-2001) and by the European Commission 50th framework Contract HPRN-CT-2000-00149.

References

[1] L.N. Hand, Phys. Rev. **129**, 1834 (1963).

[2] L.N. Hand, RX-933 (1961).

[3] M. Gourdin, Nuovo Cim. **21**, 1094 (1961).

[4] R.H. Dalitz and D.R. Yennie, Phys. Rev. **105**, 1598 (1957).

[5] D.R. Yennie, M.M. Levy and D.G. Ravenhall, Rev. Mod. Phys. **29**, 144 (1957).

[6] V.M. Budnev et al., Phys. Rep. **C 15**, 181 (1975).

[7] N. Arteaga et al., Phys. Rev. **D 52**, 4920 (1995).

[8] OPAL Coll., G. Abbiendi et al., Eur. Phys. J. **C 11**, 409 (1999).

[9] R. Nisius, Phys. Rept. **332**, 165 (2000).

[10] M. Krawczyk, hep-ph/0012179 (2000). Invited talk at PHOTON 2000: International Workshop on Structure and Interactions of the Photon (Including 13th International Workshop on Photon-Photon Collisions), Ambleside, Lake District, England, 26-31 Aug 2000.

[11] PLUTO Coll., C. Berger et al., Phys. Lett. **B 142**, 119 (1984).

[12] L3 Coll., M. Acciarri et al., Phys. Lett. **B 483**, 373 (2000).

[13] C. Friberg and T. Sjostrand, Eur. Phys. J. **C 13**, 151 (2000).

[14] C. Friberg, Nucl. Phys. Proc. Suppl. **82**, 124 (2000).

[15] C. Friberg, hep-ph/0005048 (2000).

[16] C. Friberg and T. Sjostrand, JHEP **0009**, 010 (2000).

[17] C. Friberg and T. Sjostrand, Phys. Lett. **B 492**, 123 (2000).

[18] C. Friberg, hep-ph/0010264 (2000).

[19] J. Chyla and M. Tasevsky, Eur. Phys. J. **C 16**, 471 (2000).

[20] J. Chyla, Phys. Lett. **B 488**, 289 (2000).

[21] J. Chyla, 0010055 (2000).

[22] J. Chyla and M. Tasevsky, Eur. Phys. J. **C 18**, 723 (2001).

[23] R. Brown and I. Muzinich, Phys. Rev. **D 4**, 1496 (1971).

[24] H. Georgi and H.D. Politzer, Phys. Rev. Lett. **40**, 3 (1978).

[25] R.N. Cahn, Phys. Lett. **B 78**, 269 (1978).

[26] G. Kopp, R. Maciejko and P.M. Zerwas, Nucl. Phys. **B 144**, 123 (1978).

[27] A. Mendez, Nucl. Phys. **B 145**, 199 (1978).

[28] J. Chay, S.D. Ellis and W.J. Stirling, Phys. Lett. **B 269**, 175 (1991).

[29] J. Chay, S.D. Ellis and W.J. Stirling, Phys. Rev. **D 45**, 46 (1992).

[30] K. A. Oganesian et al., Eur. Phys. J. **C 5**, 681 (1998).

[31] M. Ahmed and T. Gehrmann, Phys. Lett. **B 465**, 297 (1999).

[32] ZEUS Coll., J. Breitweg et al., Phys. Lett. **B 481**, 199 (2000).

[33] U. Jezuita-Dąbrowska and M. Krawczyk, in preparation (2001).

[34] S.J. Brodsky, J.F. Gunion and R. Jaffe, Phys. Rev. **D 6**, 2487 (1972).

[35] S.J. Brodsky et al., Phys. Lett. **B 449**, 306 (1999).

[36] P. Hoyer, M. Maul and A. Metz, Eur. Phys. J. **C 17**, 113 (2000).

[37] G. Kramer, D. Michelsen and H. Spiesberger, Eur. Phys. J. **C 5**, 293 (1998).

[38] CTEQ Coll., H. L. Lai et al., Eur. Phys. J. **C 12**, 375 (2000).

7 Electron-Nucleus Scattering

7.1 Electron-Nucleus Collisions at THERA

L. Frankfurt[1], V. Guzey[2], M. McDermott[3] and M. Strikman[4]
[1]*Nuclear Physics Dept., School of Physics and Astronomy, Tel Aviv University, 69978 Tel Aviv, Israel.*
[2]*Special Research Centre for the Subatomic Structure of Matter (CSSM), Adelaide University, 5005, Australia.*
[3]*Division of Theoretical Physics, Department of Mathematical Sciences, University of Liverpool, Liverpool L69 3BX, England.*
[4]*Department of Physics, Penn State University, University Park, PA 16802-6300, USA.*

7.1.1 Executive Summary

The nuclear option at THERA provides an ideal and unique opportunity to investigate the black body limit (BBL) of high energy Deep Inelastic Scattering (DIS) of highly virtual photons off heavy nuclear targets and thereby probe Quantum Chromodynamics (QCD) in a new regime. At high enough energies, whichever hadronic configuration the photon fluctuates into, the interaction at given impact parameter with the heavy nuclear target will eventually reach its geometrical limit corresponding to the scattering from a black disk. An attractive likely feature of the approach to the BBL regime for a large nucleus is that the interaction is strong although the coupling constant is small. Predictions for many observables are qualitatively different within the BBL from those of the standard leading twist DGLAP [1] regime. The most striking predictions for inclusive observables include: (i) the nuclear structure functions behave as $F_2^A \propto \pi R_A^2 Q^2 \ln(1/4m_N R_A x)$, with a $1/x$ dependence slower than that predicted by DGLAP (this is in contrast with the nucleon case in which $F_2^N \propto Q^2 \pi R_N^2 (1 + c_N \ln^2 1/x) \ln 1/x$ whose x dependence is comparable with the DGLAP prediction, here R_A, R_N are radii of nucleus and nucleon), (ii) the ratio of nuclear and nucleon structure functions decreases with $1/x$, $F_2^A/F_2^N \propto 1/(1+c_N \ln^2 1/x)$. Major new features for the final states in DIS are: (i) a much softer leading hadron

spectra with enhanced production of high p_t jets in inclusive and diffractive processes, (ii) the inclusive diffractive cross section reaches nearly half of the total cross section, (iii) a weakly Q^2-dependent parameter-free cross section for exclusive vector meson electroproduction.

It is possible that the black limit will be reached for certain gluon-induced DIS processes off nucleons within THERA kinematics. However, nuclei have two very clear and useful advantages over nucleon targets. Firstly, because the target is extremely Lorentz contracted, the partons of individual nucleons are piled up on one another. This means that for a given photon-target centre of mass energy the black limit will be reached *much earlier* in nuclei. Secondly, scattering from the edge of nucleons, which remains grey even at very high energies, (and competes with the BBL contribution) is heavily suppressed for large nuclei. The purpose of the rest of this report is to expand on the details for the interested reader.

7.1.2 Introduction

The standard theoretical approach to inclusive Deep Inelastic Scattering (DIS) of a virtual-photon off a target, $\gamma^*(q) + T(p) \to X$, uses a factorization theorem [2] to prove that in the limit of large photon virtuality ($q^2 = -Q^2 \ll 0$), leading twist (LT) terms dominate in the Operator Product Expansion [3] of the relevant hadronic matrix elements. This corresponds to a factorization of short and long distance contributions and leads to an attractive physical picture of the virtual photon scattering off electrically charged "point-like" partonic constituents within the target, with its associated approximate Bjorken [4] scaling (which states that structure functions, for example, F_L and F_2, only depend on the ratio $x = Q^2/2p \cdot q$). The application of the renormalization group to perturbative Quantum Chromodynamics (pQCD), embodied in the DGLAP [1] evolution equations, corrects this naive picture and leads to logarithmic scaling violations. These equations describe how the long-distance boundary conditions, the parton distributions of the quarks and gluons, (and ultimately F_L and F_2) change logarithmically with Q^2.

It is now understood that this decomposition in terms of twists should become inapplicable in pQCD at sufficiently small x (i.e. the higher twist (HT) terms, which are formally suppressed by positive integer powers of $1/Q^2$, become numerically important). However, in practice, it is very difficult to distinguish HT effects in the inclusive structure functions from uncertainties in the input parton distributions for a nucleon target, because DIS off the nucleon edge masks the importance of the HT effects. We will explain that the theoretical description of DIS off heavy nuclei is significantly simpler than that for a nucleon target. The energy and Q^2 dependence of structure functions of heavy nuclei, and specific properties of final states, can serve as clear signatures of a new regime, the black body limit (BBL) regime, where significant contributions to the dynamics of the strong interactions from all twists are expected.

For the past decade, pQCD has been used extremely successfully to describe inclusive DIS processes (see e.g. [5]). Many new phenomena specific to small-x physics have been discovered experimentally and explained by pQCD. New QCD factorization

theorems for certain hard processes (such as diffractive scattering [6], exclusive vector meson production [7, 8] and Deeply Virtual Compton Scattering [9]) have been proven. These factorization theorems were used to predict and describe qualitatively new small-x hard scattering phenomena. In particular, hard exclusive processes for both nucleon and nuclear targets, with properties strikingly different from those familiar from soft hadronic processes, were predicted and observed (several experimental [10] and theoretical [11–13] reviews are available in the literature). These include: (i) the complete transparency of nuclear matter in coherent pion diffraction into two jets off a nuclear target (predicted in [14] and later observed in [15]) and in exclusive photoproduction of J/ψ mesons off nuclei [16], (ii) a fast increase with increasing energy of cross sections of hard exclusive processes [17]: high Q^2 exclusive ρ, ϕ, J/ψ meson production [7, 18–21] and exclusive photoproduction of J/ψ and Υ mesons [22, 23] and low-x exclusive photon production in DIS (Deeply Virtual Compton Scattering [24]), (iii) an almost universal and small slope of the t-dependence of hard exclusive processes (predicted in [25]), (iv) a small and process/scale dependent rate of change of the slope of t-dependence of exclusive processes with energy, α', (v) confirmation that QCD is flavour blind in hard (high Q^2) exclusive vector meson (ρ and ϕ mesons) electroproduction. These theoretical and experimental discoveries have moved the focus of investigations in QCD to new frontiers.

A seminal and extremely important experimental observation is the fast increase with $1/x$ of the proton structure function, F_2, at small x discovered by the H1 [26] and ZEUS [27] collaborations at HERA. The implied fast increase of the proton parton densities raises several challenging questions for DIS at even higher energies:

- Will it remain sufficient to use the leading twist DGLAP evolution equation (to a given accuracy in logarithms in Q^2) or will it become necessary to resum [28–30] the large logs in energy that appear at each order in the perturbative expansion (i.e. for the regime in which $\alpha_s(Q^2)\ \ln(x_0/x) \sim \mathcal{O}(1)$) ?

- Does diffusion in parton transverse momenta lead to a breakdown of (collinear) factorization for leading twist pQCD, and a non-trivial mixing of perturbative and non-perturbative effects, in a kinematic regime in Q^2 which is assumed to be safe at higher x ?

- Will the increase of the parton distributions lead to an experimentally-accessible new pQCD regime, where the coupling constant is small but the interaction is strong ? If so, how can one distinguish between this new regime and the standard one in which the LT DGLAP equations are applicable ?

- Will the structure functions and cross sections of hard exclusive processes continue to increase with energy or will their growth be tamed to avoid violation of unitarity of the S-matrix (applied to the hard interactions of the hadronic fluctuations of the photon) ?

- Since the same QCD factorization theorems which lead to successful description of hard processes predict a rapid increase of HT effects with increasing energy,

how important will the latter effects be for the interpretation of the small-x data ?

In the following we explain that one has a good chance to answer these questions by studying electron-nucleus collisions at THERA. We will formulate several theoretical predictions, based mostly on general properties of space-time evolution of high-energy scattering, which can serve as signals of new hard QCD phenomena.

DIS at high energies is most easily formulated in the target rest frame (this approach has become known as *the dipole picture* for reasons that will become apparent below). In this frame, the photon fluctuates into a hadronic system (a quark anti-quark colour triplet *dipole*, to lowest order in α_s) a long distance, $1/2m_T x \gg R_T$, upstream of the target. This system interacts briefly with the target and eventually the hadronic final state is formed. The formation time of the initial state hadronic fluctuations, and of the final state, is typically much longer than the interaction time with the target. This allows the process to be factorized into a wavefunction for the formation of the initial state, an interaction cross section with the target, and a wavefunction describing the formation of the final state. In this frame, the standard LT result of pQCD, at leading log accuracy, may be re-expressed using the following well-known interaction cross-section [14, 18, 19, 31] for the scattering of the $q\bar{q}$ dipole with the target (for an explicit derivation see [32]):

$$\hat{\sigma}_{\mathrm{pQCD}}(d_\perp^2, x) = \frac{\pi^2}{3}\, d_\perp^2\, \alpha_s(\bar{Q}^2)\, xG^T(x, \bar{Q}^2)\,. \tag{7.1.1}$$

which is a generalization of the two-gluon exchange model of [33] (see also references in [12]). Here $d_\perp$ is the transverse diameter of the dipole, xG^T is the leading-log gluon distribution of the target sampled at a scale $\bar{Q}^2 = \lambda/d_\perp^2$, with λ a logarithmic function of Q^2. There are of course corrections, involving more complicated partonic configurations such as $q\bar{q}g$, which in general can not be described (except in special circumstances) using the interactions of dipoles of a given colour configuration. However, the description of small-x processes in terms of an *interaction cross section* for the hadronic fluctuations of the photon remains a useful one.

For heavy nuclear targets, it is legitimate to neglect a logarithmic increase of the effective radius of the target with increasing energy. In this case there is, of course, a natural geometrical upper limit to the size of this inelastic interaction cross section given approximately by the transverse cross-sectional area of the target:

$$\hat{\sigma}_{\mathrm{pQCD}} \leq \sigma_{\mathrm{black}} = \pi R_T^2\,. \tag{7.1.2}$$

It seems plausible that small-x physics of the next generation of accelerators will be a combination of two generic phenomena, *generalised colour transparency* and *complete opacity* (absorption), which correspond to two different kinematical limits. In one limit, when x is fixed and $Q^2 \to \infty$, hard processes exhibit numerous colour transparency phenomena, which can be described in terms of various generalisations of the QCD factorization theorem. In another limit, when Q^2 is fixed and $x \to 0$, the interaction cross

section increases with decreasing x (increasing energy), which leads to increased absorption by the target. Hence, in this kinematical limit, the approximation of complete absorption, which could naturally be termed "the black body limit (BBL)", seems to be a promising guide to predict new distinctive hard QCD phenomena. Colour Transparency is a generic name used to describe the fact that small colourless configurations do not interact strongly with hadrons, which is reflected by the inclusion of the transverse diameter squared, $d_\perp^2$, in (7.1.1). However, for a fixed dipole size (and neglecting for a moment an increase with increasing energy of the radius of a target which can be justified for heavy nuclear targets only), if the gluon density of the target continues to rise with increasing $1/x$, the interaction cross section will eventually reach its geometrical limit (cf. (7.1.2)). This is basically what is meant by complete opacity.

The validity of the BBL can be justified for DIS processes off heavy nuclear targets since contributions of colour transparency, and various peripheral phenomena (which complicate studies of BBL for nucleon targets) are suppressed. In the BBL, the nuclear structure function $F_2^A(x, Q^2)$ is predicted to behave as $R_A^2 Q^2 \ln 1/x$ with decreasing x, which is slower than the x-behaviour predicted by the DGLAP evolution equations. Since the nucleon is "gray" rather than "black" as seen by the incoming high-energy fluctuation, peripheral effects are important and contribute to the total electron-nucleon DIS cross section (these effects lead to an increase of the essential impact factors with increasing energy). The nucleon structure function (gluon distribution) behave as $F_2^N\,(xG^N) \propto Q^2 R_N^2 \ln^3 1/x$ in the black body limit. In both the nuclear and nucleon cases, the expression for the total cross sections is a direct generalization of the Froissart unitarity limit [34] to DIS (see subsection 7.1.3). One has to distinguish two features of these results. Firstly, the predicted Q^2-independence of total cross sections grossly violates Bjorken scaling and serves as a very clean signal of the onset of the BBL regime. Secondly, the predicted energy (or x) dependence of the total electron-nucleon (but not electron-nucleus) cross section (nucleon structure functions) can probably be accommodated within the DGLAP LT pQCD framework by a suitable subtle re-tuning of the initial conditions (this has been the pattern in the era of HERA). Hence, it would be difficult to distinguish between the DGLAP and black body approximations and predictions thereof for the nucleon structure functions. A much more promising way to identify the BBL regime is to investigate the difference between the x dependence of nucleon structure function and the structure functions of heavy nuclei, as well as final states in DIS on nucleons and nuclei for which the BBL predicts several rather striking new phenomena.

By fixing Q^2 and decreasing x, one proceeds from the DGLAP regime to the BBL regime. Theoretical models attempting to quantify deviations from the DGLAP approximation and define the kinematical boundaries of the applicability of the DGLAP equations agree that the effects, which are responsible for the inapplicability of the DGLAP dynamics, are enhanced for nuclear targets by approximately a factor of $A^{1/3}$ if the approximation is made that the HT effects and nuclear shadowing of parton distributions are a correction [35]. Neglecting non-perturbative nuclear shadowing of the gluon distribution, one can estimate the ratio of the critical x at which the BBL regime sets in for DIS on nuclei and nucleon, as $x_A(\mathrm{BBL})/x_N(\mathrm{BBL}) \approx (A/2)^{1/(3n)}$ (the factor n

comes from the energy dependence of the nucleon structure function F_2^N in the form $F_2^N \propto x^{-n}$). The factor 1/2 in this relation accounts for the difference between the nucleon radius, $r_N = 0.85$ fm, and a mean inter-nucleon distance in nuclei, $r_{NN} = 1.7$ fm.

Note that the complication of taking non-perturbative nuclear shadowing in nuclear parton distributions into account slightly reduces the advantage of using nuclear targets over nucleon ones for studying higher twist effects.

Since the DGLAP QCD evolution equations are leading twist equations, any violations of the DGLAP equation would signal a non-negligible role of higher twist effects. Therefore, a unique feature of electron-nucleus collisions is that by studying DIS on nuclear targets one can not only amplify the higher twist effects but also study them as a function of the target thickness (by varying nucleon number A).

In order to summarize the above discussion, we would like to re-emphasize that using nuclear beams in THERA has significant advantages over using a proton beam in studying new QCD phenomena such as the perturbative regime of very high parton densities and the transition from the DGLAP regime to black body scattering[1]. Since these phenomena depend on the nucleon number, A, measurements of various observables as a function of A will be necessary. Fortunately this will be practical at THERA. The BBL interpretation of many phenomena, including the difference between the x-dependence of heavy nucleus and nucleon structure functions and some properties of final states, does not require knowledge of nuclear effects. It is clear that a consistent and complete interpretation of some experimental data would require reliable information about traditional nuclear effects at small x, primarily nuclear shadowing. However, as we shall explain in detail in Sect. 7.1.5, using the profound connection between nuclear shadowing in inclusive electron-nucleus DIS and hard electron-proton diffraction, the QCD factorization theorem and modern fits to the diffractive data, one can significantly reduce uncertainties in the predictions of the leading twist part of nuclear parton densities.

The rest of this section is organized as follows. The black body limit is discussed in Sect. 7.1.3. We demonstrate that predictions made in the BBL are strikingly different from those obtained within the DGLAP approximation, especially for final states in DIS diffraction on nuclei. Precursors of the BBL can be studied by analysing the departure from the leading twist DGLAP evolution equation using the unitarity of the S-matrix for hard interactions as a guide. In Sect. 7.1.4, we discuss the relevant effects for a range of nuclei at central impact parameters. It is found that our predictions are sensitive to the amount of leading twist nuclear shadowing, which is considered in Sect. 7.1.5. It is also demonstrated that in a wide range of x and Q^2, leading twist shadowing dominates over higher twist shadowing, used frequently in eikonal-type models. After briefly considering experimental requirements in Sect. 7.1.6, we conclude in Sect. 7.1.7.

[1]Formally, the notion of parton densities is defined in the leading twist approximation only. Thus, when discussing physics beyond the DGLAP approximation, one should be cautious and explicit in using the term "parton density".

7.1.3 The black body limit and its signals in DIS final states

The leading twist (LT) approximation of perturbative QCD successfully describes DIS of photons on hadronic targets [5] and predicts a rapid increase [2] of structure functions with increasing energy (decreasing x). Within the LT approximation, there is no mechanism which would slow down or tame the rapid growth of the structure functions [3].

However, it is clear that a rapid power-like growth of the structure functions (at a given impact parameter) cannot continue forever [4] and, hence, the LT approximation must be violated at very small x. Therefore, some higher-twist mechanism is required to explain the taming of the structure functions. A practical and almost model-independent approach to the taming of the structure function is based on the analysis of the unitarity of the S-matrix for the interaction of spatially small quark-gluon wave packets.

7.1.3.1 Unitarity and the black body limit

The most direct way to understand the constraints which are imposed by unitarity of the scattering matrix (for hadronic fluctuations of the virtual photon) on the nucleon and nucleus structure functions is to use the *impact-parameter representation* for the scattering amplitude. As explained in the introduction, in the target rest frame the incoming photon interacts with the target via its partonic fluctuations. Since the interaction time is much shorter than the life-time of the fluctuations at small x, the DIS amplitude can be factorised in three factors: one describing the formation of the fluctuation, another – the hard interaction with the target, and a final factor describing the formation of the hadronic final state. The $q\bar{q}$ dipole is the dominant fluctuation at short transverse distances, and we consider its interaction primarily in what follows.

Within this high-energy factorization framework the structure functions, F_L and F_T, may be written in the following simple way

$$F_{L,T}(x,Q^2) = \int dz\, d^2d_\perp |\psi^\gamma_{L,T}(z,d^2_\perp,Q^2)|^2 \frac{Im\, A(s,t=0,d^2_\perp)}{s}\,, \tag{7.1.3}$$

where $\psi^\gamma_{L,T}(z,d^2_\perp,Q^2)$ are the light-cone wavefunctions of the longitudinally and transversely polarised virtual photon, respectively, z is the photon momentum fraction carried by one of the dipole constituents, s is the invariant energy of the dipole-target system ($s=(P+q)^2$ for the $q\bar{q}$ dipole), $t \approx -|\vec{q}'_\perp|^2$ is the momentum transfer and $d_\perp$ is the dipole's transverse diameter.

[2] This can be either introduced by hand at the initial evolution scale or generated by QCD evolution [36].

[3] One can show by direct pQCD calculations that the taming (shadowing) of parton densities at small x considered in eikonal and parton recombination models is a higher twist effect.

[4] At the same time, conventional nucleon structure functions integrated over all impact parameters may increase with increasing energy even faster (according to the $\propto \ln^3 1/x$ law) than predicted by DGLAP.

The dipole-target scattering amplitude $A(s,t,d_\perp^2)$ can be expressed via the corresponding amplitude, $f(s,b,d_\perp^2)$, in impact-parameter, b, space ($b = b_\perp$ is Fourier conjugate to $q'_\perp$):

$$A(s,t,r^2) \equiv 2s \int d^2b\, e^{i\vec{q}'\cdot\vec{b}} f(s,b,r^2) \ . \tag{7.1.4}$$

The scattering amplitude $f(s,b,d_\perp^2)$ is related to the total cross section for the scattering of dipoles of fixed transverse diameter, $d_\perp$, by the optical theorem:

$$\sigma_{\rm tot}(s,d_\perp^2) = 2 \int d^2b\, Im\, f(s,b,d_\perp^2) \ . \tag{7.1.5}$$

The unitarity of the scattering S-matrix [37] ($S_{ab} = \delta_{ab} + i f_{ab}$, $S^\dagger_{ac} S_{cb} = \delta_{ab}$) imposes the following conditions [5] on the scattering amplitudes (for each b, a continuum analogy of angular momentum in a partial wave analysis in non-relativistic quantum mechanics):

$$Im f_{aa}(s,b,d_\perp^2) = \frac{1}{2}(f^\dagger_{aa} f_{aa} + \Sigma_{c,c\neq a} f^\dagger_{ac} f_{ca}) \ , \tag{7.1.6}$$

where "a,c" are labels for definite states (on the right hand side we suppress the variables $s, b, d_\perp$ for clarity). The first and second terms on the right hand side of (7.1.6) involve elastic and inelastic final states, respectively.

The black body limit (BBL) assumes that: (i) configurations with the impact parameters satisfying $b^2 \leq b^2_{\rm max}$ are completely absorbed by target, i.e. the elastic matrix elements of the S-matrix are zero for those impact parameters: $S_{aa}(b \leq b_{\rm max}) = \delta_{aa} + i f_{aa}(b \leq b_{\rm max}) = 0$. This implies that $Im f_{aa}(s, b <_{\rm max}, d_\perp^2) = 1$, and leads to $|f_{aa}(s,b,d_\perp^2)|^2 = \Sigma_{c,c\neq a} |f_{ac}(s,b,d_\perp^2)|^2$ that is to the equality of the elastic and inelastic contributions to the total cross section. (ii) the region $b^2 \leq b^2_{\rm max}$ gives the dominant contribution to the scattering amplitude (7.1.5). The great advantage of the BBL is that calculations of the amplitudes of some small-x processes do not require specific model assumptions. Moreover, as will be discussed later, the BBL approximation seems to be realistic for DIS on heavy nuclear targets.

The dependence of $f(s,b,d_\perp^2)$ on the impact parameter, b, at large b follows from analytic properties of the scattering amplitude $A(s,t,d_\perp^2)$ in t-plane. A simple analysis leads to $f(s,b,d_\perp^2) = c\, \exp(-\mu b)$ at large b, where $c \propto x G^T(x,d_\perp^2) \propto 1/x^n$. Hence, following Froissart [34, 37] we may evaluate the maximal impact parameter characterising the black body limit. One obtains $b^2_{\rm max} \propto 1/\mu^2 \ln^2 1/x$ for a nucleon target, and $b^2_{\rm max} = R_A^2$ for a heavy nuclear target (R_A being the radius of the nucleus). Note that the difference between $b^2_{\rm max}$ for the nucleon and nuclear case reflects the fact that the nucleon target is not a homogeneous sphere but rather an object with an extended diffuse edge.

[5] A rather straightforward way to deduce unitarity of the S-matrix is to consider amplitudes for the scattering of bound states of fictitious heavy quarks Q and the prove that, for sufficiently large mass of the quarks M_Q and small x, dipole scattering would dominate. In order to complete the derivation, one also needs to use the fact that QCD is flavour blind if the resolution scales are chosen appropriately.

Using these relationships, for the total dipole-nucleon scattering cross section (see also (7.1.5)) in the BBL approximation, one obtains

$$\hat{\sigma}_{\rm tot}(s, d_\perp^2) = 2\pi(R_N^2 + 4c_N \ln^2 1/x)\,. \tag{7.1.7}$$

In addition to the total cross section, one can examine the t-dependence of the cross section, corresponding to the amplitude in (7.1.4), defined through its slope, B:

$$\frac{d\ln\sigma(s,t)}{dt}\Big|_{t=0} = B = B_0 + 2\alpha'_{\rm eff}\ln 1/x = \frac{\int d^2b\, b^2 f(s,b,d_\perp^2)}{2\int d^2b\, f(s,b,d_\perp^2)}\,, \tag{7.1.8}$$

where $\alpha'_{\rm eff} \equiv d\ (B/2)/d\ln 1/x$. We use above that the t-dependence of the real and imaginary parts of the amplitude is the same. In the BBL, one obtains

$$\begin{aligned} B &= \frac{b_{\rm max}^2}{4} = \frac{R_T^2}{4} + c_T \ln^2 1/x\,, \\ \alpha'_{\rm eff} &= c_T \ln 1/x\,. \end{aligned} \tag{7.1.9}$$

Here R_T is the radius of the target, c_T is a factor which is similar for nucleon and nucleus targets. Hence for practical purposes, one can neglect c_T for heavy nuclear targets.

Finally, the proton structure function (at fixed Q^2) in the BBL reads

$$F_2^p(x,Q^2) \propto \sum_i e_i^2 Q^2 \frac{2\pi R_N^2}{12\pi^3}(1 + \frac{4c_N^2}{R_N^2}\ln^2 x_0/x)\ln 1/x\,. \tag{7.1.10}$$

Here the sum is taken over electric charges e_i of active quark flavours i. Note that the additional factor of $\ln 1/x$ in (7.1.10) as compared to (7.1.7) is due to the contribution of large masses resulting from the singular nature of the photon wavefunction. This reflects the logarithmic divergence of renormalization coupling constant for the electric charge (cf. (7.1.13) below). As one sees from (7.1.10), general principles of QCD and, in particular, the BBL approximation, do not exclude a fast ($\ln^3 1/x$) increase of the structure functions of a nucleon at $x \to 0$. In addition, the contribution from dipoles with the impact parameters larger than $b_{\rm max}$ or sufficiently small dipoles (which are assumed to give a small contribution in the BBL approximation) should continue to increase with increasing energy as dictated by the DGLAP approximation of QCD. Thus, in practice, it would be very difficult, or even impossible, to distinguish the BBL prediction (7.1.10) from a similarly rapid growth predicted by the DGLAP equation and to search for saturation effects in inclusive nucleon structure functions. Hence, one should turn to DIS on nuclear targets in order to search for distinct signals of BBL dynamics.

The use of nuclei has two clear advantages. Firstly, scattering at large impact parameters, where the interaction is far from the BBL over a wide range of energies (the edge effects), is suppressed by the factor R_N/R_A. Secondly, in a broad range of impact parameters, $b \le R_A$, the nuclear thickness is practically b-independent and much larger than in a nucleon. Hence, DIS on sufficiently heavy nuclei can serve as

a good testing ground for the application of the BBL and will allow us to pinpoint some distinctive features of it. For example, as follows from the above discussion, the unitarity of S-matrix significantly tames the rapid grows of the nuclear structure functions and predicts the unitarity limit

$$F_2^A(x,Q^2) = \sum_i e_i^2 Q^2 \frac{2\pi R_A^2}{12\pi^3} \ln 1/4 m_N R_A x \,. \tag{7.1.11}$$

Over the last few years a number of models, using the infinite momentum frame, were suggested in order to explain the dynamics of DIS at small x by building the nuclear wave function from large gluon fields and assuming a certain saturation of the parton densities (for the review and references see e.g., [38]). In many respects, these models and the BBL approximation are similar.

The BBL in DIS from a heavy nucleus at small x was first considered by Gribov [39], before the discovery of QCD. Gribov assumed that each hadronic fluctuation of the virtual photon interacts with the target nucleus with the same maximal strength allowed by unitarity. Such an assumption, supported by the observed cross sections of hadron-nucleus interactions, was natural for understanding the dynamics of soft strong interactions in models predating QCD.

Thus, in the black body limit, DIS on nuclei is dominated by the dissociation of the incoming virtual photon into its hadronic fluctuations, which subsequently interact with the target with the same scattering cross sections $2\pi R_A^2$, and then hadronize into final states with mass M. The transverse and longitudinal nuclear structure functions may be conveniently formulated as an integral over produced masses

$$F_T^A(x,Q^2) = C \int_{M^2_{\rm min}}^{M^2_{\rm max}} dM^2 \, \frac{2\pi R_A^2}{12\pi^3} \frac{Q^2 M^2 \rho(M^2)}{(M^2+Q^2)^2} \,, \tag{7.1.12}$$

$$F_L^A(x,Q^2) = C \int_{M^2_{\rm min}}^{M^2_{\rm max}} dM^2 \, \frac{2\pi R_A^2}{12\pi^3} \frac{Q^4 \rho(M^2)}{(M^2+Q^2)^2} \,, \tag{7.1.13}$$

where $\rho(M^2) = \sigma^{e^+e^-\to \rm hadrons}(M^2)/\sigma^{e^+e^-\to\mu^+\mu^-}(M^2)$. In the BBL, the coefficient $C = 1$. The upper cutoff, $M^2_{\rm max} \ll W^2 \approx 2q_0 m_N$, comes from the nuclear form factor:

$$-\frac{t_{\rm min} R_A^2}{3} \approx \frac{(M^2+Q^2)^2}{4q_0^2} R_A^2/3 \approx m_N^2 x^2 \frac{R_A^2}{3} \ll 1 \,. \tag{7.1.14}$$

The key element of the derivation of (7.1.13) is the observation that in the BBL, as a result of orthogonality of the wave functions of the eigenstates of QCD Hamiltonian with different energies, the non-diagonal transitions between states with different M^2 are zero. This enables one to write the structure functions as a single dispersive integral as is done in (7.1.13). Since (7.1.13) leads to a cross section for $\gamma^* A$ scattering grossly violating Bjorken scaling ($\sigma_{\rm tot}^{\gamma^* A}(x,Q^2) \propto \pi R_A^2 \ln(1/x)$ instead of $\propto 1/Q^2$), the BBL has been considered for some time to be an artifact of the pre-QCD physics. This is especially so since, within the parton model, the aligned jet model removed this gross

scaling violation [40]. However, for consistency of the target rest frame and infinite momentum frame descriptions, an exponential suppression with decreasing $d_\perp^2$ of the cross section of interaction of small-size configurations with hadrons was assumed to be required. This fact was subsequently explained and understood in terms of the QCD factorization theorem for the scattering of small dipoles, colour neutrality of the dipole and asymptotic freedom for hard processes in QCD (and the "suppression" was realised only to be only a single power in $d_\perp^2$, cf. (7.1.1)).

In perturbative QCD, the dipole-target cross section (7.1.1), rapidly increases with increasing energy since the gluon density rapidly increases with decreasing x. Hence, if the increase of the interaction cross section is not tamed by some mechanism, it will reach values expected for the black body limit (i.e. tens of mb, cf. (7.1.2)).

Properties of the BBL in QCD are somewhat different from those within the Gribov picture due to a significant probability of smaller than average size configurations in the photon wave function, for which the conditions of the black body limit are not satisfied. As a result, the interaction of such small-size configurations is not tamed. Thus, in contrast to the Gribov approach, only a fraction of all configurations will interact according to the BBL approximation and therefore $C < 1$ in (7.1.13).

Using (7.1.1), it is straightforward to estimate the kinematical boundaries where the unitarity limits may be reached. Indeed, the requirement that $\sigma_{\rm el} \leq \sigma_{\rm tot}/2$ [18, 25] (also assuming that (7.1.1) is applicable for the range of x in which the taming is necessary) indicates that for some gluon-induced hard processes the unitarity limit should be well within the reach of an electron-nucleus collider at HERA/THERA (for a review see [11]).

One can also make an interesting prediction about nuclear shadowing. Since the x-dependence of the nuclear structure function of (7.1.11) is significantly weaker than that for the proton structure function of (7.1.10), nuclear shadowing is not saturated (as is often assumed in the limit of fixed Q^2 and $x \to 0$), and we find

$$\frac{F_2^A(x,Q^2)}{AF_2^N(x,Q^2)} \propto \frac{R_A^2}{AR_N^2}\frac{1}{1+4c_N^2R_A^2\ln^2 1/x} \ . \tag{7.1.15}$$

However, at unrealistically small x, where the impact parameters become significantly larger than R_A, this effect will disappear.

In summary, since the contributions of small configurations (which have not reached the black body limit) remain significant in a wide range of x and Q^2, studies of the total cross sections are a rather ineffective way to the search for the onset of the BBL regime. In particular, it may be rather difficult to distinguish the BBL from DGLAP approximation with different initial conditions in this way.

In what follows we shall demonstrate that studies of DIS final states provide a number of clear signatures of the onset of the BBL regime, which will be qualitatively different from the leading twist regime. For simplicity, we will assume that the BBL is reached for a significant part of the cross section and, hence, restrict our discussion to DIS on a large nucleus so that edge effects (which are important in the case of scattering off a nucleon) can be neglected.

7.1.3.2 Diffractive final states

The use of Gribov's orthogonality argument (to neglect non-diagonal transitions in (7.1.13)) allows the integrals over the masses to be removed in the expressions for the structure functions and, since diffraction is 50% of the total cross section in the BBL, we immediately find for the spectrum of diffractive masses:

$$\frac{dF_T^{D(3)}(x,Q^2,M^2)}{dM^2} = \frac{\pi R_A^2}{12\pi^3}\frac{Q^2M^2\rho(M^2)}{(M^2+Q^2)^2} ,$$
$$\frac{dF_L^{D(3)}(x,Q^2,M^2)}{dM^2} = \frac{\pi R_A^2}{12\pi^3}\frac{Q^4\rho(M^2)}{(M^2+Q^2)^2} . \tag{7.1.16}$$

Moreover, the spectrum of hadrons in the centre of mass of the diffractively produced system should be the same as in e^+e^- annihilation. Hence, the dominant diffractively-produced final state will have two jets with a distribution over the centre of mass emission angle proportional to $1+\cos^2\theta$ for the transverse case and $\sin^2\theta$ for the longitudinal case:

$$\frac{dF_T^{D(3)}(x,Q^2,M^2)}{dM^2 d\cos\theta} = \frac{3}{8}(1+\cos^2\theta)\frac{\pi R_A^2}{12\pi^3}\frac{Q^2M^2\rho(M^2)}{(M^2+Q^2)^2} , \tag{7.1.17}$$

$$\frac{dF_L^{D(3)}(x,Q^2,M^2)}{dM^2 d\cos\theta} = \frac{3}{4}\sin^2\theta\frac{\pi R_A^2}{12\pi^3}\frac{Q^4\rho(M^2)}{(M^2+Q^2)^2} . \tag{7.1.18}$$

The transverse momentum of the jet, p_t, and the longitudinal fraction of photon energy, z, carried by the jet are related to the diffractive mass, M, and the angle, θ, as follows (we neglect here the quark masses as compared to Q, M):

$$p_t = \frac{M}{2}\sin\theta ,$$
$$z = (1+\cos\theta)/2 . \tag{7.1.19}$$

Hence, in the BBL, diffractive production of high p_t jets is strongly enhanced:

$$\langle p_t^2(jet)\rangle_T = 3M^2/20 ,$$
$$\langle p_t^2(jet)\rangle_L = M^2/5 . \tag{7.1.20}$$

This is to be compared to the leading twist approximation where it is $\propto \ln Q^2$. The relative rate and distribution of the jet variables for the three jet events (originating from $q\bar{q}g$ configurations) will be also the same as in e^+e^- annihilation and hence is given by the standard expressions for the process $e^+e^- \to q\bar{q}g$ (see e.g. [41]).

An important advantage of the diffractive BBL signal is that these features of the diffractive final state should hold for $M^2 \le Q^2_{BBL}$ even for $Q^2 \ge Q^2_{BBL}$ because configurations with transverse momenta $\le Q_{BBL}/2$ still interact in the black regime

(and correspond to transverse size fluctuations for which the interaction is already black).

Another interesting feature of the BBL is the spectrum of the leading hadrons in the virtual photon fragmentation region produced in DIS. The spectrum is essentially given by the θ-dependence of (7.1.17) and (7.1.18). For fixed M^2, the jet distribution over z for transversely polarised photons is simply

$$\frac{d\sigma_T}{dz} \propto 1 + (2z-1)^2 \,. \tag{7.1.21}$$

Similarly, for longitudinally polarised photons,

$$\frac{d\sigma_L}{dz} \propto \; z(1-z) \,. \tag{7.1.22}$$

If no special separation procedure is undertaken, at small x one actually measures $\sigma_L + \epsilon\sigma_T$ (ϵ is the photon polarisation). In this case, combing (7.1.17) and (7.1.18) we find:

$$\frac{d(\sigma_T + \epsilon\sigma_L)}{dz} \propto \frac{M^2}{8Q^2}(1 + (2z-1)^2) + \epsilon z(1-z) \,. \tag{7.1.23}$$

Exclusive vector meson production in the BBL is in a sense a resurrection of the original vector meson dominance model [42] without off-diagonal transitions. The amplitude for the vector meson-nucleus interaction is proportion to $2\pi R_A^2$ (since each configuration in the virtual photon interacts with the same BBL cross section). This is markedly different from the requirements [43] for matching generalised vector dominance model (see e.g., [44]) with QCD in the scaling limit, where the non-diagonal matrix elements are large and lead to strong cancellations. Hence, we can factorize out the cross section for the dipole interaction from the overlap integral between wavefunctions of virtual photon and vector meson to obtain for the dominant electroproduction of vector mesons

$$\begin{aligned} \frac{d\sigma^{\gamma_T^* + A \to V + A}}{dt} &= \frac{M_V^2}{Q^2}\frac{d\sigma^{\gamma_L^* + A \to V + A}}{dt} = \\ \frac{(2\pi R_A^2)^2}{16\pi}\frac{3\Gamma_V M_V^3}{\alpha(M_V^2+Q^2)^2}\frac{4\,\left|J_1(\sqrt{-t}R_A)\right|^2}{-tR_A^2}, \end{aligned} \tag{7.1.24}$$

where Γ_V is the electronic decay width $V \to e^+e^-$, α is the fine-structure constant, and $J_1(x)$ is the Bessel function. Thus the parameter-free prediction is that in the BBL at large Q^2 vector meson production cross sections have a $1/Q^2$ behaviour, in stark contrast to an asymptotic behaviour of $1/Q^6$ predicted in perturbative QCD [7, 18, 19].

In order to observe the onset of the BBL regime for a nucleon target, one should consider scattering at small impact parameters. However, a direct comparison of the BBL prediction for small b with data is very difficult since, in the BBL, the amplitude oscillates as a function of t. Also, in the case of a proton target, a significant nucleon spin-flip amplitude may mask these oscillations.

7.1.3.3 Inclusive spectra

In the leading twist approximation, the QCD factorization theorem is valid and leads to universal spectra of leading particles (independent of the target) for the scattering off partons of the same flavour. Fundamentally, this can be explained by the fact that, in the Breit frame, the fast parton which is hit by the photon carries practically all of the photon's light-cone momentum ($z \to 1$). Due to QCD evolution, this parton acquires virtuality $\sim Q^2$, and a rather large transverse momentum, k_t (which is still $\ll Q^2$). So, in pQCD, quark and gluons emitted in the process of QCD evolution and in the fragmentation of highly virtual partons together still carry all the photon momentum. In contrast, in the BBL, configurations in which partons carry all of the photon momentum form only part of cross section of leading hadron production. Another part is from inelastic collisions of configurations where all partons carry appreciable momentum fractions and large relative transverse momenta (these configurations are rather similar to the case of diffractive scattering (see e.g. (7.1.17) and (7.1.18))). Hence, in the BBL case, the spectrum of leading hadrons (in the direction of the virtual photon) is expected to be much depleted.

The inclusive spectrum of leading hadrons can be estimated as due to the independent fragmentation of quark and antiquark of virtualities $\geq Q^2$, with z and $p_\perp$ distributions given by (7.1.17) and (7.1.18) (cf. the case of diffractive production of jets discussed above). The independence of fragmentation is justified because large transverse momenta of quarks dominate in the photon wave function (cf. eqs. (7.1.17, 7.1.18, 7.1.19) and because of the weakness of the final state interaction between q and $\bar{q}$, since the α_s is small and the rapidity interval is of the order of one. Obviously, this leads to a gross depletion of the leading hadron spectrum as compared to the leading twist approximation situation where leading hadrons are produced in the fragmentation region of the parton which carries essentially all momentum of the virtual photon [6]. Taking the production of multi-jet states like $q\bar{q}g$ into account will further enhance this scaling violation. If we neglect gluon emissions in the photon wave function, we find, for instance:

$$\frac{dN^{\gamma_T^*/h}}{dz} = 2 \int_z^1 D^{q/h}(z/y, Q^2) \frac{3}{4}(1 + (2y-1)^2) dy \,, \tag{7.1.25}$$

for the total differential multiplicity of leading hadrons produced by transversely polarised virtual photons, in the BBL. $D^{q/h}(z/y, Q^2)$ is the fragmentation function of a quark with flavour q into the hadron h. Here we use that $D^{u/h}(z/y, Q^2) = D^{d/h}(z/y, Q^2)$ and neglect a small difference in the fragmentation functions of light and heavy quarks.

An illustration of the results of the calculation of $dN^{\gamma_T^*/h}/dz$ is presented in Fig. 1. We normalise the distribution to the leading twist case by using realistic up-quark fragmentation functions at $Q^2 = 2$ GeV^2 [45] (the up and down quark distributions are similar and we neglect the small difference induced by including further flavours). One

[6] Qualitatively, this pattern is similar to the one expected in the soft region since the spectrum of hadrons produced in hadron-nucleus interactions is much softer than for hadron-nucleon interactions.

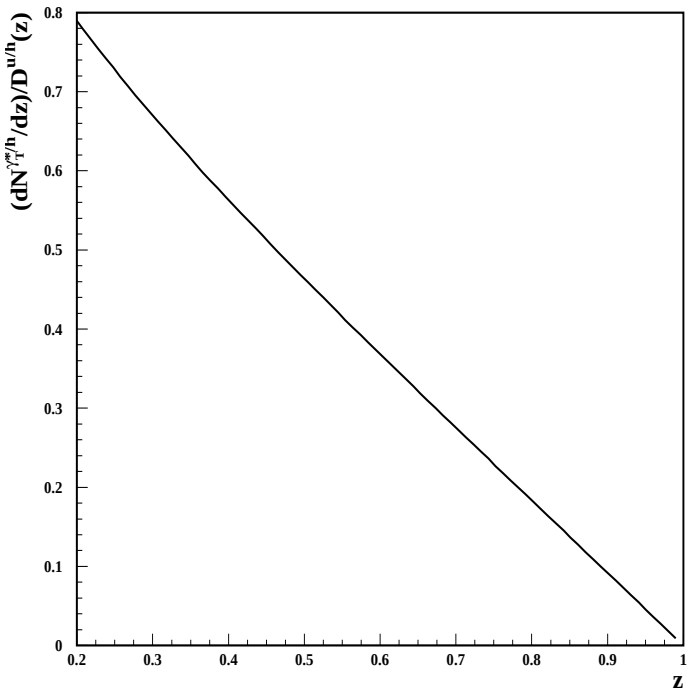

Figure 1: *The total differential multiplicity normalized to the up quark fragmentation function [45], $(dN^{\gamma_T^*/h}/dz)/D^{u/h}(z,Q^2)$, as a function of z at Q^2=2 GeV^2 calculated in the BBL using (7.1.25).*

can see from the figure that a gross violation of the factorization theorem is expected in the BBL. The spectrum of leading hadrons is much softer at large z, with an excess multiplicity at $z \leq 0.1$. Note that the use of leading twist fragmentation functions in the above expression probably underestimates absorption. So the curve in Fig.1 can be considered as a conservative lower limit for the amount of suppression.

With an increase of Q^2 we expect a further softening related to a change in the partonic structure of the virtual photon wave function. Progressively more configurations contain extra hard gluons, which fragment independently in the BBL, further amplifying deviations from the standard leading twist predictions.

Another important signature of the BBL is the change of p_t distributions with decreasing x (at fixed Q^2). The spectrum of the leading hadrons should broaden due to increased p_t of the fragmenting partons. Hence, the most efficient strategy would be to select leading jets in the current fragmentation region and examine the z and p_t-dependence of such jets. Qualitatively, the effect of broadening of p_t-distributions is similar to the increase of the p_t distribution in the model [46], although final states in DIS were not discussed in this model.

An important advantage of inclusive scattering off a nucleus is the possibility to use a centrality trigger. For example, one could use the number of nucleons emitted in the nucleus decay (soft nucleons in the nucleus rest frame) to select scattering at the central impact parameters. Such a selection allows the effective thickness of the

nucleus to be increased, as compared to the inclusive situation, by a factor ~ 1.5 and, hence, allows for the BBL to be reached at significantly larger x. The signal for the BBL will be a change of the spectrum with centrality of the collisions, in contrast to the LT case where no such correlation is expected. Note that the lack of absorption of leading particles in DIS off nuclei at the fixed target energies and $Q^2 \geq 2$ GeV^2 is well established experimentally, see e.g. [47].

To summarise, predictions for a number of simple final state observables in the black body limit are distinctly different from those made in the leading twist approximation and, hence, will provide model-independent tests of the onset of the BBL.

7.1.4 Unitarity constraints for electron-nucleus DIS

While predictions for inclusive DIS and DIS final state observables in the BBL are distinct, one still would like to determine the kinematical region where the regime of the BBL sets in. One way to address this issue it to examine the unitarity of the S-matrix for the interactions of purely perturbative QCD fluctuations.

7.1.4.1 The interaction of small colour dipoles with hadrons

The dipole picture of electron-target DIS is valid when the lifetime of the fluctuation is much longer than the interaction time with the target. Equally, this relation may be expressed in terms of the *coherence length*, l_{coh}, of the fluctuation (relative to the target radius). This length is given by the average longitudinal distances (Ioffe distances) in the correlator of the electromagnetic currents which determine the structure function $F_2(x, Q^2)$. A simple analysis shows that $l_{coh} \sim 1/(2m_N x)$. At HERA l_{coh} can reach values of 10^3 fm (for moderate Q^2 only). As Q^2 increases, the scaling violations lead to a gradual reduction of l_{coh} at fixed x and ultimately to the dominance of longitudinal distances $\sim R_N$ (for a discussion see [11]).

In the target rest frame, when l_{coh} is sufficiently large, the virtual photon can fluctuate into a variety of partonic configurations containing various numbers of partons and involving different transverse sizes. The simplest is a $q\bar{q}$ dipole, which dominates at very small distances. Since under $\mathrm{SU}(3)_c$ transformations the quark and the anti-quark transform in the fundamental representation (like 3 and $\bar{3}$) the name "colour triplet" is often used for the $q\bar{q}$ pair (although overall its colour is of course neutral). The $q\bar{q}$-dipole of a small diameter interacts with a hadronic target with an interaction cross section given by (7.1.1). Another important photon fluctuation is the one consisting of a quark, anti-quark and gluon, with a relatively large transverse momentum between the quark and the anti-quark. Such configurations effectively transform in the adjoint representation (effectively 8, $\bar{8}$) and so are known as the *$q\bar{q}g$ colour octet dipole*. There are of course other $q\bar{q}g$ configurations, for example those in which the gluon and either the quark or anti-quark have a large relative transverse momentum (these merely correspond to the $\mathcal{O}(\alpha_s)$ corrections to the colour triplet dipole) and other more general configurations which do not correspond to dipoles at all.

For the case of scattering of colour octet dipoles off a target, the corresponding

cross section is enhanced a colour factor (given by the ratio of the Casimir operators of $SU(3)_c$), $C_F(8)/C_F(3) = 9/4$ [25, 32, 48]:

$$\begin{aligned} \hat{\sigma}^{\text{octet}}_{\text{pQCD}}(d_\perp^2, x) &= \frac{9}{4}\,\hat{\sigma}^{\text{triplet}}_{\text{pQCD}}(d_\perp^2, x) \\ &= \frac{3\pi^2}{4}\, d_\perp^2\, \alpha_s(\bar{Q}^2)\, xG_T(x, \bar{Q}^2)\,. \end{aligned} \tag{7.1.26}$$

Both (7.1.1) and (7.1.26) predict cross sections steeply rising with increasing energy (driven by the rise of the gluon density with decreasing x). Fitting the energy dependence in the form [7] $\sigma_{\text{pQCD}}(s, Q^2) \propto s^{n(Q^2)}$, one finds

$$\begin{aligned} n\ (Q^2 = \ 4\ \text{GeV}^2) &\approx 0.2\ , \\ n\ (Q^2 = 40\ \text{GeV}^2) &\approx 0.4\ . \end{aligned} \tag{7.1.27}$$

One of the manifestations of the behaviour predicted by (7.1.27) is the Q^2-behaviour of the measured exclusive vector meson production. The interaction cross sections of (7.1.1) and (7.1.26) may be thought of as a complimentary description of the physics described by the leading log QCD evolution equations at small x. However, an accurate determination of the relation between $\bar{Q}^2$ and the transverse size $d_\perp$ in these equations requires a next-to-leading order QCD analysis in this framework which has not been done yet. Numerical studies [19, 31] based on matching of the $d_\perp$-space and Q-space expressions for $\sigma_L(x, Q^2)$, lead to $\lambda \sim 9 - 10$ for a sufficiently broad range of Q^2 and x. With this choice of λ, a good description of the recent inclusive DIS electron-proton data was obtained (with a suitable extrapolation to large $d_\perp$ [31]) without any further fitting. As already mentioned, λ is a logarithmically-decreasing function of the dipole size $d_\perp$. In particular, at large values of $d_\perp$, $d_\perp \geq 0.3$ fm, where connection between $d_\perp^2$ and Q^2 is rather sensitive to non-perturbative effects, one expects a decrease of λ with increasing $d_\perp^2$. On the other hand, it was found that variations in λ do not significantly effect values of $\hat{\sigma}_{\text{pQCD}}(d_\perp^2, x)$. Hence, our following estimates of the unitarity constraints, which are made using (7.1.1) and (7.1.26), are insensitive to a possible decrease of λ at large $d_\perp^2$.

7.1.4.2 Unitarity constraints

The rapid increase of the cross sections given in (7.1.1) and (7.1.26) with decreasing x cannot continue forever, otherwise the unitarity of the S-matrix will be violated (see (7.1.6)). The unitarity boundary $Im\ f(s, b, d_\perp^2) = 1$ can be expressed in terms of the pQCD dipole cross section as

$$\hat{\sigma}^{\text{inel}}_{\text{pQCD}} = \sigma^{\text{el}} = \sigma^{\text{tot}}/2\ , \tag{7.1.28}$$

and is applicable to any hadronic target. For a nucleus, with the atomic number A, $\hat{\sigma}^{\text{inel}}_{\text{pQCD}}$ cannot exceed its geometric limit πR_A^2. Thus, generalising (7.1.1) and (7.1.26)

[7] Such fit is useful in practical applications. Perturbative QCD predicts the behaviour $\propto a + b \ln 1/x + c \ln^2 1/x$ for the HERA energy range since radiation of $\leq$ 1-2 hard gluons is possible in the multi Regge kinematics at HERA.

for a nuclear target, we obtain the following kinematical restrictions imposed by the unitarity of the S-matrix for $x \ll 1/4R_A m_N$:

$$\sigma_A^{q\bar{q}}(d_\perp^2, x) = \frac{\pi^2}{3} d_\perp^2 \left[xG^A(x, \bar{Q}^2)\right] \alpha_s(\bar{Q}^2) \lesssim \pi R_A^2,$$
$$\sigma_A^{q\bar{q}g}(d_\perp^2, x) = \frac{3\pi^2}{4} d_\perp^2 \left[xG^A(x, \bar{Q}^2)\right] \alpha_s(\bar{Q}^2) \lesssim \pi R_A^2 \ , \qquad (7.1.29)$$

where $xG^A(x, \bar{Q}^2)$ is the nuclear gluon density. The kinematical boundaries following from these equations are presented as curves in the x-$\bar{Q}$ plane in Figs. 14-17 of [11].

The unitarity constraints are even more stringent for DIS on nuclei at central impact parameters b, $b \leq R_A$. This is essentially equivalent to scattering off a cylinder of the length $2R_A$ oriented along the reaction axis. Obviously, in this case, edge effects are suppressed and one also gains an additional factor of ~ 1.5 on the left hand side of (7.1.29) due to the increased density of nucleons. The nuclear gluon distribution at a given impact parameter b is introduced as [49]

$$xG^A(x, Q^2, b) \equiv A \ xG^N(x, Q^2) \ f^A(x, Q^2, b) \ T^A(b) \ , \qquad (7.1.30)$$

where the function $f^A(x, Q^2, b)$ describes the amount of nuclear shadowing, $T^A(b) = \int_{-\infty}^{\infty} dz \rho^A(b, z)$ and $\int d^2b T^A(b) = 1$. Note that nuclear shadowing is larger at central impact parameters then in the situation when one averages over all impact parameters. Now, the unitarity constraints for DIS on nuclei at central impact parameters immediately follow from (7.1.29) for colour triplet

$$1.5 \times \frac{\pi^2}{3} r^2 \left[xG^A(x, \bar{Q}^2, b = 0)\right] \alpha_s(\bar{Q}^2) \lesssim \pi R_A^2 \ , \qquad (7.1.31)$$

and colour octet dipoles

$$1.5 \times \frac{3\pi^2}{4} r^2 \left[xG^A(x, \bar{Q}^2, b = 0)\right] \alpha_s(\bar{Q}^2) \lesssim \pi R_A^2 \ . \qquad (7.1.32)$$

The kinematical regions prohibited by these unitarity constraints (defined by $x < x_{\rm lim}, \bar{Q} < Q_{\rm eff}$) lie to the left of the curves in Figs. 2 and 3 (on the boundary $\bar{Q} \equiv Q_{\rm eff}, x \equiv x_{\rm lim}$). For the nucleon gluon density we used the CTEQ4L [50] parameterization evaluated at the scale $Q^2 = 4$ GeV^2. For each nucleus, we present scenarios with the highest and lowest shadowing (see Sect. 7.1.5). The curves with more shadowing lie below the ones with less shadowing, for all Q^2. To illustrate the trends given by (7.1.31), the curves are extended to the region $x \geq 1/(4R_A m_N)$ where, strictly speaking, the unitarity constraints (of (7.1.31) and (7.1.32)) should not be directly applied.

As one can see from Figs. 2 and 3, effects associated with the unitarity constraints are expected, in a wide range of x and Q^2, to be covered by THERA. Regardless of the nature of such effects, strong modifications of the gluon field in heavy nuclei (as compared to the incoherent sum of the nucleon fields) appear to be unavoidable.

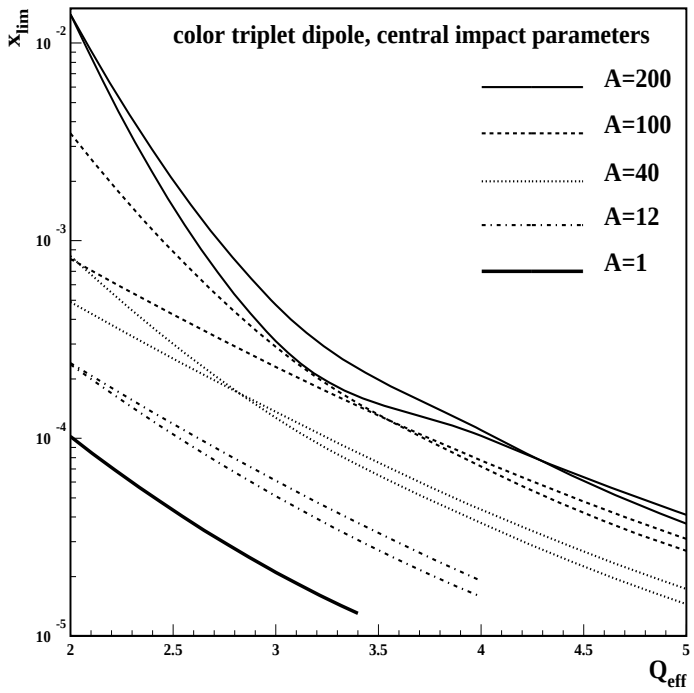

Figure 2: *Unitarity boundaries for the interaction of the colour triplet dipole with nuclei at central impact parameters. Regions to the left of each curve are prohibited by the unitarity bound of (7.1.31). Two sets of curves are given for each nucleus correspond to two different models of leading twist shadowing (as discussed in subsection 7.1.5).*

In summary, in the search for the BBL we observe that employing nuclear targets allow us to gain substantially in the region where higher twist effects become important. However, the presence of the leading twist nuclear shadowing reduces the magnitude of this gain. It is very important that in a wide range Q^2 the unitarity limit is reached at relatively large x so that $\ln Q^2/\Lambda^2_{\rm QCD}$ is comparable to $\ln x_0/x$ (where $x_0 \sim 0.05$ is the starting point for the gluon emission in the $\ln 1/x$ evolution). Hence, the diffusion to the small transverse momenta is likely to be a correction. Therefore non-perturbative QCD, with a large coupling constant, is unlikely to be relevant for the taming of the structure functions.

7.1.5 Nuclear shadowing and diffraction

A long time ago Gribov [51] established an unambiguous connection between the cross section of small-t diffraction of a hadron off a nucleon and the amount of shadowing in the interaction of the same hadron with a nucleus, for the limit in which only two nucleons of the nucleus are involved. Applying Gribov's formulae to describe photon-deuteron scattering, the effect of nuclear shadowing for the total cross section can be

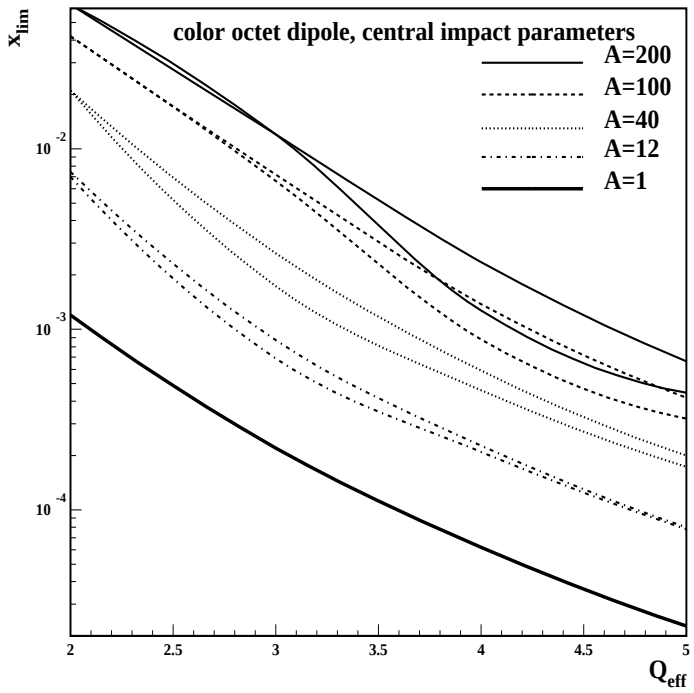

Figure 3: *Unitarity boundaries for the interaction of colour octet dipole with various nuclei at central impact parameters. Regions to the left of each curve are prohibited by the unitarity bound of (7.1.32). Two sets of curves are given for each nucleus correspond to two different models of leading twist shadowing (as discussed in subsection 7.1.5).*

expressed [8] as [52]

$$\sigma_{\rm shad} = \frac{\sigma_{\rm tot}(eD) - 2\sigma_{\rm tot}(ep)}{\sigma(ep)} = \frac{(1-\lambda^2)}{(1+\lambda^2)} \frac{\frac{d\sigma_{\rm diff}(ep)}{dt}\big|_{t=0}}{\sigma_{\rm tot}(ep)} \frac{1}{8\pi R_D^2} \ , \tag{7.1.33}$$

where λ is the ratio of real to imaginary parts of the amplitude for diffractive DIS, and R_D is the deuteron radius. For small x, λ may be as large as $0.2 \div 0.3$, which results in $(1-\lambda^2)/(1+\lambda^2) \sim 0.8 \div 0.9$. For simplicity, we have neglected the longitudinal nuclear form factor (which leads to a cutoff of the integral over the produced masses, cf. e.g., (7.1.13))

It is worth emphasising that (7.1.33) does not require the dominance of the leading twist in diffraction. The only assumption, which is due to a small binding energy of the deuteron and which is also known to work very well in calculations of hadron-nucleus total and elastic cross sections, is that the nucleus can be described as a multi-nucleon system [9]. Under these natural assumptions, one is essentially not sensitive to any

[8] The contribution of the real part of the diffractive scattering amplitude was neglected in [51] since it was assumed that the total cross section is energy-independent.

[9] The condition that the matrix element $< A|T[J_\mu(y), J_\nu(0)]|A >$ (which defines the nuclear structure function and total cross section) involves only nucleonic initial and final states is not so obvious in the infinite momentum frame. However, it is implemented in most of the light-cone models [35, 53].

details of the nuclear structure, such as short-range nucleon correlations, etc.

7.1.5.1 Inclusive diffraction at HERA and predictions for nuclear parton densities

The Gribov approximation has been applied to the description of shadowing in nuclear DIS for a long time. The first calculations were performed in [54, 55] before the advent of HERA and, hence, required modelling of diffraction in DIS. This modelling was based on the QCD extension of the Bjorken aligned jet model [54], and produced a reasonable description of the NMC data [56]. More recently, an explicit use of the HERA diffractive data allowed an essentially parameter-free description of these data [57] to be provided.

Two important features of the HERA inclusive diffractive data [58, 59] are the approximate Bjorken scaling for the diffractive parton densities and a weak dependence of the total probability of diffraction $P_{\rm diff}$ on Q^2: $P_{\rm diff} \sim 10\%$ at $Q^2 \geq 4$ GeV^2. The first observation is in line with the Collins factorization theorem [60] which states that in the Bjorken limit, the diffractive structure functions $f_j^D(\beta, Q^2, x_{I\!P}, t)$ satisfy the DGLAP evolution equations ($\beta = x/x_{I\!P} \approx Q^2/(Q^2+M^2)$ and $x_{I\!P} \approx (M^2+Q^2)/2q\cdot(p-p')$ is the fraction of the proton's momentum carried by the diffractive exchange).

A relatively small value of the probability of diffraction (as compared to the case of πN scattering) indicates that the average strength of the interaction leading to diffraction is correspondingly small. To characterise this strength it is instructive to treat diffraction in the S-channel picture using the eigenstates of the scattering matrix [61]. Such an approach is complementary to the picture of the factorization theorem. The use of the optical theorem leads to the following definition of the effective strength of the interaction (for diffraction in nucleon collisions and shadowing in nuclear collisions):

$$\sigma^j_{\rm eff}(x,Q^2) \equiv 16\pi \frac{\frac{d\sigma^j_{\rm diff}}{dt}\Big|_{t=0}}{\sigma^j_{\rm tot}(x,Q^2)} \ . \tag{7.1.34}$$

Here the superscript j indicates which hard parton is involved in the elementary hard process of the cross section $\sigma_{\rm tot}(x,Q^2)$. This equation allows the average cross section for configurations which contribute to quark-induced and gluon-induced diffraction to be extracted.

Recently a number of phenomenological analyses of HERA inclusive diffractive and diffractive jet production data were performed within the leading twist approximation for hard diffraction. We have compared several of these analyses [58, 62, 63] and found that they lead to fairly similar values of $\sigma^j_{\rm eff}$, especially if a matching at large diffractive masses to the soft factorization was implemented (for details see [64]).

The results for $\sigma^j_{\rm eff}$ for up quarks and gluons are presented in Fig. 4. We used results of two analyses of the HERA diffractive data (by the H1 collaboration [58], labelled by "H1" in the figure, and by Alvero *et al.* [62], labelled by "ACWT+"). The diffractive parton densities of [62] were extended to the region of small β by requiring consistency with the soft factorization theorem. Three curves (solid, dashed and dotted) represent the Q^2-evolution of $\sigma^j_{\rm eff}$. While the Q^2-evolution is not very significant for $\sigma^u_{\rm eff}$ of the

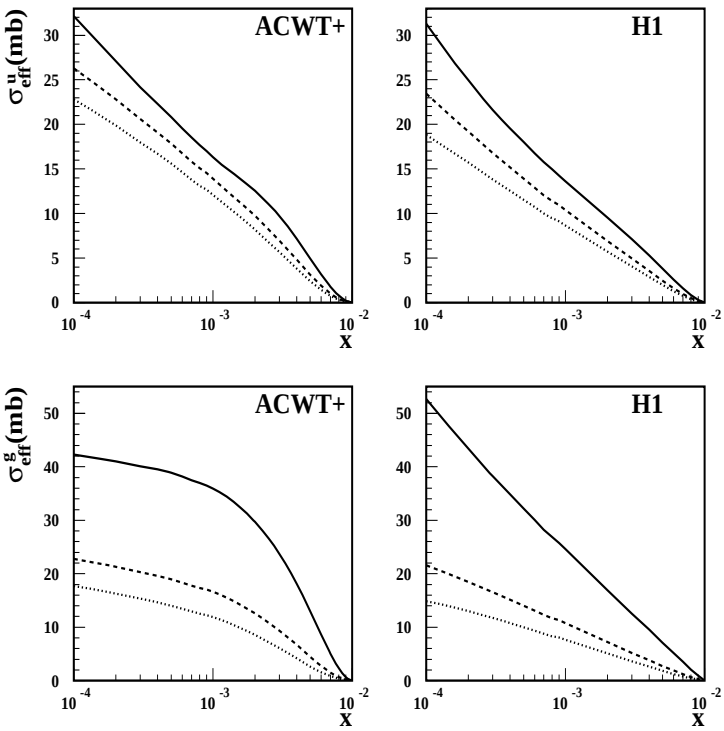

Figure 4: *The effective cross section for nuclear shadowing (or nucleon diffraction) of (7.1.34), σ^j_{eff}, for a parton of type $j = u, g$, as a function of Bjorken x at several values of Q^2. The solid curve is for $Q = 2$ GeV, the dashed curve is for $Q = 5$ GeV, the dotted one is for $Q = 10$ GeV. Two representative [63] sets of diffractive parton distributions have been used in the curves labelled by "ACWT+" [62] and "H1" [58] (see text).*

up quark, it decreases σ^g_{eff} rather rapidly for gluons. This rapid change is explained by large scaling violations for $xG^N(x, Q^2)$.

Combining the Gribov theory with the Collins factorization theorem and comparing the QCD diagrams for hard diffraction and for nuclear shadowing arising from the scattering off two nucleons (see Fig. 5), one can prove [65] that, in the low thickness limit, the leading twist nuclear shadowing is unambiguously expressed through the diffractive parton densities $f^D_j(x/x_{I\!P}, Q^2, x_{I\!P}, t)$ of ep scattering:

$$f_{j/A}(x, Q^2)/A = f_{j/N}(x, Q^2) - \frac{1}{2}\frac{1-\lambda^2}{1+\lambda^2}\int d^2b \int_{-\infty}^{\infty} dz_1 \int_{z_1}^{\infty} dz_2 \int_x^{x_0} dx_{I\!P}$$
$$\times \rho_A(b, z_1)\rho_A(b, z_2)\cos(x_{I\!P} m_N(z_1 - z_2)) f^D_{j/N}\left(\beta, Q^2, x_{I\!P}, t\right)\Big|_{k_t^2=0}, \qquad (7.1.35)$$

where $f_{j/A}(x, Q^2)$ and $f_{j/N}(x, Q^2)$ are the inclusive parton densities, ρ_A is the nucleon density in the nucleus. At moderately small values of x, one should also add a term related to the longitudinal distances comparable to the inter-nucleon distances in the nucleus. This additional term can be evaluated using information on the enhancement of the gluon and valence quark parton densities at $x \sim 0.1$ at the initial scale

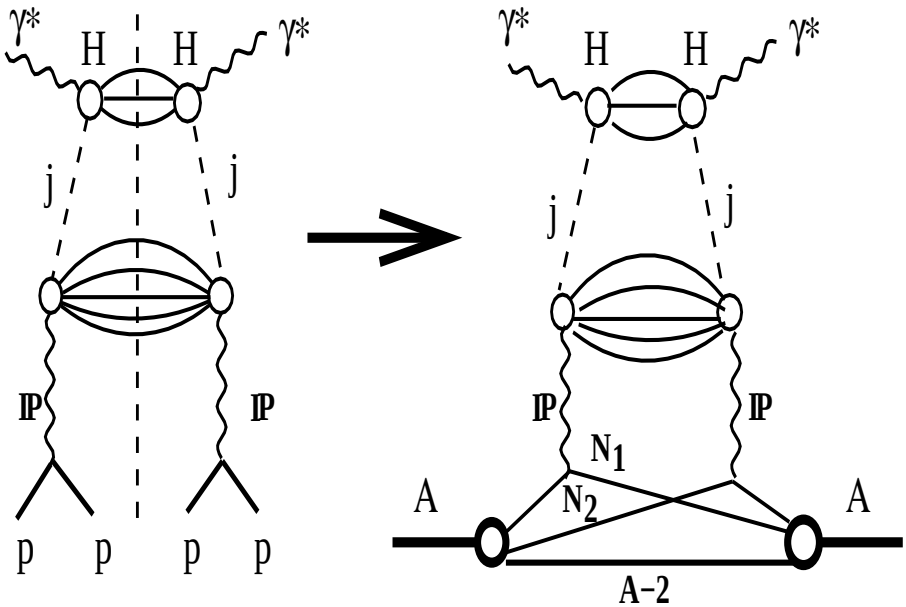

Figure 5: *Diagrams demonstrating the relationship between hard electron-proton diffraction, involving a parton of type j, and nuclear shadowing in inclusive DIS. Here the Pomeron symbol, IP, merely represents a generic label for vacuum exchange.*

Q_0^2. This would slightly diminish nuclear shadowing at higher Q^2 via the Q^2 evolution. To summarise the results of (7.1.35), the nuclear shadowing effect given by $(1 - f_{j/A}(x, Q^2)/Af_{j/N}(x, Q^2))$, is proportional to $\sigma^j_{\rm eff}(x, Q^2)$.

For $N \geq 3$ nucleons, we need to establish which configurations in the photon wavefunction dominate in diffraction. There are two extreme alternatives, i.e. a dominance of either hadronic-size configurations (as indicated by the aligned jet model) or of small size ($\sim 1/Q$) fluctuations. Figure 6 represents the corresponding diagrams (contributing to nuclear shadowing).

One can determine which of these extremes is closer to reality by comparing the effective cross section characterising diffraction (7.1.34) with the cross section, $\sigma_{\rm pQCD}(d_\perp^2, x)$, for the double interaction of a dipole with a small and fixed diameter $d_\perp \sim 1/Q$, within the eikonal approach, given by (7.1.1). Thus, for the x-range studied at HERA at $Q^2 \geq 4$ GeV^2 ($x \sim 0.001$) , large-size configurations dominate, while the small dipoles contribute little to the bulk of the inclusive diffractive cross section. This can also be seen from a comparison of the amount of nuclear shadowing in F_L^A calculated within the leading twist and eikonal approaches. This is consistent with the experimental observation that the t-slope of the inclusive diffraction ($B \sim 7$ GeV^{-2}) is significantly larger than for the processes where small-size dipole dominate ($B \sim 4.5$ GeV^{-2}). At lower $x \sim 10^{-4}$, small dipoles may become much more important due to the increase of $\hat{\sigma}_{\rm pQCD}$ due to the QCD evolution.

It is well known that total, elastic and inelastic diffractive cross sections for the interactions of hadrons with nuclei are quantitatively well-described within the scattering

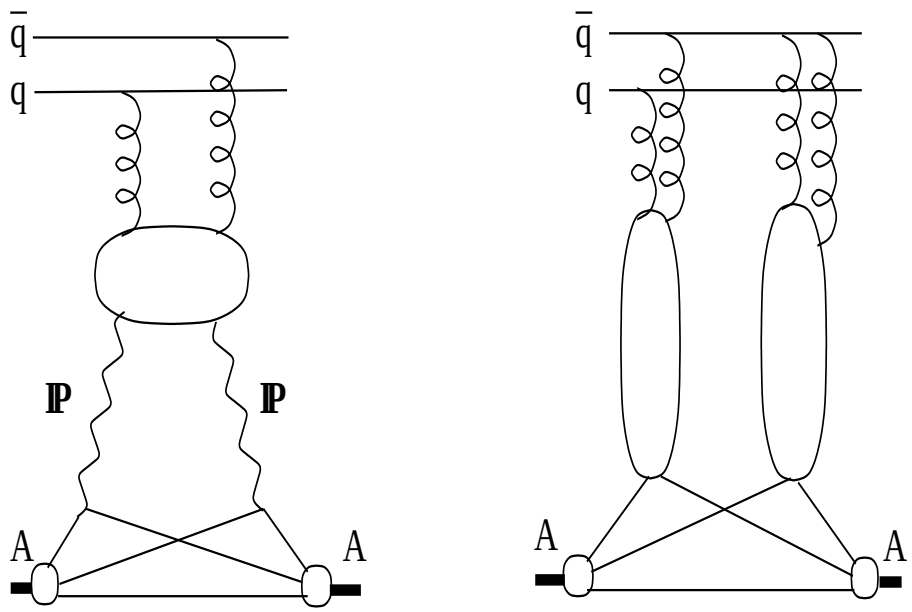

Figure 6: *Typical diagrams for the leading twist (left) and eikonal (right) models for nuclear shadowing involving a small dipole and two nucleons. The curly lines represent gluons. In the diagram on the right the blob and its attached legs represent the gluon distribution of the nucleon. The Pomeron symbol, $I\!P$, in the diagram on the left merely represents a generic label for vacuum exchange.*

eigenstate approximation [61], which is a generalization of the eikonal approximation. Since, at $Q^2 = 4$ GeV^2, relatively soft interactions give the dominant contribution to diffraction, interactions with $N \geq 3$ nucleons can be considered using a generalised eikonal model with an effective cross section given by (7.1.34). We found that, due to a relatively small value of σ^q_{eff}, the amount of nuclear shadowing for F_2^A is relatively modest (as compared to the nuclear gluon distribution) and is practically independent of fluctuations of the effective cross section (when σ_{eff} is kept fixed) [66]. The Q^2-dependence of shadowing is taken into account via the DGLAP evolution equations. Recently, we performed an extensive comparison of different parametrisations of the diffractive structure functions [64]. The results will update the analysis [65] to include a range of modern parameterizations of the quark and gluon diffractive parton densities. Using the effective cross sections presented in Fig. 4 and generalising (7.1.35) to include the rescattering terms with $N \geq 3$ nucleons, we are able to produce predictions for up quark and gluon parton distributions for a number of nuclei. As an example Fig. 7 represents the ratio of nuclear to nucleon up quark and gluon parton distributions for nuclei of ^{12}C (carbon) and ^{206}Pb (lead). Note that since the models we used provide good fits to the HERA diffractive data for $F_2^D(x, Q^2, x_{I\!P})$, they effectively take into account higher twist terms, if they are present in the data.

Hence, we conclude that combining the Gribov theory with the factorization theorem for inclusive diffraction and experimental information from HERA provides reli-

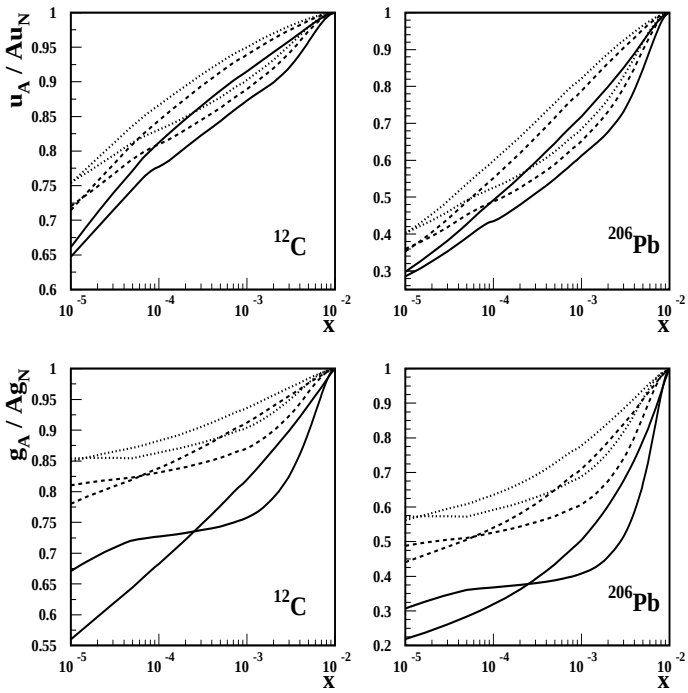

Figure 7: *The ratio of nuclear to nucleon up-quark and gluon parton distributions as a function of x, scaled by nucleon number, A. Two representative [63] sets of diffractive parton densities, "ACWT+" [62] and "H1" [58], are used to calculate nuclear shadowing (see text) for each nucleon and taken together they give an indication of the spread of theoretical predictions. The solid, dashed, and dotted curves are for $Q = 2, 5, 10$ GeV, respectively.*

able predictions for nuclear parton distributions and, hence, for F_2^A in the HERA and THERA experimental ranges.

7.1.5.2 Gluon shadowing

We explained above that since the interaction of the colour octet dipole is enhanced by a factor 9/4 relative to a colour triplet [25, 32, 48], one expects, for processes sensitive to such configurations, an earlier onset of the regime where unitarity effects may become important.

The leading twist mechanism of nuclear shadowing is connected to the amount of the leading twist diffraction in gluon-induced reactions. The larger strength of the perturbative interaction as well as stronger non-perturbative interactions up to a scale ~ 2 GeV in the gluon channel suggest that the gluon-induced diffraction should occur with a large probability.

This is consistent with another interesting feature of the current HERA diffractive data (shared by the diffractive data from the proton colliders), i.e. a very important role of the gluons in hard diffraction. In the language of the diffractive community, the

"perturbative Pomeron" is predominantly built of gluons. To quantify this statement it is convenient to define the probability of diffraction for a hard probe which couples to a parton j [65]:

$$P_j(x,Q^2) = \frac{\int dt dx_{I\!P}\ f_j^D(x/x_{I\!P}, Q^2, x_{I\!P}, t)}{f_j(x,Q^2)}\,. \tag{7.1.36}$$

A large probability of diffraction in the gluon channel:

$$\begin{aligned} P_g(x \le 10^{-3}, Q^2 = \ 4\ \mathrm{GeV}^2) \ &\sim\ 0.4\,, \\ P_g(x \le 10^{-3}, Q^2 = 10\ \mathrm{GeV}^2) \ &\sim\ 0.2\,, \end{aligned} \tag{7.1.37}$$

leads via (7.1.36) to a large σ^g_{eff} (see Fig. 4) and, hence, to the prediction of *a large leading twist shadowing* for $G^A(x \le 10^{-2}, Q^2)$ (see Fig. 7). Interactions of small dipoles are more important in the gluon case than in the quark case. Nevertheless, if we use the eikonal approximation (in the same spirit as for $q\bar{q}$ dipoles) to estimate the relative importance of the leading and higher twist effects, we find that up to fairly small x in a wide range of Q^2, the leading twist terms dominate. Note that in this case one should use $\sigma_{q\bar{q}N}$ from [31] rescaled by the factor 9/4 even for the dipole sizes where non-perturbative effects could be important. A comparison of Figs. 2 and 3 suggests that the higher twist effects appear to be more important in the gluon channel than in the quark channel. Also, the gluon induced interactions of a projectile with several nucleons are much more important and more sensitive to details of the interaction dynamics. However, with $\sigma^g_{\mathrm{eff}} \sim 40$ mb, a large leading twist shadowing in the gluon channel appears to be unavoidable. It seems to be large enough to reduce strongly the gluon densities. However, even this strong reduction can not prevent the violation of unitarity for the interaction of colour octet systems with heavy nuclei, as can be seen from Fig. 3. For scattering at central impact parameters, this may already occur at $Q \sim 2$ GeV for the whole x range, $x \le 1/(4m_N R_A)$.

7.1.5.3 Shadowing in the interaction of small dipoles with nuclei

For several small-x processes, we can probe the interactions of a small colour dipole with the nucleus directly. These include $\sigma_L(x,Q^2)$, $\sigma(\gamma + A \to J/\psi + A)$ and $\sigma(\gamma_L^* + A \to \rho + A)$.

We argued above that the eikonal approximation for fixed small $d_\perp$ leads to much weaker absorption effects than the leading twist shadowing. The eikonal approach is also inconsistent with the QCD factorization theorem for the production of vector mesons [8] which leads at small x to [7]

$$\frac{\frac{d\sigma}{dt}(\gamma_L^* A \to VA)\big|_{t=0}}{\frac{d\sigma}{dt}(\gamma_L^* N \to VN)\big|_{t=0}} \approx \left[\frac{F_L^A(x,Q)}{F_L^N(x,Q)}\right]^2 \approx \left[\frac{xG^A(x,Q)}{xG^N(x,Q)}\right]^2\,. \tag{7.1.38}$$

Another observable sensitive to the difference between the leading twist and eikonal approaches is F_L^A. It can be expressed via nuclear parton distributions (we consider

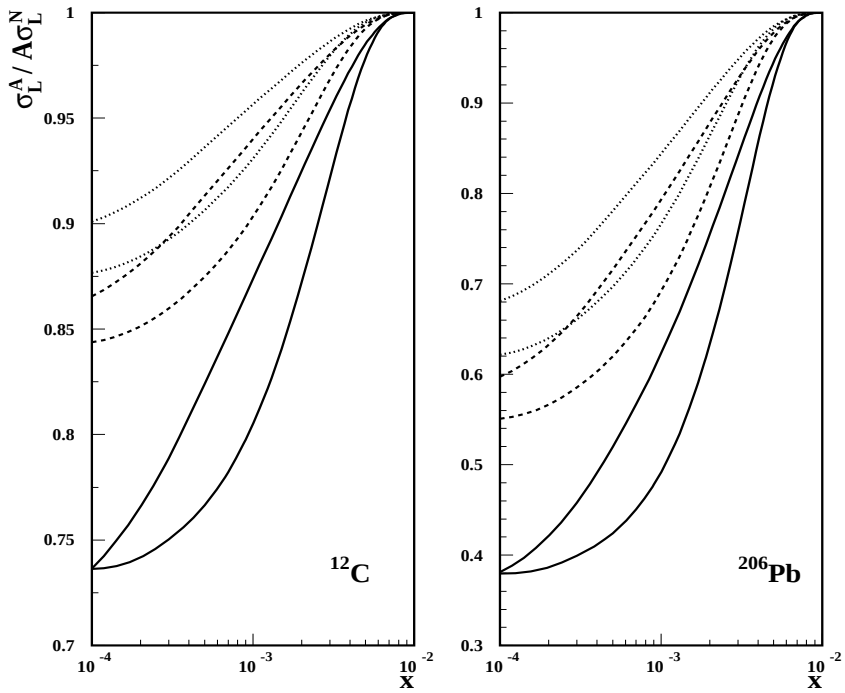

Figure 8: *The ratio of total cross sections for longitudinally polarised photons scattering on nuclear and nucleon targets, $\sigma_L^A/(A\sigma_L^N)$, as function of x for Carbon and Lead. Two representative [63] sets of diffractive parton densities are used, "ACWT+" [62] and "H1" [58], to calculate nuclear shadowing. The solid, dashed and dotted curves are for $Q = 2, 5, 10$ GeV, respectively.*

the leading order in α_s expression):

$$F_L^A(x,Q^2) = \frac{2\alpha_s(Q^2)}{\pi}\int_x^1 \frac{dy}{y}(x/y)^2\Big(\sum_{i=1}^{n_f} e_i^2(1-x/y)yG^A(y,Q^2) + \frac{2}{3}F_2^A(y,Q^2)\Big)\ . \tag{7.1.39}$$

The amount of nuclear shadowing for σ_L^A can be expressed by the ratio

$$\frac{F_L^A}{AF_L^N} = \frac{\int_x^1 \frac{dy}{y}(x/y)^2\Big((1-x/y)\ \sum_i e_i^2\ yG^A(y,Q^2) + 2F_2^A(y,Q^2)/3\Big)}{A\int_x^1 \frac{dy}{y}(x/y)^2\Big((1-x/y)\sum_i e_i^2\ yG^N(y,Q^2) + 2F_2^N(y,Q^2)/3\Big)}\ . \tag{7.1.40}$$

Results using (7.1.40) are presented in Fig. 8 for the same parameterizations as in the previous figures.

The impact-parameter eikonal approximation for $x \ll 1/(4m_N R_A)$ (where finite coherence length effects, which cannot be unambiguously treated in the eikonal approximation, can be safely neglected), leads to substantially smaller shadowing for the interaction of small dipoles (see Fig. (15) of [18]). The cleanest way to observe this

effect would be to study coherent J/ψ production. THERA would be able to cover a broad range of $x = (M^2_{J/\psi} + Q^2)/W^2$ starting from the region of colour transparency (amplitude proportional to nucleon number A) and extending to the colour opacity regime where there is a strong reduction of the amplitude (see Fig. 9).

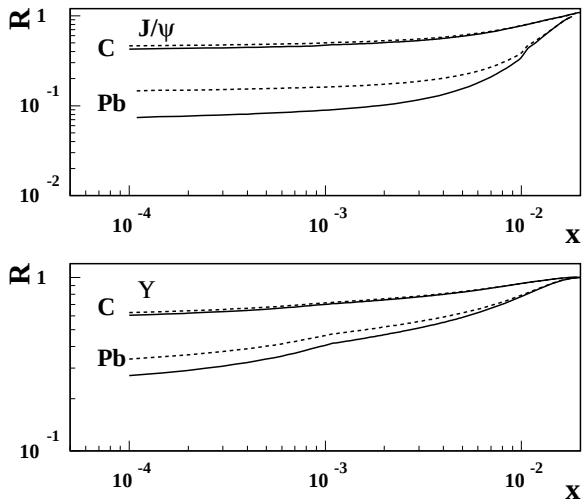

Figure 9: *The colour opacity effect for the ratio, R, of the coherent production of J/ψ and Υ from Carbon and Lead, normalized to the value of this ratio at $x = 0.02$, calculated in the leading twist models of gluon shadowing [65] both with (dashed curves) and without (solid curves) taking the fluctuations of the cross section into account.*

7.1.5.4 Total cross section of coherent inclusive diffraction

There is a deep connection between shadowing and the phenomenon of diffractive scattering off nuclei. The simplest way to investigate this connection is to apply the AGK cutting rules [67]. Several processes contribute to diffraction on nuclei: (i) coherent diffraction in which the nucleus remains intact, (ii) break-up of the nucleus (without producing of hadrons in the nucleus fragmentation region), (iii) rapidity gap events (with hadron production in the nucleus fragmentation region). In [52] we found that for $x \leq 3 \cdot 10^{-3}, Q^2 \geq 4$ GeV^2, the fraction of the DIS events with rapidity gaps reaches about 30-40% for heavy nuclei, with a fraction of the events of type (iii) decreasing rapidly with A. Recently, together with M. Zhalov one of us (MS) investigated the dependence of the fraction of the events due to coherent diffraction and due to the break-up of the nucleus on the strength of the interaction, $\sigma^j_{\rm eff}$. We found that this fraction increases with $\sigma^j_{\rm eff}$ rather slowly. Thus, it is not sensitive to fluctuations of $\sigma_{\rm eff}$. One can see from Fig. 10 that one expects a significantly smaller fraction for

quark-induced processes ($\approx 35\%$) of coherent events than for gluon-induced processes ($\approx 45\%$). We also found that the ratio of diffraction with and without nuclear break-up is small (10-20%) in a wide range of nuclei, and weakly depends on $\sigma_{\rm eff}$. Hence, it would be pretty straightforward to extract coherent diffraction by simply using anti-coincidence with a forward neutron detector, especially in the case of heavy nuclei (see discussion in [68]).

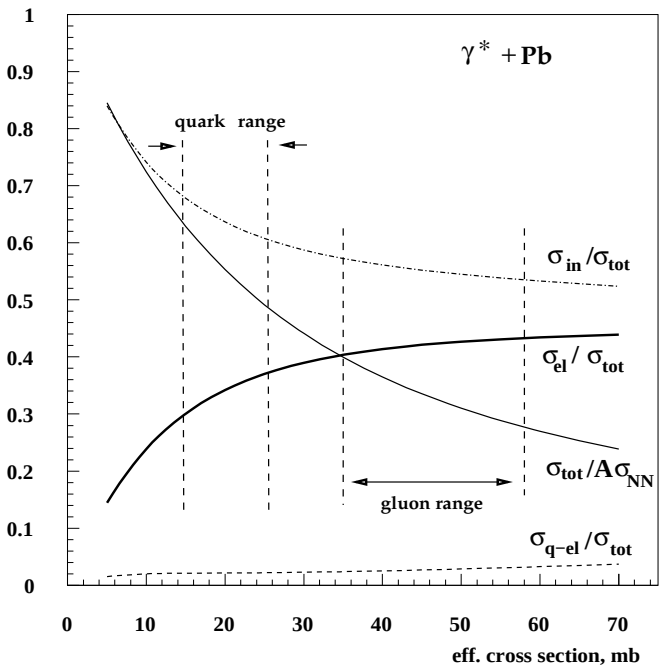

Figure 10: *Fractions of the total cross section, given by inelastic scattering (in), coherent (el) and incoherent (q−el) diffractive scattering cross sections as a function of the average interaction strength for quarks and gluons (σ^j_{eff} of (7.1.34), cf. Fig. 4) for scattering off Lead.*

It is worth emphasising that the proximity of $\sigma_{\rm el}/\sigma_{\rm tot}$ to 1/2 does not necessarily imply the proximity of the BBL in the sense of hard physics (it may also occur in the soft aligned-jet type scenario). A key distinction in this regard is in the dominance of the dijet production, broadening of the p_t distributions, etc, as discussed in Sect. 7.1.3.

Other manifestations of leading twist shadowing include a strong A-dependence of the fluctuations of the central multiplicity distribution of the produced hadrons [52], and strong modifications of the leading hadron spectrum [65] for rapidities where the diffractive contribution is small. This is also in marked contrast to the black body limit, where major modifications occur already at the highest rapidities.

7.1.6 Experimental considerations

The expected nuclear effects in the small-x region are large enough so that measurements of the ratios of the corresponding quantities for electron-nucleus and electron-nucleon scattering with an accuracy of only a few percent will be sufficient. Hence, the luminosities required for the first run of measurements are rather modest. The estimates of [69] indicate that luminosities of about 1 pb^{-1} per nucleus would be sufficient for measurements of a number of important inclusive observables which include ratios of the structure functions, the A-dependence of global features of diffractive cross sections, ratios of the leading particle spectra and fluctuations of the multiplicity in the central rapidity range. Luminosities of the order of 10 pb^{-1} per nucleus will be necessary to measure gluon densities via $2 + 1$ jet events directly, to observe the pattern of colour opacity in exclusive vector meson production and to establish differential diffractive parton densities of nuclei.

Requirements for the detector are practically the same as for the study of small-x electron-proton scattering. The only additional requirement is for forward neutron detectors with specifications similar to that for the ZEUS forward neutron calorimeter (FNC). These will be needed to trigger on central inelastic collisions by selecting events where a larger than average number of neutrons is produced. Note that for small x collisions at central impact parameters the virtual photon interacts inelastically with $\sim A^{1/3}$ nucleons. On the basis of an analysis [68] of E-665 data on the production of soft neutrons at $x \sim 0.03$ [70], we estimate that the average number of soft neutrons produced in the central collisions will be ~ 20 (as compared to ~ 4 for peripheral inelastic collisions). Overall, a strong correlation between the number produced nucleons and centrality of the event is expected at small x (as is also the case for hadron-nucleus scattering). As we explained above, such detectors would allow the breakdown of leading twist QCD to be studied in runs with a single heavy nucleus.

A FNC-type neutron calorimeter would have nearly 100% acceptance for the neutrons from nuclear break-up. Since the average number of such neutrons exceeds one for $A \geq 16$, a FNC-type detector would allow an effective tagging of nuclear break-up. Hence, it would also simplify studies of diffractive processes with nuclei. The separation of the three classes of diffractive events (coherent scattering, nuclear break-up producing nuclear fragments (mostly neutrons and protons) in the forward direction, and diffractive dissociation with meson production in the nucleus fragmentation region from non-diffractive reactions) is very similar to the selection of diffractive events in the ep case (see the previous subsection). The contribution of diffractive dissociation to the overall diffractive cross section is significantly smaller than in the ep case. The experimental signatures for this class of reactions are similar to ep scattering since the energy flow in the forward direction is expected to have almost the same topology. Calorimetric coverage down to $\theta \leq 1^0$ in the forward region (see Sect. 2.3) will allow for the detection of most dissociative reactions. Nuclear break-up is expected to constitute about 10% of coherent diffraction for a wide range of model parameters (see Fig. 10). In the case of coherent exclusive processes, such as coherent vector meson production, detection of the process will be further simplified since the average transverse momenta

of coherently produced vector mesons are $p_t \leq 2/R_A^2$, which is much smaller than for exclusive processes with protons.

7.1.7 Conclusions

The nuclear program at THERA has a very strong potential for the discovery of a number of interesting new high energy (small x) phenomena, including quark and gluon shadowing (for kinematics in which longitudinal distances are much larger than the heavy nuclear radius), hard coherent diffraction off nuclei and colour opacity in the production and interaction of small colour singlets. Crucially, for the first time, it will provide several effective tools for unambiguously probing the black body limit of photon-nuclear collisions, thereby investigating QCD in a new regime of strong interactions with a small coupling constant.

Acknowledgements

We thank A.H. Mueller for a useful discussion and GIF, ARC, PPARC and DOE for support. LF and MS thank INT for hospitality during the time this work was completed.

References

[1] V.N. Gribov and L.N. Lipatov, Sov. J. Phys. **15**, 438,625 (1972);
Yu.L. Dokshitzer, Sov. Phys. JETP **46**, 641 (1977);
G. Altarelli and G. Parisi, Nucl. Phys. **B 126**, 298 (1977).

[2] J.C. Collins, D.E. Soper, and G. Sterman, Nucl. Phys. **B 308**, 833 (1988).

[3] H. Georgi and H.D. Politzer, Phys. Rev. **D 9**, 416 (1974);
D. Gross and F. Wilczek, Phys. Rev. **D 9**, 980 (1974).

[4] J.D. Bjorken, Phys. Rev. **179**, 1547 (1969).

[5] M. Glück, E. Reya and A. Vogt, Eur. Phys. J. **C 5**, 461 (1998);
A.D. Martin et al., Eur. Phys. J. **C 4**, 463 (1998);
CTEQ Coll., H. Lai et al., Eur. Phys. J. **C 12**, 375 (2000).

[6] J.C. Collins, Phys. Rev. **D 57**, 3051 (1998).

[7] S.J. Brodsky et al., Phys. Rev. **D 50**, 3134 (1994).

[8] J.C. Collins, L. Frankfurt and M. Strikman, Phys. Rev. **D 56**, 2982 (1997).

[9] J.C. Collins and A. Freund, Phys. Rev. **D 59**, 074009 (1999).

[10] H. Abramowicz and A. Caldwell, Rev. Mod. Phys. **71**, 1275 (1999).

[11] L. Frankfurt, V. Guzey and M. Strikman, J. Phys. **G 27**, R23 (2001).

[12] M. Wüsthoff and A.D. Martin, J. Phys. **G 25**, R309 (1999).

[13] A. Hebecker, Phys. Rep. **331**, 1 (2000).

[14] L. Frankfurt, G.A. Miller and M. Strikman, Phys. Lett. **B 304**, 1 (1993);
B. Blattel et al., Phys. Rev. Lett. **71**, 896 (1993).

[15] E791 Coll., E.M. Aitala et al., *Observation of color-transparency in diffractive dissociation of pions*, [hep-ex/0010044];
Direct measurement of the pion valence quark momentum distribution, the pion light-cone wave function squared, [hep-ex/0010043].

[16] M. Sokoloff et al., Phys. Rev. Lett. **57**, 3003 (1986).

[17] L. Frankfurt and M. Strikman, Phys. Rev. Lett. **63**, 1914 (1989), *Erratum-ibid.* **64**, 815 (1990).

[18] L.L. Frankfurt, W. Koepf and M. Strikman, Phys. Rev. **D 54**, 3194 (1996).

[19] L.L. Frankfurt, W. Koepf and M. Strikman, Phys. Rev. **D 57**, 512 (1998).

[20] M.G. Ryskin, Z. Phys. **57**, 89 (1993).

[21] A.D. Martin, M.G. Ryskin and T. Teubner, Phys. Rev. **D 55**, 4329 (1997); Phys. Rev. **D 56**, 3007 (1997); Phys. Rev. **D 62**, 014022 (2000).

[22] L.L. Frankfurt, M.M. McDermott and M. Strikman, JHEP **9902**, 002 (1999); JHEP **0103**, 045 (2001);

[23] A.D. Martin, M.G. Ryskin and T. Teubner, Phys. Lett. **B 454**, 339 (1999).

[24] L. Frankfurt, A. Freund and M. Strikman, Phys. Rev. **D 58**, 114001 (1998), *Erratum-ibid.* **D 59**, 119901 (1999); Phys. Lett. **B 460**, 417 (1999).

[25] H. Abramowicz, L.L. Frankfurt, and M. Strikman, DESY 95-047, March 1995; Proceedings of SLAC Summer Inst., 1994, pp. 539-574;
Surveys High Energ. Phys. **11**, 51 (1997).

[26] H1 Coll., S. Aid et al., Nucl. Phys. **B 470**, 3 (1996).

[27] ZEUS Coll., M. Derrick et al., Z. Phys. **C 72**, 399 (1996).

[28] V.S. Fadin, E.A. Kuraev and L.N. Lipatov, Phys. Lett. **B 60**, 50 (1975); Sov. Phys. JETP **45**, 199 (1977);
I.I. Balitsky and L.N. Lipatov, Sov. J. Nucl. Phys. **28**, 822 (1978); V.S. Fadin and L.N. Lipatov, Phys. Lett. **B 429**, 127 (1998).

[29] G. Camici and M. Ciafaloni, Phys. Lett. **B 412**, 396 (1997).

[30] J.R. Forshaw and D.A. Ross, *Quantum Chromodynamics and the Pomeron*, (Cambridge Univ. Press (1997) 248p).

[31] M. McDermott et al., Eur. Phys. J. **C 16**, 641 (2000).

[32] L. Frankfurt, A. Radyushkin and M. Strikman, Phys. Rev. **D 55**, 98 (1997).

[33] F.E. Low, Phys. Rev. **D 12**, 163 (1975).

[34] M. Froissart, Phys. Rev. **123**, 1053 (1961).

[35] A.H. Mueller and J. Qiu, Nucl. Phys. **B 268**, 427 (1986).

[36] A. De Rejula et al., Phys. Rev. **D 10**, 1649 (1974).

[37] R.J Eden et al., *The Analytic S-matrix*, (Cambridge Univ. Press (1966), 287p).

[38] A.H. Mueller, Nucl. Phys. **B 335**, 115 (1990); Nucl. Phys. **B 558**, 285 (1999).

[39] V.N.Gribov, Zh. Exp. Teor. Fiz. **57**, 1306 (1969).

[40] J.D. Bjorken and J.B. Kogut, Phys. Rev. **D 8**, 1341 (1973).

[41] R.K. Ellis, W.J. Stirling and B.R. Webber, *QCD and collider physics*, (Cambridge Univ. Press (1996) 435p, Cambridge Monographs on Particle Physics, Nuclear Physics and Cosmology, Vol. 8).

[42] J.J. Sakurai, Phys. Rev. Lett. **22**, 981 (1969).

[43] L. Frankfurt, V. Guzey and M. Strikman, Phys. Rev. **D 58**, 094039 (1998).

[44] H. Fraas, B.J. Read and D. Schildknecht, Nucl. Phys. **B 86**, 346 (1975);
G. Cvetic, D. Schildknecht and A. Shoshi, Acta. Phys. Pol. **B 30**, 3265 (1999);
A. Donnachie and G. Shaw, in: *Electromagnetic interactions of hadrons, Vol.2*, 169, eds. A. Donnachie and G. Shaw (Plenum, New York (1978));
G. Shaw, Phys. Rev. **D 47**, R3676 (1993);
G. Shaw, Phys. Lett. **B 228**, 125 (1989);
P. Ditsas and G. Shaw, Nucl. Phys. **113**, 246 (1976).

[45] L. Bourhis et al., *Next-to-leading order determination of fragmentation functions*, [hep-ph/0009101].

[46] J. Jalilian-Marian et al., Phys. Rev. **D 59**, 034007 (1999); *Erratum-ibid.* **D 59**, 099903 (1999) and references therein;
L. McLerran and R. Venugopolan, Phys. Rev. **D 49**, 2233 (1994).

[47] European Muon Coll., J. Ashman et al. Z. Phys. **C 52**, 1 (1991).

[48] W. Buchmüller, A. Hebecker and M.F. McDermott, Nucl. Phys. **B 487**, 283 (1997), *Erratum-ibid.* **B 500**, 621 (1997).

[49] L. Frankfurt, M. Strikman and S. Liuti, *Parton Distributions In Hard Nuclear Collisions*, in "Brookhaven 1990, Experiments and detectors for a relativistic heavy ion collider", 103.

[50] H.L. Lai et al., Phys. Rev. **D 55**, 1280 (1996).

[51] V.N. Gribov, Zh. Exp. Teor. Fiz. **57**, 1309 (1969); Sov. Phys. JETP **30**, 709 (1970).

[52] L. Frankfurt and M. Strikman, Phys. Lett. **B 382**, 6 (1996).

[53] L. McLerran and R. Venugopalan, Phys. Rev. **D 50**, 225 (1994).

[54] L.L. Frankfurt and M.I. Strikman, Phys. Rep. **160**, 235 (1988).

[55] L.L. Frankfurt and M.I. Strikman, Nucl. Phys. **B 316**, 340 (1989).

[56] New Muon Coll., P. Amaudruz et al., Nucl. Phys. **B 441**, 3 (1995).

[57] A. Capella et al., Eur. Phys. J. **C 5**, 111 (1998).

[58] H1 Coll., C. Adloff et al., Z. Phys. **C 76**, 613 (1997).

[59] ZEUS Coll., J. Breitweg et al., Eur. Phys. J. **C 6**, 43 (1999).

[60] J.C. Collins, Phys. Rev. **D 57**, 3051 (1998).

[61] E. Feinberg and Ya. Pomeranchuk, Suppl. Nuovo Cim. **111**, 652 (1956);
M. Good and W. Walker, Phys. Rev. **D 120**, 1857 (1960).

[62] L. Alvero, et al. Phys. Rev. **D 59**, 074022 (1999).

[63] F. Hautmann, Z. Kunszt and D.E. Soper, Nucl. Phys. **B 563**, 153 (1999).

[64] L. Frankfurt et al., in preparation.

[65] L. Frankfurt and M. Strikman, Eur. Phys. J. **A 5**, 293 (1999).

[66] L. Alvero, L.L. Frankfurt and M.I. Strikman, Eur. Phys. J. **A 5**, 97 (1999).

[67] V. Abramovskii, V.N. Gribov, and O.V. Kancheli, Sov. J. Nucl. Phys. **18**, 308 (1974).

[68] M. Strikman, M.G. Tverskoii and M.B. Zhalov, Phys. Lett. **B 459**, 37 (1999).

[69] M. Arneodo et al., *Nuclear beams in HERA*, in "Hamburg 1995/96, Future physics at HERA", 887, [hep-ph/9610423].

[70] E665 Coll., M.R. Adams et al., Phys. Rev. Lett. **74**, 5198 (1995).

8 Real Photon-Proton Scattering

8.1 Gamma Options of the THERA Collider

O. Çakır[a], A. K. Çiftçi[a], S. Sultansoy[b,c], Ö. Yavaş[a] and M. Yılmaz[b]
[a]*Ankara University, 06100 Ankara,TURKEY*
[b]*Gazi University, 06500 Ankara, TURKEY*
[c]*Academy of Sciences, H. Cavid Ave. 143, Baku, AZERBAIJAN*

8.1.1 Introduction

Gamma options, namely γp and γA colliders are unique to THERA, and, can not be realised at standard (ring-ring type) lepton-hadron machines such as HERA, LEP$*$LHC and μp colliders. Reasons for this uniqueness are explained in refs [1–3]. Due to the advantage of the spectrum of the back-scattered photons, gamma options have advantages for investigation of almost all processes involving virtual photons at THERA itself. In this section we summarize main parameters and physics goals of gamma options of THERA.

8.1.2 Luminosity considerations

Earlier, the idea of using high energy photon beams obtained by Compton backscattering of laser light off a beam of high energy electrons was considered for γe and $\gamma\gamma$ colliders (see [4] and references therein.) Then the same method was proposed for constructing γp colliders on the base of linac-ring type ep machines and rough estimations of the main parameters of γp collisions are given in [5]. In general, from technical point of view γp and γA colliders are similar to TESLA based γe collider. The well-known formulae for γe option [6, 7] are modified for γp collider in [1], where the dependence of different parameters on the distance z between conversion region and collision point was analyzed and some design problems were considered.

Using upgraded parameters of both TESLA electron beam with $E_e = 250$ GeV ($n_e = 2 \times 10^{10}$, $n_b = 5264$, $\sigma_z = 0.3$ mm, $\Delta t_b = 211.37$ ns and $f_{rep} = 5$ Hz) and HERA proton beam (given in Table 8.1.1), one can easily obtain $\sqrt{s_{\gamma p}^{\max}} = 0.9$ TeV and $L = 5.3 \times 10^{30}$ cm^{-2}s^{-1}at $z = 0$ m. Here we take into account the electron to

photon conversion coefficient 0.65 [4] and a factor of two coming from smallness of the photon bunch transverse sizes.

Using the formulae from [1], below we illustrate main features of γp collisions. Dependence of the luminosity on the distance z is presented in Figure 1 for three different choices of laser and electron beam helicities. In order to reduce dependence on

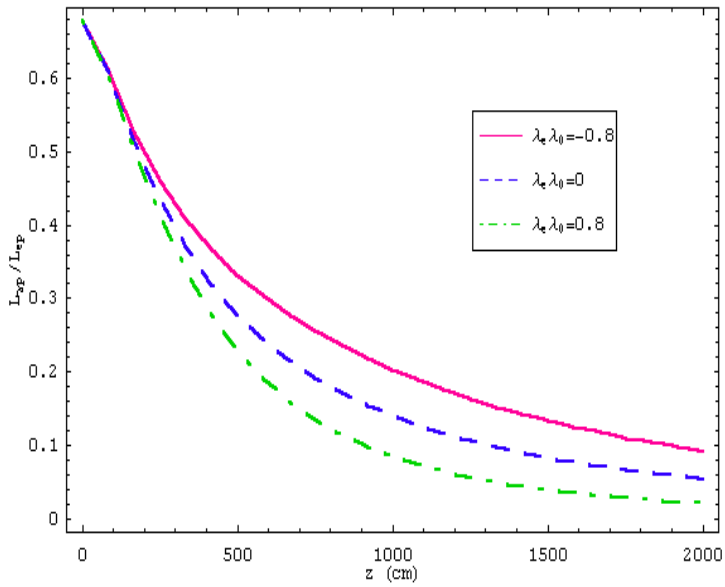

Figure 1: *Dependence of the luminosity on the distance z for γp collider*

electron and proton beam parameters, we give γp luminosity in terms of ep luminosity in this figure. As one can see, the luminosity slowly decreases with the increasing z (factor $\sim$1/2 at $z = 5$ m) and opposite helicity values for laser and electron beams are advantageous. Additionally, a better monochromatization of high-energy photons seen by proton bunch can be achieved by increasing the distance z (see Figure 2). Luminosity distribution as a function of γp invariant mass at $z = 10$ m is plotted in Figure 3.

In the γA option sufficiently high luminosity can be achieved at least for light nuclei because the main limitation comes from intra-beam scattering (IBS) and it is known that emittance growth time is proportional to Z^2/A. For illustration we consider Carbon nucleus beam with parameters given in last column of the Table 8.1.1. The dependence of luminosity on the distance between conversion region and interaction point is plotted in Figure 4.

Let us remind that an upgrade of the luminosity by a factor 3-4 may be possible by applying a "dynamic" focusing scheme [8, 9]. Further increase of luminosity will require the cooling of nucleus beam in the HERA ring [10].

In general, there are two possible choices for γp interaction region: head-on collisions and collisions with a small angle (crab crossing). Also, for both possibilities, there are

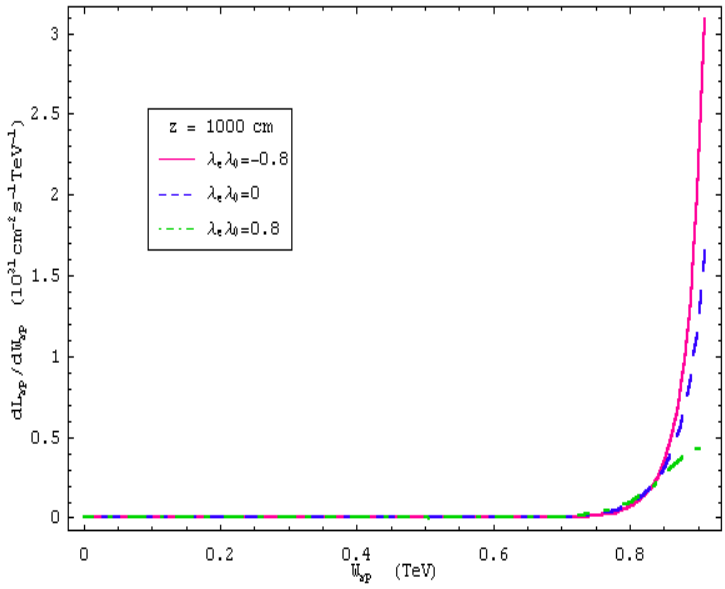

Figure 2: *Luminosity distribution as a function of γp invariant mass for three different values of z*

two options: with deflection of the electron beam and without deflection. For the first option the synchrotron radiation on proton beam line and detector can lead to some problems. In the second option residual electron-proton beam-beam tune shift effect should be kept under control. The work on these subjects is going on. Let us mention that the larger distance between the conversion region and the interaction point has advantages for solving design problems. In difference from the γe option of TESLA, where this distance should be of order of mm, for γp option even at $z = 5$ m we loose only the half of the luminosity (see Figures 1 and 4).

8.1.3 Physics goals

Partial list of physics goals of the THERA based γp collider contains [2, 11]:

- Total cross-section at TeV scale, which can be extrapolated from existing low energy data as $\sigma(\gamma p \to hadrons) \approx 100 \div 200$ μb
- Two-jet events, about 10^4 events per working year with $p_t > 100$ GeV
- Heavy quark pairs, $10^7 \div 10^8$ $(10^6 \div 10^7, 10^2 \div 10^3)$ events per working year for $c\bar{c}$ $(b\bar{b}$, $t\bar{t})$ pair production
- Hadronic structure of the photon
- Single W production, $10^4 \div 10^5$events per working year

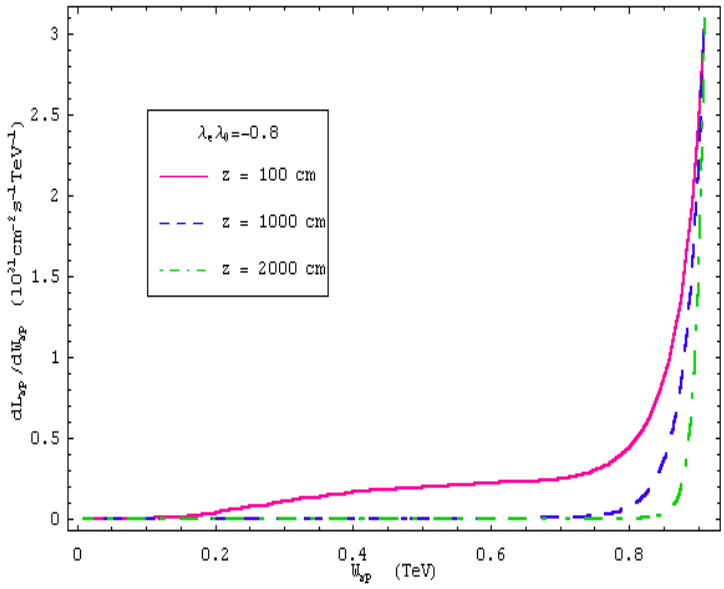

Figure 3: *Luminosity distribution as a function of γp invariant mass at $z = 10$ m for choice of three different electron polarization*

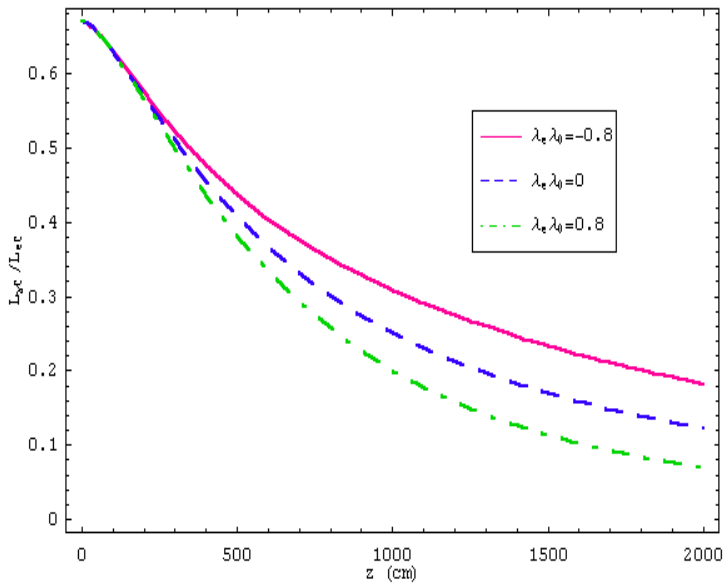

Figure 4: *The dependence of luminosity on the distance z for γC collider*

- Excited quarks ($u^*$and d^*) with $m \leq 1$ TeV
- Single production of t-quark and fourth family quarks due to anomalous γ-c-Q or γ-u-Q (Q=t, u_4) and γ-s-d_4 or γ-d-d_4 interactions.

The polarization of converted photons will provide important advantages. In addition, γp collider with longitudinally polarized proton beam will be the powerful tool for investigation of spin content of the proton.

Preliminary list of physics goals of the THERA based γA collider contains [2, 11]:

- Total cross-section to clarify real mechanism of very high energy γ-nucleus interactions
- Investigation of a hadronic structure of the photon in nuclear medium
- According to the VMD, proposed machine will be also ρ-nucleus collider
- Formation of quark-gluon plasma at very high temperatures but relatively low nuclear density
- Gluon distribution at extremely small x_g in nuclear medium ($\gamma A \to QQ + X$)
- Investigation of both heavy quark and nuclear medium properties ($\gamma A \to J/\Psi(Y)+ X, J/\Psi(Y) \to l^+l^-$)
- Existence of multi-quark clusters in nuclear medium and a few-nucleon correlation.

In our opinion γA collider is the most promising option of the TESLA$\otimes$HERA complex, because it will give unique opportunity to investigate small $x_g$region in nuclear medium [12]. Indeed, due to the advantage of the real γ spectrum, heavy quarks will be produced via γg fusion at characteristic

$$x_g \approx \frac{5 \times m^2_{c(b)}}{0.8 \times (Z/A) \times s_{ep}},$$

which is approximately $(2 \div 3) \cdot 10^{-5}$ for charmed and $(2 \div 3) \cdot 10^{-4}$ for beauty hadrons. The number of $c\overline{c}$ and $b\overline{b}$ pairs which will be produced in γC collisions, can be estimated as $10^6 \div 10^7$ and $10^5 \div 10^6$ per working year, respectively. Therefore, one will be able to investigate small x_g region in details. For this reason very forward detector in γ-beam direction will be useful for investigation of small x_g region due to registration of charmed and beauty hadrons.

The advantages of the gamma options from physics point of view in the cases of pair production of heavy quarks at γp collider and study of hadronic structure of real photons were shown in the corresponding section of the TESLA TDR.

Finally, in principle, high energy γ beam can be re-used to measure polarized gluon distributions using polarized nucleus targets [13]. The integrated luminosity of γN collisions will be of order of 1 fb^{-1}per working year and polarization asymmetry can be measured with statistical precision $\approx 1\%(0.3\%)$ using D*-tagging (single muon tagging). Of course, detailed analysis of design problems (γ-beam transportation, target and detector issues etc.) is needed.

Table 8.1.1: *Upgraded Parameters of Proton and Carbon Beams*

	p	C
Beam Energy, TeV	1	6
No. of particles/bunch, 10^{10}	10	0.8
No. of bunches per ring	94	94
ε_p^N, $10^{-6}\pi\cdot$rad$\cdot$m	1	1.4
β_p^*, cm	10	20
σ_z, cm	10	15

References

[1] A.K. Çiftçi et al., Nucl. Instrum. Meth. **A 365**, 317 (1995).

[2] R. Brinkmann et al., *Linac-ring type colliders: Fourth way to TeV scale.* Preprint DESY-97-239 (physics/9712023), 1997.

[3] S. Sultansoy, *The post-HERA era: Brief review of future lepton hadron and photon hadron colliders.* Preprint DESY-99-159 (hep-ph/9911417), 1999.

[4] V.I. Telnov, Nucl. Instrum. Meth. **A 294**, 72 (1990).

[5] S.F. Sultanov, *Prospects of the future ep and γp colliders: Luminosity and physics.* Report IC/89/409, ICTP, Trieste, 1989.

[6] I.F. Ginzburg et al., Nucl. Instrum. Meth. **205**, 47 (1983).

[7] I.F. Ginzburg et al., Nucl. Instrum. Meth. **A 219**, 5 (1984).

[8] R. Brinkmann and M. Dohlus. Preprint DESY-M-95-11, 1995.

[9] R. Brinkmann, Turkish J. Phys. **22**, 661 (1998).

[10] M. Gentner et al., Nucl. Instrum. Meth. **A 424**, 277 (1999).

[11] S. Sultansoy, Turkish J. Phys. **22**, 575 (1998).

[12] L. Frankfurt and M. Strikman. Preprint DESY 99-087, 1999.

[13] S.I. Alekhin, Eur. Phys. J. **C 11**, 301 (1999).